Vol. 46 No. 2 (2025)

ARCHIVES OF THERMODYNAMICS

ISSN: 1231-0956
ISSN: 2083-6023 (Online)

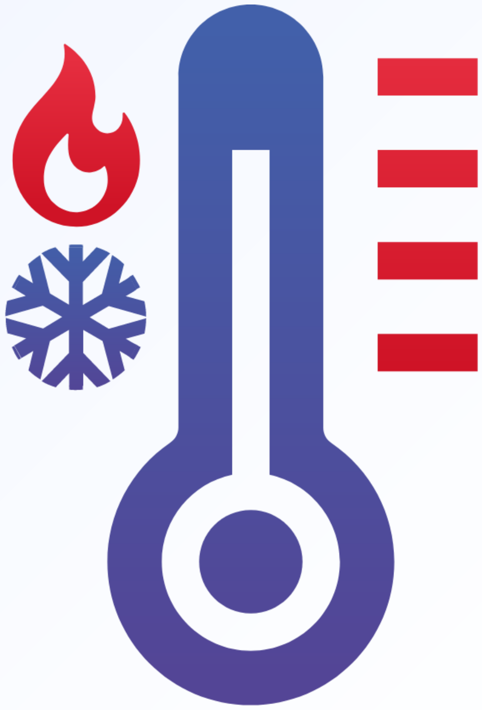

Co-published by

Institute of Fluid Flow Machinery
Polish Academy of Sciences

Committee on Thermodynamics and Combustion
Polish Academy of Sciences

WYDAWNICTWO IMP PAN

archives of thermodynamics **appears since 1980**

Aims and Scope

The aim of the quarterly journal Archives of Thermodynamics (AoT) is to disseminate knowledge between scientists and engineers worldwide and to provide a forum for original research conducted in the field of thermodynamics, heat transfer, fluid flow, combustion and energy conversion in various aspects of thermal sciences, mechanical and power engineering. Besides original research papers, review articles are also welcome.

The journal scope of interest encompasses in particular, but is not limited to:

- Classical and extended non-equilibrium thermodynamics
- Thermodynamic analysis including exergy
- Thermodynamics of heating and cooling
- Thermodynamics of nuclear power generation
- Thermodynamics in defence engineering
- Advances in thermodynamics
- Experimental, theoretical and numerical heat transfer
- Thermal and energy system analysis
- Renewable energy sources including solar energy
- Secondary fuels and fuel conversion
- Heat and momentum transfer in multiphase flows
- Nanofluids
- Energy transition
- Advanced energy carriers
- Energy storage and efficiency
- Energy in buildings
- Hydrogen energy
- Combustion and emissions
- Turbomachinery
- Thermal and energy system analysis
- Integrated energy systems
- Distributed energy generation
- Thermal incineration of wastes
- Waste heat recovery.

Supervisory Editors

- K. Badyda, Warsaw University of Technology, Poland
- M. Lackowski, Institute of Fluid Flow Machinery, Gdańsk, Poland

Honorary Editor

- J. Mikielewicz, Institute of Fluid Flow Machinery, Gdańsk, Poland

Editor-in-Chief

- P. Ocłoń, Cracow University of Technology, Cracow, Poland

Section Editors

- A.C. Benim, Duesseldorf University of Applied Sciences, Germany
- P. Lampart, Institute of Fluid Flow Machinery, Gdańsk, Poland
- S. Polesek-Karczewska, Institute of Fluid Flow Machinery, Gdańsk, Poland
- I. Szczygieł, Silesian University of Technology, Gliwice, Poland
- A. Szlęk, Silesian University of Technology, Gliwice, Poland

Technical Editors

- J. Frączak, Institute of Fluid Flow Machinery, Gdańsk, Poland
- S. Łopata, Institute of Fluid Flow Machinery, Gdańsk, Poland

Members of Programme Committee

- D. Kardaś, Inst. Fluid Flow Mach., Gdańsk, Poland (chairman)
- J. Badur, Inst. Fluid Flow Mach., Gdańsk, Poland
- T. Chmielniak, Silesian Univ. Tech., Gliwice, Poland
- P. Furmański, Warsaw Univ. Tech., Poland
- R. Kobyłecki, Częstochowa Univ. Tech., Poland
- S. Pietrowicz, Wrocław Univ. Sci. Tech., Poland
- J. Wajs, Gdańsk Univ. Tech., Poland

International Advisory Board

- J. Bataille, Ecole Centr. Lyon, France
- A. Bejan, Duke Univ., Durham, USA
- W. Błasiak, Royal Inst. Tech., Stockholm, Sweden
- G.P. Celata, ENEA, Rome, Italy
- L.M. Cheng, Zhejiang Univ., Hangzhou, China
- M. Colaco, Federal Univ. Rio de Janeiro, Brazil
- J.M. Delhaye, CEA, Grenoble, France
- M. Giot, Univ. Catholique Louvain, Belgium
- K. Hooman, Univ. Queensland, Australia
- D. Jackson, Univ. Manchester, UK
- D.F. Li, Kunming Univ. Sci. Tech., China
- K. Kuwagi, Okayama Univ. Science, Japan
- J.P. Meyer, Univ. Pretoria, South Africa
- S. Michaelides, Texas Christian Univ., USA
- M. Moran, Ohio State Univ., USA
- W. Muschik, Tech. Univ., Berlin, Germany
- I. Müller, Tech. Univ., Berlin, Germany
- H. Nakayama, JAEA, Japan
- S. Nizetic, Univ. Split, Croatia
- H. Orlande, Federal Univ. Rio de Janeiro, Brazil
- M. Podowski, Rensselaer Polyt. Inst., USA
- R.V. Rao, Sardar Vallabhbhai Nat. Inst. Techn., India
- A. Rusanov, Inst. Mech. Eng. Probl., Kharkiv, Ukraine
- A. Vallati, Sapienza Univ. Rome, Italy
- M.R. von Spakovsky, Virginia Polyt. Inst., USA
- H.R. Yang, Tsinghua Univ., Beijing, China

Vol. 46 No. 2 (2025)

ARCHIVES
OF THERMODYNAMICS

ISSN: 1231-0956
ISSN: 2083-6023 (Online)

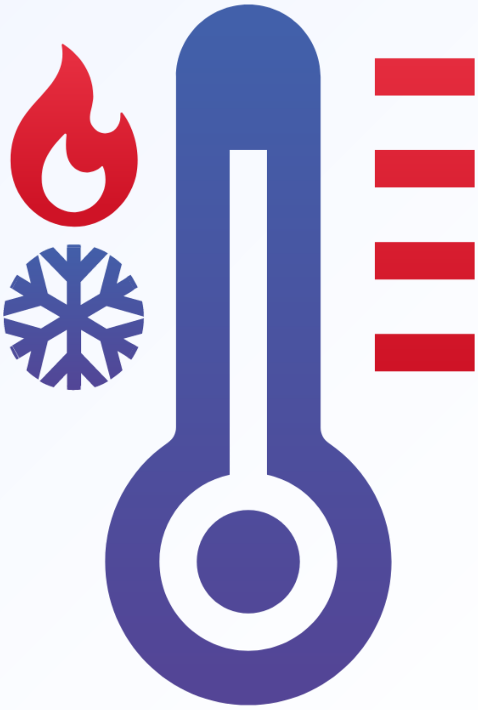

Co-published by

Institute of Fluid Flow Machinery
Polish Academy of Sciences

Committee on Thermodynamics and Combustion
Polish Academy of Sciences

WYDAWNICTWO
IMP PAN

Editorial Office
IMP PAN Publishers
Institute of Fluid Flow Machinery, Fiszera 14, 80-231 Gdańsk, Poland,
Phone: (+48) 58-341-12-71 int. 230, e-mail: redakcja(at)imp.gda(.)pl
https://www.imp.gda.pl/archives-of-thermodynamics/
Journals PAS – Electronic Library Polish Academy of Sciences
https://journals.pan.pl/ather

Subscription outside Poland

From 2024, Archives of Thermodynamics appear only in electronic version as an open access journal. However, printed archive volumes or issues are still available. The price of a full volume outside Poland is **120 EUR**. The price of a single issue is **30 EUR**. Archived volumes or issues are available on request. Orders should be sent directly to IMP PAN Publishers:
Institute of Fluid-Flow Machinery,
Fiszera 14, 80-231 Gdansk, Poland,
e-mail: redakcja(at)imp.gda.pl or jfrk(at)imp.gda(.)pl or jrybka(at)imp.gda(.)pl.
Payments should be transferred to the bank account of IMP PAN:
IBAN 28 1130 1121 0006 5498 9520 0011 at Bank Gospodarstwa Krajowego; Code SWIFT: GOSKPLPW.

Prenumerata w Polsce

Od 2024, czasopismo ukazuje się tylko w formie elektronicznej otwartej. Osiągalne są jednak wydania papierowe archiwalne. Cena pojedynczego numeru wynosi **50 PLN**. Cena rocznika **200 PLN**. Zamówienia z określeniem numeru (rocznika), nazwiskiem i adresem odbiorcy należy kierować bezpośrednio do Wydawcy:
Instytut Maszyn Przepływowych PAN
ul. Fiszera 14, 80-231 Gdańsk,
e-mail: redakcja(at)imp.gda(.)pl lub jfrk(at)imp.gda(.)pl lub jrybka(at)imp.gda(.)pl.
Wpłaty prosimy kierować na konto Instytutu Maszyn Przepływowych PAN:
nr 28 1130 1121 0006 5498 9520 0011 w Banku Gospodarstwa Krajowego.

Articles in Archives of Thermodynamics are abstracted and indexed within:

Arianta • Baidu Scholar • BazTech • Cabell's Directory • Chemical Abstracts Service (CAS) – CAplus • CNKI Scholar (China National Knowledge Infrastucture) • CNPIEC • EBSCO • Elsevier – SCOPUS • Genamics JournalSeek • Google Scholar • Inspec • Index Copernicus • J-Gate • Journal Citation Reports (ESCI) • Journal TOCs • Naviga (Softweco) • POL-index • Polymer Library • Primo Central (ExLibris) • ProQuest • ReadCube • SCImago (SJR) • TDNet • TEMA Technik und Management • Ulrich's Periodicals Directory/Ulrichsweb • Web of Science (Core Collection) • WorldCat (OCLC)

ISSN 1231-0956
ISSN 2083-6023 (Online)

Publication funding of this journal is provided by resources of the Polish Academy of Sciences and the Institute of Fluid Flow Machinery

Archives of Thermodynamics, Vol. 46, No. 2, 2025

Contents

Co-published by
Institute of Fluid-Flow Machinery
Polish Academy of Sciences
Committee on Thermodynamics and Combustion
Polish Academy of Sciences

http://www.imp.gda.pl/archives-of-thermodynamics/

ARCHIVES
OF THERMODYNAMICS

Analysis of the feasibility of using Invar process pipes in multichannel cryogenic helium transfer lines based on the second law of thermodynamics

Pawel Duda*, Maciej Chorowski, Ziemowit Malecha, Jarosław Poliński

Wroclaw University of Science and Technology, Wybrzeże Stanisława Wyspiańskiego 27, 50-370 Wrocław, Poland
*Corresponding author email: pawel.duda@pwr.edu.pl

Received: 29.12.2024; revised: 20.02.2025; accepted: 21.02.2025

Abstract

This work describes examples of the use of cryogenic lines and their designs, referring in detail to typical structural nodes found in cryogenic transfer lines. As a special case, multichannel cryogenic transfer lines are described, in which the process pipes are made of Invar. This has a significant impact on the number of internal supports and the method of thermal shrinkage compensation, which directly impact into reduced heat input during the transfer of cryogenic media. The second law of thermodynamics and the Gouy-Stodola theorem are discussed from the perspective of their application in optimizing and evaluating heat and mass transfer devices. The next part of the work presents the internal structure of the selected 250 m multichannel cryogenic transfer line. Several variants of the method of supporting process pipes have been presented and compared with the solution using Invar. For each solution, an entropy analysis was carried out in order to select the best design in terms of the entropy generated in the process pipes. From the examples presented, it is proven that entropy minimization method can be used for complex optimization of entire cryogenic distribution systems, as well as their individual components.

Keywords: Cryogenic; Cryogenic lines; Entropy minimization; Invar

Vol. 46(2025), No. 2, 5–13; doi: 10.24425/ather.2025.154196

Cite this manuscript as: Duda, P., Chorowski, M., Malecha, Z., & Poliński, J. (2025). Analysis of the feasibility of using Invar process pipes in multichannel cryogenic helium transfer lines based on the second law of thermodynamics. *Archives of Thermodynamics*, 46(2), 5–13.

1. Introduction

Big Science research infrastructure, like particle accelerators, free electron lasers, tokamaks and other machines, makes an extensive use of helium cryogenics, allowing a stable operation of superconducting magnets and superconducting radio frequency cavities in temperatures as low as 1.8 K (superfluid helium). Cold helium, in most cases in a supercritical thermodynamic state, is transferred from the helium refrigerator to the cryomodules comprising the magnets and the cavities with the use of cryogenic distribution systems (CDS). Cryogenic distribution systems typically consist of multichannel cryogenic cold helium transfer lines and so-called valve boxes interconnecting the transfer line with the cryostats. The role of cryogenic transfer lines is not only to supply cold helium to the valve boxes, but also to recover and transfer to the cryoplant cold helium vapours leaving the cryomodules. In most cases, the multichannel helium cryogenic transfer lines comprise four process lines: supercritical helium supply line, cold helium vapours return line, thermal shield cooling inlet line and thermal shield cooling outlet line. All the process lines are located in the vacuum vessel and are surrounded by an actively cooled thermal shield. This, along with a multilayer insulation (MLI) covering the process lines and thermal shield, constitutes highly effective thermal insulation of the process lines, which is essential for the proper operation of any cryogenic helium device [1]. Exemplary

Nomenclature

d – inside diameter, m
D – outside diameter, m
E – Young's Modulus, GPa
f – pipe deflection, m
g – gravitational acceleration, m^2/s
L – length of the pipe, m
$\dot{m}$ – mass flow rate, kg/s
P – power, W
p – pressure, Pa
$\dot{q}$ – heat flux, W
$\dot{S}$ – entropy flux, W/K
T – temperature, K
w – medium flow velocity, m/s
x – allowable distance between sliding supports, m

Greek symbols

Δ – difference
λ – flow coefficient (Darcy friction factor)
ζ – local pressure loss coefficient
ρ – density, kg/m^3
Σ – sum

Subscripts and Superscripts

A – ambient
C – cryogen
INV – Invar
He – helium
in – input value
out – output value

Abbreviations and Acronyms

AMTF – accelerator module test facility
DESY – Deutsches Elektronen Synchrotron
FCC – Future Circular Collider
XATL – cryogenic transfer line for supercritical helium transport from the Hadron-Electron Ring Accelerator refrigerator to accelerator module test facility hall
XFEL – X-Ray Free Electron Laser

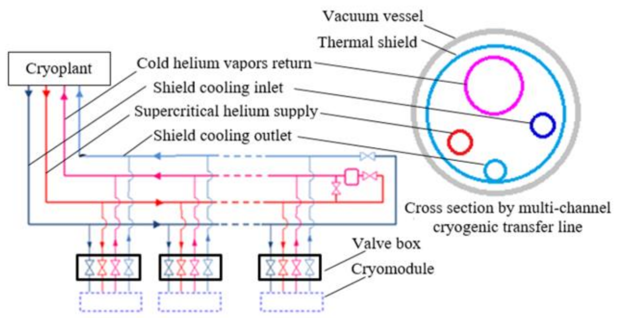

Fig. 1. Generic cryogenic distribution system with 4-channel helium transfer line.

cross-section of 4-channel helium transfer line is depicted in Fig. 1.

Due to the huge size of research facilities, such as the Large Hadron Collider (LHC), the planned Future Circular Collider (FCC) at CERN (*Conseil Européen pour la Recherche Nucléaire*) or the International Thermonuclear Experimental Reactor (ITER), it is necessary to transfer cryogenic fluids over considerable distances to cool superconducting elements [2–4].

The length of multichannel helium transfer lines may differ from tens meters to several kilometers. They may be located in outer space or in deep underground accelerator tunnels. The longest single multichannel helium transfer line is used for suppling the Large Hadron Collider magnets along one sector of the machine at the distance of 3.3 km [5].

The specific power of cryogenic refrigerators, defined as the power requirement at 300 K to produce one watt of cooling power at 4.5 K, is currently around 220 W [6]. This results from the fact that in an ideal, Carnot cycle the 1 watt of cooling power at 4.5 K temperature requires minimum 65 W of electric power, while today's state-of-art helium refrigerators are characterized by thermodynamic efficiencies in the range of 30–40% of Carnot cycle efficiency [7,8]. This means that even a slight reduction in heat input to the cryogenic medium during its transfer to the cryostats has a huge impact on reducing the power needed to drive the cryogenic refrigerator, thus, on reducing the energy consumption of the entire research device. The radiation and convection heat transfer to the process pipes can be reduced to almost negligible values by the use of insulation vacuum and multilayer insulation [9]. What is very difficult to be avoided are heat fluxes conducted by material of the mechanical internal supports of the process lines that constitute the thermal bridges between the room and process lines temperatures, and which in the cryogenic transfer line design cannot be avoided. On the other hand, the supports are the elements of the transfer lines characterized by the greatest repeatability in the entire structure. Therefore, thermal optimization of supports, or limiting their number, effectively affects the significant improvement of the thermal efficiency of the entire transfer line.

From a novelty perspective, the impact of using Invar process pipes on the mechanical, thermal, and hydraulic properties of the pipeline has been examined. By applying the entropy generation minimization method, the effect of using Invar process pipes and a new support system has been distilled into a clear and quantifiable parameter for engineers. This parameter represents the actual additional power required to compensate for the irreversibilities occurring in pipelines with the tested thermal and structural properties.

Entropy generation is a fundamental concept in thermodynamics and statistical mechanics, playing a pivotal role in understanding the behaviour of various physical systems. It provides critical insights into the irreversibility and inefficiency of processes and is intrinsically linked to the second law of thermodynamics. According to this law, the entropy of a system increases over time. Irreversibilities in physical processes lead to the generation of entropy. The concept of entropy generation has numerous applications across fields such as chemistry, biology, engineering, and environmental science. The optimization of process efficiency and the minimization of energy losses have prompted extensive investigation into entropy generation by engineers and scientists [10]. Khan et al. [11] applied the second law of thermodynamics to determine the total entropy rate, considering three distinct forms of irreversibility: heat transfer, fluid friction, and the Darcy-Forchheimer relation. Mohanty et al. [12] examined the effects of entropy production on the peristaltic transport of micropolar nanofluids. Nadeem [13] conducted research on entropy analysis in the stagnation-point flow of a hybrid nanofluid. The variation in fluid properties was investigated in terms of the velocity field, entropy generation, and induced magnetic field, with respect to the mixed convection parameter.

By employing optimization methods based on the second law of thermodynamics, it is possible to account for thermal processes, flow processes, and design parameters that describe the optimized system. The primary advantage of the described method lies in its ability to simultaneously consider multiple physical parameters that characterize various thermodynamic and mechanical states. However, a potential disadvantage is that the optimization results, which indicate the entropy generation rate, may be challenging for engineers to intuitively interpret. This contrasts with thermal or flow optimizations, where the outcomes are typically represented by measurable quantities such as heat flux or pressure drop. In such cases, the Gouy-Stodola theorem and the real efficiency of thermal-flow machines provide valuable insight. By using the entropy generation rate, these concepts enable the determination of the theoretical and real additional power required for the operation of the analysed system. The real additional power, necessary to overcome the irreversibilities present in the system, represents a clear and practical parameter for engineers.

2. Methodology based on second law of thermodynamics

The second law of thermodynamics implies that during each irreversible process, the sum of entropy of the system and its surroundings increases. For an integrated entropy generation, additional power necessary to overcome the irreversibilities accompanying the flow of cryogen in the transfer pipes, can be calculated from the Gouy-Stodola theorem described by the following equation [14,15]:

$$P_{Ad} = T_A \dot{S}, \tag{1}$$

where: P_{Ad} − additional power necessary to overcome the irreversibilities, T_A − ambient temperature, $\dot{S}$ − entropy flux.

Equation (1) suggests that thermal objects should demonstrate possibly low entropy flux increases, especially in the processes of heat exchange and medium transfer. In cryogenic transfer lines, entropy increase is caused by two processes: pressure drop of the medium in the process pipe and heat exchange due to temperature difference between the cryogen and the surroundings [16]:

$$\dot{S} = \sum_i \dot{S}_{\Delta T} + \sum_j \dot{S}_{\Delta p}, \tag{2}$$

where $\sum_i \dot{S}_{\Delta T}$ is the sum of entropy fluxes generated due to temperature differences and $\sum_j \dot{S}_{\Delta p}$ is the sum of entropy fluxes generated due to pressure drops in the pipeline. The processes of entropy generation in the process pipe of a cryogenic transfer line are shown in Fig. 2.

Entropy increase due to heat transfer can be calculated using the following formula:

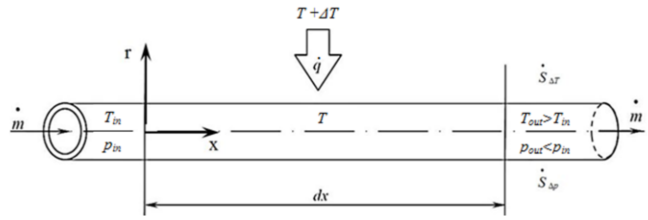

Fig. 2. Processes of entropy increase in a pipeline segment having length *dx*; $\dot{m}$ – mass flow rate of the transferred medium, $\dot{q}$ – heat flux, T – temperature of the medium, $T+\Delta T$ – ambient temperature, p – pressure, indexes *in* – input value, *out* – output value [14].

$$\dot{S}_{\Delta T} = \frac{\dot{q}}{T} - \frac{\dot{q}}{T+\Delta T}. \tag{3}$$

The second entropy source is pressure drop caused by local and linear flow resistivities described as

$$\dot{S}_{\Delta p} = \frac{\dot{m}}{\rho T}\Delta p = \frac{\dot{m}w^2}{2T}\left(\lambda\frac{L}{d} + \sum_n \zeta_n\right), \tag{4}$$

where: ρ – density of medium, Δp − pressure drops in the pipeline, w − medium flow velocity, λ − flow coefficient (Darcy friction factor), L − length of the pipe, d − diameter of the pipe, $\Sigma_n \zeta_n$ – the sum of local pressure loss coefficient.

The entropy production is increasing with the decrease of the process pipe temperature, which makes this entropy source especially important in cryogenic conditions. Equation (3) takes a special form for cryogenic liquid transfer:

$$\dot{S}_{\Delta T} = \frac{\dot{q}\Delta T}{T_C^2\left(1+\frac{\Delta T}{T_C}\right)}, \tag{5}$$

where $\Delta T = T_A - T_C$, and T_C is the cryogen temperature.

This paper employs entropy analysis to compare three cryogenic lines of identical length, diameter of process pipes, and flow rates of the cryogen. Consequently, the entropy fluxes generated due to flow resistance are equivalent across all cases. The differences in entropy fluxes generated by heat leaks by process pipe support systems can be attributed to the materials used and the configuration of the pipe supports.

3. Process pipes support systems in multichannel cryogenic transfer line

In every multichannel cryogenic transfer line, several fundamental types of supports for process pipes are present. A generic schematic of a 250-meter section of the transfer line, along with all types of process pipe supports, is presented in Fig. 3. The pipeline is divided into 12-meter modules, which facilitate trans-

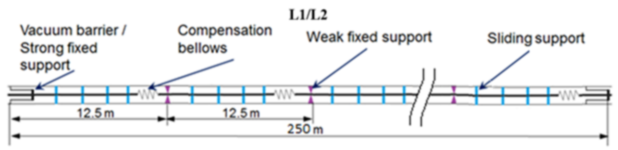

Fig. 3. The support systems for the process pipes of the typical multi-channel cryogenic transfer line.

portation. Each module is equipped with expansion bellows that mitigate the increase in stresses generated by the thermal contraction of the process pipes. The reduction of stresses resulting from thermal contraction, achieved through the use of expansion joints, is currently the most common method of compensation employed in cryogenic transfer lines. This approach necessitates the use of all the types of process pipe supports described below.

The most frequently recurring support in a cryogenic line is the sliding support. The purpose of the sliding support is to determine the vertical position of the process pipes while allowing them to move axially relative to each other and to the thermal shield [17]. In addition to sliding supports, there are two types of fixed supports. The 'strong' fixed support is designed to transfer relatively large forces generated by the compensation bellows, which are subjected to the pressure of the flowing cryogenic medium and is usually installed at the ends of a given section consisting of multiple straight section modules. The 'weak' fixed support is installed in each transfer line module that contains compensation bellows, and its task is to determine the radial and axial position of the process pipes, ensuring the correct operation of the bellows.

The use of compensation bellows implies the application of an appropriate support scheme to ensure bellows mechanical stability. This system requires the fix support on one side of the bellows and 4 sliding supports on the other side, all at a distance no larger than that specified by the bellows manufacturer. Therefore, regardless of the transfer line module length (distance between the individual fixed supports), transfer lines containing compensation bellows must include sliding supports for the process pipes.

The situation will be different for transfer lines, where the process lines are made of Invar. Due to one order of magnitude lower thermal expansion of Invar than stainless steel [18], in this case, the process lines do not require bellows to compensate for thermal shrinkage. This allows for the elimination of expansion bellows and weak fixed supports throughout the analysed structure, as presented in Fig. 4. In addition, the sliding supports between the strong supports are needed only for preventing the process line against the self-weight slanging. What is more, the lack of the bellows further reduces system energy loses related with fluid flow pressure drop.

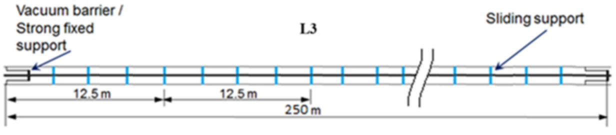

Fig. 4. The support systems for the process pipes for the case L3.

4. Case study

Three 250 m long straight segments of multichannel transfer lines L1, L2 and L3 were compared in order to examine how changing the support systems for process pipes influences the entropy fluxes generated in the process pipes and the additional power required to overcome the irreversibilities, which accompany the cryogen flow. Table 1 presents the geometric and thermodynamic parameters of the process pipes taken into account during the subsequent considerations in this paper.

Table 1. Operating parameters of transfer lines L1–L3.

Process line	Dimension	Operating parameters		
		p, MPa	T, K	$\dot{m}$, kg/s
Supercritical helium supply '5 K'	Ø60.3 × 2	0.35	5.0	0.015
Cold helium vapours return '4.5 K'	Ø88.9 × 2.3	0.12	4.5	0.015
Thermal shield cooling inlet '45 K'	Ø48.3 × 2	1.70	45.0	0.010
Thermal shield cooling outlet '60 K'	Ø48.3 × 2	1.67	60.0	0.010

As shown in Table 1, in one multichannel line, a cryogenic medium with different thermodynamic parameters is transported through the process pipes – the supply pipe carries high-pressure supercritical helium, and the return pipe carries a gaseous or two-phase medium with low pressure. Additionally, a gaseous helium with a higher temperature range is sent through the pipe used to cool the thermal shields [19].

The support systems for the process pipes of the tested multichannel transfer lines sections for cases L1 and L2 are schematically shown in Fig. 3. The arrangement of sliding supports in the case of L2 is the same as in the case of L1. The only difference is the functional separation of one sliding support used in the case of L1 into three independent supports. The third case under consideration uses the same sliding supports as described for case L2, however the process pipes are made of Invar.

4.1. Cryogenic line using a standard type of sliding supports – L1

The first analysed case L1 is a standard solution based on the cross section of cryogenic transfer line (XATL1) used to supply helium to devices located in the accelerator module test facility (AMTF) hall for the European X-ray free electron laser (XFEL) accelerator operating at the Deutsches Elektronen Synchrotron (DESY) research centre in Hamburg (see Fig. 5). The geometric parameters of the described line were used as a starting point for optimization based on the method of minimizing the entropy generated.

Figure 5 shows a sliding support of the XATL1 that mechanically connects three process pipes: 5 K supply, 4.5 K return and 45 K inlet. This support rests on a thermal shield with a temperature of 60 K.

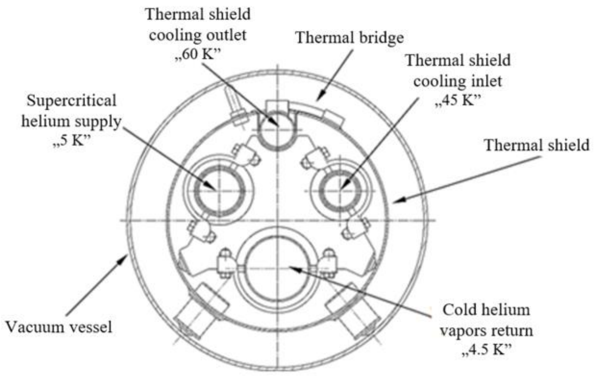

Fig. 5. Cross-section through the typical multichannel transfer line [20].

The presented solution allows for easy assembly of the transfer line and using only one design type of sliding support to support all process pipes. The disadvantage of this solution is the thermal connection of process lines with different temperatures, which results in an undesirable heat flow between the lines.

As already mentioned, in addition to sliding supports, there are two types of fixed supports in cryogenic lines. The geometry of the weak and strong fixed support used in the described analysis is shown in Figs. 6 and 7, respectively.

As it turns out, the method of supporting the process lines and, in particular, which process lines will be supported by a common support, have a very significant impact on the thermal efficiency of the cryogenic transfer line [21].

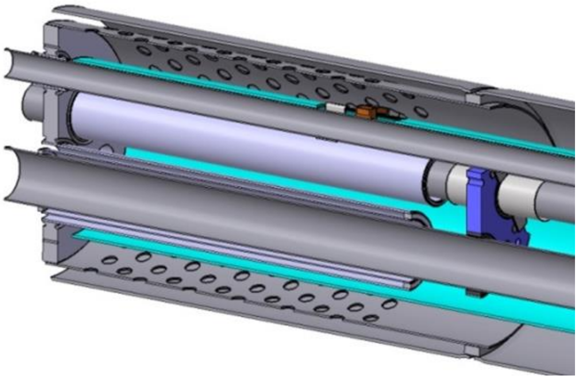

Fig. 6. Strong fixed support in transfer line.

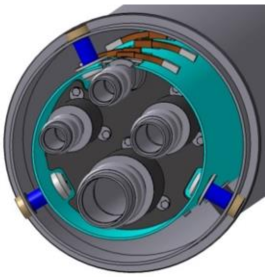

Fig. 7. Weak fixed support in transfer line.

4.2. Cryogenic line using a new type of sliding supports – L2

In order to avoid any unwanted thermal contacts in the sliding supports of the L2 line, additional types of supports were designed, as shown in Fig. 8, L2/L3 case. In this solution, the 45 K inlet line has separate, low heat-conduction support that is attached to the thermal shield. This eliminates heat flow from 45 K line to the 5 K supply line, as it is in the L1 case.

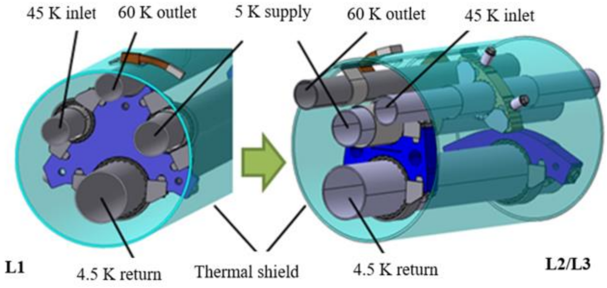

Fig. 8. Modification of the support system for the process pipes in the L2 and L3 line with reference to L1.

Another solution that thermally improves the sliding support system for the process lines is to use the support for the 5 K supply and 4.5 K vapour return lines only. In this case, the 4.5 K line acts as the mechanical support for the 5 K line and is sliding supported at a different location on the thermal shield. In such solution, there is almost no heat conduction between the 5 K and 4.5 K lines through the common sliding support, because the temperature difference is negligible and the support material has low thermal conductivity. Reduction of heat fluxes to the supply pipes allows reductions in the amounts of helium flowing, entails compensations of lower heat fluxes and thus offers a possibility to use smaller-diameter process pipes, to which less heat flows by radiation.

5. Results and discussion

5.1. Calculations of entropy 888fluxes generated in transfer line L1

In order to identify heat fluxes to the particular process pipes and to determine the resultant entropy fluxes, each support was subjected to thermal analysis. Each element of the model was assigned material properties, represented as a function of temperature. In order to determine the temperature field, boundary conditions were introduced by setting a temperature value inside each of the process pipes, as shown in Fig. 9.

In order to allow thermal comparison between the supports in the L1−L3 transfer lines, the influence of thermal radiation was not included. The temperatures inside each of the process pipes were set in accordance with the values provided in Table 1. With the temperature field and heat flux densities in the whole model known, heat exchange paths between individual process pipes could be identified. The temperature field in the investigated model is shown in Fig. 10.

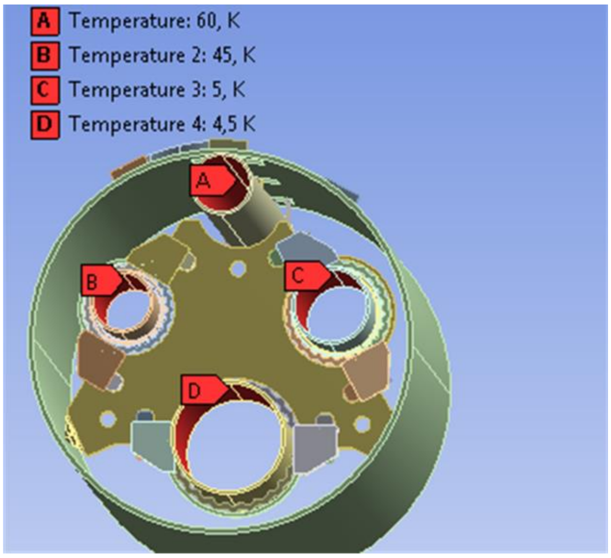

Fig. 9. Boundary conditions set for the process pipe sliding support in the L1 line.

In a similar way, the heat fluxes transferred to the process lines through strong and weak fixed supports were determined. Based on the general Eq. (5), its specific form was derived, which, utilizing the values of heat fluxes for individual process lines allows calculation the entropy fluxes generated in the transfer line by a given type of support:

$$\Sigma\dot{S} = n\sum_i \dot{S} = n\Sigma_i \frac{\dot{q}_i(T_A - T_i)}{T_i^2\left(1+\frac{T_A-T_i}{T_i}\right)}, \qquad (6)$$

where $\sum_i \dot{S}$ is the sum of entropy fluxes generated in process pipe due to heat flux, $\dot{q}_i$– heat flux to i-th the process pipe, and T_i is the temperature of i process pipe.

Table 2 includes the values of both heat fluxes and entropy fluxes.

The sliding support used in this model thermally connects pipes having a temperature of approximately 5 K with pipes for thermal shield cooling, which have temperatures of 45 K and 60 K. Such a connection results in heat flux in the location of the support, from the 45 K and 60 K pipes to the approx. 5 K pipes, causing negative entropy fluxes in the pipes for thermal shield cooling.

Using Eq. (4) and considering the flow and geometric parameters of the process pipes provided in Table1, the pressure losses and the corresponding fluxes of entropy generated for each process pipe were determined. As shown in Table 3, the entropy fluxes due to pressure losses relative to the entropy fluxes generated due to heat fluxes are negligibly low, so they will not be considered further.

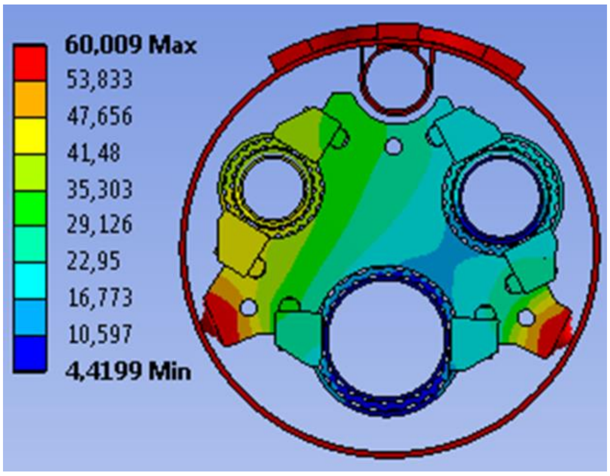

Fig. 10. Temperature field for the process pipe sliding support in the L1 line.

Table 3. Pressure losses and the corresponding fluxes of entropy calculated for the L1 case.

5 K Supply		4.5 K Return		45 K Supply		60 K Return		$\Sigma\dot{S}_{\Delta p}$ per 250m W/K
Δp Pa	$\dot{S}_{\Delta p}$ W/K	Δp Pa	$\dot{S}_{\Delta p}$ W/K	Δp Pa	$\dot{S}_{\Delta p}$ W/K	Δp Pa	$\dot{S}_{\Delta p}$ W/K	
14.3	0.000	11.0	0.002	167	0.002	230	0.003	0.007

5.2. Calculations of entropy fluxes generated in transfer line L2

In order to avoid any unwanted thermal contacts in the sliding supports of the L2 line, additional types of supports were introduced as shown in Figs. 8, 11 and 12.

Heat fluxes and the corresponding entropy fluxes for supports in the L2 transfer line were identified analogically to the procedure used in the sliding supports of the L1 transfer line. Figure 11 shows boundary conditions set for the thermal analysis of the supports. Figure 12 shows set temperature fields calculated for each type of the process pipe supports.

The results served to calculate values of heat fluxes through all supports to individual process pipes and the corresponding

Table 2. Heat fluxes to the process lines and the generated entropy fluxes calculated for the L1 case.

Type of support	5 K Supply		4.5 K Return		45 K Supply		60 K Return		Pieces per 12.5 m module	Pieces per 250 m segment	$\Sigma\dot{S}\Delta T$, W/K
	$\dot{q}$, W	$\dot{S}_{\Delta T}$, W/K	$\dot{q}$, W	$\dot{S}_{\Delta T}$, W/K	$\dot{q}$, W	$\dot{S}_{\Delta T}$, W/K	$\dot{q}$, W	$\dot{S}_{\Delta T}$, W/K			
Sliding	0.24	0.04	0.53	0.11	-0.19	0.00	-0.58	-0.01	4	80	11.5
Weak fix	0.04	0.01	0.06	0.01	0.01	0.00	22.90	0.31	1	20	6.5
Strong fix	0.17	0.03	0.31	0.06	0.10	0.00	7.02	0.09	1*	2	0.4

*Strong fix support is only in the first and last module.

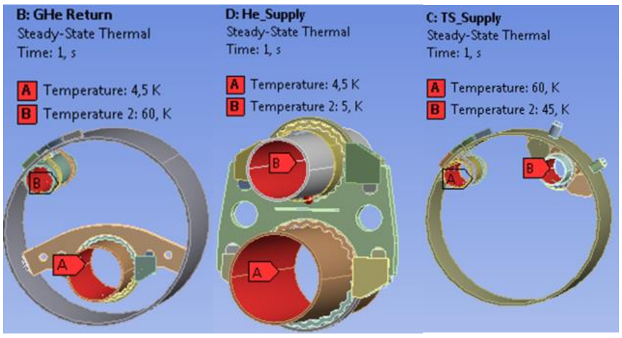

Fig. 11. Boundary conditions set for the process pipe sliding supports in the L2 line.

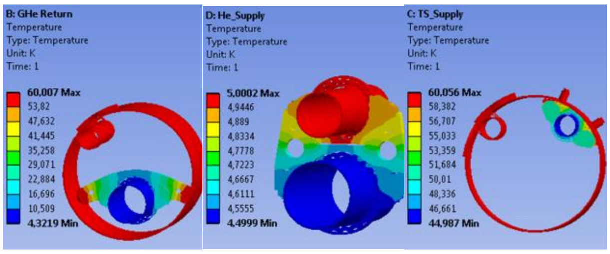

Fig. 12. Temperature fields calculated for the process pipe sliding supports in the L2 line.

entropy fluxes. Table 4 presents the results for all supports in line L2.

The sliding support system used in the L2 line significantly reduces heat fluxes to the supercritical helium supply line (5 K), as the pipe is thermally connected to the support pipe having a similar temperature. The heat leaks to the vapours return pipe (4.5 K) is likewise reduced, as the 45 K pipe is thermally connected directly to the thermal shield. Connecting the 45 K pipe directly to the thermal shield causes increased heat fluxes to this pipe. However, these heat leaks generate a smaller entropy flux than in the solution used for the L1 transfer line.

5.3. Calculations of entropy fluxes generated in transfer line L3

In the case of L3, where the process pipes are made of Invar, there is no necessity for the use of expansion joints. Consequently, there is also no justification for the application of light fixed supports to determine the axial and radial positioning of the process pipes at each of the expansion joints.

The sliding supports used in case L3 are identical to those in case L2. The number and position of sliding supports in case L2 is largely determined by the presence of compensation bellows. In case L3, where compensation bellows do not occur, the number and position of sliding supports is determined by the permissible value of the deflection arrow of the process pipes. For the purposes of this analysis, the permissible deflection arrow of the process pipes was assumed at 25×10^{-4} m. For the deflection arrow defined in this way, the distance between sliding supports should not exceed 3 m. The allowable distance between the individual sliding supports has been calculated on the basis of the following formula:

$$x = min\left|\sqrt[4]{\frac{87fE\left(D_i^4-d_i^4\right)}{20g\left(\rho_{INV}\left(D_i^2-d_i^2\right)+\rho_{He}d_i^2\right)}}\right|_i^1, \tag{7}$$

where f is the allowable value of process pipe deflection, E is the Young's modulus, D_i is the outside diameter of the i-th process pipe, d_i is the inside diameter of the i-th process pipe, ρ_{INV} is the Invar density, ρ_{He} is the density of helium transferred through the i-th process pipe, g is the acceleration of gravity.

The need to maintain a maximum distance of 3 m between sliding supports means that the number of sliding supports in the pipeline using process pipes made of Invar is the same as in the case of the L2 line. The difference between the support system for the L2 and L3 transfer lines is the absence of compensation bellows in the L3 line, which significantly reduces the entropy fluxes generated during the cryogen flow. Additionally, the most reliable transfer line is without bellows, which can be produced by using the Invar material [22]. Using a design without compensation bellows allows not only to limit heat leaks, but also to reduce the failure rate of the pipeline, as the bellows are the most failure-prone element of a cryogenic line [23]. Moreover, each compensation bellows requires an additional weld on the process pipe and the weld seam also becomes a potential failure spot. Although the probability of failure due to weld rapture is lower than the probability of compensation bellows rapture [24], reducing the number of welds has a significant role in reducing the failure rate of cryogenic transfer lines.

5.4. Summary of L1–L3 results

The application of second law of thermodynamic methods facilitates the optimization and characterization of cryogenic systems. Knowing the heat flows through the supports and the entropy fluxes generated as a result of them for each of the analysed cases of transfer lines from Eq. (1), one can determine the additional

Table 4. Heat fluxes to the process pipes and the generated entropy fluxes calculated for the sliding support system of the L2 transfer line (data provided for one support of each type).

Type of support	**5 K Supply**		**4.5 K Return**		**45 K Supply**		**60 K Return**		**Pieces per 12.5 m module**	**Pieces per 250 m segment**	**$\Sigma\dot{S}_{\Delta T}$, W/K**
	$\dot{q}$, W	**$\dot{S}_{\Delta T}$, W/K**	**$\dot{q}$, W**	**$\dot{S}_{\Delta T}$, W/K**	**$\dot{q}$, W**	**$\dot{S}_{\Delta T}$, W/K**	**$\dot{q}$, W**	**$\dot{S}_{\Delta T}$, W/K**			
Sliding	0.00	0.00	0.45	0.09	0.38	0.00	-0.83	-0.01	4	80	6.7
Weak fix	0.04	0.01	0.06	0.01	0.01	0.00	22.9	0.31	1	20	6.5
Strong fix	0.17	0.03	0.31	0.06	0.10	0.00	7.02	0.09	1*	2	0.4

*Strong fix support is only in the first and last module.

Table 5. The summary of the generated entropy fluxes and theoretical and real additional power for each analysed pipeline case.

	5 K Supply	4.5 K Return	45 K Inlet	60 K Outlet			
	$\dot{S}_{\Delta T}$, W/K	$\dot{S}_{\Delta T}$, W/K	$\dot{S}_{\Delta T}$, W/K	$\dot{S}_{\Delta T}$, W/K	$\Sigma\dot{S}_{\Delta T}$, W/K	P_{AdT}, W	P_{AdR}, kW
L1	3.74	9.09	-0.08	5.66	18.41	5431	18.10
L2	0.20	7.77	0.17	5.40	13.54	3994	13.31
L3	0.04	7.53	0.17	-0.69	7.04	2112	6.92

P_{AdT} and P_{AdR} are the theoretical and real additional power required to overcome irreversibilities associated with heat leaks during pipeline flow ($P_{AdR} = P_{AdT}/0.3$).

power necessary to overcome the irreversibilities accompanying the flow [25,26]. In order to determine the actual additional power required to overcome the described irreversibilities, it is necessary to take into account the thermodynamic efficiency of the cryogenic refrigerator, which, as indicated in Section 1, is 0.3 Carnot efficiency. Table 5 presents a summary of the generated entropy fluxes and theoretical and real additional power for each analysed pipeline case.

6. Conclusions

The results for the 250 m segments of the L1, L2 and L3 design type transfer lines demonstrate that the use of new sliding supports system shown in the L2 and L3 design significantly reduces the additional power which would need to be supplied to the condensing unit if only one type of sliding support was used for all process pipes. The obtained results indicate also that using cryogenic transfer lines with Invar process pipes rather than stainless steel pipes reduces the number of supports present in the transfer line and limits the entropy fluxes generated during the flow. It is proved that transfer line using Invar process pipes to be the best solution from a thermodynamic point of view and allows reduction the operating costs of the studied multichannel cryogenic transfer line by more than 2.5 times. This study shows that using cryogenic transfer lines comprising Invar process pipes offer the possibility to significantly improve thermodynamic parameters and at the same time to increase the mechanical stability of the pipeline, as no compensation bellows need to be used in the process pipes.

The use of the process pipes made of Invar in cryogenic transfer lines is currently very rare, because the cost of Invar pipes themselves is very high, which significantly increases the installation costs. However, in the case of long installations, as is the case for the Future Circular Collider accelerator, it is possible to purchase large series of Invar pipes, which significantly reduces the investment costs. Taking into account the results of this analysis, it can be stated that in the case of appropriately long installations, it is reasonable to use Invar process pipes, which reduce operating costs and increase the reliability of the pipeline.

Based on the performed analysis it can be concluded that an optimization approach based on the use of the second law of thermodynamics and Gouy-Stodola theory allows a comprehensive assessment of the thermodynamic efficiency of systems, in which there is a mass flow of fluids with different thermodynamic parameters. Entropy in this case plays the role of a common denominator, which can be easily converted into the additional power required to be supplied to the device to compensate the effects of irreversibility. The presented method can therefore be used for complex optimization taking into account thermal, flow and design parameters of entire distribution systems, as well as their individual components such as transfer lines, valve boxes or execution modules.

Acknowledgements

The work has been supported by the National Centre of Nuclear Research at Warsaw in the framework of Polish in-kind contribution to the construction of the European Free Electron Laser XFEL and by CERN at Geneva in the framework of conceptual design of Future Circular Collider cryogenic system.

References

[1] Deng, B.C., Yang, S.Q., Xie, X.J., Wang, Y.L., Pan, W., Li, Q., & Gong, L.H. (2019). Thermal performance assessment of cryogenic transfer line with support and multilayer insulation for cryogenic fluid. *Applied Energy*, 250, 895−903. doi: 10.1016/j.apenergy.2019.05.025

[2] Rohan, D., Ghosh, P., & Chowdhury, K. (2011). Application of parallel heat exchangers in helium refrigerators for mitigating effects of pulsed load from fusion devices. *Fusion Engineering and Design*, 86(4-5), 296−306. doi: 10.1016/j.fusengdes.2011.01.133

[3] Iwamoto, A., Nobutoki, M., Kumaki, T., Higaki, H., Hamaguchi, S., Takahata, K., Imagawa, S., Mito, T., Takada, S., & Nadehara, K. (2017). In-situ calibration method of orifice flow meter equipped in 600 W helium refrigerator/liquefier with variable temperature supplies. *Fusion Engineering and Design*, 123, 107−110. doi: 10.1016/j.fusengdes.2017.05.045

[4] Benedikt, M., & Zimmermann, F. (2016). Status of the Future Circular Collider Study. *25th Russian Particle Accelerator Conference*, 21-25 Nov., Saint Petersburg, Russia, TUYMH01. doi: 10.18429/JACoW-RuPAC2016-TUYMH01

[5] Collier, P. (2015). The technical challenges of the Large Hadron Collider. *Philosophical Transactions A: Mathematical, Physical and Engineering Sciences*, 373, 20140044. doi: 10.1098/rsta.2014.0044

[6] Gistau-Baguer, G. (2020). *Cryogenic Helium Refrigeration for Middle and Large Powers*. In International Cryogenics Monograph Series, Weisend II, J.G., Jeong, S. (eds.). Springer Nature Switzerland AG. doi: 10.1007/978-3-030-51677-2

[7] Quack, H.H. (1994). *Maximum efficiency of helium refrigeration cycles using non-ideal components*. In *Advances in Cryogenic Engineering,* vol. 39, Kittel, P. (ed.). Springer, Boston, MA. doi: 10.1007/978-1-4615-2522-6_148

[8] Van Sciver, S.W. (2012). *Helium Cryogenics* (1st ed.). In

International Cryogenics Monograph Series, Timmerhause K.D., Rizzuto, C. (eds.). Springer. doi: 10.1007/978-1-4419-9979-5

[9] Chorowski, M., Choudhury, A., Datta, T.S., & Polinski, J. (2008). Synthesis of the multilayer cryogenic insulation modeling and measurments. *AIP Conference Proceedings*, 985(1), 1367–1374. doi: 10.1063/1.2908496

[10] Khan, M.N., Ahmad, S., Wang, Z., Hussien, M., Alhuthali, A.M.S., & Ghazwani, H.A. (2024). Flow and heat transfer insights into a chemically reactive micropolar Williamson ternary hybrid nanofluid with cross-diffusion theory. *Nanotechnology Reviews*, 13(1), 20240081. doi: 10.1515/ntrev-2024-0081

[11] Khan, M.N., Ahmad, S., Wang, Z, Ahammad, N.A., & Elkotb, M.A. (2023). Bioconvective surface-catalyzed Casson hybrid nanofluid flow analysis by using thermodynamics heat transfer law on a vertical cone. *Tribology International*, 188, 108859. doi: 10.1016/j.triboint.2023.108859

[12] Mohanty, B., Mohanty, S., Mishra, S.R., & Pattnaik, P.K. (2021). Analysis of entropy on the peristaltic transport of micropolar nanofluid: a simulation obtained using approximate analytical technique. *The European Physical Journal Plus*, 136, 1139. doi: 10.1140/epjp/s13360-021-02150-z

[13] Nadeem, S., Ishtiaq, B., Akkurt, N., & Ghazwani, H.A. (2023). Entropy optimized flow of hybrid nanofluid with partial slip boundary effects and induced magnetic field. *International Journal of Modern Physics B*, 37(29), 2350252. doi:10.1142/s0217979223502521

[14] Bejan, A. (1980). Second law analysis in heat transfer. *Energy*, 5(8-9), 712−732. doi: 10.1016/0360-5442(80)90091-2

[15] Mahmud, S., & Fraser, R.A. (2002). Second law analysis of the heat transfer and fluid flow inside a cylindrical annular space. *Exergy an International Journal*, 2(4), 322−329. doi: 10.1016/S1164-0235(02)00078-X

[16] Bejan, A. (1995). Entropy Generation Minimization. The Method of Thermodynamic Optimization of Finite-Size Systems and Finite-Time Processes. CRC Press. doi: 10.1201/9781482239171

[17] Pietsch, M., Rummel, T., Nagel, M., Bosch, H.S.F., & Carovani, F. (2023). Development, design and installation of multichannel transfer lines at W7-X under extreme geometrical constraints. *Fusion Engineering and Design*, 188, 113429. doi: 10.1016/j.fusengdes.2023.113429

[18] Duda, P., Chorowski, M., & Polinski, J. (2017). Impact of process parameters and design options on heat leaks of straight cryogenic distribution lines. *Physical Review Accelerators and* Beams, 20, 033202. doi: 10.1103/PhysRevAccelBeams.20.033202

[19] Duda, P., Chorowski, M., & Polinski, J. (2020). Entropy analysis of support systems in multi-channel cryogenic lines. *IOP Conference Series: Materials Science and Engineering*, 755, 012065. doi: 10.1088/1757-899X/755/1/012065

[20] Rusiński, E., Chorowski, M., Iluk, A., Fydrych, J., & Malcher, K. (2014). Selected aspects related to the calculations and design of a cryogenic transfer line. *Archives of Civil and Mechanical Engineering*, 14(2), 231−241. doi: 10.1016/j.acme.2013.11.003

[21] Chuang, P.-S., Chang, S.-H., Chiou, W.-S., Hsiao, F.-Z., Li, H.-C., Liao, W., Lin, T.-F., & Tsai, H. (2016). Development of multi-channel line for the NSRRC cryogenic system. *7th International Particle Accelerator Conference*, 8-13 May, Busan, Korea. doi: 10.18429/JACoW-IPAC2016-TUPMB050

[22] Thakkar, A., & Vyas, M.I. (2011). Design & analysis of bellows free cryogenic transfer line. *2nd International Conference on Current Trends in Technology 'NUiCONE-2011'*, 8-10 Dec., Ahmedabad, India.

[23] Cadwallader, L.C. (2010). *Vacuum bellows, vacuum piping, cryogenic break and copper joint failure rate estimates for ITER design use*. Idaho National Laboratory, INL/EXT-10-18973, USA. doi: 10.2172/983360

[24] Cadwallader, L.C. (1992). *Cryogenic system operating review for fusion application*. Idaho National Engineering Laboratory, Technical Raport, EGG-FSP-10048, ON: DE92012509, USA. doi: 10.2172/5550141

[25] Kirkconnell, C.S., & Curran, D.G.T. (2002). Thermodynamic optimization of multi-stage cryogenic systems. *AIP Conference Proceedings*, 613(1), 1123−1132. DOI: 10.1063/1.1472137

[26] Hånde, R., & Wilhelmsen, Ø. (2019). Minimum entropy generation in a heat exchanger in the cryogenic part of the hydrogen liquefaction process: On the validity of equipartition and disappearance of the highway. *International Journal of Hydrogen Energy*, 44(29), 15045−15055. doi: 10.1016/j.ijhydene.2019.03.229

Co-published by
Institute of Fluid-Flow Machinery
Polish Academy of Sciences
Committee on Thermodynamics and Combustion
Polish Academy of Sciences

http://www.imp.gda.pl/archives-of-thermodynamics/

ARCHIVES OF THERMODYNAMICS

Impact of water cooling on photovoltaic modules performance in Polish climate conditions – a case study

Weronika Janowicz, Michał Pomorski, Piotr Kolasiński*

Department of Thermodynamics and Renewable Sources of Energy, Wrocław University of Science and Technology,
Wybrzeże Stanisława Wyspiańskiego 27, Wrocław 50-370, Poland
*Corresponding author email: piotr.kolasinski@pwr.edu.pl

Received: 14.08.2024; revised: 06.03.2025; accepted: 10.03.2025

Abstract

Atmospheric conditions, such as for example ambient temperature, may have the influence on temperature of a photovoltaic (PV) module. The greatest impact is exerted by solar radiation intensity, leading to an increase in the temperature of photovoltaic cells. As the temperature of the module increases, the efficiency and thus the generated power decreases. The cooling systems capable of lowering the temperature of the module, thus improving its efficiency may be promising solution to this problem. This paper presents the results of a study on the effect of water cooling of a photovoltaic module. The experiments were conducted in Poland using the test stand composed of two photovoltaic modules. One module was equipped with a water cooling system at its front surface while the second module was treated as the reference. Thanks to such a test setup design it was possible to study the influence of atmospheric conditions on the change of photovoltaic module temperature, power output and amount of energy generated by the cooled and reference module. Two cooling methods concerning the timing of cooling water flow activation/deactivation were investigated. The first method involved a fixed cooling time and intervals, while the second method adjusted the cooling water flow activation and deactivation time based on the surface temperature of the module. As a result of the conducted research, a maximum decrease of 17.6 K of photovoltaic module temperature and a maximum power increase of ca. 5%, using the cooling system, was achieved. Furthermore, a correlation between cooling efficiency and cloud cover was described, as well as a method for determining cooling water flow. It was found that better cooling results are obtained when employing a cooling activation and deactivation method based on temperature dependence.

Keywords: Photovoltaic module; PV cell temperature; PV cooling system; PV module efficiency

Vol. 46(2025), No. 2, 15–28; doi: 10.24425/ather.2025.154903

Cite this manuscript as: Janowicz, W., Pomorski, M., & Kolasiński, P. (2025). Impact of water cooling on photovoltaic modules performance in Polish climate conditions – a case study. *Archives of Thermodynamics*, 46(2), 15–28.

1. Introduction

Climate change, partly caused by the use of conventional fossil fuel-based energy systems for electricity generation, can be mitigated by incorporating a greater share of renewable energy sources into the electricity generation system [1]. One of the most important sources of renewable energy that can potentially be used to change the energy mix and thus decarbonise the energy systems is solar radiation. Photovoltaic installations are one of the possible technologies that can be applied for solar radiation harvesting [2,3]. In recent years, there has been a significant increase in the installed power of photovoltaic installations observed worldwide (an average annual increase was equal to ca. 25%), reaching the power of 1.05 TW in 2022 [4]. In Poland, an even more rapid growth of installed photovoltaic (PV) power is observed, which reached the power of 16.9 GW at the end of 2023 [5]. Such a rapid growth of PV installations power in Poland is largely caused by the increasing number of prosumer PV

Nomenclature

A – surface area, m^2
E – energy, Wh
G – solar irradiance, W/m^2
P – power, W
q – flow rate, l/min
T – temperature, K
U – voltage, V

Greek symbols

γ – temperature coefficient at the maximum power point, %/K
δ – relative difference
Δ – change in value
η – efficiency, %

Subscripts and Superscripts

a – ambient
c – photovoltaic cell
el – electrical energy
v – volumetric

Abbreviations and Acronyms

A – cooled module
B – comparison module
PV – photovoltaic
STC– standard test conditions

microinstallations, whose share in installed power at the end of 2022 was equal to 72% [6]. Figure 1 shows the change in installed photovoltaic power on a global, European and Polish scale. An increase in installed PV power directly translates into an increase in the amount of electricity generated from such installations. Figure 2 shows the change in the amount of electricity generated by PV installations in Poland and its share in the total electricity amount generated from all sources.

The maximum efficiency of commercially available photovoltaic modules is nowadays equal to ca. 20−22% [6]. In real operating conditions, the PV module efficiency varies and depends on different variables, such as e.g. atmospheric conditions, which may affect the operating temperature of the PV cells and the amount of harvested solar radiation. The most important parameters related to atmospheric conditions include solar irradiance, ambient temperature, wind speed, precipitation and air pollution (i.e. content of dust and other pollutants) [6−8]. The intensity of solar radiation is an important factor on which the power generated by a PV module directly depends. What is more, at the same time, the intensity of solar radiation is causing the PV cell heating, which results in a decrease of its efficiency. An increase in ambient temperature also heats the cells (i.e. to the ambient temperature level). At the same time, due to ambient temperature increase, the cooling intensity of the modules decreases, which results in a negative effect of increasing temperature of PV cells. Wind also influences the operation of photovoltaic modules. On the one hand, it positively influences and helps in better heat removal from the module surface, thus lowering the cell temperature. On the other hand, wind influence can be negative, because it can carry pollutants such as dust or leaves, which may partially cover PV modules and consequently reduce their efficiency. Wind-borne volatile pollutants such as dust, sand, pollen and others may stick to the surface of the module, causing it to be shaded and thus reducing the generated power. In this aspect, the wind can also have a positive effect by removing contaminants from the module surface. Rainfall can also have a positive effect on the operation of photovoltaic modules. Water may remove contaminants from the module surface, allowing more solar energy to reach the cells. At the same time, water acts as a coolant, which reduces the cell temperature and thus increases efficiency.

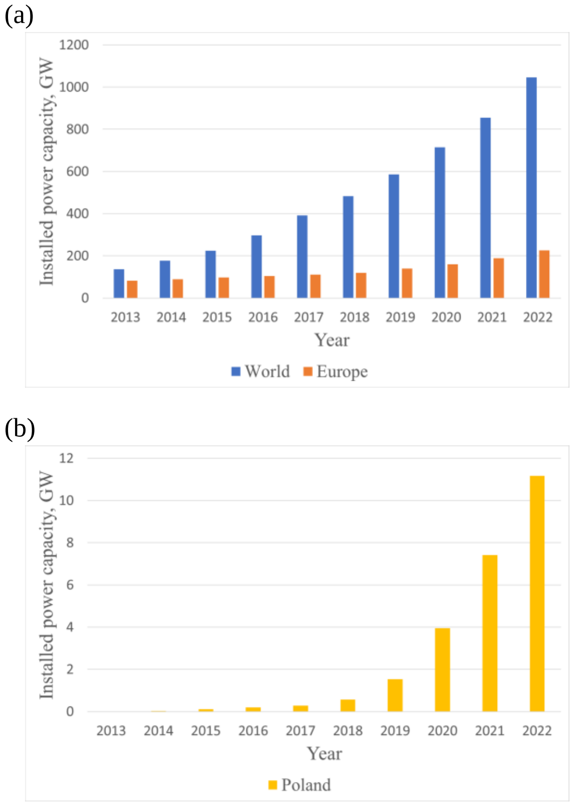

Fig. 1. Installed power of photovoltaic systems: (a) data for World and Europe; (b) data for Poland. Own elaboration based on [4].

A number of models that can be used for determining PV cell temperature as a function of various atmospheric conditions can

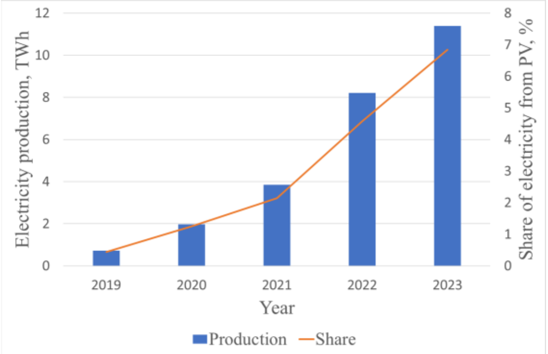

Fig. 2. Electricity production from PV and its share in Poland energy production. Own elaboration based on [5].

be found in the literature [6,9−11]. On the basis of these models, it is possible to determine the influence of individual atmospheric conditions on the cell temperature. These models are different depending on the module and installation type. Solar irradiance has a linear effect on the change in cell temperature. An increase of solar irradiance by 100 W/m^2 at a constant ambient temperature results in an increase of cell temperature by 3.1 K according to the Mondol et al. model [6] and by 1.75 K if the cell temperature is determined using the Tselepis model [6]. The change in the cell temperature as a function of the change in solar irradiance depends on the type of module and usually ranges between 1.8 K and 4.93 K [9]. Also, a change in ambient temperature causes a linear change in cell temperature. Ambient temperature increase by 1 K results in an increase of cell temperature by ca. 1 K, however, it depends on the type of PV module [9]. Using the Mondol et al. model, this increase can be determined as 1 K, while using Tselepis model a value of 1.1 K is obtained [6]. Wind has a positive effect on the cell temperature, causing an intensification of PV module cooling. Models that take wind speed into account can deviate from a linear character and cause large discrepancies in the obtained modelling results, due to the very strong influence of the module's position and thus the intensity of cooling. Based on selected models (i.e. Markvart [9], Kurtz et al. [9], Chenni [9], Skoplaki and Palyvos [6]), an average decrease of cell temperature of 0.6 K to 2 K per 1 m/s of wind speed can be determined at constant solar irradiance and ambient temperature. The most rapid decrease in cell temperature is observed at low wind speeds, which can be clearly seen from the Skolpaki and Palyvos model [6].

In Polish climatic conditions, the temperature of PV cells can reach 70°C [12], and depends on the temperature coefficient of maximum power and the way of the PV system installation (i.e. roof-top or ground-mounted installation). Figure 3 shows the change of ambient (T_a) and cell temperature (T_c), which were determined from the Kurtz et al. model using the annual variation of ambient temperature for Wrocław. Figure 4 shows the variation of module efficiency (η) resulting from the change in the cell temperature. Presented data were obtained for a PV module featuring a temperature coefficient of power at maximum power point of $\gamma = -0.340$ %/K, i.e. the module used in this study. This means that the achievable power and thus the efficiency of this module decrease by 3.4% for each increase of cell temperature by 10 K. The efficiency of the module was determined using the following formula:

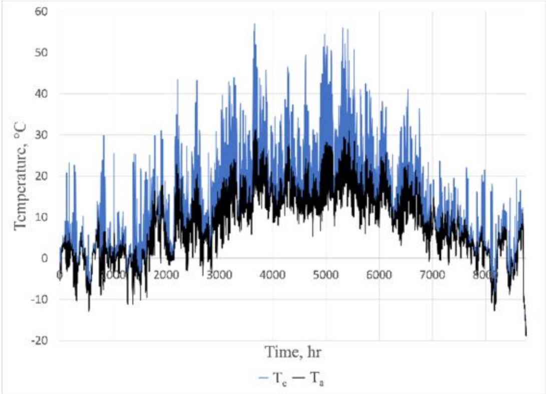

Fig. 3. Annual variation of ambient temperature in Wroclaw and photovoltaic cell temperature determined from Kurtz et al. model. Own elaboration based on [13,14].

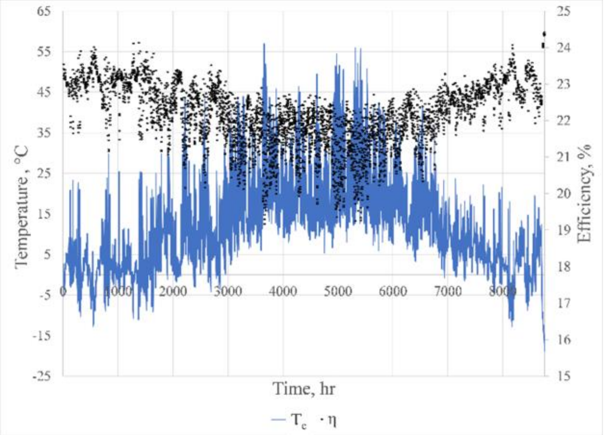

Fig. 4. Annual variation of PV cell temperature and module efficiency determined for $\gamma = -0.340$ %/K. Own elaboration based on [13,14].

$$\eta = \eta_{STC}\left[1 + \frac{\gamma}{100}(T_c - T_a)\right], \tag{1}$$

where η_{STC} is the efficiency under STC conditions (i.e. standard test conditions defined as: cell temperature of 25°C, solar irradiance of 1000 W/m^2 and air mass factor of AM1.5), T_c is the photovoltaic cell temperature and T_a is the ambient temperature, and γ is the temperature coefficient of power at maximum power point.

From the above analysis, it can be seen that by lowering the operating temperature of photovoltaic cells, it is possible to increase the energy conversion efficiency of the module and thus increase the module power and electricity production. It should also be noted that application of module cooling may contribute to reducing the amplitude and frequency of cell temperature fluctuations, reduce the cell thermal load, limit their degradation and extend their operating time [15].

2. Review of methods applied for photovoltaic modules cooling

There are many methods that can be applied for photovoltaic modules cooling, i.e. active, which require a power supply for their operation, and passive, which do not need additional energy input [15−21].

Water is one of the substances which can be used to cool PV modules. As a cooling medium for PV modules, it has many advantages over air. These include a higher value of the thermal conductivity coefficient and specific heat, thanks to which the modules can be cooled in a shorter time. It also has the ability to clean the PV module against dust accumulation, which is particularly important in deserts, agricultural and polluted areas.

It can be applied for passive cooling by immersing the modules in water or placing the modules on the water surface. In active cooling methods, water can be directly applied as a coolant to cool the top or bottom surface of the module. The top surface can be cooled by forcing a film of liquid to flow down on the module surface or by spraying it on the module surface to mimic rainfall. The bottom surface can also be cooled by direct water sprinkling or by forcing the water flow through a heat exchanger (cooler) adjacent to its surface. A comprehensive description of water cooling methods can be found in the review [22].

Water (or other fluids) can also be used to cool photovoltaic modules in photovoltaic/thermal (PV/T) systems. In [23], the authors highlighted the positive features of PV/T systems and their great application potential. They presented an innovative thermal collector for a PV/T system and presented the obtained research results. It was estimated that, at a sufficiently matched water flow rate and inlet temperature, the tested system achieves an electrical efficiency of 17.79% and a thermal efficiency of 76.13%, which is significantly better than in the case of other solutions available in the literature. A study of module cooling in a PV/T system was also carried out in [24]. The study showed that, as a result of the cooling system used, energy production increased by 14.1% and electrical efficiency increased to 19.8% compared to 17.4% for the module without the applied cooling system. Experimental results related to the cooling of a monocrystalline and polycrystalline PV module were presented in [25]. It was observed that there is a linear relationship between the module efficiency and its temperature. As a result of the applied cooling, the average temperature was 13.6% lower (for the monocrystalline module) and 7.2% lower (for the polycrystalline module) compared to the case without cooling. The decrease in average temperature of the modules resulted in increased modules' efficiency (by 13% and 6.2%, respectively). In [26], the numerical research aimed at determining the influence of atmospheric conditions (i.e. ambient temperature, solar irradiance and wind speed) on the cooling of the back surface of the PV module using water flowing in a channel was carried out. The obtained results proved that water cooling is an effective method, and that the best results are achieved at high ambient temperatures and high irradiance values. It was also observed that the influence of wind on the cooling process is less important than the influence of ambient temperature and irradiance. The maximum increase of module efficiency by 52% (compared to a PV module without cooling) was found during the study. The results of a numerical study on the PV module cooling were also published in [27]. It was observed that the modelled cooling system was able to reduce the module temperature by 6 K. In [28], the authors presented the results of a study on cooling the front and back surfaces of the PV module. The research was carried out in India. The front surface was drip-cooled by water flow, while the back surface was cooled by the application of wet grass. The research results showed that the average temperature drop of the PV module was 21.23%, which resulted in a 28.60% increase in module power. The researchers also found that cooling the front surface of the module gives a more noticeable effect.

High impact in lowering the PV modules temperature is achieved by cooling their front surface. Therefore, many researchers are dealing with this type of cooling. In [29], the authors presented a mathematical model describing the heat transfer mechanism in a module with cooling applied to its front surface and validated this model using a test stand located in India. The validation showed good agreement between modelled and experimentally obtained data, and the study showed that the application of the cooling system resulted in a reduction of module surface temperature (from 56.67°C to 39.44°C) and an increase of its efficiency (from 12.74% to 14.29%). In [30], the authors conducted a study on cooling the front surface of a PV module by sprinkling water on it with the help of nozzles and made an attempt to optimise the number, geometry and position of the nozzles. It was found that a cooling system consisting of 3 nozzles with a 90-degree opening angle, which are supplied with water at a pressure of 1.5 bar reduces the module temperature by 24 K and improves its efficiency from 11.18% to 13.27% if the cooling system is operated in 30 s spray and 180 s pause time sequences. A study of spray cooling of a photovoltaic module is also reported in [31]. The applied cooling technique was based on the simultaneous cooling of both the front and back surfaces of the PV module. The tests were conducted in a Mediterranean climate location. The experimental results showed that by cooling both the front and back surfaces simultaneously, it was possible to reduce the module temperature from 54°C to 24°C, which resulted in a 16.3% increase of maximum module power and a 14.1% increase of module efficiency. In [32], a mathematical model was developed to determine the optimal cooling cycle of the modules' front surface through water flow. The model was validated by performing an experiment carried out in Egypt. Based on the model of the heating and cooling rate of the module, it was found that the panels achieve the highest energy output if the panel temperature reaches the maximum allowable temperature of 45°C. In [33], the results of a study and exergy analysis on cooling monocrystalline modules by cooling water flow were reported. The obtained results are valid for Laos climate and showed an increase in the exergy efficiency of the module from 2.91% (in the case of the module without an applied cooling system) to 12.76% (in the case of the module with an applied cooling system). The results of tests on cooling the front surface of a module equipped with reflectors, which focus solar radiation, are presented in [34]. The tests were carried out in Iraq and it was observed that the temperature of the cooled module decreased to 36.5°C compared to the temperature of 64.1°C observed for the module without the applied cooling system. An increase in power output by 24.4% and electrical efficiency from 14.2% to 17% due to the use of focusing reflectors and cooling was observed. In [35], the authors presented the results of the simulation of water cooling of PV modules using single nozzles. The influence of the nozzle position on the obtained results was analysed. It was assessed that the droplet size is a key parameter that plays a very important role in the contact effectiveness of the sprayed liquid stream. In [36], researchers from Poland presented their findings on cooling the front surface of the PV module by liquid film flow and by sprinkling water to mimic rain. A decrease of module temperature from 45°C to 25°C was achieved. Better results were achieved by cooling the module with a water film, and continuous cooling led to a 20% increase in power output.

The above literature review shows that the problem of photovoltaic module cooling is vital and has been addressed by many researchers. Unfortunately, most of the research is carried out in regions where climate conditions significantly differ from Central European regions where climate conditions significantly differ from Central European climate or carried out only in laboratory conditions using low-power photovoltaic modules. Specific differences in Polish climate conditions compared to other regions of the world where experimental investigations on PV module cooling have been conducted include lower ambient temperatures (resulting in a lower maximum temperature reached by the modules), fewer sunny hours per year (leading to a shorter requirement for module cooling), and consequently, fewer opportunities to increase the amount of energy produced. Despite the fact that Poland experiences continental climatic conditions, and consequently, there may be significantly fewer days characterised by high temperatures compared to, for example, Mediterranean countries, thus reducing the need for module cooling, it may still be necessary. However, it is worth noting that in Poland, during the summer months, ambient temperatures do not differ much from those in Mediterranean countries; only the duration of their occurrence is shorter. The application of module cooling is not only related to a possible increase in the amount of energy generated by modules, but also to increasing their longevity. The application of cooling reduces the amplitude and frequency of cell temperature fluctuations, decreases thermal loads, and consequently contributes to limiting cell degradation, thereby extending cell operational lifespan.

The authors decided to fill the research gap related to PV module cooling analysis in Poland. Therefore, the present study is aimed at investigating the effect of drip cooling of 410 W monocrystalline PV modules, which are operating in Polish climate conditions. The research is aimed at assessing the temperature reduction rate of PV modules in a temperate climate and investigating the feasibility of real benefits from the application of a drip cooling method.

3. Description of experimental set up and mathematical model

3.1. Description of experimental test stand

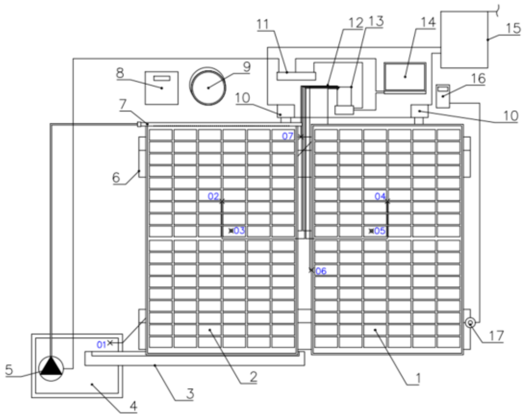

Fig. 5. Test stand scheme: 1 – comparison module (*B*) Longi LR5-54HPH-410M; 2 − cooled module (*A*) Longi LR5-54HPH-410; 3 – trough; 4 − water tank; 5 − diaphragm pump; 6 − concrete blocks; 7 – dispenser; 8 – scales; 9 – bucket; 10 − power optimizer SolarEdge S500; 11 − power supply; 12 − T-type thermocouples; 13 − measuring system National Instruments (basis USB - cDAQ-9174, measurement card NI 9212, compact cassette NI TB-9212); 14 − computer; 15 − inverter SolarEdge SE5K-RW0TEBNN4; 16− universal meter DT-30B; 17 − pyranometer Kipp & Zonen SP Lite.

The experimental test stand was commissioned in the Renewable Energy Laboratory, which is located on the flat roof of the campus building of Wrocław University of Science and Technology in Poland. The photovoltaic modules used for the analyses were inclined at an angle of 30° to the roof surface and facing south. A scheme of the test stand is presented in Fig. 5. The main components of the stand are two photovoltaic modules of the same type, whose catalogue data are presented in Table 1. These modules are made in half-cut technology and are assembled on concrete blocks (6). On one of the modules, the cooling system is installed. This module is further referred to as module *A* (2). The second module does not have a cooling system installed and is treated as a reference module to compare measurement results. This module is further referred to as module *B* (1). The test stand is equipped with water cooling system, which is composed of a pump (5) (used for pumping water from a tank (4) to a dispenser (7), which is assembled on the front surface of the module), a tank (4), a dispenser (7) (made of PVC pipe featuring a diameter of 1", in which a set of 68 holes, each featuring a diameter 2.5 mm and spaced by a pitch of 15 mm are drilled) and a trough (3), which directs the cooling water flowing out from the cooling system back to the tank. A bucket (9) and scale (8) are used to measure the cooling water mass flow. Each module is connected to an optimiser (10) and an inverter (15) for direct current (DC) to alternating current (AC) conversion. The experimental data from the measuring system is collected by a National Instruments data acquisition (DAQ) system equipped with an NI 9212 card (13), working with a laptop (14) equipped with LabVIEW software. Seven T-type (Cu-CuNi) thermocouples with a measurement accuracy of ±0.5 K (12) were used to measure temperature at different points of the system. Locations of thermocouples are marked with blue numbers (01−07) in

Table 1. Catalogue data of the photovoltaic modules used in the experiment.

Name	**Catalogue data**
Type of module	Silicon, mono-crystalline
Manufacturer	Longi Group
Model	LR5-54HPH-410M
Rated power	410 W
Performance in STC	21%
Temperature coefficient of the current short circuit	α = 0.050 %/K
Temperature coefficient of the voltage of an open circuit	β = -0.265 %/K
Temperature coefficient of maximum power	γ = -0.340 %/K
Surface area	1.953 m^2

Fig. 5. The first (01) was immersed in water in the tank, the second (02) was attached to the front surface of the cooled module, the third (03) was attached to the back surface of the cooled module, the fourth (04) was attached to the front surface of the comparison module, the fifth (05) was attached to the back surface of the comparison module, the sixth (06) was used to measure the ambient temperature in front of the surface of the modules, and the seventh (07) was used to measure the ambient temperature in the shade. The maximum measuring error of the NI 9212 temperature measuring system is equal to ±0.02 K. Measurement of the solar irradiance was possible by application of a Kipp & Zonen SP Lite pyranometer (17), which was transmitting a voltage signal to the DT-830B type universal multimeter (16). A solar irradiance value was then calculated from the measured voltage (U) using the following formula:

$$G = \frac{10^6 \cdot U}{71}. \tag{2}$$

The maximum measuring error of the solar irradiance measuring system is equal to ±2.4%. The pump, laptop and NI data acquisition (DAQ) system were connected to the power supply (11).

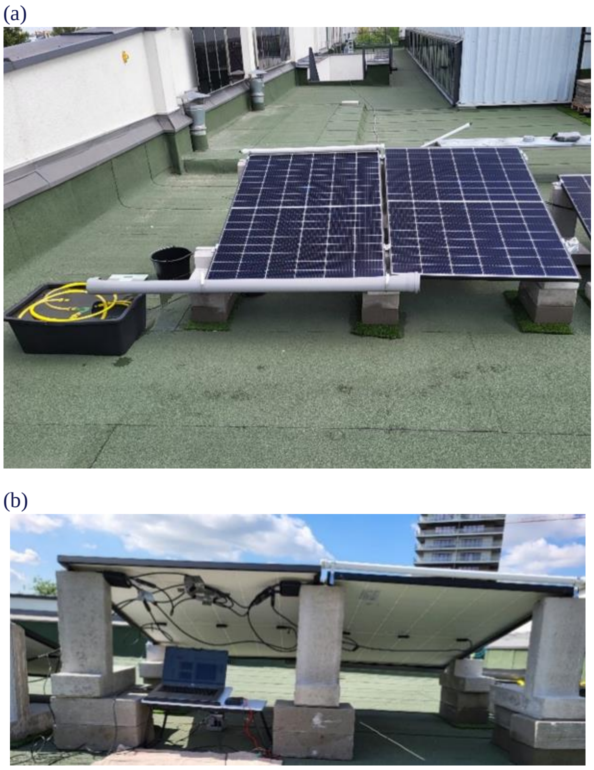

Fig. 6. Photograph of the test stand: (a) front view; (b) back view.

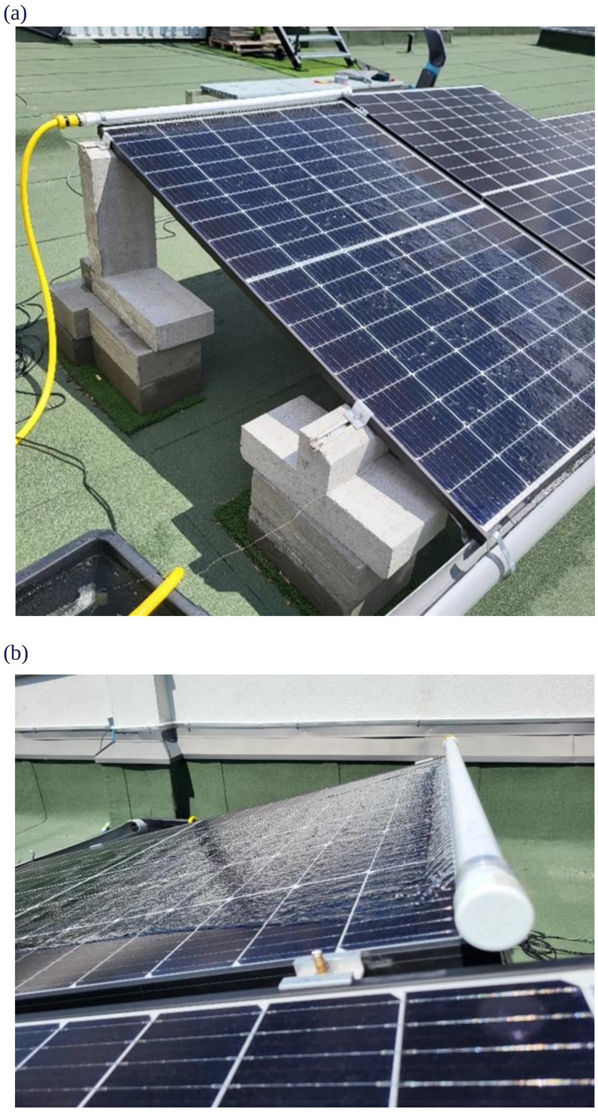

Fig. 7. Photograph of the test stand: (a) water-washed module; (b) water outflow from the dispenser.

Photographs of the test stand front and back are presented in Figs. 6a and 6b, respectively. Figure 7a shows the general view of a water-washed PV module, while Fig. 7b visualises the water outflow from the dispenser.

3.2. Experimental procedure

Experiments were carried out in the summer of 2023 and lasted three days. A description of the weather conditions, the times of the experiments and their duration are summarised in Table 2.

Table 2. Experimental conditions.

	Day 1 **29.06.2023**	**Day 2** **30.06.2023**	**Day 3** **08.07.2023**
Weather conditions	Maximum temperature in the shade: 30.3°C, sky partly covered by clumped clouds (further referred to as cloudy sky conditions)	Maximum temperature in the shade: 28.6°C, sky completely covered by stratus clouds (further referred to as completely overcast sky conditions)	Maximum temperature in the shade: 37.6°C, cloudless sky (further referred to as cloudless sky conditions)
Experiment start time	11:10 a.m.	10:20 a.m.	10:10 a.m.
Experiment end time	2:30 p.m.	12:25 p.m.	3:15 p.m.
Duration of experiment	3 hr 20 min	2 hr 5 min	5 hr 5 min

The temperature measurements were recorded automatically by a data acquisition system. Voltage readings were taken at five-minute intervals on a universal multimeter connected to the pyranometer. These results were then converted into a solar irradiance value using Eq. (2). The mean value of the cooling water flow rate was obtained after converting the mass flux values measured by the weighing method and was equal to 6.27 l/min, 14.33 l/min, 15.33 l/min for the following days, respectively.

On each experimental day, the cooling water flow occurred under different conditions. During experiments, which were performed in cloudy sky conditions (i.e. day 1), the condition for switching on the cooling water pump was that the temperature difference between the temperature of the back surface of the cooled PV module and the ambient temperature in the shade was equal to at least 10 K. Cooling water pump was switched off when the temperature difference reached 5 K. During experiments which were performed in completely overcast sky conditions (i.e. day 2), experiment on module cooling was started at 10.35 a.m. and ended at 12.05 p.m. That day, the cooling water flow was switched on and off periodically (i.e. 1 min water flow once every 30 min of experimental time). During experiments, which were performed in cloudless sky conditions (i.e. day 3), the experiment on module cooling was started at 10.20 a.m. and ended at 3.05 p.m. That day, the cooling water flow was also switched on and off periodically (i.e. 1.5 min water flow once every 15 min of experimental time). The detailed information on the cooling water flow during experiments is presented in Table 3.

Table 3. Cooling water flow during experiments.

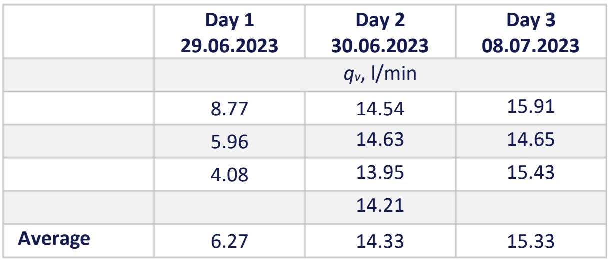

	Day 1 29.06.2023	Day 2 30.06.2023	Day 3 08.07.2023
		q_v, l/min	
	8.77	14.54	15.91
	5.96	14.63	14.65
	4.08	13.95	15.43
		14.21	
Average	6.27	14.33	15.33

By connecting a SolarEdge optimiser to each module, it was possible to access the software, which provides detailed data for PV modules. Therefore, it was possible to read data about the power generated by each module and the daily amount of electricity generated by each module. The accuracy of electrical power measurement using the SolarEdge system is ±5%.

3.3. Description of mathematical model

The power of the module, defined for a cell temperature specified in STC (i.e. 25°C), is calculated from the formula

$$P_{T\_STC} = \frac{\eta_{STC}}{100} A \times G, \tag{3}$$

where A is the surface area of the module and G is the solar irradiance.

The change in PV module power is related to the change in cell temperature (relative to the STC temperature) and was calculated using the formula

$$\Delta P = P_{T\_STC} \frac{\gamma}{100}, \tag{4}$$

The power generated by the module can be calculated using the formula

$$P = P_{T\_STC} + \Delta P(T_c - T_{STC}) \tag{5}$$

where T_{STC} is the cell temperature specified in STC.

If it is not possible to directly measure the temperature of photovoltaic cells, it is possible to calculate it using the temperature models. Temperature models that take into account meteorological variables and/or material variables, or system configuration, are used for this purpose. The models used in this paper are presented below. Equation (6) is the Mondol et al. temperature model [9]:

$$T_c = T_a + 0.031G. \tag{6}$$

Equation (7) is the Tselepis temperature model [9]:

$$T_c = 30 + 0.0175(G - 150) + 1.14(T_a - 25). \tag{7}$$

The relative difference in the sum of the daily electricity produced by the modules is calculated using the following formula:

$$\delta E_{el} = \frac{E_{el\_B} - E_{el\_A}}{E_{el\_B}}, \tag{8}$$

where E_{el_A} is the amount of electricity generated by module *A* and E_{el_B} is the amount of electricity generated by module *B*.

4. Results and discussion

The results of the temperature and solar irradiance measurements, which were made during three series of experiments, are presented in Figs. 8–10. The curves show the variation of the temperatures of the back surface of the cooled module (T_{A_back}), the back surface of the comparison module (T_{B_back}), the ambient in the shade (T_{a_shadow}) and the cooling water in the tank (T_{H2O}). The solar irradiance values (G) were highlighted on the graphs by yellow points. The purple bars show the time of cooling water flow on the module surface during the experiments (the cooling water flow rates are reported in Table 3).

4.1. Results of experiments performed in cloudy sky conditions

The first part of the experiments was performed in cloudy sky conditions, which caused varied solar irradiance conditions (see Fig. 8). Due to the partial cloud cover, the lowest irradiance was equal to 148 W/m^2, while the highest was equal to 1183 W/m^2. Significant variations in this value affect the shape of the curve corresponding to the temperature of the back surface of the comparison module (*B*), which is also characterised by a large difference between the values of the highest and lowest temperature (i.e. 28.3°C and 51.2°C). The proportional dependence of the module temperature on the solar irradiance is apparent. In the case of the cooled module (*A*), its lowest temperature was

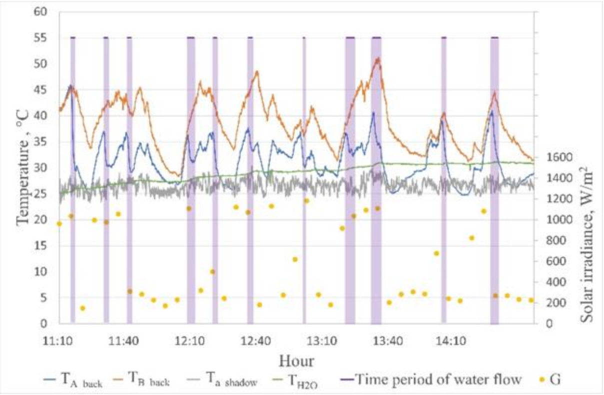

Fig. 8. Variation of PV panel, cooling water and ambient temperature, and solar irradiance, for experiments performed in cloudy sky conditions.

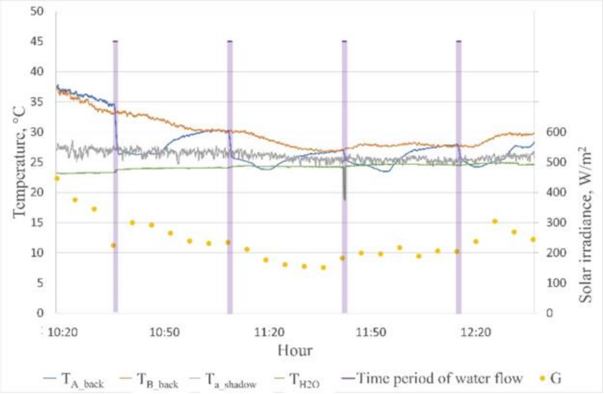

Fig. 9. Variation of PV panel, cooling water and ambient temperature, and solar irradiance, for experiments performed in completely overcast sky conditions.

equal to 24.7°C, while the highest temperature (observed after the first cooling) was equal to 41.0°C. The maximum temperature difference between the modules was equal to 17.6 K, which clearly shows the positive effect of water cooling. At the beginning of the experiment, the cooling water temperature was equal to 25.2°C, while at the end of the experiment it increased to 30.8°C. The maximum observed cooling water temperature was equal to 31.2°C. In addition to the increase of cooling water temperature, which was caused by the absorption of heat from the back of the PV module, the cooling water may also be warmed up due to absorption of heat from solar radiation falling on the black water tank. A steeper rise in the temperature is noticeable in the cooling water temperature curve during the time of water flow, just after the flow, and then during the absence of water flow. The average ambient temperature during the experiment was equal to 26.6°C.

4.2. Results of experiments performed in completely overcast sky conditions

The second part of the experiments was performed in completely overcast sky conditions. For this reason, less dynamic variations in the solar irradiance and thus of the temperature of the reference module were observed (see Fig. 9) compared to experiments, which were performed in cloudy sky conditions. The irradiance value changes between 151 W/m^2 and 445 W/m^2, while the temperature of the reference module (*B*) varies between 26.7°C and 37.3°C. The maximum temperature of the cooled module (*A*) after the first cooling cycle was equal to 30.5°C, while the minimum was equal to 23.5°C. Compared to the cooling method used during the experiments performed in cloudy sky conditions (when the water flow was regulated depending on the difference between the PV module temperature and the ambient temperature), during the experiments performed in completely overcast sky conditions, the cooling water flow was periodic and not temperature-dependent. The maximum observed difference between the temperatures of the modules was equal to 7.6 K. Due to the low solar activity during the experiments, which were performed in completely overcast sky conditions, the module did not reach as high a temperature as in the experiments performed in cloudy sky conditions. This is also caused by the lower amount of heat absorbed by the cooling water. The observed increase of water temperature in this case was equal to 1.5 K. The sharp drop in cooling water temperature during the time of the third flow is due to a measurement error. The average ambient temperature during the experiments, which were performed in completely overcast sky conditions, was equal to 26.1°C.

Considering the experiments, which were conducted in cloudy and completely overcast sky conditions, a significant difference is noticeable in the maximum temperature reached by the comparison module (*B*). The maximum value of the module temperature observed for the experiments performed in cloudy sky conditions was equal to 51.2°C, while for experiments performed in completely overcast sky conditions, this temperature was equal to 37.3°C, despite comparable average ambient temperatures during both experiments (i.e. 26.6°C and 26.1°C, respectively). Therefore, it can be concluded that not the ambient temperature, but the solar irradiance is mainly influencing the module temperature. During the experiments carried out in cloudy sky conditions, solar irradiance reached much higher maximum values (equal to 1183 W/m^2) compared to the maximum value of solar irradiance observed during the experiments performed in completely overcast sky conditions (equal to 446 W/m^2).

4.3. Results of experiments performed in cloudless sky conditions

The third part of the experiments was performed in cloudless sky conditions. Temperature variations of PV panel, cooling water and ambient, as well as solar irradiance for these experiments are presented in Fig. 10. At the beginning of the experiment, the solar irradiance value of 777 W/m^2 was observed and it reached a maximum value of 989 W/m^2 at 12:25 p.m. The lowest irradiance value was equal to 763 W/m^2 and was observed at the end of the experiment. It is worth to note that the maximum observed solar irradiance for experiments performed in cloudless sky conditions (08.07.2023) was 194 W/m^2 lower than the solar irradiance value observed during experiments performed in cloudy sky conditions (29.06.2023). The temperature of the reference module (*B*) varied between 38.3°C and 53.3°C. During experi-

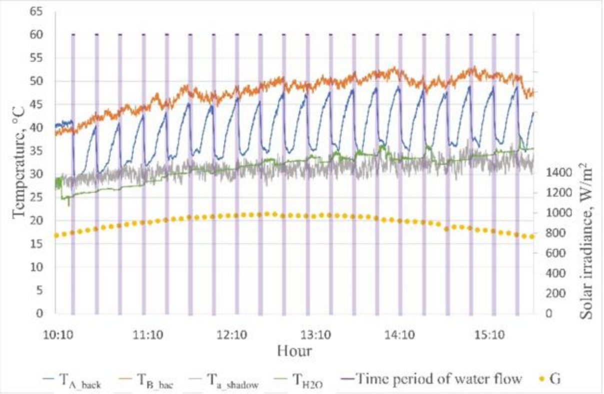

Fig. 10. Variation of PV panel, cooling water and ambient temperature, and solar irradiance, for experiments performed in cloudless sky conditions.

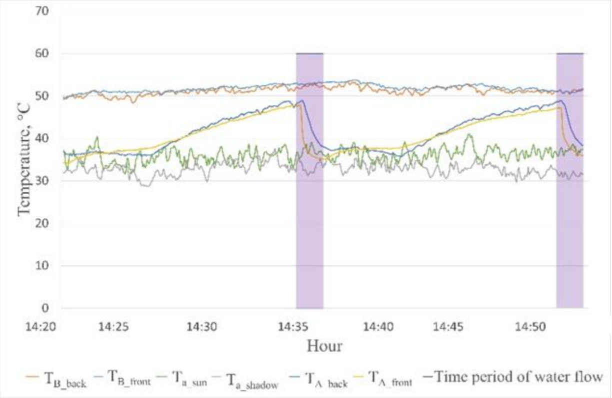

Fig. 11. Variation of PV panel and ambient temperature during experiments performed in cloudless sky conditions (data presented for 30 min of experiment time).

ments, which were performed in cloudless sky conditions, the maximum module temperature during the entire experimental research was observed. The cooling water flow during these experiments was periodic and not dependent on the observed temperatures. The lowest temperature of 28.7°C and the highest temperature of 49°C were observed for the cooled module. The maximum temperature difference between the modules was equal to 16.1°C. The temperature of the cooled module (*A*) fluctuated considerably and the maximum temperature reached by the cooled module was very high (due to the applied periodic cooling water flow). The temperature of the cooling water increased from 27.1°C to 35.4°C at the end of the experiment due to the heating of the cooling water during flow on the PV module surface, the direct heating of the water tank by solar radiation and the need of refilling the tank by adding a fresh, colder water. The average ambient temperature during experiments conducted in cloudless sky conditions was equal to 31.1°C.

When the experimental results obtained for different water flow condition are compared, it is worth to pay attention to the maximum temperature of the cooled module (*A*). During the experiments, which were performed in cloudy sky conditions, the cooling water flow was dependent on the temperature difference between the temperature of the cooled module (*A*) and the temperature of the ambient. For these experimental conditions, the difference between the maximum temperature of the cooled module (*A*) and the comparison module (*B*) was equal to 10.2 K. During the experiments, which were performed in completely overcast and cloudless sky conditions, the temperature differences were considerably smaller, and in certain cases the temperature of the cooled module (*A*) was comparable to the temperature of the reference module (*B*). The main aim of PV module cooling is to keep its temperature at a relatively low and constant value. Therefore, obtained experimental results prove that it may be preferable if the cooling water flow on the PV module surface will be temperature temperature-dependent, not switched on and off periodically. This aim could also be achieved if the water flow sequences were more frequent, but in order to minimise the water losses and limit the consumption of energy needed to drive the feed pump, it may be beneficial to regulate the length and frequency of flow sequences depending on the module temperature.

Figure 11 visualises variations of the module and ambient temperature during the experiments, which were performed in cloudless sky conditions. This graph summarises the temperature measured on the front and back surfaces of the modules, as well as the ambient temperature in the shade (i.e. at the back of the modules) and in front of the modules. To make the results more readable, selected measurement data (i.e. for 30 min of experiment time) is presented in Fig. 11. The average ambient temperature behind and in front of the modules during the experiments performed in cloudless sky conditions was equal to 31.3°C and 33.7°C, respectively. A discrepancy of measured values can also be seen for the temperature of the front and back sides of the modules. In the case of the comparison module, most of the time the temperature of its front side is higher than the temperature of its back side. This may be due to the effect of direct radiation falling on the front thermocouple. For the cooled module (*A*), the temperature ratio between the front surface and the back surface is influenced by the cooling water flow on the PV module surface and thus changes periodically. Before the first cooling water flow, the temperature of the front surface of the cooled module was higher than the temperature of its back surface, which can be explained similarly as in the case of the comparison module. After the first and each subsequent cooling process, the temperature of the back side of the module was higher than the temperature of its front side. Water, which is flowing down on the front surface of the PV module, firstly cools this surface. Each component of the PV module is characterised by specific thermal conductivity, as well as thermal inertia, which have the influence on the response time to the applied cooling. Once the water flow on the surface ends, the temperatures of the front and back surfaces of the module equalise. The front surface temperature then rises steadily, at one stage reaching a higher value than the value of the back surface temperature. Then the drop in this temperature is observed. The steady increase in the front surface temperature may be due to the fact that a certain volume of water remains in the vicinity of the thermocouple and affects the measured value. The front surface of the PV module is constantly exposed to sunlight, which probably causes that this surface reaches a higher temperature than the back surface. It should also be taken into account that a certain amount of liquid remains on the surface of the module after the cooling water flow is stopped. This water evaporates, which mainly intensifies the cooling of the front surface, but it also may result in a higher temperature of the back surface of the module at the end of the cycle, before the next cooling water flow. In addition, the drop of the cooled module (*A*) temperature occurs with some delay from the start of the cooling water flow, due to the time needed to fill the dispenser and reach the module surface.

Figure 12 shows the measured and modelled temperature variations of the comparison module (*B*). The green line shows the mean value of the measured front and back temperatures of the module. The orange line shows the module temperature calculated from the Mondol et al. model (see Eq. (5)) [9], while the dark blue line shows the temperature calculated from the Tselepis model (see Eq. (6)) [9]. These models are based on two variables, i.e. ambient temperature and solar irradiance. This figure shows that the Tselepis model better approximates the obtained experimental results. The maximum difference between the modelled value and the measured value is 14.4%, while for the Mondol et al. model this difference is equal to 33.7%. The mean difference between the measured and calculated values is equal to 5.3% (for the Tselepis model) and 23.1% (for the Mondol et al. model).

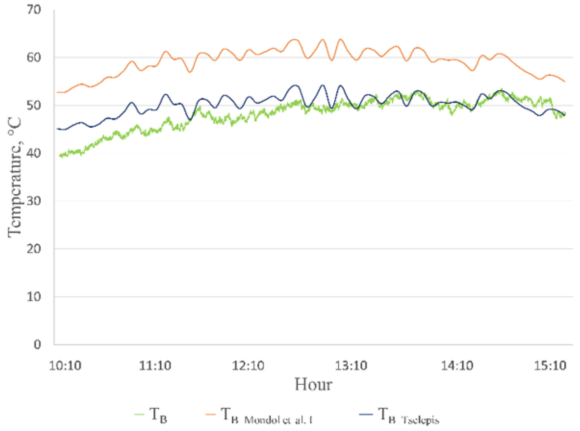

Fig. 12. Measured and modelled temperature variations of comparison module (*B*) during experiments performed in cloudless sky conditions.

4.4. Analysis of the amount of electricity generated by modules during the experiments

In order to assess the effect of the cooling system application on the generated electricity, the daily sum of electricity ($E_{\_el}$) generated by the comparative (*B*) and cooled (*A*) modules was analysed. This data was collected over 49 days (from April 1, 2023, to July 23, 2023) and visualized in Fig. 13 with blue (E_{el_B}) and yellow (E_{el_A}) dots, representing the comparative and cooled modules, respectively. The data is arranged from highest to lowest values relative to the comparison module (*B*). The SolarEdge application was utilized for data collection, facilitated by optimizers installed on the modules.

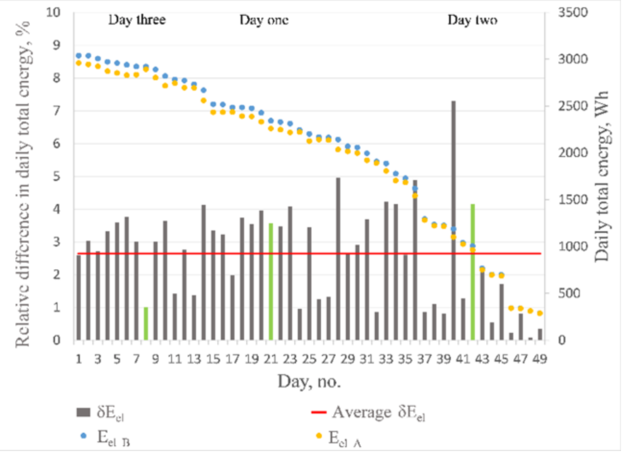

Fig. 13. The amount of electricity generated daily by the modules and the relative difference in the obtained values.

Despite both modules being of the same type and manufactured by the same company, it is observed that each day, the comparison module (*B*) generated more electricity than the cooled one (which may be attributed to internal differences). Additionally, Fig. 13 illustrates that the daily electricity generated by the cooled module (*A*) is, on average, 2.64% lower than that generated by the comparison module (*B*), as indicated by the red line. Smaller differences are noticeable when daily electricity gains are low. The relative difference in the sum of generated electricity is described by Eq. (8). These differences were calculated for each day of the experiment, visualized by grey bars, and considered in the analysis of the module cooling efficiency.

Experimental days during which water cooling was actively applied to module *A* are denoted by green bars in Fig. 13. It can be observed that during the experiments which were performed in cloudless sky conditions, when module *A* was cooled, the relative difference in the sum of generated electricity dropped to 1%, significantly lower than the average value. Conversely, during the experiments, which were performed in completely overcast and cloudy sky conditions, the values are higher than the average. This effect can probably be explained by the presence of a cooling water film on the PV module surface. Besides reducing the module temperature, water flow may also restrict the absorption of solar radiation by the module. In case of experiments, which were conducted when the sky was cloudless and solar radiation intensity was relatively high, the positive effect of module cooling by water flow and the reduction of its temperature outweighed the effect of limited absorption of solar radiation caused by the presence of the cooling water film on the module surface. However, on other experimental days when the sky was cloudy, the limited absorption of solar radiation caused by the cooling water film might have resulted in the cooled module (*A*) generating less electricity. In such cases, the positive effect of cooling may not be as visible.

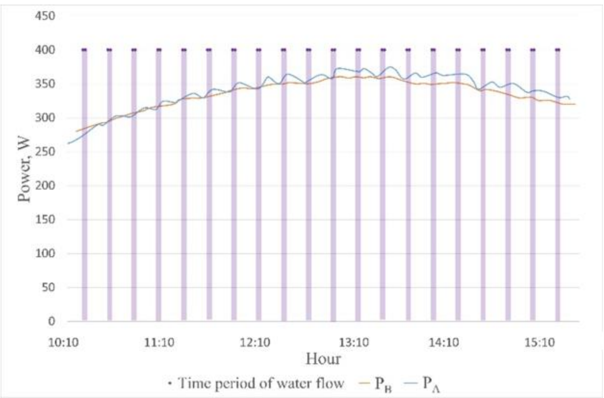

Fig. 14. The variation of measured module power during experiments performed in cloudless sky conditions (power values were obtained from the SolarEdge application).

4.5. Analysis of photovoltaic module power during the experiments

Module power analysis was carried out during experiments, which were performed in cloudless sky conditions using SolarEdge software. The variation of measured module power is presented in Fig. 14. Differences are noticeable between the power of the comparison module (B) and the cooled module (A). The cooled module achieves higher power values (maximum difference of ca. 15 W is observed), which represents a power increase by 4% compared to the comparison module power (B). A direct correlation can be seen between the power achieved by the PV module and the cooling water flow.

Figure 15 shows the variation of modules power calculated using Eqs. (3), (4) and (5). These calculations could be made using measured solar irradiance and the temperature of the modules. Compared to measured values of power, which are presented in Fig. 14, there are higher power values obtained for the cooled module (*A*) and the dependence of a calculated power value on the cooling water flow.

A comparison of the measured and calculated power values for the cooled module (*A*) is presented in Fig. 16. The maximum difference between the measured power value and the calculated value is about 40 W, thus a relative error is equal to 15%. The shape of the two presented characteristics is similar. The differences in the measured and calculated values may be due to the assumption adapted in calculations (i.e. it was assumed that the solar irradiance was perpendicular to the inclined module surface, while the solar irradiance perpendicular to a flat surface was measured experimentally).

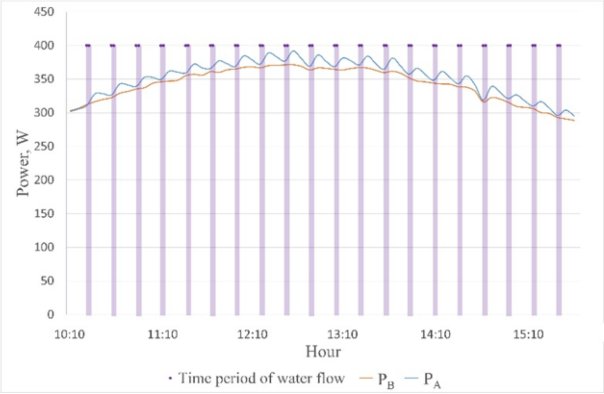

Fig. 15. The variation of module power during experiments performed in cloudless sky conditions (power was calculated using the calculation model presented in Section 3.3).

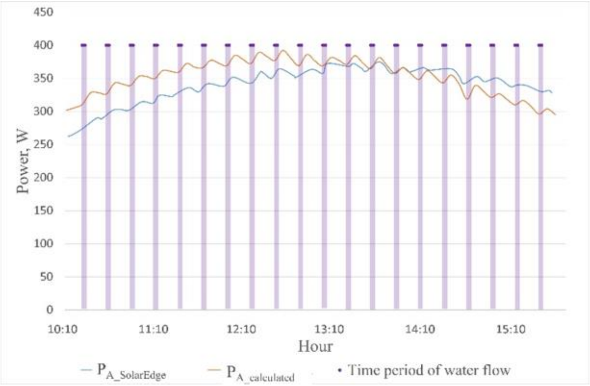

Fig. 16. Variation of the measured and calculated power of the cooled module during experiments performed in cloudless sky conditions.

5. Summary and conclusions

The research was aimed to assess the impact of temperate climate atmospheric conditions on the temperature and on the electrical parameters achieved by the PV module, as well as evaluating the possibility of improving the energy conversion efficiency of the PV module by the application of a water cooling of its front surface.

The study showed that solar irradiance has the greatest influence on the PV module temperature. During the experiments, which were performed in cloudy and completely overcast sky conditions, the average ambient temperature differed. The solar radiation intensity during experiments, which were performed in cloudy sky conditions, reached values exceeding 1000 W/m^2, while during experiments performed in completely overcast sky conditions it reached nearly 500 W/m^2. The maximum temperature of the comparison module (*B*) for these experiments reached 51.2°C and 37.3°C, respectively.

The effect of the water cooling of the module was observed during the tests. During cooling, the temperature of the module was reduced to values close to the cooling water temperature. The maximum differences between the temperature of the comparison module (*B*) and the cooled module (*A*) reached values of 17.6 K, 7.6 K and 16.1 K for consecutive experiments.

The type of system used to determine water flow influences the maximum temperature reached by the cooled module. The application of temperature-dependent cooling water flow system (which was used during experiments performed in cloudy sky conditions) resulted in reaching lower maximum module temperature compared to the maximum temperature of comparison module. Thus, by application of this type of water cooling system it is possible to limit the modules operational temperature range. A different effect was observed for the periodic cooling water flow during the other experiments.

There is a noticeable difference in the temperature of the front and back surfaces of the module. For the cooled module (*A*), most of the time the back surface temperature was higher than the temperature of the front surface, and during cooling water flow, the cooling of the back surface is delayed. For the comparison module (*B*), the front surface temperature was higher than the back surface temperature.

The gains in the daily amount of electricity generated by the cooled module (*A*) are dependent on the weather conditions (mainly on the cloud cover and the solar irradiance). For a cloudless sky conditions, there is a noticeable growth observed in the amount of electricity generated by the cooled module. For cloudy sky conditions, cooling is not efficient or even may have negative influence on the module operating conditions.

During the experiments, which were performed in cloudless sky conditions, there was an increase in the cooled module (*A*) power observed compared to the comparison module (*B*). The maximum increase of ca. 4% was obtained. This is relatively low value compared to the data presented for installations tested in warmer climates than Polish. In Table 4, a comparison of the obtained research results with data published in literature is presented, illustrating differences between the results obtained in different climatic conditions.

The output power of PV modules can be clearly compared based on the results obtained during experiments, which were performed in cloudless sky conditions. The maximum output power of the cooled module was 374.5 W, while the output power of comparative module was equal to 360.7 W at the same time (i.e. an increase in output power by 3.83% was obtained). The maximum power increase of the cooled module was 5.64%, while the average power increase of the cooled module between 11 a.m. and 3 p.m. was equal to 7.6 W.

From the obtained research results, it can be concluded that to achieve a better cooling effect, the water cooling installation should be designed and regulated to enable periodic activation and deactivation of the cooling water flow based on the PV module temperature. In a large PV installation, a good solution appears to be the utilization of an underground water tank, which can dissipate the heat contained in the cooling water to the ground and utilize rainwater to replenish any water losses in the cooling system. It is worth to note that the application of module cooling is not only related to a possible increase in the amount of energy generated by modules, but also to increasing their longevity. The application of cooling reduces the amplitude and frequency of cell temperature fluctuations, decreases thermal loads, and consequently contributes to limiting their degradation, thereby extending their operational lifespan.

Further work could focus on determining and optimizing the periods of time during which the PV module cooling system would be activated, as well as the optimal cell temperature.

Based on the work carried out, the following most important conclusions can be drawn:

1. Solar irradiance has the greatest influence on the photovoltaic module temperature;
2. The maximum module temperature reduction was 7.6−17.6 K (depending on atmospheric conditions);
3. The maximum electrical output power increased by 5.65%;
4. To achieve a better cooling effect, the water cooling installation should be designed and regulated to enable periodic activation and deactivation of the cooling water flow based on the photovoltaic module temperature

Table 4. Comparison of the obtained research results with data published in the literature.

Reference	Cooling method	Location	Results
Kumar et al. [29]	Water flow	India, Chennai	• Decrease of the daily average module temperature from 56.67°C to 39.44°C • Increase of the average daily module electrical efficiency to 14.29%, compared to 12.74% (without cooling)
Moharram et al. [32]	Water flow	Egypt, Cairo	• Highest energy output is obtained if the panel temperature reaches the maximum allowable temperature of 45°C • Module temperature reduction by 10 K • Increase of module electrical efficiency of 12%
Chanphavong et al. [33]	Water flow	Laos	• Decrease of the highest module temperature from 65.7°C to 36.5°C • Increase of the average exergy efficiency of module to 12.76% compared to 2.91% (without cooling)
Zubeer et al. [34]	Water flow (with solar concentration system)	Iraq, Duhok	• Decrease of the module temperature from 64.1°C to 36.5°C • Increase of the module electrical efficiency to 17% compared to 14.2% (without cooling) • Increase of electric power output of 24.4%
Benato et al. [30]	Spraying the upper surface of the module	indoor test	The ON/OFF cycle in which water is sprayed for 30 s and remains turned off for 180 s constitutes the best compromise among mean surface temperature reduction and PV efficiency improvement: • Module temperature reduction – 24.31 K • Increase of module electrical efficiency to 13.27% compared to 11.18% (without cooling) • Increase of the amount of generated electricity from 178.88 W to 212.31 W
Nizetic et al. [31]	Spraying both sides of the module	Croatia, Split	• Decrease of the average module temperature from 54°C to 24°C • Increase of module electrical efficiency of 16.3% • Increase of electric power output of 14.1%

References

[1] Paraschiv, L.S., & Paraschiv, S. (2023). Contribution of renewable energy (hydro, wind, solar and biomass) to decarbonization and transformation of the electricity generation sector for sustainable development. *Energy Reports*, 9(9), 535−544. doi: 10.1016/j.egyr.2023.07.024

[2] Haas, R., Duic, N., Auer, H., Ajanovic, A., Ramsebner, J., Knapek, J., & Zwickl-Bernhard, S. (2023). The photovoltaic revolution is on: How it will change the electricity system in a lasting way. *Energy*, 265, 1-14. doi: 10.1016/j.energy.2022.126351

[3] Izdebski, W., & Kosiorek, K. (2023). Analysis and evaluation of the possibility of electricity production form small photovoltaic installations in Poland. *Energies*, 16, 944. doi: 10.3390/en16020944

[4] Lebedys, A., Akande, D., Elhassan, N., Escamilla, G., Arkhipova, I., & Whiteman, A. (2023). Renewable capacity statistics 2023. *International Renewable Energy Agency*, Abu Dhabi.

[5] Zatorska, M., Wrońska, I., Mikołajuk, H., Stępniak, E., & Galewski, K. Informacja statystyczna o energii elektrycznej. *Biuletyn miesięczny Agencji Rynku Energii S.A.*, 12(324), 12(336), 12(348), 12(360).

[6] Janowicz, W., Mika, H., Woźniak, A., &., Pomorski, M. (2023). Wpływ warunków atmosferycznych na pracę modułów fotowoltaicznych. *Instal*, 3, 16−22. doi: 10.36119/15.2023.3.2

[7] Hasan, K., Yousuf, S.B., Tushar, M.S.H.K, Das, B.K., Das, P., & Islam, M.S. (2022). Effects of different environmental and operational factors on the PV performance: A comprehensive review. *Energy Science and Engineering*, 10(2), 656−675. doi: 10.1002/ese3.1043

[8] Aslam, A., Ahmed, N., Qureshi, S.A., Assadi, M., & Ahmed, N. (2022). Advances in solar PV systems; A comprehensive review of PV performance, influencing factors, and mitigation techniques. *Energies*, 15(20), 7595. doi: 10.3390/en15207595

[9] Santos, L.O., Carvalho, P.C.M., & Carvalho Filho, C.O. (2022). Photovoltaic Cell Operating Temperature Models: A Review of Correlations and Parameters. *IEEE Journal of Photovoltaics*, 12(1), 179–190. doi: 10.1109/jphotov.2021.3113156

[10] Coskun, C., Toygar, U., Sarpdag, O., & Oktay, Z. (2017). Sensitivity analysis of implicit correlation for photovoltaic module temperature: A review. *Journal of Cleaner Production*, 164, 1474–1485. doi: 10.1016/j.jclepro.2017.07.080

[11] Skoplaki, E., & Palyvos, J.A. (2009). Operating temperature of photovoltaic modules: A survey of pertinent correlations. *Renewable Energy*, 34(1), 23−29. doi: 10.1016/j.renene.2008.04.009

[12] Matuszczyk, P., Popławski, T., & Flasza, J. (2015). The influence of solar radiation and temperature module on selected parameters and the power rating of photovoltaic panels. *Przegląd Elektrotechniczny*, 91(12), 159−162 (in Polish). doi: 10.15199/48.2015.12.40

[13] Janowicz, W., Woźniak, A., Mika, H., & Pomorski, M. (2023). Annual analysis of the performance of a PV module with a cooling system. *Instal*, 9, 32−37, (in Polish). doi: 10.36119/15.2023.9.3

[14] *Data for building energy calculations. Typical meteorological years and statistical climate data for building energy calculations.* https://www.gov.pl/web/archiwum-inwestycje-rozwoj/dane-do-obliczen-energetycznych-budynkow [accessed 11 Feb. 2024] (in Polish).

[15] Sharaf, M., Yousef, M.S., & Huzayyin, A.S. (2022). Review of cooling techniques used to enhance the efficiency of photovoltaic power systems. *Environmental Science and Pollution Research*, 29, 26131−26159. doi: 10.1007/s11356-022-18719-9

[16] Siecker, J., Kusakana, K., & Numbi, B.P. (2017). A review of solar photovoltaic systems cooling technologies. *Renewable and Sustanable Energy Reviews*, 79, 192−203. doi: 10.1016/j.rser.2017.05.053

[17] Dwivedi, P., Sudhakar, K., Soni, A., Solomin, E., & Kirpichnikova, I. (2020). Advanced cooling techniques of P.V. modules: A state of art. *Case Studies in Thermal Engineering*, 21, 1−17. doi: 10.1016/j.csite.2020.100674

[18] Nabil, T., & Mansour, T.M. (2022). Augmenting the performance of photovoltaic panel by decreasing its temperature using various cooling techniques. *Results in Engineering*, 15, 100564. doi: 10.1016/j.rineng.2022.100564

[19] Elavarasan, R.M., Nadarajah, M., & Pugazhendhi, R. (2024). An experimental investigation on coalescing the potentiality of PCM, fins and water to achieve sturdy cooling effect on PV panels. *Applied Energy*, 356, 122371. doi: 10.1016/j.apenergy.2023.122371

[20] Majumder, A., Kumar, A., Innamorati, R., Mastino, C.C., Cappellini, G., Baccoli, R., & Gatto, G. (2023). Cooling methods for standard and floating PV panels. *Energies*, 16(24), 7939. doi: 10.3390/en16247939

[21] Pathak, S.K., Sharma, P.O., Goel, V., Bhattacharyya, S., Aybar, H.S., & Meyer, J.P. (2022). A detailed review on the performance of photovoltaic/thermal system using various cooling methods. *Sustainable Energy Technologies and Assessments*, 51, 101844. doi: 10.1016/j.seta.2021.101844

[22] Bhakre, S.S., Sawarkar, P.D., & Kalamkar, V.R. (2021). Performance evaluation of PV panel surfaces exposed to hydraulic cooling – A review. *Solar Energy*, 224, 1193−1209. doi: 10.1016/j.solener.2021.06.083

[23] Yildirim, M.A., Cebula, A., & Sułowicz, M. (2022). A cooling designe for photovoltaic panels – Water-based PV/T system. *Energy*, 256, 124654. doi: 10.1016/j.energy.2022.124654

[24] Shalaby, S.M., Elfakharany, M.K., Moharram, B.M., & Abosheiasha, H.F. (2022). Experimental study on the performance of PV with water cooling. *Energy Reports*, 8(1), 957−961. doi: 10.1016/j.egyr.2021.11.155

[25] Bashir, M.A., Ali, H.M., Amber, K.P., Bashir, M.W., Ali, H., Imran, S., & Kamran, M.S. (2018). Performance investigation of photovoltaic modules by back surface water cooling. *Thermal Science*, 22(6/A), 2401−2411. doi: 10.2298/TSCI160215290B

[26] Wu, G., Liu, Q., Wang, J., & Sun, B. (2021). Thermal analysis of water-cooled photovoltaic cell by applying computational fluid dynamics. *Journal of Thermal Analysis and Calorimetry*, 144(5), 1741−1747. doi: 10.1007/s10973-020-10283-z

[27] Bin Ehtesham, M.S., Ahmad, S., & Sui, Y. (2019). Water cooling system of PV panel. *AIP Conference Proceedings*, 2324(1), 050013 (*Proceedings of the 13th International Conference on Mechanical Engineering (ICME2019)*, 18-20 Dec. 2019, Dhaka, Bangladesh). doi: 10.1063/5.0037593

[28] Panda, S., Panda, B., Jena, C., Nanda, L., & Pradhan, A. (2023). Investigating the similarities and differences between front and back surface cooling for PV panels. *Materials Today: Proceedings*, 74(2), 358−363. doi: 10.1016/j.matpr.2022.08.424

[29] Kumar, R.S., Nagarajan, P.K., Subramani, J., & Natarajan, E.A. (2019). Detailed mathematical modelling and experimental validation of top water cooled solar PV module. *FME Transactions*, 47(3), 591−598.

[30] Benato, A., Stoppato, A., Vanna, F., & Schiro, F. (2021). Spraying cooling system for PV modules: Experimental measurements for temperature trends assessment and system design feasibility. *Designs*, 5(2), 25. doi: 10.3390/designs5020025

[31] Nižetić, S., Čoko, D., Yadav, A., & Grubišić-Čabo, F. (2016). Water spray cooling technique applied on a photovoltaic panel: The performance response. *Energy Conversion and Management*, 108, 287−296. doi: 10.1016/j.enconman.2015.10.079

[32] Moharram, K.A., Abd-Elhady, M.S., Kandil, H.A., & El-Sherif, H. (2013). Enhancing the performance of photovoltaic panels by water cooling. *Ain Shams Engineering Journal*, 4(4), 869−877. doi: 10.1016/j.asej.2013.03.005

[33] Chanphavong, L., Chanthaboune, V., Phommachanh, S., Vilaida, X., & Bounyanite, P. (2022). Enhancement of performance and exergy analysis of a water-cooling solar photovoltaic panel. *Total Environment Research Themes*, 3-4, 100018. doi: 10.1016/j.totert.2022.100018

[34] Zubeer, S.A, & Ali, O.M. (2022). Experimental and numerical study of low concentration and water-cooling effect on PV module performance. *Case Studies in Thermal Engineering*, 34, 102007. doi: 10.1016/j.csite.2022.102007

[35] Mzad, H., & Otmani, A. (2021). Simulation of photovoltaic panel cooling beneath a single nozzle based on a configurations framework. *Archives of Thermodynamics*, 42(1), 115−128. doi: 10.24425/ather.2020.136950

[36] Luboń, W., Pełka, G., Janowski, M., Pająk, L., Stefaniuk, M., Kotyza, J., & Reczek, P. (2020). Assessing the impact of water cooling on PV modules efficiency. *Energies*, 13(10), 2414. doi: 10.3390/en13102414

Co-published by
Institute of Fluid-Flow Machinery
Polish Academy of Sciences
Committee on Thermodynamics and Combustion
Polish Academy of Sciences

http://www.imp.gda.pl/archives-of-thermodynamics/

ARCHIVES OF THERMODYNAMICS

Thermal analysis of acetone and water in closed loop pulsating heat pipe

Haider Ali[a], Muhammad Amjad[a], Muhammad Ishaq[a], Mohammed Marshad R. Alharbi[b], Krzysztof Kędzia[c], Ahmed Zubair Jan[c*]

[a]Department of Mathematics, COMSATS University Islamabad, Vehari Campus, Vehari 61100, Pakistan
[b]Ministry of Education, Saudi Arabia
[c]Faculty of Mechanical Engineering, Wroclaw University of Science and Technology, Wroclaw, Poland
*Corresponding author email: ahmed.jan@pwr.edu.pl

Received: 08.12.2023; revised: 23.06.2024; accepted: 29.10.2024

Abstract

Thermal conductivity and transition are the two stages of a closed loop pulsating heat pipe's operation. A device called a closed loop pulsating heat pipe transfers heat at various heat inputs. The thermal performance of the closed loop pulsating heat pipe is impacted by various types of modifications. Heat transfer characteristics of the closed loop pulsating heat pipe are to be observed using computational fluid dynamics analysis. The aim of this study is to improve the heat conductivity of the closed loop pulsating heat pipe with the changing filling ratio. This study presents the closed loop pulsating heat pipe modeling by using ANSYS Workbench. ANSYS Fluent is considered to model the above stated phenomenon and computational fluid dynamics simulations are performed for different variations of temperature and filling ratio. The model is analyzed at 200W–300W heat flux for 100–400 iterations and the vaporized form is obtained. The temperature and iterations variations are the key parameters of the study. It is concluded that the temperature of the evaporator increased more at different levels of time as compared to the temperature of the condenser. In this analysis, by giving different heat inputs and evaporator sections, the heat flux in the condenser section is observed. It is concluded that the time and heat flux are the most affecting parameters in this study.

Keywords: Heat transfer; Closed loop pulsing heat pipes; Thermal analysis; ANSYS workbench; Computational fluid dynamics

Vol. 46(2025), No. 2, 29–37; doi: 10.24425/ather.2025.154917

Cite this manuscript as: Ali, H., Amjad, M., Ishaq, M., Alharbi, M.M.R., Kędzia, K., & Jan, A.Z. (2025). Thermal Analysis of Acetone and Water in Closed Loop Pulsating Heat Pipe. *Archives of Thermodynamics*, 46(2), 29−37.

1. Introduction

An effective method of transferring heat between hot and cold sources is a closed loop pulsing heat pipe (CLPHP). An oscillating pulsating heat pipe (PHP) is another name for a pulsating heat pipe. CLPHP is in thermal contact with the condenser section from one side which is the end of the tube and the other is the evaporator section. After providing heat to the evaporator, the condenser section oscillates with liquid plugs and vapour bubbles. The plugs alternate between hot and cold regions.

CLPHPs are powerful heat transfer innovations with high thermal performance. The idea of CLPHP was introduced by Akachi [1] in 1990. PHP has been designed so that heat moves

Nomenclature

c – specific heat, J/(kg·K)
D – diameter of CLPHP, m
f – surface tension, N/m
k – Boltzmann constant, J/K
p – pressure, N/m^2
T – temperature, K
u – velocity, m/s

Greek symbols

μ – dynamic viscosity, Pa·s
ρ – density, kg/m^3
σ – vapour-liquid surface tension coefficient, N/m

Subscripts and Superscripts

g – gas
l – liquid

Abbreviations and Acronyms

CLPHP	– closed loop pulsating heat pipe
CFD	– computational fluid dynamics
PHP	– pulsating heat pipe
VOF	– volume of fluid (method)

fluid. CLPHP must have two portions: heat receiving and radiating portions. PHP is a technology that transfers heat in the condenser area and gets it from the evaporator section. The flow of fluid and vapour is formed and a capillary action is formed.

Suresh and Bhramara [2] performed computational fluid dynamics (CFD) analysis of a single-turn PHP by using Ansys CFX. They considered different filling ratios of 60%, 70% and 80% and found a 60% filling ratio to be the best choice under different conditions. They concluded and suggested that a 60% filling ratio shows better heat transfer characteristics.

To attain the alternating vapour-liquid state, the PHP diameter must satisfy specific criteria. So, a formula was presented by Wang et al. [3] to measure the allowable inner diameter of PHP:

$$0.7\sqrt{\frac{\sigma}{(\rho_l-\rho_g)g}} \le D \le 2\sqrt{\frac{\sigma}{(\rho_l-\rho_g)g}}.$$

From the above equation, it can be noted that the surface tension has a great impact on the inner diameter of a closed-loop PHP.

Reddy et al. [4] analysed the thermal performance of ethanol and distilled water experimentally with a filling ratio of 50%. They used copper to construct PHP and the inner diameter was considered to be 2 mm. They concluded that the thermal performance of ethanol is finer than that of distilled water. Girish et al. [5] considered acetone, ethanol and methanol as working fluids in the analysis of CLPHP. Different heat inputs from 7 W to 15 W with filling ratios from 60% to 80% were considered. By increasing the heat coefficient of working fluids, the thermal resistance was reduced. Among all the considered working fluids, Acetone produces good results with a heat input of 13 W and a 60% filling ratio. Rudresha et al. [6] performed the CFD analysis of water and ethylene alcohol by utilizing Ansys. They concluded that the surface tension and thermal performance of water are better than those of the ethylene alcohol at the 60% filling ratio.

Betancur et al. [7] investigated PHP in a vertical position with various heat power inputs. A copper tube was utilized with five U-turns, 10 channels of planner serpentine, and an external and internal diameter of 4.76 mm and 3.18 mm, respectively. The thermal performance and flow along the tube were examined. Distilled water with a 50% filling ratio was considered as the working fluid and it was deduced that the motion of flow was reduced as a result of hindrance in the liquid film creation caused by the superhydrophobic coating.

Li and Li [8] analysed the application of PHP in high-performance central processing units (CPUs). Numerous high-power CPUs are utilized in data centres, which leads to the production of heat. They examined the whole research on CLPHP and different factors affecting the performance of PHP. The system's processor, storage, power supply, chip and voltage regulator are heat-generating components. Their research guided future research and engineering applications. The thermal performance of CLPHP was examined by Haque et al. [9] experimentally and by performing CFD simulations in Ansys. They considered the acetone-acetone vapours for this analysis. They calculated the thermal coefficient using the thermocouple temperature distribution. The CLPHP was built of copper, with a diameter of 1.95 mm and a total length of 540 mm. Different heat inputs were considered. They concluded that the increased heat transfer coefficient, reduced thermal resistance and heat transfer properties of CLPHP gave a good performance at a filling ratio of 60%.

Xue and Qu [10] used the high-speed camera to investigate the connection between PHP thermos hydrodynamics and flow patterns. In PHP, ammonia was utilized as a working fluid. PHP was made of quartz glass and had 6 turns and the outer diameter and inner diameter were considered to be 6 mm and 2 mm, respectively. The filling ratio was considered to be 70% with different heat inputs from 25 W to 250 W. They described the influence of vapour plugs, liquid slugs and also the velocity of the vapour. Pachghare and Mahalle [11] experimentally analysed the thermal performance of CLPHP. CLPHP was constructed of copper, having external and internal diameters of 3.6 mm and 2 mm, respectively. Different heat inputs were given from 10 W to 100 W and the filling ratio was fixed at 50% for all the experiments. The length of the adiabatic section, evaporation section and condenser section was kept at 50 mm. Water, ethanol, methanol, acetone and certain binary mixtures were assumed to be working fluids for this experiment. They concluded that a crucial factor for the thermal performance of CLPHP is the operating fluid, and acetone gave the best results among all the working fluids assumed.

Due to higher heat flux dissipation, electronic components' efficiency and performance have improved. Many devices have proved to be useful in microelectronic thermal management. In this field (thermal management of electronics), PHP cooling was an emerging and new technique. Baitule and Pachghare [12] used this technique to analyse the thermal performance of

CLPHP experimentally. The internal and external diameters of the copper-based evaporator and condenser portion were assumed to be 2 mm and 3 mm, respectively. The whole length of CLPHP was 1080 mm and the analysis was done on vertical surfaces with various heat loads ranging from 10 W to 100 W with a gap of 10 W per step. Acetone, methanol, water and ethanol were tested in CLPHP as working fluids for different filling ratios from 0% to 100% with a gap of 20% in each step. The results depicted that a lower thermal resistance, heat transfer characteristics, and greater CLPHP heat transfer coefficient produced superior results for various heat inputs at a 60% filling ratio. Patel and Mehta [13] investigated the thermal performance of 9-turn CLPHP. The inner and outer diameters were assumed to be 2 mm and 4 mm respectively. The lengths of the adiabatic, evaporator and condenser sections were considered 100 mm, 40 mm, and 50 mm, respectively. Throughout the trial, the working fluid was water, with a fixed filling ratio of 50%. Evaporator heaters were positioned in various orientations, including horizontal (90^0), vertical top (180^0), and bottom (0^0), as well as the inclined top (135^0) and bottom (45^0), to study the gravitational effect. The heat input ranged from 10 W to 50 W. The outcomes showed how gravity and input heat flux affected the thermal efficiency of CLPHP. From this perspective, Yeswanth and Bhaskara Rao [14] manipulated the geometry to investigate the thermal performance of a single-loop closed PHP. Geometry was modified by changing the surface area on the condenser side. To enhance the capacity for heat transfer, the best geometry was discovered. Rahman et al. [15] experimentally investigated the thermal efficiency of CLPHP with and without fins. Water and acetone were taken as working fluids for both cases. The values of the filling ratio were taken as 40%, 50%, 60% and 70%. The values of the angle of inclination were considered to be 0^0, 30^0, 45^0 and 60^0 and the heat input was taken from 10W to 100W in the stages of 10W. CLPHP was constructed from a copper tube, and its inner and outer diameters were assumed to be 2mm and 3mm, respectively. The results depicted that better results were observed for acetone and water for the 70% and 50% filling ratio, respectively, at an inclination angle of 0^0 for both cases.

Pachghare and Mahalle [16] experimentally analysed the copper-made CLPHP having an internal and external diameter of 2 mm and 3.6 mm, respectively. Water-methanol, water-ethanol and water-acetone binary mixtures were chosen as the working fluids. The distances of the adiabatic, evaporator and condenser sections were considered 170 mm, 42 mm and 50 mm, respectively, using a fixed filling ratio. The findings showed that the thermal resistance reduced gradually up to a heat input of 40 W and thereafter became reasonably stable. It was concluded that water-acetone gave the best results in comparison to the other considered fluids. Sree et al. [17] used CFD to examine the influence of several parameters on the thermal performance of CLPHP. Water was used as the working fluid, and CLPHP was manufactured with internal diameters of 2 mm and outer diameters of 3 mm. Different heat inputs were taken which were 16 W, 32 W and 48 W. The temperature, liquid volume fractions and pressure variations between three portions of CLPHP were described for various assimilations of the geometry of CLPHP, and the experimental and CFD results of thermal performance were compared. Yang et al. [18] analysed the operational limitation of CLPHP which was made up of 40 copper tubes with internal diameters of 1 mm and 2 mm, and the filling ratios were 30%, 50% and 70%. In the analysis, the effect of filling ratio, different heat inputs, operational orientation and inner diameter was calculated. They concluded that the inner diameter of 2mm gave the best results as compared to 1mm and also the 50% filling ratio was ideal in both cases.

PHP has gained great attention from theoretical and experimental research in recent times. Khandekar et al. [19] gave further visualization results to emphasize the complexity of the mathematical formulation of the modelling challenge. The results included a thorough analysis of the CLPHP modelling methodologies currently in use. The significant challenges that were embroiled in the modelling of such devices were thoroughly examined. It was uncommon to see a combination of such mechanisms and events, such as flooding or bridging, bubble agglomeration and changes in flow regime, bubble nucleation and collapse, pumping action, temperature, pressure and non-equilibrium conditions. They concluded that each of these factors affects well how a gadget conducts heat. The attempts to characterize the device in terms of controllable thermomechanical boundary conditions and a basic problem were made by Khandekar and Groll [20].

For CLPHPs, Xu et al. [21] offered the visualization with high-speed flow findings that showed that there is a bulk circulation flow that is long-lasting and shifts the direction of flow. The sine oscillation waves were visible. However, the local oscillating waves were overlaid and had brief periods and modest oscillation amplitudes. They concluded that the oscillation flow in PHP was caused by the sophisticated coupled effects of coalescence, bubble nucleation and condensation.

Khan and Nadeem [22] explored the heat and mass transfer for Maxwell nanofluid and concluded that the time relaxation parameter is one of the key parameters in this case. Khan et al. [23] investigated the ternary hybrid nanomaterials and noted that the slip parameter and Darcy-Forchheimer parameter were the key parameters in this study. Fourier's heat flux model was implemented by Khan et al. [24] to compute the heat transfer rate of a micropolar fluid. They observed an enhancement in heat transfer with an increment in the micro-polar parameter. Some other latest articles in this field are presented in the reference list as [24−29]. Ju et al. [30] provided information about the stability of oil droplets by varying certain parameters. Khan et al. [31] considered the Casson nanomaterials to compute the entropy generation numerically and the impact of inclusive parameters. Khan et al. [32] depicted that the Soret and Dufour numbers are the key parameters in analysing the Maxwell fluid. Tian et al. [33] experimentally studied the heat transfer phenomena due to electric fields and macro-structured surfaces during electrospray cooling. Khan et al. [34] modelled the partial differential equations for microelectromechanical systems and performed the stability analysis by employing the homotopy perturbation method. Khan et al. [35] depicted that the Yamada-Ota model has proficient outcomes in comparison to the Xue model for heat exchangers.

The existing literature includes the experimental results of these types of models leaving a gap for CFD simulations. In the current study, the thermal performance of CLPHP will be analysed using the Ansys 2021 R2. Acetone, acetone vapours and water are taken as working fluids which were not considered for this specific case before. Due to this consideration, the numerical results will be established and these will be useful in validating the results experimentally.

2. Materials and methods

2.1. Governing equations

For a two-phase flow, the gas-liquid interaction is recognized as the volume of fluid (VOF). The general method to model such flow utilizing a sole fluid creation based on the VOF method is pursued for shaping the slug in the capillaries. This phenomenon could be expressed using the following equations:

$$\nabla \cdot \vec{u} = 0,$$

$$\frac{\partial(\rho\vec{u})}{\partial t} + \nabla \cdot (\vec{u} \cdot \rho\vec{u}) = -\nabla p + \nabla \cdot [\mu(\nabla\vec{u} + (\nabla\vec{u})^T)] + \vec{f_\sigma},$$

$$\frac{\partial(\rho c T)}{\partial t} + \nabla \cdot (\rho c \vec{u} T) = \nabla \cdot (k \nabla T),$$

where $\vec{u}, \rho, \mu, p, T, k, \vec{f_\sigma}$ and c are the velocity vector, density, dynamic viscosity, pressure, temperature, thermal conductivity, surface tension and specific heat, respectively. The above stated equations are solved utilizing the VOF method.

The CLPHP filling ratio is taken to be 70%. Water and acetone are the operating fluids, and the internal and external dimensions are 2 mm and 3 mm, respectively. The size of the evaporator, condenser and adiabatic section is considered to be 116 mm, 53 mm, and 50 mm, respectively. The heat flux is given as 200W. The model of a two-turn PHP is designed in Ansys Fluent software. In this analysis, the temperature difference is to be determined between the condenser and evaporator.

2.2. CFD simulation

This study aims to analyse the thermal performance of CLPHP with the variations in the evaporator section under load conditions using acetone, acetone vapours, and water as working fluids. This simulation is made in CFD software ANSYS 2021 R2.

Also, the flow paradigm of the above-stated working fluids inside the CLPHP is to be noted to suggest the trajectory. Furthermore, the temperature differences in the condenser and evaporator are considered performance parameters.

2.2.1. Methodology

Based on the literature cited above, the article by Giri and Pachghare [36] is considered to define the basic parameters. This article was restricted to only a few conditions. In this study, it is extended to certain variations in different parameters. CFD analysis is performed using certainly suitable schemes and the simulation is performed until the achievement of the required convergence criterion.

2.3. Geometry and meshing

The work of Giri and Pachghare [36] is considered to construct the basic geometry. The grid-independent test is performed for each model and the solution is also independent of the mesh resolution.

2.3.1. Geometry

The CLPHP is designed in ANSYS workbench. CLPHP is based on three sections: the evaporation section, the adiabatic section, and the condenser section which are shown in Figs. 1, 2 and 3, respectively. The copper domain is not deemed in the modelling of geometry. Only the fluid domain is under consideration in this case. Dimensions of CLPHP are demonstrated below in Table 1.

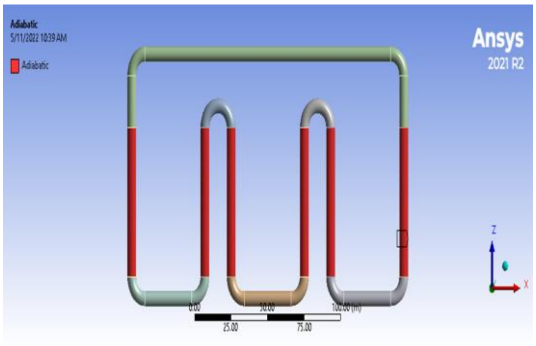

Fig. 1. Adiabatic section.

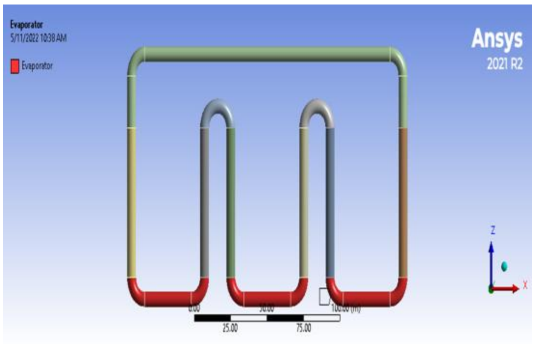

Fig. 2. Evaporator section.

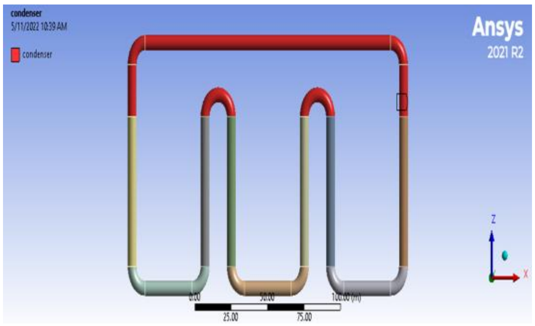

Fig. 3. Condenser section.

Table 1. Details of CLPHP geometry.

Specifications	**Dimensions**
Inner diameter	3 mm
Outer diameter	5 mm
Evaporator section length	116 mm
Condenser section length	53 mm
Adiabatic section length	50 mm

2.3.2. Meshing

A mesh is a grid that is made of points and cells. In the meshing, complex geometries are divided into elements. It depends on the shape of the geometry. When the geometry area is larger, more cells are created, which means the calculations take longer time. On the other hand, if the geometry area is smaller, fewer cells are created, so the calculations take less time. Meshing allows us to visualize the flow pattern inside the tube. Creating more cells improves the accuracy of the results, while fewer cells lead to less precise outcomes. In this analysis, we used a cell size of 0.3 mm. Near the walls, we made the mesh elements smaller to ensure better accuracy in capturing details close to the outer walls of the CLPHP The number of nodes and number of elements in the generated mesh are 384 438 and 453 381, respectively. The section of CLPHP with water vapour is shown in Fig. 4. In this analysis, the filling ratio of CLPHP is taken at 70% which is shown in Fig. 5. This meshing process is done by using the ANSYS Fluent. The working fluid is considered water and acetone.

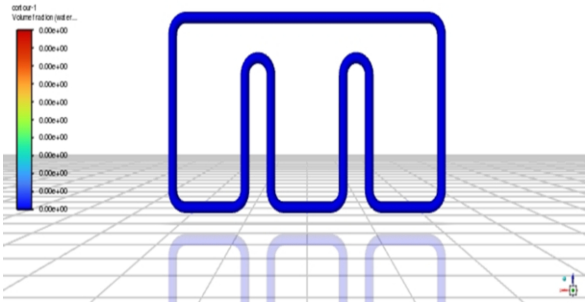

Fig. 4. CLPHP with vapour.

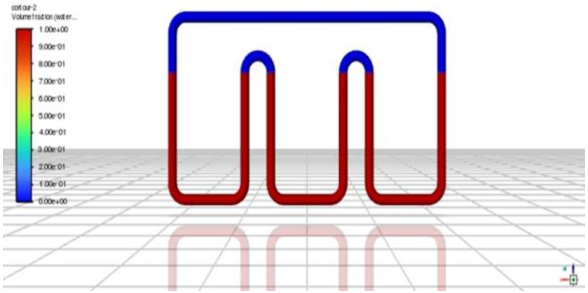

Fig. 5. CLPHP with a mixture of fluids.

2.4. Analysis settings

The steady-state analysis is conducted in Fluent although a major part of the thermal analysis with the phenomena of phase change is primarily a transient case. The analysis is performed to confirm the state of the fluid whether it is steady-state or transient. The variation between a steady-state simulation and its transient solution is that this simulation neglects much of the cross and higher-order terms. These terms all approach zero in a steady state, exerting minimal influence on the outcome. Similarly, transient simulations encompass all these terms. Generally, this implies that the aforementioned model has a better convergence as fewer terms have to be modelled and some transient non-linearity is neglected. For some specific cases, this leads to convergence.

In this section, the mesh is checked. To recognize the peak aspect ratio and lowest orthogonal quality, the report quality is checked. We use the multiphase model because it has three phases: vapour, gas and liquid. In the solver settings, we used a transient pressure-based approach, and considered velocity in absolute terms. The energy equation is kept on. In the models, the volume of the fluid is enabled, the formulation is taken as implicit, and body force is also enabled. Three phases are taken and the type of phase can be defined in the options. Phase pairs can be defined in the 'phase attraction' and surface tension coefficients are also enabled. The options: continuum surface force, wall adhesion and jump adhesion are also kept on. Then, at the end of the multiphase model, we will set the mass transfer. After this, in the viscous option, the k–ε model is enabled as standard, enhanced wall treatment, thermal effect and curvature correction are also selected. Then, in the materials section, working fluids are selected which are acetone, acetone vapour and water in this case. Then, the properties of fluids like density, specific heat, thermal conductivity and viscosity are defined. The wall temperature and the filling ratio are defined in the CLPHP finally. The filling of fluid is shown below in the figures.

2.5. Basic settings for the domain

CLPHP is divided into three domains, i.e. the adiabatic region, condenser and evaporator. Furthermore, the adiabatic region is partitioned into two domains to encompass the rise in CLPHP from the evaporator at the base.

2.6. Boundary conditions

200 W and 300 W heat fluxes were applied to the evaporator region with 100, 200, 300 and 400 iterations. The heat flux is considered to be negligible for the adiabatic region. In the condenser region, a lower heat flux was given. The VOF model is utilized to obtain CFD results. In all domains, the no-slip condition is applied.

2.7. Condenser

In the condenser section, the velocity and relative pressure are negligible. Primarily, as there is only low-pressure air, there will be low turbulent flow in the condenser section. The volume fraction for the binary mixture of fluid and vapours is 0 while for air, it is 1. Upon completion of heating to the evaporator, the thermal boundary condition is applied with a fixed temperature of 302 K.

2.8. Evaporator

The same as in the condenser section, the velocity and relative pressure are negligible. In the evaporator, the values (0, 1, 0) are used to represent the vapour and the binary mixture of air and fluid. Across all domains, the no-slip condition is applied.

2.9. Material selection

The properties of the analysed fluids are listed in Table 2. For comparison, data for water are also given.

Table 2. Properties of fluid.

Fluid	Density, kg/m³	Specific heat, J/(kg·K)	Thermal conductivity, W/(m·K)	Dynamic viscosity, Pa·s
C_3H_6O	761	2160	0.18	0.000331
C_3H_6O - Vapour	2.37	2160	0.18	0.014
H_2O	998	4181	0.644	0.001003

3. Results and discussion

The filling ratio of the closed loop pulsating pipe is taken at 70%. The working fluids for this analysis are acetone and water. In this analysis, results are obtained by giving different heat inputs. Figure 6 shows the results obtained by applying a heat flux of 200 W after 100 iterations. Similarly, Fig. 7 shows the results after 200 iterations, Fig. 8 after 300 iterations, and Fig. 9 after 400 iterations, all with the same heat flux of 200 W. The vapour of acetone is illustrated in Fig. 10. Moving on, Fig. 11 presents the results for a heat flux of 300 W after 100 iterations. Figures 12, 13 and 14 show the results after 200, 300, and 400 iterations, respectively, with the same heat flux. The vapour of acetone is shown again in Fig. 15, and the final results are summarized in Fig. 16. The increment in the heat power input reduces the thermal resistance. While at low input of heat flux, enough perturbations are not generated and it results in the restriction of bubble pumping action. So, this phenomenon results in the poor performance. The heat transfer coefficient is improved with an enhancement in the heat input. Still, higher input heat fluxes resulted in bulk flow taking a fixed direction that did not reverse with time. This circulation was manifested as the adjacent tube became alternately hot and cold. Interestingly, in such a case the lowest thermal resistance was observed.

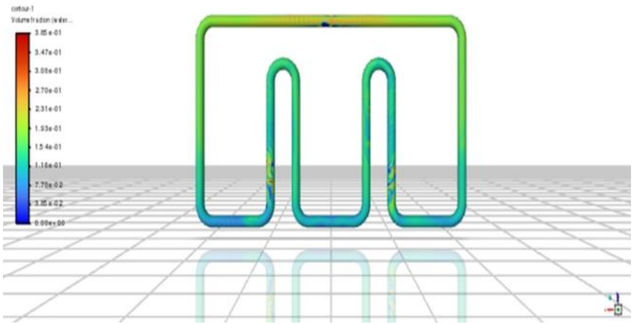

Fig. 6. Temperature contours at 200 W heat flux after 100 iterations for water-acetone.

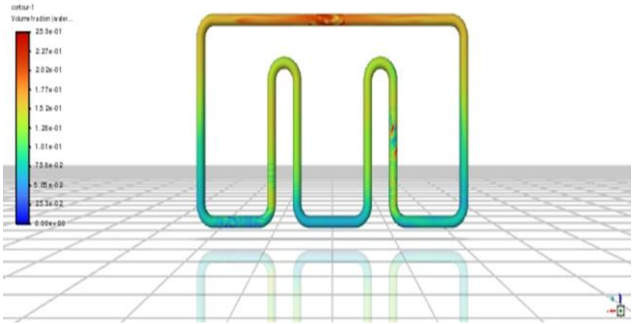

Fig. 7. Temperature contours at 200 W heat flux after 200 iterations for water-acetone.

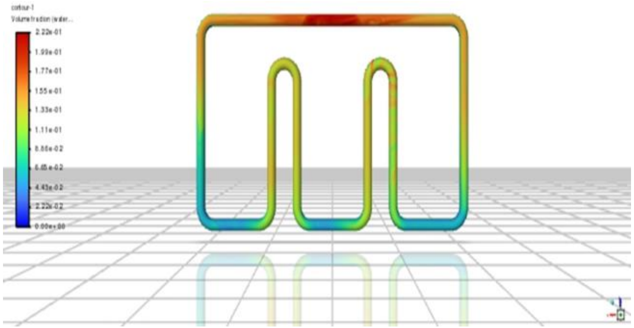

Fig. 8. Temperature contours at 200 W heat flux after 300 iterations for water-acetone.

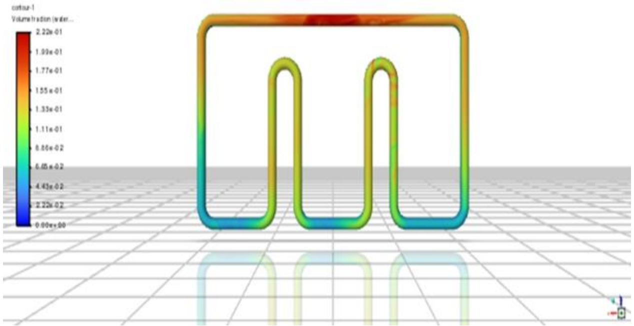

Fig. 9. Temperature contours at 200 W heat flux after 400 iterations for water-acetone.

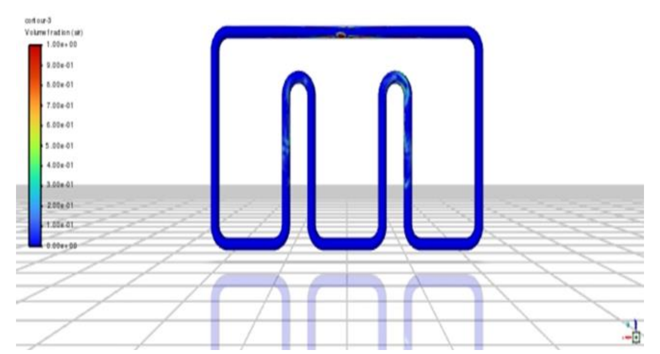

Fig. 10. Vapourized acetone at 200 W heat flux.

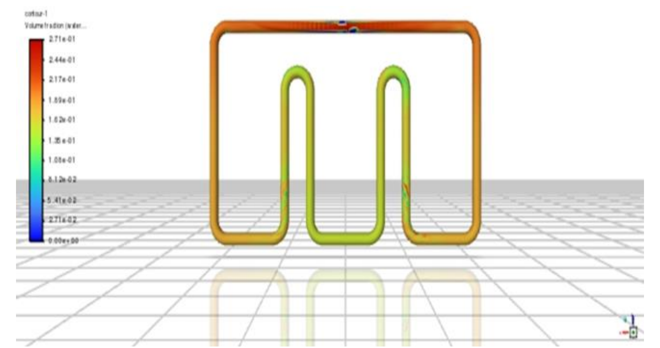

Fig. 11. Temperature contours at 300 W heat flux after 100 iterations for water-acetone.

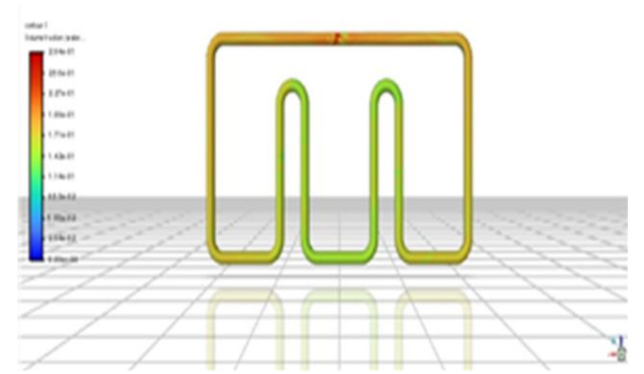

Fig. 12. Temperature contours at 300 W heat flux after 200 iterations for water-acetone.

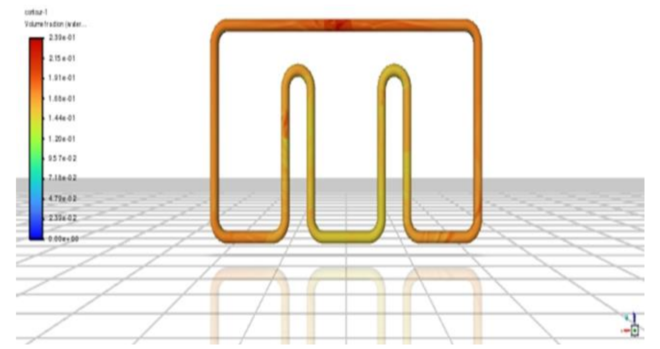

Fig. 13. Temperature contours at 300 W heat flux after 300 iterations for water-acetone.

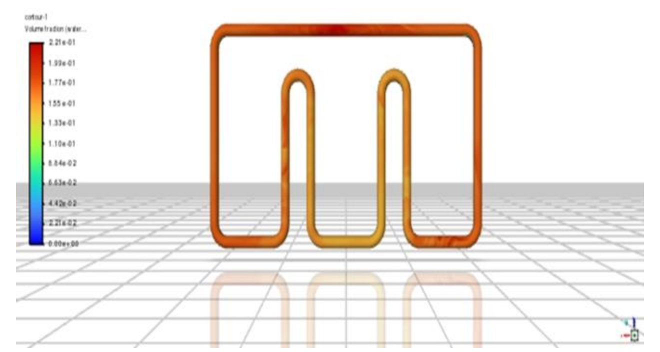

Fig. 14. Temperature contours at 300 W heat flux after 400 iterations for water-acetone.

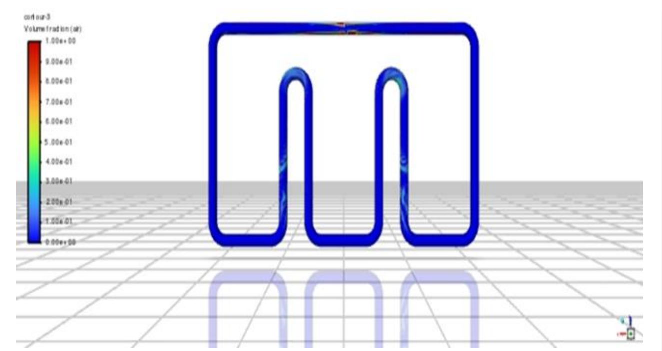

Fig. 15. Vapourized acetone at 300 W heat flux.

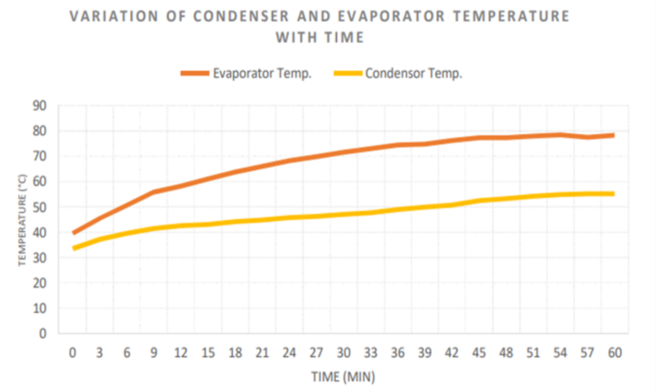

Fig. 16. Evaporator temperature and condenser temperature vs. time.

The above graph (Fig. 16) depicts the comparison of variations of evaporator and condenser temperature versus time. The temperature gradually enhances over time for both the condenser and evaporator. At the beginning of the heat transfer rate, the temperature rises gradually. Whenever the heat transfer rate increases, the rate of temperature rise decreases until it changes to a steady state which shows that it becomes constant. In the beginning, the difference between the condenser and evaporator temperature is lower and rises gradually. The optimum filling ratio for CLPHP in this study is 70%, which most adequately combines the advantages of the following two aspects: the latent heat along with the pumping action of the bubbles, and the sensible heat transport of the liquid slugs.

4. Conclusions

CFD analysis is used (ANSYS Fluent) to study the heat transfer characteristics of CLPHP. The working fluids are acetone and water. It is observed from the presented contours, as the time step size increases, the volume fraction of acetone-liquid decreases when the heat load is applied at the evaporator section. It was also observed that the acetone-liquid volume fraction decreases as the heat load increases in the CLPHP. This happens because the heat load increases at the evaporator section then the acetone-liquid to vapour phase transformation time is reduced. It is concluded that:

1. The thermal resistance and operating time of the PHP decrease as the heat input to the CLPHP increases.

2. If we apply more heat flux to the fluid, it cools down gradually. On the other hand, applying less heat flux causes it to cool more slowly.

3. When heat flux is applied to the evaporator, less heat is transferred to the condenser compared to the evaporator. Over time, the temperature in the condenser stabilizes and becomes nearly constant.

4. As shown in Fig. 16, at T=0, the evaporator's temperature is around 40°C, while the condenser's temperature is about 32°C. After 18 minutes, the evaporator's temperature rises to 62°C, and that of the condenser reaches approximately 43°C. By 60 minutes, the evaporator heats up to around 79°C, and the condenser reaches about 55°C.

5. From these observations, it is clear that the evaporator's temperature increases more significantly over time compared to the condenser's temperature.

6. In the future, this study can be expanded by exploring variations in the filling ratios and introducing additional parameters like the Grashof and Prandtl numbers.

References

[1] Akachi, H. (1990). *Structure of heat pipe*. U.S. Patent 4 921 041.

[2] Suresh, Z.V., & Bhramara, B. (2016). CFD Analysis of single turn pulsating heat pipe. *International Journal of Scientific and Engineering Research*, 7(6), 238−244.

[3] Wang, J., Xie, J., & Liu, X. (2019). Investigation on the performance of closed-loop pulsating heat pipe with surfactant. *Applied Thermal Engineering*, 160, 113998. doi:10.1016/j.applthermaleng.2019.113998

[4] Reddy, D.R., Reddy, K.H., & Balajiganesh, N. (2017). Performance Analysis of Pulsating Heat Pipes Using Various Fluids. *International Journal of Engineering and Manufacturing Science*, 7(2), 281−291.

[5] Girish, S., Lavanya, K., & Krishna, P.G. (2017). CFD analysis of Pulsating heat pipe using different fluids. *International Journal of Mechanical Engineering and Technology*, 8(6), 804-812.

[6] Rudresha, S., Goyal, P., Pandey, P., Sharma, M., & Srivastav, M. (2021). CFD Analysis of Single Turn Pulsating Heat Pipe by Comparing Ethylene Alcohol & Water. *International Journal of Mechanical Engineering and Technology*, 8(7), 2273−2279.

[7] Betancur, L., Mangini, D., Mantelli, M., & Marengo, M. (2020). Experimental study of thermal performance in a closed loop pulsating heat pipe with alternating superhydrophobic channels. *Thermal Science and Engineering Progress*, 17, 100360. doi: 10.1016/j.tsep.2019.100360

[8] Li, C., & Li, J. (2021). Passive Cooling Solutions for High Power Server CPUs with Pulsating Heat Pipe Technology. *Frontiers in Energy Research*, 9. doi: 10.3389/fenrg.2021.755019

[9] Haque, M.M.A., Azizuddin, D.M., & Rehman, M.M.K. (2016). CFD and Volume Fraction Analysis of Closed Loop Pulsating Heat Pipe (CLPHP). *Journal of Mechanical and Civil Engineering*, 13(5), 88–94. doi: 10.9790/1684-1305048894

[10] Xue, Z.H., & Qu, W. (2017). Experimental and theoretical research on an ammonia pulsating heat pipe: New full visualization of flow pattern and operating mechanism study. *International Journal of Heat and Mass Transfer*, 106, 149−166. doi: 10.1016/j.ijheatmasstransfer.2016.09.042

[11] Pachghare, P.R., & Mahalle, A.M. (2013). Effect of pure and binary fluids on closed loop pulsating heat pipe thermal performance. *Procedia engineering*, 51, 624−629. doi: 10.1016/j.proeng.2013.01.088

[12] Baitule, D.A., & Pachghare, P.R. (2013). Experimental analysis of closed loop pulsating heat pipe with variable filling ratio. *International Journal of Mechanical Engineering and Robotic Research*, 2(3), 113−121.

[13] Patel, V.M., & Mehta, H.B. (2016). Influence of Gravity on the Performance of Closed Loop Pulsating Heat Pipe. *18th International Conference on Fluid Mechanics and Thermal*., 12−13 Jan., 18(1), Part V. Zurich, Switzerland. *International Journal of Mechanical and Mechatronics Engineering*, 10(1), 219−223.

[14] Yeswanth, A., & Bhaskara Rao T.S.S. (2016). CFD Analysis on pulsating heat pipe to improve heat transfer. *International Journal of Research and Innovation in Thermal Engineering*, 3.1, 107−111.

[15] Rahman, M.L., Kader, M.F., Rahman, M.Z., & Ali, M. (2016). Experimental investigation on thermal performance of a closed loop pulsating heat pipe without fin and with fin structure. *American Journal of Mechanical Engineering*, 4(6), 209−214. doi: 10.12691/ajme-4-6-1

[16] Pachghare, P.R., & Mahalle, A.M. (2014). Thermohydro-dynamics of closed loop pulsating heat pipe: an experimental study. *Journal of Mechanical Science and Technology*, 28(8), 3387−3394. doi: 10.1007/s12206-014-0751-9

[17] Sree, N.S., Sudheer, N.V.S.S., & Bhramara, P. (2018). Thermal analysis of closed loop pulsating heat pipe. *International Journal of Mechanical and Production Engineering Research and Development*, 8(2), 21−36. doi:10.24247/ijmperdapr20183

[18] Yang, H., Khandekar, S., & Groll, M. (2008). Operational limit of closed loop pulsating heat pipes. *Applied Thermal Engineering*, 28(1), 49−59. doi: 10.1016/j.applthermaleng.2007.01.033

[19] Khandekar, S., Charoensawan, P., Groll, M., & Terdtoon, P. (2003). Closed loop pulsating heat pipes Part B: visualization and semi-empirical modeling. *Applied Thermal Engineering*, 23(16), 2021−2033. doi: 10.1016/S1359-4311(03)00168-6

[20] Khandekar, S., & Groll, M. (2004). An insight into thermo-hydrodynamic coupling in closed loop pulsating heat pipes. *International journal of thermal sciences*, 43(1), 13−20, doi: 10.1016/S1290-0729(03)00100-5

[21] Xu, J.L., Li, Y.X., & Wong, T.N. (2005). High speed flow visualization of a closed loop pulsating heat pipe. *International Journal of Heat and Mass Transfer*, 48(16), 3338−3351. doi: 10.1016/j.ijheatmasstransfer.2005.02.034

[22] Khan, M.N., & Nadeem, S. (2020). Theoretical treatment of bio-convective Maxwell nanofluid over an exponentially stretching sheet. *Canadian Journal of Physics*, 98(8), 732−741. doi: 10.1139/cjp-2019-0380

[23] Khan, M.N., Ahmad, S., Alrihieli, H.F., Wang, Z., Hussien, M.A., & Afikuzzaman, M. (2023). Theoretical study on thermal efficiencies of Sutterby ternary-hybrid nanofluids with surface catalyzed reactions over a bidirectional expanding surface. *Journal of Molecular Liquids*, 391, 123412. doi: 10.1016/j.molliq.2023.123412

[24] Khan, M.N., Nadeem, S., & Muhammad, N. (2020). Micropolar fluid flow with temperature-dependent transport properties. *Heat Transfer*, 49(4), 2375−2389. doi: 10.1002/htj.21726.

[25] Khan, M.N., Hussien, M.A., Allehiany, F.M., Ahammad, N.A., Wang, Z., & Algehyne, E.A. (2023). Variable fluid properties and concentration species analysis of a chemically reactive flow of micropolar fluid between two plates in a rotating frame with cross diffusion theory. *Tribology International*, 189, 108943. doi: 10.1016/j.triboint.2023.108943

[26] Ahmad, S., Khan, M.N., & Nadeem, S. (2020). Mathematical analysis of heat and mass transfer in a Maxwell fluid with double stratification. *Physica Scripta*, 96(2), 025202. doi: 10.1088/1402-4896/abcb2a

[27] Khan, M.N., Ahmed, A., Ahammad, N.A., Wang, Z., Hassan, A.M., & Elkotb, M.A. (2023). Chemotaxis bioconvection in swirling flow of Maxwell fluid with diffusion-thermo and thermal-diffusion effects. *Case Studies in Thermal Engineering*, 49, 103334. doi: 10.1016/j.csite.2023.103334

[28] Ahsan, N., Nauman Aslam, M., Khan, M.N, & Elseesy, I.E. (2023). Thermal features of Darcy-Forchheimer on a micropolar fluid flow over a curved stretching surface with homogenous-heterogeneous reactions. *Numerical Heat Transfer A*, 1−15. doi: 10.1080/10407782.2023.2251082

[29] Khan, M.N., Khan, A.A., Wang, Z., Alrihieli, H.F., M. Eldin, S., Aldosari, F.M., & Elseesy, I.E. (2023). Flow investigation of the stagnation point flow of micropolar viscoelastic fluid with modified Fourier and Fick's law. *Scientific Reports*, 13(1), 9491. doi: 10.1038/s41598-023-36631-1

[30] Ju, M., Li, B., Wu, Y., Wang, Z., Sun, Z., Zhan, S., & Wang, J. (2023). Oil droplet migration in the coupling of electric field and nano-confined shearing flow field: A molecular dynamics study. *Journal of Molecular Liquids*, 388, 122813. doi: 10.1016/j.molliq.2023.122813

[31] Khan, M.N., Ahmad, S., Wang, Z., Ahammad, N.A., & Elkotb, M.A. (2023). Bioconvective surface-catalyzed Casson hybrid nanofluid flow analysis by using thermodynamics heat transfer law on a vertical cone. *Tribology International*, 188, 108859. doi: 10.1016/j.triboint.2023.108859

[32] Khan, M.N., Ahmed, A., Ahammad, N.A., Wang, Z., Hassan, A.M., & Elkotb, M.A. (2023). Chemotaxis bioconvection in swirling flow of Maxwell fluid with diffusion-thermo and thermal-diffusion effects. *Case Studies in Thermal Engineering*, 49, 103334. doi: 10.1016/j.csite.2023.103334

[33] Tian, J., He, C., Chen, Y., Wang, Z., Zuo, Z., Wang, J., & Xiong, J. (2024). Experimental study on combined heat transfer enhancement due to macro-structured surface and electric field during electrospray cooling. *International Journal of Heat and Mass Transfer*, 220, 125015. doi: 10.1016/j.ijheatmasstransfer.2023.125015

[34] Khan, M.N., Haider, J.A., Wang, Z., Gul, S., Lone, S.A., & Elkotb, M.A. (2024). Mathematical modelling of the partial differential equations in microelectromechanical systems (MEMS) and its applications. *Modern Physics Letters B*, 38(05), 2350207. doi: 10.1142/S021798492350207X

[35] Khan, M.N., Aldosari, F.M., Wang, Z., Yasir, M., Afikuzzaman, M., & Elseesy, I.E. (2024). Overview of solar thermal applications of heat exchangers with thermophysical features of hybrid nanomaterials. *Nanoscale Advances*, 6(1), 136−145. doi: 10.1039/D3NA00481C

[36] Giri, K.C., & Pachghare, P. R. (2021). Study of Thermal Performance of Closed Loop Pulsating Heat Pipe using Computational Fluid Dynamics. *International Journal for Research in Applied Science and Engineering Technology*. 9(9), 1384−1388. doi: 10.22214/ ijraset.2021.38088

Co-published by
Institute of Fluid-Flow Machinery
Polish Academy of Sciences
Committee on Thermodynamics and Combustion
Polish Academy of Sciences

http://www.imp.gda.pl/archives-of-thermodynamics/

ARCHIVES OF THERMODYNAMICS

The temperature distribution in the ground on the two types of pipes of underground heating network

Dariusz Jakubek[a], Marzena Nowak-Ocłoń[a*], Petar Sabev Varbanov[b], Maciej Sułowicz[c]

[a]Energy Department, Cracow University of Technology, al. Jana Pawła II 37, Cracow, 31-864, Poland
[b]Sustainable Process Integration Lab, NETME Centre, Brno Univ. of Technology, Technická 2896/2, Brno, 616 69, Czech Republic
[c]Faculty of Electrical and Computer Engineering, Cracow University of Technology, Warszawska 24, Cracow, 31–155, Poland
*Corresponding author email: marzena.nowak-oclon@pk.edu.pl

Received: 30.08.2024; revised: 01.04.2025; accepted: 15.04.2025

Abstract

District heating systems commonly utilize pre-insulated pipes arranged in either a parallel or TwinPipe configuration. This study compares the temperature distribution in the ground, as determined by a numerical 3D model, with experimental measurements conducted on a dedicated test setup. The analysis includes several district heating pipe variants (DN40, DN50 and DN65), and their counterparts in a single parallel pre-insulated system. The results obtained from laboratory experiments and numerical simulations show strong agreement, confirming the reliability of the proposed approach. The novelty of this work lies in the integration of experimental data and numerical simulations to improve the accuracy of heat loss estimations. The relative error between the computational and experimental models remains below 10%, ensuring high precision in the findings. The presented results provide valuable design insights for optimizing insulation thickness and pipe layout configurations in district heating networks. These findings contribute to the development of more efficient and sustainable thermal energy distribution systems.

Keywords: District Heating Network; Heat loss; Heat transfer; Temperature distribution

Vol. 46(2025), No. 2, 39–47; doi: 10.24425/ather.2025.154904

Cite this manuscript as: Jakubek, D., Nowak-Ocłoń, M., Varbanov, P.S., & Sułowicz, M. (2025). The temperature distribution in the ground on the two types of pipes of underground heating network. *Archives of Thermodynamics*, 46(2), 39–47.

1. Introduction

In Europe, more than 40% of final energy is used to heat buildings [1]. One way to provide heat is through district heating networks. It works especially well in large cities where these networks are very extensive and access to them is more easily available. In order to achieve the most energy-efficient district heating network (DHN), it is necessary to choose the appropriate source of heat for its supply and its distribution method. The use of heat pumps and other renewable energy sources is considered to reduce the amount of fossil fuel use and greenhouse gas (GHG) emissions, as discussed by Lund et al. [2].

For transporting the energy carrier within the DHN, pre-insulated pipes are currently used in single and TwinPipe arrangements. Both types of pipes can be used in underground and aboveground networks. When delivering the medium to the building at the required temperature to compensate for heat losses, it is necessary to use the required materials and pipes that will ensure it. Maximizing energy efficiency requires minimizing heat losses in the pipes. The analysis of energy efficiency of

Nomenclature

D	– diameter, m
h	– heat transfer coefficient, W/(m^2 K)
H	– depth of foundation, m
k	– thermal conductivity, W/(m K)
q	– heat losses, W/m
R	– thermal resistance, (m K)/W
t	– fluid temperature, °C

Greek symbols

ρ	– density, kg/m^3
σ	– relative error, %

Subscripts and Superscripts

gr	– ground
ins	– insulation
r	– return
s	– supply
w	– wall

Abbreviations and Acronyms

BEM	– boundary element method
CIPP	– cured-in-place pipe
DHN	– district heating network
FEM	– finite element method
FVM	– finite volume method
GA	– genetic algorithm
GHG	– greenhouse gas
TOTS	– two supply/one return, triple pipe structure
5GDHC	– 5th generation district heating and cooling (network)

such district heating networks is investigated in many works, including pipes located in the ground.

The approach to thermal-ecological analysis was presented in the paper of Ziębik and Stanek [3]. The method uses cumulative exergy consumption and thermo-ecological costs as criteria in the analysis. The authors advocate the application of these criteria to overall processes instead of local exergy efficiency studies. However, the illustration of the concept is not well developed leaving the need for a more systematic presentation of the approach.

One possible measure for reducing heat losses is to lower the operating temperature levels of the fluid circulating inside the DHN. In 3rd generation DHN, the supply operating temperature is $t_s < 100$°C and return $t_r < 45$°C; in 4th generation DHN, these parameters take values for the supply temperature $t_s \sim 70$°C and return $t_r \sim 25$°C [4]. Fourth-generation systems should involve integration of renewables into the network [5]. If, in addition to heating, the district heating network also provides cooling, this is referred to as 5th Generation District Heating and Cooling Network (5GDHC) [6].

Merlet et al. [7] proposed a methodology to optimize the multi-stakeholder temperature reduction in the design of district heating distribution networks. The authors applied identification of the system bottlenecks and focused the retrofit measures on them, formulating dynamic optimisation problems.

The energy and economic benefits of reducing grid temperatures using different heat sources have been analysed by Geyer et al. [8]. The authors discussed that in the case of alternative heat technologies, such as heat pumps and solar panels, higher monetary sensitivity is observed compared to traditional heat technologies. Thus, future heat networks are expected to have higher economic benefits and monetary savings.

The economic optimisation of the insulation thickness of buried double pipes was analysed by Li et al. [9] aiming to minimise energy losses. The developed a model to optimise insulation and minimum total annual cost, and demonstrated the different effects of sensitivity factors on the parameters. The focus was on only one type of pipe found in the district heating network studied.

The thermal and economic analysis was made by Nowak-Ocłoń and Ocłoń [10]. It shows, by means of an analytical heat loss model, the cost effectiveness of TwinPipe in comparison with various types of single pre-insulated pipe. However, the heat loss here was determined in a simplified one-dimensional approach.

Ocłoń et al. [11] in another paper made a comparison between a numerical method and an analytical method for determining heat loss in underground heating network pipes. The calculations were performed for different diameters of two types of pipe systems: single pipes and TwinPipe arrangement. Differences between the results of calculations using the analytical model (1D) and the numerical model (2D) did not exceed 10%. The three dimensional space was neglected there.

Wang et al. [12] in their work proposed a method for estimating the heat loss of a ground heat network based on hourly measurements in each section of the network, which a genetic algorithm (GA) was used to solve. This method of optimization makes it possible to detect a more precise location of insulation or conductor defects in the network. The calculation results showed good agreement with the measured results. This model may not be suitable for real-time applications where computer resources or high-speed data processing capabilities may be limited.

Chicherin [13] in his work proposed another way to determine heat loss. He created a model that took into account the correlation between the amount of heat produced and outdoor temperatures by considering a linear regression function. The difference between the results from this method and the results from the actual heat losses in the existing analysed network ranges from 0.4% to 1.2%. Sartor et al. [14] proposed a dynamic model that determines the temperature of the medium taking into account ambient losses and the thermal inertia of the pipe. The finite volume method (FVM) was used. The results from the 1D model were compared with the results from the 2D model. The calculations were made using ANSYS software. The method may have been validated on specific case studies in certain regions, which may limit its generalizability to other areas with different geographical, economic or infrastructural characteristics. Wider validation in different contexts would be required to ensure its wider applicability.

Danielewicz et al. [15] compared the results of numerical calculations of heat loss in pre-insulated pipes with the results of in-situ measurements. The validation process confirmed the high quality of the model, as the differences between the ground temperatures were about 0.1°C. The calculations were carried out for a single type of pre-insulated pipe laid in parallel. The three-dimensional numerical model is computationally demanding, which may limit its practical application in large-scale or real-time scenarios. A simplified model was presented in the work of Jakubek et al. [16]. They compared the results of heat losses in the ground calculated by analytical solution (1D model) with the measurements on the dedicated experimental setup. Calculations were performed for different diameters (DN40, DN50, DN65) and pipe types: TwinPipe system and a single pre-insulated system. The difference between them was less than 10% based on the type of system.

Chen et al. [17] proposed a mathematical model for calculating the economic efficiency of a pipeline network by optimising the structural parameters involved in laying these pipes, based on the TOTS (two supply/one return, triple pipe structure) heat loss theory of a fourth generation district heating system. Suitable parameters were identified for which the total loss cost would be the lowest. Thermal analysis of the same fourth generation TOTS pipe system was analysed in the article by Xu et al. [18]. The heat losses for this type of network system have been calculated using an analytical model, and the numerical simulations have a high accuracy, with a deviation of 2%. The proposed heat loss model provides an innovative solution for low temperature district heating systems. It introduces additional complexity in terms of design, installation and maintenance compared to traditional two-pipe systems. It can lead to higher initial costs and requires specialist knowledge. Further research and validation is needed to assess its practicality, economic viability and long-term performance under different real-world conditions.

An analysis of the energy efficiency of another type of district heating network: flexible pre-insulated double pipes with symmetrical or asymmetrical insulation, double pipes and triple pipes was carried out by Dalla Rosa et al. [19]. Using a 2D model based on the Finite Element Method (FEM), the heat loss was determined and the results were verified with good agreement with experimental measurements and analytical formulae. The energy saving potential of asymmetric double pipe insulation, double pipe insulation and triple pipe insulation is about 10%, depending on the type of system. The method is based on simplifications: homogeneous soil conditions, constant flows or thermal steady states, which may not reflect all the complexities of real district heating systems. In order to apply it more widely, further validation would be required, taking into account the specific context, economic factors and potential technological advances.

Krawczyk and Teleszewski [20], in their work, proposed changing the cross-sectional geometry of the thermal insulation in double heating from round to ovoid in order to reduce heat losses in networks. Heat loss was determined using a boundary element method (BEM) plotting program, and the results showed that the larger insulation area in the supply pipe contributed to a reduced heat flux density around the supply pipe, resulting in a significant reduction in heat loss. Due to geographical limitations, the specificity of the solutions used, and the need for further long-term analyses, a cautious approach is necessary when attempting to generalize the results to other heating systems.

Teleszewski et al. [21] proposed the use of a quadruple-heated pre-insulated network and utilized a 2D numerical model to compare the heat loss results of single and double pipes. The results contributed to a significant reduction in heat losses compared to the existing single pre-insulated network (up to 57.1%). To apply the results on a larger scale or in other regions, further research should be conducted, including an economic assessment of this solution and its impact on the operational flexibility of the heating system.

Jing et al. [22] proposed the use of cured-in-place pipe (CIPP) liners with improved insulation function to reduce heat loss, which reduced the heat loss of the ageing pipe by 55.4% in numerical calculations. To better assess the potential of the proposed method, further research and validation in various contexts are necessary.

The presented studies have demonstrated methods for determining heat losses and their reduction in district heating networks. To gain a better understanding of the problem in these networks, it is also necessary to consider its impact on the ground during operation. In this article, the temperature distribution in the ground during the operation of district heating networks was analysed for two of the most popular types of pipes: single parallel pre-insulated pipes system and TwinPipe system (two pipes in one insulation). The calculations were carried out on a 3D model using CFD analysis in Ansys software [23] for three different diameters: DN40, DN50 and DN65. The results were compared with test bench measurements.

2. Experimental setup

In this chapter, the experimental setup will be presented, where the operation of the heating network system was simulated. Temperature measurements were conducted on two representative types of pipes.

The experimental laboratory stand (Fig. 1) is used to determine the heat losses and temperature distribution in the underground district heating network. The analysis concerns two types of pipes – two separate preinsulated pipes (parallel layout) and two pipes in one preinsulated system (TwinPipe).

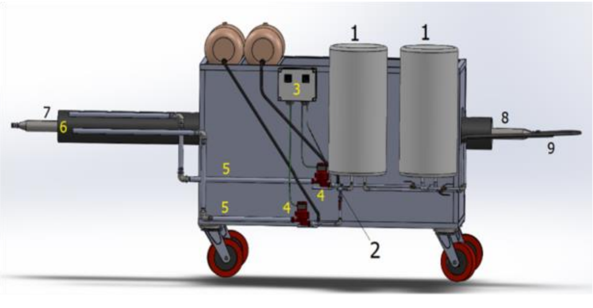

Fig. 1. The 3D model of the experimental laboratory setup.

The schematic diagram of the working medium is shown in Fig. 2. The demineralized water is heated to the desired temperature in two independent open systems (electric storage heater). The main function was the initialisation of the hydrostatic pressure for centrifugal pumps and removing the air bubbles from the system by using a non-pressure tank.

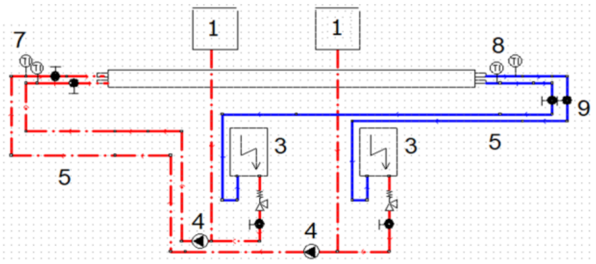

Fig. 2. The circulation flow diagram of the experimental-stand device.

The markings shown in Fig. 1 and Fig. 2 are described as follows:

- no 1 – the electric water heater tank for supply and return pipe,
- no 2 – temperature measurement sensors (two separate),
- no 3 – temperature regulators,
- no 4 – centrifugal pumps,
- no 5 – pipeline,
- no 6 – preinsulated pipe,
- no 7, 8 – temperature measurement points – inlet and outlet,
- no 9 – flow measurements point.

Each of the circuits has two separate temperature measurement sensors. Information about the liquid temperature goes to the temperature regulators which turn on or off the heater system. The refrigerant goes to the pumps forcing the liquid circulation. Then, through an insulated pipeline, it goes to one of the examined types of preinsulated pipes. The temperature is measured at the inlet and at the outlet of preinsulated pipes. Measurement of the flow with a turbine sensor is located at the outlet of the pipeline.

The temperature was measured with a digital thermometer, which measures temperatures from –55°C to +125°C (–67°F to +257°F). The accuracy from –10°C to +85°C is ± 0.5°C. The frequency of the measurements was 1 Hz at the same time in all measurement points. The location of the temperature sensors depends on the system used. The temperature is measured at the inlet and outlet of the pre-insulated pipes and on the outer surface of the casing. For the variant with single pipes, two sections of pre-insulated pipes with a length of 3.0 m (length of the insulated surface) were mounted to the device. The diagram of the location of the temperature sensors is presented in Fig. 3.

Sensors No. 3 – No. 6, No. 13 – No. 16 are sensors recording the temperature on the outer surface of the pipes. Sensors No. 9 – No. 12 are sensors recording the temperature of the soil between the supply and return pipes (Fig. 3).

The arrangement of the temperature sensors for TwinPipe configuration is shown in Fig. 4. The sensors were recording the temperature of the outer surface of the pipe in the soil. The parameters were checked before heating up activity. The estimated proportion of the clay and sandy soil in the compound is 50/50.

Sensors No. 3 – No. 6, are sensors recording the temperature on the outer surface of the pipe.

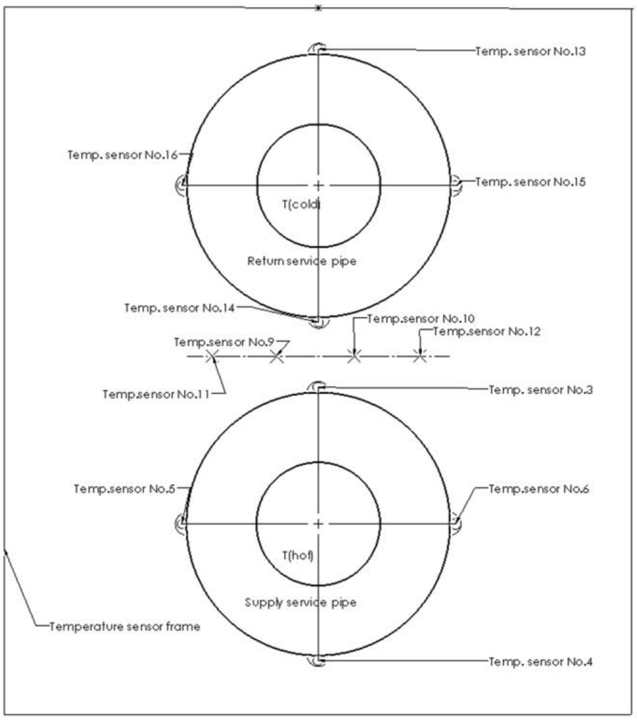

Fig. 3. Arrangement of temperature sensors.

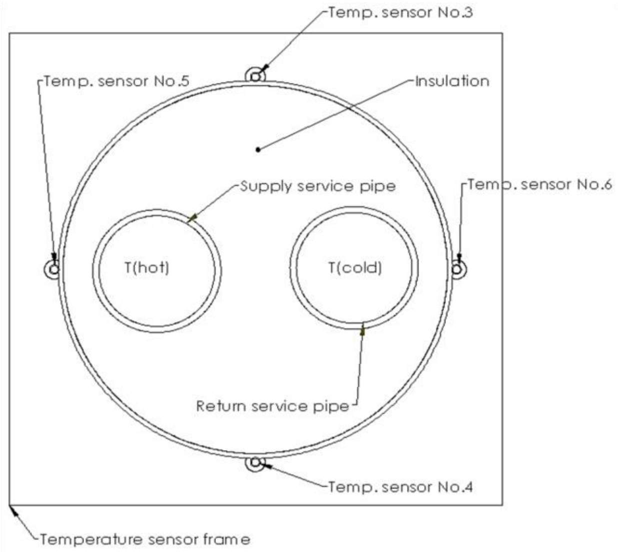

Fig. 4. Arrangement of temperature sensors for TwinPipe configuration.

2.1. Parameters of the soil, linear dimensions of single parallel pre-insulated system and TwinPipe system

The parameters of the soil used at the experimental laboratory setup are presented in the following:

- thermal conductivity coefficient: $k_{gr} = 2.2$ W/(m K),
- degree of moisture: 24%,
- density: $\rho = 1800$ kg/m^3.

The presented results refer to average parameters of the soil used in trials. The parameters were checked before heating up activity. Pure sandy soil is characterized by high proportion of the sand and little clay. They are quicker to warm up in comparison to clay soil but tend to dry in summer. The pure clay soil remains wet and coils in winter, clay soil has an ability to hold high amounts of water. In order to that warming up takes longer. The estimated proportion of the clay and sandy soil in the compound is 50/50.

Based on the research [23], the soil with 5% of humidity compared to the soil with 15% of humidity gives a 50% higher heat transfer coefficient, 0.62 W/(m K) and 1.20 W/(m K), respectively. The heat conductivity coefficient depends on the density of soil. For the humidity of 20%, and the densities of 1000 kg/m^3 and 2000 kg/m^3, it is 0.5 W/(m K) and 1.4 W/(m K), respectively.

The experimental laboratory stand was designed based on information included in standards for TwinPipes [24] and for single pre-insulated pipes in a parallel configuration [25]. Parameters of the pre-insulated pipes system and linear dimensions are shown as follows (Fig. 5).

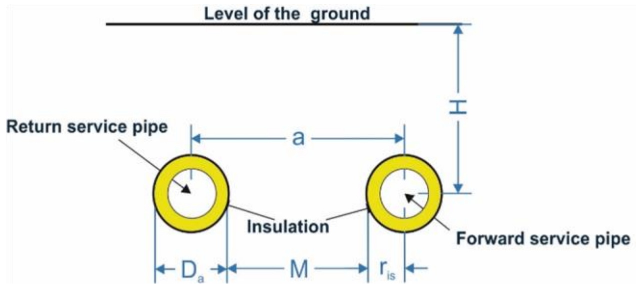

Fig. 5. Scheme of the underground preinsulated single pipe system.

Linear dimensions are included in Table 1.

Table 1. The parameters of the underground preinsulated parallel pipe system for DN40, DN50 and DN65.

	DN40	DN50	DN65
a [mm]	170	170	170
M [mm]	30	45	60
D_a [mm]	140	125	110
H [mm]	455	455	455
r_{is} [mm]	70.0	62.5	55.0
h_m [mm]	385.0	392.5	400.0

Material and insulation (polyurethane rigid foam insulation – PUR) properties meet the requirements included in the norm EN 253:2019+A1:2023 [26].

Parameters of the TwinPipe system and its linear dimensions are shown in Fig. 6 and in Table 2.

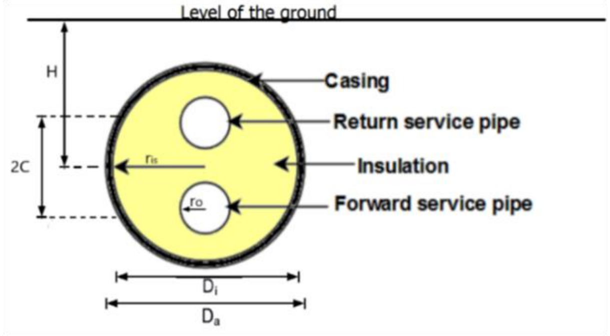

Fig. 6. Scheme of the underground TwinPipe system.

Table 2. The parameters of the underground TwinPipe system for DN40, DN50 and DN65.

	DN65	DN50	DN40
a [mm]	48.05	40.15	34.15
D_a [mm]	225.0	200.0	160.0
H [mm]	385.0	392.5	400.0
r_{is} [mm]	108.3	95.8	75.8
r_o [mm]	38.05	30.15	24.15

3. The numerical model

The temperature distribution analysis was conducted using Ansys software. DesignModeler was utilized for geometric modelling, while the Fluent module was employed for simulating temperature distribution in the ground near the district heating network [27]. The results were also compared with experimental data. A three-dimensional heat conduction equation is solved to determine the maximum temperature within the heating network $T = T(x, y, z)$. The heating network is composed of layers tube (t), insulation (ins) and ground (gr). The convective heat transfer occurs between the fluid flowing inside the supply (s) and return (r) tubes.

- For the tube domain:

$$k_t \frac{\partial^2 T}{\partial x^2} + k_t \frac{\partial^2 T}{\partial y^2} + k_t \frac{\partial^2 T}{\partial z^2} = 0; \tag{1}$$

- For the insulation domain:

$$k_{ins} \frac{\partial^2 T}{\partial x^2} + k_{ins} \frac{\partial^2 T}{\partial y^2} + k_{ins} \frac{\partial^2 T}{\partial z^2} = 0\,; \tag{2}$$

- For the ground domain

$$k_{gr} \frac{\partial^2 T}{\partial x^2} + k_{gr} \frac{\partial^2 T}{\partial y^2} + k_{gr} \frac{\partial^2 T}{\partial z^2} = 0, \tag{3}$$

where: x, y – are Cartesian coordinates of a specified point that belongs to the heat transfer domain, k – is the thermal conductivity specified for the different computational domains, i.e. for the tube wall material $k_t = 30$ W/(m K), for the insulation material $k_{ins} = 0.042$ W/(m K), for the soil layer $k_{gr} = 2.2$ W/(m K).

The boundary conditions are:

- For the supply pipe:

$$k_t \frac{\partial T}{\partial r}\Big|_{r=r_{in}} = h_s(T - T_s); \tag{4}$$

- For the return pipe:

$$k_t \frac{\partial T}{\partial r}\Big|_{r=r_{in}} = h_r(T - T_s), \tag{5}$$

where r_{in} is an inner radius of the supply/return pipe; h_s and h_r are the water side heat transfer coefficients from the supply (s) and return (r) side.

The mesh boundary conditions are prepared in the Design Modeler module. The geometry and mesh discretization is shown in Fig. 7. The multizone method with prism mapping was applied. The minimum edge length is 0.13163 m. The number of nodes and elements are 68488 and 58265, respectively. The element size is defined as 0.008 m. Five layers of inflation with a 1.2 rate of growth are used on “hot” and “cold” areas.

Fig. 7. The geometry model after discretization process (mapped mesh type applied: prism).

The applied boundary conditions according to the temperature, thermal conductivity and fluid flow are as follows:

- Inlet_1:
  - Velocity magnitude: 1 m/s,
  - Fluid temperature: 85°C,
- Inlet_2:
  - Velocity magnitude: 1 m/s,
  - Fluid temperature: 45°C,
- Soil_clay:
  - Temperature: 19°C.

The number of iterations is 500. The parameters of the layers of each geometry correspond to the values obtained during laboratory investigations.

The temperature of the fluid inside the pipes was imposed as a boundary condition, with values based on the results obtained from laboratory experiments. The heat transfer coefficients on the fluid side (h_s, h_r) were assumed as constant values, in accordance with the model assumptions and based on the measurement data.

4. Results and discussion

The selected results of measurements, computations, and comparisons, covering three measurement series for different sizes of pre-insulated pipes in single parallel and TwinPipe configurations. The thermal conductivity of the insulation had been verified separately for each case. Temperature results are from the steady state thermal condition (approx. after 3.5 h of heating up). The initial temperature of the soil was used in the numerical simulation as input data.

The experimental data, computations, and comparison of results for the single parallel configuration pipes for different diameters are shown in Figs. 8–10. In these figures, (a) are the results from an experimental stand, and (b) are the results from temperature distribution simulations. The temperature values in the ground (nodes 9–12 in Fig. 3) are presented in Tables 3–5.

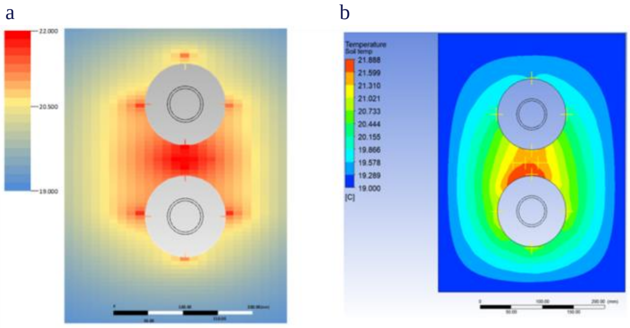

Fig. 8. Temperature distribution on the single parallel configuration DN40 – experimental stand (a), numerical simulation (b).

Table 3. The average temperature from an experimental stand and numerical analysis for single parallel configuration (DN40).

		Numerical simulation	Experimental stand	Relative error σ [%]
Temp. of the soil between pipes [°C]	No. 9	21.55	20.80	3.61
	No. 10	21.55	20.55	4.87
	No. 11	21.05	19.55	7.67
	No. 12	21.25	19.90	6.78
Ave. temp. of soil [°C]		21.35	20.75	2.89

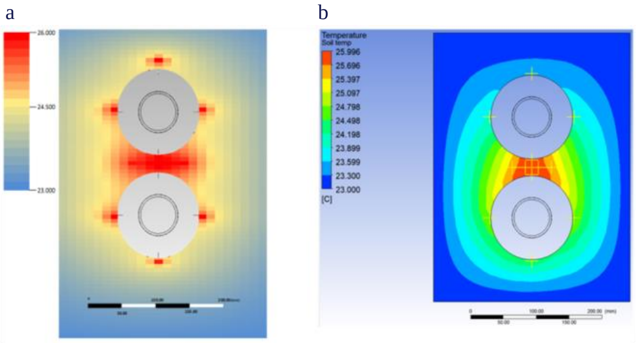

Fig. 9. Temperature distribution on single parallel configuration DN50 – experimental stand (a), numerical simulation (b).

Table 4. The temperature from an experimental stand and numerical analysis for single parallel configuration (DN50).

		Numerical simulation	Experimental stand	Relative error σ [%]
Temp. of the soil between pipes [°C]	No. 9	25.85	25.30	2.17
	No. 10	25.85	25.75	0.39
	No. 11	25.55	25.60	0.20
	No. 12	25.55	24.60	3.86
Ave. temp. of soil [°C]		25.70	25.30	1.58

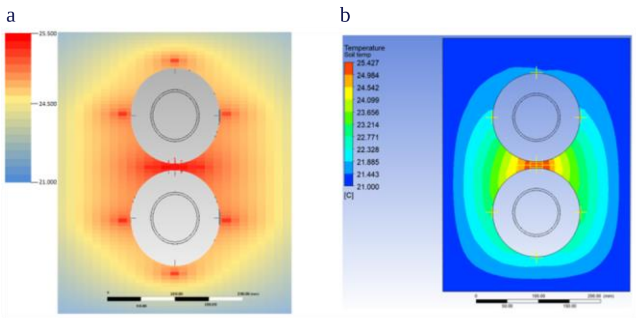

Fig. 10. Temperature distribution on single parallel configuration DN65 – experimental stand (a), numerical simulation (b).

Table 5. The temperature from an experimental stand and numerical analysis for single parallel configuration (DN65).

		Numerical simulation	Experimental stand	Relative error σ [%]
Temp. of the soil between pipes [°C]	No. 9	25.25	24.50	3.06
	No. 10	25.35	24.25	4.54
	No. 11	24.55	23.30	5.36
	No. 12	24.65	23.20	6.25
Ave. temp. of soil [°C]		24.95	23.80	4.83

The results of calculations for the second type of pipes configuration – TwinPipe system are presented below in Figs. 11–13. The temperature values in the ground (nodes 3–6 in Fig. 4) are presented in Tables 6–8.

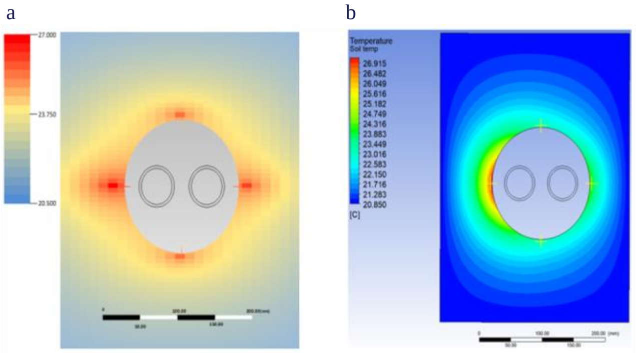

Fig. 11. Temperature distribution on TwinPipe configuration DN40 – experimental stand (a), numerical simulation (b).

Table 6. The temperature from an experimental stand and numerical analysis for TwinPipe configuration (DN40).

		Numerical simulation	Experimental stand	Relative error σ [%]
Temp. of the soil between pipes [°C]	No. 3	21.35	20.30	5.17
	No. 4	21.45	20.40	5.15
	No. 5	26.75	25.30	5.73
	No. 6	22.85	22.40	2.01
Ave. temp. of soil [°C]		23.10	22.70	1.76

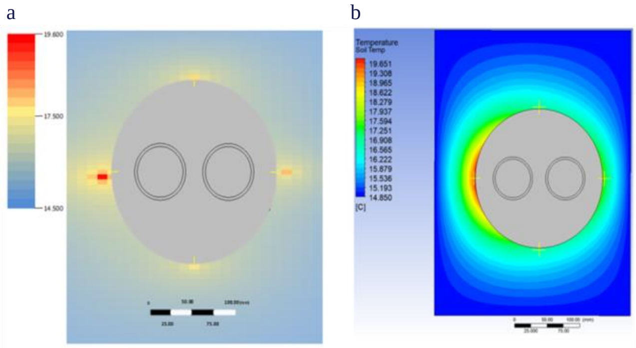

Fig. 12. Temperature distribution on TwinPipe configuration DN50 – experimental stand (a), numerical simulation (b).

Table 7. The temperature from an experimental stand and numerical analysis for TwinPipe configuration (DN50).

		Numerical simulation	Experimental stand	Relative error σ [%]
Temp. of the soil between pipes [°C]	No. 3	16.85	15.20	10.86
	No. 4	16.75	15.30	9.48
	No. 5	19.55	17.80	9.83
	No. 6	17.45	15.60	11.86
Ave. temp. of soil [°C]		17.65	16.00	10.31

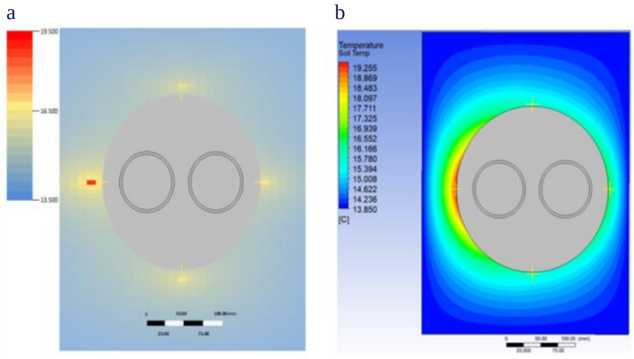

Fig. 13. Temperature distribution on TwinPipe configuration DN65 – experimental stand (a), numerical simulation (b).

Table 8. The temperature from an experimental stand and numerical analysis for TwinPipe configuration (DN65).

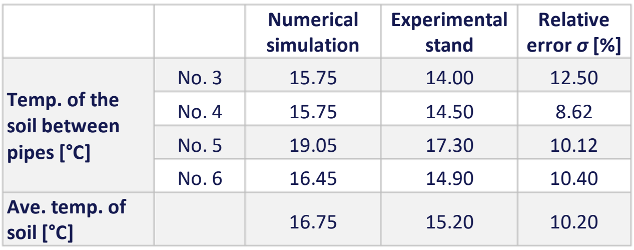

		Numerical simulation	Experimental stand	Relative error σ [%]
Temp. of the soil between pipes [°C]	No. 3	15.75	14.00	12.50
	No. 4	15.75	14.50	8.62
	No. 5	19.05	17.30	10.12
	No. 6	16.45	14.90	10.40
Ave. temp. of soil [°C]		16.75	15.20	10.20

The difference between the numerical calculation and the measured results for the ground temperature distribution around the district heating network pipe varies between 0.2% and 12% (approximately 5% for single parallel pipes and 10% for TwinPipe).

Figures 8–13 show how to interpret the temperature distribution in the ground, where the greatest losses occur. Knowing these values gives you the opportunity to propose design solutions that will reduce heat loss in the areas concerned.

5. Conclusions

This paper presents an analysis of the temperature distribution in the surrounding soil, determined through numerical heat transfer simulations. The computed temperature values were compared with experimental measurements obtained from a dedicated test setup. The agreement between the experimental results and numerical modelling of the heating network's temperature distribution is satisfactory, with a relative error of less than 10%. Specifically, the difference between the computational approach and experimental data is approximately 5% for the single pre-insulated pipe system and 10% for the TwinPipe system. Additionally, the temperature drop between the heating medium and the surrounding ground is lower for the TwinPipe configuration.

The proposed model can serve as a practical tool for the design, optimization and retrofitting of district heating networks. Additionally, it can be extended to analyse the interaction between underground heating networks and other energy infrastructure. Future research should focus on expanding the numerical model to incorporate transient heat transfer effects and different soil compositions, further improving the accuracy of heat loss predictions.

References

[1] European Commission: Energy statistical country datasheets, February 2021.

[2] Lund, H., Duic, N., Østergaard, P.A., & Mathiesen, B.V. (2018). Future district heating systems and technologies: On the role of smart energy systems and 4th generation district heating. *Energy*, 165, 614–619. doi: 10.1016/j.energy.2018.09.115

[3] Ziębik, S., & Stanek, W. (2023). Energy efficiency – selected thermo-ecological problems. *Archives of Thermodynamics*, 41(2), 277–299. doi: 10.24425/ather.2020.133633

[4] Jiang, M., Rindt, C., & Smeulders, D.M.J. (2022). Optimal Planning of Future District Heating Systems – A Review. *Energies*, 15(19), 7160. doi: 10.3390/en15197160

[5] Buffa, S., Cozzini, M., D'Antoni, M., Baratieri, M., & Fedrizzi, R. (2019). 5th generation district heating and cooling systems: A review of existing cases in Europe. *Renewable and Sustainable Energy Reviews*, 104, 504–522. doi: 10.1016/j.rser.2018.12.059

[6] Lund, H., Werner, S., Wiltshire, R., Svendsen, S., Thorsen, J.E., Hvelplund, F., & Mathiesen, B.V. (2014). 4th Generation District Heating (4GDH). *Energy*, 68, 1–11. doi: 10.1016/j.energy.2014.02.089

[7] Merlet, Y., Baviere, R., & Vasset, N. (2023). Optimal retrofit of district heating network to lower temperature levels. *Energy*, 282, 128386. doi: 10.1016/j.energy.2023.128386

[8] Geyer, R., Krail, J., Leitner, B., Schmidt, R.-R., & Leoni, P. (2021). Energy-economic assessment of reduced district heating system temperatures. *Smart Energy*, 2, 100011. doi: 10.1016/j.segy.2021.100011

[9] Li, F., Jie, P., Fang, Z., & Wen, Z. (2021c). Determination of the optimal economic insulation thickness of buried double pipes for district heating systems. *Frontiers in Energy*, 15(1), 170–185. doi: 10.1007/s11708-020-0680-5

[10] Nowak-Ocłoń, M., & Ocłoń, P. (2020). Thermal and economic analysis of preinsulated and TwinPipe heat network operation. *Energy*, 193, 116619. doi: 10.1016/j.energy.2019.116619

[11] Ocłoń, P., Nowak-Ocłoń, M., Vallati, A., Quintino, A., & Corcione, M. (2019). Numerical determination of temperature distribution in heating network. *Energy*, 183, 880–891. doi: 10.1016/j.energy.2019.06.163

[12] Wang, H., Meng, H., & Zhu, T. (2018). New model for onsite heat loss state estimation of general district heating network with hourly measurements. *Energy Conversion and Management*, 157, 71–85. doi: 10.1016/j.enconman.2017.11.062

[13] Chicherin, S. (2022). A method for assessing heat losses in developing countries with a focus on operational data of a district heating (DH) system. *Sustainable Energy Grids and Networks*, 30, 100616. doi: 10.1016/j.segan.2022.100616

[14] Sartor, K., Thomas, D., & Dewallef, P. (2018) A comparative study for simulating heat transport in large district heating networks. *Heat Technology*; 36, 301–308. doi: 10.18280/ijht.360140.

[15] Danielewicz, J., Śniechowska, B., Sayegh, M.A., Fidorów, N., & Jouhara, H. (2016). Three-dimensional numerical model of heat losses from district heating network pre-insulated pipes buried in the ground. *Energy*, *108*, 172–184. doi: 10.1016/j.energy.2015.07.012

[16] Jakubek, D., Ocłoń, P., Nowak-Ocłoń, M., Sułowicz, M., Varbanov, P.S., & Klemeš, J.J. (2023). Mathematical modelling and model validation of the heat losses in district heating networks. *Energy*, 267, 126460. doi: 10.1016/j.energy.2022.126460

[17] Chen, X., Ren, L., Zheng, Q., Yang, G., Akkurt, N., Liu, L., Liu, Z., Qiang, Y., Yang, H., Xu, Q., & Ding, Y. (2023). Heat loss optimization and economic evaluation of a new fourth generation district heating triple pipe system. *Applied Thermal Engineering*, 233, 121160. doi: 10.1016/j.applthermaleng.2023.121160

[18] Xu, Q., Wang, K., Zou, Z., Zhong, L., Akkurt, N., Feng, J., Xiong, Y., Han, J., Wang, J., & Du, Y. (2021). A new type of two-supply, one-return, triple pipe-structured heat loss model

based on a low temperature district heating system. *Energy*, 218, 119569. doi: 10.1016/j.energy.2020.119569

[19] Dalla Rosa, A., Li, H., & Svendsen, S. (2011). Method for optimal design of pipes for low-energy district heating, with focus on heat losses. *Energy*, 36(5), 2407–2418. doi: 10.1016/j.energy.2011.01.024

[20] Krawczyk, D.A., & Teleszewski, T.J. (2019). Reduction of heat losses in a pre-insulated network located in central Poland by lowering the operating temperature of the water and the use of egg-shaped thermal insulation: A case study. *Energies*, 12(11), 2104. doi: 10.3390/en12112104

[21] Teleszewski, T.J., Krawczyk, D.A., & Rodero, A. (2019). Reduction of heat losses using quadruple heating pre-insulated networks: A case study. *Energies*, 12(24), 4699. doi: 10.3390/en12244699

[22] Jing, M., Zhang, S., Fu, L., Cao, G., & Wang, R. (2023). Reducing heat losses from aging district heating pipes by using cured-in-place pipe liners. *Energy*, 273, 127260. doi: 10.1016/j.energy.2023.127260

[23] Nikiforova, T., Savytskyi, M., Limam, K., Bosschaerts, W., & Belarbi, R. (2013). Methods and results of experimental researches of thermal conductivity of soils. *Energy Procedia*, 42, 775–783. doi: 10.1016/j.egypro.2013.12.034

[24] EN 15698–1: 2020. (2020) *District heating pipes – Preinsulated bonded twin pipe systems for directly buried hot water networks – Part 1: Twin pipe assembly of steel service pipe, polyurethane thermal insulation and outer casting of polyethylene*.

[25] EN 13941:2020. (2020) *Design and installation of the preinsulated bonded pipe systems for district heating*.

[26] European Committee for Standardization (CEN). EN 253:2019+A1:2023. (2023). *Preinsulated bonded pipe systems for directly buried hot water networks - Pipe assembly of steel service pipe, polyurethane thermal insulation and outer casing of polyethylene. Requirements and test methods*.

[27] *Ansys Academic Research Mechanical*, *Release 19.2* (2018), Pittsburgh, USA.

Co-published by
Institute of Fluid-Flow Machinery
Polish Academy of Sciences
Committee on Thermodynamics and Combustion
Polish Academy of Sciences

http://www.imp.gda.pl/archives-of-thermodynamics/

ARCHIVES OF THERMODYNAMICS

Concept of a test stand for electricity generation from waste heat using wet steam

Wiesław Zima[a*], Artur Cebula[a], Karol Morański[a], Jerzy Cisek[b]

[a]Department of Energy, Cracow University of Technology, Al. Jana Pawła II 37, Cracow 31-864, Poland
[b]Mechanical Department, Cracow University of Technology, Al. Jana Pawła II 37, Cracow 31-864, Poland
*Corresponding author email: wieslaw.zima@pk.edu.pl

Received: 31.01.2025; revised: 05.03.2025; accepted: 10.03.2025

Abstract

The paper presents a concept of an innovative test stand for converting waste heat into electricity using wet steam. Two expanders will be tested, i.e. a rotary blower and a scroll compressor, which have been adapted for reverse cycle operation. The main objective of the stand is to verify experimentally the feasibility of the effective use of an innovative wet steam cycle for waste heat recovery. To verify the design assumptions, as well as the stand configuration and parameters, preliminary simulations were carried out in Ebsilon software. The solution innovation lies in using wet steam to enhance waste heat recovery. Wet steam is generated on the test stand by injecting water into saturated steam using a specially designed nozzle system. In this way, steam dryness can be controlled precisely and proper conditions are created for the expander operation. Saturated steam is generated in the boiler installed at the laboratory of the Department of Energy of the Cracow University of Technology. The test stand will enable the system operation and an assessment of the system's potential applications. This will help to improve the energy efficiency of waste heat utilization and reduce emissions.

Keywords: Waste heat; Wet steam; Expanders; Preliminary results of simulation; Test stand design

Vol. 46(2025), No. 2, 49–56; doi: 10.24425/ather.2025.154905

Cite this manuscript as: Zima, W., Cebula, A., Morański, K., & Cisek, J. (2025). Concept of a test stand for electricity generation from waste heat using wet steam. *Archives of Thermodynamics*, 46(2), 49–56.

1. Introduction

In recent decades there has been a significant increase in the demand for various forms of energy. This increase affects all areas of the economy and is associated with the growth in the world's population and the improvement in the quality of life. Consequently, one of the needs that arise is to implement new distributed generation systems. Therefore, the world literature notes an increased activity in the field of research on new solutions enabling efficient use of various energy sources, including industrial waste heat [1]. The rapid development of the world economy in recent decades is confirmed in [2], which also emphasizes the fact that the recovery of low-temperature waste heat is of high importance for energy savings and emission reduction. However, the recovery faces a number of problems, such as the mismatch between the waste heat supply and demand, or the high investment outlays required for distributed waste heat recovery. The authors of [2] presented the prospects for solving these problems. Woolley et al. presented interesting analyses of waste heat [3]. According to them, the industrial sector consumes a third of global energy, of which up to 50% is ultimately wasted in the form of heat. The problem here is the correct identification of the heat quantity and quality. To solve it, a methodology is proposed for selecting appropriate waste heat recovery technologies and making decisions based on economic benefits. The conclusions resulting from the above publications are also confirmed in [4,5]. The former additionally indicates the capabilities and potential of waste heat recovery in the European Union.

Nomenclature

c – specific heat, kJ/(kg K)
h – enthalpy, kJ/kg
$\dot{m}$ – mass flow rate, kg/h
r – heat of vaporization, kJ/kg
p – pressure, MPa
s – entropy, kJ/(kg K)
t – temperature, °C
x – steam quality

Greek symbols

η – efficiency
Φ – power, kW

Subscripts and Superscripts

c – condensation
g – power generator
in – internal
is – isentropic
m – mechanical
s – steam
w – water
1 – inlet
2 – outlet
$'$ – boiling water
$''$ – saturated steam

Abbreviations and Acronyms

DECUT – Department of Energy of the Cracow University of Technology
ORC – organic Rankine cycle
PE-ORC – partially evaporated organic Rankine cycle
TFC – trilateral flash cycle
WSC – wet steam cycle

Mass and volume flows of waste, as well as temperature levels, are identified. The latter provides a quantitative estimate of global waste heat in various sectors of the economy until 2030. This is combined with an assessment of the environmental impact of waste heat fluxes.

In the literature there are many publications on the use of waste heat, including electricity production. A very popular way of heat utilization is the well-known organic Rankine cycle (ORC), which is widely described in the literature [6]. A review of theoretical and experimental studies on the use of ORC for waste heat recovery is presented in [7]. The paper also includes an analysis of the impact of the cycle configuration, the working fluid, and the operating conditions on the system performance. In many cases, however, ORCs are realized using flammable [8] or toxic [9] agents, the leakage of which is inevitable. A certain level of toxicity and flammability can only be accepted if the leaks are very low. The level of the fluid thermal stability should also be taken into consideration. The literature includes analyses related to various modifications of the organic Rankine cycle. They are mainly theoretical works concerning, for example, the dual-loop ORC for diesel engine waste heat recovery [10], turbine bleeding or regeneration, or both [11]. The analyses carried out in [11] indicate that the ORC integrated with turbine bleeding and regeneration is characterized by the highest heat efficiency.

Another way of utilizing waste heat, widely reported in the literature, is the so-called trilateral flash cycle (TFC). Unlike the ORC, the working liquid in TFC expands from the saturated liquid phase to a two-phase mixture. The significant reduction in exergy losses due to a heat exchanger where no evaporation takes place is the main advantage of TFC. The works in this field are mainly theoretical. In [12], the use of the Engineering Equation Solver is proposed to design TFC. Theoretical energy and exergy analyses are performed for various working fluids, and it is found that the twin-screw expander is the most suitable expander technology for the TFC application. It should be noted here that [13] is one of the first works where twin-screw expanders are indicated as the most suitable option for the TFC operation. A numerical model of a two-phase twin-screw expander and its integration with a TFC system model for low-temperature heat-to-electricity conversion applications are shown in [14]. In contrast to [12−14], in [15] a piston engine is proposed for TFC. In this case, however, it is very important that the liquid should not enter the piston chamber. According to the authors of [15], the biggest advantage of the process is the substantial reduction in exergy losses for the TFC process compared to ORC.

Many papers focus on comparing the performance of ORCs and TFCs. Interesting results are shown in [16], where the electricity generation exergy efficiency is found to be 14−29% higher for TFC compared to ORC. In [17], a solar pond is analysed as a low-temperature heat source for electricity generation. In this case, the results indicate that the ORC energy efficiency is higher than that of TFC.

The few experimental papers available in the literature relate to, for example, a TFC system in which a stationary converging-diverging nozzle with an impulse turbine is used as the expander [18]. The authors of [19] present the results obtained using a prototype system where the function of the expander is performed by a modified twin-screw compressor. An analysis of energy and exergy efficiency is performed using experimental data. The measured efficiency of the twin-screw expander reached about 18%.

The above review of the literature indicates that most theoretical and experimental works are related to the use of the twin-screw expander in waste heat utilization processes. Apart from twin-screw expanders, others are also used, such as vane expanders, scroll expanders and pistol expanders. The comparative assessment of different volumetric expanders presented in [20] confirms that screw expanders are the most suitable devices for waste heat utilization. Considering technical constraints and operational performance, scroll expanders are only slightly inferior to them, and they are also the subject of research and analysis. Du et al. [21] emphasize that due to the lack of efficient low-grade heat recovery technologies, the heat is heavily wasted. They performed a thermodynamic and computational fluid dynamics (CFD) analysis of the scroll expander with respect to a system of energy recovery from a low-grade heat source (127°C) using CO_2. The obtained results were successfully verified on a test stand. A detailed numerical analysis of the impact of various operating parameters on the steady- and transient-state efficiency of the scroll expander is presented in [22]. To obtain an accurate and efficient model of the scroll expander, a method is proposed in [23] that combines the residual ANFIS (adaptive-network-based fuzzy inference system) model with the mechanistic model. The method's high accuracy is confirmed experimentally.

In the literature, it is difficult to find publications on the use of the wet steam cycle (WSC) to convert waste heat into electricity. Being a new technology, WSC has not been sufficiently described yet. WSC should be understood as a thermodynamic cycle in which the expander is supplied with wet steam. In this way, the expansion process in the expander begins and ends in the wet steam region. The partially evaporated organic Rankine cycle (PE-ORC) shows some similarities with WSC [1]. The PE-ORC is a transition cycle between ORC and TFC. The paper [1] is theoretical in nature. However, there are no documented experimental results related to the use of wet steam as a fluid driving the expander. Only occasional information can be found, such as the commercial offer presented in [24], where it is proposed that wet steam energy should be converted into electricity using a twin screw turbine.

An interesting solution is presented in [25]. The report presents the conversion of residual steam into electricity using a rotary blower. To the authors' best knowledge, there are no other studies on the use of the rotary blower in the process of waste heat conversion into electricity.

Considering the literature review presented above, a decision was made to carry out experimental studies related to the use of WSC for the production of electricity from waste heat. Because twin-screw expanders are widely described in the literature, a scroll expander and a rotary blower are proposed for this purpose, as these devices are tolerant of wet steam. Using them to realize a WSC is a new approach to the problem of waste heat utilization. This paper presents preliminary results of calculations and simulations of wet steam cycles, along with a concept of the test stand. Based on the results, a scroll expander, a rotary blower and an alternator with appropriate parameters were selected. The stand will be constructed in the near future at the laboratory of the Department of Energy of the Cracow University of Technology (DECUT).

2. Preliminary computations and simulations

To select expanders and a generator with appropriate parameters, preliminary thermodynamic calculations of selected cycles were performed. The obtained results were compared with the results of simulations carried out using the Ebsilon Professional program [26]. The calculations and the simulations were carried out mainly to select the power of the above-mentioned devices, and to determine the level of steam dryness at their outlet. The input data for the calculations were derived from the steam parameters obtained on the DECUT laboratory current test stand. The stand is equipped, among other things, with a boiler generating mass flow $\dot{m}_s$ = 700 kg/h of saturated steam with a pressure of p = 1 MPa and a temperature of approx. 180°C. The boiler is fired with fuel oil. To obtain wet steam with a set level of dryness, an appropriate mass flow of water with a temperature of about 105°C, taken from the thermal degasser, will be injected into the saturated steam pipeline. The resulting wet steam will then be directed to the expander connected to the generator.

Preliminary calculations were carried out for both expanders, assuming that wet steam expanded to atmospheric pressure at the scroll expander outlet, and to a pressure of 8.5 bar at the rotary blower outlet. Based on commercially available devices, it was further assumed that the rotary blower was fed with the entire mass flow of the generated wet steam, whereas the scroll expander – with about a third.

Selected preliminary calculations and the results obtained therefrom are presented below. Example calculations were performed for both expanders assuming that the steam dryness at their inlet was 0.8. Among other things, the following quantities were calculated: the required mass flow of injection water, the level of the steam dryness at the expander outlet, and the power obtained on the shaft.

2.1. Scroll expander

To obtain wet steam, water with a temperature of approx. 100°C will be injected into the saturated steam produced in the boiler. To heat this water to a saturation temperature (180°C for the pressure of 1 MPa), part of the saturated steam mass flow will condense.

Using a simple power balance equation,

$$\dot{m}_w c_w \Delta t_w = \dot{m}_c r, \tag{1}$$

and a relation describing the steam dryness level (steam quality),

$$x_1 = \frac{\dot{m}_s - \dot{m}_c}{(\dot{m}_s - \dot{m}_c) + (\dot{m}_w + \dot{m}_c)}, \tag{2}$$

the required mass flow of injection water $\dot{m}_w$ = 41.2 kg/h and the mass flow of condensing steam $\dot{m}_c$ = 7.03 kg/h were obtained. These values were obtained assuming that $\dot{m}_s$ = 200 kg/h and x_1 = 0.8.

Next, using the following relations:

$$h_1 = h_1' + x_1 r_1, \tag{3}$$

$$s_1 = s_1' + x_1(s_1'' - s_1'), \tag{4}$$

the enthalpy and entropy of wet steam at the expander inlet were calculated, giving the values of 2374.5 kJ/kg and 5.696 kJ/(kgK), respectively.

The following formula for isentropic expansion:

$$x_{2is} = \frac{s_2 - s_2'}{(s_2'' - s_2')} \tag{5}$$

was used to calculate steam dryness at the outlet of the expander (assuming expansion to atmospheric pressure). The result was 0.726.

Next, using formulae

$$h_{2is} = h_2' + x_{2is} r_2, \tag{6}$$

$$h_2 = h_1 - \eta_{in}(h_1 - h_{2is}) \tag{7}$$

and assuming isentropic expansion and internal efficiency η_{in} = 40%, wet steam enthalpies at the expander outlet were found.

The enthalpy values are 2057.2 kJ/kg and 2247.6 kJ/kg, respectively. The scroll expander internal efficiency is based on [20,27], where the value is given for the steam cycle. According to the authors of [27], the operating capacity of the scroll expander does not depend on the inlet steam dryness. This is a big advantage of such an expander. Owing to it, its usefulness in the case of wet steam, and even in hot water conditions, is increased. The calculated quantities are illustrated in Fig. 1.

The steam dryness at the scroll expander outlet, calculated using the formula

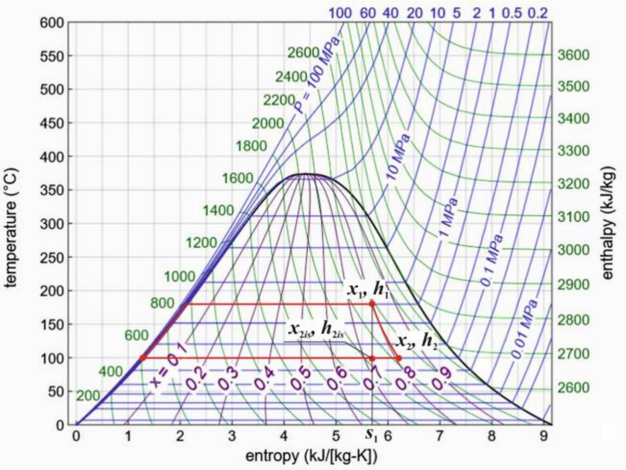

Fig. 1. Scroll expander cycle.

$$x_2 = \frac{h_2 - h_2'}{r_2}, \tag{8}$$

is 0.810.

The available power on the shaft, calculated as

$$\Phi = \frac{(\dot{m}_s + \dot{m}_w)\eta_m (h_1 - h_2)}{3600}, \tag{9}$$

is 7.652 kW. The power achieved in the generator (assuming the generator efficiency of 0.9) totals 6.887 kW.

The results of the simulations performed using the Ebsilon Professional program under the above assumptions are shown in Fig. 2. The simulation data were the parameters of the steam generated in the boiler and the parameters of injection water. The obtained results fully agree with the results of calculations – formulae (1)−(9). Slight discrepancies were observed in the case of the power on the shaft and the power achieved in the generator. This is solely related to the accuracy of the enthalpy and entropy determination.

2.2. Rotary blower

The same calculations were performed for the rotary blower, assuming that $\dot{m}_s$ = 700 kg/h. As there is no literature data on the operation of the rotary blower as an expander, it was assumed that wet steam expanded to a pressure of 8.5 bar and internal efficiency η_{in} = 20%.

Using Eqs. (1)–(9), the following results were obtained:

- injection water mass flow $\dot{m}_w$ = 144.2 kg/h,
- condensing steam mass flow $\dot{m}_c$ = 24.6 kg/h,
- wet steam enthalpy at the expander inlet h_1 = 2374.5 kJ/kg,
- wet steam entropy at the expander inlet s_1 = 5.696 kJ/(kg K),

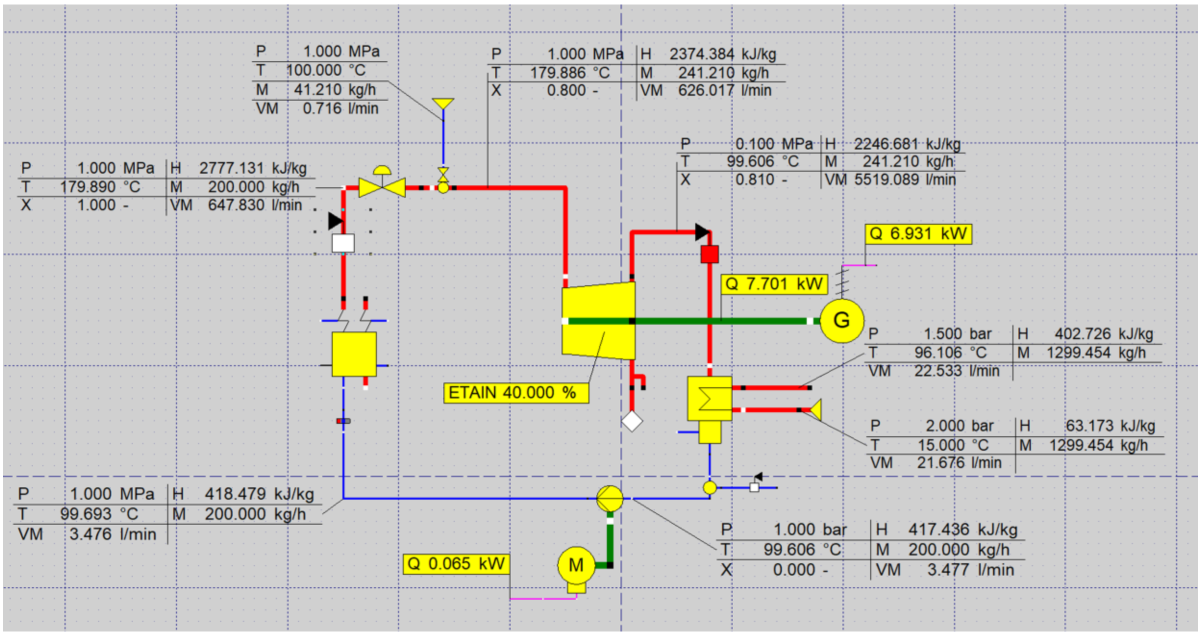

Fig. 2. Ebsilon Professional simulation of a cycle realised using a scroll expander.

- steam dryness at the expander outlet $x_{2is} = 0.793$ (for isentropic expansion),
- wet steam enthalpy at the expander outlet $h_{2is} = 2348.7$ kJ/kg (for isentropic expansion),
- wet steam enthalpy at the expander outlet $h_2 = 2369.7$ kJ/kg (assuming $\eta_{in} = 20\%$),
- steam dryness at the rotary blower outlet $x_2 = 0.803$,
- power on the shaft $\Phi = 1.013$ kW,
- power achieved in the generator (assuming the generator efficiency of 0.9) $\Phi_g = 0.912$ kW.

Selected results of the calculations are shown in Fig. 3. The results of the simulations carried out in the Ebsilon Professional program are illustrated in Fig. 4. The simulation input data were the rated parameters of the boiler steam and the parameters of injection water. As in the case of the scroll expander, the results fully agree with the results of calculations. Like before, slight discrepancies were observed in the case of the power on the shaft and the power achieved in the generator.

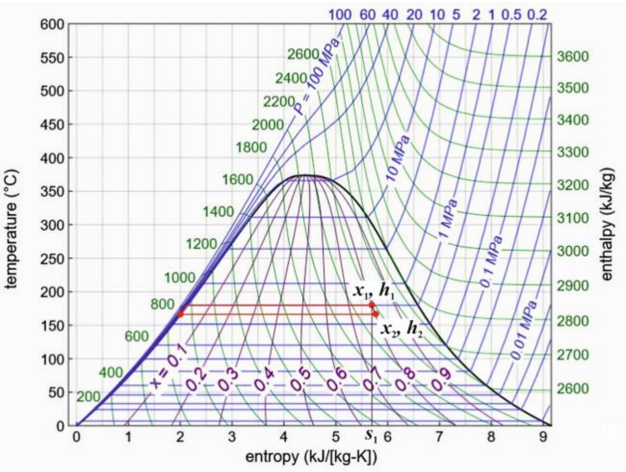

Fig. 3. Rotary blower cycle.

3. Test stand design

The stand design is based on the oil-fired boiler already existing at the DECUT laboratory. Its view is shown in Fig. 5. As previously mentioned, the boiler rated output is 700 kg/h of saturated steam with a pressure of 1 MPa.

Fig. 5. View of the boiler and its equipment.

Based on the calculation and simulation results presented in Section 2, the following devices were selected for experimental studies:

- oil-free scroll compressor (Fig. 6 and Table 1),
- rotary blower (Fig. 7 and Table 2),
- alternator (Fig. 8 and Table 3).

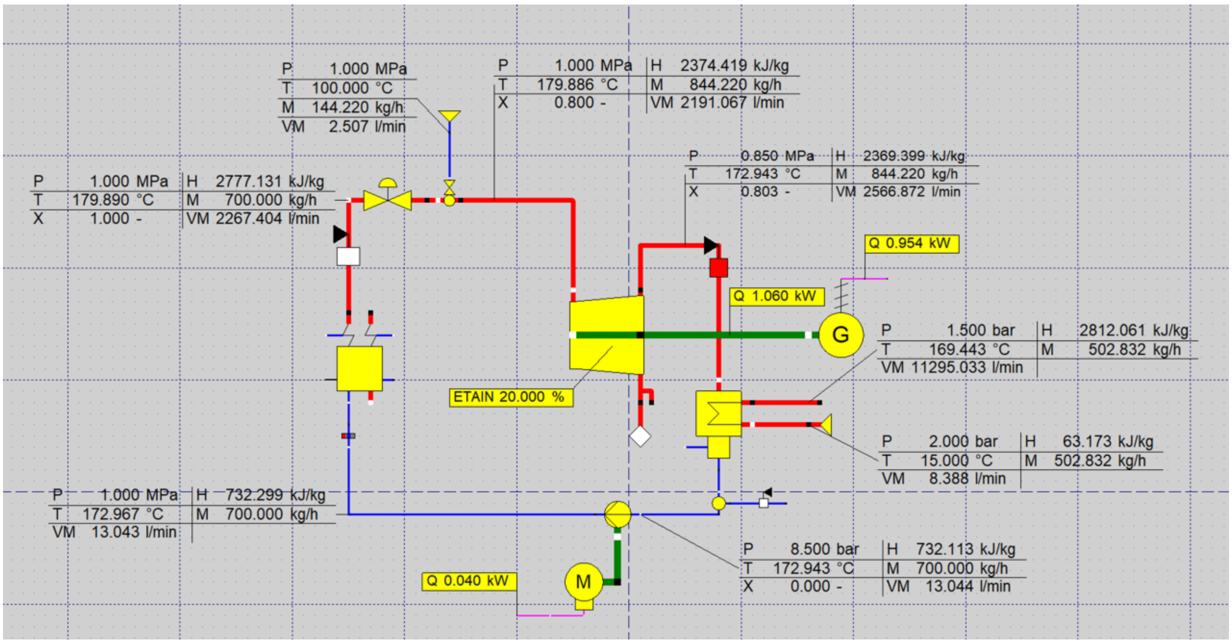

Fig. 4. Ebsilon Professional simulation of a cycle realised using a rotary blower.

Fig. 6. View of the selected oil-free scroll compressor.

Fig. 7. View of the selected rotary blower.

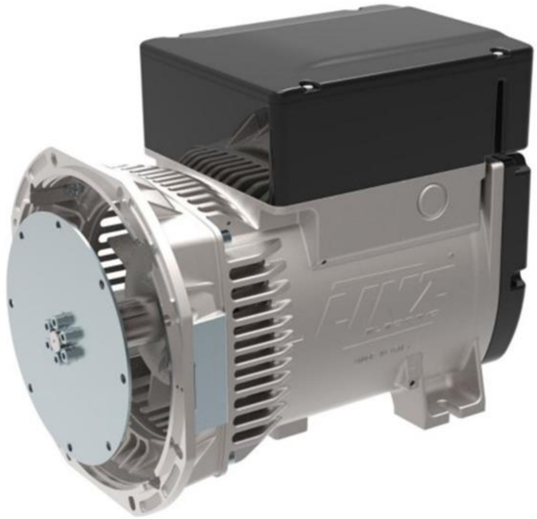

Fig. 8. View of the selected alternator.

Table 1. Selected parameters of the scroll compressor (HitachI SRL-7.5CB).

Parameter	Value	Unit
Maximum working pressure	10	bar
Steam volume flow	~0.7	m^3/min
Power	7.5	kW
Rotational speed	3100	min^{-1}

Table 2. Selected parameters of the rotary blower (Kaeser Omega 42P).

Parameter	Value	Unit
Rated air volume flow	15.91	m^3/min
Minimum rotational speed	900	min^{-1}
Maximum rotational speed	4800	min^{-1}

Table 3. Selected parameters of the alternator (Alternator E1S13S A/4, three-phase synchronous alternator with brushes; compound, 4 poles).

Parameter	Value	Unit
Rated power at 50 Hz	8	kVA
Rated power factor	0.8	–
Air flow requirement	5.4	m^3/min
Maximum over speed	2250	min^{-1}
Frequency	50	Hz
Series star voltage	400/230	V
Efficiency	~85	%

A diagram of the extension of the existing test stand for experimental testing of the selected devices (a scroll compressor and a rotary blower adapted for reverse cycle operation) is shown in Fig. 9.

The stand will also be equipped with a data acquisition system. The following quantities will be measured and collected: the wet steam mass flow, the fluid pressure and temperature at the inlet and outlet of the expanders, rotational speed at different values of the wet steam volume flow, and the amount of generated electricity.

The selected devices (the scroll compressor and the rotary blower) were preliminarily tested for operation in a reverse cycle. Air compressed up to approx. 5 bar was used for this purpose (Fig. 10). No quantity was measured during the tests; the correctness of the device operation was only assessed visually and acoustically.

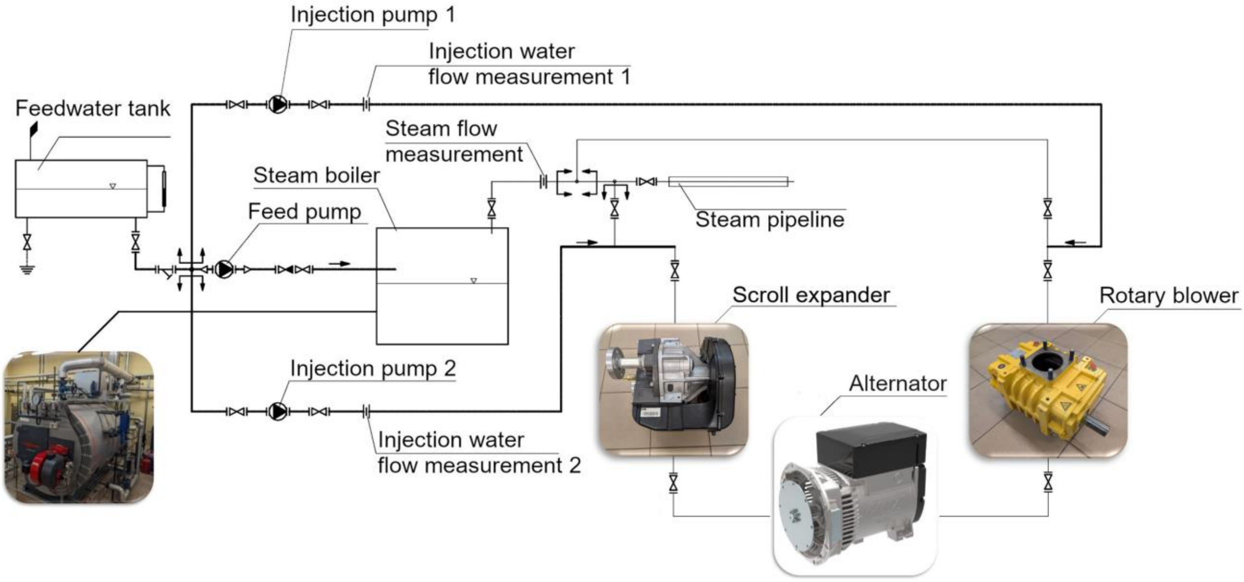

Fig. 9. Diagram of the current test stand at the DECUT laboratory, including the wet steam generation system, expanders and alternator.

Fig. 10. Preliminary tests of the selected devices during their operation in a reverse cycle.

4. Conclusions

The paper presents the concept of a test stand to empirically confirm the possibility of effective utilization of an innovative WSC for waste heat recovery. As part of the research work, it is planned to develop a system enabling the implementation of cycles not used before and using wet steam as a working fluid in the temperature range of approx. 150°C to approx. 450°C. This requires the use of wet steam-tolerant expanders. The solution proposed herein is truly universal and will have an impact on the reduction of CO_2 emissions into the atmosphere.

A vast majority of the waste heat recovery systems now in use are based on well-known ORC systems. They make use of refrigerants/low-boiling liquids. Today’s refrigerants are being replaced by agents that have a less harmful impact on the environment. These substitutes have a low global warming potential (GWP), but some are still harmful, flammable or toxic. In the planned solution, the working fluid is water/steam, and it does not have the adverse properties of refrigerants.

Based on a detailed review of the literature, it was possible to select the scroll compressor and the rotary blower for experimental studies. Obviously, these devices are originally intended for increasing gas pressure at the expense of the supplied electrical energy. After minor modifications, these machines will be fed with wet steam and generate mechanical energy used to drive the generator. The idea of such use is based on the already known trilateral cycle, in which boiling water is fed into an expander where evaporation occurs during the expansion process. As part of this work, it is proposed that the above-mentioned cycle should be developed further for the heat recovery technology by implementing:

- WSC for a wide range of wet steam quality,
- TFC enhancement by the supply of wet steam,
- the use of a wet steam-tolerant expander.

The proposed WSC combines the advantages of the conventional saturated steam process with the thermodynamic advantages of the TFC process.

Preliminary calculations and simulations enabled the selection of a scroll compressor, a rotary blower, and an alternator with appropriate parameters, adapted to the parameters of the saturated steam generated in the boiler installed at the DECUT laboratory. In the near future, the existing test stand will be expanded to the necessary extent. The extension will include, among other things, the generation of wet steam with a set level of dryness, the connection of a scroll compressor, a rotary blower and an alternator, and a data acquisition system.

Some risks that may occur during the stand operation are obtaining wet steam at a set dryness level and adapting the expanders to wet steam.

Acknowledgements

This research is funded in whole by the National Science Centre, Poland (grant UMO-2022/47/B/ST8/02108)

References

[1] Daniarta, S., Kolasiński, P., & Imre, A.R. (2021). Thermodynamic efficiency of trilateral flash cycle, organic Rankine cycle and partially evaporated organic Rankine cycle. *Energy Conversion and Management*, 249, 114731. doi: 10.1016/j.enconman.2021.114731

[2] Xu, Z.Y., Wang, R.Z., & Yang, Ch. (2019). Perspectives for low-temperature waste heat recovery. *Energy*, 176, 1037–1043. doi: 10.1016/j.energy.2019.04.001

[3] Woolley, E., Luo, Y., & Simeone, A. (2018). Industrial waste heat recovery: A systematic approach. *Sustainable Energy Technologies and Assessments*, 29, 50–59. doi: 10.1016/j.seta.2018.07.001

[4] Panayiotou, G.P., Bianchi, G., Georgiou, G., Aresti, L., Argyrou, M., Agathokleous, R., Tsamos, K.M., Tassou, S.A., Florides, G., Kalogirou, S., & Christodoulides, P. (2017). Preliminary assessment of waste heat potential in major European industries. *Energy Procedia*, 123, 335–345. doi: 10.1016/j.egypro.2017.07.263

[5] Firth, A., Zhang, B., & Yang, A. (2019). Quantification of global waste heat and its environmental effects. *Applied Energy*, 235, 1314–1334. doi: 10.1016/j.apenergy.2018.10.102

[6] Macchi, E., & Astolfi, M. (Eds.) (2016). *Organic Rankine cycle (ORC) power systems: Technologies and applications.* Woodhead Publishing.

[7] Mahmoudi, A., Fazli, M., & Morad, M.R. (2018). A recent review of waste heat recovery by Organic Rankine Cycle. *Applied Thermal Engineering*, 143, 660–675. doi: 10.1016/j.applthermaleng.2018.07.136

[8] Tian, H., Wang, X., Shu, G., Wu, M., Yan, N., & Ma, X. (2017). A quantitative risk-assessment system (QR-AS) evaluating operation safety of Organic Rankine Cycle using flammable mixture working fluid. *Journal of Hazardous Materials*, 338, 394–409. doi: 10.1016/j.jhazmat.2017.05.039.

[9] Klimaszewski, P., Zaniewski, D., Witanowski, Ł., Suchocki, T., Klonowicz, P., & Lampart, P. (2019). A case study of working fluid selection for a small-scale waste heat recovery ORC system. *Archives of Thermodynamics*, 40(3), 159–180. doi: 10.24425/ather.2019.129999

[10] Song, J., & Gu, Ch. (2015). Performance analysis of a dual-loop organic Rankine cycle (ORC) system with wet steam expansion for engine waste heat recovery. *Applied Energy*, 156, 280–289. doi: 10.1016/j.apenergy.2015.07.019

[11] Safarian, S., & Aramoun, F. (2015). Energy and exergy assessments of modified organic Rankine cycles (ORCs). *Energy Reports*, 1, 1–7. doi: 10.1016/j.egyr.2014.10.003

[12] Bianchi, G., McGinty, R., Oliver, D., Brightman, D., Zaher, O., Tassou, S.A., Miller, J., & Jouhara, H. (2017). Development and analysis of a packaged trilateral flash cycle system for low grade heat to power conversion applications. *Thermal Science and Engineering Progress*, 4, 113–121. doi: 10.1016/j.tsep.2017.09.009

[13] Smith, I.K. (1993). Development of the trilateral flash cycle system: Part 1: Fundamental considerations. *Proceedings of the Institution of Mechanical Engineers, Part A: Journal of Power and Energy*, 207, 179–194. doi: 10.1243/pime_proc_1993_207_032_02

[14] Bianchi, G., Marchionni, M., Miller, J., & Tassou, S.A. (2020). Modelling and off-design performance optimisation of a trilateral flash cycle system using two-phase twin-screw expanders with variable built-in volume ratio. *Applied Thermal Engineering*, 179, 115671. doi: 10.1016/j.applthermaleng.2020.115671

[15] Steffen, M., Löffler, M., & Schaber, K. (2013). Efficiency of a new triangle cycle with flash evaporation in a piston engine. *Energy*, 57, 295–307. doi: 10.1016/j.energy.2012.11.054

[16] Fischer, J. (2011). Comparison of trilateral cycles and organic Rankine cycles. *Energy*, 36, 6208–6219. doi: 10.1016/j.energy.2011.07.041

[17] Zeynali, A., Akbari, A., & Khalilian, M. (2019). Investigation of the performance of modified organic Rankine cycles (ORCs) and modified trilateral flash cycles (TFCs) assisted by a solar pond. *Solar Energy*, 182, 361–381. doi: 10.1016/j.solener.2019.03.001

[18] Iqbal, M.A., Rana, S., Ahmadi, M., Date, A., & Akbarzadeh, A. (2020). Experimental study on the prospect of low-temperature heat to power generation using trilateral flash cycle (TFC). *Applied Thermal Engineering*, 172, 115139. doi: 10.1016/j.applthermaleng.2020.115139

[19] Guerron, G., Nicolalde, J.F., Martínez-Gómez, J., & Dávila, P. (2024). Implementation of a waste heat recovery prototype facility based on the Rankine cycle with a twin-screw expander. *Applied Thermal Engineering*, 257(A), 124233. doi: 10.1016/j.applthermaleng.2024.124233

[20] Imran, M., Usman, M., Park, B.-S., & Lee, D.H. (2016). Volumetric expanders for low grade heat and waste heat recovery applications. *Renewable and Sustainable Energy Reviews*, 57, 1090–1109. doi: 10.1016/j.rser.2015.12.139

[21] Du, Y., Tian, G., & Pekris, M. (2023). Unsteady and three-dimensional computational fluid dynamics modelling of scroll expander for low-grade waste heat recovery transcritical carbon dioxide micro-scale power system. *Energy Conversion and Management*, 282, 116857. doi: 10.1016/j.enconman.2023.116857

[22] Zhen, K., Shi, L., Zhang, Y., & Peng, B. (2024). Performance prediction and regression analysis of scroll expander based on response surface methodology. *Case Studies in Thermal Engineering*, 60, 104766. doi: 10.1016/j.csite.2024.104766

[23] Ma, X., Lv, X., Li, Ch., & Li, K. (2023). Accurate modelling of the scroll expander via a mechanism-incorporated data-driven method. *International Journal of Refrigeration*, 155, 32–46. doi: 10.1016/j.ijrefrig.2023.09.005

[24] Heliex Power Technology. *Twin screw turbine*. https://www.heliexpower.com/technology [accessed 24 Apr. 2024].

[25] Kaeser (2011). Report Spring 2011. http://www.kaeser.com

[26] STEAG Energy Services GmbH (2019). *Ebsilon Professional Version 14.02 – Release (Patch 2).*

[27] Kim, H.J., Ahn, J.M., Park, I., & Rha, P.C. (2007). Scroll expander for power generation from a low-grade steam source. *Proceedings of the Institution of Mechanical Engineers, Part A: Journal of Power and Energy*, 221(5), 705−711. doi: 10.1243/09576509JPE392

Co-published by
Institute of Fluid-Flow Machinery
Polish Academy of Sciences
Committee on Thermodynamics and Combustion
Polish Academy of Sciences

http://www.imp.gda.pl/archives-of-thermodynamics/

ARCHIVES OF THERMODYNAMICS

Numerical analysis of the effect of chemical reaction and heat source on MHD hyperbolic tangent fluid flow across a non-linear stretching sheet in a porous medium

Srinivas Reddy Kallem[a], Siva Reddy Sheri[a*], Alfunsa Prathiba[b], Gollapalli Shankar[c]

[a]Department of Mathematics, GSS, GITAM (Deemed to Be University), Hyderabad, Telangana-502329, India
[b]Department of Mathematics, CVR College of Engineering, Telanagana-501510, India
[c]Department of Mathematics, B V Raju Institute of Technology, Narsapur, Medak, Telanagana-502313, India
*Corresponding author email: sreddy7@yahoo.co.in

Received: 10.09.2024; revised: 01.02.2025; accepted: 03.02.2025

Abstract

This study investigates the influence of chemical reactions, heat sources, and magnetohydrodynamic effects on the flow of hyperbolic tangent fluid over a nonlinear stretching sheet in a porous medium. Despite significant research on magnetohydrodynamic flows, the combined effects of magnetohydrodynamics, chemical reactions and heat on hyperbolic tangent fluid flow in porous media have not been fully explored, especially under varying electromagnetic conditions. This gap is critical in applications such as geothermal energy extraction, petroleum recovery, polymer processing and cooling systems for electronics. The governing equations for mass, momentum, energy and species transport are transformed into a dimensionless system using similarity transformations and solved numerically using the implicit finite difference method with MATLAB's "bvp4c" solver. Key parameters, including magnetic field strength, porosity, chemical reaction rate and heat source/sink are analysed for their effects on velocity, temperature and concentration profiles. Notably, varying magnetic field strengths significantly influence flow characteristics, offering insights into the behaviour of hyperbolic tangent fluid under different electromagnetic conditions. Results of this study show that magnetohydrodynamic interactions, chemical processes and thermal effects significantly affect the flow dynamics and heat transfer. Additionally, as the Darcy number increases and the permeability of the porous medium rises, so do the shear rates within the pores. This observation underscores the intricate relationship between the shear-thinning behaviour of heat transfer fluids and permeability, providing valuable insights for optimizing flow dynamics in porous media relevant to energy extraction and material processing applications.

Keywords: Chemical reaction; Tangent hyperbolic nanofluid; Heat source; Magnetohydrodynamic effects; Porous medium

Vol. 46(2025), No. 2, 57–67; doi: 10.24425/ather.2025.154906

Cite this manuscript as: Kallem, S.R., Sheri, S.R., Prathiba, A., & Shankar, G. (2025). Numerical analysis of the effect of chemical reaction and heat source on MHD hyperbolic tangent fluid flow across a non-linear stretching sheet in a porous medium. *Archives of Thermodynamics*, 46(2), 57–67.

1. Introduction

The mathematical modelling of heat and mass transfer in nanofluid (NF) flow has sparked widespread attention due to its broad ramifications in a variety of disciplines of applied research and advanced technology. It has several uses in geosciences, the petroleum sector, biotechnology, and biomedicine. As a result, various researchers have studied magnetohydrodynamic (MHD) convection mass and heat transfer in NF flow problems. Shankar Goud et al. [1] numerically analysed the effects of the Eckert and Prandtl numbers on MHD natural convection of an electrically conducting, incompressible viscous fluid flowing through a perpendicular microchannel. The study considered conduction in non-conducting walls and temperature/velocity slip. The coupled momentum and induction equations, accounting for the induced magnetic field, were transformed into nonlinear ordinary differential equations (ODEs) using similarity variables and solved numerically using MAT-

Nomenclature

C – concentration profile, mol
C_f – skin friction coefficient
C_w – concentration of fluid at the wall, mol
C_∞ – ambient concentration of fluid, mol
D_B – Brownian diffusion coefficient, m^2/s
D_T – thermophoresis diffusion coefficient, m^2/s
Ec – Eckert number
$f'(\eta)$– velocity profile
g – gravitational acceleration, m^2/s
$g(\eta)$– dimensionless concentration profile
M – magnetic parameter
n – fluid shear thinning behaviour
Nbt – thermophoretic parameter
Nc – Brownian motion parameter
Nu$_x$– local Nusselt number
Pr – Prandtl number
Q – heat source parameter
R – radiation parameter
Rc – chemical reaction parameter
Re$_x$ – local Reynolds number
Sc – Schmidt number
Sh$_x$ – local Sherwood number
T – fluid temperature, K
T_w – surface temperature, K
T_∞ – ambient temperature, K
u, v – velocity components, m/s
u_w – velocity at the wall, m/s
We – Weissenberg number
x, y – Cartesian coordinates, m

Greek symbols

α – thermal diffusivity, m^2/s
Γ – positive time constant
η – dimensionless similarity variable
$\theta(\eta)$– temperature profile
μ – dynamic viscosity, Pa·s
ν – kinematic viscosity, m^2/s
ρ – density, kg/m^3
σ – electrical conductivity, S/m

Subscripts and Superscripts

∞ − condition at the free stream
w − condition at the surface

Abbreviations and Acronyms

ANN − artificial neural networks
HTF − hyperbolic tangent fluid
MHD– magnetohydrodynamic
NF − nanofluid
NSP – nonlinear stretching plate
NSS – nonlinear stretching sheet

LAB. Graphical results showed that increasing the Hartmann and magnetic Prandtl numbers significantly reduces the volume flow rate. Al Oweidi et al. [2] investigated entropy generation in MHD mixed convection of a Casson nanofluid with Arrhenius activation energy over a nonlinearly stretching sheet and solved it numerically with MATLAB's bvp4c solver. The study showed that increasing the slip parameter increases temperature and decreases entropy generation, while the Brinkman number and concentration gradient have opposing effects on entropy. The Eckert number's influence on temperature is amplified by the presence of nanoparticles. The results were validated by comparison with previous studies. Jamshed et al. [3] explored the effect of electromagnetic radiation and convective slippery circumstances on second-grade nanofluids with permeability. Pal [4] investigated heat and mass transfer in the two-dimensional stagnation-point flow of an incompressible viscous fluid over a stretching vertical sheet, considering the effects of buoyancy force and thermal radiation. Their results, presented in tabular form, demonstrated that thermal radiation leads to an increase in the skin friction coefficient, local Nusselt number and Sherwood number. Asogwa et al. [5] studied Cu-H_2O nanofluids flow past the upright Riga plate, comparing isothermal and ramped wall temperature scenarios. Kandasamy et al. [6] analysed the impact of temperature-dependent fluid viscosity, chemical reactions and thermophoresis on MHD free convective heat and mass transfer in the presence of heat generation/absorption, considering flow over a porous stretching sheet. Dharmaiah et al. [7] numerically analysed heat and mass transfer with viscous dissipation, Joule dissipation and activation energy. Building upon this work, Goud et al. [8] extended the investigation to explore the role of Joule heating and activation energy on MHD heat and mass transfer flow in the presence of thermal radiation. Elbashbeshy and Bazid [9] investigated the thermal transport characteristics of NF flow across an unstable stretched sheet, considering the wobbliness metric and ”Prandtl number” (Pr). Raptis [10] explored radiant heat transfer and spontaneous convection in porous media. Cortell [11] studied heat transfer in the flow of a viscous fluid over a nonlinear stretching plate (NSP). Xuan and Li [12] conducted a theoretical investigation of the thermal conductivity of nanofluids, accounting for the volume fraction, shape and size of nanoparticles.

The HTF model is a popular variant of the classic ”non-Newtonian model” used in chemical engineering because it is computationally efficient, durable and practical. In contrast to empirical connections, this rheological model is based on the liquid kinetic theory, making it a more basic and dependable alternative. Although no one model can completely represent the complicated features of non-Newtonian fluids, the hyperbolic tangent model is an effective tool for understanding their behaviour. Researchers have used this model to examine several elements of non-Newtonian fluid dynamics. For instance, the MHD flow of HTF around a stretched cylinder using the Keller box method was investigated by Malik et al. [13]. Naseer et al. [14] studied the steady boundary layer flow and heat transfer of a tangential hyperbolic fluid flow in the presence of a vertically stretched cylinder. Hayat et. al. [15] investigated the chemically reactive flow of HTF with heat radiation and dual stratification in a porous medium. Nadeem and Akram [16] explored an extensive study on the peristaltic transport of HTF in an asymmetric channel. Reddy et al. [17] in their investigations on MHD hyperbolic tangent fluid flow across a non-linear stretching sheet in a porous medium, focused instead on boundary layer flow and thermophysical properties by implementing the Keller box method. Additional relevant studies involving stretching sheets can be found in the literature, Upadhya et al. [18] and Nadeem and Akram [19].

Convective flow accompanied by concurrent mass and heat transport with chemical reactions is a ubiquitous phenomenon in various applications. Notably, such methods are widespread in the chemical field, power generation and cooling sectors, dyeing, chemical vapour plating on surfaces, nuclear reactor cooling and fossil fuel sectors. Chemical reactions are categorized as either consistent or diverse processes, depending on whether they manifest at a junction or as a singular-phase reaction within a volume. A uniform-phase reaction occurs evenly throughout a given medium, whereas a heterogeneous reaction is restricted to a particular zone or phase surface. The rate of reaction is primarily concentration-dependent, and for first-order reactions, it varies linearly with the concentration. For instance, the creation of smog is a first-order chemical reaction that occurs uniformly throughout the phase, resulting from the discharge of NO_2 from vehicles and chimneys, which exhibits similar behaviour to unburned hydrocarbons skyborne with sunlight influence, to produce “acetyl peroxyl nitrate” $C_2H_3NO_5$, forming a photochemical smog envelope. Sheikh et al. [20] investigated in their study an MHD flow and focused on the effect of chemically reactive species over a stretching sheet, considering thermal radiation and partial slip. Nasir et al. [21] considered the 3D radiative flow of a tangent hyperbolic fluid across a porous stretched sheet using artificial neural networks (ANN) backpropagation and Bayesian regularization. The Cattaneo-Christov flow model, heat radiation, chemical processes and ion slip effects were all included in their study, which used MATLAB's BVP4C solver to train ANN. ANN obtained a great accuracy ($R2 = 1$, MSE $\approx 10{-}11$), reducing the fluid velocity with increased porosity and magnetic parameters, while increasing the thermal profile. Their discoveries have major implications for modern cooling and heating technology. Gaffar et al. [22] explored thermal convection flow of magnetized tangent hyperbolic fluid around a spinning cone in a porous medium using the Brinkman-Darcy-Forchheimer model. The Keller Box approach was used to investigate the fluctuations in velocity, temperature, skin friction and Nusselt number with respect to critical factors. The results revealed that raising the Weissenberg number, Forchheimer number and radiative flux lowered velocities while increasing temperature, whereas higher Darcy numbers increased the velocity near the cone but decreased the temperature.

Further in line with those findings, the study of Shehzad et al. [23] also observes a more rapid decrease in the concentration profile compared to the fluid velocity with an increase in the suction parameter. These findings provide valuable insights into the behaviour of Casson fluids under the combined influence of MHD, mass transfer and chemical reactions.

This study aims to explore the flow dynamics and heat transfer characteristics of a two-dimensional magnetohydrodynamic nanofluid incorporating the hyperbolic tangent velocity model over a nonlinearly stretching sheet. As an extension of the work of Amjad et al. [24] and Ahmed et al. [25], the analysis focuses on understanding the interplay between nonlinear stretching effects, magnetic field influence and nanofluid properties to provide deeper insights into the behaviour of such complex fluid systems. The partial differential equations (PDEs) that govern the flow with the corresponding boundary conditions are transformed into highly nonlinear ODEs using a similarity transformation. The resulting ODEs were numerically solved using the bvp4c solver. The effects of varying key metrics on the velocity, temperature and concentration profiles were examined through graphs.

2. Problem description

In this model (Fig. 1), we consider the ongoing movement of HTF with a fixed density through a nonlinear stretching sheet (NSS). The stretching sheet speed in the *x*-direction is defined as $u = u_w(x) = Bx^{1/3}$, whilst that in the *y*-direction is orthogonal. We postulated a two-dimensional incompressible layer of boundary fluid and investigated the impact of magnetohydrodynamics (MHD). The *y*-axis receives a tunable transverse magnetic field $B = B_0 x^{-1/3}$ (where B_0 is the magnetic flux). T_∞, T_w, C_w and C_∞ denote the ambient temperature, wall temperature, surface concentration and ambient concentration of the fluid, respectively.

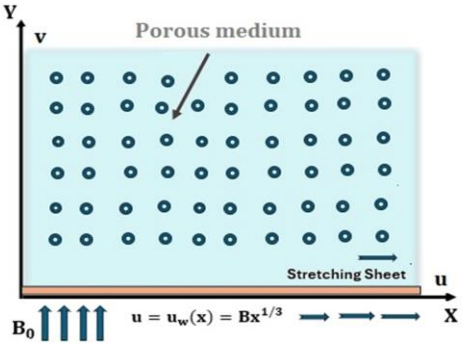

Fig. 1. A systematic depiction of the physical representation.

The theoretical equations for the numerical simulation of the hyperbolic tangent fluid (HTF) flow together with the postulated boundary circumstances are shown below (Amjad et al. [24]):

$$\frac{\partial u}{\partial x} + \frac{\partial v}{\partial y} = 0, \tag{1}$$

$$u\,\frac{\partial u}{\partial x} + v\,\frac{\partial\, u}{\partial y} = \vartheta\left((1-n) + \sqrt{2}n\Gamma\frac{\partial u}{\partial y}\right)\frac{\partial^2 u}{\partial y^2} - \frac{\sigma\, B_0^2(x)}{\rho}u +$$

$$-\frac{\vartheta}{K}\,u\ + g\,\beta^*(T - T_\infty) + g\,\beta_c(C - C_\infty), \tag{2}$$

$$u\frac{\partial T}{\partial x} + v\frac{\partial T}{\partial y} = \alpha\frac{\partial^2 T}{\partial y^2} + \frac{\rho_p\, c_p}{\rho\, c}\left[D_B\frac{\partial C}{\partial y}\frac{\partial T}{\partial y} + \frac{D_T}{T_\infty}\left(\frac{\partial T}{\partial y}\right)^2\right] + \frac{\mu}{\rho c}\left(\frac{\partial u}{\partial y}\right)^2 +$$

$$+\alpha\frac{\partial q_r}{\partial y} + \frac{Q_0}{\rho\, c}\,(T - T_\infty), \tag{3}$$

$$u\frac{\partial C}{\partial x} + v\frac{\partial C}{\partial y} = \frac{D_T}{T_\infty}\frac{\partial^2 T}{\partial y^2} + D_B\frac{\partial^2 C}{\partial y^2} - R_0(C - C_\infty). \tag{4}$$

The associated boundary conditions are Ahmed et al. [25]:

$$\text{at } y=0, \begin{cases} u = u_w(x) = Bx^{1/3} \\ v = 0 \\ T = T_w \\ C = C_w \end{cases} \quad \text{as } y \to \infty, \begin{cases} u \to 0 \\ T \to 0 \\ C \to 0 \end{cases}. \quad (5)$$

Here, $n, \sigma^*, K, \mu, \vartheta, \Gamma, B_0, \rho, c, Q_0, R_0, q_r, \alpha, \beta_c, \beta^*, \rho_p$ and c_p represent shear-thinning behaviour of the fluid, Stefan-Bolzmann constant, porous medium permeability, dynamic viscosity, kinematic viscosity, time constant, magnetic field, density, specific heat, heat source coefficient, chemical reaction coefficient, radiative heat flux, thermal diffusivity, concentration expansion coefficient, thermal expansion coefficient, density and specific heat of particle, respectively. Using the following similarity transformations (Amjad et al. [24])

$$\begin{Bmatrix} u = \frac{\partial \Psi}{\partial y} = Bx^{1/3} f'(\eta) \\ v = -\frac{\partial \Psi}{\partial x} = -\frac{\sqrt{\vartheta B}}{3\,x^{1/3}}\left[2f(\eta) - \eta f'(\eta)\right] \\ \eta = \frac{y}{x^{1/3}}\sqrt{\frac{B}{\vartheta}}, g = \frac{C - C_\infty}{C_w - C_\infty}, \theta = \frac{T - T_\infty}{T_w - T_\infty} \\ q_r = \frac{16\,\sigma^* T_\infty^3}{3\,k\,k^*}\frac{\partial T}{\partial y} \\ K_0 = K\,x^{-2/3} \end{Bmatrix}. \quad (6)$$

in Eqs. (2), (3), (4) and (5) leads to the dimensionless form of equations as:

$$[(1-n) + n\,\mathrm{We} f''] * f''' - \frac{f'^2}{3} - M \cdot f' + \frac{2}{3} f \cdot f'' +$$

$$-\mathrm{Da} \cdot f' + \mathrm{Gr} \cdot \theta + \mathrm{Gc}\, g = 0, \quad (7)$$

$$\frac{2}{3}\,\mathrm{Pr}\;\theta' f + \left[1 + \frac{4R}{3}\right]\theta'' + \frac{Nc}{\mathrm{Le}} g'\theta' + \frac{Nc}{\mathrm{Le}\,Nbt}\theta'^2 +$$

$$+\mathrm{Pr}\,Q\,\theta + \mathrm{Pr}\,\mathrm{Ec}\,f''^2 = 0, \quad (8)$$

$$g' + \frac{2}{3}\,\mathrm{Sc}\;g' f + \frac{1}{Nbt}\theta'' - \mathrm{Sc}\,R_c\,g = 0. \quad (9)$$

Then dimensionless BC (boundary conditions) are:

$$at\ \eta = 0, \begin{cases} f' = 1 \\ f = 0 \\ \theta = 1 \\ g = 1 \end{cases} \quad as\ \eta \to \infty, \begin{cases} f' \to 0 \\ \theta \to 0 \\ g \to 0 \end{cases}. \quad (10)$$

The dimensionless parameters used in these equations are:

$$\begin{Bmatrix} \mathrm{We} = \sqrt{\frac{2B^3}{\vartheta}}, M = \frac{\sigma B_0^2}{B\,\rho}\,x^{\frac{2}{3}}, \mathrm{Gr} = \frac{g\,\beta^*\,(T_w - T_\infty)}{B^2\,x^{-\frac{1}{3}}}, \mathrm{Le} = \frac{\alpha}{D_B} \\ \mathrm{Gc} = \frac{g\,\beta_c\,(C_w - C_\infty)}{B^2\,x^{-\frac{1}{3}}}, R = \frac{4\,\sigma^* T_\infty^3}{k\,k^*}, \mathrm{Pr} = \frac{\vartheta}{\alpha} = \frac{\mathrm{Sc}}{\mathrm{Le}}, \mathrm{Sc} = \frac{\vartheta}{D_B} \\ Nc = \frac{\rho_p\,c_p}{\rho\,c}\,(C_w - C_\infty),\ Nbt = \frac{D_B T_\infty\,(C_w - C_\infty)}{D_T\,(T_w - T_\infty)} \\ Q = \frac{Q_0\,x^{2/3}}{B\,\rho\,c},\ \mathrm{Ec} = \frac{u_w^2}{c\,(T_w - T_\infty)},\ \mathrm{Da} = \frac{\vartheta}{B\,K_0},\ R_c = \frac{R_0\,x}{u_w} \end{Bmatrix}. \quad (11)$$

Here, R_c, R, Le, Ec, Gr, Gc, k, k^* and Ψ represent chemical reaction factor, radiation factor, Lewis number, Eckert number, thermal, solutal Grashof numbers, thermal expansion, mean absorption coefficient and stream function.

The skin friction coefficient C_f, Nu_x (Nusselt number), Sh_x (Sherwood number) are given below:

$$\begin{Bmatrix} C_f = \frac{\tau_w}{\rho\,u_w^2},\ \tau_w = \mu \left.\frac{\partial u}{\partial y}\right|_{y=0} \\ \mathrm{Nu}_x = \frac{x q_w}{k\,(T_w - T_\infty)},\ q_w = -k \left.\frac{\partial T}{\partial y}\right|_{y=0} \\ \mathrm{Sh}_x = \frac{x q_s}{D_B\,(C_w - C_\infty)},\ q_s = -D_B \left.\frac{\partial C}{\partial y}\right|_{y=0} \end{Bmatrix}. \quad (12)$$

Here, τ_w, q_w and q_s represent shear stress, surface heat flux and mass flux.

The above equations after applying the similarity transformation and simplification are given as:

$$\begin{Bmatrix} C_f\,\mathrm{Re}_x = \left[(1-n) + \frac{n}{2}\,\mathrm{We}\,f''(0)\right] f''(0) \\ \frac{\mathrm{Nu}_x}{\mathrm{Re}_x} = -\theta'(0) \\ \frac{\mathrm{Sh}_x}{\mathrm{Re}_x} = -g'(0), \\ \text{where: } \mathrm{Re}_x = \frac{u_w^2}{\sqrt{B^3\,\vartheta}} = x^{2/3}\sqrt{B/\vartheta} \end{Bmatrix}. \quad (13)$$

3. Mathematical procedure

The system of coupled nonlinear ordinary differential equations (ODE) as derived in Eqs. (7)–(9), subject to the boundary conditions (BC) defined in Eq. (10), were solved numerically using MATLAB's bvp4c solver. This solver employs a finite difference method based on the 3-stage Lobatto IIIa formula (LeVeque [26]). To utilize bvp4c, Eqs. (7)–(9), are first transformed into a set of coupled first-order ODEs, enabling the problem to be formulated as a boundary value problem. A finite value of $\eta \to \infty$ was assumed for $\eta = 40$ – the far-field boundary condition. The bvp4c solver requires three inputs: the ODE function (odes), boundary condition residual function (bcs) and an initial guess for the solution and mesh (solinit). Numerical solutions were then obtained for various parameters of the governing equations: the power-law index n, Weissenberg number We, Prandtl number Pr, magnetic parameter M, Brownian motion parameter Nbt, thermophoresis parameter Nc and Darcy number Da. The ordinary differential Eqs. (7)–(9), as well as the boundary conditions in Eq. (10), are transformed into a first-order equation system by introducing new variables. The following transformation is applied:

$$y_1 = f(\eta), \qquad y_1{}' = y_2,$$

$$y_2 = f'(\eta), \qquad y_2{}' = y_3,$$

$$y_3 = f''(\eta), \qquad y_3{}' = \frac{\frac{(y_2)^2}{3} + M\,y_2 - \frac{2}{3}y_1\,y_3 + \mathrm{Da}\;y_2 - \mathrm{Gr}\;y_4 - Gc\;y_6}{(1-n) + n\,\mathrm{We}\;y_3},$$

$$y_4 = \theta\,(\eta), \qquad y_4{}' = y_5,$$

$$y_5 = \theta'(\eta),$$

$$y_5{}' = \frac{-\frac{2}{3}\mathrm{Pr}\;y_1\,y_5 - \frac{Nc}{\mathrm{Le}}y_5\,y_7 - \frac{Nc}{\mathrm{Le}\,Nb_t}(y_5)^2 - \mathrm{Pr}\,Q\;y_4 - \mathrm{Pr}\,\mathrm{Ec}\;(y_3)^2}{\left[1 + \frac{4R}{3}\right]},$$

$$y_6 = g\,(\eta), \qquad y_6{}' = y_7,$$

$$y_7 = g'(\eta), \qquad y_7{}' = -\frac{2}{3}\,\mathrm{Sc}\;y_1\,y_7 - \frac{y_5'}{Nb_t} + S_c\,R_c\,y_6,$$

subjected to:

$$y_1(0) = a, \quad y_2(0) = b, \quad y_3(0) = b_1, \quad y_4(0) = b,$$

$$y_5(0) = b_2, \quad y_6\,(0) = b, \quad y_7\,(0) = b_3,$$

$$y_2\,(\infty) = a, \quad y_4\,(\infty) = a, \quad y_6\,(\infty) = a,$$

where: $a = 0$, $b = 1$.

4. Results and discussion

This segment delivers graphs and tables showing how different physical parameters affect dimensionless speed, temperature and concentration. Table 1 shows the effect of the parameters n, M and the Weissenberg number (We) on the skin friction coefficient $\text{Re}_x C_f$, Ahmed et al. [25]. Skin friction rises with both n and M, but decreases with the Weissenberg number for Da=Gr=Gc=0. Table 2 shows how n, We, M, Pr, Le, Nc, Nbt and Sc affect $-\theta'(0)$ and $-g'(0)$, R=Ec=0. It is seen that $-\theta'(0)$ rises with Pr, Le, Nbt and Sc, whereas it decreases with n, We, M and Nc. Similarly, the Sherwood number $-g'(0)$ grows with Nc, Nbt and Sc, but decreases with n, We, M, Pr and Le. Table 3 shows the numerical findings for the Nusselt number $-\theta'(0)$ for various We and Pr values. Tables 1–3 show that our findings are congruent with those of Ahmed et al. [25]. The influence of the metrics Rc, R, Q, M and Da on the velocity profile can be observed from Figs. 2–6.

Table 1. Effect of n, We, M on skin friction coefficient $\text{Re}_x C_f$ with Da = Gr = Gc = 0.

n	We	M	$\text{Re}_x C_f$ [25]	$\text{Re}_x C_f$
0.1	0.5	0.5	0.932163	0.943621
0.2			1.016640	1.16139
0.3			1.096308	1.124345
0.3	0.1		0.808646	0.823561
	0.2		0.800995	0.829672
	0.3		0.793042	0.793240
		0.1	0.600077	0.600100
		0.2	0.648990	0.648899
		0.3	0.694237	0.694221

Table 2. Effect of n, We, M, Pr, Le, Nc, Nbt, Sc on $-\theta'(0)$, $-g'(0)$ for R=Ec=0.

n	We	M	Pr	Le	Nc	Nbt	Sc	$-\Theta'(0)$ [25]	$-g'(0)$ [25]	$-\Theta'(0)$	$-g'(0)$
0.1								0.209793	0.627703	0.209534	0.628793
0.2								0.200519	0.610165	0.202132	0.612128
0.3								0.189534	0.587607	0.188235	0.589021
0.3	0.1							0.191385	0.597856	0.198037	0.598213
	0.2							0.190240	0.595289	0.196452	0.596253
	0.3							0.189048	0.592585	0.189274	0.593630
		0.1						0.218816	0.645472	0.219125	0.646203
		0.2						0.209244	0.629025	0.208269	0.629294
		0.3						0.200779	0.613862	0.201943	0.614204
			0.1					0.063744	0.635271	0.064247	0.636367
			0.2					0.091398	0.622241	0.092156	0.623464
			0.3					0.122145	0.609816	0.123206	0.609048
			0.5	0.1				0.001045	0.651501	0.002105	0.652479
				0.2				0.016199	0.646421	0.017345	0.646532
				0.3				0.039595	0.649343	0.038649	0.649689
					0.1			0.212768	0.576634	0.213185	0.577839
					0.2			0.205897	0.579276	0.206064	0.571094
					0.3			0.199232	0.581832	0.199568	0.582120
						0.1		0.104454	0.046621	0.156023	0.047864
						0.2		0.139576	0.224951	0.138673	0.225207
						0.3		0.154879	0.330159	0.155783	0.331075
							0.1	0.206840	-0.005330	0.207356	-0.006552
							0.2	0.204218	0.026183	0.205720	0.025294
							0.3	0.201683	0.062341	0.202075	0.063360

Table 3. Effect of We, Pr on $-g'(0)$.

We	Pr	$-g'(0)$ [25]	$-g'(0)$
0.0	0.5	0.319	0.322
0.2		0.318	0.321
0.4		0.317	0.320
	0.2	0.231	0.234
	0.6	0.348	0.351
	1.2	0.521	0.524

In Fig. 2, the increased chemical reaction rate leads to a decreased fluid velocity. A possible explanation for this could be that higher reaction rates lead to increased consumption of reactants, which might result in a less dense and slower-moving fluid. Beyond $\eta \sim 2.5$, the velocity likely enters a regime where the system reaches an equilibrium or a steady state. Here, the effects of Rc diminish, due to the velocity profile flattening out as it approaches a far-field condition, the influence of dominant forces, inertial forces overtaking the variations induced by Rc.

In Figs. 3 and 4, increased heat source/sink and radiation values lead to the increased fluid velocity. For $\eta < 1$, the flow is likely dominated by viscous forces in the boundary layer or near-wall area. Radiation effects are weaker here, leaving the velocity profile essentially unaltered. For $\eta > 1$, radiation has a greater impact on the flow field due to the increased temperature, reduced viscosity from shear-thinning, and enhanced thermal expansion effects.

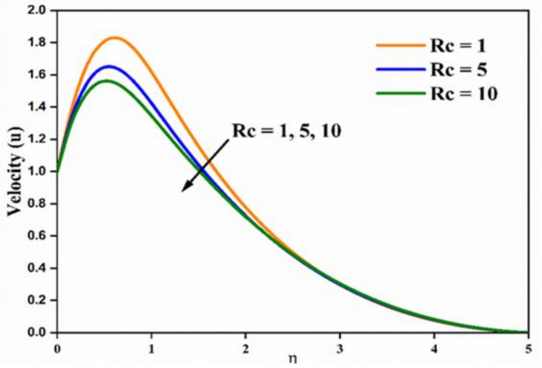

Fig. 2. Velocity variations with *Rc*.

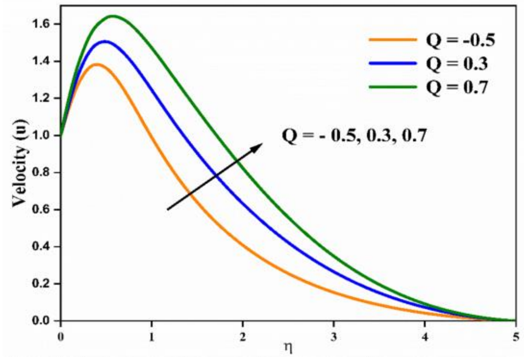

Fig. 3. Velocity variations with *Q*.

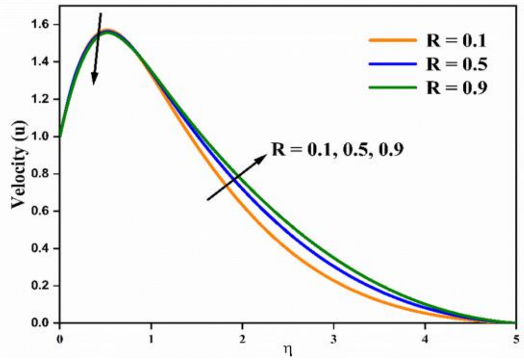

Fig. 4. Velocity variations with *R*.

In Fig. 5, the increased magnetic field strength (M) leads to the decreased fluid velocity. This is consistent with the principles of MHD, where the magnetic field exerts a drag force on the conducting fluid, opposing its motion. The reduced Lorentz force affects as the flow passes away ($\eta > 3$) from the border zone, the magnetic field impact lessens and the velocity becomes insensitive to M.

Tangential hyperbolic fluids often exhibit shear-thinning behaviour, meaning their viscosity decreases with increasing shear rate. As Da increases, the permeability of the porous medium increases, potentially leading to higher shear rates within the pores (Fig. 6). This increased shear rate could cause a significant decrease in the fluid viscosity, counteracting the increased permeability, and result in a net decrease in velocity. With uniform flow through porous medium beyond a certain distance ($\eta > 3$), the flow reaches a domain where the influence of the porous medium resistance (connected to Da) is no longer substantial, and the velocity profile stabilizes.

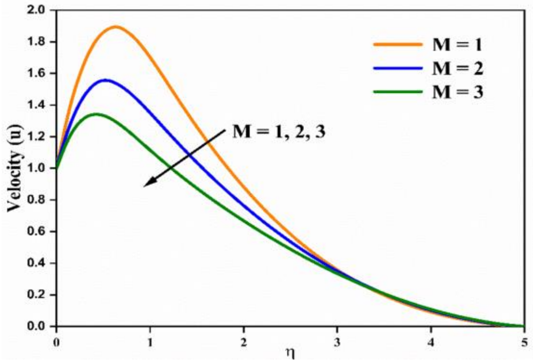

Fig. 5. Velocity variations with *M*.

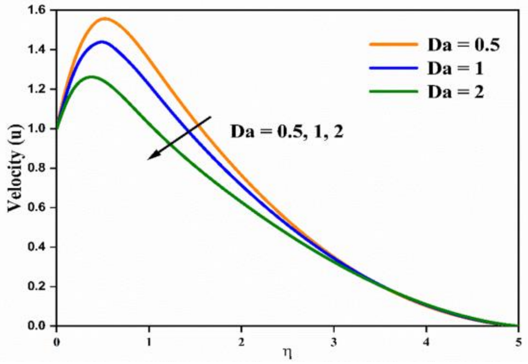

Fig. 6. Velocity variations with Da.

Figure 7 explores the temperature profile for varying values of the chemical reaction parameter *Rc*. The observed behaviour suggests a transition in the nature of heat transfer around $\eta = 2$. In this model, the influence of chemical reactions or other complex phenomena is represented by a term, $S(\eta) = Sc \cdot Rc \cdot g(\eta)$ in the energy equation. For $\eta < 2$, $S(\eta)$ acts as a heat sink (endothermic), leading to a decrease in temperature with increasing *Rc*. Conversely, for $\eta > 2$, $S(\eta)$ acts as a heat source (exothermic), resulting in the expected increase in temperature with increasing *Rc*.

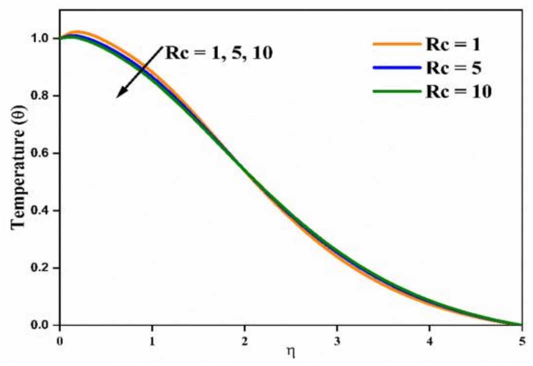

Fig. 7. Temperature variations with *Rc*.

In Figs. 8 to 11, increased heat source, radiation, magnetic field and Da values lead to the increased fluid temperature. Heat source: adding heat to a system naturally increases its temperature. Magnetic field: a magnetic field can induce currents in a conductive fluid, leading to resistive heating. Darcy number: the Darcy number is related to fluid flow through porous media. A higher Da generally indicates greater flow, which can enhance heat transfer and increase the temperature. Radiation: increased radiation will lead to greater absorption of radiant energy, thus lifting the temperature.

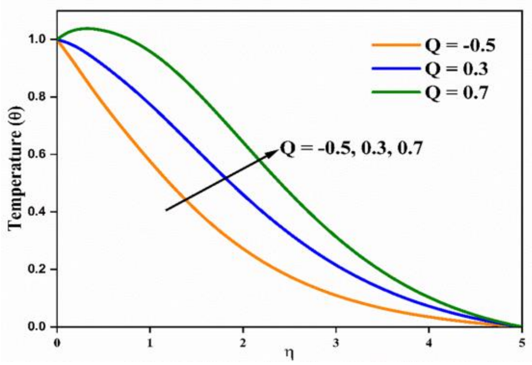

Fig. 8. Temperature variations with Q.

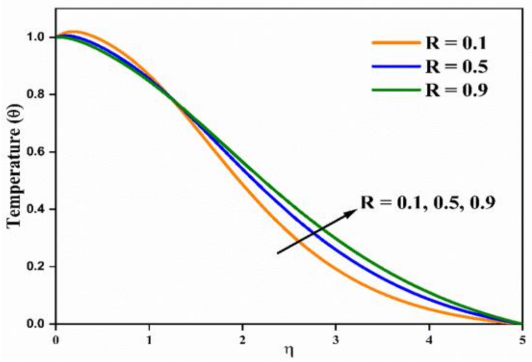

Fig. 9. Temperature variations with R.

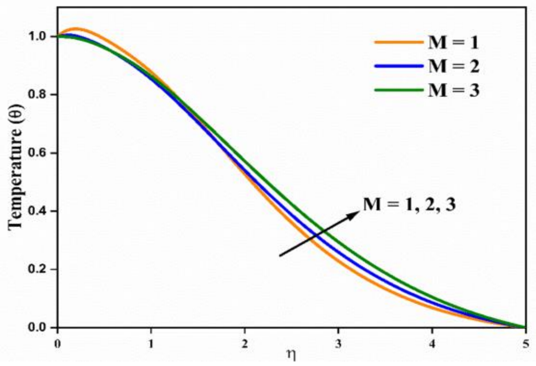

Fig. 10. Temperature variations with M.

In Fig. 9, at smaller η values ($\eta < 1.3$), heat conduction is a more dominant mode of heat transfer. The influence of radiation is less pronounced in this region and other factors like the stretching surface or fluid properties cause a decrease in temperature despite the increase in R. Around $\eta = 1.3$, there is a transition region where the balance between conduction and radiation shifts. The increasing radiation might start to have a more significant effect, counteracting the factors that were causing the temperature to decrease at smaller η values. For larger η values ($\eta > 1.3$), radiation likely becomes the dominant mode of heat transfer. The increase in R directly leads to an increase in temperature in this region.

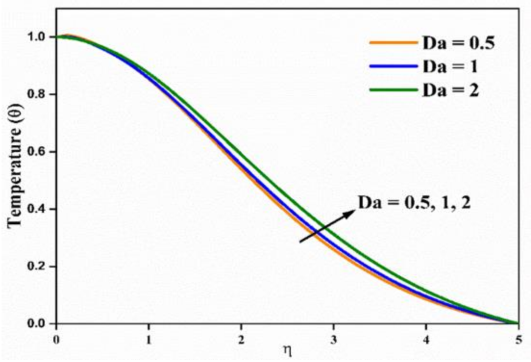

Fig. 11. Temperature variations with Da.

Figs. 10 and Fig. 11 explore the temperature profiles for varying values of the magnetic parameter (M) and Darcy number (Da). A distinct split behaviour is observed, for $\eta < 1.5$ approximately, increasing M leads to a decrease in temperature, while the opposite trend is observed for $\eta > 1.5$. This suggests a competition between several physical effects. Increasing M strengthens the Lorentz force, which can suppress convective heat transfer in certain regions while enhancing it in others. Similarly, increasing Da suppress the temperature field for $\eta < 1$; for $\eta > 1$, having opposing effects on the temperature. The combined influence of M and Da, coupled with the effects of buoyancy (represented by Gr), the boundary conditions at the stretching sheet and the non-linear nature of the governing equations lead to the complex temperature distribution observed. It was found that the influence of other parameters, such as Pr and Le is crucial.

The chemical reaction parameter Rc influences the fluid dynamics because the chemical reaction affects momentum and energy transfer due to changes in concentration or thermal gradients. This is where the velocity is sensitive to Rc and a decrease in concentration profile is observed due to the combined effects of the chemical reaction and fluid resistance as observed in Fig. 12.

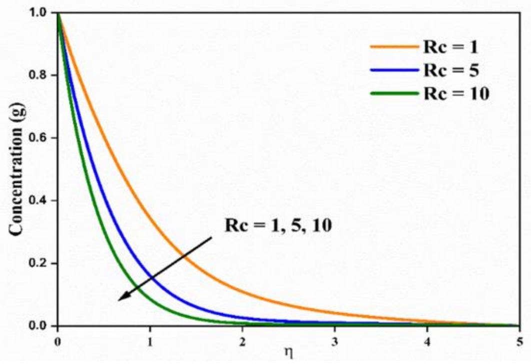

Fig. 12. Concentration profile with Rc.

Since velocity, temperature and concentration profiles are coupled in the boundary layer, any effect of *Rc* on the fluid flow is localized near the surface (small η). At large η, the influence of chemical reactions vanishes, leading to identical profiles regardless of the value of *Rc*.

As shown in Fig. 13, the effect of heat on concentration depends on the heat source parameter. Exothermic reactions tend to shift towards reactants at higher temperatures, potentially leading to increased reactant concentration. Endothermic reactions shift towards products at higher temperatures, potentially leading to a decreased reactant concentration.

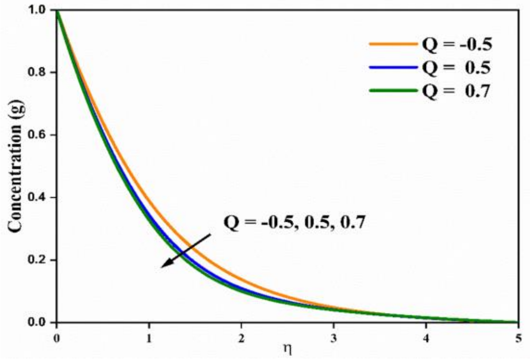

Fig. 13. Concentration profile with *Q*.

From Figs. 14 and 15 we observe that increased radiation and magnetic parameter values lead to the rise in the concentration profiles. There is a poor coupling between *R* and *M* and other system parameters, resulting in little visible variations.

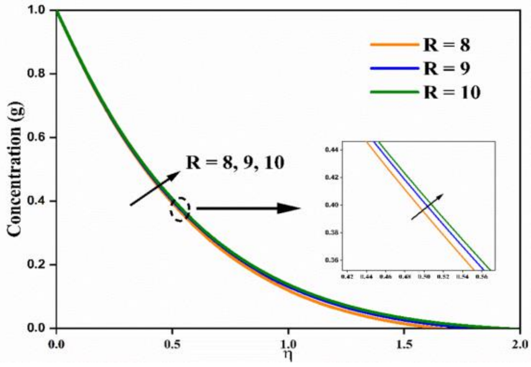

Fig. 14. Concentration profile with *R*.

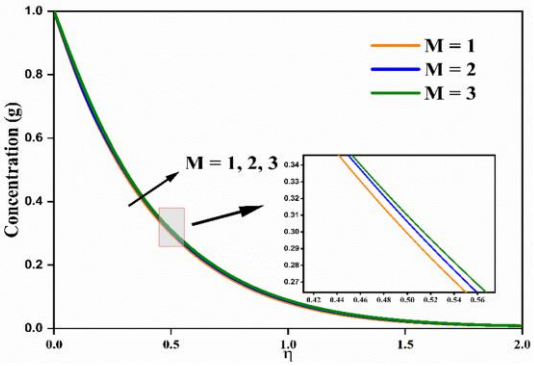

Fig. 15. Concentration profile with *M*.

The Schmidt number describes the relative effectiveness of momentum diffusion (viscosity) compared to mass diffusion. A higher Sc means that momentum diffusion dominates, which can lead to thinner boundary layers and potentially higher concentration gradients near a surface, but lower concentrations overall (Fig. 16).

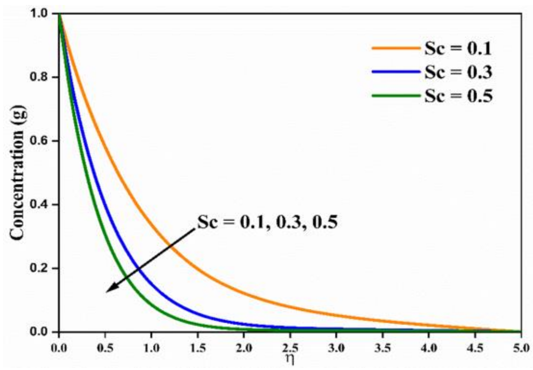

Fig. 16. Concentration profile with Sc.

The impact of the different metrics on the drag coefficient and Nu can be visualized from Figs. 17 to 23. The skin friction coefficient exhibits a complex interplay with the magnetic field, fluid elasticity, flow behaviour and slip parameter. While increasing the magnetic field strength initially enhances skin friction, this effect reverses beyond a certain threshold.

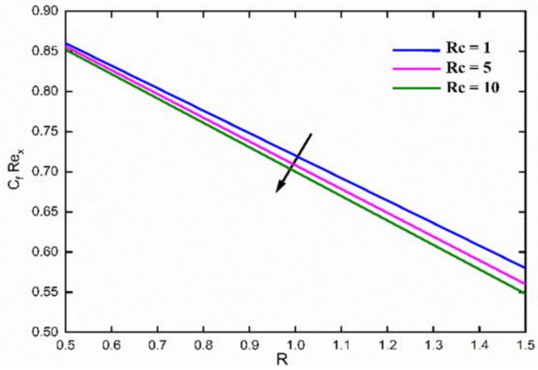

Fig. 17. Influence of *Rc* and *R* on drag coefficient.

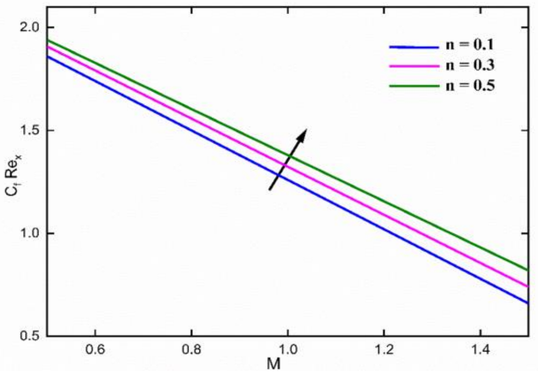

Fig. 18. Influence of *n* and *M* on drag coefficient.

Similarly, the coefficient initially rises with the increasing power-law index, indicating a complex relationship between flow behaviour and friction. Increased fluid elasticity, represented by the Weissenberg number, generally reduces skin friction, following a downward parabolic trend.

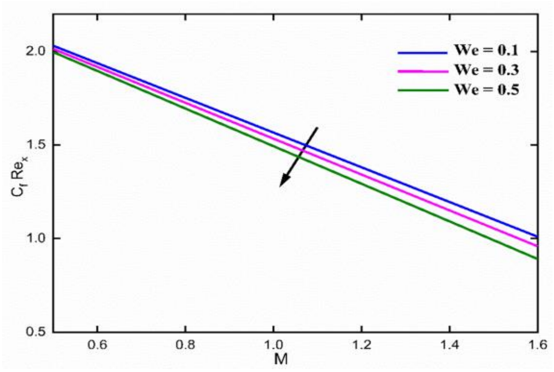

Fig. 19. Influence of We and *M* on drag coefficient.

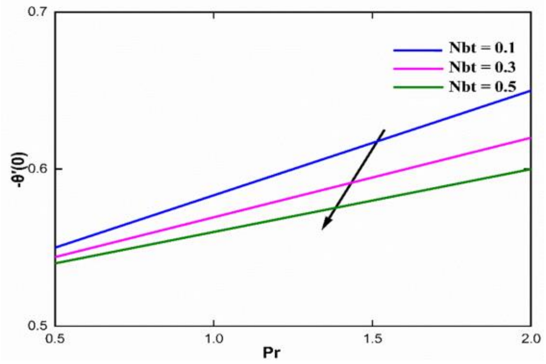

Fig. 20. Influence of *Nbt* and Pr on local Nusselt number.

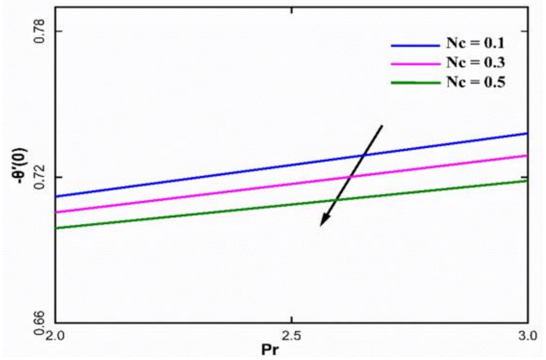

Fig. 21. Influence of *Nc* and Pr on local Nusselt number.

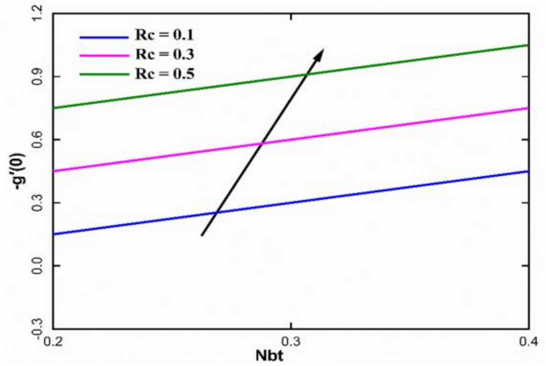

Fig. 22. Influence of *Rc* and *Nbt* on local Sherwood number.

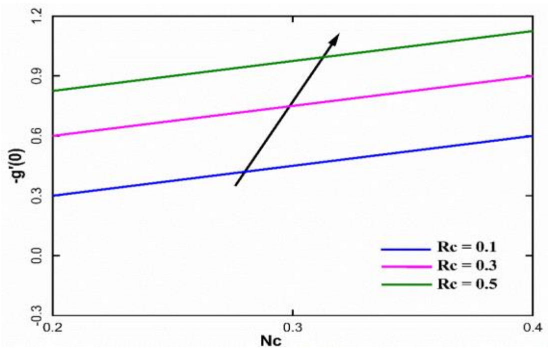

Fig. 23. Influence of *Rc* and *Nc* on local Sherwood number.

The heat transfer rate, represented by the local Nusselt number, is influenced by several factors. Higher values of the thermophoresis parameter, power-law index (*n*), and conversely, increasing the convective parameter enhances the local Nu, suggesting improved heat transfer.

Notably, the power-law index (*n*), which describes the fluid's flow behaviour, has a consistently negative impact on the local Nu at the surface, meaning a more shear-thinning fluid will exhibit reduced heat transfer.

5. Conclusions

The numerical values for the parameters in this study were selected within realistic ranges observed in relevant engineering applications, such as microelectronics cooling, heat exchangers, and geothermal systems. For example, the Weissenberg number (We), which characterizes the fluid's elasticity, was varied to represent both Newtonian and viscoelastic behaviours, enabling a comprehensive investigation of how fluid elasticity influences the flow. A range of values was explored for each parameter to thoroughly analyse its impact on flow and heat transfer, providing a detailed understanding of their effects on velocity, temperature and concentration profiles. Furthermore, the chosen values were benchmarked against those used in previous studies on similar nanofluid, non-Newtonian and MHD flow problems, allowing for direct comparison and validation of the present results with existing literature.

In this investigation, the non-dimensional parameter values $n = 0.5$, We = 0.5, $M = 2$, Da = 0.5, Gr = 5, Gc = 5, Pr = 0.72, $R = 0.5$, $Nc = 0.5$, Le = 3, $Nbt = 5$, $Q = 0.5$, Ec = 0.5, Sc = 0.5, $Rc = 10$ were used. These variables are treated as constants except for changed parameters in the graphs. Boundary layer flow and heat transfer of HTF fluid with nanosized particles via a stretched sheet are often described in relation to thermal radiation, convective heating, Weissenberg number and magnetic field metric. Through the application of similarity transformation, the boundary layer equations controlling the flow issue are reduced to a pair of high order non-linear ODEs.

Using MATLAB’s bvp4c, the resultant ODEs are numerically solved.

The fundamental results of the investigation are:

1. Increasing the Weissenberg number We or power-law index *n* thins the velocity boundary layer.

2. Radiation, however, increases the thickness of the thermal boundary layer.
3. Velocity, temperature and concentration fields for the flow of tangent hyperbolic fluid decline with the chemical reaction parameter.
4. The fluid velocity and temperature increase and the concentration profile drops with the increasing values of heat source/sink parameter.
5. The energy field is enhanced with the intensifying effect of porous parameter, but the velocity curve of HTF decreases.
6. Similarly, the skin friction coefficient C_f decreases as the slip parameter increases.
7. An increase in the Weissenberg number acts to reduce the skin friction coefficient.
8. Furthermore, the Weissenberg number has a diminishing effect on the local Nusselt number.
9. The convective metric and power-law index demonstrate opposite effects on the local Nusselt number.

References

[1] Shankar Goud, B., Pramod Kumar, P., & Malga, B.S. (2022). Induced magnetic field effect on MHD free convection flow in nonconducting and conducting vertical microchannel walls. *Heat transfer*, 51(2), 2201–2218. doi: 10.1002/htj.22396

[2] Al Oweidi, K.F., Jamshed, W., Goud, B.S., Ullah, I., Usman, Mohamed Isa, S.S.P., El Din, S.M., Guedri, K., & Jaleel, R.A. (2022). Partial differential equations modeling of thermal transportation in Casson nanofluid flow with Arrhenius activation energy and irreversibility processes. *Scientific Reports*, 12(1), 20597. doi: 10.1038/s41598-022-25010-x

[3] Jamshed, W., Ramesh, G.K., Roopa, G.S., Nisar, K.S., Safdar, R., Madhukesh, J.K., Shahzad, F., Isa, S.S.P.M., Shankar Goud, B., & Eid, M.R. (2022). Electromagnetic radiation and convective slippery stipulation influence in viscous second grade nanofluid through penetrable material. *ZAMM-Journal of Applied Mathematics and Mechanics (Zeitschrift für Angewandte Mathematik und Mechanik)*, e202200002. doi: 10.1002/zamm.202200002

[4] Pal, D. (2009). Heat and mass transfer in stagnation-point flow towards a stretching surface in the presence of buoyancy force. *Meccanica*, 44(2), 145–158. doi: 10.1007/s11012-008-9155-1

[5] Asogwa, K.K., Kumar, K.T., Goud, B.S., & Chohan, J.S. (2023). Significance of nanoparticle shape factor and buoyancy effects on a parabolic motion of EMHD convective nanofluid past a Riga plate with ramped wall temperature. *The European Physical Journal Plus*, 138(6), 1–13. doi: 10.1140/epjp/s13360-023-04170-3

[6] Kandasamy, R., Muhaimin, I., & Saim, H.B. (2010). Lie group analysis for the effect of temperature-dependent fluid viscosity with thermophoresis and chemical reaction on MHD free convective heat and mass transfer over a porous stretching surface in the presence of heat source/sink. *Communications in Nonlinear Science and Numerical Simulation*, 15(8), 2109–2123. doi: 10.1016/j.cnsns.2009.09.016

[7] Dharmaiah, G., Goud, B.S., Shah, N.A., & Faisal, M. (2023). Numerical analysis of heat and mass transfer with viscous dissipation, Joule dissipation, and activation energy. *International Journal of Ambient Energy*, 44(1), 2090–2102. doi: 10.1080/01430750.2023.2224335

[8] Shankar Goud, B., & Dharmaiah, G. (2023). Role of Joule heating and activation energy on MHD heat and mass transfer flow in the presence of thermal radiation. *Numerical Heat Transfer, Part B: Fundamentals*, 84(5), 620–641. doi: 10.1080/10407790.2023.2215917

[9] Elbashbeshy, E.M.A., & Bazid, M.A.A. (2004). Heat transfer over an unsteady stretching surface. *Heat Mass Transfer*, 41, 1–4. doi: 10.1007/s00231-004-0520-x

[10] Raptis, A. (1998). Radiation and Free Convection Flow through a Porous Medium. *International Communications in Heat and Mass Transfer*, 25(2), 289–295. doi: 10.1016/S0735-1933(98)00016-5

[11] Cortell, R. (2007). Viscous flow and heat transfer over a nonlinearly stretching sheet. *Applied Mathematics and Computation*, 184(2), 864–873. doi: 10.1016/j.amc.2006.06.077

[12] Xuan, Y., & Li, Q. (2000). Heat transfer enhancement of nanofuids. *International Journal of Heat and Fluid* Flow, 21(1), 58−64. doi: 10.1016/S0142-727X(99)00067-3

[13] Malik, M.Y., Salahuddin, T., Hussain, A., & Bilal, S. (2015). MHD flow of tangent hyperbolic fluid over a stretching cylinder: Using Keller box method. *Journal of Magnetism and Magnetic Materials*, 395, 271–276. doi: 10.1016/j.jmmm.2015.07.097

[14] Naseer, M., Malik, M.Y., Nadeem, S., & Rehman, A. (2014). The boundary layer flow of hyperbolic tangent fluid over a vertical exponentially stretching cylinder. *Alexandria Engineering Journal*, 53(3), 747–750. doi: 10.1016/j.aej.2014.05.001

[15] Hayat, T., Qayyum, S., Ahmad, B., & Waqas, M. (2016). Radiative flow of a tangent hyperbolic fluid with convective conditions and chemical reaction. *European Physical Journal Plus*, 131(12). doi: 10.1140/epjp/i2016-16422-x

[16] Nadeem, S., & Akram, S. (2009). Peristaltic Transport of a Hyperbolic Tangent Fluid Model in an Asymmetric Channel. *Zeitschrift für Naturforschung A*, 64(9–10), 559–567. doi: 10.1515/zna-2009-9-1004

[17] Reddy, B.N., Dodda, R., & Reddy, B.S. (2024). A Numerical Investigation on Boundary Layer Flow of MHD Tangent Hyperbolic Fluid Flow over a Stretching Sheet with Slip Boundary Conditions. *Journal of Advanced Research in Fluid Mechanics and Thermal Sciences*, 120(1), 122–139. doi:10.37934/arfmts.120.1.122139

[18] Upadhya, S.M., Raju, S.S.K., Raju, C.S.K., & Mnasri, C. (2020). Arrhenius Activation and Zero Mass Flux Conditions on Nonlinear Convective Jeffrey Fluid over an Electrically Conducting and Radiated Sheet. *Arabian Journal for Science and Engineering*, 45(11), 9095–9109. doi: 10.1007/s13369-020-04687-0

[19] Nadeem, S., & Akram, S. (2011). Magnetohydrodynamic peristaltic flow of a hyperbolic tangent fluid in a vertical asymmetric channel with heat transfer. *Acta Mechanica Sinica*, 27(2), 237−250. doi: 10.1007/s10409-011-0423-2

[20] Sheikh, M., Hasnain, J., Abid, N., & Abbas, Z. (2024). Chemically reactive mhd flow through a slendering stretching sheet subjected to non-linear radiation flow over a linear and non-linear stretching sheet. *Facta Universitatis, Series: Mathematics and Informatics*, 39(2), 265−278. doi: 10.22190/fumi230413018s

[21] Nasir, S., Berrouk, A.S., & Aamir, A. (2024). Efficiency analysis of solar radiation on chemical radioactive nanofluid flow over a porous surface with magnetic field. *Case Studies in Thermal Engineering*, 63, 105231. doi: 10.1016/j.csite.2024.105231

[22] Gaffar, S.A., Bég, O.A., Kuharat, S., & Bég, T.A. (2024). Computation of hydromagnetic tangent hyperbolic non-Newtonian flow from a rotating non-isothermal cone to a non-Darcy porous medium with thermal radiative flux. *Physics Open*, 19, 100216. doi: 10.1016/j.physo.2024.100216

[23] Shehzad, S.A., Hayat, T., Qasim, M., & Asghar, S. (2013). Effects of mass transfer on MHD flow of Casson fluid with chemical reaction and suction. *Brazilian Journal of Chemical Engineering*, 30(1), 187–195. doi:10.1590/S0104-66322013000100020

[24] Amjad, M., Khan, M.N., Ahmed, K., Ahmed, I., Akbar, T., & Eldin, S.M. (2023). Magnetohydrodynamics tangent hyperbolic nanofluid flow over an exponentially stretching sheet: Numerical investigation. *Case Studies in Thermal Engineering*, 45, 102900. doi: 10.1016/j.csite.2023.102900

[25] Ahmed, I., Alghamdi, M., Amjad, M., Aziz, F., Akbar, T., & Muhammad, T. (2023). Numerical investigation of MHD flow of hyperbolic tangent nanofluid over a non-linear stretching sheet. *Helion*, 9(7), e17658. doi: 10.1016/j.heliyon.2023.e17658

[26] LeVeque, R.J. (2007). *Finite difference methods for ordinary and partial differential equations*. *Steady-state and time-dependent problems*. Society for Industrial and Applied Mathematics. Philadelphia, USA.

Co-published by
Institute of Fluid-Flow Machinery
Polish Academy of Sciences
Committee on Thermodynamics and Combustion
Polish Academy of Sciences

http://www.imp.gda.pl/archives-of-thermodynamics/

ARCHIVES OF THERMODYNAMICS

Electro-osmotic and magnetohydrodynamic flow of Maxwell nanofluid over Darcy-Forchheimer porous medium with Soret-Dufour effects

Amudhini M, Poulomi De*

Department of Mathematics, School of Advanced Sciences, Vellore Institute of Technology, Chennai-600127, Tamilnadu, India
*Corresponding author email: poulomide12@yahoo.com

Received: 16.07.2024; revised: 09.09.2024; accepted: 08.10.2024

Abstract

In this study, we investigate the potential impacts of the thermo-diffusion and diffusion-thermo effects on electro-osmotic flow of Maxwell nanofluid across the stretching sheet. Magnetic and electric field over Darcy-Forchheimer flow and chemical reaction are also included. This study is vital in areas such as microfluidics, medical applications, and thermal management, where manipulating nanofluids under electromagnetic fields is essential. Through similarity transformation, the governing equations are turned into a collection of non-linear ordinary differential equations. The numerical results for the changed equations are obtained using the fifth order Runge-Kutta-Fehlberg technique with a shooting method. It has been established that if the Forchheimer number and electro-osmotic parameter increase, the velocity profile drops. As the diffusion-thermo effect grows so does the temperature profile. Similarly, the thermo-diffusion effect increases along with the concentration profile. The skin friction coefficient decreases by 10% and 23%, for the magnetic parameter increases from 0.4 to 2 and the Forchheimer number rises from 1 to 5, respectively. Additionally, with an increase in the Dufour number from 1.5 to 2, the Nusselt number decreases by 9%, while the Sherwood number increases by 33%. This research provides a more comprehensive analytical framework by integrating multiple physical effects such as Soret and Dufour effects, magnetic and electric fields, and porous media, thereby enhancing applications in microfluidic devices for precise fluid control, biomedical engineering for improved drug delivery and tissue engineering, thermal management for more efficient electronic cooling systems, environmental remediation for effective pollution control, and materials science for developing smart materials and nanocomposites.

Keywords: Maxwell nanofluid; Magnetohydrodynamics, Electro-osmotic forces; Darcy porous medium; Cross diffusion effects

Vol. 46(2025), No. 2, 69–81; doi: 10.24425/ather.2025.154907

Cite this manuscript as: M, A., & De, P. (2025). Electro-osmotic and magnetohydrodynamic flow of Maxwell nanofluid over Darcy-Forchheimer porous medium with Soret-Dufour effects. *Archives of Thermodynamics*, 46(2), 69–81.

1. Introduction

The capability to move a liquid caused by an electric field that is applied over a porous medium is referred to as electro-osmosis. The electro-osmotic force is induced from the collision of the electro-magnetic field that meets the ion in the liquid, which results in an overall movement of the fluid. Electro-osmotic flow is useful in a variety of domains, including microfluidics, chromatography, and electrokinetic separations. It is frequently used to regulate fluid motion in small-scale systems.

Nanofluids are made up of colloids containing nanoscale-sized particles, which are typically called nanoparticles that are dispersed throughout a base fluid like ethylene glycol, water or oil. Choi and Eastman [1] established the theoretical idea of

Nomenclature

a – parameter
B_0 – magnetic field strength, T
c_p – specific heat, J/(kg K)
c_s – concentration susceptibility, m^3/kg
C – concentration, mol/m^3
C_{fx} – coefficient of local skin friction
C_w – concentration at the surface of the sheet, mol/m^3
C_∞ – ambient concentration, mol/m^3
D_B – Brownian diffusion coefficient, m^2/s
D_T – thermophoresis diffusion coefficient, m^2/s
D_m – mass diffusivity, m^2/s
Df – Dufour number
e – electronic charge, C
E – electric field strength, N/C
E_1 – electric field parameter
Ec – Eckert number
E_x – applied electro-osmotic force, N
f – dimensionless stream function
F – non-uniform inertia force
Fr – Forchheimer number
k – thermal conductivity, W/(m K)
k_p – permeability of porous medium, m^2
k_1 – rate of chemical reaction
K – porosity parameter
K_B – Boltzmann constant, 1/(K mol)
K_T – thermo-diffusion ratio, 1/K
Kr – chemical reaction parameter
M – magnetic parameter
m_e – electroosmotic parameter
$\bar{n}_0$ – bulk concentration,
$\bar{n}^+$, $\bar{n}^-$ – cations and anions
Nb – Brownian motion parameter
Nt – thermophoresis parameter
Nu$_x$ – local Nusselt number
Pr – Prandtl number
q_w, q_m – heat and mass flux, W/m^2, kg/(m^2 s)
Re$_x$ – local Reynolds number
Sc – Schmidt number
Sr – Soret number
Sh$_x$ – local Sherwood number
T – temperature of the fluid, K
T_w – temperature at the sheet's surface, K
T_∞ – ambient temperature, K
T_{av} – average temperature, K
u, v – fluid velocity in x- and y-direction, m/s
u_w – stretching velocity of sheet, m/s
U_{hs} – Helmholtz-Smoluchowski velocity, m/s
x, y – Cartesian coordinates, m
Z_v – charge balance
$(\cdot)'$ – differentiation with respect to η

Greek symbols

α – thermal diffusivity, m^2/s
β^* – Maxwell parameter
Γ – dimensional variable
$\bar{\Gamma}$ – electric potential, V
ε – dielectric permittivity
η – similarity variable
θ – temperature function
λ – fluid relaxation time, s
λ_e – Debye length, m
μ – dynamic viscosity of fluid, kg/(m s)
ν – kinematic viscosity of fluid, m^2/s
ξ – dimensionless similarity variable
ρ – density of fluid, kg/m^3
ρ_e – density of the total ionic energy, J/m^3
σ – electrical conductivity, S/m
τ – ratio of effective heat capacity of nanoparticle and base fluid
ϕ – concentration function

nanofluids by attempting to sustain different nanoparticles made from metals and metal oxides in various base fluids. Wong and De Leon [2] discussed existing and next-generation uses involving nanofluids, highlighting their better controlled heat transfer qualities and unique features. In a comparable manner, Jama et al. [3] evaluated the creation of metallic and nonmetallic nanofluids, in addition to the endurance of created nanofluids, plus also covered physical and thermal characteristics, as well as nanofluid applications. De et al. [4] evaluated the flow of nanofluid across the shrinking sheet utilizing thermal radiation and compared it to earlier studies. Kariko et al. [5] studied the flow of thixotropic nanofluid containing gyrotatic microorganisms along a vertical surface under convective conditions using active and passive controls. Yaseen et al. [6] analysed the flow of tri-hybrid nanofluid with gyrotactic microorganisms and Cattaneo-Christov model with a comparison of cone, wedge and plate, and concluded that heat transfer in a cone is greater than in other geometries. Akram et al. [7] investigated the flow of an Eyring-Powell hybrid nanofluid through an elliptical conduit with a concurrent entropy generation. Shah et al. [8] studied the magnetohydrodynamic (MHD) flow of Sutterby nanofluid via a Riga plate, including heat production. Shahzad et al. [9] investigated the peristaltic flow of hybrid nanofluid over an elliptical multi-stenotic artery, and the importance of the parameters was evaluated using a fuzzy environment. They also used entropy generation to reduce energy loss. Akbar et al. [10] explored the flow of Carreau-Yasuda nanofluid past an expanding sheet with the impacts of magnetic field, heat generation and variable thermal conductivity. Among these models, Maxwell fluid represents a type of non-Newtonian fluid. Maxwell fluids have a linear viscoelastic behaviour and are frequently employed for describing complicated fluids such as polymer melts or solutions that have both viscous and elastic effects. Knowing the rheological behaviour of Maxwell fluids is critical in a variety of industrial processes, including polymer and other material processing. Hayat et al. [11] explored the three-dimensional flow of Maxwell nanofluid together by employing convective and magnetic effects through a stretching sheet and numerically solved it using the homotopy analysis method. Through a porous expanding surface, Nagendramma et al. [12] reported the steady and incompressible transport of Maxwell nanofluid involving slip boundary conditions, thermal radiation and viscous dissipation. Using the Keller box method, Jamshed [13] numerically solved the problem of entropy generation in the MHD two-dimensional flow of Maxwell nanofluid across an infinite horizontal surface containing viscous dissipation and thermal radiation effects. Murtaza et al. [14] used the Fourier sine transform and Laplace transform to precisely solve the problem of the electro-osmotic flow of Maxwell nanofluid along the existence of the field of electric charge into a conduit amid two plates which are parallel. Sultana et al. [15] examined the flow of a Maxwell hybrid fluid across a spinning disc in a porous media, taking into account suction effects and analyzing entropy generation.

The electromagnetohydrodynamic (EMHD) flow of fluid has been used in a variety of technological fields recently because of its benefits. The Lorentz force, which is produced by passing an electrical current over the channel in the direction of a perpendicular magnetic field, is the basis for the EMHD flow phenomenon. The electro-magnetohydrodynamic flow through the riga plate with buoyancy forces was studied by Pantokratoras and Magyari [16], who used a finite difference approach to tackle the issue. Buren and Jian [17] used the perturbation approach to solve the two-dimensional, unsteady, incompressible electro-magnetohydrodynamic flow in a microparallel channel containing slightly transverse corrugated walls. The simplified finite difference method (SFDM) was used by Irfan et al. [18] to solve the steady transport of nanofluid past the stretching sheet that is non-linear with electric and magnetic fields, porosity and heat generation/absorption. The electro-magnetohydrodynamic micropolar nanofluids involving slip conditions going along an expanded sheet are explored by Muhammad et al. [19] at its stagnation point flow.

Porous media, which are defined by interconnected void spaces, are used in a variety of engineering sectors, including environmental remediation, oil reservoir engineering, groundwater management and other areas. They aid in the comprehension and optimization of fluid flow in both naturally occurring and artificial systems. So, researchers are quite interested in it. An equation known as the Darcy law describes how fluid moves through a porous material. A fluid flow that defines the Darcy law is referred to as non-Darcy fluid movement. In spite of suction velocity and heat radiation, Raptis [20] studied the two dimensions and steady movement of the fluid with viscous properties through a medium that is porous on an infinite plate. Hayat et al. [21] use the homotopy analysis method (HAM) to solve the magnetohydrodynamic flow of a fluid that is not compressible but viscous through a porous medium via a vertically expanding sheet at its stagnation point. Qing et al. [22] investigated chemical reaction, heat radiation and magnetohydrodynamic flow of Casson nanofluid across a porous stretching/shrinking surface. Sajid et al. [23] studied the Maxwell nanofluid Darcy-Forchheimer transport across a linear stretching sheet combined with thermal conductivity, activation energy, as well as non-linear thermal radiation. Sangetha and De [24] studied the transport of a nanofluid containing microorganisms, implanted in a non-Darcy porous medium, as it passed over a convectively heated surface. Mohanty et al. [25−27] investigated the Darcy-Forchheimer flow of a hybrid nanofluid in a variety of scenarios, including flow past a moving needle under thermal radiation and Cattaneo-Christov heat flux, as well as past a disc influenced by Marangoni convection, thermo-solutal Marangoni convection, and activation energy, using entropy production analysis. Sohail et al. [28] investigated the flow of tri-hybrid pseudo-plastic fluid in the presence of a non-Darcy porous medium across a stretched sheet.

When distinct species or components within a mixture display varying rates of diffusion, this phenomenon is referred to as cross diffusion. Mass and thermal transfer processes, specifically in mixtures or multi-component fluids, are associated with the Soret and Dufour effects. The phenomenon wherein all the parts of a mixture travel with various speeds along a temperature gradient is referred to as the Soret effect, or thermal diffusion effect. The Dufour effect, sometimes referred to as diffusion-thermo effect, indicates that a temperature gradient can be induced by a concentration gradient and vice versa, resulting in the linked transfer of mass and heat. On a porous media with thermo-diffusion and diffusion-thermo effects, Moorthy and Senthilvadivu [29] investigated the thermal and mass transfer in a buoyancy-driven flow through a vertical surface. Using thermo-diffusion and diffusion-thermo effects, Partha et al. [30] explored the influence of double dispersion upon thermal and mass transfer by free convection over a vertical surface containing a non-Darcy conducting fluid filled with porous media. Ramzan et al. [31] researched on the mixed convective transport that occurs in a Maxwell nanofluid across a porous vertically expanded surface combining the thermo-diffusion and diffusion-thermo effects. Venkateswarlu and Narayana [32] researched the mixed convection flow of the Maxwell fluid through a vertical stretched sheet in combination with the context of magnetic field, Joule heating, chemical reactions and the Soret and Dufour effects. De [33] analysed the unsteady flow of a free convective Eyring-Powell magneto nanofluid mixed with Soret and Dufour effects past a semi-infinite vertical plate. Temjennaro and Hemanta [34] and Mathews and Hymavathi [35] considered an unsteady MHD flow with variable fluid properties.

1.1. Significance and uniqueness of the current work

This research peeps into the effects of the Soret and Dufour effects, magnetic and electric fields, and electro-osmotic force on the Darcy-Forcheimer flow and heat and mass transfer properties of Maxwell nanofluid. The novelty of this study is found in its detailed approach to modelling the intricate interactions among these factors, offering new insights into the behaviour of Maxwell nanofluids under the combined study of Soret-Dufour effect and electro-osmotic effect in the non-Darcy porous medium:

- A topic that has not been widely examined in past research.
- Understanding the concept of boundary layer can provide insights into overall effectiveness of nanofluids.
- It has potential applications in industry sectors such as cooling systems, crystal formation and magnetic drug targeting.
- It examines how non-Darcy porous media affect the heat and mass transfer in a Maxwell nanofluid, by filling a gap in literature and increasing our understanding of the complicated fluid behaviour of porous media.

- This offers the framework for future research to interact between the thermo-diffusion and diffusion-thermo effects in nanofluids, which helps to improve prediction accuracy in engineering.

The significance of the study lies in the following:

- Effective heat transmission may be achieved via thermomagnetic pumping, which makes use of the combination of nanofluids with EMHD.
- Darcy-Forchheimer flow models are useful to investigate fluid flow over high velocity porous medium in water purification and desalination processes.
- Thermo-diffusion effect and diffusion-thermo effect in Maxwell fluid are used in cooling strategies in electronic devices.
- To optimize the transfer of heat in electro-kinetic heat exchangers, electro-osmotic force can be employed combined with Maxwell nanofluids.
- For physical comprehension, the velocity profile, temperature profile and concentration profile for various parameters are illustrated.

2. Mathematical formulation

Consider the steady, viscous, incompressible and Darcy-Forchheimer stream of Maxwell nanofluid over the porous medium. The flow is limited to the $y > 0$ plane. Nonetheless, the *x*-axis is tracked along the flow path, and the *y*-axis is selected orthogonal to the *x*-axis, in order to characterize the physical issue under consideration using the Cartesian coordinate system. Furthermore, an electroosmotic flow (EOF) is added to the sheet. The magnetic field occurs normally to the sheet, which is represented as $B = (0, B_0, 0)$, and the electric field $E = E(x)$ is generated from the applied magnetic field. Ohm's law $J = \sigma(E + V \times B)$ applies to both the magnetic and electric fields wherein V is the fluid velocity field, σ is the electrical conductivity and J is the Joule current. Moreover, the sheet is expanded over the path of the flow with a constant origin as a result of the action of opposing forces that are equal. Nevertheless, the fluid flow happened as a result of the sheet expanding in the line of *x*-axis (ref. Fig. 1, Zaher et al. [37]).

The governing equation of the Maxwell nanofluid flow equations are given below, with the aid of the boundary layer and above assumption which is obtained from Suraih Palaiah et al. [36]:

$$\frac{\partial u}{\partial x} + \frac{\partial v}{\partial y} = 0, \tag{1}$$

$$u\frac{\partial u}{\partial x} + v\frac{\partial u}{\partial y} = \nu\frac{\partial^2 u}{\partial y^2} - \lambda\left(u^2\frac{\partial^2 u}{\partial x^2} + v^2\frac{\partial^2 u}{\partial y^2} + 2uv\frac{\partial^2 u}{\partial x \partial y}\right) - \frac{\sigma}{\rho c_p}\left({B_0}^2 u - EB_0\right) - \frac{\mu}{k_p}u - \frac{F}{\sqrt{k_p}}u^2 + \rho_e E_x, \tag{2}$$

$$u\frac{\partial T}{\partial x} + v\frac{\partial T}{\partial y} = \frac{k}{\rho c_p}\frac{\partial^2 T}{\partial y^2} + \frac{\mu}{\rho c_p}\left(\frac{\partial u}{\partial y}\right)^2 + \tau\left[D_B\frac{\partial C}{\partial y}\frac{\partial T}{\partial y} + \frac{D_T}{T_\infty}\left(\frac{\partial T}{\partial y}\right)^2\right] + \frac{\sigma}{\rho c_p}(uB_0 - E)^2 + \frac{D_m K_T}{T_m}\frac{\partial^2 T}{\partial y^2}, \tag{3}$$

$$u\frac{\partial C}{\partial x} + v\frac{\partial C}{\partial y} = D_B\frac{\partial^2 C}{\partial y^2} + \frac{D_T}{T_\infty}\frac{\partial^2 T}{\partial y^2} + \frac{D_m K_T}{T_m}\frac{\partial^2 T}{\partial y^2} - k_1(C - C_\infty). \tag{4}$$

In the above Eqs. (1)−(4), μ, ν, λ, ρ, k_p, σ, c_p, D_B, D_T, k_1 represent the viscosity, kinematic viscosity, relaxation time, density, permeability of the porous medium, electrical conducivity, specific heat, Brownian motion coefficient, thermophoresis diffusion coefficient and chemical reaction rate.

The continuity principle is embodied in Eq. (1), which guarantees mass conservation. The momentum equation is given by Eq. (2), where the second term on the right-hand side represents

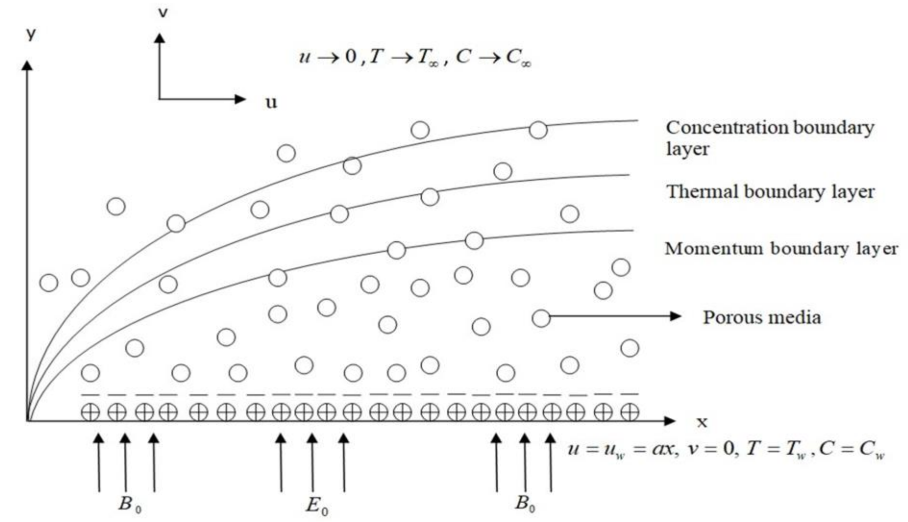

Fig. 1. Illustration of fluid flow.

the Maxwell fluid, the third term describes the behaviour of the magnetic and electric fields, the fourth term is due to the impact of porous media, the next term characterizes the Darcy-Forchheimer flow, and the last term refers to the electro-osmotic force. The energy equation is given by Eq. (3), where the second term on the right denotes the viscous dissipation, the third term represents the essence of Brownian motion and thermophoresis effect, the next term refers to the Joule heating and the last term denotes the Dufour effect. A chemical process is represented by the term at the right of Eq. (4); before that, the Soret effect is denoted, which appears in the concentration equation.

For the above Eqs. (1)–(4), the boundary conditions are (Suraih Palaiah et al. [36]):

$$u = u_w = ax, \quad v = 0, \quad T = T_w, \quad C = C_w \quad \text{at} \quad y = 0,$$
$$u \to 0, \quad T \to T_\infty, \quad C \to C_\infty \quad \text{as} \quad y \to \infty. \tag{5}$$

The boundary conditions in Eq. (5) are governed by the surface temperature and concentration, with consistent velocity at the surface and by the ambient temperature and concentration with zero velocity at the outer edge of the boundary layer.

The partial differential equations (PDEs) (2)–(4) are converted into the ordinary differential equations (ODEs) by the following similarity transformations from Suraih Palaiah et al. [36]:

$$\eta = \sqrt{\frac{a}{\nu}}y, \quad u = axf'(\eta), \quad v = -\sqrt{a\nu}f(\eta),$$
$$\theta(\eta) = \frac{T-T_\infty}{T_w-T_\infty}, \quad \phi(\iota) = \frac{C-C_\infty}{C_w-C_\infty}. \tag{6}$$

3. Examining electro-osmotic flow using boundary layer flow

The following can be obtained from the Gaussian law (Zaher et al. [37]):

$$\nabla \cdot E = \frac{\rho_e}{\varepsilon}, \tag{7}$$

where ε is the dielectric permittivity and ρ_e is the overall ionic energy density. Since it is believed that the electric field is conservative, the electric potential $\bar{\Gamma}$ is written as follows:

$$E = -\nabla\bar{\Gamma}. \tag{8}$$

Substituting Eq. (8) into Eq. (7)

$$\nabla \cdot \nabla\bar{\Gamma} = \nabla^2\bar{\Gamma} = -\frac{\rho_e}{\varepsilon}. \tag{9}$$

The Boltzmann distribution is described by the total density of charged particles, which is symbolized as (Abdelsalam et al. [38]):

$$\rho_e = -Z_v e(\bar{n}^- - \bar{n}^+), \tag{10}$$

where the term $\bar{n}^- = \bar{n}_0 e^{-\frac{eZ_v}{T_{av}K_B}\bar{\Gamma}}$ denotes the anions and $\bar{n}^+ = \bar{n}_0 e^{\frac{eZ_v}{T_{av}K_B}\bar{\Gamma}}$ denotes the cations. The Debye-Huckel linearization principle states that $\frac{eZ_v}{T_{av}K_B} << 1$. Reducing Eq. (10), we get

$$\rho_e = \frac{\varepsilon}{{\lambda_e}^2}\bar{\Gamma}, \tag{11}$$

where $\partial/\partial x \to 0$ in Eq. (9), leading to:

$$\frac{d^2\bar{\Gamma}}{dy^2} = \frac{1}{\lambda_e^2}\bar{\Gamma}. \tag{12}$$

Using the following transformation

$$\Gamma = \frac{\bar{\Gamma}}{\xi}, \quad \eta = \sqrt{\frac{a}{y}}y,$$

Eq. (12) is transformed to:

$$\frac{d^2\Gamma}{d\eta^2} = m_e^2\Gamma,$$

where $m_e = \sqrt{\frac{\nu}{a}\frac{1}{\lambda_e}}$ is the electro-osmotic parameter.

The outcome of the above equation with boundary conditions $\Gamma = 1$ at $\eta = 0$ and $\Gamma \to \infty$ at $\eta \to \infty$ is

$$\Gamma = \exp(-m_e\eta). \tag{13}$$

The transformed ordinary differential Eqs. (2)–(4) are:

$$f''' - \beta^*(f^2f''' - 2ff'f'') + ff'' - f'^2 + M(E_1 - f') - Kf' - \mathrm{Fr}f'^2 + U_{hs}m_e^2\mathrm{e}^{-m_e\eta} = 0, \tag{14}$$

$$u\theta'' + \Pr f\,\theta' + \Pr \mathrm{E}\,cf''^2 + \Pr N\,b\theta'\phi' + \Pr N\,t\theta'^2 + \Pr M\,\mathrm{Ec}(f' - E_1)^2 + \Pr \mathrm{D}\,\mathrm{f}\phi'' = 0,. \tag{15}$$

$$\phi'' + \mathrm{Sc}f\phi' + \frac{Nt}{Nb}\mathrm{Sc}\theta'' + \mathrm{SrSc}\theta'' - \mathrm{KrSc}\phi = 0. \tag{16}$$

The boundary conditions for the above equations are:

$$f(0) = 0, f'(0) = 1, \ \theta(0) = 1, \ \varphi(0) = 1 \text{ at } \eta = 0,$$
$$f'(\infty) \to 0, \ \theta(\infty) \to 0, \ \varphi(\infty) \to 0 \text{ as } \eta \to \infty. \tag{17}$$

The dimensionless parameters in Eqs. (14)–(16) are given below: $\beta^* = \lambda a$ is a Maxwell fluid parameter, $M = \frac{\sigma B_0}{\rho a}$ is a magnetic parameter, $E_1 = \frac{E}{B_0 u_w}$ is the electric field parameter, $K = \frac{\mu}{k_p a}$ is the porosity parameter, $\mathrm{Fr} = \frac{Fx}{\sqrt{k_p}}$ is the Forchheimer number, $U_{hs} = \frac{\varepsilon\xi E_x}{\nu u_w}$ is the Helmholtz-Smoluchowski velocity, $m_e = \sqrt{\frac{a}{\nu}\frac{1}{\lambda_e}}$ is the electro-osmotic parameter, $\Pr = \frac{\nu}{\alpha}$ is the Prandthl number, $\mathrm{Ec} = \frac{u_w^2}{c_p(T_w - T_\infty)}$ is the Eckert number,

$Nb = \frac{\tau D_B}{\nu}(C_w - C_\infty)$ is the Brownian motion parameter, $Nt = \frac{\tau D_T}{\nu T_\infty}(T_w - T_\infty)$ is the thermophoresis parameter, $\mathrm{Df} = \frac{D_m K_T}{\nu c_s c_p}\frac{(C_w - C_\infty)}{(T_w - T_\infty)}$ is the Dufour number, $\mathrm{Sc} = \frac{\nu}{D_B}$ is the Schmidt number, $\mathrm{Sr} = \frac{D_m K_T}{\nu T_m}\frac{(T_w - T_\infty)}{(C_w - C_\infty)}$ is the Soret number, $\mathrm{Kr} = \frac{k_1}{a}$ is the chemical reaction parameter.

The local skin-friction coefficient (C_{fx}), the Nusselt number (Nu_x) and the Sherwood number (Sh_x) for the current study are as follows:

$$C_{fx} = \frac{\tau_w}{\rho u_w^2}, \quad \mathrm{Nu}_x = \frac{x q_w}{k(T_w - T_\infty)}, \quad \mathrm{Sh}_x = \frac{x q_m}{D_B(C_w - C_\infty)}, \tag{18}$$

where $\tau_w = \mu\left(\frac{\partial u}{\partial y}\right)_{y=0}$ is the wall shear stress, $q_w = -k\left(\frac{\partial T}{\partial y}\right)_{y=0}$ is the heat flux and $q_m = -D_B\left(\frac{\partial C}{\partial y}\right)_{y=0}$ is the mass flux.

Equations (18) are reduced to non-dimensional form as follows:

$$C_{fx}\mathrm{Re}_x^{\frac{1}{2}} = f''(0), \quad \mathrm{Nu}_x\,\mathrm{Re}_x^{-\frac{1}{2}} = -\,\theta'(0),$$
$$\mathrm{Sh}_x\,\mathrm{Re}_x^{-\frac{1}{2}} = -\,\varphi'(0), \tag{19}$$

where $\mathrm{Re}_x = ax^2/\nu$.

4. Numerical methods

Employing the fifth order Runge-Kutta-Fehlberg method combined with a shooting method, one can determine the accepted finite values of $\eta \to \infty$ and solve the non-linear ODEs (14)–(16). The values n_∞ are found by picking a set of initial estimate values for various physical variables and repeating the method unless two consecutive values of $f''(0)$, $\theta'(0)$ and $\varphi'(0)$ are deviated by less than a specified tolerance. This approach reduces Eqs. (14)–(16) to seven simultaneous ODE's with the following consequences:

$$f_1' = f_2,$$
$$f_2' = f_3,$$
$$f_3{}' = \frac{1}{1-\beta^* f_1^2}\left[f_2^2 - 2\beta^* f_1 f_2 f_3 - f_1 f_3 - M(E_1 - f_2) - K f_2 - \mathrm{Fr} f'^2 + U_{hs} m_e^2 \mathrm{e}^{-m_e^2 \eta}\right],$$
$$f_4' = f_5,$$
$$f_5' = -\left(\frac{\mathrm{Pr}}{l} - \mathrm{PrDfSc}\frac{Nt}{Nb} - \mathrm{PrDfScSr}\right)[f_1 f_5 + \mathrm{Ec} f_3^2 + Nb f_5 f_7 + Nt f_5^2 + M\mathrm{Ec}(f_2 - E_1)^2 - \mathrm{DfSc} f_1 f_7 + \mathrm{Df}Kr\, f_6],$$
$$f_6' = f_7,$$
$$f_7' = -\mathrm{Sc} f_1 f_7 - \frac{Nt}{Nb} f_5' - \mathrm{SrSc} f_5' + Kr\mathrm{Sc} f_6.$$

Here $f_1 = f$, $f_2 = f'$, $f_3 = f''$, $f_4 = \theta$, $f_5 = \theta'$, $f_6 = \varphi$, $f_7 = \varphi'$.

The following are the transformed boundary conditions:

$$f_1 = 0, \quad f_2 = 1, \quad f_3 = c_1, \quad f_4 = 1$$
$$f_5 = c_2, \quad f_6 = 1, \quad f_7 = c_3 \quad \text{at} \quad \eta = 0,$$
$$f_2 = 0, \quad f_4 = 0, \quad f_6 = 0 \quad \text{at} \quad \eta \to \infty.$$

The values $f''(0)$, $\theta'(0)$ and $\varphi'(0)$ are found using the initial guess values c_1, c_2, and c_3 until they satisfy the boundary conditions. The fifth order Runge-Kutta method is employed to achieve highly accurate results with a convergence threshold of 10^{-8}. This ensures that the numerical solutions are precise and reliable, allowing for a detailed understanding of the fluid flow behaviour.

5. Results and discussion

The graphs represented in this section depict the significance of the parameters mentioned in Eqs. (14)–(16) with the help of boundary condition in Eq. (17) for the steady flow conduct, temperature and concentration distribution. The Nusselt numbers for a subset of Prandtl numbers are compared in order to validate the current study. It is assumed that $Nt = Nb = 0.1$, $\mathrm{Sc} = 1.0$ and all other parameters are set to zero. There is an excellent compromise in contrast to the previously published research of [26–28] and it is presented in Table 1.

Table 1. Comparative analysis of outcomes for the Nusselt number $-\ \theta'(0)$ with $Nt = Nb = 0.1$, $\mathrm{Sc} = 1.0$; all other parameters set to zero.

Pr	Wang [39]	Reddy Gorla et al. [40]	Khan and Pop [41]	Present
0.07	0.0656	0.0656	0.0663	0.06592
0.2	0.1691	0.1691	0.1691	0.16889
0.7	0.4539	0.5349	0.4539	0.45465
2.0	0.9114	0.9114	0.9113	0.91132

Furthermore, it is shown that when Pr values rise, heat transfer improves. The study's findings are illustrated graphically for particular parameter ranges such as: $0.5 \le \beta^* \le 12.5$, $0.5 \le M \le 8.5$, $0.1 \le E_1 \le 0.4$, $1 \le K \le 5$, $0.3 \le \mathrm{Fr} \le 5$, $0.5 \le U_{hs} \le 5.0$, $0.4 \le m_e \le 9.0$, $5.0 \le \mathrm{Pr} \le 9.0$, $0 \le \mathrm{Ec} \le 0.3$, $0.3 \le Nb \le 11.0$, $0.8 \le Nt \le 3$, $0.1 \le \mathrm{Df} \le 2.5$, $2 \le \mathrm{Sc} \le 4$, $0.05 \le \mathrm{Sr} \le 0.5$, and $0.3 \le Kr \le 4.5$. These intervals were chosen to guarantee manageable computation and ensure convergence under the specified conditions.

The influence of Maxwell fluid parameter (β^*) on the velocity profile is shown in Fig 2. The relaxation time (λ) increases with an increase in β^*, which enhances the fluid's elastic nature. As a result, the viscosity rises, causing greater resistance to flow and the velocity profile falls. Physically, this represents the greater dominance of elastic effects, which slow down the fluid velocity since it takes longer to recover after deformation. The same trend occurs in Suraih Palaiah et al. [36].

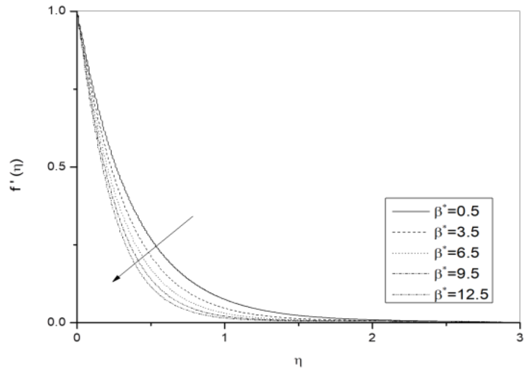

Fig. 2. Effect of Maxwell fluid parameter on velocity profile.

Figure 3 illustrates the impact of magnetic parameter (M) upon velocity distribution. The force that acts on the fluids is the Lorentz force which opposes the fluid velocity. This causes an increase in the resistance of flow and a fall in the velocity profile. A similar pattern is observed in the study of Jamshed [13].

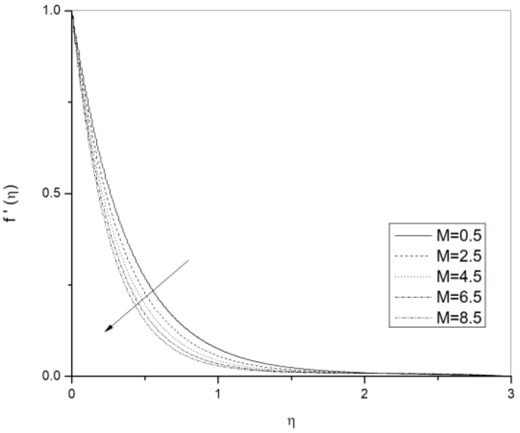

Fig. 3. Contribution of magnetic parameter to velocity distribution.

The influence of the porosity parameter (K) on the velocity profile is displayed in Fig. 4. The flow resistance rises as the porosity parameter grows because the voids in the porous medium get bigger. As an outcome, the velocity profile gets decreased. A comparable pattern is noted by Mohanty et al. [27]. Figure 5 shows the impact of the Forchheimer number (Fr) on the velocity distribution. It is discovered in which the Forchheimer number rises, the boundary layer thickens because the Forchheimer number represents inertial drag effects in porous media. This results in adding resistance to the fluid motion. As a result, the velocity profile decreases. The same trend is observed in the work of Mohanty et al. [27].

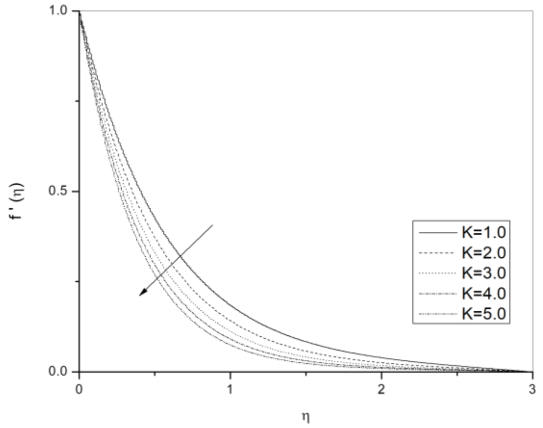

Fig. 4. Effect of porosity parameter on velocity distribution.

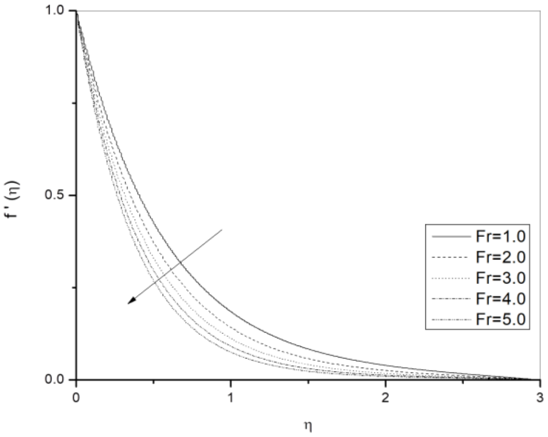

Fig. 5. Effect of Forchheimer number on velocity distribution.

Figure 6 illustrates how the velocity profile is affected by the Helmholtz-Smoluchowski velocity (U_{hs}). As the Helmholtz-Smoluchowski velocity rises, it causes particles that are charged in electric fields produced in the electro-osmotic flow to travel at an average faster velocity. That results in increases of the velocity distribution by reducing the resistance. The similar pattern is noted by Zaher et al. [37].

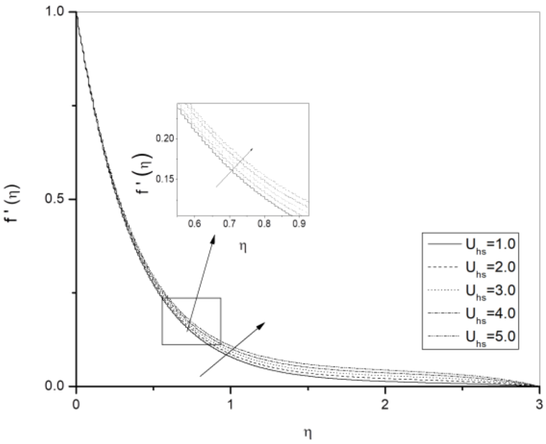

Fig. 6. Effect of Helmholtz-Smoluchowski velocity on velocity profile.

Figure 7 depicts the consequence of electro-osmotic parameter (m_e) upon the velocity profile. As the electro-osmotic parameter increases it leads to creating an electric double layer (EDL) in the flow which strengthens the electrostatic forces near the charged surface by creating more drag. This increases resistance of the fluid flow, and thereby decreases the velocity distribution. A comparable trend is noted in the study conducted by Hegazy et al. [42].

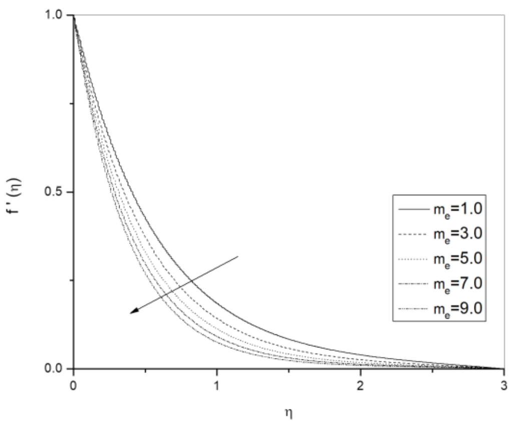

Fig. 7. Effect of electro-osmotic parameter on velocity distribution.

As seen in Fig. 8, a rise in the temperature distribution is implied by a booster in the Prandtl number. Thermal diffusivity becomes more prevalent over kinematic viscosity as by definition, as the Prandtl number increases. The same pattern is observed by Kumar et al. [43].

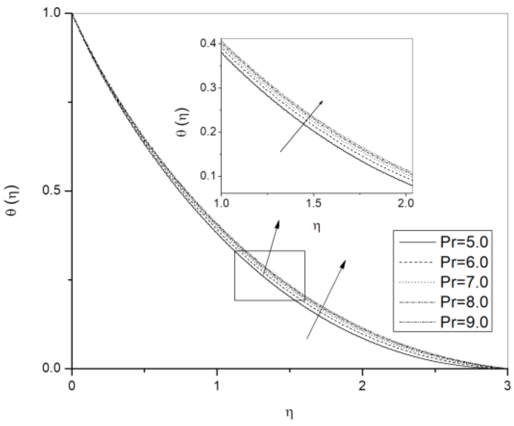

Fig. 8. Effect of Prandtl number on temperature profile.

A growth in the Eckert number (Ec) indicates a decrease in the temperature profile, as shown in Fig. 9. The kinetic energy dissipation may be of greater importance in the flow than the heat transmission if the Eckert number rises. This could contribute to a drop in the temperature distribution by decreasing the capacity of kinetic energy conversion to thermal energy. This trend is occurred in Palanimani [44]. Figure 10 demonstrates the way that the thermophoresis parameter (Nt) consequences the temperature profile. The temperature distribution rises when Nt is increased because it is found that nanoparticles at the hot boundary layer are being moved in the direction of the cold fluid by the thermophoretic force. This force redistributes the heat and results in an increase of the temperature profile. A comparable pattern is noted in Ragupathi et al. [45]. Figure 11 depicts the effects of the Dufour number (Df) on temperature profile. Thermal diffusivity to mass diffusivity is expressed as a Dufour number. An increased Dufour number suggests that thermal diffusivity is more vital than mass diffusivity. It follows that a rise in the temperature profile is the outcome of heat transfer effects predominating over mass transfer effects. The same trend occurs in De [33].

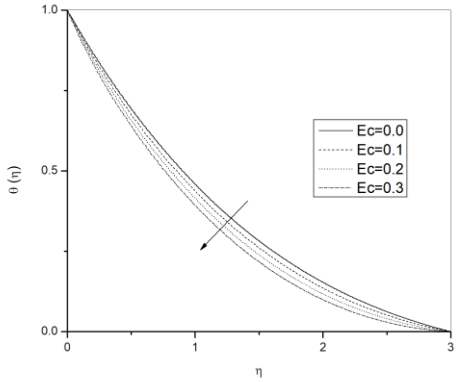

Fig. 9. Effect of Eckert number on temperature profile.

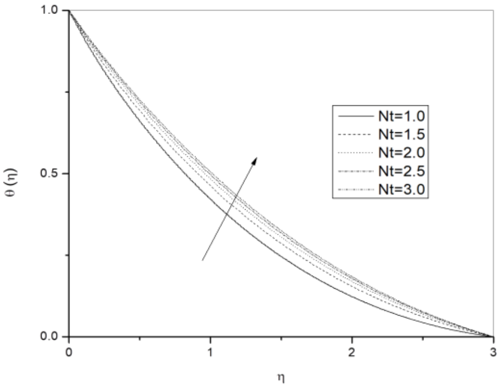

Fig. 10. Effect of thermophoresis parameter on temperature profile.

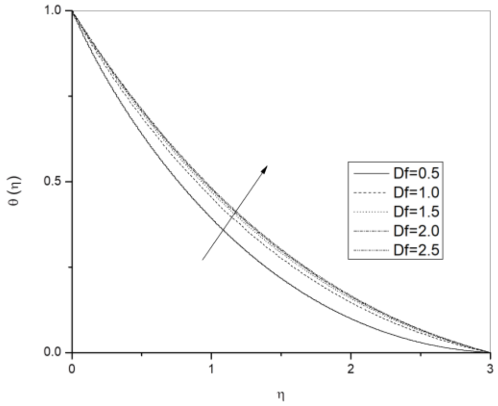

Fig. 11. Effect of Dufour number on temperature profile.

Figure 12 shows how a change in the Brownian motion parameter (Nb) causes the concentration distribution to increase. The chaotic movement of nanoparticles in suspension in the carrier fluid is called Brownian motion. A rise in Brownian motion results in moving particles more vigorously and randomly and hence, evens out the concentration of particles across the fluid by reducing the difference between high and low concentration regions. Thus, as the value of Nb increases, the concentration decreases. A similar pattern is observed by Awan et al. [46].

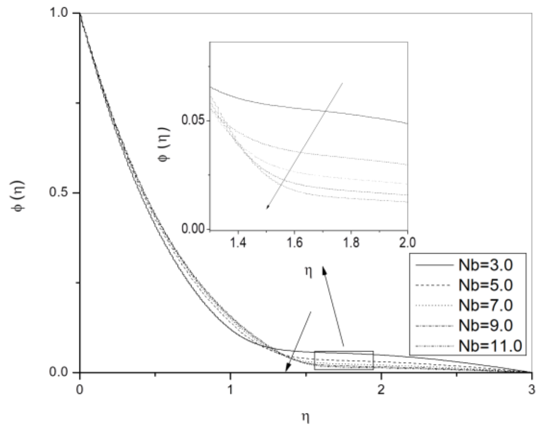

Fig. 12. Effect of Brownian motion parameter on concentration profile.

The consequence of Schmidt number (Sc) on concentration distribution is revealed in Fig. 13. The kinematic viscosity to mass diffusivity ratio is represented as the Schmidt number. A rise in Schmidt number raises kinematic viscosity and lowers mass diffusivity and it results in a fall in concentration gradients and a decrease in concentration profiles.

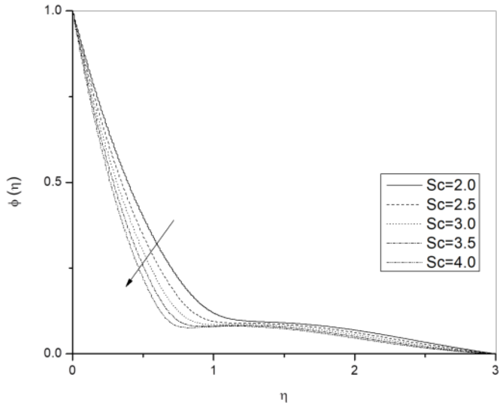

Fig. 13.The influence of Schmidt number on concentration distribution.

Soret number's influence over the concentration profile is shown in Fig. 14. A boost in the Soret number (Sr) leads to an enhancement in the concentration profile because thermal diffusion has a major impact on the flow of species within a fluid mixture, leading the concentration profile to rise. A similar pattern is observed by De [33]. Figure 15 shows the impact of chemical reaction parameter (Kr) on the concentration distribution. An increase in chemical reaction parameter causes the concentration profile to decrease because the reactant concentrations may fall more rapidly, resulting in a more noticeable reduction in concentration gradients within the fluid. The same trend is found by Raza et al. [47].

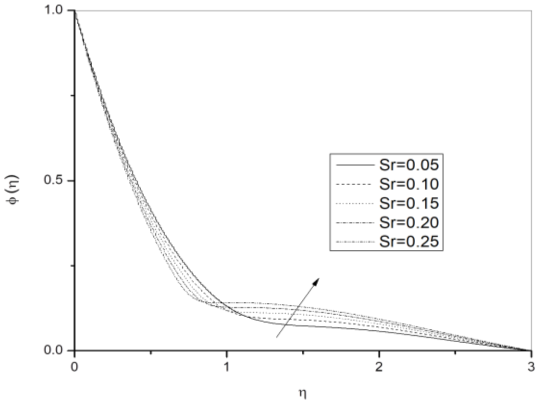

Fig. 14.Effect of Soret number on concentration profile.

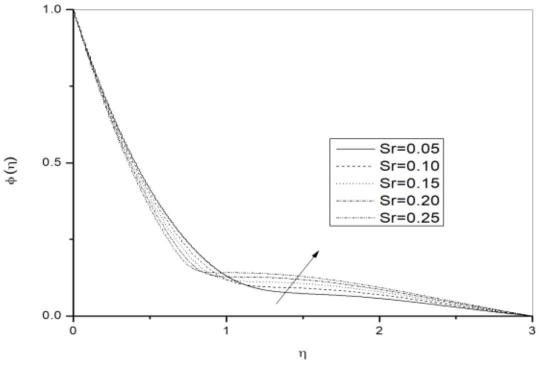

Fig. 15. Effect of Soret number on concentration profile.

Table 2 describes the skin friction coefficient for different parameters including the Maxwell fluid parameter, magnetic field parameter, electric field parameter, porosity parameter, Forchheimer number, Helmholtz-Smoluchowski velocity and electro-osmotic parameter. An increase in Maxwell fluid parameter, magnetic parameter, porosity parameter, Forchheimer number and electro-osmotic parameter decreases the skin friction coefficient due to the reduction in velocity gradient near the wall, whereas an increase in electric field parameter and Helmholtz-Smoluchowski velocity increases the skin friction coefficient. Table 3 represents the Nusselt number and Sherwood number for different parameters including the Prandtl number, Eckert number, Brownian motion parameter, thermophoresis parameter, Dufour number, Schmidt number, Soret number and chemical reaction parameter. Increasing the Prandtl number, thermophoresis parameter, Dufour number and Soret number reduces the Nusselt number by decreasing the convective heat transfer and increases the Sherwood number by strengthening mass transfer. Conversely, an increase in Eckert number, Brownian motion, Schmidt number and chemical reaction parameter leads to an increase in Nusselt number and a decrease in Sherwood number.

Table 2. Skin friction coefficient for different parameters.

β^*	M	E_1	K	Fr	U_{hs}	m_e	$f''(0)$
0.5	0.5	0.2	3.0	0.3	0.5	0.4	-2.15952
1.5							-2.27339
2.5							-2.38406
0.5	0.4						-2.14594
	1.2						-2.25369
	2.0						-2.35878
	0.5	0.1					-2.18365
		0.3					-2.13543
		0.5					-2.08362
		0.2	1.0				-1.63064
			3.0				-2.15952
			5.0				-2..58216
			3.0	1.0			-2.26370
				3.0			-2.53863
				5.0			-2.78723
				0.3	1.0		-2.14220
					3.0		-2.07310
					5.0		-2.00428
					0.5	1.0	-2.14424
						3.0	-2.17148
						5.0	-2.17659

Table 3. Nusselt and Sherwood number for different parameters.

Pr	Ec	Nb	Nt	Df	Sc	Sr	Kr	$-\Theta(0)$	$-\varphi(0)$
5.0	0.2	0.3	0.8	1.2	0.8	0.5	0.3	0.54207	0.08890
7.0								0.53824	0.09971
9.0								0.53616	0.10554
6.2	0.1							0.50781	0.18830
	0.2							0.53946	0.09627
	0.3							0.57110	0.00424
	0.2	0.1						0.39941	0.16694
		0.2						0.46790	0.13298
		0.3						0.53945	0.09266
			1.0					0.51018	0.07099
			2.0					0.44849	0.06762
			3.0					0.42697	0.21223
			0.8	1.0				0.55726	0.04461
				1.5				0.52217	0.14643
				2.0				0.50539	0.19515
				1.2	0.3			0.45908	0.12628
					0.9			0.55407	0.09038
					1.5			0.63317	0.05616
					0.8	0.1		0.56699	0.08725
						0.5		0.53946	0.09627
						0.9		0.51777	0.10322
						0.5	0.1	0.47846	0.11703
							0.3	0.53946	0.09626
							0.5	0.60206	0.07332

6. Conclusions

This article examined the numerical solutions of two-dimensional, incompressible, electro-osmotic and Darcy-Forchheimer flow of the Maxwell nanofluid with the effects of electric and magnetic fields, Soret and Dufour effects, and chemical reaction over a porous medium. The results of these findings have been potentially used to improve industrial processes by increasing heat transfer in cooling systems, enhancing chemical reactor efficiency, refining filtering and separation procedures, expanding oil recovery technologies, and developing more effective medication delivery systems. Our research led us to the conclusions that:

- When the Maxwell fluid parameter, porosity parameter, Forchheimer number and electro-osmotic parameter are increased, the velocity profile decreases.
- The velocity develops as the magnetic parameter, electric field parameter and Helmholtz-Smoluchowski velocity rises.
- As the Prandtl number, thermophoresis parameter, and Dufour number rise, the temperature profile rises.
- The temperature profile narrows as the Eckert number rises.
- When the Brownian motion parameter, Schmidt number or chemical reaction parameter are increased, the concentration profile decreases.
- In the case where the Soret number grows, so does the concentration profile.
- The skin friction increases by 4% when the electric field parameter increases from 0.1 to 0.5. The Eckert number increases the Nusselt number by 35% and decreases the Sherwood number by 44%.

The future direction emphasizes the emergence of novel modelling approaches for industrial and technical applications, giving significant insights into the complicated behaviour of fluid flow which is investigated in this paper. Our work will focus on analysing how these effects impact the fluid flow behaviour and heat and mass transfer rates, and determining which parameters should be optimized to design more efficient systems, optimize processes, and improve material performance in fields such as nanotechnology, biotechnology and energy storage.

7. Limitation and future scope

When it comes to getting exact answers for boundary value problems, the fifth order Runge-Kutta method with the shooting technique is quite effective. However, in order to get the best convergence outcomes, one must be careful regarding initial guesses in the shooting technique. The applicability of this study's findings may be limited to specific conditions such as selected nanofluid, flow parameters and boundary conditions. Future research could expand upon this investigation by exploring various non-Newtonian fluids or hybrid models across various different geometries and certain analysis like sensitivity analysis, entropy generation and stability analysis can be performed.

References

[1] Choi, S.U.S., & Eastman, J.A. (1995). Enhancing thermal conductivity of fluids with nanoparticles. *ASME International Mechanical Engineering Congress & Exposition*, Nov. 12-17, San Francisco, USA.

[2] Wong, K.V. & De Leon, O. (2010). Applications of nanofluids: Current and future. *Advances in Mechanical Engineering*, 2, 519659. doi:10.1155/2010/519659

[3] Jama, M., Singh, T., Gamaledin, S.M., Koc, M., Samara, A., Isaifan, R.J., & Atieh, M.A. (2016). Crictical review on nanofluids: preparation, characterization, and applications. *Journal of Nanomaterials*, 2016(1), 717624. doi: 10.1155/2016/6717624

[4] De, P., Mondal, H., & Bera, U.K. (2016). Dual solutions of heat and mass transfer of nanofluid over a stretching/shrinking sheet with thermal radiation. *Meccanica*, 51,117−124. doi: 10.1007/s11012-015-0205-1

[5] Koriko, O.K., Shah, N.A., Saleem, S., Chung, J.D., Omowaye, A.J., & Oreyeni, T. (2021). Exploration of bioconvection flow of MHD thixotropic nanofluid past a vertical surface coexisting with both nanoparticles and gyrotactic microorganisms. *Scientific Reports*, 11, 16627. doi: 10.1038/s41598-021-96185-y

[6] Yaseen, M., Rawat, S.K., Shah, N.A., Kumar, M., & Eldin, S M. (2023). Ternary hybrid nanofluid flow containing gyrotactic microorganisms over three different geometries with Cattaneo-Christov model. *Mathematics*, 1(5), 1237. doi: 10.3390/math11051237

[7] Akram, M., Shahzad, M.H., Ahammad, N.A., Gamaoun, F., Awan, A.U., Hamam, H., & Alroobaea, R. (2024). Rheology of Eyring-Powell hybrid nanofluid flow under the peristaltic effects through an elliptical conduit: Analytical investigation. *Results in Physics*, 59, 107602. doi: 10.1016/j.rinp.2024.107602

[8] Shah, S.A.A., Qayyum, S., Nadeem, S., Alzubadi, H., Ahammad, N.A., Awan, A.U., & Alroobaea, R. (2025). Thermal characterization of Sutterby nanofluid flow under Riga plate: Tiwari and Das model. *Modern Physics Letters B*, 39(3) 2450421. doi: 10.1142/S0217984924504219

[9] Shahzad, M.H., Awan, A.U., Guedri, K., Fadhl, B.M., & Oreijah, M. (2024). Entropy-based investigation of blood flow in elliptical multi-stenotic artery with hybrid nanofluid in a fuzzy environment: Applications as drug carriers for brain diseases. *Engineering Applications of Artificial Intelligence*, 130, 107695. doi: 10.1016/j.engappai.2023.107695

[10] Akbar, A.A., Awan, A.U., Nadeem, S., Ahammad, N.A., Raza, N., Oreijah, M., Guedri, K. & Allahyani, S.A. (2024). Heat transfer analysis of Carreau-Yasuda nanofluid flow with variable thermal conductivity and quadratic convection. *Journal of Computational Design and Engineering*, 11(1), 99−109. doi: 10.1093/jcde/qwae009

[11] Hayat, T., Muhammad, T., Shehzad, S.A., Chen, G.Q., & Abbas, I.A. (2015). Interaction of magnetic field in flow of Maxwell nanofluid with convective effect. *Journal of Magnetism and Magnetic Materials*, 389, 48−55. doi: 10.1016/j.jmmm.2015.04.019.

[12] Nagendramma, V., Kumar, R.K., Prasad, P.D., Leelaratnam, A., & Varma, S.V. (2016). Multiple slips and radiation effects on Maxwell nanofluid flow over a permeable stretching surface with dissipation. *Journal of Nanofluids*, 5(6), 817−825. doi: 10.1166/jon.2016.1273.

[13] Jamshed, W. (2021). Numerical investigation of MHD impact on Maxwell nanofluid. *International Communications in Heat and Mass Transfer*, 120, 104973. doi: 10.1016/j.icheatmasstransfer.2020.104973

[14] Murtaza, S., Iftekhar, M., Ali, F., & Khan, I. (2020). Exact analysis of non-linear electro-osmotic flow of generalized Maxwell nanofluid: application in concrete based nano-materials. *IEEE Access*, 8, 96738-96747. doi: 10.1109/ACCESS.2020.2988259

[15] Sultana, N., Shaw, S., Nayak, M.K., & Mondal, S. (2023). Hydromagnetic slip flow and heat transfer treatment of Maxwell fluid with hybrid nanostructure: Low Prandtl numbers. *International Journal of Ambient Energy*, 44(1), 947−957. doi: 10.1080/01430750.2022.2158370

[16] Pantokratoras, A., & Magyari, E. (2009). EMHD free-convection boundary layer flow from a Riga-plate. *Journal of Engineering Mathematics*, 64, 303−315. doi: 10.1007/s10665-008-9259-6

[17] Buren, M. & Jian, Y. (2015). Electromagnetohydrodynamic (EMHD) flow between two transversely wavy microparallel plates. *Electrophoresis*, 36(14), 1539−1548. doi: 10.1002/elps.201500029

[18] Irfan, M., Farooq, M.A., & Iqra, T.A. (2020). A new computational technique design for EMHD nanofluid flow over a variable liquid characteristics. *Frontiers in Physics*, 8, 66. doi: 10.3389/fphy.2020.00066

[19] Muhammad Atif, S., Abbas, M., Rashid, U., & Emadifar, H. (2021). Stagnation point flow of EMHD micropolar nanofluid with mixed convection and slip boundary. *Complexity*, 2021(1), 3754922. doi: 10.1155/2021/3754922.

[20] Raptis, A. (1998). Radiation and free convection flow through a porous medium. *International Communications in Heat and Mass Transfer*, 25(2), 289−295. doi: 10.1016/S0735-1933(98)00016-5

[21] Hayat, T., Abbas, Z., Pop, I., & Asghar, S. (2010). Effects of radiation and magnetic field on the mixed convection stagnation-point flow over a vertical stretching sheet in a porous medium. *International Journal of Heat and Mass Transfer*, 53(1-3), 466−474. doi: 10.1016/j.ijheatmasstransfer.2009.09.010

[22] Qing, J., Bhatti, M.M., Abbas, M.A., Rashidi, M.M., & Ali, M.E. (2016). Entropy generation on MHD Casson nanofluid flow over a porous stretching/shrinking surface. *Entropy*, 18(4), 123. doi: 10.3390/ e18040123

[23] Sajid, T., Sagheer, M., Hussain, S., & Bilal, M. (2018). Darcy-Forchheimer flow of Maxwell nanofluid flow with nonlinear thermal radiation and activation energy. *AIP Advances*, 8(3), 035102. doi: 10.1063/1.5019218

[24] Sangeetha, E, & De, P. (2021). Darcy-Forchheimer porosity effects on nanofluid with motile gyrotactic microorganisms over convectively heated surface. *Nanoscience and Technology: An International Journal*, 12(4), 19−38. doi: 10.1615/NanoSciTechnolIntJ.2021037367

[25] Mohanty, D., Mahanta, G., Chamkha, A.J., & Shaw, S. (2023). Numerical analysis of interfacial nanolayer thickness on Darcy-Forchheimer Casson hybrid nanofluid flow over a moving needle with Cattaneo-Christov dual flux. *Numerical Heat Transfer, Part A: Applications*, 86(3), 399−423. doi: 10.1080/10407782.2023.2263906

[26] Mohanty, D., Sethy, N., Mahanta, G., & Shaw, S. (2023). Impact of the interfacial nanolayer on Marangoni convective Darcy-Forchheimer hybrid nanofluid flow over an infinite porous disk with Cattaneo-Christov heat flux. *Thermal Science and Engineering Progress*, *41*, 101854. doi: 10.1016/j.tsep.2023.101854

[27] Mohanty, D., Mahanta, G., Byeon, H., Vignesh, S., Shaw, S., Khan, M. Ijaz, Abduvalieva, D., Govindan, V., Awwad, F.A., & Ismail, E.A.A. (2023). Thermo-solutal Marangoni convective Darcy-Forchheimer bio-hybrid nanofluid flow over a permeable disk with activation energy: Analysis of interfacial nanolayer thickness. *Open Physics*, 21(1), 20230119. doi: 10.1515/phys-2023-0119

[28] Sohail, M., El-Zahar, E.R., Mousa, A.A.A., Nazir, U., Althobaiti, S., Althobaiti, A., Shah, N.A., & Chung, J.D. (2022). Finite element analysis for ternary hybrid nanoparticles on thermal enhancement in pseudo-plastic liquid through porous stretching sheet. *Scientific Reports*, 12, 9219. doi: 10.1038/s41598-022-12857-3.

[29] Moorthy, M.B.K., & Senthilvadivu, K. (2012). Soret and Dufour effects on natural convection flow past a vertical surface in a porous medium with variable viscosity. *Journal of Applied Mathematics*, 2012(1), 634806. doi: 10.1155/2012/634806

[30] Partha, M.K., Murthy, P.V., & Raja Sehkhar, G.P. (2006). Soret and Dufour effects in a non-Darcy porous medium. *ASME Journal of Heat and Mass Transfer*, 128(6), 605−610. doi: 10.1115/1.2188512

[31] Ramzan, M., Bilal, M., Chung, J.D., & Farooq, U. (2016). Mixed convective flow of Maxwell nanofluid past a porous vertical stretched surface − An optimal solution. *Results in Physics*, 6, 1072−1079. doi: 10.1016/j.rinp.2016.11.036

[32] Venkateswarlu, B., & Narayana, P.V.S. (2017). Soret and Dufour effects on MHD flow of a Maxwell fluid over s stretching sheet with Joule heating. *Frontiers in Heat and Mass Transfer*, 9(11), 1−10. doi: 10.5098/hmt.9.11

[33] De, P. (2019). Soret-Dufour effects on unsteady flow of convective Eyring-Powell magneto nanofluids over a semi-infinite vertical plate. *BioNanoScience*, 9, 7−12. doi: 10.1007/s12668-018-0583-7

[34] Temjennaro, J., & Hemanta, K. (2023). Soret and Dufour effects on an unsteady MHD flow about a permeable rotating vertical cone with variable fluid properties. *Archives of Thermodynamics*, 45(1), 75−86. doi: 10.24425/ather.2024.150440

[35] Mathews, J., & Hymavathi, T. (2024). Unsteady magnetohydrodynamic free convection and heat transfer flow of Al2O3–Cu/water nanofluid over a non-linear stretching sheet in a porous medium. *Archives of Thermodynamics*, 45(1), 165–173. doi: 10.24425/ather.2024.150449

[36] Palaiah, S.S., Basha, H., Reddy, G.J, & Sheremet, M.A. (2021). Magnetized dissipative Soret effect on chemically reactive Maxwell fluid over a stretching sheet with joule heating. *Coatings*, 11(5), 528. doi: 10.3390/coatings11050528

[37] Zaher, A.Z., Ali, K.K., & Mekheimer, K.S. (2021). Electroosmosis forces EOF driven boundary layer flow for a non-Newtonian fluid with planktonic microorganism: Darcy Forchheimer model. *International Journal of Numerical Methods for Heat & Fluid Flow*, 31(8), 2534−2559. doi: 10.1108/HFF-10-2020-0666

[38] Abdelsalam, S.I., Mekheimer, K.S., & Zaher, A.Z. (2020). Alterations in blood stream by electroosmotic forces of hybrid nanofluid through diseased artery: Aneurysmal/stenosed segment. *Chinese Journal of Physics*, 67, 314−329. doi: 10.1016/j.cjph.2020.07.011

[39] Wang, C.Y. (1989). Free convection on a vertical stretching surface. *ZAMM - Journal of Applied Mathematics and Mechanics*, 69(11), 418−420. doi: 10.1007/BF00853952

[40] Reddy Gorla, R.S., & Sidawi, I. (1994). Free convection on a vertical stretching surface with suction and blowing. *Applied Scientific Research*, 52, 247-57. doi: 10.1007/BF00853952

[41] Khan, W.A., & Pop, I. (2010). Boundary-layer flow of a nanofluid past a stretching sheet. *International Journal of Heat and Mass Transfer*, 53(11–12), 2477−2483. doi: 10.1016/j.ijheatmasstransfer.2010.01.032.

[42] Hegazy, N., Eldabe, N.T., Abouzeid, M., Abousaleem, A., & Alana, A. (2023). Influence of both chemical reaction and electro-osmosis on MHD non-Newtonian fluid flow with gold nanoparticles. *Egyptian Journal of Chemistry*, 66(10), 191−201. doi: 10.21608/ejchem.2023.190175.7526

[43] Kumar, K.G., Gireesha, B.J., Rudraswamy, N.G., & Krishnamurthy, M.R. (2019). An unsteady flow and melting heat transfer of a nanofluid over a stretching sheet embedded in a porous medium. *International Journal of Applied Mechanics and Engineering*, 24(2), 245−258. doi: 10.2478/ijame-2019-0016

[44] Palanimani, P.G. (2007). Effects of chemical reactions, heat, and mass transfer on nonlinear magnetohydrodynamic boundary layer flow over a wedge with a porous medium in the presence of ohmic heating and viscous dissipation. *Journal of Porous Media*, 10(5), 489−502. doi: 10.1615/JPorMedia.v10.i5.60

[45] Ragupathi, P., Ahammad, N.A., Wakif, A., Shah, N.A., & Jeon, Y. (2022). Exploration of multiple transfer phenomena within viscous fluid flows over a curved stretching sheet in the co-existence of gyrotactic micro-organisms and tiny particles. *Mathematics*, 10(21), 4133. doi: 10.3390/math10214133

[46] Awan, A.U., Qayyum, S., Nadeem, S., Ahammad, N.A., Gepreel, K.A., Alharthi, M., & Alosaimi, M. (2024). Analysis of chemical characteristics of engine-oil-based Prandtl hybrid nanofluid flow. *ZAMM - Journal of Applied Mathematics and Mechanics/Zeitschrift für Angewandte Mathematik und Mechanik*, 104(8), e202400050. doi: 10.1002/zamm.202400050

[47] Raza, Q., Qureshi, M.Z.A., Khan, B.A., Kadhim Hussein, A., Ali, B., Shah, N.A., & Chung, J.D. (2022). Insight into dynamic of mono and hybrid nanofluids subject to binary chemical reaction, activation energy, and magnetic field through the porous surfaces. *Mathematics*, 10(16), 3013. doi: 10.3390/math10163013

Co-published by
Institute of Fluid-Flow Machinery
Polish Academy of Sciences
Committee on Thermodynamics and Combustion
Polish Academy of Sciences

http://www.imp.gda.pl/archives-of-thermodynamics/

ARCHIVES OF THERMODYNAMICS

Modelling the heat transfer of nanofluid towards a radiating stretching sheet of varying thickness using thermal flux

Pragya Pandey[a], Dhatchana Moorthy Kavitha[b*], Thangaraju Lawanya[b]

[a]Department of Mathematics, SRM Institute of Science and Technology, Ramapuram, Chennai – 600 089, Tamil Nadu, India
[b]Department of Mathematics, Saveetha School of Engineering, Saveetha Institute of Medical and Technical Sciences, Saveetha Nagar, Thandalam, Chennai – 602 105, Tamil Nadu, India
Corresponding author email: soundarkavitha@gmail.com

Received: 10.06.2024; revised: 21.08.2024; accepted: 03.10.2024

Abstract

The present paper targets the flow of fluid with Fe_3O_4 particles as nanomaterial over a non-linear elongated sheet with changing width. The process holds vital importance in various industries like paper manufacturing, extrusion of dyes and filaments, atomic reactors and many more. Nanofluids depict special features which give them the potential to be also used in power engines, refrigerators, power plants as well as pharmaceutical processes. Hence, the presented model is designed to intensify the rate of heat transfer and to reduce energy wastage, and tailor for the optimal selection of parameters like conductivity as well as viscosity, which will improve the effectiveness of the heat transfer process. The main idea behind this investigation is to calculate the effect of electromagnetohydrodynamics, Biot number, Eckert number, radiation along with the absorption factor. In this paper, the flow is modelled by using Navier-Stokes equations which are customised to Prandtl boundary layer equations. The Adams-Bashforth predictor-corrector is used to obtain numerical solutions. The present study helps to potentially improve and achieve the desired quality of the stretching sheet. Moreover, a negligible amount of activation energy is required, finding an economical way to get suitable outputs.

Keywords: Nanofluid; Nanoparticles; Stretching sheet; Thermal radiation; Viscosity; Electromagnetohydrodynamics

Vol. 46(2025), No. 2, 83–91; doi: 10.24425/ather.2025.154908

Cite this manuscript as: Pandey, P., Kavitha, D.M, & Lawanya, T. (2025). Modelling the heat transfer of nanofluid towards a radiating stretching sheet of varying thickness using thermal flux. *Archives of Thermodynamics*, 46(2), 83–91.

1. Introduction

Engineers in the domain of computational fluid dynamics (CFD) are curious to explore the cooling mechanism of elongated sheet due to its wide variety of practical importance. In many factories, different domains have utilized the cooling of stretching sheets to obtain the desired quality of the sheet. Although many liquids have been tried as cooling agents, nanofluids have been found superior in comparison to all other fluids. The fluid flow over this type of sheet has many uses in industrial processes like manufacturing parts of aircrafts, extraction of fibres from glass, manufacturing of polymer sheets, drawing filaments and dyes, and many more. The quality of sheets relies upon on rate of cooling as well as heat removal. Many scientists studied the mechanism of action of nanofluids in various geometrical shapes. In [1], copper nanofluids flow over an elongated sheet is explored. An exact solution of a thin fluid layer flowing over a stretching sheet was found in [2]. The combination of dust particles mixed

Nomenclature

A – variable viscosity parameter
A^* – space-dependent coefficient
b – stretching constant
B, B_o – magnetic field strength, T
B^* – time-dependent coefficient
Bi – Biot number
c – stretching parameter
C_p – heat capacity, J kg^{-1} K^{-1}
E, E_0 – electric field strength, N C^{-1}
E_1 – electric field parameter
Ec – Eckert number
f – base fluid
f' – velocity parameter
h – step size
k – kth iteration
k^* – mean absorption coefficient
M – magnetic field parameter
n – parameter of velocity power index
N – coefficient related to stretching sheet
Nu – Nusselt number
Pr – Prandtl number
q''' – non-uniform flux
qr – radiative heat flux, W m^{-2}
Rd – parameter of radiation
T – fluid temperature, K
T_∞ – free stream temperature, K
U_w – wall velocity, m s^{-1}
u, υ – components of velocity along x- and y-axis, m s^{-1}
x, y – Cartesian coordinates, m

Greek symbols

α – wall thickness parameter
ε – infinitesimal small
η – non-dimensional similarity variable
θ – dimensionless temperature
ϑ – viscosity parameter
κ – thermal conductivity, W m^{-1} K^{-1}
μ – dynamic viscosity, kg m^{-1} s^{-1}
ν – kinematic viscosity, m^2 s^{-1}
ρ – density, kg m^{-3}
σ – electric conductivity, S m^{-1}
σ^* – Stefan-Boltzmann constant, W m^{-2} K^{-4}
ϕ – volume fraction
ψ – streamline function

Subscripts and Superscripts

f – base fluid
nf – nanofluid
t – tri
p – particle
s – solid
w – wall
$'$ – differentiation with respect to η

Abbreviations and Acronyms

FEM – finite element method
EMHD – electromagnetohydrodynamics
MHD – magnetohydrodynamics

with nanoparticles flowing over a stretched plate was investigated with novel mathematical modelling in [3]. The flow induced by nanofluid over an exponentially stretchable plate was surveyed in [4] by considering the impact of viscous dissipation. The thermophysical characteristics of nanofluid flow along a vertical plate due to porous media along tiny sized suspensions were studied with a novel method in [5]. The situation dealing with free convection inside a cavity taking into account nanoparticles dispersed in the base fluid was solved numerically in [6]. The impact of dust grains dispersed on a stretched surface was investigated in [7]. The process of dispersing particles in liquids over an increasingly stretching sheet was studied and framed in [8] with viscous dissipation and magnetohydrodynamics (MHD) taken into account. The comparison of heat transfer in a normal fluid and nanofluid flow using different nanoparticles on a stretching surface was studied in [9]. The nanoparticle's shape was examined in [10] at a point of the magneto stagnation flow with a dual combination of effects of chemical reaction and thermal radiation. A 3D modelling of magneto flow of nanofluids over a disc was presented in [11]. The Casson flow stimulated due to gyrotactic microbes in a conical shape was solved using the Homotopy Analysis Method (HAM). Lately, the impact of magnetic nanofluid over a moving disc was deducted in [12]. The impact of MHD on nanofluid flow over an inclined stretched plate bearing an unsteady thin film flow was examined in [13].

MHD flow in nanofluids has attracted attention due to its extraordinary potential to control the rate of heat transfer. Magnetohydrodynamics is mainly derived from 3 terms: magneto, hydro and dynamics – the term was coined in [14]. The process of flow with magnetohydrodynamics on a stretched plate up to a stagnation point was investigated in [15] and estimated numerically using the finite difference method. Buongiorno's model was considered as a base to study MHD flow of nanofluid over an extending plate taking the slip factor into account [16]. A case of bidirectional MHD flow of nanofluid with Hall current and heat flux over a stretching sheet was solved by [17]. It was noticed that Hall current and heat flux boosted the quality of the sheet. Many studies related to MHD are utilized in improving machine efficiency [18–20] and serve as the motivation for the current effort. Additionally, it is noted that studies on heat transfer have utilized linear extending sheets. To document the impact of electromagnetohydrodynamic (EMHD), a non-linear elastic sheet of varying thickness has also been incorporated with boundary-layer flow of a nanofluid. Changing width of stretching sheets holds actual uses in industries, including appliance constructions and patterns, nuclear reactor mechanisation, filament extrusion, paper industry and several other fields [21–24]. Velocity slip along ternary nanofluid over a stretching sheet was enquired in [25] and concluded that the inclusion of three different nanoparticles accelerated the conduction of heat. Hybrid nanofluid over a porous stretched sheet was investigated in [26]. Natural convection of hybrid nanofluid in a quadrantal enclosure was studied in [27]. The study signified the role of magnetic field in the process of heat removal. The process was investigated by taking equal proportions of water and ethyl glycol. The dual effect of two particle nanofluid and magnetic field was analysed in [28–29]. Radiating hybrid nanofluid flow with the Hall effect over a stretching/shrinking sheet was scrutinised in [29]. Statistical modelling of radiative hybrid nanofluid was meticulously solved in [30]. Darcy-Forchheimer flow of hybrid nanofluids with melting heat transfer over a porous rotating disk was investigated in [31]. Gyrotactic and heat transfer of water with MHD taking single-walled carbon nanotubes (SWCNT) as nanoparticles was studied in [32].

This study aims to provide new horizons to the effects of heat transfer using iron oxide nanofluid, which is cost-effective over a non-linear stretching sheet with changing width. The effects of thermal radiation, changing heat flux, viscous dissipation, electromagnetohydrodynamics and ohmic heating are taken into account. Furthermore, the effects of Nusselt number and skin friction coefficient have been calculated. This study is significant to obtain better quality of a stretching sheet which holds vital industrial importance, and it proves to be another milestone in the computational fluid dynamic in the field of nanofluids.

2. Methods and materials

A two-dimensional nanofluid with water as a base is made to flow over a stretching sheet of changing thickness. The nature of sheet is non-linear (Fig. 1). The velocity of fluid is given by $U_w(x) = b(x + c)^n$ [33], where b is a constant, c is the extending parameter and n is the exponential parameter. The direction along the stretching plate is considered an x axis. The EMHD force is considered to act along a y axis. The variation of thickness is taken as $y = N(x + c)(1 - n)/2$. It is assumed that the pressure difference does not alter the length of the sheet. N is taken as a minor factor for this purpose. The application of two forces of equal magnitude and opposite direction leads to the elongation of the plate through its slit.

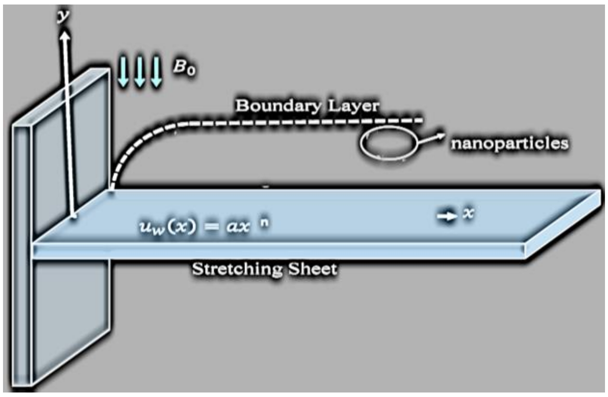

Fig. 1. Three different boundary layers.

In order to maintain the Reynolds number in a low range, electric and magnetic fields are applied perpendicular to the flow direction. The mathematical transformations for electric and magnetic fields can be formulated as $E(x) = E_0(x + c)^{\frac{n-1}{2}}$ and $B(x) = B_0(x + c)^{\frac{n-1}{2}}$, [17], respectively. The temperature difference due to layers of fluids is assumed to be zero. Furthermore, the effects of non-uniform heat flux, viscous dissipation, and Joule heating are incorporated with Prandtl's boundary layer equations:

$$\frac{\partial u}{\partial x} + \frac{\partial v}{\partial y} = 0, \tag{1}$$

$$\rho_{nf}\left(u\frac{\partial u}{\partial x} + v\,\frac{\partial u}{\partial y}\right) = \frac{\partial}{\partial y}[\mu(T)] + \frac{\sigma_{tnf}{B_0}^2 u}{\rho_{tnf}} + $$

$$+\sigma_{nf}[E(x)B(x) - B(x)^2 u], \tag{2}$$

$$(\rho C_p)_{nf}\left(u\frac{\partial T}{\partial x} + v\,\frac{\partial T}{\partial y}\right) = k_{nf}\frac{\partial^2 T}{\partial y^2} + $$

$$+\frac{16\sigma^*}{3k^*}\frac{\partial^2 T}{\partial y^2} + \mu_{nf}\left(\frac{\partial u}{\partial y}\right)^2 + q''' + \sigma_{nf}[uB(x) - E(x)]^2, \tag{3}$$

using boundary conditions represented by the equations:

$$u = U_w(x) = (x + c)^n,\; y = 0,$$

$$-k\,\frac{\partial T}{\partial y} = h(T_w - T) \quad \text{at} \quad y = N(x + c)^{\frac{n-1}{2}} \quad \text{and} \tag{4}$$

$$u \to 0,\quad T \to T_\infty \;\text{ as }\; y \to \infty,$$

where the components of speed along coordinate axes are represented by u and v; T is the temperature fluid temperature, ρ_{nf} is the density, σ_{nf} is the measure of electrical conduction, $\alpha_{nf} = \frac{k_{nf}}{(\rho C_p)_{nf}}$ is the thermal diffusivity, σ^* symbolises the Stefan-Boltzmann constant and k^* symbolises the average value of absorption. The coefficient of viscosity [16] is tailored by the equation:

$$\mu(T) = \mu^*[a_1 + b_1\,(1 - \theta)(T_w - T_\infty)], \tag{5}$$

where μ^* is a standard reference viscosity, whereas a_1, b_1 are assumed to be constants. q''' that appears in Eq. (3) is the non-uniform value of heat flux and is computed by:

$$q''' = \frac{k_{nf}U_w(x)}{v_f(x+c)}\,[A^*(T_w - T_\infty) + B^*(T - T_\infty)], \tag{6}$$

where A^* and B^* are heat generation and absorption parameters, respectively.

2.1. Conversion of equations

To solve the given partial differential equations, it is necessary to introduce the following dimensionless variables:

$$\psi = (b\,\vartheta_{nf})^{\frac{1}{2}} x f(\eta), \tag{7}$$

$$\eta = \left[\frac{(n+1)b(x+c)^{n-1}}{2\vartheta}\right]^{\frac{1}{2}} y, \tag{8}$$

$$u = b(x + c)^n\, f'(\eta), \tag{9}$$

$$v = -\left[\frac{(n+1)b(x+c)^{n-1}}{\vartheta}\right]^{\frac{1}{2}}\left[f(\eta) + \eta f'(\eta)\frac{n-1}{n+1}\right], \qquad (10)$$

$$T = T_w(x), \qquad (11)$$

where $\psi(x,y)$ is the streamline function and $u = \frac{\partial\psi}{\partial y}$ and $v = -\frac{\partial\psi}{\partial x}$, η is a similarity variable, and the temperature is non-dimensionlised as follows:

$$\theta(\eta) = \frac{T-T_\infty}{T_w-T_\infty}. \qquad (12)$$

It is necessary to convert the partial differential formulas to ordinary differential equations:

$$A_0\{[a_1 + A(1-\theta)]f''' - A\theta' f''\} +$$
$$+A_1\left(f'''f - \frac{2n}{n+1}f'^2\right) + A_2M(E_1 - f') = 0. \qquad (13)$$

$$\theta''\left(A_4 + \frac{4}{3}\mathrm{Rd}\right) + \mathrm{Pr}\left[A_0\mathrm{Ec}f''^2 + A_2\mathrm{Ec}M(f'-E_1)^2 +\right.$$
$$\left.+A_3f\theta' - A_3f'\theta\left(\frac{1-n}{1+n}\right)\right] + A_4\frac{2}{n+1}(Af' + B\theta) = 0. \qquad (14)$$

where the prime (′) denotes differentiation concerning η and

$$f(\eta) = \left(\frac{1-n}{1+n}\right)\alpha, \qquad f'(\eta) = 1,$$
$$\theta'(\eta) = -\mathrm{Bi}[1-\theta(0)] \text{ at } \eta = 0;$$
$$f'(\eta) = 0, \qquad \theta(\eta) = 0 \quad \text{as} \quad \eta \to \infty.$$

The non-dimensional parameters are given by:

$$M = \frac{2\sigma_f B_0^2}{\rho_f b(n+1)}, \qquad E_1 = \frac{E_0}{B_0 b(x+c)^n},$$

$$\mathrm{Rd} = \frac{4\sigma T_\infty^3}{kk_f}, \qquad \mathrm{Ec} = \frac{b^{2(x+c)^2}}{(C_p)_f(T_w-T_\infty)},$$

$$\mathrm{Pr} = \frac{\vartheta_f(C_p)_f}{k_f}, \qquad \alpha = N\left(\frac{b(n+1)}{2\vartheta_f}\right)^{\frac{1}{2}},$$

$$\mathrm{Bi} = \frac{h}{k_f}\left[\frac{2\vartheta_f(x+c)}{b(n+1)}\right]^{1-n}, \quad A = b_1(T_w - T_\infty),$$

where M symbolises magnetic field intensity, E_1 – magnitude of electric field, Rd – radiation parameter, Pr represents the Prandtl number, Ec is the Eckert number, α – wall thickness, Bi – Biot number, A_0, A_1,. A_2, A_3 and A_4 are unknown constants (dimensionless coefficients).

2.2. Thermophysical properties of nanofluid

To calculate fixed values, the thermophysical properties of water and iron oxide are presented in Table 1.

The volume fraction ϕ of nanoparticles determines the heat capacity, thermal conductivity and viscosity of the nanofluids. The nanofluid's effective density is given by

$$\rho_{nf} = (1-\phi)\rho_f + \phi\rho_s \qquad (15)$$

and the heat capacitance of nanofluid by

$$\left(\rho C_p\right)_{nf} = (1-\phi)(\rho C_p)_f + \phi(\rho C_p)_s. \qquad (16)$$

According to Brinkman [34], the dynamic viscosity of a nanofluid is as below:

$$\mu_{nf} = \frac{\mu_f}{(1-\phi)^{2.5}}, \qquad (17)$$

$$\frac{k_{nf}}{K_f} = \frac{(k_s+2k_f)-2\phi\,(k_f-k_s)}{(k_s+2k_f)+\phi\,(k_f-k_s)}. \qquad (18)$$

The electrical conductivity of a nanofluid can be given by

$$\sigma_{nf} = 1 + \frac{3\phi\left(\frac{\sigma_p}{\sigma_f}-1\right)}{\left(\frac{\sigma_p}{\sigma_f}+2\right)-\left(\frac{\sigma_p}{\sigma_p}-1\right)\phi}\sigma_f. \qquad (19)$$

2.3. Skin friction coefficient

The skin friction coefficient C_f can be derived from

$$C_f = \frac{\tau_w}{\rho_f U_w^2},$$

where $\tau_w = \mu_{nf}\left(\frac{\partial u}{\partial x}\right)_{y=N(x+c)^{\frac{n-1}{2}}}$. Using the above equations, we get

$$C_f\mathrm{Re}_x^{\frac{1}{2}} = \frac{A_0}{A_4}\left(\frac{n+1}{2}\right)^{\frac{1}{2}} f'(0). \qquad (20)$$

2.4 Nusselt number

The concept of the Nusselt number can be modified for nanofluids. The Nusselt number for nanofluids is given by:

$$\mathrm{Nu} = \frac{(x+c)q_w}{k_f(T_w-T_f)},$$

where $q_w = -k_{nf}\left(\frac{\partial T}{\partial y}\right)_{y=N(x+c)^{\frac{n-1}{2}}}$. Using the above we get

$$\mathrm{Nu}\mathrm{Re}_x^{\frac{1}{2}} = -A_4\left(\frac{n+1}{2}\right)^{\frac{1}{2}}\theta'(0). \qquad (21)$$

2.5. Solution of the problem

Numerical methods are efficient tools to deal with non-homogeneous equations with higher order accuracy. The system of nonlinear ordinary differential equations (ODE) is converted into 5 linear equations. The Adams-Bashforth predictor-corrector method was utilized to fetch the solution. It is a linear multistep methodology, which helps our results to be more accurate by utilizing the quantitative value of the last step.

The calculation works can be divided into two phases, first to get appropriate values as a predictor and the Adams-Moulton method to get a corrector.

The first order system for $\theta(\eta)$ and $f(\eta)$ is as follows:

$$g_1 = f', \quad g_2 = g_1', \quad g_3 = g_2', \qquad (22)$$

$$g_3 = {g_2}' = \frac{1}{[a_1+A(1-\theta)]}\left[A\,\theta_1 f_2 - \frac{B_1}{B_0}\left(g^2 f - \frac{2}{n+1}g_1^2\right) - \frac{B_2}{B}M(E_1 - g_1)\right], \tag{23}$$

$$\theta_1 = \theta', \quad \theta_2 = {\theta_1}', \tag{24}$$

$$\theta_2 = {\theta_1}' = \frac{1}{1+\frac{4}{3}\mathrm{Rd}}\left\{\Pr\left[\frac{B_0}{B_4}\mathrm{Ec}f_2^2 + \frac{B_2}{B_4}\mathrm{Ec}M(E_1 - g_1)^2 + \frac{B_3}{B}f\theta_1\left(\frac{1-n}{1+n}\right)\right]\right\}. \tag{25}$$

Along with the boundary conditions

$$f\,(\eta) = \left(\frac{1-n}{1+n}\right)\alpha, \quad f'(\eta) = 1\,, \quad \theta'(\eta) = -\mathrm{Bi}[1 - \theta(0)] \quad \text{at } \eta = 1 \tag{26}$$

$$f'(\eta) = 0, \quad \theta(\eta) = 0 \quad \text{as} \quad \eta \to \infty$$

where:

$$B_0 = \frac{\mu_{nf}}{\mu_f} = \frac{1}{(1-\phi)^{2.5}}, \tag{27}$$

$$B_1 = \frac{\rho_{nf}}{\rho_f} = (1-\phi)\rho_f + \phi\frac{\rho_p}{\rho_f}, \tag{28}$$

$$B_2 = \frac{\sigma_{nf}}{\sigma_f} = 1 + \frac{3\phi\left(\frac{\sigma_p}{\sigma_p}-1\right)}{\left(\frac{\sigma_p}{\sigma_f}+2\right)-\left(\frac{\sigma_p}{\sigma_p}-1\right)\phi}, \tag{29}$$

$$B_3 = \frac{(\rho C_p)_{nf}}{(\rho C_p)_f} = (1-\phi) + \phi\frac{(\rho C_p)_s}{(\rho C_p)_f}, \tag{30}$$

$$B_4 = \frac{k_{nf}}{K_f} = \frac{(k_s+2k_f)-2\phi\,(k_f-k_s)}{(k_s+2k_f)+\phi\,(k_f-k_s)}. \tag{31}$$

Initial values are obtained with the help of the 4th order Runge-Kutta method. Afterwards, the explicit fourth order predictor is given by the formula:

$$y_{n+1,corr} = y_n + \frac{1}{24}(9y'_{n+1} - 59y'_n + 37y'_{n-1} - 9y'_{n-2}). \tag{32}$$

The final values of $f'(u,b)$ (ambient velocity calculated by predictor) are calculated from Eq. (32) by subtracting from boundary values. A similar methodology is used to fetch $\theta(u,b)$ (ambient temperature calculated by the predictor). If results are larger than ε, then initial guesses are changed and the secant method is employed for making another guess. The process is repeated until we get the similarity variable. The value of the similarity variable is assumed from 0 to ∞, η_0 represents the initial value of the similarity variable, however, the solution converges by assigning its value up to 5.

The differential operator is defined by Eqs. (33) and (34):

$$\frac{df}{d\eta} = q(\eta, f), \quad f(\eta_0) = f_0, \tag{33}$$

$$\frac{d\theta}{d\eta} = q(\eta, \theta), \quad \theta(\eta_0) = \theta_0. \tag{34}$$

The formula for the Adams-Bashforth predictor approach is given by Eqs. (35) and (36):

$$f_{k+1} = f_k + \frac{3h}{2}q(\eta_k, f_k) - \frac{h}{2}q(\eta_{k-1}, f_{k-1}), \tag{35}$$

$$\theta_{k+1} = \theta_k + \frac{3h}{2}q(\eta_k, \theta_k) - \frac{h}{2}q(\eta_{k-1}, \theta_{k-1}). \tag{36}$$

whereas the Adams-Moulton formula by Eqs. (37) and (38):

$$f_{k+1} = f_k + \frac{h}{2}q(\eta_{k+1}, f_{k+1}) - \frac{h}{2}q(\eta_k, f_k), \tag{37}$$

$$\theta_{k+1} = f_k + \frac{h}{2}q(\eta_{k+1}, \theta_{k+1}) - \frac{h}{2}q(\eta_k, \theta_k), \tag{38}$$

where h is the step size. The obtained results were verified and compared with the previous analysis.

3. Analysis of results

The effects of various thermophysical parameters are shown by suitable graphs. The quantities considered are heat generation or absorption factor, the wall thickness, electric and magnetic field factors and viscous dissipation. Table 2 is designed to match the outputs with earlier studies. The results obtained are in perfect match with the earlier analyses.

Figure 2 shows the influence of n on the temperature and velocity profile. The velocity shoots up as the value of n increases, resulting in more fluid to be displaced and hence increasing in the velocity associated with the boundary layer. The increase in velocity ultimately lowers the heat transfer rate.

The velocity is decreased when the fluid is closer to the sheet, resulting in reduction of the boundary layer. Because of the wall thickness parameter, the temperature gradient similarly demonstrates a downfall. Figure 3 guides the importance of incorporation of magnetic factor which influences both the temperature gradient and speed. Increasing the magnetic field reduces the nanofluid flow. This is expected as an increasing value of the MHD parameter of electrically charged nanoparticles results in an increase of the Lorentz force, a force which retards the motion of fluid. This property is useful to fetch the desired velocity. The graph shows that the magnetic field is inversely related to the velocity factor.

Figure 4 exhibits the role of viscous dissipation in the temperature profile. The Eckert number shows a relation between the kinetic energy of nanofluid flow and the enthalpy difference between the surrounding area and the wall to represent the heat dissipation. This is in alignment with the study conducted in [8] in the absence of magnetic field. The dimensionless temperature for various Rd values is also displayed in Fig. 4. The radiation parameter is designed to detect the rate of heat transfer. An increase in radiation accelerates the amount of heat transfer which leads to an increase in boundary layer thickness. Therefore, both the temperature gradient and boundary layer thickness assume higher values with the increasing Rd. The radiation effect is designed to customize the fluid velocity.

Table 2. Thermophysical parameters.

Pr	Gul et al. [8]	Saeed et al. [9]	Present study
2.0	0.9113	0.9114	0.9110
6.2	1.5797	1.5796	1.5786
7.0	1.8954	1.8954	1.8964
20.0	1.3539	1.3539	1.3539

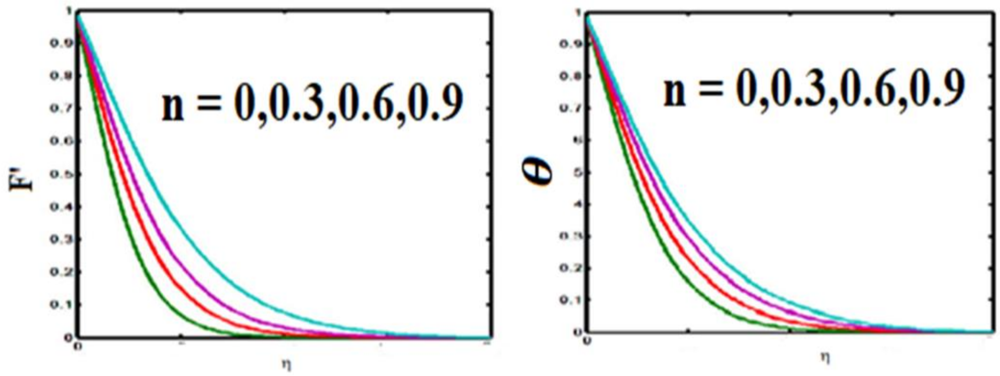

a)

b)

Fig. 2. Effect of *n* on velocity (a) and temperature (b).

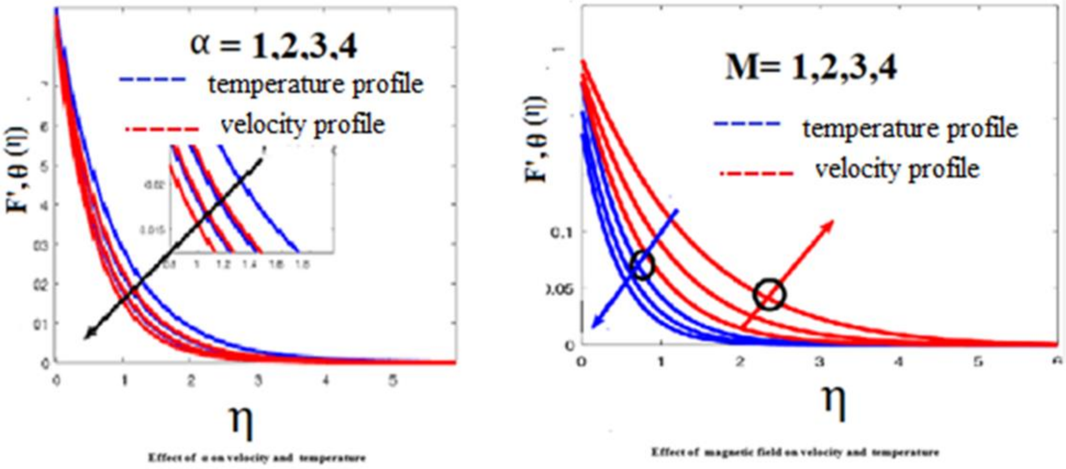

Fig. 3. The effect of magnetic field on velocity and temperature.

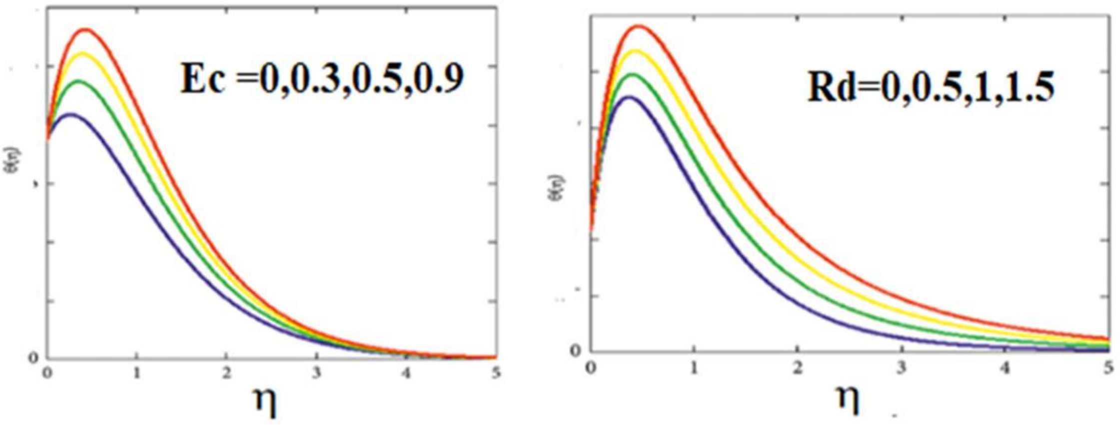

Fig. 4. Influence of Eckert number and radiation parameter on temperature.

Figure 5 illustrates the effect of Biot number (Bi). The Biot number, which represents the ratio of convective heat transfer to conductive heat transfer, significantly influences the thermal boundary conditions. As observed, increasing the Biot number leads to a higher temperature gradient near the surface, indicating enhanced heat transfer at the boundary. This result shows an excellent agreement with [9].

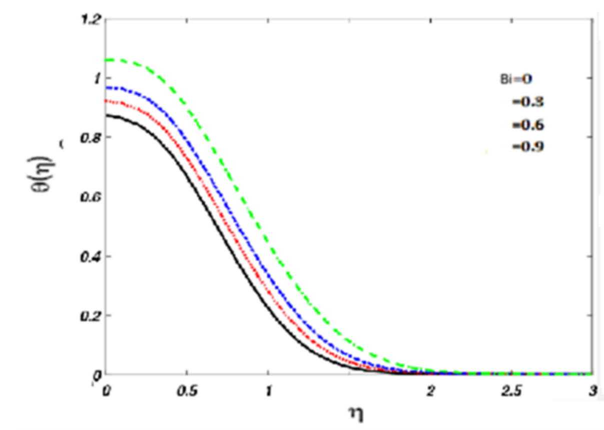

Fig. 5. Influence of Biot number on temperature.

Fig 6 highlights the impact of the space-dependent heat generation/absorption parameter A* on the temperature distribution. The left graph shows the effect of positive values of A*, representing heat generation, while the right graph depicts the effect of negative values of A*, corresponding to heat absorption. It is on a par with the study conducted in [11]. It was found that the dispersion of heat exhaust energy causes the temperature gradient to be larger, enhancing the values of A^*. The effect of heat absorption or generation factor on temperature can be visualised in Fig. 7. The graphs show that an increase in values of B^* rises the values of the temperature gradient. It is also found that while assigning negative values to B^* there is more heat absorption and a decrease in value of temperature gradient.

The result matches with outcomes of study conducted in [12]. The comparison of present results with Shah et al. [17] is presented in Fig 8. The results obtained are comparable and show an acceptable level of agreement.

4. Conclusions

The current work concentrates on flow simulation of copper carrying nanofluids along an elongated surface with varying width in association with electromagnetohydrodynamic (EMHD)

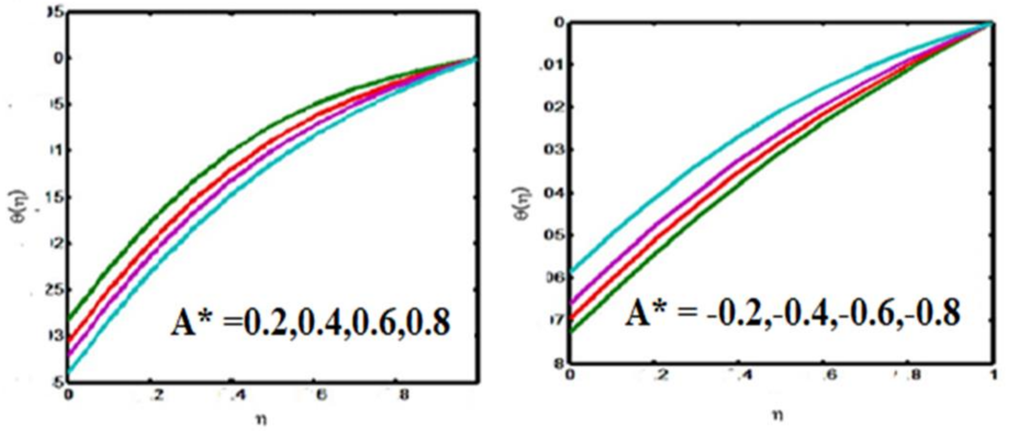

Effect of positive A* on temperature

Effect of negative A* on temperature

Fig. 6. The effect of heat absorption and generation factor on the temperature distribution.

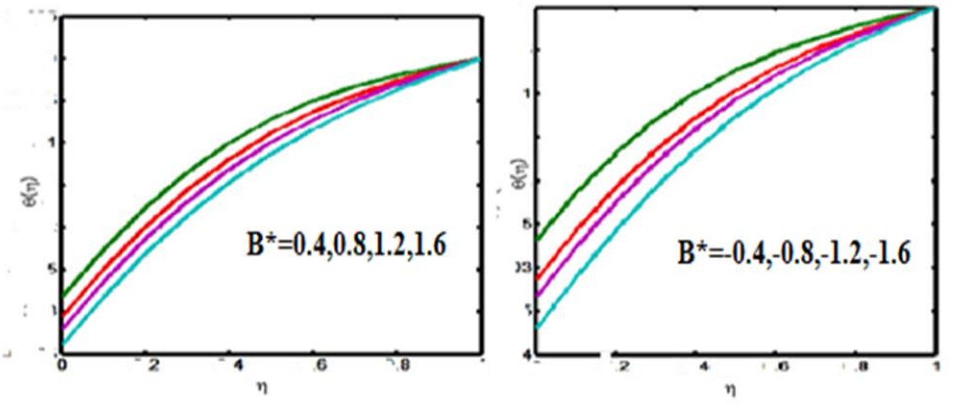

Effect of positive B* on temperature

Effect of negative B* on temperature

Fig. 7. Effect of positive and negative values of the space-dependent parameter on the temperature distribution.

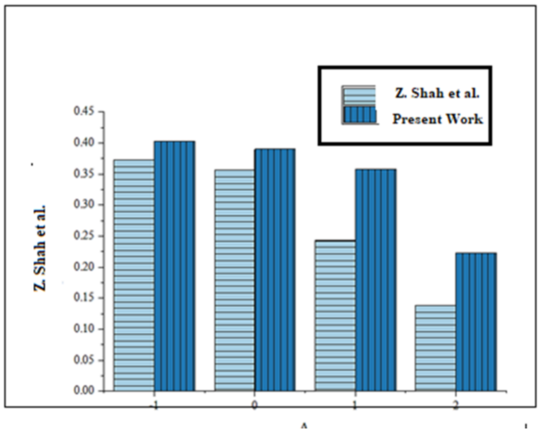

Fig. 8. Comparison of present study with Shah et al. [17].

flow. It also incorporates the heat flux with radiation phenomenon, which have a favourable effect on the flow behaviour. A survey has been conducted on the effects of an electrically charged particle-filled magnetic field on heat flux values, fluid with varied viscosity, and so on an extended surface with varying thickness. Diagrammatic representations of the temperature and velocity profiles are employed to analyse the influence of various physical parameters. The key findings from this investigation are summarized as follows:

- The comparative study of the obtained results using the Adams-Bashforth method with earlier investigation holds a good agreement, and also constitutes a validation of the proposed methodology;
- The temperature profile becomes more noticeable for the enhanced radiation parameters, nanoparticle fraction, and Eckert number; however, the opposite pattern is noticed for the increasing stretching parameter and Prandtl number;
- The increase in nanoparticle concentration, in association with the nonlinear stretching factor, reduces the nanofluid velocity;
- There is a noticeable reduction in the shear rate coefficient noticed for the increasing particle concentration, while it overshoots the heat transfer rate;
- While the power index of velocity term increases, both the nanofluid velocity and the nanofluid temperature also increase;
- Due to an increase in the boundary thickness factor, both the temperature as well as velocity of the fluid decrease;
- For increasing positive values, the time-dependent and space-dependent heat generation/absorption parameter contributes to heat generation, thereby increasing the temperature. Conversely, increasing the magnitude of negative values enhances heat absorption, which reduces the temperature.

The novelty of the present study is that it not only illustrates the physical properties of the parameters under conditions, but also provides a base for future research by associating the momentous role of magnetic and electric fields in customizing fluid velocity, which can be favourable for industrial sector dealing with stretching sheets. Further investigations using different concentrations, will be helpful in producing a finished product of the desired quality. The key points of this research can be successfully applied for further scientific investigation using stretching sheets.

References

[1] Khan, W.A., & Pop, I. (2010). Boundary-layer flow of a nanofluid past a stretching sheet. *International Journal of Heat and Mass Transfer,* 53(11-12), 2477–2483. doi: 10.1016/j.ijheatmasstransfer.2010.01.032

[2] Ibrahim, W., & Shankar, B. (2013). MHD boundary layer flow and heat transfer of a nanofluid past a permeable stretching sheet with velocity, thermal and solutal slip boundary conditions. *Computers & Fluids,* 75, 1−10. doi: 10.1016/j.compfluid.2013.01.014

[3] Gireesha, B., Sowmya, G., Khan, M.I., & Öztop, H.F. (2020). Flow of hybrid nanofluid across a permeable longitudinal moving fin along with thermal radiation and natural convection. *Computer methods and programs in biomedicine,* 185, 105166. doi: 10.1016/j.cmpb.2019.105166

[4] Makarem, M.A., Bakhtyari, A., & Rahimpour, M.R. (2018). A numerical investigation on the heat and fluid flow of various nanofluids on a stretching sheet. *Heat Transfer – Asian Research,* 47(2), 347–365. doi: 10.1002/htj.21307

[5] Ghalambaz, M., Groşan, T., & Pop, I. (2019). Mixed convection boundary layer flow and heat transfer over a vertical plate embedded in a porous medium filled with a suspension of nano-encapsulated phase change materials. *Journal of Molecular Liquids,* 293, 111432. doi: 10.1016/j.molliq.2019.111432

[6] Hajjar, A., Mehryan, S., & Ghalambaz, M. (2020). Time periodic natural convection heat transfer in a nano-encapsulated phase-change suspension. *International Journal of Mechanical Sciences,* 166, 105243. doi: 10.1016/j.ijmecsci.2019.105243

[7] Saeed, A., Kumam, P., Nasir, S., Gul, T., & Kumam, W. (2021). Non-linear convective flow of the thin film nanofluid over an inclined stretching surface. *Scientific Reports,* 11, 18410. doi: 10.1038/s41598-021-97576-x

[8] Mathew, A., Areekara, S., Sabu, A., & Saleem, S. (2021). Significance of multiple slip and nanoparticle shape on stagnation point flow of silver-blood nanofluid in the presence of induced magnetic field. *Surfaces and Interfaces,* 25, 101267. doi: 10.1016/j.surfin.2021.101267

[9] Krishnamurthy, M., Prasanna Kumara, B., Gireesha, B., & Gorla, R.S. (2015). Effect of viscous dissipation on hydromagnetic fluid flow and heat transfer of nanofluid over an exponentially stretching sheet with fluid-particle suspension. *Cogent Mathematics,* 2, 1050973. doi: 10.1080/23311835.2015.1050973

[10] Senthilraja, S., Vijayakumar, K., & Gangadevi, R. (2015). A comparative study on thermal conductivity of Al_2O_3/water, CuO/water and Al_2O_3–CuO/water nanofluids. *Digest Journal of Nanomaterials and Biostructures,* 10(4), 1449–1458.

[11] Chamkha, A., Doostanidezfuli, A., Izadpanahi, E., & Ghalambaz, M. (2017). Phase-change heat transfer of single/hybrid nanoparticles-enhanced phase-change materials over a heated horizontal cylinder confined in a square cavity. *Advanced Powder Technology,* 28(2), 385–397. doi: 10.1016/j.apt.2016.10.009

[12] Sharma, K., & Kumar, S. (2023). Impacts of low oscillating magnetic field on ferrofluid flow over upward/downward moving rotating disk with effects of nanoparticle diameter and nanolayer. *Journal of Magnetism and Magnetic Materials,* 575, 170720. doi: 10.1016/j.jmmm.2023.170720.

[13] Gopal, D., Saleem, S., Jagadha, S., Ahmad, A., Almatroud, A.O., & Kishan, N. (2021). Numerical analysis of higher order chemical reaction on electrically MHD nanofluid under influence of viscous dissipation. *Alexandria Engineering Journal*, 60(1), 1861–1871. doi: 10.1016/j.aej.2020.11.034

[14] Sowmya, G., Gireesha, B.J., & Madhu, M. (2020). Analysis of a fully wetted moving fin with temperature-dependent internal heat generation using the finite element method. *Heat Transfer,* 49(4), 1939–1954. doi: 10.1002/htj.21701

[15] Alsaedi, A., Hayat, T., Qayyum, S., & Yaqoob, R. (2020). Eyring-Powell nanofluid flow with nonlinear mixed convection: Entropy generation minimization. *Computer Methods and Programs in Biomedicine,* 186, 105183. doi: /10.1016/j.cmpb.2019.105183

[16] Fang, T., Zhang, J., & Zhong, Y. (2012). Boundary layer flow over a stretching sheet with variable thickness. *Applied Mathematics and Computation,* 218(13), 7241–7252. doi: 10.1016/j.amc.2011.12.094

[17] Shah, Z., Ramzan, M., Kumam, P., Khan, W., Watthayu, W., & Kumam, W. (2022). Bidirectional flow of MHD nanofluid with Hall current Cattaneo-Christove heat flux towards the stretching sheet. *Plos One*, 17(4), e0264208. doi: 10.1371/journal.pone.0264208

[18] Khader, M.M., & Megahed, A.M. (2013). Numerical solution for boundary layer flow due to a nonlinearly stretching sheet with variable thickness and slip velocity. *The European Physical Journal Plus*, 128, 100. doi: 10.1140/epjp/i2013-13100-7

[19] Alawi, O.A., Sidik, N.A.C., Xian, H.W., Kean, T.H., & Kazi, S.N. (2018). Thermal conductivity and viscosity models of metallic oxides nanofluids. *International Journal of Heat and Mass Transfer*, 116, 1314–1325. doi: 10.1016/j.ijheatmasstransfer.2017.09.133

[20] Suresh, S., Venkitaraj, K.P., Selvakumar, P., & Chandrasekar, M. (2012). Effect of Al_2O_3–Cu/water hybrid nanofluid in heat transfer. *Experimental Thermal and Fluid Science,* 38, 54–60. doi: 10.1016/j.expthermflusci.2011.11.007

[21] Momin, G.C. (2013). Experimental investigation of mixed convection with water-Al_2O_3 & hybrid nanofluid in inclined tube for laminar flow. *International Journal of Scientific and Technology Research,* 2(12), 195–202.

[22] Takabi, B., & Salehi, S. (2014). Augmentation of the heat transfer performance of a sinusoidal corrugated enclosure by employing hybrid nanofluid. *Advances in Mechanical Engineering,* 6, 147059. doi: 10.1155/2014/147059

[23] Devi, S.P.A., & Devi, S.S.U. (2016). Numerical investigation of hydromagnetic hybrid Cu–Al_2O_3/water nanofluid flow over a permeable stretching sheet with suction. *International Journal of Nonlinear Sciences and Numerical Simulation*, 17(5), 249–257. doi: 10.1515/ijnsns-2016-0037

[24] Ghalambaz, M., Doostani, A., Izadpanahi, E., & Chamkha, A. (2017). Phase-change heat transfer in a cavity heated from below: The effect of utilizing single or hybrid nanoparticles as additives. *Journal of the Taiwan Institute of Chemical Engineers,* 72, 104–115. doi: 10.1016/j.jtice.2017.01.010

[25] Shuguang, Li., Puneet, V., Saeed, A.M., Singhal, A., Fuad, A.M., Yarimi, Al., & Ijaz Khan, M. (2024). Analysis of the Thomson and Troian velocity slip for the flow of ternary nanofluid past a stretching sheet. *Scientific Reports,* 14(1), 2340−2351. doi: 10.1038/s41598-024-83032-z

[26] Prajapati, V.J., & Meher, R. (2024). Analysis of MHD tangent hyperbolic hybrid nanofluid flow with different base fluids over a porous stretched sheet. *Journal of Taibah University for Science,* 18(1), 2300851. doi: 10.1080/16583655.2023.2300851

[27] Khan, M.S., Ahmad, S., Shah, Z., Vrinceanu, N., Mansoor, H., & Alshehri, M. (2024). Natural convection heat transfer of a hybrid nanofluid in a permeable quadrantal enclosure with heat generation. *Case Studies in Thermal Engineering*, 56, 104207. doi: 10.1016/j.csite.2024.104207.

[28] Alsabery, A.I., Armaghani, T., Chamkha, A.J., & Hashim, I. (2020). Two-phase nanofluid model and magnetic field effects on mixed convection in a lid-driven cavity containing heated triangular wall. *Alexandria Engineering Journal,* 59(1), 129−148. doi: 10.1016/j.aej.2019.12.017.

[29] Jameel, M., Shah, Z., Shafiq, A., Rooman, M., Vrinceanu, N., Alshehri, A., & Islam, S. (2023). Statistical and entropy optimization modeling for radiative hybrid nanofluid flow with Hall effect over exponential stretching/shrinking plate. *International Journal of Thermofluids*, 20, 100398. doi: 10.1016/j.ijft.2023.100398

[30] Shah, Z., Sulaiman, M., Dawar, A., Alshehri, M.H., & Vrinceanu, N. (2024). Darcy-Forchheimer MHD rotationally symmetric micropolar hybrid-nanofluid flow with melting heat transfer over a radially stretchable porous rotating disk. *Journal of Thermal Analysis and Calorimetry*, 149, 14625–14641, doi: 10.1007/s10973-024-12986-z

[31] Muhammad, K., Abdelmohsen, S.A., Abdelbacki, A.M., & Ahmed, B. (2022). Darcy-Forchheimer flow of hybrid nanofluid subject to melting heat: A comparative numerical study via shooting method. *International Communications in Heat and Mass Transfer,* 135, 106160. doi: 10.1016/j.icheatmasstransfer.2022.106160

[32] Shah, Z., Sulaiman, M., Khan, W., Vrinceanu, N., & Alshehri, M.H. (2024). Gyrotactic microorganism's and heat transfer analysis of water conveying MHD SWCNT nanoparticles using fourth-grade fluid model over Riga plate. *Case Studies in Thermal Engineering*, 55, 104119. doi: 10.1016/j.csite.2024.104119

[33] Adel, M., Khader, M.M., & Ahmad, H. (2024). MHD nanofluid flow and heat transfer caused by a stretching sheet that is heated convectively: an approximate solution using ADM. *Case Studies in Thermal Engineering*, 60, 104683. doi: /10.1016/j.csite.2024.104683

[34] Brinkman, H.C. (1952). The viscosity of concentrated suspensions and solutions. *Journal of Chemical Physics,* 20(4), 571−571. doi: 10.1063/1.1700493

Co-published by
Institute of Fluid-Flow Machinery
Polish Academy of Sciences
Committee on Thermodynamics and Combustion
Polish Academy of Sciences

http://www.imp.gda.pl/archives-of-thermodynamics/

ARCHIVES OF THERMODYNAMICS

Heat transfer optimization of MHD unsteady separated stagnation-point flow of a hybrid ferrofluid with heat generation

Amirul Zaqwan Azman[a], Norihan Md Arifin[a*], Nur Syahirah Wahid[a],
Mohd Ezad Hafidz Hafidzuddin[b]

[a]Department of Mathematics & Statistics, Faculty of Science, Universiti Putra Malaysia, 43400, UPM Serdang, Selangor, Malaysia
[b]Centre of Foundation Studies for Agricultural Science, Universiti Putra Malaysia, 43400 UPM Serdang, Selangor
*Corresponding author email: norihana@upm.edu.my

Received: 23.12.2024; revised: 04.03.2025; accepted: 20.03.2025

Abstract

The heat transfer optimization for magnetohydrodynamic unsteady stagnation-point flows and the thermal progress with the effect of heat generation is performed using the response surface methodology. The first step in this study involves reducing the mathematical model of partial differential equations and boundary conditions into non-linear ordinary differential equations via similarity transformations. Numerical solutions of the emerged system are obtained using the bvp4c solver. As observed from this study, the magnitude of the skin friction coefficient and heat transfer rate rises with the suction parameter. The statistical analysis and optimization done using the response surface methodology revealed that the suction parameter highly impacts the local Nusselt number. The maximum sensitivity of the heat transfer rate is towards the magnetic and suction parameters.

Keywords: Stagnation-point flow; Magnetohydrodynamic; Hybrid ferrofluid; Heat generation; Permeable

Vol. 46(2025), No. 2, 93–102; doi: 10.24425/ather.2025.154909

Cite this manuscript as: Azman, A.Z., Arifin, N.M., Wahid, N.S., & Hafidzuddin, M.E.H. (2025). Heat transfer optimization of MHD unsteady separated stagnation-point flow of a hybrid ferrofluid with heat generation. *Archives of Thermodynamics*, 46(2), 93–102.

1. Introduction

Heat transfer has been the focus of many researchers due to its wide application. One important material property that controls heat transfer efficiency is thermal conductivity, a higher conductivity allows thermal energy to move through the medium more quickly. Magnetohydrodynamics (MHD) describes the behaviour of electrically conducting fluids and has crucial applications in engineering, astrophysics and fusion energy research. For example, axisymmetric MHD Homann flow over a stretching and spiralling disk in the stagnation region was analysed by Khan et al. [1]. Many studies have found that solid-type nanoparticles with high thermal conductivity can raise the fluid thermal conductivity to intensify the heat transfer rate. Nanofluids, consisting of a blend of two distinct nanoparticles dispersed in a base liquid, are employed to boost heat transfer efficiency owing to their enhanced thermal conductivity compared to the base liquid. These fluids have shown promising results in improving energy efficiency in various applications, especially industries that require thermal management. Choi and Eastman [2] were the first to introduce the concept of nanofluids. Later, Eastman et al. [3] investigated their thermal conductivity and heat transfer properties. Since then, numerous researchers have conducted extensive theoretical studies on the thermal conductivity of nanofluids. Recently, Sarfraz et al. [4] examined Walter's B nanofluid heat and mass flow, and dual solutions were obtained. They show that the activation energy parameter enhances mass distribution in both solutions.

Nomenclature

B_0 – magnetic field effect, T
C – number centre points
C_p – heat capacity, J/(kg·K)
c – coefficients
F – number of factors
k – thermal conductivity, W/(m·K)
M – dimensionless magnetic parameter
N – number of independent variables
Nu – Nusselt number
Pr – Prandtl number
Q_H – dimensionless heat generation parameter (or Q)
Q_h – heat generation effect, W/m^3
q_w – local Nusselt number
Re – Renolds number
S – dimensionless suction parameter
T_w – wall temperature, K
T_∞ – farfield temperature, K
t – time, s
t_{ref} – constant reference time, s
u, v – component velocity, m/s
u_0 – velocity of the plate, m/s
u_e – free stream velocity, m/s
υ_0 – mass suction/injection, m/s
υ_w – velocity of wall mass transfer, m/s
x, y – Cartesian coordinate, m
x_0 – displacement of the plate, m
$x1$ – coded symbol for the magnetic parameter
$x2$ – coded symbol for the heat generation parameter
$x3$ – coded symbol for the suction parameter

Greek symbols

α – strength of free stream velocity
β – unsteadiness parameter
μ – dynamic viscosity, kg/(m·s)
ν – kinematic viscosity, m^2/s
ρ – density, kg/m^3
σ – electrical conductivity, S/m
τ – local skin friction coefficient
ϕ – nanoparticles volume fraction

Subscripts and Superscripts

f – base fluid
hnf – hybrid nanofluid
nf – mono nanofluid

Abbreviations and Acronyms

ANOVA – analysis of variance
DOE – design of experiment
MHD – magnetohydrodynamics
RSM – response surface methodology
USSP – unsteady separated stagnation point (flow)

Ferrofluid is a stable colloidal mixture where ferromagnetic particles are suspended in a liquid, using standard base fluids such as water, oil and similar liquids. The composition of a ferrofluid includes three key components; magnetic nanoparticles, a dispersion medium (the carrier liquid) and a dispersant. Hybrid ferrofluid is a unique heat transfer fluid because it can be controlled magnetically and is ideal for wide applications. Several researchers have investigated the efficiency of hybrid ferrofluid as a heat transfer fluid. The stagnation-point flow on exponentially stretching/shrinking surfaces for hybrid ferrofluids with magnetic effect was examined by Anuar et al. [5], and significant improvement was found in utilizing hybrid ferrofluids. The unsteady hybrid ferrofluid flow over a cylinder examined by Saranya et al. [6] also considerably benefits from the viscous–ohmic dissipative effect. To evaluate the impact of the unsteadiness parameter on the thermal rate, Waini et al. [7] studied the unsteady MHD flow of hybrid ferrofluid over a rotating disk. Another numerical study on the effects of MHD and heat generation for the time-dependent separated stagnation-point flow of hybrid ferrofluid on a moving plate was carried out by Khashi'ie et al. [8]. Many other works reported in this field [9–11].

The influence of heat generation or absorption plays a crucial role in altering the temperature distribution in various applications, particularly those involving dissociating fluids and chemical reactions. The study of unsteady stagnation-point flow in hybrid nanofluids has gained significant interest due to its applications in industries such as cooling systems, chemical processes and thermal management technologies. Hybrid nanofluids, which combine two or more types of nanoparticles in a base fluid, exhibit superior thermal and flow properties compared to conventional fluids or mono-nanofluids. Unsteady stagnation-point flow describes the time-dependent interaction of fluid meeting a surface perpendicularly before diverging tangentially. The introduction of hybrid nanofluids to this flow system has been studied extensively for its ability to enhance heat transfer and fluid dynamics. Zainal et al. [12] investigated the thermophysical properties of the unsteady separated stagnation-point flow past a moving plate by a hybrid nanofluid. Khan et al. [13] concluded that the combination of Al_2O_3 and Cu nanoparticles in hybrid nanofluids improves thermal conductivity and increases the heat transfer rate. Their research shows that the heat generation parameter further enhances temperature profiles, while heat absorption mitigates thermal effects. The unsteadiness parameter, representing time-dependent changes in flow behaviour, significantly affects velocity and temperature profiles. Mahmood and Khan [14] found that decreasing unsteadiness enhances heat transfer but increases flow resistance. Additional studies of flow via the boundary layer and heat transfer are available in [15–19].

A variety of studies have investigated heat sources or sinks that depend on temperature across different geometrical configurations. Hybrid nanofluid slip flow over an exponentially stretching/shrinking permeable sheet with heat generation was analysed by Wahid et al. [20]. Consequently, the thermal boundary layer thickness is observed to expand with heat generation and contract with heat absorption. Further analyses on the effects of heat generation were discussed in [21,22]. Furthermore, Yasir and Khan [23] studied the impact of internal heat generation on thermal transport processes. Heat generation, whether due to chemical reactions, exothermic processes or Ohmic heating, significantly influences the thermal behaviour of fluids in engineering applications. It alters the thermal boundary layer, affecting heat transfer rates and overall system efficiency.

Frequently studied is flowing over the stagnation point, which describes the behaviour of the fluid flow near the region of a surface situated in a stationary or moving body. Recent studies on the stagnation-point flow of hybrid nanofluids with MHD have highlighted their enhanced thermal performance and fluid dynamics, particularly under magnetic field influence and varying nanoparticle concentrations. Numerical analyses, such as in a three-dimensional non-axisymmetric Homann flow of Al_2O_3/H_2O nanofluids, demonstrate improved heat transfer and skin friction with increased magnetic parameters but a decline in performance with higher unsteadiness, alongside stability validation of dual solutions [24]. The study of MHD stagnation-point flow of hybrid nanofluids, particularly alumina-graphene/water, explores the influence of magnetic and wall permeability parameters on buoyancy-driven dual similarity solutions over a permeable plate [25]. Findings highlight that these parameters extend the solution range and reduce boundary layer thicknesses, with assisting flow yielding higher skin friction and Nusselt numbers compared to opposing flow regimes. Khashi'ie et al. [26] studied MHD unsteady separated stagnation-point flow and revealed that dual solutions occur in decelerating flow, with critical parameters like the Hartmann number, and acceleration significantly influences boundary layer behaviour and thermal performance. Zainodin et al. [27] investigated the stagnation-point flow of hybrid ferrofluids in the presence of MHD, incorporating magnetite and cobalt ferrite nanoparticles in water, highlighting the effects of magnetic fields, viscous dissipation, Joule heating and convective boundary conditions. Key findings include dual solutions under opposing and assisting flows, enhanced skin friction with nanoparticle addition, reduced heat transfer rates due to magnetic fields and viscous effects, and significant thermal rate improvement with higher Biot numbers.

Following the brief literature review, a potential gap was discovered in studying the problem of MHD unsteady separated stagnation-point flow and the thermal progress of Fe_3O_4 – $CoFe_2O_4$ over a permeable plate subject to heat generation. This work is an extension of the research of Khashi'ie at al. [8], and in the current study, an optimal solution for different dimensionless parameters has been predicted using statistical tools, namely the response surface methodology (RSM). RSM is a robust statistical technique that has been used to obtain the optimal heat transfer rate [28–30].

2. Mathematical model

The modelling of heat transfer in ferrofluid over a permeable moving plate with heat generation has numerous practical applications across engineering, energy systems and biomedical fields. The integration of ferro-nanofluid, which contains magnetic nanoparticles, allows for enhanced control through external magnetic fields. This capability enables specialized applications, including electronic cooling, thermal protection systems, aerodynamic heating management and solar thermal energy optimization.

Hence, this paper covers the unsteady two-dimensional MHD axisymmetric stagnation-point flow and heat transfer of hybrid nanofluid over a permeable moving plate with heat generation illustrated in Fig. 1. The frame of reference (x, y) is chosen in such a way that the x-axis is along the direction of the plate and the y-axis is normal to the plate. In this problem, the velocity of the plate is defined as $u_0(t) = \partial x_0(t)/\partial t$, where $x_0(t)$ and t are the plate displacement and time, respectively. The free stream velocity, $u_e(t) = \frac{\alpha(x - x_0(t))}{t_{ref} - \beta t} + u_0(t)$, where t_{ref} is the constant reference time, is parallel to the plate. Also, the wall mass transfer velocity is denoted as $v_w(t) = -v_0/\sqrt{t_{ref} - \beta t}$ (where $\upsilon_0 < 0$ is the mass suction, and $\upsilon_0 > 0$ is the mass injection). In addition, α refers to the strength of free stream velocity outside the boundary layer region. For the unsteadiness parameter, $\beta > 0$ and $\beta < 0$ refer to unsteady accelerating and decelerating parameters, respectively, and $\beta = 0$ denotes a steady boundary layer flow. The permeability of the plate, alongside the unsteadiness of the flow, and the external magnetic field introduce asymmetry in the flow properties (velocity, temperature) across the domain (see [8,31]).

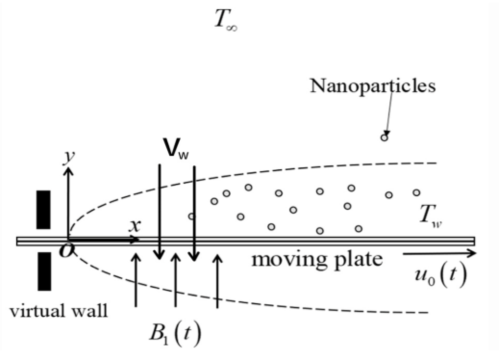

Fig. 1. Geometry of the problem.

The water-based (H_2O) hybrid nanofluid incorporates two distinct types of nanoparticles, magnetic-cobalt ferrite (Fe_3O_4 – $CoFe_2O_4$). Table 1 presents the properties of thermophysical for each ferroparticle and the based fluid. The mixture of ferroparticles with its based fluid is presumed to be in thermal equilibrium.

Table 1. Thermophysical properties of H_2O, Fe_3O_4 and $CoFe_2O_4$ [4].

Thermophysical properties	**H_2O (*Bf*)**	**Fe_3O_4**	**$CoFe_2O_4$**
ρ, kg/m^3	997.1	5180	4908
C_p, J/(kg K)	4179	670	700
k, W/(m K)	0.613	9.8	3.6
σ, S/m	5.5×10^{-6}	0.74×10^{6}	1.1×10^{7}

Using the conservations law, the flow field and energy equations can be modelled as follows:

$$u_x + v_y = 0, \tag{1}$$

$$u_t + uu_x + vu_y = (u_e)_t + u_e(u_e)_x + \frac{\mu_{hnf}}{\rho_{hnf}}u_{yy} +$$

$$-\frac{\sigma_{hnf}}{\rho_{hnf}}B_0^2(u - u_e), \tag{2}$$

$$T_t + uT_x + vT_y = \frac{k_{hnf}}{(\rho C_p)_{hnf}} T_{yy} + \frac{Q_h}{(\rho C_p)_{hnf}} (T - T_\infty), \quad (3)$$

$$\begin{gathered} u = u_0(t), \quad v = v_w, \quad T = T_w \quad \text{at} \quad y = 0, \\ u \longrightarrow u_e, \quad T \longrightarrow T_\infty \quad \text{at} \; y \longrightarrow \infty. \end{gathered} \quad (4)$$

Following Khashi'ie et al. [4], the transformation for Eqs. (1) to (4) is as follows:

$$\begin{gathered} u = \alpha \frac{x - x_0(t)}{t_{ref} - \beta t} f'(\eta) + u_0(t), \quad v = -\alpha \sqrt{\frac{\nu_f}{t_{ref} - \beta t}} f(\eta), \\ \theta(\eta) = \frac{T - T_\infty}{T_w - T_\infty}, \eta = \frac{y}{\sqrt{\nu_f (t_{ref} - \beta t)}}. \end{gathered} \quad (5)$$

By using Eq. (5) and after performing the necessary calculation, the following dimensionless momentum and energy equations are attained:

$$\begin{gathered} \frac{\mu_{hnf}/\mu_f}{\rho_{hnf}/\rho_f} f''' + \alpha(ff'' - f'^2 + 1) - \beta\left(\frac{1}{2}\eta f'' + f' - 1\right) + \\ - \frac{\sigma_{hnf}/\sigma_f}{\rho_{hnf}/\rho_f} M^2 (f' - 1) + 1 = 0, \end{gathered} \quad (6)$$

$$\begin{gathered} \frac{k_{hnf}/k_f}{\Pr (\rho C_p)_{hnf}/(\rho C_p)_f} \theta'' + \alpha f \theta' + \\ - \frac{1}{2}\beta \eta \theta' + \frac{Q_H}{(\rho C_p)_{hnf}/(\rho C_p)_f} \theta = 0, \end{gathered} \quad (7)$$

with boundary conditions:

$$\begin{gathered} f(0) = S, \quad f'(0) = 0, \quad \theta(0) = 1, \\ f'(\eta) \to 1, \quad \theta(\eta) \to 0, \quad \text{as} \quad \eta \to \infty, \end{gathered} \quad (8)$$

where $M^2 = \sigma_f B_0^2/(\nu\rho)_f$ is the Hartmann number also known as the magnetic field parameter, $\Pr = (\mu C_p)_f/k_f$ is the Prandtl number, $Q_H = Q_h/(\mu C_p)_f$ is the heat generation and $S = -v_0/\alpha\sqrt{\nu_f}$ is the suction parameter. The correlations for the hybrid nanofluid properties are shown in Table 2.

Table 2. Correlations of hybrid nanofluid.

Properties	**Hybrid nanofluid correlation**
Density	$\rho_{hnf} = \phi_1\rho_1 + \phi_2\rho_2 + (1 - \phi_{hnf})\rho_f$
Dynamic viscosity	$\mu_{hnf} = \frac{\mu_f}{(1-\phi_{hnf})^{2.5}}$, where: $\phi_{hnf} = \phi_1 + \phi_2$
Electrical conductivity	$\sigma_{hnf} = \frac{\left(\sigma_2 + 2\sigma_{nf} - 2\phi_2(\sigma_{nf} - \sigma_2)\right)k_{nf}}{\sigma_2 + 2\sigma_{nf} + \phi_2(\sigma_{nf} - \sigma_2)}$, where: $\sigma_{nf} = \frac{\left(\sigma_1(2\phi_1 + 1) + 2\sigma_{Bf}(1 - \phi_1)\right)\sigma_f}{\sigma_f(\phi_1 + 2) + \sigma_1(1 - \phi_1)}$
Heat capacity	$(\rho C_p)_{hnf} = (1 - \phi_{hnf})(\rho C_p)_f + \phi_1(\rho C_p)_{s1} + \phi_2(\rho C_p)_{s2}$
Thermal conductivity	$k_{hnf} = \frac{\left(k_2 + 2k_{nf} - 2\phi_2(k_{nf} - k_2)\right)k_{nf}}{k_2 + 2k_{nf} + \phi_2(k_{nf} - k_2)}$, where: $k_{nf} = \frac{\left(k_1 + 2k_f - 2\phi_1(k_f - k_1)\right)k_f}{k_1 + 2k_f + \phi_1(k_f - k_1)}$

The local skin friction coefficient and the local Nusselt number are mathematically defined and computed as [25]:

$$\begin{gathered} \tau_w = \mu_{hnf}(v_x + u_y)_{y=0}, \\ q_w = -k_{hnf}(T_x + T_y)_{y=0}, \end{gathered} \quad (9)$$

where τ_w and q_w denote the shear stress and the heat flux at a point on the surface of the sheet, respectively. By substituting Eq. (5) into Eq. (9), it yields:

$$\frac{\sqrt{\nu_f (t_{ref} - \beta t)}^3}{\alpha \mu_f (x - x_0(t))} \tau_w = \frac{\mu_{hnf}}{\mu_f} f''(0) \quad (10)$$

$$\frac{\sqrt{\nu_f (t_{ref} - \beta t)}}{k_f (T_w - T_\infty)} q_w = -\frac{k_{hnf}}{k_f} \theta'(0) \quad (11)$$

Here, Eqs. (10) and (11) describe the local skin friction and local Nusselt number, respectively.

3. Results and discussion

The solutions of Eqs. (6) and (7), subject to boundary conditions (8), were numerically obtained using the MATLAB's bvp4c solver. Preliminary guesses, optimal boundary layer thickness and various parameter values were carefully selected and adjusted within MATLAB to ensure the most accurate results. The suction effect, S, is considered in this current study. Non-unique or dual solutions for Eqs. (6) and (7) under the conditions of Eq. (8) were found for specific parameter values. The thermal and flow performances of $Fe_3O_4 - CoFe_2O_4/H_2O$ were examined and presented in Figs. 2–6, illustrating the variations with the magnetic parameter $M = 0, 0.2, 0.4$, heat generation parameter $Q = 0, 0.1, 0.2$, and suction parameter $S = 0.1, 0.2, 0.3$. Other physical parameters were kept constant throughout the analysis: the Prandtl number $\Pr = 6.2$, volume fractions of the nanoparticles $\phi_1 = \phi_2 = 0.01$, free stream velocity strength $\alpha = 1$.

Figures 2 to 4 illustrate the velocity and temperature profiles under varying values of magnetic field parameters M and heat generation parameter Q as the governing parameters. All graphical results satisfy the boundary conditions specified in Eq. (8), confirming the validity of the model.

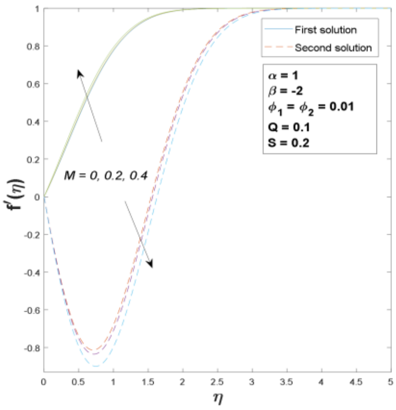

Fig. 2. Velocity profile with varied *M*.

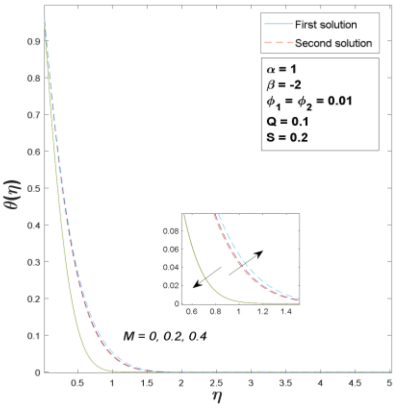

Fig. 3. Temperature profile with varied *M*.

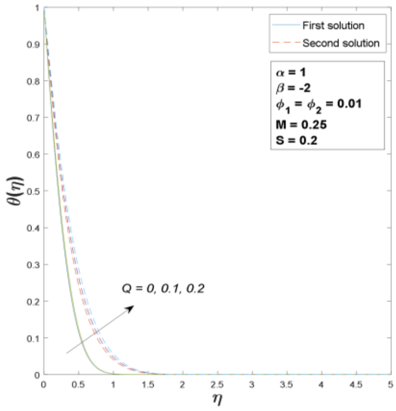

Fig. 4. Temperature profile with varied *Q*.

In Fig. 2, the velocity profile increases with higher M, while the temperature profile decreases for the first solution. Both magnetic field and unsteady separated stagnation-point (USSP) flow do not diminish the velocity profile, as the acceleration parameter stabilizes vorticity and facilitates the motion of Fe_3O_4 – $CoFe_2O_4/H_2O$. The reduction in the temperature profile seen in Fig. 3 results from the active transfer of heat from the particles into the surrounding cooler surface. The heat generation parameter Q does not influence the flow dynamics; thus, only the temperature profiles are shown in Fig. 4. Both solutions for the temperature profile expand with increasing Q, indicating a reduction in the heat transfer rate. This expansion signifies a higher temperature distribution within the fluid, reducing the surface's temperature gradient. Since the heat transfer rate is directly proportional to the temperature gradient, the overall effect is a decreased heat transfer efficiency. This means that the temperature spreads more uniformly across the fluid, reducing the steepness of the temperature gradient near the surface. Since heat transfer depends on this gradient, the overall heat transfer rate reduces, making the system less efficient at dissipating heat.

Figs. 5 and 6 illustrate the profiles of velocity and temperature with varying values of S as the testing factor. Here, the unsteadiness parameter β is set at a value $\beta = -2$. All profiles adhere to the boundary conditions in Eq. (8) confirming the model validity. Increasing the suction parameter S causes the velocity profile to increase (approach closer to the boundary) in the first solution, but reduce (move further from the boundary) in the second solution. However, both temperature profiles asymptotically approach the given boundary conditions.

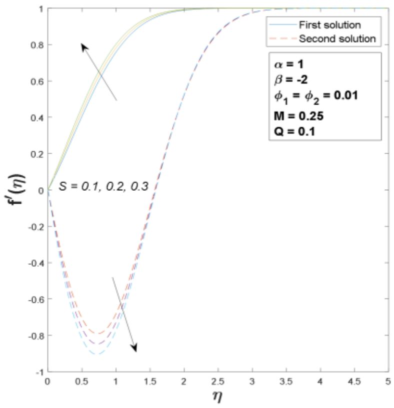

Fig. 5. Velocity profile with varied *S*.

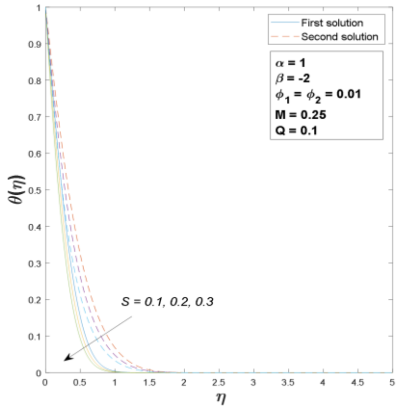

Fig. 6. Temperature profile with varied *S*.

Physically, suction reduces the thickness of the thermal boundary layer by drawing cooler fluid toward the surface, which steepens the temperature gradient at the wall, and enhances the velocity gradient. This process removes the lower-energy, slower-moving fluid from the boundary layer, thereby thinning it. This leads to improved heat transfer from the surface to the fluid, enhancing the overall heat exchange. Previous studies have highlighted that the heat generation parameter interacts differently with suction. A higher velocity gradient translates into a greater shear stress at the wall, increasing the local skin friction coefficient.

The influence of the suction parameter S, on the behaviour of $f''(0)$ and $-\theta'(0)$ with respect to the unsteadiness parameter $\beta_s \leq \beta \leq 1$ are presented in Fig. 7 and Fig. 8.

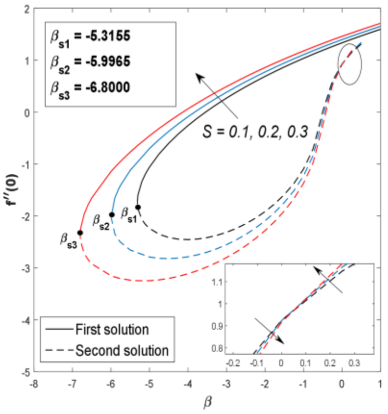

Fig. 7. $f''(0)$ for various S.

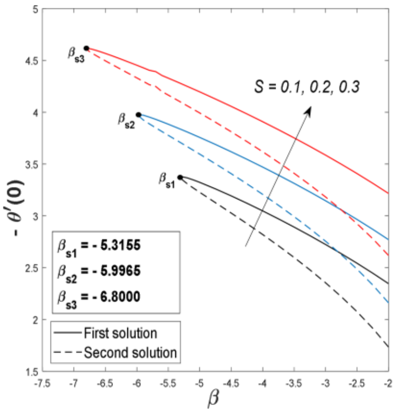

Fig. 8. $-\theta'(0)$ for various S.

In stagnation-point flow with heat generation, such as in Fe_3O_4–$CoFe_2O_4/H_2O$, suction improves heat removal efficiency, leading to enhanced heat transfer from the surface. Stabilizing the boundary layer and maintaining higher shear stress near the wall, suction helps prevent flow separation. By increasing shear stress near the wall, suction enhances momentum transfer, preventing the detachment of the boundary layer and mitigating flow separation. This stabilization not only improves aerodynamic performance but also enhances convective heat transfer by maintaining a thinner thermal boundary layer. Consequently, suction serves as an effective method for increasing heat transfer efficiency by promoting better energy exchange between the surface and the fluid. Therefore, previous research on dual solutions suggests that the first set of solutions of Eqs. (6) and (7) are stable and physically feasible, while the second set is not.

Multiple solutions are observed for specific values of the governing parameters, extending up to the separation point (critical value of β_s). It is evident that increasing the suction parameter S expands β_s. Specifically, $\beta_{s1} = -5.3155$, $\beta_{s2} = -5.9965$ and $\beta_{s3} = -6.8000$ for S = 0.1, 0.2, 0.3, respectively. Moreover, the suction parameter increased both $f''(0)$ and $-\theta'(0)$ as $\beta \to +\infty$ but a reduction in $f''(0)$ and an upsurge of $-\theta'(0)$ could be observed for the first solution as $\beta \to \beta_s$.

4. Response Surface Methodology

Response Surface Methodology (RSM) is an empirical model that employs the use of statistical techniques to relate input variables to the response. RSM is utilized where the response surface of the heat transfer rate is simulated based on numerical experiments to enhance and optimize the data to determine the optimal values of physical parameters. Some of the widely used experimental designs of RSM compared in terms of its characteristics and efficiency are included, which helps to point out the importance of the design of experiments (DOE) in optimization using RSM. In this study, RSM is applied to determine the optimal conditions and identify which input variables have a significant impact on the heat transfer performance.

In this model, RSM, implemented using Minitab, is utilized to obtain the optimum heat transfer by calculating the local Nusselt number, (response = $Re_x^{-1/2}Nu_x = (k_{hnf}/k_f)\theta'(0)$), influenced by three factors: magnetic effect, heat generation, and suction. To perform RSM, the uncoded symbols for these factors were converted into coded symbols, as shown in Table 1. Each parameter is categorized into three levels: low (–1), medium (0), and high (+1), as depicted in Table 3.

Table 3. Varied values of uncoded factors assigned to coded values.

Uncoded symbol	Coded symbol	Level		
		Low (–1)	Medium (0)	High (+1)
M	*x*1	0.25	0.5	0.75
Q	*x*2	0.1	0.2	0.3
S	*x*3	0.1	0.2	0.3

The formula $N = 2^F + 2F + C$ is used to determine the number of runs required, where F represents the number of factors and C represents the number of centre points. To ensure sufficient representation of both factorial and centre points, a total of $N = 20$ trials were conducted, with $F = 3$ and $C = 6$. Table 4 presents 20 runs computed using the involved factors and responses through a face-centred composite design. The following general quadratic regression model is used:

$$\text{response} = \mathrm{Re}_x^{-1/2}\mathrm{Nu}_x =$$
$$c_o + \sum_{i=1}^{N} c_i\, x_i + \sum_{i=1}^{N} c_{ii}\, x_i^2 + \sum_{i=1}^{N-1}\sum_{i=1}^{N} c_{ij}\, x_i x_j\ , \quad (12)$$

where the response is the dependent parameter or outcome, c represents the coefficient, N is the number of independent variables (factors), and x denotes the factor.

The results are summarized in Table 5 through an analysis of variance (ANOVA). A parameter is considered statistically significant if its p-value is less than 0.05, indicating a 95% confidence level. It can be observed that all variables demonstrated significance with p-values less than 0.05. As a result, these terms are significant in the correlation of Eq. (12). The final response correlation is then provided as:

$$\begin{aligned}\mathrm{Re}_x^{-1/2}\mathrm{Nu}_x &= 2.15690 + 0.02659\,x1 - 1.31010\,x2 + \\ &+4.04582\,x3 + 0.04281\,x1^2 - 0.2160\,x2^2 + \\ &+1.1375\,x3^2 + 0.04002\,x1x2 + \\ &-0.08002x1x3 + 0.75007x2x3. \qquad (13)\end{aligned}$$

It can be observed from the coefficients of $x1$ and $x3$ in Eq. (13) that these terms positively affect the response, whereas $x2$ has a negative impact. This implies that the local parameters M and suction parameter S decrease with an increase in Q. Physically, this means that removing the slower-moving fluid near the surface enhances heat transfer, and when the fluid itself is generating heat, there is less need for external heat transfer, reducing the efficiency of convective cooling. This observation is consistent with and encapsulates the numerical results presented in the preceding section.

Table 4. Experimental design and response values on $\mathrm{Re}_x^{-1/2}\mathrm{Nu}_x$.

Runs	**Coded values**			**Real values**			**Response**
	x1	*x2*	*x3*	***M***	***Q***	***S***	
1	-1	-1	-1	0.25	0.1	0.1	2.45568
2	1	-1	-1	0.75	0.1	0.1	2.48798
3	-1	1	-1	0.25	0.3	0.1	2.19294
4	1	1	-1	0.75	0.3	0.1	2.23017
5	-1	-1	1	0.25	0.1	0.3	3.36643
6	1	-1	1	0.75	0.1	0.3	3.39166
7	-1	1	1	0.25	0.3	0.3	3.13462
8	1	1	1	0.75	0.3	0.3	3.16292
9	-1	0	0	0.25	0.2	0.2	2.77836
10	1	0	0	0.75	0.2	0.2	2.80882
11	0	-1	0	0.5	0.1	0.2	2.91144
12	0	1	0	0.5	0.3	0.2	2.66607
13	0	0	-1	0.5	0.2	0.1	2.34131
14	0	0	1	0.5	0.2	0.3	3.26327
15	0	0	0	0.5	0.2	0.2	2.79091
16	0	0	0	0.5	0.2	0.2	2.79091
17	0	0	0	0.5	0.2	0.2	2.79091
18	0	0	0	0.5	0.2	0.2	2.79091
19	0	0	0	0.5	0.2	0.2	2.79091
20	0	0	0	0.5	0.2	0.2	2.79091

Table 5. Analysis of variance (ANOVA) for $\mathrm{Re}_x^{-1/2}\mathrm{Nu}_x$.

Source	**DF**	**Adj SS**	**Adj MS**	**F-value**	**P-value**
Model	9	2.27993	0.25333	5134957.5	0
Linear	3	2.27874	0.75958	15396786.77	0
x1	1	0.00236	0.00236	47770.77	0
x2	1	0.15042	0.15042	3049066.69	0
x3	1	2.12596	2.12596	43093522.85	0
Square	3	0.00071	0.00024	4774.17	0
x1*x1	1	0.00002	0.00002	399.12	0
x2*x2	1	0.00001	0.00001	260.04	0
x3*x3	1	0.00036	0.00036	7212.23	0
2-Way Interaction	3	0.00049	0.00016	3311.55	0
x1*x2	1	0.00001	0.00001	162.35	0
x1*x3	1	0.00003	0.00003	648.96	0
x2*x3	1	0.00045	0.00045	9123.36	0
Error	10	0	0		
Lack-of-Fit	5	0	0	*	*
Pure Error	5	0	0		
Total	19	2.27993			

The Nusselt number increases with higher values of magnetic field parameter. Further insights into the interaction effects between independent variables on the response can be obtained using RSM. These interactions are visualized through contour and surface plots, as illustrated in Fig. 9.

In Fig. 9a, the plot suggests a stronger correlation between Nu_x and $x2$ compared to $x1$. As $x2$ increases, there is a noticeable reduction in the response value. While the response value increases with $x1$, the rate of increase appears to be more gradual. Furthermore, there is a more noticeable dependence of the response value on $x3$ than on $x1$. While $x1$ does influence the response value, it appears to be less pronounced than that of $x3$, the higher the value of $x3$, the higher the response value achieved at any $x1$ as shown in Fig. 9b. As presented in Fig. 9c, the response value shows a strong positive correlation with a high value of $x3$. The gradient is steep, meaning that increasing $x3$ causes a significant increase in response value. Hence, the magnetic field M and suction S have a favourable impact on maximizing the heat transfer rate, as the magnetic field interacts with moving fluid particles, enhancing mixing and improving heat dissipation. In contrast, the heat generation parameter Q reduces the local Nusselt number, as an increase in Q leads to a flatter temperature profile, decreasing the surface temperature gradient and consequently lowering both the local Nusselt number and heat transfer efficiency.

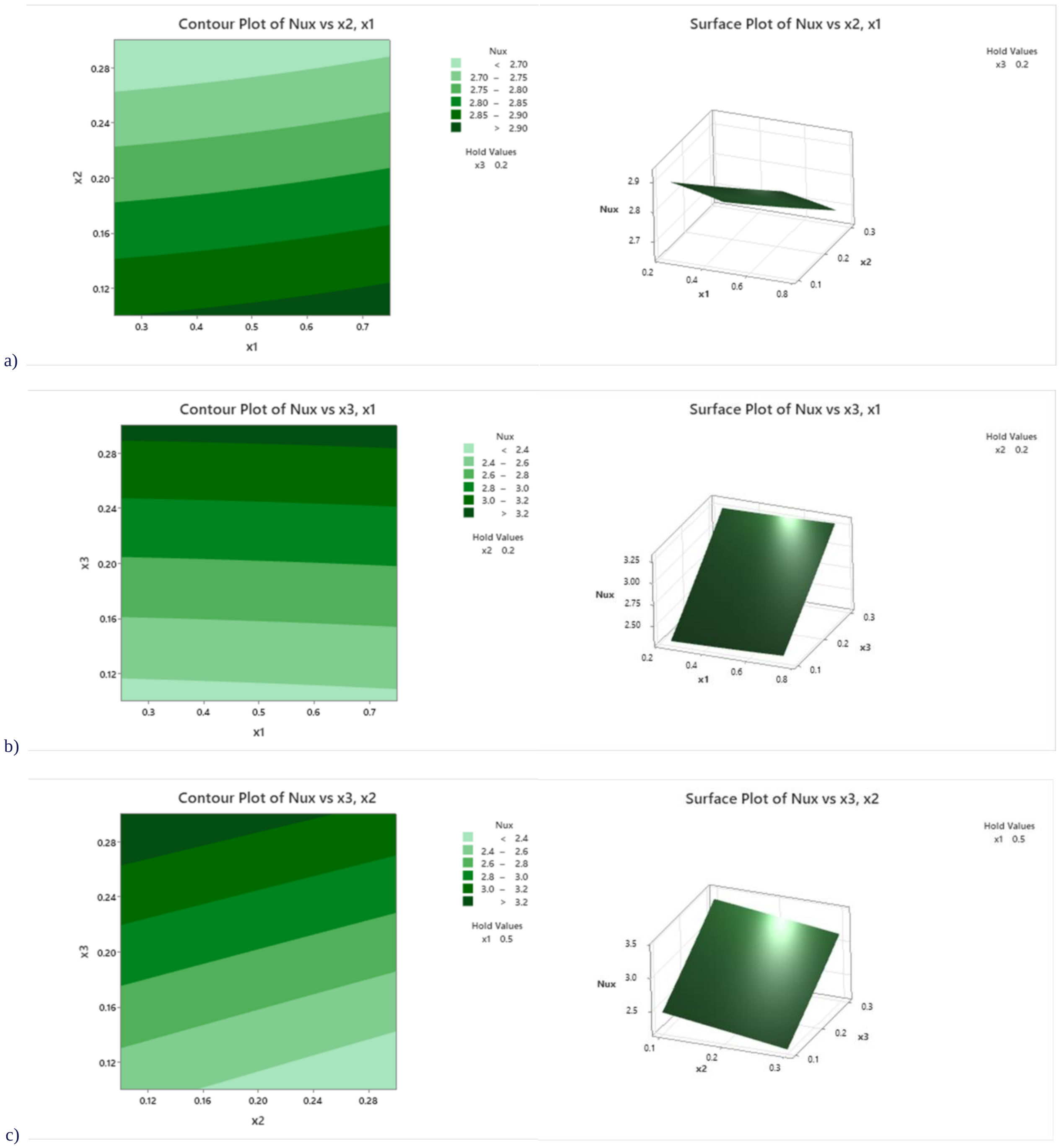

a)

b)

c)

Fig. 9. Contour and surface plots of response (heat transfer) for different combinations of coded parameters.

Finally, the optimization of the local Nusselt number is presented in Table 6. The objective of this optimization is to maximize the local Nusselt number, thereby improving heat transfer performance in the current flow scenario. Achieving desirability of 99.98%, the local Nusselt number reaches an optimized value of 3.39138 when the magnetic effect and suction parameters are at their maximum, while the heat generation parameter is minimized.

Table 6. Optimal value of the response.

Solution	***x*1**	***x*2**	***x*3**	**Response fit**	**Composite desirability**
1	0.75	0.1	0.3	3.39138	0.999769

5. Conclusions

Thermal progress of unsteady separated stagnation-point flow with the presence of magnetic field, heat generation and suction in hybrid ferrofluid has been successfully analysed. The current investigation used an approach that combined numerical and optimization techniques to examine flow and heat transfer. The similarity transformation technique reduces partial differential equations and boundary conditions into non-linear ordinary differential equations. The dual solution was obtained numerically by utilizing the bvp4c solver in MATLAB. Further, the optimal heat transfer rate was determined by employing the response surface methodology. This study specifically examines the novelty, which is the suction effect. The important discoveries are listed as follows:

- A dual solution was obtained with the first one being the stable and physically feasible.
- Increasing M expands the velocity profile.
- The temperature profile decreases for the first solution, indicating the stabilizing effect of the magnetic field.
- Q primarily affects the temperature profile, with higher values reducing the heat transfer rate.
- An increase in S broadens the range of $f''(0)$ and $-\theta'(0)$, reduces boundary layer thickness, stabilizes the flow, prevents flow separation and increases the skin friction coefficient.
- As the unsteadiness parameter $\beta \rightarrow \beta_s$, $-\theta'(0)$ increases for the first solution, demonstrating the effectiveness of suction in optimizing thermal performance.
- The combined effect of suction and magnetic field enhances the heat transfer efficiency, with the suction playing a crucial role in improving heat removal, particularly in stagnation-point flow scenarios.
- The highest heat transfer rates occur at the maximum magnetic field and suction values, while the lowest heat generation results in optimal heat dissipation.

In conclusion, the findings of this study offer significant contributions to the field of fluid dynamics by providing a deeper understanding of fluid flow behaviour and heat transfer mechanisms in hybrid ferrofluids. The research highlights the influence of key parameters, such as the magnetic field, suction and heat generation on thermal performance, which can be beneficial for applications in cooling systems, biomedical engineering and advanced thermal management technologies. Since this study focuses on the flow of hybrid nanofluids containing spherical-shaped nanoparticles, future research could explore the effects of different nanoparticle shapes. Incorporating additional conditions or effects could further extend the applicability of the current flow model to real-world scenarios. As this study is limited to numerical and statistical investigations of thermal behaviour, experimental validation may be considered in future work.

References

[1] Khan, M., Sarfraz, M., & Zehra, R. (2022). Energy transport near Homann stagnation point flow over a spiraling disk with Cattaneo–Christov theory. *International Journal of Modern Physics B*, 36(25), 2250171. doi: 10.1142/S0217979222501715

[2] Choi, S.U., & Eastman, J.A. (1995). Enhancing Thermal Conductivity of Fluids With Nanoparticles. *ASME International Mechanical Engineering Congress & Exposition*, No. ANL/MSD/CP-84938, CONF-951135-29. November 12–17, San Francisco, USA.

[3] Eastman, J.A., Choi, S.U.S., Li, S., Yu, W., & Thompson, L.J. (2001). Anomalously increased effective thermal conductivities of ethylene glycol-based nanofluids containing copper nanoparticles. *Applied Physics Letters*, 78(6), 718–720. doi: 10.1063/1.1341218

[4] Sarfraz, M, Muhammad, K. Alrihieli, H.F., & Abdelmohimen, M.A.H. (2025). Heat and mass transfer analysis in flow of Walter's B nanofluid: A numerical study of dual solutions. *Journal of Applied Mathematics and Mechanics / Zeitschrift für Angewandte Mathematik und Mechanik*, 105(1), e202300951. doi: 10.1002/zamm.202300951

[5] Anuar, N.S., Bachok, N., & Pop, I. (2021). Influence of MHD hybrid ferrofluid flow on exponentially stretching/shrinking surface with heat source/sink under stagnation point region. *Mathematics*, 9(22), 2932. doi: 10.3390/math9222932

[6] Saranya, S., Al-Mdallal, Q.M., & Javed, S. (2021). Shifted Legendre collocation method for the solution of unsteady viscous-ohmic dissipative hybrid ferrofluid flow over a cylinder. *Nanomaterials*, 11(6), 1512. doi: 10.3390/nano11061512

[7] Waini, I., Khashi'ie, N.S., Kasim, A.R.M., Zainal, N.A., Hamzah, K.B., Arifin, N.M., & Pop, I. (2022). Unsteady magnetohydrodynamics (MHD) flow of hybrid ferrofluid due to a rotating disk. *Mathematics*, 10(10), 1658. doi: 10.3390/math10101658

[8] Khashi'ie, N.S., Waini, I., Zainal, N.A., Hamzah, K.B., Kasim, A.R.M., Arifin, N.M., & Pop, I. (2022). Thermal Progress of Unsteady Separated Stagnation Point Flow with Magnetic Field and Heat Generation in Hybrid Ferrofluid. *Nanomaterials*, 12(18), 3205. doi: 10.3390/nano12183205

[9] Rosli, W.M.H.W., Mohamed, M.K.A., Sarif, N.M., & Ong, H.R. (2023). Convective Boundary Layer Flow of Williamson Hybrid Ferrofluid over a Moving Flat Plate with Viscous Dissipation. *Journal of Advanced Research in Fluid Mechanics and Thermal Sciences*, 112(1), 176–188. doi: 10.37934/arfmts.112.1.176188

[10] Idris, S., Jamaludin, A., Nazar, R., & Pop, I. (2023). Heat transfer characteristics of magnetized hybrid ferrofluid flow over a permeable moving surface with viscous dissipation effect. *Heliyon*, 9(5). doi: 10.1016/j.heliyon.2023.e15907

[11] Zainodin, S., Jamaludin, A., Nazar, R., & Pop, I. (2023). Effects of higher order chemical reaction and slip conditions on mixed

convection hybrid ferrofluid flow in a Darcy porous medium. *Alexandria Engineering Journal*, 68, 111–126. doi: 10.1016/j.aej.2023.01.011

[12] Zainal, N.A., Nazar, R., Naganthran, K., & Pop, I. (2022). Unsteady separated stagnation-point flow past a moving plate with suction effect in hybrid nanofluid. *Mathematics*, 10(11), 1933. doi: 10.3390/math10111933

[13] Khan, A., Jamshed, W., Eid, M.R., Pasha, A.A., Tag El Din, E.S.M., Khalifa, H.A.E.-W., & Alharbi, S.K. (2022). Unsteady electro-hydrodynamic stagnating point flow of hybridized nanofluid via a convectively heated enlarging (dwindling) surface with velocity slippage and heat generation. *Symmetry*, 14(10), 2136. doi: 10.3390/sym14102136

[14] Mahmood, Z., & Khan, U. (2023). Unsteady three-dimensional nodal stagnation point flow of polymer-based ternary-hybrid nanofluid past a stretching surface with suction and heat source. *Science Progress*, 106(1), 00368504231152741. doi: 10.1177/00368504231152741

[15] Khashi'ie, N S., Arifin, N.M., & Pop, I. (2022). Unsteady axisymmetric radiative Cu-Al_2O_3/H_2O flow over a radially stretching/shrinking surface. *Chinese Journal of Physics*, 78, 169–179. doi: 10.1016/j.cjph.2022.06.003

[16] Sarfraz, M., Khan, M, Al Zubaidi, A. & Saleem, S. (2023). Insights into the thermodynamic efficiency of Homann-Agrawal hybrid nanofluid flow. *Alexandria Engineering Journal*, 82, 178–185. doi: 10.1016/j.aej.2023.09.074

[17] Khan, M., Sarfraz, M. Mehmood, S. & Ullah, M.Z. (2022). Irreversibility process analysis for SiO_2-MoS_2/water-based flow over a rotating and stretching cylinder. Journal of Applied Biomaterials & Functional Materials, 20, 1–15. doi: 10.1177/22808000221120329

[18] Sarfraz, M. & Khan, M, (2024). Energy optimization of water-based hybrid nanomaterials over a wedge-shaped channel. *Scientia Iranica*, 31(1), 71–82. doi: 10.24200/sci.2023.60254.6689

[19] Sarfraz, M., Yasir, M & Khan, M. (2023). Exploring dual solutions and thermal conductivity in hybrid nanofluids: a comparative study of Xue and Hamilton–Crosser models. *Nanoscale Advances*, 50 (23), 6695–6704. doi: 10.1039/D3NA00503H

[20] Wahid, N.S., Arifin, N.M., Khashi'ie, N.S., & Pop, I. (2020). Hybrid nanofluid slip flow over an exponentially stretching/shrinking permeable sheet with heat generation. *Mathematics*, 9(1), 30. doi: 10.3390/math9010030

[21] Eid, M.R., & Nafe, M.A. (2022). Thermal conductivity variation and heat generation effects on magneto-hybrid nanofluid flow in a porous medium with slip condition. *Waves in Random and Complex Media*, 32(3), 1103–1127. doi: 10.1080/17455030.2020.1810365

[22] Bakar, S.A., Wahid, N.S., Arifin, N.M., & Khashi'ie, N.S. (2022). The flow of hybrid nanofluid past a permeable shrinking sheet in a Darcy–Forchheimer porous medium with second-order velocity slip. *Waves in Random and Complex Media*, 1–18. doi: 10.1080/17455030.2021.2020375

[23] Yasir, M., & Khan, M. (2024). Thermal efficiencies of Ohmic cobalt ferrite and magnetite hybrid ferrofluid flow over an exponentially vertically shrinking surface. *Alexandria Engineering Journal*, 90, 120–128. doi: 10.1016/j.aej.2024.01.055

[24] Zainal, N.A., Nazar, R., Naganthran, K., & Pop, I. (2020). Unsteady three-dimensional MHD non-axisymmetric Homann stagnation point flow of a hybrid nanofluid with stability analysis. *Mathematics*, 8(5), 784. doi: 10.3390/math8050784

[25] Pop, I., Rostami, M.N., & Dinarvand, S. (2021). Dual similarity solutions because of mixed convective flow of a double-nanoparticles hybrid nanofluid: critical points and stability analysis. *International Journal of Numerical Methods for Heat & Fluid Flow*, 31(11), 3319–3342. doi: 10.1108/HFF-09-2019-0714

[26] Khashi'ie, N.S., Wahid, N.S., Arifin, N.M., & Pop, I. (2022). Magnetohydrodynamics unsteady separated stagnation-point (USSP) flow of a hybrid nanofluid on a moving plate. *ZAMM-Journal of Applied Mathematics and Mechanics/Zeitschrift für Angewandte Mathematik und Mechanik*, 102(6), e202100410. doi: 10.1002/zamm.202100410

[27] Zainodin, S., Jamaludin, A, Nazar, R & Pop, I., (2023). MHD Mixed Convection Flow of Hybrid Ferrofluid through Stagnation-Point over the Nonlinearly Moving Surface with Convective Boundary Condition, Viscous Dissipation, and Joule Heating Effects, *Symmetry*, 15(4), 878. doi: 10.3390/sym15040878

[28] Algehyne, E.A., Ahammad, N.A., Elnair, M.E., Zidan, M., Alhusayni, Y.Y., El-Bashir, B., & Alzahrani, F. (2023). Entropy optimization and response surface methodology of blood hybrid nanofluid flow through composite stenosis artery with magnetized nanoparticles (Au-Ta) for drug delivery application. *Scientific Reports*, 13(1), 9856. doi: 10.1038/s41598-023-36931-6

[29] Mishra, S., Panda, S., & Baithalu, R. (2024). Enhanced heat transfer rate on the flow of hybrid nanofluid through a rotating vertical cone: a statistical analysis. *Partial Differential Equations in Applied Mathematics*, 11, 100825. doi: 10.1016/j.padiff.2024.100825

[30] Yahaya, R.I., Arifin, N.M, Mustafa, M.S., Pop, I., Ali, F.M., & Isa, S.S.P. M., (2025). Mixed convection hybrid nanofluid flow past a non-isothermal cone and wedge with radiation and convective boundary condition: Heat transfer optimization. *Case Studies in Thermal Engineering*, 66, 105768. doi: 10.1016/j.csite.2025.105768

[31] Dholwy, S. (2016). Magnetohydrodynamic Unsteady Separated Stagnation-Point flow of a viscous Fluid over a Moving Plate. *Journal of Applied Mathematics and Mechanics / Zeitschrift für Angewandte Mathematik und Mechanik*, 96, 707–720. doi: 10.1002/zamm.2014

Co-published by
Institute of Fluid-Flow Machinery
Polish Academy of Sciences
Committee on Thermodynamics and Combustion
Polish Academy of Sciences

http://www.imp.gda.pl/archives-of-thermodynamics/

ARCHIVES OF THERMODYNAMICS

Preparation of Mullite Porous Ceramics by the Composite Method of Foaming and Pore-Forming Agent Method

Huayun Sun

School of Metallurgy, Shandong Vocational College of Industry, Zibo, 256414, China
Corresponding author email: sunmzh66@163.com

Received: 08.02.2025; revised: 27.03.2025; accepted: 15.04.2025

Abstract

To prepare mullite porous ceramics with low thermal conductivity and high strength, taking kyanite tailings and α-Al_2O_3 as the main raw materials, the mixture after adding sawdust and foaming agents was cast into shape and heated at different temperatures. The bulk density, porosity and mechanical properties of the sample were tested at room temperature. The phase composition and microstructure were analyzed using X-ray diffraction and scanning electron microscopy. The results show that as the sawdust addition increased, the apparent porosity of the sample increased; the compressive strength and the thermal conductivity decreased. Increasing the firing temperature can promote the densification, improve the compressive strength and increase the thermal conductivity of the sample. When the firing temperature was increased to 1500°C, the ceramic reaction was basically completed. When the sawdust content was low, the sawdust was almost surrounded by the material, and the pore distribution was relatively dispersed. As the sawdust content increased, the pore distribution became more concentrated, and there were more connected pores. When the sawdust addition was 10% (w) and the heat treatment temperature was 1500°C, the mullite porous ceramics would have high compressive strength and low thermal conductivity.

Keywords: Foaming method; Pore-forming agent method; Mullite porous ceramics

Vol. 46(2025), No. 2, 103–109; doi: 10.24425/ather.2025.154910

Cite this manuscript as: Sun, H. (2025). Preparation of Mullite Porous Ceramics by the Composite Method of Foaming and Pore-Forming Agent Method. *Archives of Thermodynamics*, 46(2), 103–109.

1. Introduction

Porous ceramic materials have these properties such as low bulk density and low thermal conductivity. Related research on porous ceramic materials has attracted more and more attention [1–3]. Porous ceramic materials are widely applied in catalyst carriers [4–5], filtration and separation [6,7], heat insulation [8,9], sound absorption [10], and electronic components [11,12]. Especially in the current situation of extremely severe environmental pollution and energy shortage, the demand for materials with better performance is constantly increasing [13,14]. Due to its porous nature, porous ceramics can reduce thermal radiation and heat convection, thereby lowering the thermal conductivity. It is an excellent thermal insulation material that is of great significance for environmental protection and carbon emission reduction [15].

Widespread technical applications of mullite ceramics stem from their optimal properties such as high thermal stability, excellent thermal shock resistance, low density, low thermal expansion and electrical conductivity, as well as appropriate strength and fracture toughness [16–18]. In addition, mullite ceramics have low gas permeability, optimal creep resistance, high compressive strength, and good corrosion resistance at high temperatures [19]. Due to its optimal thermal and mechanical

Nomenclature

w – share of raw materials, %

Abbreviations and Acronyms

SEM – scanning electron microscopy
XRD – X-ray diffraction

properties, mullite has become an important material for traditional and advanced ceramics [20].

In this work, the foaming method and the pore-forming agent method are combined to form multi-level pores inside the material, aiming to improve the strength and reduce the thermal conductivity of the material. The effects of adding sawdust and heat treatment temperature on the densification, microstructure and physical properties of the samples are studied, aiming to improve the strength of mullite porous ceramic materials and reduce their thermal conductivity.

2. Experiment

2.1. Raw materials

The main raw materials used in this experiment were α-Al_2O_3 micropowder produced by Kaifeng Special Refractories Co., Ltd., China, and kyanite produced in Hainan province, China. The specific chemical compositions of the raw materials are shown in Table 1.

Table 1. Chemical composition of raw materials.

Raw material	w, %										Particle size
	SiO_2	Al_2O_3	Fe_2O_3	CaO	MgO	K_2O	Na_2O	TiO_2	ZrO_2	I.L	µm
Kyanite	35.24	56.73	0.88	0.02	0.81	0.01	0.02	0.02	3.25	3.02	25.72
α-Al_2O_3	0.13	98.88	0.07	0.02	0.02	0.008	0.008	0.005		0.859	2.27

The additives include sawdust (from Hebei province, China, passing through a 0.5 mm sieve, used as a pore-forming agent), polyvinyl alcohol (PVA, analytical grade, used as a binder), aluminium sol (from Shandong province, China, with a solid content of 20%), carboxymethyl cellulose (CMC, analytical grade, used as a thickener), and NG10 (produced by Wuhan Shanda Chemical Co., Ltd., China, used as a foaming agent).

2.2. Sample preparation

The ingredients were prepared according to the ratio of m(kyanite):m(Al_2O_3 micropowder) = 74.57:25.43. First, the prepared raw materials, PVA (3.5% (w)) and CMC (0.1% (w)) were placed into a planetary ball mill for grinding. The ratio of grinding ball, material and water was 3.6:3:1. Then, 5% (w), 10% (w), 15% (w) and 20% (w) sawdust was added separately to the ball-milled materials, followed by the foaming agent. After rapid stirring, the mixture was poured into moulds. After drying at room temperature for 24 hours, the samples were demoulded and further dried at 110°C for 24 hours. Finally, the samples were heat-treated in a high-temperature furnace at 1450°C and 1500°C, respectively, as shown in Fig. 1.

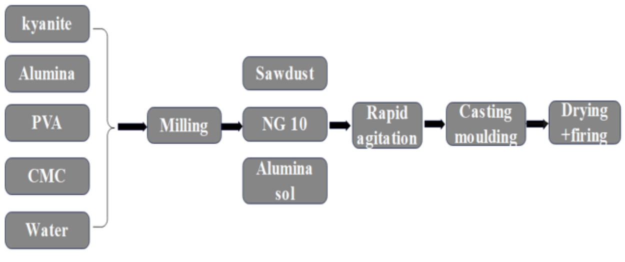

Fig. 1. Preparation process of mullite porous ceramics.

2.3. Analysis and testing

According to GB/T 2997-2000, the apparent porosity and bulk density of the heat-treated samples were measured using an apparent porosity and bulk density tester (Model XQK-04, Luoyang Precondar Instruments for Testing Refractoriness Co., Ltd., China). According to GB/T 5072.2-2004, the compressive strength of the heat-treated specimens at room temperature was tested using a microcomputer-controlled electronic universal testing machine (Shenzhen WANCE Testing Equipment Co., Ltd., China). According to GB/T 5988-2007, the linear change rate of the samples heat-treated at 1450°C and 1500°C was measured. Referring to the international standard ISO 22007-2, the thermal conductivity of the specimens at room temperature was measured using a Hot Disk thermal property analyser (Model TPS2500S, Hot Disk AB, Sweden).

3. Results and discussion

3.1. Effects of heat-treatment temperature and sawdust addition on the phase changes of samples

Figure 2 shows the variation rules of the phases of mullite porous ceramics with different sawdust additions at different heat-treatment temperatures.

It can be observed from the X-ray diffraction (XRD) patterns of the three samples that an increase in the heat-treatment temperature is conducive to the formation of the mullite phase. Specifically, the peak values of the characteristic peaks of the mullite phase in the mullite porous ceramic samples prepared at 1500°C are higher than those prepared at 1450°C. Therefore, from the phase growth trend of the samples, the quantity of the mullite phase is higher when the heat-treatment temperature is 1500°C. This indicates that the combination of various phases is better at this temperature, resulting in the formation of more mullite phases. The internal reaction of the mullite porous ceramic prepared by heat-treatment at 1500°C is basically completed. Specifically, kyanite reacts with α-Al_2O_3 micropowder to form mullite, and zircon decomposes and reacts with α-Al_2O_3 micropowder to form mullite and zirconia. As a phase that can undergo phase transformation at high temperatures to improve and toughen materials, the formation of zirconia in materials is beneficial for improving their thermal shock resistance.

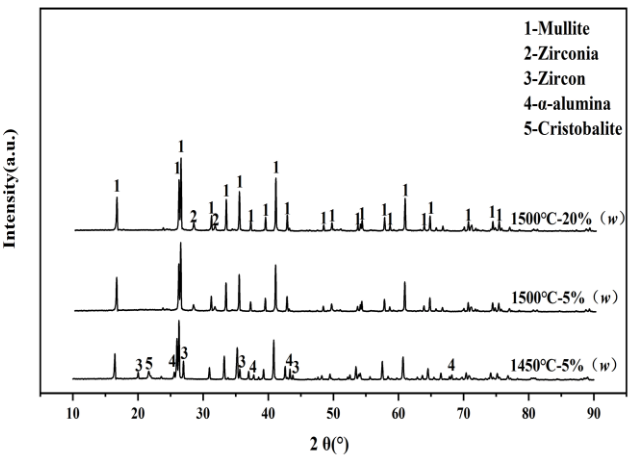

Fig. 2. XRD patterns of mullite porous ceramics prepared with different amounts of sawdust added at different sintering temperatures.

3.2. Effects of heat-treatment temperature and sawdust additions on the permanent linear change rate of sample heating, apparent porosity and bulk density

Figure 3a shows the permanent linear change rate upon heating of the prepared mullite porous ceramics with different sawdust addition amounts at different heat-treatment temperatures. With the increase of the heat-treatment temperature, the permanent linear change rate shows a downward trend. Taking the sawdust addition amount of 5% (*w*) as an example, the permanent linear change rate upon heating of the specimen prepared by heat-treatment at 1450°C is –0.22%, and that of the specimen prepared by heat-treatment at 1500°C is –0.44%. With the increase of the heat-treatment temperature, the diffusion coefficient increases, and the mutual reaction between the raw materials in the mullite porous ceramics proceeds more completely. The shrinkage of the specimen intensifies, resulting in a decrease in the permanent linear change rate upon heating. When the heat-treatment temperature is the same, as the sawdust addition increases, the permanent linear change rate of the samples after heating increases. As the sawdust addition increases from 5% (*w*) to 20% (*w*), the permanent linear change rate of the specimen after heating prepared by heat-treatment at 1450°C increases from –0.22% to –0.01%, and that prepared by heat-treatment at 1500°C increases from –0.44% to –0.19%. This change is caused by two aspects: First, as the sawdust addition increases, the relative content of the solid matrix in the sample decreases. Since the deformation of the sample is mainly borne by the solid matrix, the reduction in the matrix content implies a decrease in deformation. Therefore, under the same temperature, the permanent linear change rate of the sample will increase (with the absolute value decreasing). Second, the pores in the sample can accommodate the shrinkage of the matrix. When the matrix shrinks, the pores, by virtue of their own cavity structures, provide additional space for the shrinking matrix. To a certain extent, the shrinkage of the matrix is alleviated, and from a macroscopic perspective, the samples have a relatively high permanent linear change rate.

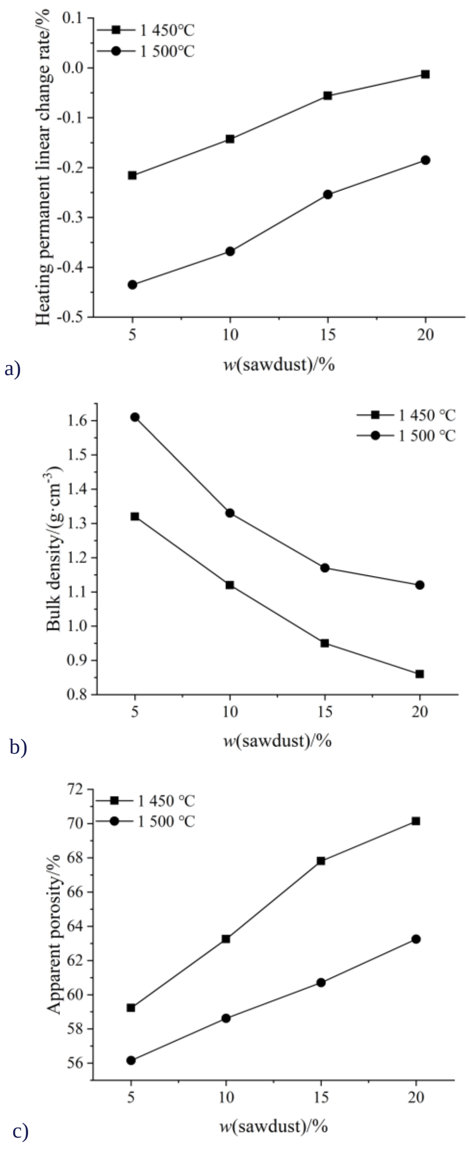

Fig. 3. The physical properties of mullite porous ceramics prepared by sawdust addition at different heat treatment temperatures:
a) Heating permanent linear change rate, b) Bulk density change,
c) Apparent porosity change.

Figures 3b and 3c show the changes in the bulk density and apparent porosity of the prepared mullite porous ceramic specimens with different sawdust additions at different heat-treatment temperatures. As the heat-treatment temperature increases, the apparent porosity of the prepared mullite porous ceramics decreases, while the bulk density increases. Taking the sawdust addition of 10% (*w*) as an example, the bulk density and apparent porosity of the specimen prepared by heat-treatment at 1450°C are 1.12 g·cm⁻³ and 63.25%, respectively, and those at 1500°C are 1.33 g·cm⁻³ and 58.62%, respectively. As the heat-treatment temperature increases, then the intensification of the mutual reaction between raw materials in mullite porous ceramics leads to a decrease in the permanent linear change rate during heating. This is the main reason for the above-mentioned results. When the heat-treatment temperature is the same, as the sawdust addition increases, the bulk density of the prepared mullite porous ceramics decreases, and the apparent porosity increases. As the sawdust addition increases from 5% (*w*) to 20% (*w*), the bulk density of the specimen prepared by heat-treatment at 1450°C decreases from 1.32 g·cm⁻³ to 0.86 g·cm⁻³, and the apparent porosity increases from 59.23% to 70.14%.The bulk density of the specimen prepared by heat-treatment at 1500°C decreases from 1.61 g·cm⁻³ to 1.12 g·cm⁻³, and the apparent porosity increases from 56.16% to 63.25%.

3.3. Effects of heat-treatment temperature and sawdust addition on the compressive strength at room temperature and thermal conductivity of samples

Figure 4a shows the effects of different heat-treatment temperatures and sawdust additions on the compressive strength of the samples at room temperatures. As shown in Fig. 4a, as the heat-treatment temperature increases, the compressive strength increases. Taking the sawdust addition of 15% (*w*) as an example, the compressive strengths of the specimens prepared by heat-treatment at 1450°C and 1500°C are 7.23 MPa and 7.56 MPa, respectively. As the heat-treatment temperature increases, the density of the mullite porous ceramics increases, and the pores decrease. At the same time, the intensification of the reaction between raw materials leads to high bonding strength. This is the main reason for the above-mentioned results. When the heat-treatment temperature is the same, as the sawdust addition increases, the compressive strength decreases. When the sawdust addition increases from 5% (*w*) to 20% (*w*), the compressive strength of the specimen prepared by heat-treatment at 1450°C decreases from 9.85 MPa to 6.39 MPa; that at 1500°C decreases from 10.65 MPa to 6.75 MPa. The increase in sawdust addition leads to a decrease in the density of the mullite porous ceramics and an increase in the pores after heat-treatment, ultimately resulting in a decrease in the compressive strength of the material.

Figure 4b shows the effects of different heat-treatment temperatures and sawdust additions on the thermal conductivity of the specimens at room temperature. As shown in Fig. 4b, as the heat-treatment temperature increases, the thermal conductivity increases. Taking the sawdust addition of 20% (*w*) as an example, the thermal conductivity of the specimens prepared by heat-treatment at 1450°C and 1500°C is 0.210 W·(m·K)⁻¹ and 0.214 W·(m·K)⁻¹ respectively. As the heat-treatment temperature increases, the density of the mullite porous ceramics increases. Since the heat-transfer efficiency of the solid phase is much higher than that of the gas phase, the decrease in the porosity is the main reason for the increase in the thermal conductivity. When the heat-treatment temperature is the same, as the sawdust addition increases, the thermal conductivity of the prepared mullite porous ceramics decreases. As the sawdust addition increases from 5% (*w*) to 20% (*w*), the thermal conductivity of the specimen prepared by heat-treatment at 1450°C decreases from 0.227 W·(m·K)⁻¹ to 0.210 W·(m·K)⁻¹; that at 1500°C decreases from 0.269 W·(m·K)⁻¹ to 0.214 W·(m·K)⁻¹. The increase in sawdust addition leads to a decrease in the density of the mullite porous ceramics and an increase in the porosity, thereby reducing the heat conducted by the solid phase and ultimately resulting in a decrease in the thermal conductivity of the material.

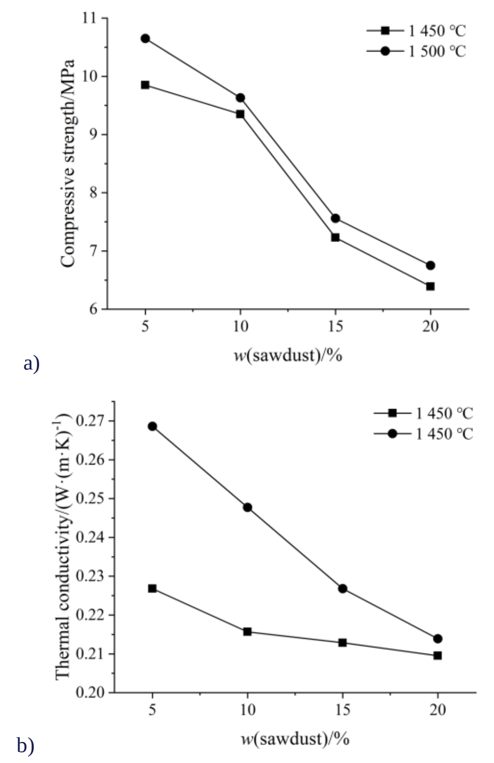

Fig. 4. The influence of sawdust additions on the compressive strength and thermal conductivity of mullite porous ceramics at different sintering temperatures: a) Compressive strength, b) Thermal conductivity.

3.4. Effects of heat treatment temperature and foaming-pore former composite method on the microstructure of samples

Figure 5 shows the scanning electron microscopy (SEM) images of specimens prepared with different sawdust additions after heat treatment at different temperatures. As shown in Figs. 5a–5d, the pores formed by sawdust have irregular shapes, rough contours and certain unevenness on the pore walls. The pores formed by the foaming agent are mostly spherical or approximately spherical. This is because gas tends to form a spherical shape with the minimum surface energy in a homogeneous medium. The pores formed by the combustion of sawdust are relatively large, with pore diameters concentrated around several hundred micrometers. In contrast, the pores generated by the decomposition of the foaming agent are smaller, usually around tens of micrometers. Pore diameters of the samples show a bimodal distribution of large and small pores. Small pores distributed in the gaps of large pores help to increase the number of pores within a limited space, thereby further increasing the porosity and specific surface area of the porous ceramics. As the sawdust addition increases, the average size of pores in the samples increases. This is the main reason for the increase in the porosity and the decrease in the strength of the samples.

Comparing Figs. 5b and 5d, it can be seen that the skeleton of the mullite porous ceramics prepared by heat treatment at 1500°C is denser. At the same time, due to sintering densification, the pores are interconnected. Comparing Figs. 5e and 5f, it can be seen that the skeleton of the mullite porous ceramics prepared by heat treatment at 1500°C is denser, with only a small number of closed pores in the skeleton. The skeleton of the mullite porous ceramics prepared by heat treatment at 1450°C is relatively loose, and most of the pores inside the skeleton are connected pores. This is a factor for the lower strength of the mullite porous ceramics prepared at 1450°C.

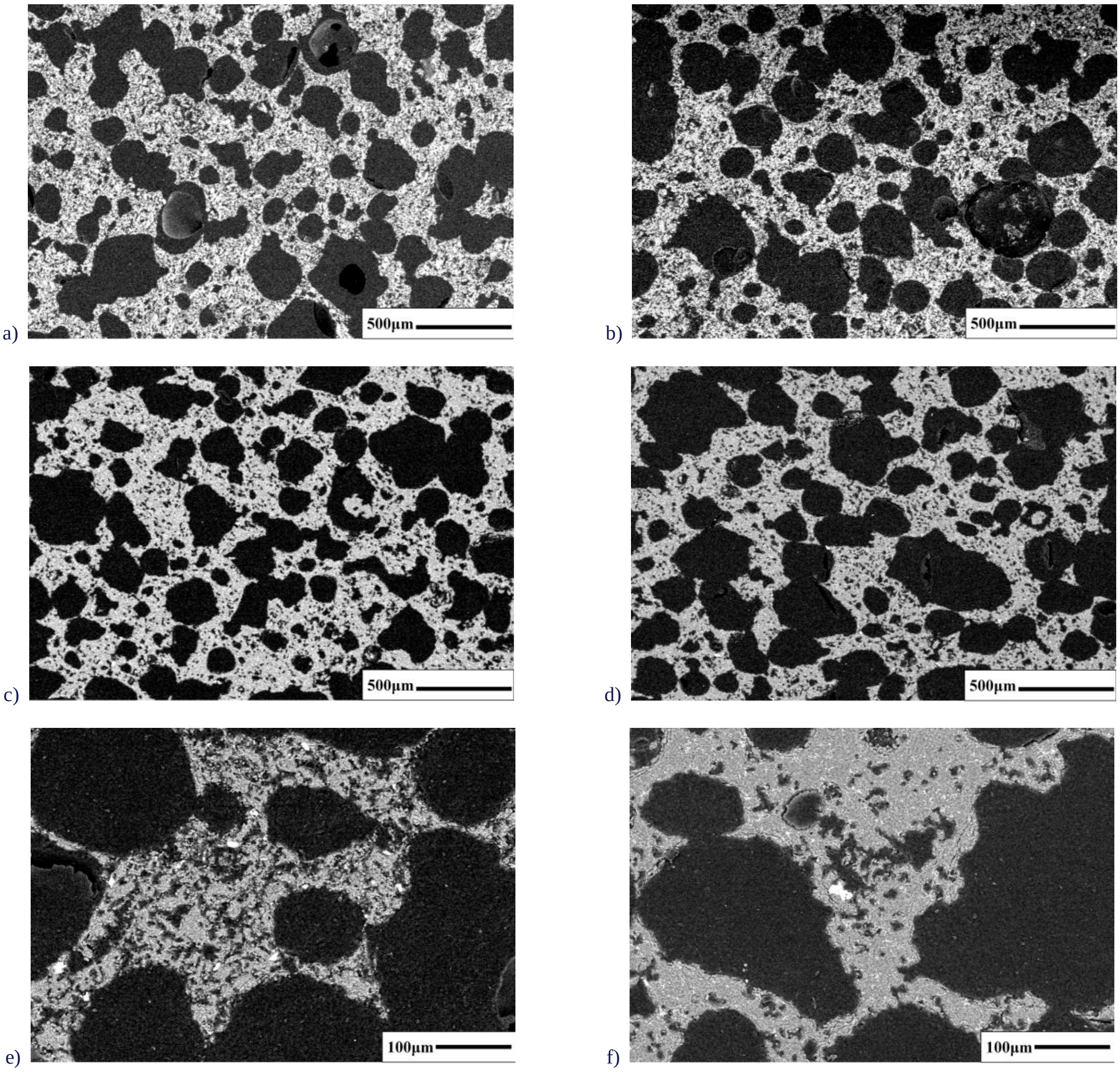

Fig. 5. SEM images of polishing samples prepared by different sawdust additions after heat treatment at different temperatures.
Sawdust: a) 5% (*w*) –1450℃, b) 20% (*w*) – 1450℃, c) 15% (*w*) – 1500℃, d) 20% (*w*) – 1500℃, e) 10% (*w*) – 1450℃, f) 10% (*w*) – 1500℃.

Figure 6 shows the SEM images of the cross-sections of specimens prepared with different sawdust additions after heat treatment at different temperatures. Comparing Figs. 6a and 6c, it can be seen that as the heat-treatment temperature increases, the thickness of pore walls becomes thinner, but more compact. Comparing Figs. 6b and 6d, it can be seen that the microstructure of the mullite porous ceramics prepared by heat treatment at 1450°C is relatively loose. Moreover, the particle morphology is diverse. Combining with the XRD results in Fig. 2, it can be determined that the raw materials have not completely reacted. The microstructure of the mullite porous ceramics prepared by heat treatment at 1500°C is relatively dense, and the difference in particle morphology is low. Combining with the XRD results in Fig. 2, it can be determined that the reaction between raw materials has been completed.

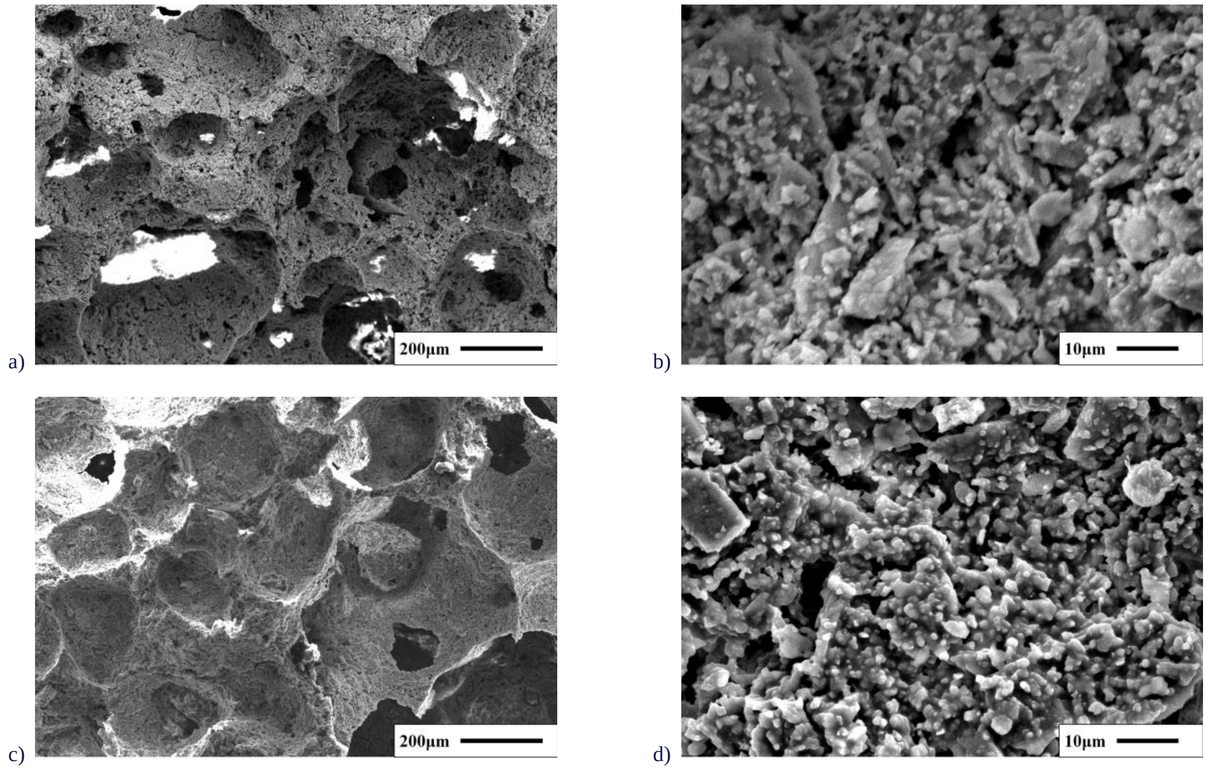

Fig. 6. SEM images of the fracture surface of the samples prepared by different sawdust additions after heat treatment at different temperatures. Sawdust: a) 5% (*w*) – 1450℃, b) 5% (*w*) – 1450℃, c) 5% (*w*) – 1500℃, d) 5% (*w*) – 1500℃.

4. Conclusions

Comprehensively comparing the mullite porous ceramic materials prepared with different sawdust additions and heat-treated at different temperatures, the following conclusions can be drawn:

1) When the sawdust addition was the same, the mullite porous ceramics prepared by heat-treatment at 1500°C have a more compact microstructure. The mutual reaction between the raw materials was more sufficient, with higher bulk density, lower apparent porosity, higher strength and relatively higher thermal conductivity;
2) The compressive strength of the prepared mullite porous ceramic materials was 6.39–10.56 MPa, and the thermal conductivity was 0.210–0.269 $W\cdot(m\cdot K)^{-1}$;
3) When the sawdust addition was 10% (*w*) and the heat-treated temperature was 1500°C, the sample had the best comprehensive performance. At room temperature, its bulk density, apparent porosity, compressive strength and thermal conductivity were 1.33 $g\cdot cm^{-3}$, 58.62%, 9.63 MPa and 0.248 $W\cdot(m\cdot K)^{-1}$, respectively.

References

[1] Pan, J.W., & Jiang, H.Y. (2024). Effect of ρ-Al_2O_3-CAC composite sintering aid on properties of porous SiC ceramics. *Refractories*, 58(05), 376–380+386. doi: 10.3969/j.issn.1001-1935.2024.05.002

[2] Wang, H., Li, S., Li, Y., Xiang, R., Luo, H., Zhou, Z., & Guo, W. (2021). Preparation of novel reticulated prickly porous ceramics with mullite whiskers. *Journal of the European Ceramic Society*, 41(1), 864–870. doi: 10.1016/j.jeurceramsoc.2020.08.001

[3] Kultayeva, S., Kim, Y.W., & Song, I.H. (2021). Effects of dopants on electrical, thermal, and mechanical properties of porous SiC ceramics. *Journal of the European Ceramic Society*, 41(7), 4006–4015. doi: 10.1016/j.jeurceramsoc.2021.01.049

[4] Arumugham, T., Kaleekkal, N.J., Gopal, S., Nambikkattu, J., Rambabu, K., Aboulella, A.M., & Banat, F. (2021). Recent developments in porous ceramic membranes for wastewater treatment and desalination: A review. *Journal of Environmental Management*, 293, 112925. doi: 10.1016/j.jenvman.2021.112925

[5] Chai, L., Zhai, W., Liu, X., Xing, G., Zhang, B., Zang, J., & Zhang, J. (2024). Room Temperature Catalysts for High Effective Degradation of Formaldehyde: Research Progresses and Challenges. *Chemistry Select*, 9(12), e202304418. doi: 10.1002/slct.202304418

[6] Liu, J.J., Yue, W.D., Xiong, F., & Shan, Y.F. (2024). Preparation of silicon carbide based porous ceramics with network cell wall and theirparticipate matter capture. *Refractories*, 58(02), 132–136. doi: 10.3969/j.issn.1001-1935.2024.02.008

[7] Zhang, M., Ning, H., Shang, J., Liu, F., & Peng, S. (2024). A robust superhydrophobic-superoleophilic PDMS/Al_2O_3/CM composite ceramic membrane: Stability, efficient emulsified oil/water separation, and anti-pollution performance. *Separation and Purification Technology*, 328, 124864. doi: 10.1016/j.seppur.2023.124864

[8] Wang, H., Li, Y., Yin, B., Li, S., He, X., Xiang, R., & Qiao, Z. (2023). Synthesis and application evaluation in lithium battery furnace of mullite insulating refractory bricks from tailings. *International Journal of Applied Ceramic Technology*, 20(5), 3237–3245. doi: 10.1111/ijac.14408

[9] Low, Z. K., Blal, N., & Baillis, D. (2024). Numerical and exper-

imental characterization of high-temperature heat transfer in a ceramic foam with dual-scale porosity. *International Journal of Heat and Mass Transfer*, 222, 125148. doi: 10.1016/j.ijheatmasstransfer.2023.125148

[10] Lou, J., He, C., Shui, A., & Yu, H. (2023). Enhanced sound absorption performance of porous ceramics with closed-pore structure. *Ceramics International*, 49(23), 38103–38114. doi: 10.1016/j.ceramint.2023.09.140

[11] Zhang, X.Y., Yang, J.J., & Li, W.H. (2021). Porous Ceramics Based on Slurry-based Addictive Manufacturing Technique – A Short Review. *Journal of the Chinese Ceramic Society*, 49(09), 1810–1827. doi: 10.14062/j.issn.0454-5648.20210221

[12] Padurariu, C., Padurariu, L., Curecheriu, L., Ciomaga, C., Horchidan, N., Galassi, C., & Mitoseriu, L. (2017). Role of the pore interconnectivity on the dielectric, switching and tunability properties of PZTN ceramics. *Ceramics International*, 43(7), 5767–5773. doi: 10.1016/j.ceramint.2017.01.123

[13] Li, Z., Li, W., You, J., Huang, J., Gan, R., Guo, J., & Zhang, X. (2024). Critical secondary resource for porous ceramics: A review on recycling of inorganic solid wastes. *Journal of the European Ceramic Society*, 44(15), 116781. doi: 10.1016/j.jeurceramsoc.2024.116781

[14] Xu, C., Hu, R., Liu, Y., Chen, Z., Liu, Z., & Han, W. (2024). Research on preparation and related properties of macro-micro porous mullite ceramic skeletons via twice pore-forming technology. *RSC Advances*, 14(18), 12624–12632. doi: 10.1039/D4RA01277A

[15] Wang, M.M., Sui, X.Y., Qi, K.Y., Xu, J., Liu, R.X., Zhou, C.L., Tang, W.Z., Duan, X.F., & Li, Z.F. (2024). Research Progress of Porous Ceramic Thermal Insulation Materials. *Bulletin of the Chinese Ceramic Society*, 43(02), 637–648. doi: 10.16552/j.cnki.issn1001-1625.20240011.004

[16] Wang, B., Liu, Y., Peng, X., Yuan, F.H., & Cheng, Y.X. (2022). Research on High Temperature Protection Property and Thermal Impact Resistance of A PS–PVD Si/Mu/YbMS Environmental Barrier Coating. *Aeronautical Manufacturing Technology*, 65(03), 64–70. doi: 10.16080/j.issn1671-833x.2022.03.064

[17] Ternero, F., Rosa, L.G., Urban, P., Montes, J.M., & Cuevas, F.G. (2021). Influence of the total porosity on the properties of sintered materials – A review. *Metals*, 11(5), 730. doi: 10.3390/met11050730

[18] Sandoval, M.L., Martinez, A.T., & Camerucci, M.A. (2021). Mechanical and thermal behavior of cellular mullite materials. *Journal of the European Ceramic Society*, 41(13), 6687–6696. doi: 10.1016/j.jeurceramsoc.2021.05.047

[19] Das, D., Lucio, M.D.S., Kultayeva, S., & Kim, Y.W. (2024). Effects of pore size on electrical and thermal properties of porous SiC ceramics. *International Journal of Applied Ceramic Technology*, 21(4), 2651–2662. doi: 10.1111/ijac.14620

[20] Li, S., Zhang, H., Li, S., Wang, J., Wang, Q., & Cheng, Z. (2024). Advances in hierarchically porous materials: Fundamentals, preparation and applications. *Renewable and Sustainable Energy Reviews*, 202, 114641. doi: 10.1016/j.rser.2024.114641

Co-published by
Institute of Fluid-Flow Machinery
Polish Academy of Sciences
Committee on Thermodynamics and Combustion
Polish Academy of Sciences

http://www.imp.gda.pl/archives-of-thermodynamics/

ARCHIVES OF THERMODYNAMICS

Sustainable air conditioning with a focus on evaporative cooling and the Maisotsenko cycle

Jan Pokorný[a*], Paweł Madejski[b], Jan Fišer[a]

[a]Faculty of Mechanical Engineering, Department of Thermodynamics and Environmental Engineering, Brno University of Technology (BUT),
Technická 2896/2, Královo Pole, 61669, Brno, Czech Republic
[b]Faculty of Mechanical Engineering and Robotics, Department of Power Systems and Environmental Protection Facilities,
AGH University of Science and Technology, al. Mickiewicza 30, 30-059 Kraków, Poland
*Corresponding author email: pokorny.j@fme.vutbr.cz

Received: 29.01.2025; revised: 05.05.2025; accepted: 27.05.2025

Abstract

Evaporative cooling can be an answer to the growing global demand for energy efficient and sustainable air conditioning. Direct evaporative cooling is the traditional method of cooling air to wet-bulb temperature. Indirect evaporative cooling uses heat exchangers with wet and dry channels to cool air indirectly, avoiding an increase in humidity. The Maisotsenko cycle is a dew point indirect evaporative cooling that allows air to be cooled below wet-bulb temperature using a heat and mass exchanger with a coupled wet and dry channel. It can be used as a stand-alone system, or as coupled with traditional refrigerant-based cooling systems, or as a heat recovery process to improve the efficiency in the power industry applications. A Python-based computational tool for simulating of 1D heat and mass transfer in the Maisotsenko cycle is presented here. It uses a spatially discretised differential equation solver and a psychrometric chart. The 1D model and experimental data from the study of Pakari were used as a reference for the initial testing. The comparison results are promising, suggesting a potential application in the design of sustainable cooling.

Keywords: Sustainability; Cooling; M-cycle; Python; 1D model

Vol. 46(2025), No. 2, 111–121; doi: 10.24425/ather.2025.154911

Cite this manuscript as: Pokorný, J., Madejski, P., & Fišer, J. (2025). Sustainable air conditioning with a focus on evaporative cooling and the Maisotsenko cycle. *Archives of Thermodynamics*, 46(2), 111–121.

1. Introduction

The challenges posed by climate change and rapid population growth, particularly in urbanizing regions, have intensified the demand for sustainable cooling technologies. Currently, India and China together account for 35% of the global population, which is approximately 8.2 billion people [1], as illustrated by the population density map in Fig. 1. According to United Nations population projections [2], the global population is expected to reach 10 billion by 2060. The combination of population growth and global warming presents challenges for governments, requiring proactive measures to address both the causes and consequences of these issues. Tackling these challenges demands innovative solutions and a shift toward more sustainable technologies, especially by rethinking energy use and emission production. „Under the Paris Agreement of 2015, every five years countries review their progress in limiting greenhouse gas emissions. The key aim is to curb the rise in global average near-surface temperature, holding it to well below 2°C above pre-industrial levels, and to pursue efforts to limit the increase to 1.5°C" [3]. In 2018 the Intergovernmental Panel on Climate Change (IPCC) published the report Global Warming of 1.5 [4], which emphasized the need for global action to halve emissions by 2030 and achieve net-zero emissions by 2050. It was projected that the 1.5°C limit could be reached between 2030 and 2052.

Nomenclature

c – specific heat capacity of air, J/(kg·K)
h – convective heat transfer coefficient, W/(m^2·K)
h_m – mass transfer coefficient, m/s
h_{fg} – latent heat of vaporization of water, J/kg
H – height of the channel, m
k – thermal conductivity, W/(m·K)
L – length of the channel, m
$\dot{m}$ – mass flow rate, kg/s
p – barometric pressure, kPa
t – time, s
T – temperature, K
U – heat transfer coefficient, W/(m^2·K)
x – axial distance along the channel, m

Greek symbols

δ – thickness, m
ε – effectiveness, %
ρ – density, kg/m^3
φ – relative humidity, %
ω – specific humidity, kg/kg$_{da}$

Subscripts and Superscripts

[0] – start point of vector (Python)
[-1] – end point of vector (Python)
a – dry air
d – dry channel air
dp – dew point
in – inlet
m – mass
out – outlet
pa – paper
pl – plastic
w – wet channel air
wf – saturated air at water film
wb – wet-bulb

Abbreviations and Acronyms

AC – air conditioning
BVP – boundary value problem
C3S – Copernicus climate change service
CFD – computational fluid dynamics
COP – coefficient of performance
DEC – direct evaporative cooling
EC – evaporative cooling
ECMWF– European Centre for Medium-Range Weather Forecasts
FDM – finite difference method
GWP – global warming potential
HMX – heat and mass exchanger
HX – heat exchanger
HVAC – heating, ventilation, air conditioning
IEC – indirect evaporative cooling
IPCC – Intergovernmental Panel on Climate Change
IVP – initial value problem
M-cycle– Maisotsenko cycle
ODEs – ordinary differential equations
PDEs – partial differential equations
TRL – technology readiness levels
VCC – vapour compression cycle

According to the recent data (November 2024) from Copernicus Climate Change Service (C3S) [5], the Earth reached this 1.5°C limit already in 2024 with the average near-surface temperature of the Earth 15°C. The prediction [6] expected that in the year 2060, there would be an increase of 2°C or even more than in the pre-industrial period in the pessimistic case scenario, which seems to be more probable today than in 2016, see Fig. 2.

The sustainability of technologies related to climate change is more important than ever, leading to a rethinking of strategies for cooling and air conditioning (AC) systems. Traditional cooling technologies, such as vapour compression cycles (VCC), rely heavily on refrigerants that significantly contribute to the greenhouse effect. Due to stricter legislation, refrigerants with high Global Warming Potential (GWP) are being phased out. The European Commission's study on cooling technologies under the revised Renewable Energy Directive underscores the importance of shifting towards renewable and energy-efficient cooling methods, away from high GWP refrigerants toward more sustainable alternatives. In the [7], the review of cooling technologies, the environmental impacts, efficiencies, and Technology Readiness Levels (TRL) are listed.

Generally, cooling systems can be based on electrical (e.g. thermoelectric Peltier modules), mechanical (e.g. VCC), acoustic, magnetic (e.g. magnetocaloric), chemical (e.g. desiccant systems, heat of reaction), hydraulic (e.g. potential energy use), thermal (e.g. absorption and adsorption, transcritical thermal compression heat pumps), and natural physical phenomena (e.g. natural convection, evaporative cooling systems).

A promising alternative to VCC in some applications are

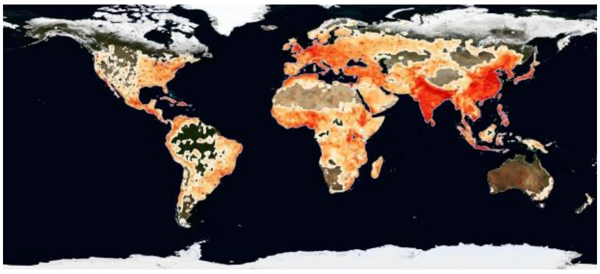

Fig. 1. Population density: processed from sources [8,9].

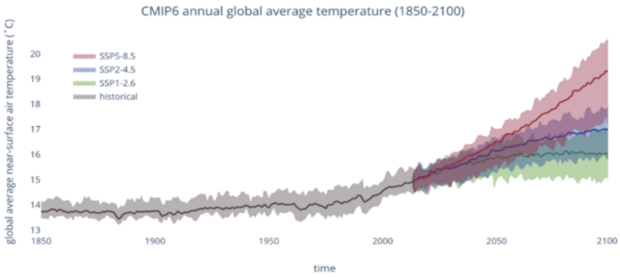

Fig. 2. Global mean temperature between 1850 and 2100. Projection from [6] published in 2016. The grey shows the past and the coloured areas show projections of future temperature based on greenhouse gas emission scenarios (red is pessimistic, blue is realistic and green is optimistic). Credit: C3S, ECMWF.

evaporative cooling (EC) systems, which generally allow for reaching the wet-bulb temperature and in this range can achieve interesting values of coefficient of performance (COP) at the expense of water consumption. By [10], the evaporative cooling can reach COP values (15–20), which are very good values in comparison with VCC (2–4), absorption/adsorption (0.6–1.2) or thermoelectric cooling by the Peltier effect (0.2–1.2). The reason for the good COP is that unlike in VCC where a compressor is used, in evaporative cooling (EC), only power supply of a fan or a water pump is needed to provide the required cooling effect, primarily through water consumption. However, the limitation of standard EC is that the cooling requirements must remain above the wet bulb temperature. The EC system can be used as a stand-alone system, or as coupled with traditional refrigerant-based cooling systems, or as a heat recovery process to improve the efficiency in the power industry applications such as turbines [11]. An example of the coupled EC and VCC system is an evaporative condenser to lower system condensing temperatures and reduce the compressor workload. A more advanced solution is the so-called M-condenser [12].

This paper focuses on EC systems for heating, ventilation, and air conditioning (HVAC) applications. The challenges related to the demand for sustainable cooling technologies have already been outlined.

The subsequent part of the introduction presents a brief literature review of evaporative cooling, including Maisotsenko cycle (M-cycle) technology; discusses the potential of EC and our research objectives, emphasizing the advanced materials, innovative structures, and system integration to enhance the efficiency of cooling technologies, especially EC systems.

Finally, the main contribution of this study is the development of a Python-based one-dimensional model of heat and mass transfer for M-cycle calculations inspired by Pakari's study [13]. His 1D model simulated in COMSOL and his experimental data were used as a reference for presented benchmark tests.

1.1. Evaporative cooling

EC can be understood as a physical process which uses the transition of liquid water to water vapour to the cooldown of the wetted surface based on the principle of adiabatic cooling. This phenomenon occurs naturally in trees and plants, which regulate water loss through micropores in their leaves; similarly, humans regulate water loss through sweat glands and pores in the skin. By the long-term adaption, they adjusted to manage control of the water loss to survive in different climatic zones. Human civilisation has used EC as a fundamental method for temperature control for centuries, utilized in various forms across different cultures – Mashrabiya architecture for cooling of buildings [14], terracotta pots for beverage and food storage etc. These traditional techniques are still widely used because of their simplicity even in the modern design of buildings. They can be combined with new architectural strategies like optimizing building orientation, incorporating advanced natural ventilation systems, integrating plants on building facades for shading and evapotranspiration, or new solar cooling technologies [15], etc. These approaches significantly contribute to lower thermal loads and reduce energy consumption of HVAC systems. The evaporative cooling can be categorized into [14]:

- Direct Evaporative Cooling (DEC) – active, passive,
- Indirect Evaporative Cooling (IEC) – wet bulb, sub-wet bulb (M-cycle),
- Combined Indirect/ Direct Evaporative Cooling (IDEC) – multi stages.

Direct Evaporative Cooling (DEC) is the traditional method of cooling air to wet bulb temperature, which can be active or passive. Active cooling typically uses a fan or water pump for increasing of efficiency. Passive cooling is naturally driven with no power consumption. DEC systems are particularly effective in dry climates, where high temperatures and low air humidity levels enhance the cooling effect. However, in humid regions, these systems may increase moisture levels, which can reduce indoor thermal comfort [16].

Indirect Evaporative Cooling (IEC) systems cool air indirectly through a heat exchanger (HX), avoiding an increase of humidity in the produced air. This makes them suitable for a broader range of climatic conditions and applications where traditional DEC systems might not be suitable [17]. HX can have different setups of wet and dry channels (counterflow, cross-flow, etc.) based on the specific application. The M-cycle is a dew point or so-called sub-wet bulb IEC that allows air to be cooled below the wet bulb temperature using a heat and mass exchanger (HMX) with a coupled wet and dry channel. Mahmood et al. [16] provided a comprehensive overview of dew point evaporative cooling.

To enhance efficiency, combined systems integrating IEC and DEC, also referred to as two-stage or multi-stage evaporative cooling systems, can be utilized. In a two-stage system, the air is initially cooled through indirect adiabatic cooling before undergoing direct adiabatic cooling in the subsequent stage. These combined systems can achieve higher cooling efficiencies while maintaining better control over humidity levels. This makes them particularly well-suited for applications where precise environmental control is required, such as in food storage and specific industrial processes. More information on combined systems can be found in [18].

The efficiency of general EC systems is typically assessed by evaluating their wet-bulb effectiveness, Eq. (1), which measures how effectively the system cools air relative to the wet-bulb temperature. The wet-bulb effectiveness ε_{wb} of the cooling system is defined, according to Pescod [19]. For the M-cycles, it also makes sense to evaluate the dew point effectiveness ε_{dp}, which is defined by Eq. (2) to express how effectively the system cools air relative to the dew point temperature [16]:

$$\varepsilon_{wb} = \frac{T_{d,in} - T_{d,out}}{T_{d,in} - T_{d,in,wb}}\,, \tag{1}$$

$$\varepsilon_{dp} = \frac{T_{d,in} - T_{d,out}}{T_{d,in} - T_{d,in,dp}}\,, \tag{2}$$

where $T_{d,in}$ is the dry channel inlet air temperature, $T_{d,out}$ is the produced air temperature at the dry channel outlet, $T_{d,in,wb}$ is the wet-bulb temperature of the air entering the dry channel and $T_{d,in,dp}$ is the corresponding dew-point temperature.

The theoretical limit of 100% effectiveness for DEC and IEC processes is the wet-bulb temperature, whereas for the M-cycle, it is the dew point temperature. The typical wet-bulb effectiveness of the DEC system ranges from 70% to 95%, depending on the air temperature and relative humidity, as well as other factors such as airflow rate and system design. The IEC system has typically an efficiency between 60–85 %. M-cycles, under very specific conditions, can achieve wet-bulb effectiveness up to 180%, as reported by Mammod et al. [16]. However, typical values range from 110% to 120%, according to Pakari and Ghani [13], and 112%, as reported by Jradi and Riffat [20]. These values correspond to dew point effectiveness of 70% to 80%.

To increase system cooling efficiency in hot humid conditions it is possible to use some desiccation technologies to reduce the air humidity at the inlet to the cooling systems. Desiccants are hygroscopic materials which are able to reduce water content from humid air in a natural way. Silica gel, calcium chloride or similar absorption/adsorption materials are typically used. The list of studies related to this topic was published in [21–27]. The sustainability of the cooling system can be even improved with the solar driven ejector [28], water pump and fan to reduce power consumption from the electricity distribution grid to zero. So, these solar powered systems have zero CO_2 emission during their operation. Ge et al. [29] reviewed solar powered rotary desiccant wheel coolant systems, and Pacak and Worek [30], Pandelidis and Anisimow [31] investigated the application of the M-cycle for these systems.

Costelloe and Finn [17] stated that: „Desiccant AC has two main disadvantages. One is direct evaporative cooling, by which moisture is added to the air. In DEC, the limitation is the wet-bulb temperature (wet-bulb effectiveness), which is almost impossible to reach by typical direct cooling. Another disadvantage is the size of the system. Both the rotary heat exchanger and the spraying chamber need significant volume".

Related to the sustainability in some regions is easy to supply salt water rather than fresh water even with a slightly lower cooling performance [32]. The wet-bulb and dew point temperate lowered with a lower barometric pressure. This is typically used to improve the efficiency of refrigeration as vacuum cooling of food [33], which is a rapid cooling technique for any porous product that has free water and uses the principle of evaporative cooling. Additionally, membrane-based vacuum air dehumidification [34] can provide a solution for building air conditioning in combination with hollow fibre membranes [35].

Another practical factor which influences the efficiency of evaporative cooling systems are pressure losses and the maintenance to avoid clogging of the evaporative system (pad) by pollutants or water stone, etc. Evaporative coolers with a sprayed bed (wet channel) differ from each other in terms of construction and the used material. The simplest construction is a free-bed evaporative cooler, which can be made of a simple material, e.g. wood chips, sponge, non-woven fabric, or cellulose pad (Fig. 3). Water is pumped and poured onto the bed, along which it trickles and reaches the lower tray, where it is pumped again and supplemented with the evaporated amount. The issues related to the sustainability of usage of different types of natural or synthetic materials pads are discussed in a literature review of Kapilan et al. [18]. For AC applications, DEC limits the technology by increasing the outcoming humidity, which is good for some agriculture applications such as chicken farms, agriculture product storage (fruit, vegetable) or AC of greenhouses. For building applications [20,37–41], IEC provides better control about humidity at the outlet and is also safer regarding the health risks associated with mould formation in the working channels, which can spread more easily in DEC.

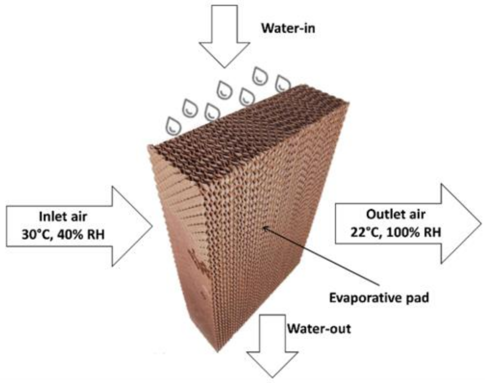

Fig. 3. Cellulose pad for direct evaporative cooling, cheap and efficient solution for cooling greenhouses, or even rooms in which higher outlet humidity does not cause problems. Source [36].

1.2. Potential of evaporative cooling

Another important aspect is determining where evaporative cooling systems are most effective, which depends largely on the Earth's climatic conditions, influenced by seasonal and time variations. The maps in Fig. 4 illustrate the average climatic conditions for May 2024, which is considered a warm month for the Northern Hemisphere, though not the hottest, which is July. The first map shows the average temperature, while the second map represents specific humidity. These maps are based on the datasets: *pressure/air.mon.mean.nc*, *shum.mon.mean.nc* from downloads.psl.noaa.gov/Datasets/ncep.reanalysis/Monthlies.

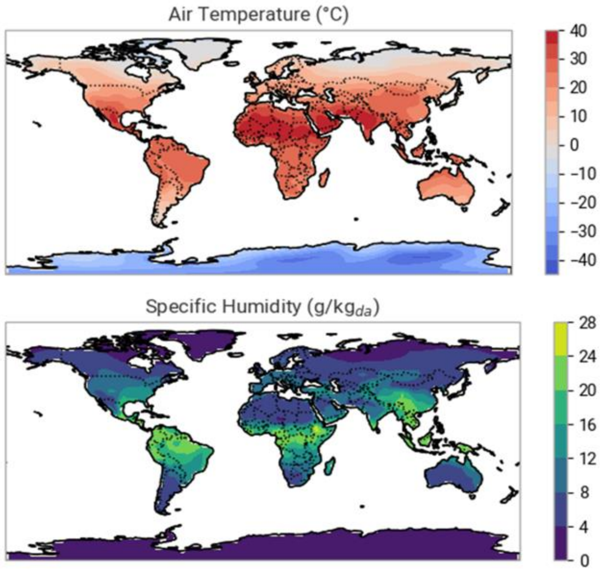

Fig. 4. Maps represent May 2024 NOAA monthly data: air temperature and specific humidity.

The dew-point and wet-bulb potential maps (Fig. 5) were calculated and visualised by EMCWF Python tool „earthkit". A similar map can be found in publications related to the storage of vegetables and fruits [42]. The potential calculations take into account the difference between average climatic conditions and the corresponding wet-bulb and dew-point temperatures.

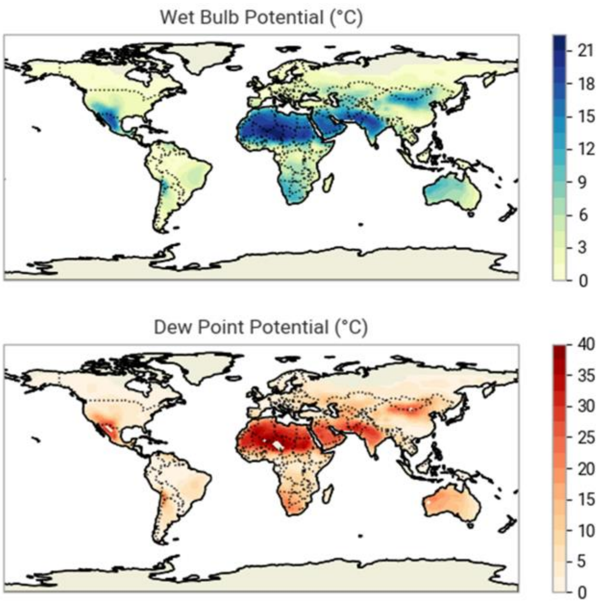

Fig. 5. Calculated wet bulb and dew point potentials for May 2024.

In these visualizations, if the wet-bulb or dew point temperature falls below 0°C, it is set to 0°C, without considering the effects of sublimation. These maps indicate that the potential for EC is the highest in regions such as India, northern China, the eastern United States, and the Middle East and North Africa. However, due to ongoing global warming, this potential is also increasing in southern and central European countries. Notably, the difference between dew-point and wet-bulb potentials highlights where the M-cycle could be most beneficial.

1.3. Maisotsenko cycle

Modern EC technologies are still evolving significantly [43,44] and in this study, we focused specifically on sub-wet bulb evaporative cooling using the M-cycle. The M-cycle represents an IEC method that enables cooling below the wet-bulb temperature by utilizing a configuration of alternating wet and dry channels within a heat and mass exchanger. The M-cycle's ability to achieve such low temperatures without the need for refrigeration makes it an attractive option for both HVAC applications and power engineering. Its versatility extends to hybrid systems, where it can be integrated with traditional refrigerant-based systems (VCC). This combination maintains high cooling capacity while reducing the environmental impact associated with conventional refrigerants.

According to Taler et al. [45], there are still challenges for research in the field of IEC and M-cycles such as: improvement of water and air distribution inside channels; developing of new materials dedicated for IEC for greater heat and mass transfer, lower pressures drops and better applicability; looking for novel solutions and connection with IEC to increase the efficiency of the systems. For example, applying a novel bare tube plastic heat exchanger to desiccant M-cycle air conditioning. Kang et al. [46] already published the numerical optimisation of such a kind of bare tube plastic heat exchanger.

1.4. Advanced materials and system integration

Our research, conducted within the framework of the Brno University of Technology (BUT), project Mechanical Engineering of Biological and Bio-inspired Systems (MEBioSys) tries to transfer bio-inspired solutions from the long-term evolution to innovative technical solutions. Our main goal is to develop and optimize innovative evaporative cooling systems, exploring the use of various materials and structures such as smart membranes, which can be used in bio-inspired evaporative pads.

In the EC system, the most important component is the wetted pad and techniques how the material of the pad absorbs and reveals water. Recent studies, including those by Mumtaz et al. [22] and Kapilan et al. [18] highlight the potential of natural fibres and materials, emphasizing their availability and the reuse of natural resources to enhance system efficiency. Understanding natural processes and materials is crucial for identifying key parameters in the design of industrial heat exchangers, such as those manufactured using advanced methods like 3D printing with additive lattice structures [47]. Strategies for water sprays and membrane designs with controlled interface layers for optimal water evaporation and vapour condensation remain also highly relevant for ongoing areas of research [48–51]. The literature review highlighted the potential of innovative materials, such as membrane-based and bio-inspired evaporative pads, to enhance the cooling system efficiency.

2. Materials and methods

This paper aims to provide Python-based computational tools for simulation and visualisation of M-cycles. The computational tool utilizes a discretized approach to model the heat exchanger, dividing the process into small sections to solve the governing equations for heat and mass transfer iteratively. This approach allows for detailed analysis of the thermal performance across different sections of the M-cycle. This paper presents the first step to reproduce the established and validated model of Pakari and Ghani [13], and compare results to ensure the validity of our Python model. This iterative process of refinement and validation is crucial for further developing a reliable computational tool. The hypothesis was given that this kind of model is able to support the design of the M-cycle, and that the model can reproduce the data from the Pakari study. The next steps will involve validating our 1D model using our own 3D-printed complex geometry. Additionally, strategies for water spraying and the use of advanced materials will be considered in the subsequent phases of our research.

2.1. Computational tool development

To support the design and optimization of EC and M-Cycle systems, a 0D/1D computational tool has been developed in Python. This tool is designed for psychrometric calculations and simulating the 1D heat and mass transfer during evaporation. The CoolProp library is used as the dataset of humid air properties. The developed Python library includes modules for calculating humid air properties using Coolprop, visualizing data on a psychrometric chart, Mollier diagram, and implementing a discretized model for heat and mass transfer calculations. For the development, the Python 3.10 and Spyder 5.5 were used. The main code requirements of libraries are: „CoolProp, matplotlib, numpy, openpyxl, plotly, pandas, scipy". These libraries allow us to create datasets compatible with Excel and interactive charts, and provide a support for the calculation of humid air properties and numerical solution for the differential equations.

2.2. Pakari's study

The experimental setup is described in the Pakari study and the details about definition of each term of the system of differential equations can be found in [13]. In this paper, we focused just on the description of the developed 1D M-cycle model in Python, which is designed to solve the heat and mass transfer in HMX including evaporation. The scheme of simulated M-cycle is depicted in Fig. 6 and it corresponds to the Pakari scheme of his experimental test bench.

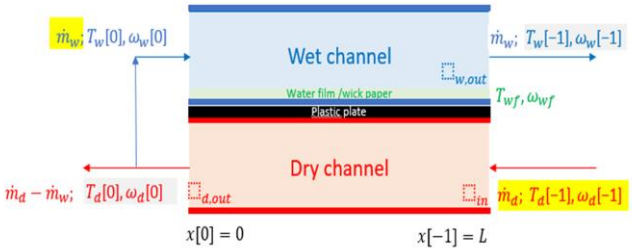

Fig. 6. Scheme of the one channel pair: dry and wet.

For the simulation, the exact dimensions of Pakari's M-cycle HMX are used. The physical constants such as the conductivity of materials (paper, plastic wall) are the same, and also the same assumption are made about flow characteristics such as the Nusselt number, etc. The Pakari HMX consists of 50 pairs of dry and wet channels in counter-current arrangement with the following geometrical parameters: channel length $L = 0.5$ m; channel height $H = 0.3$ m; heat exchanger width 0.22 m; dry channel width 2 mm; wet channel width 2 mm; plastic plate thickness $\delta_{pl} = 0.2$ mm; paper thickness $\delta_{pa} = 0.15$ mm.

Pakari experimentally investigated 15 different test cases, see Table 1, showing all input values of temperature and humidity at the dry channel inlet (T_{in}, ω_{in}) and mass flows in the dry ($\dot{m}_d$) and wet channel ($\dot{m}_w$). These inputs to the 1D M-cycle model are highlighted in yellow in Fig. 6 and in Table 1 and denoted by subscript in). The mass flows $\dot{m}_d$ and $\dot{m}_w$ are the sum of 50 pairs of the dry and wet channels. The mass flow difference $\dot{m}_d - \dot{m}_w$ is the air produced at the dry channel outlet. The primary focus of Pakari was on the produced air at the outlet of the dry channel ($T_{d,out}$, $\omega_{d,out}$) referred to in the numerical scheme as ($T_d[0]$, $\omega_d[0]$) . However, he also evaluated by his model the working air at the outlet of the wet channel ($T_{w,out}$, $\omega_{w,out}$) referred to in the numerical scheme as ($T_w[-1]$, $\omega_w[-1]$) by his 1D and 3D model. In this study, we use for verification the experimental values and also the values from his 1D model (these parameters are highlighted in grey in Fig. 6).

Table 1. Pakari's measured test data used as input for model verification.

Test No.	T_{in} (°C)	φ_{in} (%)	ω_{in} (g/kg$_{da}$)	$\dot{m}_d$ (kg/s)	$\dot{m}_w$ (kg/s)
1	29.2	43.2	10.9	0.0465	0.0154
2	30.1	43.0	8.8	0.0468	0.0153
3	30.2	30.0	8.3	0.0643	0.0193
4	30.3	31.0	8.1	0.0493	0.0157
5	30.5	34.0	9.1	0.0694	0.0256
6	30.5	38.0	7.7	0.0450	0.0108
7	35.1	28.0	9.9	0.0429	0.0157
8	35.1	35.0	11.7	0.0504	0.0165
9	35.2	43.0	10.7	0.0517	0.0167
10	39.2	42.0	11.5	0.0655	0.0246
11	40.2	29.0	11.3	0.0643	0.0143
12	43.9	22.0	10.6	0.0643	0.0143
13	43.9	22.0	11.4	0.0643	0.0155
14	44.2	17.0	10.8	0.0525	0.0252
15	44.2	17.0	9.8	0.0435	0.0147

2.3. Python model of the Maisotsenko cycle

The Python 1D model consists of the following set of differential equations describing heat and mass transfer in the M-cycle, see Eqs. (3) to (6):

- energy conservation in the dry channel (subscript d):

$$\rho_d c_d \frac{\partial T_d}{\partial t} + \dot{m}_d c_d \frac{\partial T_d}{\partial x} = UH\left(T_{wf} - T_d\right), \tag{3}$$

- energy conservation in the wet channel (subscript w):

$$\rho_w C_w \frac{\partial T_w}{\partial t} + \dot{m}_w C_w \frac{\partial T_w}{\partial x} = h_w H\left(T_{wf} - T_w\right), \tag{4}$$

- moisture conservation in the wet channel:

$$\rho_w \frac{\partial \omega_w}{\partial t} + \dot{m}_w \frac{\partial \omega_w}{\partial x} = h_m \rho_a H\left(\omega_{wf} - \omega_w\right), \tag{5}$$

- energy conservation at the water film (subscript wf):

$$\rho_w C_{wf} \frac{\partial T_{wf}}{\partial t} + h_w H\left(T_w - T_{wf}\right) + UH\left(T_d - T_{wf}\right) +$$

$$+ h_m \rho_a h_{fg}\left(\omega_w - \omega_{wf}\right) + kHL \frac{\partial^2 T_{wf}}{\partial x^2} = 0, \tag{6}$$

where ρ is the density, c – specific heat capacity, T is the temperature, ω – specific humidity, H is the height of the channel, x – spatial domain, t – time domain, and h is the convective heat transfer coefficient. Remark: ω_{wf} is saturated humid air in equilibrium with the water film and thus can be evaluated as humid air in the psychrometric chart. The value U includes the value h_d and the effect of thermal resistance of walls (plastic + paper)

$$U = 1/(1/h_d + \delta_{pl}/k_{pl} + \delta_{pa}/k_{pa}). \tag{7}$$

For the proposed model, similar assumptions were made by Pakari that HMX is insulated and there is no heat transfer to the ambience through the walls. Only temperature variations in the *x*-axis are considered. The fluid (humid air) is incompressible and viscous dissipation is negligible. The flow in the channels is laminar and fully developed, steady with a constant mass flow, heat and mass transfer coefficients. And there is no heat accumulation in the wicked paper or plastic wall. The time derivatives are proposed to simulate the dynamic behaviour of the system reacting to the varying conditions at the dry channel inlet. However, the unsteady model which is able to deal with these time terms is not yet finished and it is still under development. In this paper, only steady model results will be presented.

2.4. Discretisation and boundary conditions

The proposed set of partial differential equations (PDEs) was suggested to be solved using the Crank-Nicholson scheme for unsteady-state conditions. In this paper, we present only the steady-state solution, where the governing equations are simplified to a set of ordinary differential equations (ODEs) by setting all time derivatives to zero as Pakari did in his 1D model solved by COMSOL. The numerical solution of the resulting two-point boundary value problem (BVP) [52] is solved using the shooting method with a forward finite difference scheme for spatial discretization of $N = 1000$ elements. A finer discretisation improves the accuracy of this method while keeping the computation time within seconds. The code is designed to solve the system of ODEs for these variables:

- Temperatures: T_d (dry channel), T_w (wet channel), T_{wf} (water film),
- Specific humidity (humidity ratios): ω_d (dry channel), ω_w (wet channel), ω_{wf} (at the water film interface).

And these boundary conditions:

- Dirichlet boundary for T_d and ω_d at $x = L$ (right side of the dry channel) $T_d\,[-1] = T_{in}$; $\omega_d\,[-1] = \omega_{in}$, where T_{in}, ω_{in} are input values defined in Table 2,
- Neumann boundary condition (no heat flux) at $x = L$ for water film $dT_{wf}[-1] = 0$ and at $x = 0$ $dT_{wf}[0] = 0$,
- Coupled conditions for the wet and dry channel at $x = 0$ (left side of the dry channel) $T_w\,[0] = T_d\,[0]$ and $\omega_w\,[0] = \omega_d\,[0]$.

Table 2. Results of 1D Python model for 15 test cases (TC). $\varphi_{w,out}$ and $\varphi_{wf,out}$ were always 100 %.

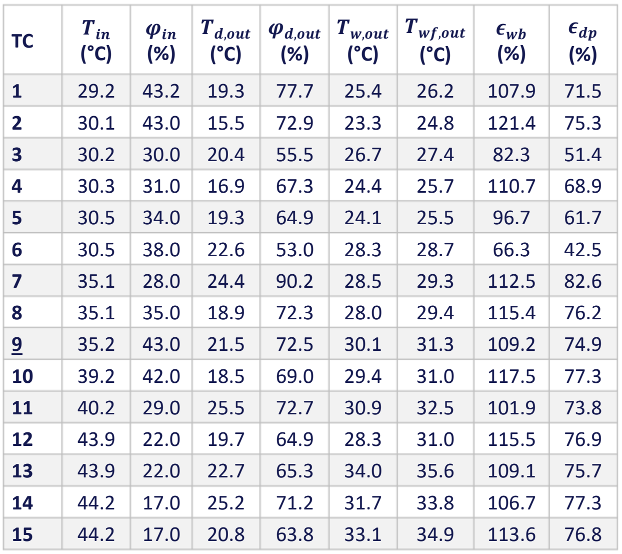

TC	T_{in} (°C)	φ_{in} (%)	$T_{d,out}$ (°C)	$\varphi_{d,out}$ (%)	$T_{w,out}$ (°C)	$T_{wf,out}$ (°C)	ϵ_{wb} (%)	ϵ_{dp} (%)
1	29.2	43.2	19.3	77.7	25.4	26.2	107.9	71.5
2	30.1	43.0	15.5	72.9	23.3	24.8	121.4	75.3
3	30.2	30.0	20.4	55.5	26.7	27.4	82.3	51.4
4	30.3	31.0	16.9	67.3	24.4	25.7	110.7	68.9
5	30.5	34.0	19.3	64.9	24.1	25.5	96.7	61.7
6	30.5	38.0	22.6	53.0	28.3	28.7	66.3	42.5
7	35.1	28.0	24.4	90.2	28.5	29.3	112.5	82.6
8	35.1	35.0	18.9	72.3	28.0	29.4	115.4	76.2
9	35.2	43.0	21.5	72.5	30.1	31.3	109.2	74.9
10	39.2	42.0	18.5	69.0	29.4	31.0	117.5	77.3
11	40.2	29.0	25.5	72.7	30.9	32.5	101.9	73.8
12	43.9	22.0	19.7	64.9	28.3	31.0	115.5	76.9
13	43.9	22.0	22.7	65.3	34.0	35.6	109.1	75.7
14	44.2	17.0	25.2	71.2	31.7	33.8	106.7	77.3
15	44.2	17.0	20.8	63.8	33.1	34.9	113.6	76.8

The shooting method solves the boundary value problem (BVP) by first converting it into an initial value problem (IVP). The method uses an initial guessed condition at $x = 0$ for the unknown temperature $T_d\,[0]$ and ω_{in}. Since no change in specific humidity occurs within the dry channel, $\omega_d\,[0] = \omega_{in}$.. For this initial guess, the solver based on the forward finite difference method provides an initial numerical solution, which is compared to the Dirichlet boundary condition at $x = L$ (dry channel inlet). The solver is run iteratively to adjust the guess until the solution of dry channel temperature matches the boundary condition with an error lower than the given tolerance of 0.01°C. So when the condition $|T_d\,[-1] - T_{in}\,[-1]| < 0.01$ is satisfied then the final solution is given. This approach ensures consistency in handling the coupled heat and mass transfer processes across the dry channel, wet channel, and water film.

The proposed iterative procedure allows us to deal with the coupling of the wet and dry channel at $x = 0$, which is a key factor for the proper simulation of the M-cycle with counter-current configuration.

3. Results

Simulations using the Python 1D model were performed for all 15 test cases from Table 1 to calculate the outlet dry and wet channel temperatures, humidity, and effectiveness. The results closely align with Pakari's experimental and simulation data.

3.1. Verification of the model on Pakari's data

The aim of this paper was to verify our Python model based on Pakari's experimental data and his 1D model. This chapter brings a summary of all simulated test cases. Table 2 presents the main results of the Python 1D M-cycle model for all test cases. The key outputs of the model are provided from the fourth column onward. Test case number 9 is underlined and highlighted because additional verification data were available for this test, see Chapter 3.2.

The verification of the simulated effectiveness is shown in Fig. 7, which compares the wet-bulb effectiveness as investigated experimentally by Pakari, simulated by Pakari's 1D model, and simulated by the Python 1D model. Additionally, these values are recalculated for the dew point effectiveness. Both calculated values of effectiveness are in good agreement with the results simulated in COMSOL by Pakari and also with experimental values.

The final verification is depicted in Fig. 8, where the outlet dry channel temperatures of the produced air are plotted and compared with Pakari's 1D model. Tolerance lines of 10% are highlighted, indicating that all test cases fall within this range, with the Python and Pakari models closely aligned. Ideally, the simulated results should lie on the diagonal of this chart to match Pakari's experimental data. Test cases 4 and 15 were closest to this ideal fit, while test case 6 was the furthest. Uncertainties during measurement and the estimation of some channel parameters should also be considered, meaning an ideal fit cannot be

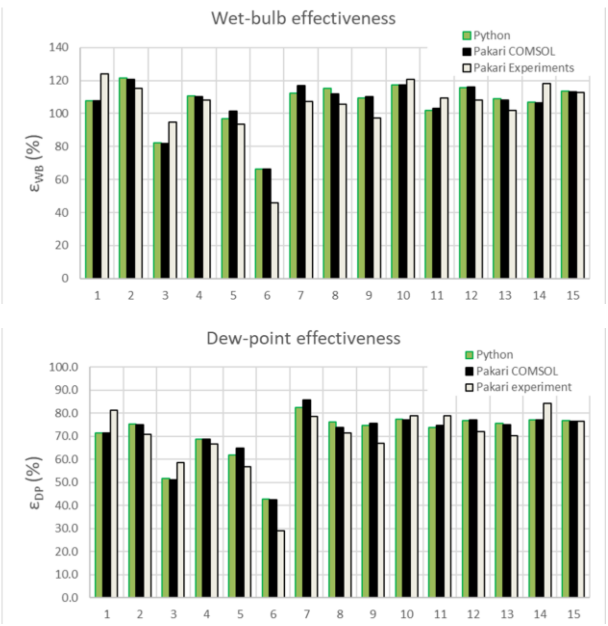

Fig.7. Wet-bulb and dew-point effectiveness experimentally investigated by Pakari, simulated by Pakari's 1D model and simulated by 1D Python model.

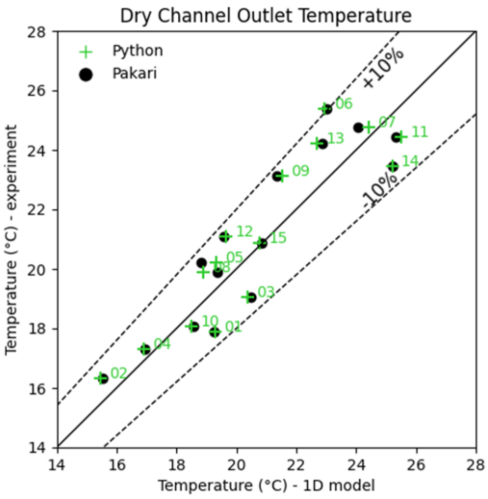

Fig. 8. Air temperatures produced at the outlet from the dry channel. The horizontal axis is from 1D model of Pakari and Python. The vertical axis are the corresponding measured data. The best agreement between simulation and measurement lies on the diagonal line of the

expected for all test cases. Still, the achieved results are very good, and the agreement between Pakari's and the Python simulation is particularly strong, indicating that the Python code verification was successful for all 15 test cases.

3.2. Verification of test case 9

Test Case 9 is highlighted in this section because it was published in the Pakari study with a more detailed analysis. For this test case, Pakari provided the resulting temperature profiles. Figure 9 compares the simulated temperature profiles with Pakari's results. Specific humidity data from the Pakari study were not available, so only simulated humidity profiles are presented. It can be observed that the water film has a higher temperature than the wet channel, which aligns with the fact that heat transfer between the wet and dry channels is mediated by the water film separating them.

Other test cases do not have these spatial data available. However, the data come from the 1D Pakari's model, not the experiment, so the comparison of these profiles is just our Python model (line) versus Pakari's model (dots). The continuous lines represent 1000 discretised points by our model and the dots do not correspond to the discretisation used by Pakari (100 points). These dots just represent the shape of the resulting profiles and are used to clearly distinguish between both models. The dry channel has a red colour, the wet channel has a blue colour, and the water film is green. The temperatures and specific humidity profiles correspond to the visualisations in the psychrometric chart (Fig. 10) and in the Mollier chart (Fig. 11).

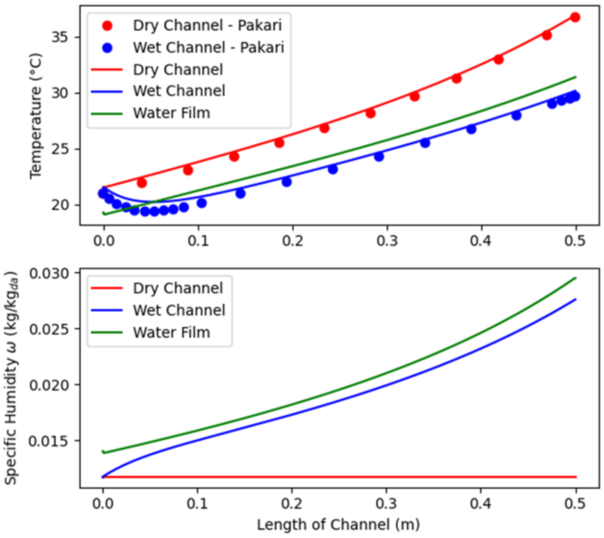

Fig. 9. Temperature and specific humidity profiles for the dry and wet channel and water film: Python model (lines) vs. Pakari's model (dots).

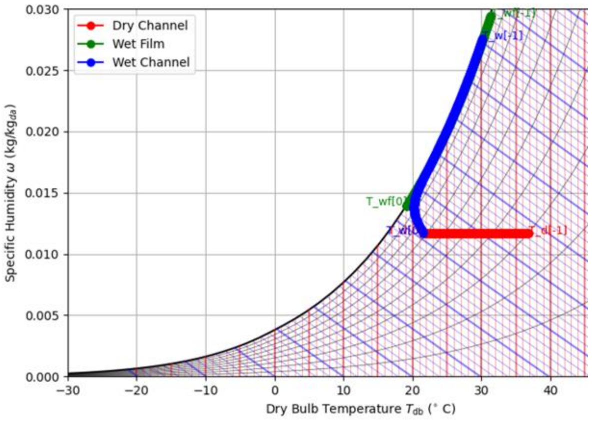

Fig. 10. Visualisation in the psychrometric chart.

During the development and testing of the model, it was found that the model is very sensitive to values of heat and mass transfer coefficient, so for each simulation, the values of these coefficients were carefully checked. The current model provides a steady solution with constant heat and mass transfer coefficients. Below are listed values for test case 9:

- h_m = 0.0224 m/s – mass transfer,
- h_w = 26.38 W/(m^2 K) – wet channel heat transfer coef.,
- h_d = 30.69 W/(m^2 K) – dry channel heat transfer coef.,
- U = 28.42 W/(m^2 K) – dry/water film heat transfer coef.

These are fundamental parameters characterising HMX and it is important to correctly calculate their values, because the model is very sensitive to them. An illustrative calculation of U by Eq. (7) for test case 9 is provided below:

$$U = 1/(1/30.69+0.0002/0.125+0.00015/0.15) = 28.42\ \mathrm{W/(m^2\,K)},$$

$$U \approx 1/(0.0326+0.0016+0.001).$$

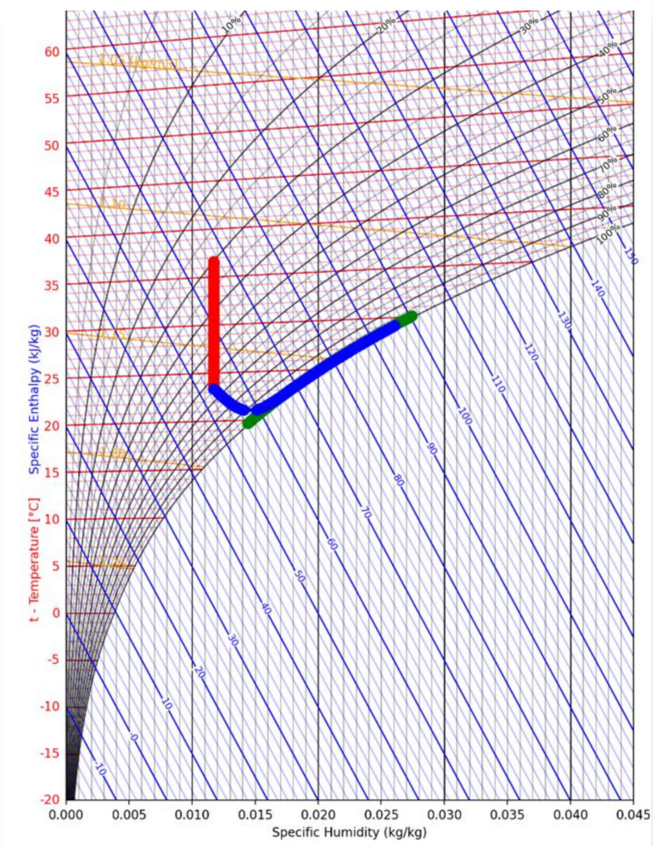

Fig.11. Visualisation in the Mollier chart.

The overall heat transfer coefficient U is given by the reciprocal of the sum of individual thermal resistances (m² K/W): convection in the dry channel $1/h_d$ = 0.0326, wicked paper δ_{pa}/k_{pa} = 0.0016 and plastic plate δ_{pl}/k_{pl} = 0.001. The last two resistances are constant and negligible; thus, the convection term is essential to adjust the M-cycle model. Another important parameter influencing the M-cycle effectiveness, apart from the inlet air temperature and humidity, is the mass flow rate in the dry and wet channels—particularly the ratio between them. This ratio is determined by the mass flow of the produced air at the dry channel outlet, which is subsequently used for cooling.

4. Conclusions

In the paper, the issues of sustainable AC were discussed related to population growth and ongoing climate change. The promising cooling technology from this point of view could be evaporative cooling. EC, particularly in dry climates, provide a promising alternative to VCC by achieving the cooling close to the wet-bulb temperature or even below by the M-cycle. We aimed our research to find new concepts of EC by implementing innovative materials, structures and ideas considering also literature sources mentioned in the introduction.

The main part of the paper was devoted to the introduction of the Python-based 1D model for the basic analysis of the M-cycle, which has been developed in the frame of the project MEBioSys. It is a Python-based computational tool for calculating heat and mass transfer in M-cycles and related psychrometric calculations, which are powered by the CoolProp library. It uses a spatially discretised differential equation solver and psychrometric chart (including the Mollier chart). Currently, the solver is just steady-state, and the unsteady solver is still under development. For the initial verification of the 1D model with a steady-state solver, the data from Pakari's study were used as a reference. Simulations of 15 test cases were performed. Our 1D model provides reasonable results and accurately fits Pakari's 1D model and his experimental data, which means that the numerical scheme is valid and can be used and adjusted for our planned experimental investigations, which will be the next step.

Currently, the model is focused solely on IEC with the M-cycle. However, we plan to enhance and extend it based on new experimental data:

- At the AGH University (under the project supported by the program „Excellence initiative – research university") the first direct evaporation test case data were collected and evaluated (not presented in this study),
- At the BUT University (under the project MEBioSys) the physical model for indirect evaporation is under development and it is planned to conduct measurements on new designs of indirect evaporative cooling using HX or even HMX (M-cycle).

The new validation datasets will be measured in the climatic chamber at BUT to evaluate the EC system under a wide range of climatic conditions. The own experiments will have an advantage of avoiding some uncertainties in interpreting simulation or experimental data from the literature. These experimental tests will also aim to enhance evaporative cooling systems through the use of new materials and structures. Based on the collected data, it will then be possible to adjust the model for different configurations of the M-cycle or, more generally, DEC/IEC systems.

In the development of our custom-designed EC system, we primarily consider the use of rapid prototyping (3D printing) supported by this 1D model. This approach is in our opinion more time-efficient than conducting full 3D CFD simulations to explore new designs. After the selection of the proper design, it is reasonable to use advanced CFD simulations of multiphase flows to adjust the 3D printed model and make refinements to improve some technical details, which can be behind the distinction of a simple 1D model or even can be hard to identify by experiments.

It can be concluded that this paper presents a promising verification result of the developed Python-based 1D model suggesting a potential application in the advanced design of sustainable cooling technologies, primarily for air conditioning.

Acknowledgements

The research was supported by the project „Mechanical Engineering of Biological and Bio-inspired Systems", funded as project No. CZ.02.01.01/00/22_008/0004634 by Programme Johannes Amos Comenius, call Excellent Research. The research was also supported by the program „Excellence initiative – research university" for the AGH University.

References

[1] Worldometer. (2024). World Population by Year. https://www.worldometers.info/world-population/population-by-country/ [accessed 13 Dec. 2024].

[2] United Nations, Department of Economic and Social Affairs, Population Division. (2022). *World Population Prospects 2022: Demographic profiles – Global*. https://population.un.org/wpp/Graphs/DemographicProfiles/Line/900 [accessed 13 Dec. 2024].

[3] Copernicus Climate Change Service. (2024). *Temperature*. Copernicus Climate Change Service. https://climate.copernicus.eu/climate-indicators/temperature [accessed 13 Dec. 2024].

[4] IPCC (2018): Global Warming of 1.5°C. [Masson-Delmotte, V., Zhai, P., Pörtner, H.-O., Roberts, D., Skea, J., Shukla, P.R., Pirani, A., Moufouma-Okia, W., Péan, C., Pidcock, R., Connors, S., Matthews, J.B.R., Chen, Y., Zhou, X., Gomis, M.I., Lonnoy, E., Maycock, T., Tignor, M., & Waterfield, T. (eds.)]. *An IPCC Special Report on the impacts of global warming of 1.5°C above pre-industrial levels and related global greenhouse gas emission pathways, in the context of strengthening the global response to the threat of climate change, sustainable development, and efforts to eradicate poverty*. Cambridge University Press, Cambridge, UK and New York, USA, 616. doi: 10.1017/9781009157940. https://www.ipcc.ch/site/assets/uploads/sites/2/2018/12/SR15_FAQ_Low_Res.pdf [accessed 13 Dec. 2024].

[5] Copernicus Climate Change Service. (2024). *Copernicus: 2024 virtually certain to be the warmest year and first year above 1.5°C.* https://climate.copernicus.eu/copernicus-2024-virtually-certain-be-warmest-year-and-first-year-above-15degc [accessed 18 Dec. 2024].

[6] Eyring, V., Bony, S., Meehl, G.A., Senior, C.A., Stevens, B., Stouffer, R.J., & Taylor, K.E. (2016). Overview of the Coupled Model Intercomparison Project Phase 6 (CMIP6) experimental design and organization, *Geoscientific Model Development*, 9(5), 1937–1958, https://doi.org/10.5194/gmd-9-1937-2016. https://gmd.copernicus.org/articles/9/1937/2016/ [accessed 13 Dec. 2024].

[7] Pezzutto, S., Novelli, A., Zambito, A., Quaglini, G., Miraglio, P., Belleri, A., Bottecchia, L., Gantioler, S., Moser, D., Riviere, P., Etienne, A., Stabat, P., Berthou, T., Kranzl, L., Mascherbauer, P., Fallahnejad, M., Viegand, J., Jensen, C., Hummel, M., & Müller, A. (2022). *Cooling technologies overview and market shares. Part 1 of the study "Renewable cooling under the revised Renewable Energy Directive ENER/C1/2018-493*". (D. G. for European Commission, Ed.). Publications Office of the European Union. doi: 10.2833/799633

[8] ASA. (2024). *May – Blue Marble Next Generation. Visible Earth.* https://visibleearth.nasa.gov/images/74042/may-blue-marble-next-generation/74044l [accessed 13 Dec. 2024].

[9] Acma, B., & Özyakali, N. (2020). Correlation Analysis of European Socioeconomic and Waste Management Structure Pursuant To EU-27 Waste Data - 2018. *Theoretical and Applied Issues of Economics*, 191–204. doi: 10.17721/tppe.2020.41.7

[10] Duan, Z., Zhan, C., Zhang, X., Mustafa, M., Zhao, X., Alimohammadisagvand, B., & Hasan, A. (2012). Indirect evaporative cooling: Past, present and future potentials. *Renewable and Sustainable Energy Reviews*, 16(9), 6823–6850. doi: 10.1016/j.rser.2012.07.007

[11] Tariq, R., Caliskan, H., & Sheikh, N.A. (2023). Maisotsenko Cycle for Heat Recovery in Gas Turbines: A Fundamental Thermodynamic Assessment. *Global Challenges*, 7(11), 2300178. doi: 10.1002/gch2.202300178

[12] Gillan, L.E., Gillan, A.D., Kozlov, A., & Kalensky, D.C. (2011). An advanced evaporative condenser through the Maisotsenko cycle. *International Journal of Energy for a Clean Environment*, 12 (2-4), 251–258. doi: 10.1615/InterJEnerCleanEnv.2013006619

[13] Pakari, A., & Ghani, S. (2019). Comparison of 1D and 3D heat and mass transfer models of a counter flow dew point evaporative cooling system: Numerical and experimental study. *International Journal of Refrigeration*, 99, 114–125. doi: 10.1016/j.ijrefrig.2019.01.013

[14] Amer, O., Boukhanouf, R., & Ibrahim, H.G. (2015). A Review of Evaporative Cooling Technologies. *International Journal of Environmental Science and Development*, 6(2), 111–117. doi: 10.7763/ijesd.2015.V6.571

[15] Prieto, A., Knaack, U., Auer, T., & Klein, T. (2019). COOLFACADE: State-of-the-art review and evaluation of solar cooling technologies on their potential for façade integration. *Renewable and Sustainable Energy Reviews*, 101, 395–414. doi: 10.1016/j.rser.2018.11.015

[16] Mahmood, M.H., Sultan, M., Miyazaki, T., Koyama, S., & Maisotsenko, V.S. (2016). Overview of the Maisotsenko cycle – A way towards dew point evaporative cooling. *Renewable and Sustainable Energy Reviews*, 66, 537–555. doi: 10.1016/j.rser.2016.08.022

[17] Costelloe, B., & Finn, D. (2003). Indirect evaporative cooling potential in air–water systems in temperate climates. *Energy and Buildings*, 35(6), 573–591. doi: 10.1016/S0378-7788(02)00161-5

[18] Kapilan, N., Isloor, A.M., & Karinka, S. (2023). A comprehensive review on evaporative cooling systems. *Results in Engineering*, 18, 101059. doi: 10.1016/j.rineng.2023.101059

[19] Pescod, D. (1979). Heat exchanger for energy saving in an air-conditioning plant. *ASHRAE Transactions*, 85(2), 238 – 251.

[20] Jradi, M., & Riffat, S. (2014). Experimental and numerical investigation of a dew-point cooling system for thermal comfort in buildings. *Applied Energy*, 132, 524–535. doi: 10.1016/j.apenergy.2014.07.040

[21] Nawaz, K., Schmidt, S.J., & Jacobi, A.M. (2016). Adsorption and Desorption Isotherms Of Desiccants for Dehumidification Applications: Silica Aerogels and Silica Aerogel Coatings on Metal Foams. *15th International Refrigeration and Air Conditioning Conference at Purdue*, July 14–17, 2016. http://Docs.Lib.Purdue.Edu/Iracc/1600 [accessed 13 Dec. 2024].

[22] Mumtaz, M., Pamintuan, B.C., Fix, A.J., Braun, J.E., & Warsinger, D.M. (2023). Hybrid membrane dehumidification and dewpoint evaporative cooling for sustainable air conditioning. *Energy Conversion and Management*, 294. doi: 10.1016/j.enconman.2023.117547

[23] Fix, A.J., Braun, J.E., & Warsinger, D.M. (2024). A general effectiveness-NTU modeling framework for membrane dehumidification systems. *Applied Thermal Engineering*, 236, 121514. doi: 10.1016/j.applthermaleng.2023.121514

[24] Kumar, A., & Yadav, A. (2016). Experimental investigation of solar driven desiccant air conditioning system based on silica gel coated heat exchanger. *International Journal of Refrigeration*, 69. doi: 10.1016/j.ijrefrig.2016.05.008

[25] Liu, L., Zeng, T., Huang, H., Kubota, M., Kobayashi, N., He, Z., Li, J., Deng, L., Li, X., Feng, Y., & Yan, K. (2020). Numerical modelling and parametric study of an air-cooled desiccant coated cross-flow heat exchanger. *Applied Thermal Engineering*, 169, 114901. doi: 10.1016/j.applthermaleng.2020.114901

[26] Pan, Q.W., Xu, J., Wang, R.Z., & Ge, T.S. (2023). Analysis on desiccant coated heat exchangers based on a new performance parameter and thermodynamic model. *Applied Thermal Engineering*, 222, 119943. doi: 10.1016/j.applthermaleng.2022.119943

[27] Tu, Y.D., Wang, R.Z, Hua, L.J, Ge, T.S, & Cao, B.Y. (2017). Desiccant-coated water-sorbing heat exchanger: Weakly-coupled heat and mass transfer. *International Journal of Heat and Mass Transfer*, 113. doi: 10.1016/j.ijheatmasstransfer.2017.05.047

[28] Abdulateef, J.M., Sopian, K., Alghoul, M.A., & Sulaiman, M.Y. (2009). Review on solar-driven ejector refrigeration technologies. *Renewable and Sustainable Energy Reviews*, 13(6–7), 1338–1349. doi: 10.1016/j.rser.2008.08.012

[29] Ge T.S., Dai, Y.J., & Wang, R.Z. (2014). Review on solar powered rotary desiccant wheel cooling system. *Renewable and Sustainable Energy Reviews*, 39, 476–497. doi: 10.1016/j.rser.2014.07.121

[30] Pacak, A., & Worek, W. (2021). Review of Dew Point vaporative Cooling Technology for Air Conditioning Applications. *Applied Sciences*, 11(3). doi: 10.3390/app11030934

[31] Pandelidis, D., & Anisimov, S. (2016). *Mathematical Modeling of the M-Cycle Heat and Mass Exchanger Used in Air Conditioning Systems*. Ph.D. Thesis, Wrocław University of Science and Technology, Wrocław, Poland.

[32] Yan, M., He, S., Gao, M., Xu, M., Miao, J., Huang, X., & Hooman, K. (2021). Comparative study on the cooling performance of evaporative cooling systems using seawater and freshwater. *International Journal of Refrigeration*, 121, 23–32. doi: 10.1016/j.ijrefrig.2020.10.003

[33] McDonald, K., & Sun, D.W. (2000). Vacuum cooling technology for the food processing industry: a review. *Journal of Food Engineering*, 45(2), 55–65. doi: 10.1016/S0260-8774(00)00041-8

[34] Lim, H., Choi, S., Cho, Y., Kim, S., & Kim, M. (2020). Comparative thermodynamic analysis of membrane-based vacuum air dehumidification systems. *Applied Thermal Engineering*, 179, 115676. doi: 10.1016/j.applthermaleng.2020.115676

[35] Yan, W., Yang, C., Liu, Y., Zhang, Y., Liu, Y., Cui, X., Meng, X., & Jin, L. (2024). A design optimization framework for vacuum-assisted hollow fiber membrane integrated evaporative water coolers. *Renewable Energy*, 230, 120848. doi: 10.1016/j.renene.2024.120848

[36] Madejski, P., & Kuś, T. (2024). *Evaporative Cooling: Lab Manual.* Katedra Systemów Energetycznych i Urządzeń Ochrony Środowiska, AGH WIMiR (in Polish).

[37] Shi, W., Ma, X., Min, Y., & Yang, H. (2024). Feasibility Analysis of Indirect Evaporative Cooling System Assisted by Liquid Desiccant for Data Centers in Hot-Humid Regions. *Sustainability*, 16(5). doi: 10.3390/su16052011

[38] Gorshkov, V. (2013). *Systems based on Maisotsenko cycle: Coolerado coolers.* Bachelor's Thesis. Building services Engineering. December 2012. Mikkelin ammattikorkeakoulu. Mikkeli University of Applied Sciences.

[39] Robichaud, R. (2007). *Coolerado Cooler Helps to Save Cooling Energy and Dollars: New Cooling Technology Targets Peak Load Reduction*. Technical Report, National Renewable Energy Lab. (NREL), Golden, CO, United States. doi: 10.2172/908968

[40] Worek, W., Khinkis, M., Kalensky, D., & Maisotsenko, V. (2012). Integrated Desiccant–Indirect Evaporative Cooling System Utilizing the Maisotsenko Cycle. *Conference Proceeding. ASME 2012 Heat Transfer Summer Conference collocated with the ASME 2012 Fluids Engineering Division Summer Meeting and the ASME 2012 10th International Conference on Nanochannels, Microchannels, and Minichannels*, July 8–12, Rio Grande, Puerto Rico, USA. doi: 10.1115/HT2012-58039

[41] Pandelidis, D., Niemierka, E., Pacak, A., Jadwiszczak, P., Cichon, A., Drag, P., Worek, W., & Cetin, S. (2020). Performance study of a novel dew point evaporative cooler in the climate of central Europe using building simulation tools. *Building and Environment*, 181, 107101. doi: 10.1016/j.buildenv.2020.107101

[42] Inobeme, A., Adetunji, C., Maliki, M., Eziukwu, C., Ngonso, B., Akhor, S., Ogundolie, F., & Dauda, W. (2023). Evaporative coolers for the postharvest management of fruits and vegetables. In *Evaporative coolers for the postharvest management of fruits and vegetables* (pp. 287–291). Elsevier. doi: 10.1016/B978-0-323-89864-5.00023-0

[43] Rogdakis, E, & Tertipis, D. (2015). Maisotsenko cycle: technology overview and energy-saving potential in cooling systems. *Energy and Emission Control Technologies*, 3, 15–22. doi: 10.2147/eect.S62995

[44] Xiao, X., & Liu, J. (2024). A state-of-art review of dew point evaporative cooling technology and integrated applications. *Renewable and Sustainable Energy Reviews*, 191, 114142. doi: 10.1016/j.rser.2023.114142

[45] Taler, J., Jagieła, B., & Jaremkiewicz, M. (2022). Overview of the M-Cycle Technology for Air Conditioning and Cooling Applications. *Energies*, 15(5). doi: 10.3390/en15051814

[46] Kang, H., Han, U., Lim, H., Lee, H., & Hwang, Y. (2021). Numerical investigation and design optimization of a novel polymer heat exchanger with ogive sinusoidal wavy tube. *International Journal of Heat and Mass Transfer,* 166, 120785. doi: 10.1016/j.ijheatmasstransfer.2020.120785

[47] Kaur, I., & Singh, P. (2021). Critical evaluation of additively manufactured metal lattices for viability in advanced heat exchangers. *International Journal of Heat and Mass Transfer,* 168, 120858. doi: 10.1016/j.ijheatmasstransfer.2020.120858

[48] Ma, X., Shi, W., Lu, L., & Yang, H. (2024). Performance assessment and optimization of water spray strategy for indirect evaporative cooler based on artificial neural network modeling and genetic algorithm. *Applied Energy*, 368, 123438. doi: 10.1016/j.apenergy.2024.123438

[49] Ma, X., Shi, W., & Yang, H. (2022). Study on water spraying distribution to improve the energy recovery performance of indirect evaporative coolers with nozzle arrangement optimization. *Applied Energy*, 318. doi: 10.1016/j.apenergy.2022.119212

[50] Wen, T., & Lu, L. (2019). Numerical and experimental study on internally cooled liquid desiccant dehumidification concerning film shrinkage shape and vapor condensation. *International Journal of Thermal Sciences*, 136, 316–327. doi: 10.1016/j.ijthermalsci.2018.10.046

[51] Zhou, B., Lv, J., Zhu, M., Wang, L., Li, S., & Hu, E. (2024). Experiment for the performance of a thin membrane inclined automatic wicking dew-point evaporative cooling device based on simulation results. *Energy and Buildings*, 308, 114021. doi: 10.1016/j.enbuild.2024.114021

[52] Press, W.H., Teukolsky, S.A., Vetterling, W.T., & Flannery, B.P. (2007). *Numerical Recipes: The Art of Scientific Computing* (3rd ed.). Cambridge University Press. New York, USA

Co-published by
Institute of Fluid-Flow Machinery
Polish Academy of Sciences
Committee on Thermodynamics and Combustion
Polish Academy of Sciences

http://www.imp.gda.pl/archives-of-thermodynamics/

ARCHIVES OF THERMODYNAMICS

Increasing the Efficiency of a Vapour Compression Refrigerating Machine through Adiabatic Air Cooling

Serhii Molskyi[a*], Oleksandr Molskyi[b], Anna Vorontsova[c]

[a]Public Union "Refrigeration Association of Ukraine", Druzhkivska St., 10, 03113, Kyiv, Ukraine
[b]State Biotechnological University, Alchevskikh St., 44, 61000, Kharkiv, Ukraine
[c]Anatolii Pidhornyi Institute of Power Machines and Systems, National Academy of Sciences of Ukraine, Komunalnykiv St., 2/10, 61046, Kharkiv, Ukraine
*Corresponding author email: molskyi@ipmach.kharkov.ua

Received: 20.02.2025; revised: 30.04.2025; accepted: 27.05.2025

Abstract

The issue of reducing energy consumption and the negative impact on the environment caused by vapour-compression refrigerating machines through the use of adiabatic air cooling technologies is considered in the paper. The climatic features of the use of adiabatic air cooling are determined using the example of four cities of Ukraine (Lviv, Kyiv, Kharkiv, Odesa). It is shown that the maximum cooling effect is observed in Kharkiv, although in terms of maximum temperatures and the duration of the warm period, this city is 6.3% inferior to Odesa. However, due to low relative humidity, the cooling efficiency was 5.4% higher. To conduct a comparative study of the effectiveness of the use of adiabatic technologies, field tests were conducted on two identical refrigerating units working under the same operating conditions, one of which was additionally equipped with an evaporative cooling system. A monitoring system, which was installed on both the original and the modernized refrigerating units, was developed to collect, accumulate and pre-process experimental data. It was determined that when using adiabatic technologies, the mass flow rate of the refrigerant is reduced compared to the original vapour-compression machine while ensuring the same cooling capacity, which in turn leads to a decrease in the load on the compressor. In turn, this leads to a decrease in the rotation frequency of the compressor electric motor, which resulted in a decrease in energy consumption by 25–28 % for the considered type of refrigerating units.

Keywords: Efficiency; Adiabatic cooling; Evaporative air cooling technologies; Air pre-cooling

Vol. 46(2025), No. 2, 123–132; doi: 10.24425/ather.2025.154195

Cite this manuscript as: Molskyi, S., Molskyi, O., & Vorontsova, A. (2025). Increasing the Efficiency of a Vapour Compression Refrigerating Machine through Adiabatic Air Cooling, *Archives of Thermodynamics*, 46(2), 123–132.

1. Introduction

The main problem the developers of refrigerating equipment have faced since the time when the first refrigerating machines were used, namely, achieving maximum refrigerating capacity with minimal energy consumption, is still relevant today [1,2].

It is relevant primarily from an environmental point of view, because the consumption of electrical energy by a refrigeration machine directly affects the ecological state of the environment. After all, electricity production at thermal power plants leads to constant CO_2 emissions [3–7].

It should also be taken into account that operated refrigerating machines loose cooling capacity over time for a number of reasons. These reasons include changes in operating modes, which have increased the heat load; increased maximum temperatures due to changing climatic conditions; retrofit (replacement) of the refrigerant due to environmental requirements; equipment ageing. Thus, the search for ways to increase the cooling capacity, reduce energy consumption and negative impact on the environment by refrigerating machines remains a pressing problem in the world.

Analysis of literature sources [8,9] showed that there are the

Nomenclature

c_p – specific isobaric heat capacity, kJ/(kg·K)
d – absolute humidity, kg/kg$_{\text{dry air}}$
G – mass flow rate, kg/s
I – specific enthalpy, kJ/kg
kF – heat transfer rate in the evaporator and condenser, W/K
m_{ref} – mass flow rate of refrigerant, kg/s
n_{h} – number of hours/year in the temperature range
t – temperature, °C
t_{in} – air temperature in front of the evaporative surface, °C
v – specific volume of vapour at the compressor suction, m^3/kg
V_{comp} – compressor volumetric flow, m^3/s

Greek symbols

$\bar{\eta}_{\text{ev}}$ – coefficient of thermal efficiency of the evaporator
$\bar{\eta}_{\text{cond}}$ – coefficient of thermal efficiency of the condenser
λ_{comp} – compressor delivery coefficient
ξ – moisture loss coefficient
$\bar{\pi}$ – compression ratio in the compressor
φ – average relative humidity, %

Subscripts and Superscripts

cond – condensation
cool – coolant from the evaporator side of the refrigeration system
ev – evaporation
ref – refrigerant

Abbreviations and Acronyms

COP – coefficient of performance
RU – refrigerating units
TRV – temperature-regulating valve

following ways to increase the cooling capacity of a refrigerating machine:

- increasing the speed of the compressor motor shaft using a frequency converter,
- reducing temperature drops of condensers and evaporators,
- reducing pressure losses in pipelines and fittings on the refrigerant discharge and suction lines,
- optimizing the processes within the refrigerating system (increasing the coefficient of operating time of the refrigerating machine and reducing thermal loads on the refrigerating system),
- additional subcooling of the liquid refrigerant at the inlet to the temperature-regulating valve (TRV).

These methods are thoroughly reviewed in the literature [8,9] and are widely used in practice.

But there is another, less common way to improve the performance of vapour compression refrigeration machines. This is to reduce the air temperature at the condenser inlet through evaporative pre-cooling.

Many literature sources are devoted to evaporative cooling as an alternative to mechanical refrigeration cooling for air conditioning depending on the climatic conditions and thermal load characteristics of the building [10]. Direct and indirect evaporative coolers are widely used in many arid regions of the world, such as the south-western United States, Australia, Western Asia and north-western China [10].

In [11], a simplified mathematical model was developed to describe heat and mass transfer between air and water in a direct evaporation cooler. The predicted results show the adequacy of the simple mathematical model for the design of a direct evaporative cooler, and that a direct evaporative cooler with a high-performance material can be well applied for air conditioning systems.

Direct evaporative cooling can significantly reduce air temperature, which is theoretically limited by the wet bulb temperature. The wet bulb temperature is the temperature that moist air has when it reaches saturation and the air enthalpy remains constant, that is, it is the limiting temperature of adiabatic cooling.

For evaporative air cooling, panels with various water-wettable materials have been developed for adiabatic systems. The paper [12] describes the influence of panel design on saturation efficiency and plant operation. These coolers can also be used as stand-alone units to cool room air to wet bulb temperature. In [12], it is not proposed to use these devices as an air pre-cooling system.

In [13], a numerical and experimental study of a new indirect evaporative cooling system is proposed. The air in this scheme is cooled to a temperature limited by the dew point temperature. This temperature is lower than the wet bulb temperature. Unsaturated moist air can be cooled to the dew point temperature while maintaining constant moisture content. At the same time, the moist air becomes saturated.

There are very few papers in the current literature devoted to the use of evaporative cooling as a pre-cooling system for air before refrigeration machines.

In [14], the operation of a pre-cooling system, which ensures a reduction in energy consumption by chillers, is considered. The system was installed in the climatic conditions of Kuwait. It is shown that the use of the adiabatic pre-cooling system for existing air conditioning leads to a significant reduction in compressor operating hours and service time, which, in turn, significantly reduces the peak power consumption of the load.

In [15,16], it is shown that when using thermodynamic analysis and thermoeconomic optimization to design operating parameters of air-to-air air conditioners, it is necessary to take into account the humidity of the ambient air. The thermoeconomic model of an air conditioner operating on a transcritical cycle with the refrigerant R744 (CO_2) has been improved in the paper. However, it is not proposed in the paper to humidify the air to increase the coefficient of performance (COP), but only to determine the effects of humidity on the plant efficiency.

In paper [17], to ensure thermal comfort indoors and energy saving in buildings, an integrated comfort control strategy, which combines the air conditioning, humidifier and ventilation system, taking into account the parameters of the environment, is proposed. The effectiveness of the proposed integrated comfort control is shown by comparing it with the indicators of traditional individual control tools. However, the air humidification proposed in the paper occurs in parallel with air conditioning and is not considered as a system of pre-cooling of air before the air conditioner.

In [18], a premise heating system using a transcritical CO_2 heat pump system with an R134a subcooling device was proposed, and the subcooling temperature was investigated theoretically and experimentally. However, although this method increases the efficiency of the heat pump, it requires the installation of an additional compressor, and therefore requires additional electricity consumption. In addition, the use of freon increases the negative impact on the environment.

A review of the literature [8–18] showed that there is not enough information on this topic. That is, either evaporative cooling is considered as an alternative for air conditioning systems [17], or adiabatic pre-cooling is considered for chillers operating in the climatic conditions of Kuwait [14]. The climate of Kuwait is exceptionally hot. It is subtropical and characterized by extremely high temperatures in the summer. Summer average maximum temperatures practically do not fall below +45°C, sometimes rising to +50°C…+55°C in the shade. Therefore, the feasibility of using an adiabatic cooling system there is determined by climatic conditions.

Therefore, the current task of this work is to clearly demonstrate the high efficiency and accessibility of adiabatic cooling technologies to improve the characteristics of industrial refrigeration systems with high cooling capacity in temperate climate zones. The accessibility of technologies implies not only the simplicity of design, installation and operation, but also the economic component, since it is associated with the cost of the adiabatic system itself, as well as the consumption of additional electricity for the operation of fans and pumps and irreversible water losses. The effect of air supercooling can be considered as a reduction in electricity consumption by the refrigeration machine, an increase in its efficiency with a rational balance of the number of operating times of the adiabatic system, taking into account investments and operational losses associated with its operation. It is clear that the appropriateness of using such systems is closely related to climatic conditions. The higher the psychometric temperature difference (the difference between air temperature and wet bulb temperature) over a longer period of the year, the more rational it seems to use adiabatic systems as pre-cooling before refrigeration machines.

Thus, the theoretical justification of increasing the efficiency of vapour-compression refrigeration machines using evaporative air pre-cooling technologies and experimental confirmation of the competitiveness of adiabatic technologies in the refrigeration industry through remote monitoring of these systems in the climatic conditions of Ukraine is an extremely urgent task

2. Evaporative cooling technologies and research methods

When calculating adiabatic cooling processes, the psychometric difference between the wet and dry bulb temperatures should be taken into account. This difference allows the use of a renewable energy resource – water – in the process of evaporative air cooling.

Air cooling can occur in various ways. The first one is direct evaporative single-stage cooling. In this case, heat is removed during the evaporation of water in the air stream, and the minimum theoretical air temperature is the wet bulb temperature. In process 1–2, the temperature during adiabatic cooling decreases, and the moisture content increases, while the enthalpy remains unchanged (Fig. 1), because this thermodynamic process is not accompanied by the removal of heat from the air.

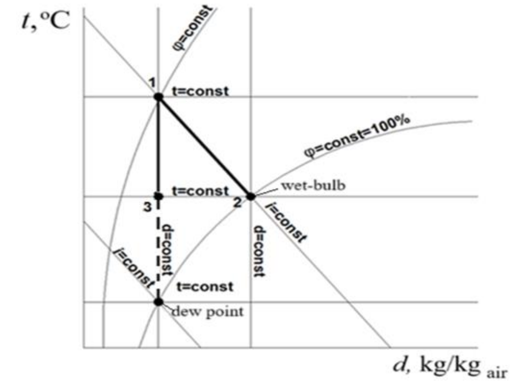

Fig. 1. Psychrometric diagram of air: 1–2 – adiabatic air cooling;
1–3 – cooling in an indirect evaporative heat exchanger.

The second one is indirect evaporative single-stage cooling. In this case, the air is cooled through the wall of the heat exchanger by a flow of coolant, which is cooled by the evaporation of water. The most accessible coolants in this case are water cooled by partial evaporation and air cooled during the evaporation of water. The minimum theoretical air temperature is the wet bulb temperature of the refrigerant circuit. During the process of temperature reduction in indirect evaporative cooling 1–3, the enthalpy decreases, and the moisture content remains unchanged (Fig. 1). The third one is evaporative two-stage cooling, which is a symbiosis of the first two methods (Fig. 2). Indirect cooling is used in the first stage, and evaporative cooling – in the second one. This method allows obtaining temperatures below the wet bulb temperature and close to the dew point temperature. In the process of lowering the temperature in two-stage cooling, the enthalpy decreases and the moisture content increases. Such systems are often offered as an alternative to “artificial cold in air conditioning systems”.

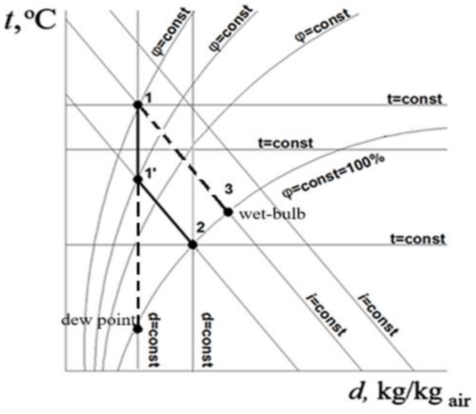

Fig. 2. Psychrometric diagram of air: 1–1' – indirect cooling
(first stage), 1'–2 – adiabatic cooling (second stage),
1–3 – adiabatic air cooling.

The parameters of moist air are determined using known equations [11].

The indicators of cooled air at the outlet of the heat exchanger (process (1–1’ in Fig. 2) are calculated according to well-known thermodynamic relations and criterion equations of heat transfer, relative humidity and air velocity. As a calculation results, temperature, relative humidity, water consumption for evaporation, cooling capacity, additional and final air moisture content are obtained.

There is not only theoretical evidence of the effect of adiabatic pre-cooling of air before the condenser, but also long-term observation of the operation of operating systems offered in the paper. Namely, remote monitoring of the efficiency of using adiabatic technologies in an industrial refrigerating unit was used in comparison with a similar machine in which humidification was absent.

It should be noted that during the study, it is also necessary to take into account such a fact as a decrease in the efficiency of evaporation systems due to a decrease in the temperature gradient with a decrease in temperature and an increase in the relative humidity of the ambient air. The weather and climatic dependence of the use of certain water evaporation systems requires careful analysis and consideration of the characteristics of a particular region. The decrease in the temperature of the wet bulb thermometer does not change so quickly, unlike the dry bulb one. Therefore, at moderate ambient temperatures, the efficiency of an air cooler may be better than that of an evaporative cooler. In this regard, methods of analysis and generalization of weather and climate data (namely, temperature and humidity of atmospheric air) to determine the climatic features of the use of adiabatic air cooling in different cities of Ukraine, which allowed to conduct a comparison of the use of technologies for reducing condensation temperatures and liquid supercooling, were also used in the paper.

3. Climatic features of the use of adiabatic air cooling

3.1. Analysis of climatic conditions in Ukraine

As noted, evaporative cooling of heat exchangers that release heat is most effective in the warm season.

But in different climatic conditions, depending on the temperature and relative humidity, the effectiveness of the evaporation technology will vary. In this regard, the calculation results of direct evaporative single-stage cooling to the wet bulb temperature in Lviv, Kyiv, Kharkiv and Odesa were analysed. A summary of the general climatic conditions and the calculated wet bulb temperature are shown for each city in Table 1.

Table 1. Evaporative cooling indicators for 4 cities of Ukraine.

t_{in}, °C	Lviv			Kyiv			Kharkiv			Odesa		
	φ, %	$t_{wet\ bulb}$, °C	n_h, h	φ, %	$t_{wet\ bulb}$, °C	n_h, h	φ, %	$t_{wet\ bulb}$, °C	n_h, h	φ, %	$t_{wet\ bulb}$, °C	n_h, h
34…36										19	18…19	12
32…34							24	18…19	36	23	18…19	38
30…32				29	18…19	36	29	18…19	120	32	18…20	136
28…30	38	18…20	36	40	19…20	147	33	17…18	243	37	18…20	252
26…28	41	17…19	171	43	18…19	276	36	16…18	327	43	17…19	364
24…26	50	17…19	288	49	17…18	432	44	16…18	378	52	17…19	372
22…24	54	16…18	411	54	16…18	537	49	15…17	462	58	17…18	504
20…22	62	15…17	501	63	15…17	588	55	14…16	564	65	16…18	677
18…20	70	15…16	618	68	15…17	693	61	14…15	633	67	14…16	606
Annual			2025			2709			2763	-		2949

3.2. Analysis of the use of single- and two-stage air cooling technology in different cities of Ukraine

The estimated air temperatures after direct single-stage cooling in multilayer evaporation panels based on aluminium foil and two-stage cooling devices in different cities of Ukraine depending on the temperature and relative humidity of the ambient air recorded by weather stations are shown in Fig. 3.

To calculate the cooling processes, a certified software from the manufacturer of evaporative panels OXYCOM (Netherlands) [19] was used. OXYCOM produces evaporative panels OXYVAP, which provide adiabatic cooling and humidification. The initial data for this software are the parameters of moist air and cooling methods.

Blue colour indicates the outdoor air temperature at the inlet to the evaporative surface in the range of +/−1°C. Orange colour indicates the average temperatures after single-stage cooling, and green colour indicates the average temperatures after two-stage cooling.

Using two-stage cooling compared to single-stage one for a specific type of evaporator increases the performance of evaporative cooling by 33%…36%.

3.3. The method of mathematical modelling to determine the operating parameters of a vapour-compression refrigeration machine

The method of mathematical modelling with lumped parameters to determine the operating parameters of a vapour-compression refrigerating machine is also used in the study. When modelling an object with lumped parameters, the mathematical model is a system of ordinary differential and algebraic equations. The method is simple in form, easily amenable to algorithmization, and takes into account the interrelation of many of its characteristics. The method for calculating the static characteristics of the

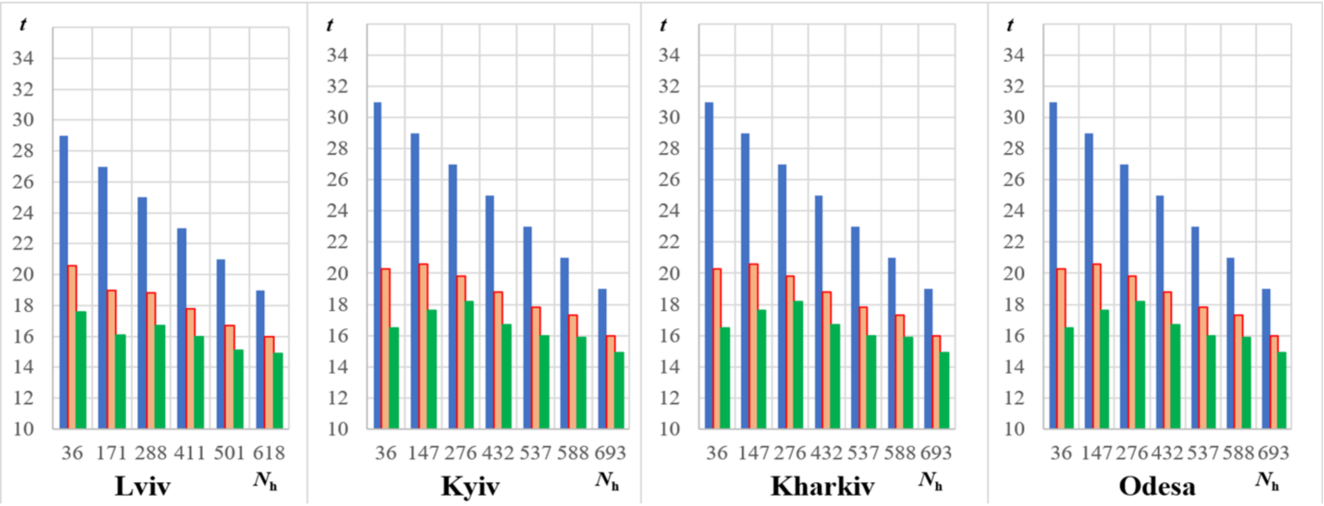

Fig. 3. Temperature performance of evaporative surfaces of direct single-stage and two-stage cooling in 4 cities of Ukraine.

operation of a refrigerating machine is based on modelling the refrigerant circulation circuit by constructing heat balance equations for the plant elements.

Fig. 4 shows a schematic diagram of a refrigeration machine with an air pre-cooling system, indicating the main points of the process. Point 1ref corresponds to the refrigerant parameters before the compressor, taking into account the refrigerant overheating by 5°C.

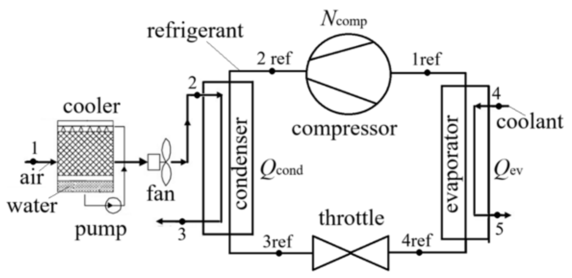

Fig. 4. Schematic diagram of a refrigeration machine with an air pre-cooling system.

The evaporator cooling capacity Q_{ev} and the condenser heating capacity Q_{cond} are determined by jointly solving the following equations:

$$Q_{ev} = m_{ref}[i_{1ref} + i_{4ref}] = G_{cool}c_{pcool}\xi\bar{\eta}_{ev}(t_4 - t_{ev}),$$

$$\bar{\eta}_{ev} = 1 - e^{-\frac{kF_{ev}}{G_{cool}c_{pcool}}};\ m_{ref} = \lambda_{comp}V_{comp}/v_{1ref},$$

$$Q_{cond} = m_{ref}[i_{2ref} + i_{3ref}] = G_2 c_{p2}\bar{\eta}_{cond}(t_{cond} - t_2),$$

$$\bar{\eta}_{cond} = 1 - e^{-\frac{kF_{cond}}{G_2 c_{p2}}},$$

where t_4, t_{ev} are the temperatures of the coolant at the evaporator inlet and the refrigerant evaporation temperature; t_2, t_{cond} are the temperatures of the moist air at the condenser inlet and the refrigerant condensation temperature.

The compressor delivery coefficient λ_{comp} can be determined by the empirical equation:

$$\lambda_{comp} = 1 - 0.05[\bar{\pi}^{0.869} - 1].$$

The vapour temperature at the compressor outlet t_{2ref} is defined as:

$$(t_{2ref} + 273.15) = (t_{1ref} + 273.15)\left[\frac{1}{\eta_{is}}\left(\bar{\pi}^{\frac{\kappa-1}{\kappa}} - 1\right) + 1\right],$$

where κ is the refrigerant adiabatic index; $\bar{\pi}$ is the compression ratio, which is defined as the ratio of the condensation pressure p_{cond} to the evaporation pressure p_{ev}; η_{is} is the compressor isentropic efficiency, which is found from equations [20]:

- at $\bar{\pi} \leq 4$

$$\eta_{is} = -0.0025153\bar{\pi}^4 + 0.0387299\bar{\pi}^3 - 0.2279675\bar{\pi}^2 + 0.5772372\bar{\pi} + 0.2758929,$$

- at $\bar{\pi} > 4$

$$\eta_{is} = -0.03\bar{\pi} + 0.892.$$

Compressor indicator power:

$$N_{comp} = m_{ref}\frac{[i_{2ref} + i_{1ref}]}{\eta_{is}}.$$

The compressor indicator power is the power consumed in the cylinder for compression and injection of vapour without taking into account the mechanical losses in the compressor and drive.

Compressor power consumption:

$$N_e = N_{comp}/\eta_e,$$

where η_e = 0.98 is the electromechanical efficiency of the compressor.

Cooling coefficient:

$$COP = \frac{Q_{ev}}{N_e}.$$

The presented method is implemented as a package of applied programs. Comparison of the results of numerical modelling with the data of air conditioner tests confirmed the efficiency of the method. The maximum discrepancy between the design and experimental values for such parameters as Q_{ev}, Q_{cond} and *COP* does not exceed 7.6%, which can be considered satisfactory for design developments.

The vapour-compression refrigeration machine MKH-80 manufactured in Ukraine, designed to produce a coolant (ice water) with a temperature of 1°C for use in technological lines of the food and chemical industries, was examined.

Freon R507 is used as the refrigerant, which circulates in the system in liquid and vapour states during machine operation.

The MKH-80 refrigeration machine has a semi-hermetic piston compressor "Frascold". The refrigeration capacity of the refrigeration machine is 80 kW, the current frequency is 50 Hz.

Hydraulic losses were not taken into account in the calculation. The thermal efficiency of the condenser was set at 60% and the evaporator at 50%. The superheat temperature of the freon is set to 2°C. At the inlet to the condenser, the temperatures of dry air and moist air were set for comparison under all the same conditions according to Table 1.

Refrigeration machine cycle calculated at $t_2 = 30°C$ and $t_2 = 20°C$ is shown in Fig. 5.

According to Table 1, the thermodynamic parameters of the refrigeration machine and the energy consumption for the compressor drive were calculated for two cities at a cooling capacity of 80 kW and a chilled water temperature at the evaporator outlet of 1°C.

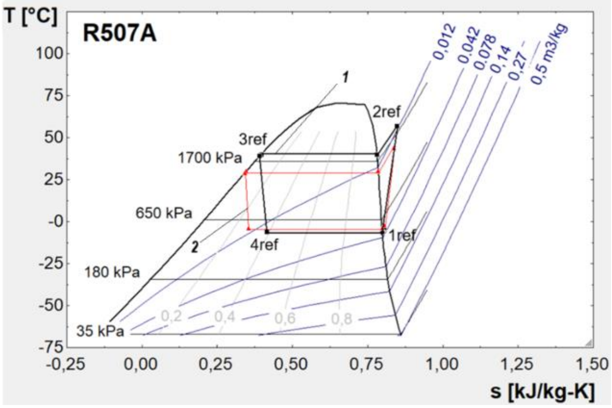

Fig. 5. Refrigeration machine cycle calculated at t_2 = 30°C (1) and t_2 = 20°C (2).

Table 2 shows summary data on temperatures and reduction in compressor power consumption ΔN_e, which was determined as its difference when dry and moist air was supplied to the condenser. Electricity savings $\Delta N_e \times n_h$ during periods n_h of high temperatures were also calculated.

Table 2. Summary data for two cities of Ukraine on temperatures and electricity savings of a refrigeration machine when feeding moist air to the condenser.

Lviv						Kharkiv					
t_2, °C	$t_{wet\ bulb}$, °C	n_h, h	t_2-$t_{wet\ bulb}$, °C	ΔN_e, kW	$\Delta N_e \times n_h$, kW·h	t_2, °C	$t_{wet\ bulb}$, °C	n_h, h	t_2-$t_{wet\ bulb}$, °C	ΔN_e, kW	$\Delta N_e \times n_h$, kW·h
						34	19	36	15	13.35	480.60
						32	19	120	13	11.21	1345.20
30	20	36	10	8.45	304.20	30	18	243	12	9.92	2410.56
28	19	171	9	7.33	1253.43	28	18	327	10	8.06	2635.62
26	19	288	7	8.26	2378.88	26	18	378	8	9.00	3402.00
24	18	411	6	4.6	1890.60	24	17	462	7	5.31	2453.22
22	17	501	5	3.71	1858.71	22	16	564	6	4.40	2481.60
20	16	618	4	2.67	1650.06	20	15	633	5	3.56	2253.48
Annual		**2025**			**9335.88**			**2763**			**17462.28**

It can be seen that the use of evaporative pre-cooling of air at the condenser inlet is 46% more effective for the climatic conditions of Kharkiv than for Lviv. By analogy with Table 2, the ΔN_e values for Odesa and Kyiv were also calculated.

Table 3 shows the total electricity savings $\Sigma \Delta N_e \times n_h$ and average electricity savings per hour $\Sigma \Delta N_e \times n_h / \Sigma n_h$ for the entire period of high temperatures for each city.

Table 3. Total electricity savings for 4 cities of Ukraine.

City	Σn_h, h	$\Sigma \Delta N_e \times n_h$, kW·h	$\Sigma \Delta N_e \times n_h / \Sigma n_h$, kW·h per hour
Lviv	2025.00	9335.88	4.61
Kharkiv	2763.00	17462.28	6.32
Kyiv	2709.00	13315.65	4.92
Odesa	2949.00	15775.30	5.35

Table 3 shows that the largest average electricity savings per hour for the entire period of high temperatures is observed in Kharkiv – 6.32 kW·h per hour, and the smallest in Lviv – 4.61 kW·h per hour. Thus, the greatest potential for the use of evaporative adiabatic pre-cooling is in Kharkiv, where the average electricity savings per hour is 15.3% higher than in Odesa (5.35 kW·h per hour), where the highest ambient temperatures are observed, but the relative humidity is higher.

There is not only theoretical evidence of the effect of adiabatic pre-cooling of air before the condenser, but also long-term observation of the operation of operating systems offered in the paper. Namely, remote monitoring of the efficiency of using adiabatic technologies in an industrial refrigerating unit was used in comparison with a similar machine in which humidification was absent.

4. Remote monitoring of the effectiveness of using adiabatic technologies

For 5 years, the company Astra LLC, Verkhniodniprovsk, has been producing, installing and investigating the operation of refrigerating machines with various adiabatic devices at cooling facilities. As a basic evaporative surface, multilayer surfaces based on the aluminium foil of the OXYVAP panel, products of the OXYCOM company, Netherlands [19,21], were used.

About 100 refrigerating machines with adiabatic devices were modular typical devices. The main consumer of cold is medium-temperature chambers of distribution centres in different regions of Ukraine. Thanks to the installed remote monitoring system, information on the effectiveness of the use of adiabatic technologies was collected.

4.1. Remote monitoring of the efficiency of using cooling air at the condenser inlet

One of the first studies (Kharkiv) was about the use of irrigation of evaporated panels OXYVAP to cool the air at the inlet to the condensers of refrigerating machines in order to reduce the energy consumption of compressors due to a decrease in the condensation temperature.

Two identical refrigerating units (RU1 and RU2), which are installed on the same site and operate with the same parameters per refrigerating chamber, were selected for the experiment (Fig. 6).

Water was supplied to the irrigated panels of the RU1 condenser from 11:20 to 15:00. No panels were installed on the RU2 condenser. The presence of panels creates additional aerodynamic resistance and reduces the volume of air passing through the condenser of the refrigeration unit. The condenser performance decrease was 28.9% (Table 4), and the calculated results using the equations in section 3.3 show a 32% condenser performance decrease.

Fig. 6. Air cooled condensers with adiabatic panels.

Table 4. Meter readings.

Meter	Start of measurement 11.20	End of measurement 15.00	Difference in indicators
Electricity RU1, kWh	20.9	83.6	62.7
Electricity RU2, kWh	29.4	117.6	88.2
Water consumption, m^3	237.173	237.745	0.572

Monitoring of equipment operation was carried out during the warm period – 154 days. Next, to demonstrate this technology, a time period of 3 hours and 40 minutes with stable high ambient temperatures (from 30°C to 32°C) was chosen.

During the experiment, the indicators of electricity meters (accuracy class 1.0), installed separately on each of the systems, and the water flow meter (accuracy class C) were monitored (Table 4).

The outdoor temperature, as well as ambient air temperature after the adiabatic surface, refrigerant condensation temperature of the refrigerating system and the temperature in the chamber were also recorded (Fig. 7). The accuracy of temperature sensor measurements is ± 0.1°C.

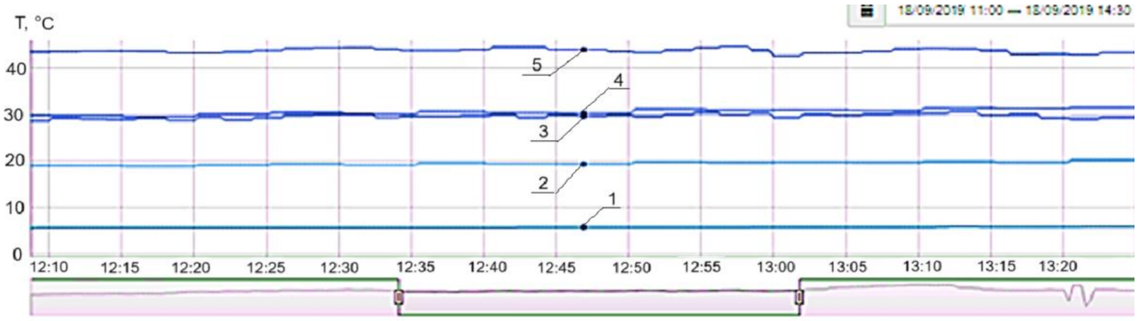

Fig. 7. Performance indicators of refrigerating units with and without adiabatic cooling of air at the condenser inlet: 1 – air temperature in the refrigerator compartment, 5.8°C, 2 – air temperature at the inlet to the RU1 condenser (after adiabatic panels), 19.4°C, 3 – RU1 condensation temperature, 29.7°C, 4 – ambient air temperature, 30.4°C, 5 – RU2 condensation temperature, 44.1°C.

Based on the results of the field experiment, the following conclusions can be drawn:

1. The water supplied to the irrigated panels evaporates and cools the air at the inlet to the condenser, which reduces the condensation temperature of the refrigerant. The graph (Fig. 7) shows that the condensation temperature of RU1 is 29.7°C, which is 14.4°C lower than the condensation temperature of the RU2 refrigerating unit and 0.8°C lower than the ambient dry bulb temperature.
2. The refrigerating system with adiabatic air cooling consumes less electricity due to the lower condensation temperature. Compressor of RU1 consumed 11.61 kW less energy than RU2 compressor during 3 hours 40 minutes of the experiment. The electricity savings were 26.58%.

3. The air temperature at the inlet to the RU1 condenser after the irrigated panel is 19.4°C. The air temperature at the inlet to the RU2 condenser corresponds to the ambient temperature of 30.4°C. The decrease in the air temperature at the inlet to the RU1 condenser occurred due to the energy of water evaporation. Water was also spent on washing the irrigated panels. The total consumption during the experiment was 572 litres in 3 hours 40 minutes.
4. The economic effect of resource conservation looks like this (2019):
   - cost of saved energy per hour: 6.87 UAH;
   - cost of water used: 1.9 UAH;
   - economic effect of resource saving per hour: 4.97 UAH;
   - probable maximum savings of up to 5571 UAH/year;
   - estimated payback period of the technology: up to 5 years.

The Euro to UAH exchange rate was: 1 Euro = 32.8267 UAH.

4.2. Remote monitoring of the efficiency of air cooling at the inlet to the subcooler

The following studies, which were conducted before the use of water evaporation systems to improve the operation of the refrigerating machine, were carried out using adiabatic panels at the air inlet to the liquid subcooler.

Two identical refrigerating systems with units RU3 and RU4, which are installed on the same site and operate with similar parameters per refrigerating chamber (Figs. 8 and 9), were also selected for the experiment.

On the RU4 system, an adiabatic liquid refrigerant subcooler was installed in front of the electronic superheat control valve (throttle) of the air cooler.

Fig. 8. Liquid subcooler with adiabatic panel.

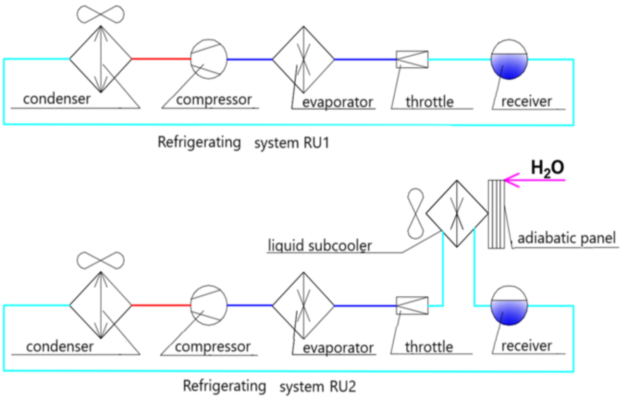

Fig. 9. Schematic diagrams of RU3 and RU4.

Remote computer monitoring data showed that at 10:22, when the water supply to the adiabatic subcooler was turned on, the operating parameters of the two systems began to differ significantly (Fig. 10).

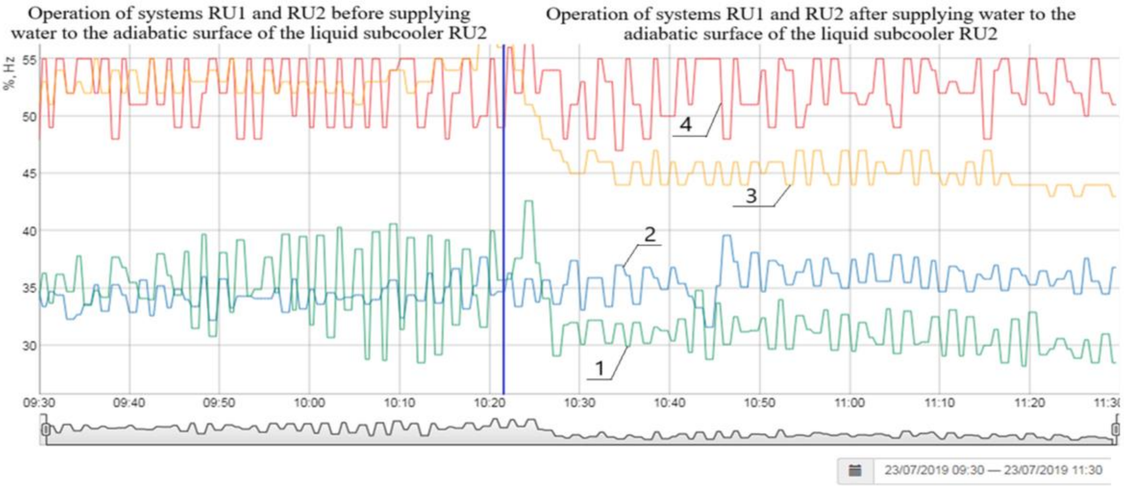

Fig. 10. Operation of refrigerating machines with and without liquid subcooling: 1 – RU2 compressor operating frequency, Hz; 2 – RU3 compressor operating frequency, Hz; 3 – opening of the RU4 system throttle; 4 – opening of the RU1 system throttle.

As a result, the liquid refrigerant in front of the throttle was subcooled from 35.7°C to 22.3°C, i.e. by 13.4°C. The ambient air temperature according to the dry bulb was 21°C, and the relative humidity was 64%.

The air temperature after the adiabatic panel was 17.1°C. The water consumption was 7.6 l/h.

To transfer the same amount of heat, a lower mass flow rate of supercooled refrigerant is required. When comparing the indicator "% valve opening", it can be seen that in the RU4 system, it is 15–20% lower than in the RU3 system.

Due to the decrease in the mass flow rate of the refrigerant, the load on the compressor decreases. Accordingly, the rotation frequency of the compressor electric motor decreases, which in turn leads to a decrease in the energy consumption of the RU4 system compressor also by 15–20% compared to the RU3 system.

5. Discussion of research results. Comparison of the operation of adiabatic systems

One of the performance indicators of evaporative cooling systems is water use. In the first experiment (Section 4.1), an adiabatic panel humidification system without recirculation was used. That is, water was supplied according to the algorithm proposed by the panel manufacturer, which took into account the periodicity of water supply depending on the temperature and humidity of the ambient air. With this method, water was not fully used in the evaporation process, but partially went into the sewer. Later, in order to reduce water consumption, the refrigerating units were equipped with a recirculation system, which allowed for a 30% reduction in water losses. But a significant factor in reducing water consumption was the transition to evaporative air cooling at the inlet to the liquid subcooler (Section 4.2). It was found that at high ambient air temperatures, the efficiency of evaporative air cooling at the inlet to the condenser is higher than while using an adiabatic subcooler. But as the temperature decreases, this difference decreases, so the choice can be made in favour of a system with a subcooler. At low air temperatures and high relative humidity, the use of an adiabatic subcooler can be more effective than the use of an adiabatic condenser.

Let's consider four options for operating a medium-temperature vapour-compression refrigerating machine at high ambient air temperatures (from 15°C to 35°C). Namely, with an air-cooled condenser, the same system with an additional air-cooled subcooler, and both systems with evaporative air cooling using adiabatic panels. The refrigerating capacity of the refrigerating machine, regardless of the operating mode and configuration, is maintained at the same level and is equal to 33.3 kW. When the air temperature at the inlet to the condenser and/or subcooler decreases, the system automatically maintains the specified refrigerating capacity through frequency control. As a result, the electric consumption of the compressor motor decreases. The lower the ambient temperature, the lower the water consumption of adiabatic systems.

Using the calculation algorithm [19], the operation of the refrigerating machine was simulated at different temperatures and humidity of the environment (Figs. 11 and 12).

This allowed us to draw the following conclusions:

- the highest energy consumption of the compressor of the machine with an air-cooled condenser without additional subcooling of the liquid refrigerant is at the inlet to the throttling element;
- the highest water consumption in the refrigerating machine with evaporative cooling of the air is at the inlet to the condenser;
- the most efficient during the period of maximum air temperatures of the warm period (minimum number of hours per year) is the use of the machine with evaporative cooling of the air at the inlet to the condenser;
- the efficiency is almost the same during the period of minimum air temperatures of the warm period (maximum number of hours per year) of the use of machines with evaporative cooling of the air at the inlet to the condenser and the subcooler;
- in third place in terms of energy efficiency in the warm period of the year is the machine with an additional subcooler of the air cooler liquid.

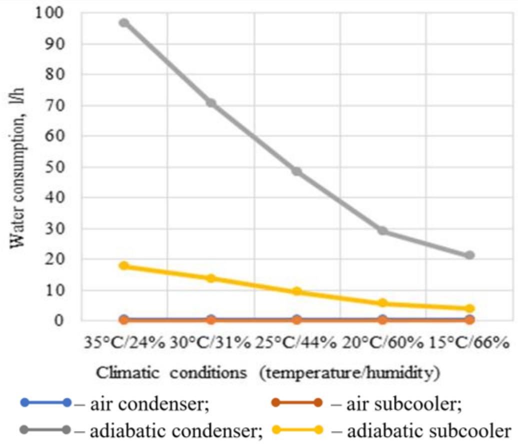

Fig. 11. Comparison of water consumption when using air condensers, liquid subcoolers and adiabatic condensers and subcoolers.

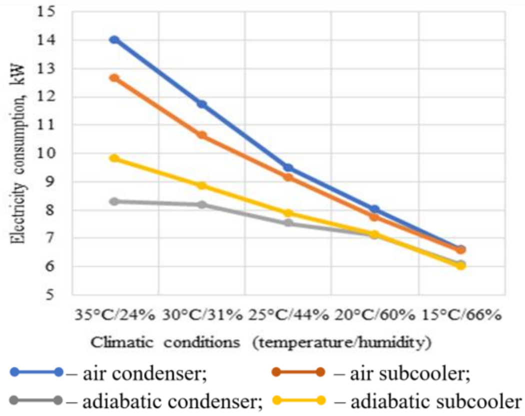

Fig. 12. Comparison of electricity when using air condensers, liquid subcoolers and adiabatic condensers and subcoolers.

Thus, water evaporation (adiabatic) systems use the enormous hidden potential of water evaporation. Increasing the performance of a refrigerating system using water evaporation is a kind of “free cooling”, that is obtaining additional cooling without using energy-intensive “machine cooling”. With the competent implementation of liquid refrigerant subcooling systems, it is possible to reduce annual electricity consumption by more than 20%.

6. Conclusions

The climatic features of the use of adiabatic air cooling in the conditions of the temperate climate zone were determined using the example of four cities of Ukraine (Lviv, Kyiv, Kharkiv, Odesa). On the example of the characteristics of the vapour-compression refrigerating machine MKH-80 (80 kW) of Ukrainian production, the average electricity saving during the warm period due to the use of evaporative pre-cooling of air at the condenser inlet was calculated. The maximum effect of evaporative pre-cooling was observed in Kharkiv, where the reduction in electricity consumption was 6.32 kWh per hour, which is 15.3% higher than in Odesa (5.35 kWh per hour), where the highest ambient temperatures are observed, but the relative humidity is higher.

A field experiment was conducted using a remote monitoring system, which collected information on the efficiency of using adiabatic technologies. Two identical industrial refrigerating units were selected for observation, one of which was equipped with a cooling system. The refrigerating units were installed on the same site and operated with the same parameters for one refrigerating chamber. It was determined that when using adiabatic technologies, the mass flow rate of the refrigerant is reduced while ensuring the same cooling capacity, which in turn leads to a decrease in the load on the compressor. Accordingly, the speed of the compressor motor decreases, which in turn leads to a decrease in energy consumption by 15–20%.

The higher the outdoor temperatures, the lower the humidity, and the longer the warm period, the higher the effectiveness of this technology. Given global climate change leading to an increase in annual temperatures, water evaporation technologies have high prospects for wider application.

References

[1] Kuznetsov, M., Tarasova, V., & Kostikov, A. (2025). Techno-economic method for the rational choice of air source heat pumps for bivalent heating systems. In *Advanced in Mechanical and Power Engineering II. CAMPE 2023. Lecture Notes in Mechanical Engineering* (pp. 153–163). Springer, Cham. doi: 10.1007/978-3-031-82979-6_16

[2] Kharlampidi, D., Kuznetsov, M., Tarasova, V., & Voytenko, E. (2017). Thermodynamic analysis of air-compression refrigerating machine based on the exergy cost theory. *Eastern-European Journal of Enterprise Technologies*, 5(8), 30–38. doi: 10.15587/1729-4061.2017.112113

[3] Kharlampidi, D., Tarasova, V., Kuznetsov, M., & Omelichkin, S. (2016). Application of graphic apparatus of C-curves for the analysis and optimization of supercritical cycles of thermotransformers. *Eastern-European Journal of Enterprise Technologies*, 5(8), 20–25. doi: 10.15587/1729-4061.2016.79988

[4] Kuznetsov, M., Kharlampidi, D., Tarasova, V., & Voytenko, E. (2016). Thermoeconomic optimization of supercritical refrigeration system with the refrigerant R744 (CO_2). *Eastern-European Journal of Enterprise Technologies*, 6(8), 24–32. doi: 10.15587/1729-4061.2016.85397

[5] Sutandi, T., Margana, A.S., Sumeru, K., & Sukri, M.F. (2020). Experimental study of R32 as a retrofit for R410A refrigerant in a residential air conditioner. *Advances in Engineering Research*, 198, 167–170. doi: 10.2991/aer.k.201221.029

[6] Zhao, D., Zhao, R., Deng, S., Zhao, L., & Chen, M. (2020). Transcritical carbon dioxide power cycle for waste heat recovery: A roadmap analysis from ideal cycle to real cycle with case implementation. *Energy Conversion and Management*, 226, 113578. doi: 10.1016/j.enconman.2020.113578

[7] Sánchez, D., Aranguren, P., Casi, A., Llopis, R., Cabello, R., & Astrain, D. (2020). Experimental enhancement of a CO_2 transcritical refrigerating plant including thermoelectric subcooling. *International Journal of Refrigeration*, 120, 178–187. doi: 10.1016/j.ijrefrig.2020.08.031

[8] Estrada, A., Córdova-Castillo, L., & Piedra, S. (2024). Enhancing vapor compression refrigeration systems efficiency via two-phase length and superheat evaporator MIMO control. *Processes*, 12(8), 1600. doi: 10.3390/pr12081600

[9] Khatri, R., & Joshi, A. (2017). Energy performance comparison of inverter based variable refrigerant flow unitary AC with constant volume unitary AC. *Energy Procedia*, 109, 18–26. doi: 10.1016/j.egypro.2017.03.038

[10] Wu, J.M., Huang, X., & Zhang, H. (2009). Theoretical analysis on heat and mass transfer in a direct evaporative cooler. *Applied Thermal Engineering*, 29(5–6), 980–984. doi: 10.1016/j.applthermaleng.2008.05.016

[11] Fouda, A., & Melikyan, Z. (2011). A simplified model for analysis of heat and mass transfer in a direct evaporative cooler. *Applied Thermal Engineering*, 31(5), 932–936. doi: 10.1016/j.applthermaleng.2010.11.016

[12] *Adiabatic fluid coolers & refrigerant condensers: Impact of pad system design on saturation efficiency and unit operation*. http://www.evapco.com/sites/evapco.com/files/2019-02/Adiabatic-Pad-Saturation-White-Paper-11.2018.pdf [accessed 28 Apr. 2025].

[13] Riangvilaikul, B., & Kumar, S. (2010). Numerical study of a novel dew point evaporative cooling system. *Energy and Buildings*, 42(11), 2241–2250. doi: 10.1016/j.enbuild.2010.07.020

[14] Bilal, S.A., & Alansari, A.A. (2021). Efficiency and energy savings provided by adiabatic pre-cooling system. *International Journal of Scientific & Technology Research*, 10(4), 86–90.

[15] Kuznetsov, M.O., Kharlampidi, D.Kh., & Tarasova, V.O. (2017). Influence of air humidity on the thermoeconomic indicators of air conditioners. *Modern Problems of Refrigeration Engineering and Technology Conference*, 21−22 September, Odesa, Ukraine. URL: https://card-file.ontu.edu.ua/handle/123456789/8571 (in Ukrainian).

[16] Kuznetsov, M.O., Tarasova, V.O., & Kostikov, A.O. (2022). Influence of airflow humidity on the optimal characteristics of air conditioners operating on a transcritical CO_2 cycle. *XI Annual Scientific Conference "Scientific Results 2022"*, 20 December, Kharkiv, Ukraine (in Ukrainian).

[17] Kim, J.W., Yang, W., & Moon, H.-J. (2017). An integrated comfort control with cooling, ventilation, and humidification systems for thermal comfort and low energy consumption. *Science and Technology for the Built Environment*, 23(2), 264–276. doi: 10.1080/23744731.2016.1258294

[18] Song, Y., & Cao, F. (2018). The evaluation of the optimal medium temperature in a space heating used transcritical air-source CO_2 heat pump with an R134a subcooling device. *Energy Conversion and Management*. 166, 409–423. doi: 10.1016/j.enconman.2018.04.052.

[19] *All there is to know about evaporative cooling (adiabatic cooling)*. https://www.oxy-com.com/evaporative-cooling [accessed 28 Apr. 2025].

[20] Matsevityy, Yu.M., Bratuta, E.G., Kharlampidi, D.Kh., & Tarasova, V.A. (2014). *System-structural analysis of steam compressor thermotransformers*. IPMach of NASU. URL: https://repository.kpi.kharkov.ua/handle/KhPI-Press/18163 (in Russian).

[21] Antonius, J., & Reinders, M. (2005). Heat exchange element, WO Patent 2005019739 A1, Mar. 3.

Co-published by
Institute of Fluid-Flow Machinery
Polish Academy of Sciences
Committee on Thermodynamics and Combustion
Polish Academy of Sciences

http://www.imp.gda.pl/archives-of-thermodynamics/

ARCHIVES OF THERMODYNAMICS

Integrated model of a biomass boiler coupled with a Stirling engine

Javier Uche[a*], Sergio Usón[b], Juan Anat Gómez[c]

[a] ENERGAIA Institute and Department of Mechanical Engineering, University of Zaragoza. Mariano Esquillor 15, 50018 Zaragoza, Spain
[b] ENERGAIA Institute and Department of Mechanical Engineering, University of Zaragoza. Maria de Luna 5, 50018 Zaragoza, Spain
[c] ENERGAIA Institute, University of Zaragoza. Mariano Esquillor 15, 50018 Zaragoza, Spain
*Corresponding author email: javiuche@unizar.es

Received: date here; revised: date here; accepted: date here

Abstract

Integration of a Stirling engine in a biomass boiler can be an interesting renewable alternative for the supply of heat and electricity in isolated homes located in areas where local biomass is available and during months when sunlight is low. Since this integration requires a careful coupling of the engine and boiler, an integrated model of these two devices is a relevant issue. In this case, a modular integrated model of a 25 kW_{th} biomass pellet boiler, fire-tube with a cylindrical water jacket, coupled to a 1 kW_e free piston Stirling engine is presented. To model the boiler, and take into account the location of the Stirling head, the zonal method was chosen, which allows estimating this temperature from an additional set of surrounding temperatures. For the Stirling engin, a model widely used to evaluate those engines was used. Various software tools have been used to integrate the model sequentially. The integrated model predicts the thermal and electrical production based on different operation parameters, such as the boiler load in 5% fractions of its load from 50 to 100%. The obtained results, which will be validated with the experimental setup, show a maximum output of approximately 600 W for the engine and a decreasing temperature profile in the combustion chamber, as a function of the partial load.

Keywords: Biomass boiler; Stirling engine; Integrated systems; Energy modelling; Cogeneration

Vol. 46(2025), No. 2, 133–141; doi: 10.24425/ather.2025.154912

Cite this manuscript as: Uche,’ J., Usón, S., & Gómez, J.A. (2025). Integrated model of a biomass boiler coupled with an Stirling engine. *Archives of Thermodynamics*, 46(2), 133–141.

1. Introduction

In the field of combined heat and power generation in the form of cogeneration, integrating a domestic biomass boiler (BB) with a Stirling engine (SE) allows for the provision of both demands [1,2]. It may be enough to meet the needs of a household, especially in isolated areas where biomass is available in certain abundance and where, in many cases, the power grid supply may be distant. Unfortunately, the high investment costs of Stirling technology make it scarcely competitive compared to other technologies, such as photovoltaics (PV). Still, it can be a cost-effective option in cold areas with low electricity demand and high heat demand for heating and domestic hot water. Alternatively, this technology may be the only feasible option in areas with low solar insolation and limited space availability for placing PV panels. Finally, the proposed scheme may complement solar energy by operating in winter when radiation is low.

The research focused on modelling and improving SE remains relevant [3] within a power range from 1 to 225 kW_e. Free piston type Stirling engine (FPSE), due to its simplicity in transmission, long operating life, low sound pollution and high efficiency, is usually selected as SE [4]. Anyway, it is very complex to design, and its start-up is also complex. Its performance has been studied in-depth for diverse typologies [5], and its efficie-

Nomenclature

a – weight coefficient (WSGG model)
A – area, m^2
c – coefficient associated to the k value (WSGG model)
c_p – specific heat, J/(kg·K)
d – hydraulic diameter, m
D – diameter of the combustion chamber, m
E – emissive power, W/m^2
f – frequency, Hz
f_r – friction coefficient
G – mass flow rate of the working fluid, kg/s
$\overline{\mathbf{gg}}$ – gas-gas DEA matrix
$\overline{\mathbf{GG}}$ – gas-gas TEA matrix
$\overrightarrow{\mathbf{G_i G_j}}$ – gas-gas DFA matrix
$\overrightarrow{\mathbf{G_i S_j}}$ – gas-surface DFA matrix
h – heat transfer coefficient, W/(m^2·K)
k – absorption coefficient of the WSGG model, m^{-1}
l – length, m
m – mass stored, kg
M – mass (in SE), kg
Nu – Nusselt number
P – pressure, Pa
Pr – Prandtl number
Q – heat rate, W
R – specific gas constant of helium (2078 J/kg·K)
$\overline{\mathbf{R}}$ – auxiliary matrix for TEA calculations
Re – Reynolds number
$\overline{\mathbf{sg}}$ – surface-gas DEA matrix
$\overline{\mathbf{SG}}$ – surface-gas TEA matrix
$\overline{\mathbf{ss}}$ – surface-surface DEA matrix
$\overline{\mathbf{SS}}$ – surface-surface TEA matrix
$\overrightarrow{\mathbf{S_i S_j}}$ – surface-surface DFA matrix
T – temperature, K
V – volume, m^3

Greek symbols

ε – emissivity, effectiveness
η – thermal efficiency
θ – crank angle, rad
λ – conductivity, W/(m·K)
μ – viscosity, Pa·s
ρ – reflectivity
σ – Stefan-Boltzmann constant, 5.67·10^{-8} W/(m^2·K^4)

Subscripts and Superscripts

c – compression
cb – combustion
cv – convection
e – expansion, electrical
j – zone
g – gases (in the combustion chamber)
h – exhaust gases (inside of water jacket), heater
i – zone, volume
j – zone, volume
k – cooler
n – grey gas number
p – internal wall
r – regenerator
rd – radiation
s – surface
th – thermal
w – water, wetted, wall

Abbreviations and Acronyms

BB – biomass boiler
µCHP– micro combined heat and power
DEA – direct exchange areas (matrix)
DFA – directed flux areas (matrix)
EES – Engineering Equation Solver
FPSE– free-piston Stirling engine
LHV – lower heating value
ORC – organic Rankine cycle
PL – part load operation
PV – photovoltaics
SE – Stirling engine
TEA – total exchange areas (matrix)
WSGG– weighted sum of grey gases (model)

ncy varied from 3% to 41% depending on the applied model. Hybrid SE-PV systems could considerably reduce CO_2 emissions by up to 69% compared with diesel generators [6]. A model of 3.9 kW$_e$ to be supplied by biomass or solar energy is presented in [7] and considered a renewable energy source. Using waste heat from SE to feed an Organic Rankine Cycle (ORC) in a cascade improves the SE performance by 63% to 66% [8]. In some cases, a program has been implemented that allows the design to be modified and the SE model to be selected to calculate its performance. However, it requires a lot of information [9]. Despite its limited commercialization and, therefore, confidentiality in the design, there are experiences of experimental validation for diverse but limited sizes. In [10], a 4.03 kW engine was optimized by combining the model and the performed tests. On the contrary, in [11], less than 1 W was tested in a small SE with also reduced efficiencies (6%). Typically, SE is powered by heat from fossil fuels. Integrated micro combined heat and power (µCHP) unit with an SE and a natural gas boiler has been studied in terms of modelling and experimentation [12], providing up to 1 kW$_e$ for domestic boilers. In [13], the overall efficiency of the µCHP unit was close to 100% based on the LHV by using an SE with N_2.

There is hardly any scientific literature on the subject of integration of a BB feeding a SE. The main works are those of Choque and Araoz [14] and Cardozo et al. [15]. Both papers analyse a 1 kW$_e$ SE coupled with a 20 or 30 kW BB. However, SE is a two-cylinder of a gamma type, and the heater is made of tubes, which is somewhat different than our SE. Damirchi et al. [16] tested diverse biomass and obtained 96 W by a small gamma type SE. Arashnia et al. [17] used the same gamma type SE but modified the previous simple BB, with similar results of low power obtained in the engine (< 100 W). This first research group has also carried out a validation with an integrated model of experiments of BB with SE [18,19]. In any case, the boiler model is able to estimate the performance but does not detail aspects of its design, which may affect a better capture of heat to obtain a maximum electrical production in the engine, as well as avoiding as far as possible the formation of ash deposits in its head.

Therefore, and after the humble analysis by the authors of the state-of-the-art integrated model of a BB with an SE, it has been found that there is no such model, at least with a similar level of detail in both pieces of equipment. An integrated, modular and flexible model that allows us to analyze the variations in certain design parameters of the biomass boiler, and to see how they affect the production and reliable operation of SE constitutes a novelty.

In this article, both BB and SE are modelled sequentially. First, the model of BB is used to obtain temperature values, particularly in the area where the heat receiver is located, which in turn is used by the SE model to estimate the expected performance of the engine. Accordingly, the integrated model aims to estimate the expected production of heat and electricity from both units, which will later be tested in an already-constructed experimental facility.

2. Materials and methods

The modelled BB is a commercial unit of 25 kW_{th} with a somewhat particular configuration (BioCurve BCH25). It is a fire tube, with the combustion gases from the combustion chamber circulating inside the tubes within a cylindrical water jacket. This boiler has the advantage of condensing water vapour of flue gases, which increases its efficiency, and has a system for cleaning the gas circuit with water.

As for SE, the approximate model basis is a 1 kW_e Free-Piston Stirling Engine (FPSE), whose working fluid is helium (Microgen/MEC, biomass Stirling converter). Its approximate operating range is for temperatures of its heat source around 180–550ºC. Figure 1 shows the diagram of the experimental facility supporting the developed models. It should be noted that, in order to increase the efficiency of SE, it has an independent cooling system. Different software tools have been used for the model, taking advantage of each of their capabilities to make it more flexible.

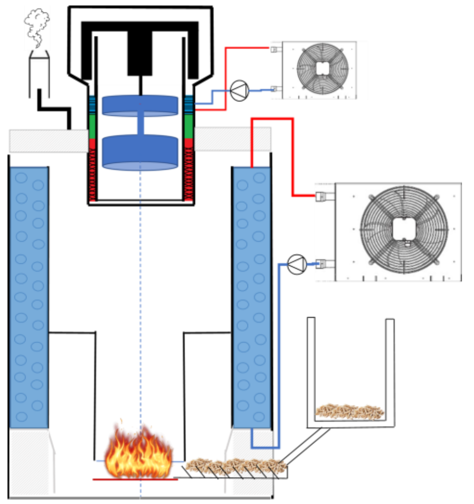

Fig. 1. Experimental facility of the hybrid BB+SE system.

2.1. Biomass boiler model

The following Fig. 2 shows the conceptual diagram of the sequenced sub-models used to solve this BB model. In the end, thirteen temperatures of the inner surface ($T_{s,i}$), nine temperatures of gases ($T_{g,i}$), eight of exhaust gases and water inside the jacket ($T_{h,i}$, $T_{w,i}$), and other less relevant eight internal temperatures are obtained ($T_{p,i}$). One of the temperatures corresponds to the approximate location of the SE head placed in a vertical position, which will be crucial for examining the performance of the engine under partial load conditions of the boiler. The position of SE in the upper part of the boiler can be seen in Figs. 1 and 3. In the experimental facility, a lifting mechanism has been introduced that allows removing the engine quickly to prevent its overheating in case of a safety trip in the boiler or the engine itself. It should be noted that a metallic piece of cylindrical shape was located in the inner part of the commercial boiler to redirect gas flow towards the water jacket, but it has been removed to introduce the SE heater; accordingly, this piece is not present in the model.

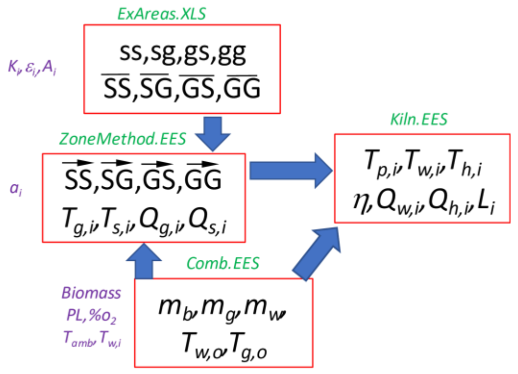

Fig. 2. Block scheme of the BB model.

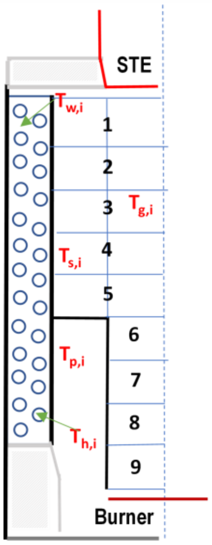

Fig. 3. Gas volumes and surfaces for the zone method in BB.

The heat rate provided by combustion and gas flow, as well as the circulating water flow rate, were provided by a model created by the Engineering Equation Solver (EES) using data from an average pellet fuel composition in Spain [20] (see Table 1) and excess of air, giving the efficiency at partial loads adjusted to the offering of around 30 biomass boiler models available on the market, where condensation is only offered in rare situations.

The zonal method with nine gas zones ($T_{g,i}$) and thirteen surfaces ($T_{s,i}$) has been developed to estimate the net radiative balance in the combustion chamber, as detailed in Fig. 3.

Table 1. Biomass averaged composition.

Chemical element	% (or kJ/kg)
C	45.4
H	5.755
N	0.087
S	0.1293
Cl	0.0054
O	40.94
W	7.628
LHV (dry basis)	17 566

The direct and total exchange areas were obtained using matrix algebra tools in Excel. Regarding the direct exchange areas (DEA), given the purely cylindrical geometry of this boiler in its simplification, the values available in Appendix 7 of the reference book on the subject [21] have been used. Based on the previously obtained DEA (surface-surface $\overline{\mathbf{ss}}$, surface-gas $\overline{\mathbf{sg}}$ and gas-gas $\overline{\mathbf{gg}}$) and the emissivities ε, reflectivities ρ and areas A of each enclosure surface, an equation for the total exchange areas (TEA) $\overline{\mathbf{SS}}, \overline{\mathbf{SG}}, \overline{\mathbf{GG}}$ can be seen in the following Eqs. (1) to (4) by using matrix algebra [22]:

$$\overline{\mathbf{SS}} = \boldsymbol{\varepsilon}\mathbf{AI} \cdot \mathbf{R} \cdot \overline{\mathbf{ss}} \cdot \boldsymbol{\varepsilon}\mathbf{I}, \tag{1}$$

$$\overline{\mathbf{SG}} = \boldsymbol{\varepsilon}\mathbf{AI} \cdot \mathbf{R} \cdot \overline{\mathbf{sg}}, \tag{2}$$

$$\overline{\mathbf{GG}} = \overline{\mathbf{gs}} \cdot \boldsymbol{\rho}\mathbf{I} \cdot \mathbf{R} \cdot \overline{\mathbf{sg}} + \overline{\mathbf{gg}}, \tag{3}$$

$$\mathbf{R} = [\mathbf{AI} - \overline{\mathbf{ss}} \cdot \boldsymbol{\rho}\mathbf{I}]^{-1}. \tag{4}$$

Subsequently, a second EES file performs the net radiative balance of the gas zones and interior surface zones of the combustion chamber, using the direct flux areas (DFA) based on the gas or surface temperatures and applying the Weighted Sum of Grey Gases (WSGG) model, which includes soot and particles due to biomass combustion, as described in [22]. The DFA $\overrightarrow{\mathbf{S_iS_j}}, \overrightarrow{\mathbf{G_iS_j}}, \overrightarrow{\mathbf{G_iG_j}}$ can be obtained for a grey-diffuse gas zone i or a surface i as a function of the abovementioned TEA for each attenuation coefficient $k_{g,n}$ of the WSGG model, as follows in Eqs. (5) to (7):

$$\overrightarrow{\mathbf{S_iS_j}} = \sum_{n=1}^{N_g} a_{s,n}(T_i) \cdot (\overline{\mathbf{SS}})_{k=k_{g,n}}, \tag{5}$$

$$\overrightarrow{\mathbf{G_iS_j}} = \sum_{n=1}^{N_g} a_{g,n}(T_{g,i}) \cdot (\overline{\mathbf{GS}})_{k=k_{g,n}}, \tag{6}$$

$$\overrightarrow{\mathbf{G_iG_j}} = \sum_{n=1}^{N_g} a_{g,n}(T_{g,i}) \cdot (\overline{\mathbf{GG}})_{k=k_{g,n}}. \tag{7}$$

The previously mentioned $a_{s,n}$ or $a_{g,n}$ weight coefficients for the WSGG model used are presented in Eqs. (8) and (9):

$$a_i = \sum_{j=1}^{N_c} c_{i,j} \left(\frac{T}{T_{ref}}\right)^{j-1}, \tag{8}$$

$$a_{i=0} = 1 - \sum_{i=1}^{N_g} a_i. \tag{9}$$

The four $k_{g,n}$ values in the WSGG model are 0 (transparent), 0.2715, 2.5005 and 39.1395 m^{-1}, respectively, each one including five $c_{i,j}$ coefficients [23], the reference temperature for normalization T_{ref} being equal to 1200 K.

Therefore, the net radiative balance for the case of a surface A_i is presented in Eqs. (10) and (11), where E_i is the emissive power of the surface A_i:

$$\sum_{j=1}^{m} \overrightarrow{S_iS_j} \cdot E_j + \sum_{j=1}^{l} \overrightarrow{G_jS_i} \cdot E_{g,j} - A_i \cdot \varepsilon_i \cdot E_i = Q_{rd,i}, \tag{10}$$

$$E_i = \sigma \cdot T_i^4. \tag{11}$$

The energy balance of a volume zone V_i is then presented in Eqs. (12) and (13), where $E_{g,i}$ is the emissive power of the gas volume i:

$$\sum_{j=1}^{l} \overrightarrow{G_jG_i} \cdot E_{g,j} + \sum_{j=1}^{l} \overrightarrow{S_jG_i} \cdot E_j + \\ -4 \cdot \sum_{n=1}^{N_g} a_{g,n} \cdot k_{g,n} \cdot V_i \cdot E_{g,i} = Q_{rd,i}, \tag{12}$$

$$E_{g,i} = \sigma \cdot T_{g,i}^4. \tag{13}$$

Finally, in this section, the energy balance (heat rate Q in steady state) of a gas zone i is formulated as in [24], including the energy from the combustion (if proceed), the one of the gas flow at the inlet and outlet of the volume, convection with the walls, and further conduction losses to the outside of the boiler, see Eq. (14):

$$Q_{cb} + Q_{rd,i} - Q_{cv,i} + Q_{g,i} - Q_{g,i-1} = 0. \tag{14}$$

The term related to convection is calculated as follows in Eqs. (15) and (16), where h, Nu, Re, λ, Pr and D are the convection coefficient, Nusselt number, conductivity, Prandtl number and diameter of the combustion chamber, respectively:

$$Q_{cv,i} = h_i \cdot A_i \cdot (T_{g,i} - T_{s,i}), \tag{15}$$

$$h_i = \frac{\mathrm{Nu}_i \cdot \lambda}{D} = \frac{0.023 \cdot \mathrm{Re}^{0.8} \cdot \mathrm{Pr} \cdot \lambda}{D}. \tag{16}$$

A simpler balance was also used for any surface A_I, considering that radiation and convection are transferred by conduction toward the water jacket.

Once the energy balance of the combustion chamber is completed, the fourth EES sub-model performs the energy balance in the internal walls ($T_{p,i}$), water jacket ($T_{w,i}$), exhaust gases inside of the jacket ($T_{h,i}$) and the lower enclosure between the area closest to the burner and the water jacket, which has a passage section reduced by half due to a metallic piece in the boiler (already included in $T_{p,i}$ or $T_{s,i}$). The input data for this latest boiler sub-model uses the inner surface temperature profile from the radiative model and gas temperature $T_{g,1}$. An energy balance closure is considered when the boiler inputs and outputs (losses in gases, walls heat rate transferred to water) are less than 50 W: if not, some boiler design parameters are modified (emissivities, generally, in some areas) and the Excel-3 EES simulation sequence is repeated.

2.2. Stirling engine model

To model FPSE is a quite complex issue, as its integrated operation of the piston and displacer on the same axis, to avoid the crankshaft mechanism present in other types of SE (α, γ), requires a dynamic model considering the characteristics of the springs and dampers that make it up [25]. Anyway, such models are related to the design of SEs rather than the analysis of their performance. In this work, the most interesting aspect is to predict the electrical generation considering the heat rate provided by the boiler according to its regime. Thus, the three well-known thermodynamic models sequentially presented by Urieli and Berchowitz [26] have been adapted from the available code implemented in MATLAB [27] and tested for some commercial SE. Figure 4 shows a schematic of the free piston Stirling engine, but placed vertically upwards, and Fig. 5 shows the sequential model developed to further integrate it with BB. The program provides both overall power and performance values, as well as cycle parameters.

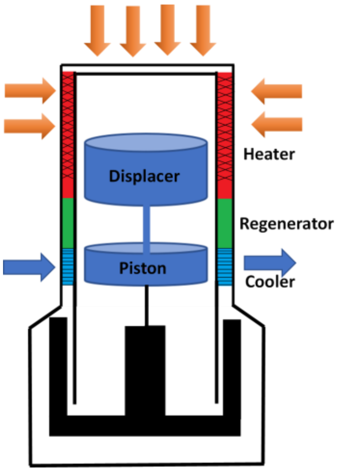

Fig. 4. Sketch of the modelled FPSE.

The model starts with the most basic scheme (Schmidt isothermal model) that provides an initial estimation of power, cycle efficiency, average working pressure and gas mass required in the cycle. Previously, the dimensions of the engine and working fluid were requested for preliminary analysis.

The second model includes a more realistic situation. Now, the compression and expansion processes are not considered isothermal but adiabatic. This implies a reduction in the efficiency of the thermodynamic cycle. The model already has a certain complexity, including solving a differential, incremental and conditioned equations system, which can be solved relatively quickly using the Runge-Kutta method.

The system consists of twenty-two variables and sixteen derivatives to be solved in a complete cycle ($\theta = 0$–2π rad), including seven derivatives that must be integrated numerically (T_c, T_e, Q_k, Q_r, Q_h, W_c, W_e), nine variables that are analytical derivatives (W, p, V_c, V_e, m_c, m_k, m_r, m_h, m_e). Six are conditional indefinite derivatives (T_{ck}, T_{he}, m_{ck}, m_{kr}, m_{rh}, m_{he}). Equations involved in the adiabatic model are included in Eqs. (17) to (47).

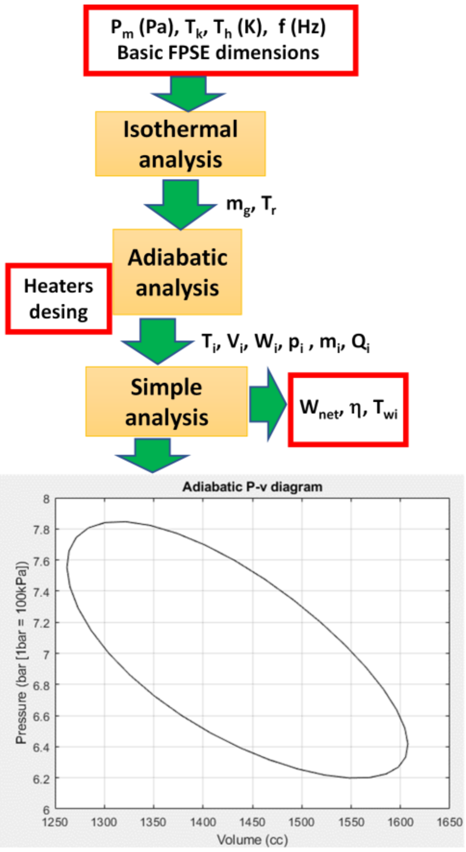

Fig. 5. Block model for FPSE.

First, Eqs. (17) and (18) are for pressure calculation and its variation in SE:

$$p = M \cdot R \,/\left(\frac{V_c}{T_c} + \frac{V_k}{T_k} + \frac{V_r}{T_r} + \frac{V_h}{T_h} + \frac{V_e}{T_e}\right), \tag{17}$$

$$dp = \frac{-\gamma \cdot p\left(\frac{dV_c}{T_{ck}} + \frac{dV_e}{T_{he}}\right)}{\frac{V_c}{T_{ck}} + \gamma\left(\frac{V_k}{T_k} + \frac{V_r}{T_r} + \frac{V_h}{T_h}\right) + \frac{V_e}{T_{he}}}. \tag{18}$$

Equations (19) to (23) are related to mass calculations in the five volumes of SE:

$$m_c = \frac{p \cdot V_c}{R \cdot T_c}, \tag{19}$$

$$m_k = \frac{p \cdot V_k}{R \cdot T_k}, \tag{20}$$

$$m_r = \frac{p \cdot V_r}{R \cdot T_r}, \tag{21}$$

$$m_h = \frac{p \cdot V_h}{R \cdot T_h}, \tag{22}$$

$$m_e = \frac{p \cdot V_e}{R \cdot T_e}. \tag{23}$$

Alternatively, Eqs. (24) to (28) estimate the mass accumulations in those five volumes:

$$dm_c = \frac{p \cdot dV_c + V_c \cdot dp/\gamma}{R \cdot T_{ck}}, \tag{24}$$

$$dm_e = \frac{p \cdot dV_e + V_e \cdot dp/\gamma}{R \cdot T_{he}}, \tag{25}$$

$$dm_k = m_k \cdot \frac{dp}{p}, \tag{26}$$

$$dm_r = m_r \cdot \frac{dp}{p}, \tag{27}$$

$$dm_h = m_h \cdot \frac{dp}{p}. \tag{28}$$

The mass flow rates between the five volumes of SE are shown in Eqs. (29) to (32); see Fig. (6) for details:

$$m_{ck'} = -dm_c, \tag{29}$$

$$m_{kr'} = m_{ck'} - dm_k, \tag{30}$$

$$m_{he'} = dm_e, \tag{31}$$

$$m_{rh'} = m_{he'} + dm_h. \tag{32}$$

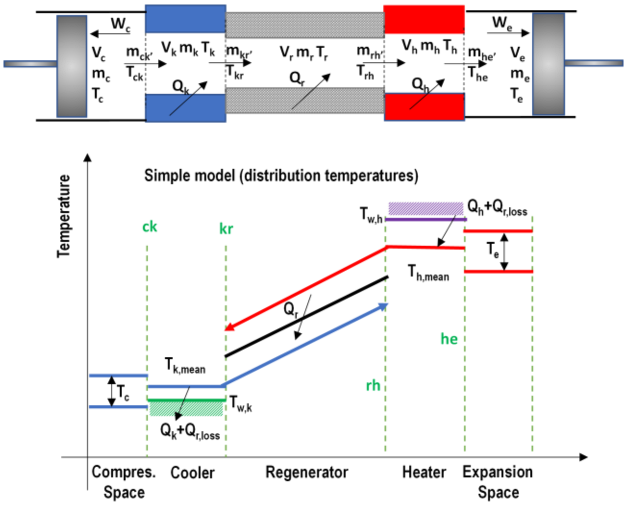

Fig. 6. Temperature profile of the simple model applied to FPSE. Adapted from [27].

Temperatures in the SE interfaces (compression-cooler and heater-expansion) are calculated depending on the mass flow rate sense, according to Eqs. (33) and (34):

$$if\ m_{ck'} > 0\ then\ T_{ck} = T_c\ else\ T_{ck} = T_k, \tag{33}$$

$$if\ m_{he'} > 0\ then\ T_{he} = T_h\ else\ T_{he} = T_e. \tag{34}$$

Then, the evolution of the temperatures in the compression and expansion volumes is estimated in Eqs. (35) and (36):

$$dT_c = T_c \cdot \left(\frac{dp}{p} + \frac{dV_c}{V_c} - \frac{dm_c}{m_c}\right), \tag{35}$$

$$dT_e = T_e \cdot \left(\frac{dp}{p} + \frac{dV_e}{V_e} - \frac{dm_e}{m_e}\right). \tag{36}$$

Energy balances in cooler, regenerator and heater volumes of SE are formulated as follows in Eqs. (37) to (39):

$$dQ_k = V_k \cdot dp \cdot \frac{c_v}{R} - c_p \cdot (T_{ck} \cdot m_{ck'} - T_k \cdot m_{kr'}), \tag{37}$$

$$dQ_r = V_r \cdot dp \cdot \frac{c_v}{R} - c_p \cdot (T_k \cdot m_{kr'} - T_h \cdot m_{rh'}), \tag{38}$$

$$dQ_h = V_h \cdot dp \cdot \frac{c_v}{R} - c_p \cdot (T_h \cdot m_{rh'} - T_{he} \cdot m_{he'}). \tag{39}$$

Finally, the work generation in SE is computed by Eqs. (40) to (43):

$$dW_c = p \cdot dV_c, \tag{40}$$

$$dW_e = p \cdot dV_e, \tag{41}$$

$$dW = dW_c + dW_e, \tag{42}$$

$$W = W_c + W_e. \tag{43}$$

The third model, curiously named Simple, also considers the heat transfer and pressure losses in the three heat exchangers of SE (heater, regenerator and cooler), especially the effectiveness of the regenerator based on parameters such as its porosity, as they significantly affect the final engine performance in terms of efficiency and generation (W). This third model is what essentially causes the different performances of SE to vary aside from the dynamic mechanism of the relative piston-displacer movement of these engines. This is due to the wide range of selections in the design of heat exchangers chosen for the heater, cooler and regenerator in this third model, which in turn is clearly dependent on the dynamic design performed.

In particular, since SE operates cyclically, the regenerator effectiveness ε is not practical in maintaining the classical definition based on the enthalpy exchange with respect to the maximum [25]. In this case, the amount of heat transferred from the gas to the regenerator in the cycle is compared with respect to the ideal adiabatic cycle, Q_r, being 0 in the worst case (no regeneration) and 1 in the best case (ideal regenerator). With a non-ideal regenerator, the working gas exits from the regenerator at a lower temperature than that of the heater. Thus, non-ideal effectiveness is then traduced into an additional heat loss $Q_{r,loss}$, see Eq. (44), thereby increasing the temperature of the hot source of SE and decreasing the cooler one, as estimated in Eqs. (45) and (46). Typical correlations for the forced convection coefficients h in the heater and cooler were used in the MATLAB code: $A_{w,i}$ their wetted areas.

$$Q_{r,loss} = (1 - \varepsilon) \cdot Q_r, \tag{44}$$

$$T_h = T_{wh} - \frac{(Q_h + Q_{r,loss}) \cdot f}{h_h \cdot A_{w,h}}, \tag{45}$$

$$T_k = T_{wk} - \frac{(Q_k - Q_{r,loss}) \cdot f}{h_k \cdot A_{w,k}}. \tag{46}$$

This parameter significantly affects the thermal efficiency η of FPSE compared to the one obtained for the adiabatic model η_i [26,28], which performs the heat transfer process at constant volume, usually in a mesh, see Eq. (47):

$$\eta = \frac{\eta_i}{\left[1 + \left(\frac{Q_r}{Q_h}\right) \cdot (1 - \varepsilon)\right]}. \tag{47}$$

The Simple method also considers the power loss associated with pressure drop dP in the three SE exchangers. As an example, Eq. (50) shows the associated dP_r to the regenerator.

$$dP = dP_h + dP_r + dP_k, \tag{48}$$

$$Pump_{loss} = \int (dP \cdot dV) \cdot f, \tag{49}$$

$$dP_r = \frac{2 \cdot f_r \cdot \mu \cdot V_r \cdot G \cdot l_r}{m_r \cdot d_r^2}. \tag{50}$$

It can be complemented with additional pressure losses due to the finite velocity of the piston or the internal conduction (*"shuttle"*) losses by the regenerator [9,29], heater and cooler walls. Still, they are not included here for the sake of simplicity. Furthermore, its value is also much lower than the power reduction associated with the Simple method. For all these reasons, the Simple method is considered the closest to the real value that an SE will measure in its operation.

3. Results analysis

3.1. Biomass boiler

Given the complexity of solving the boiler model, which is highly sensitive to the zonal method solution and especially to the emissivity of the analyzed surfaces, the modelling of the boiler has been studied with a typical excess air for this type of boiler of 10% measured in O_2 in gases, an outlet water temperature of 40°C, and an inlet water temperature depending on the partial load, which varies from 22°C to 30°C for the load range from 100% to 30%, according to the Spanish regulations regarding the certification of boiler efficiency [30]. A constant water flow rate (20 l/min) is assumed, so the outlet gas temperature is even lower at low loads since heat transmission is reduced when the gas flow rate is also reduced with the load. This temperature varies between 45°C and 49°C. This is why very similar efficiency values are obtained for this boiler throughout its possible operating range: In all cases, the thermal efficiency of the boiler yields values around 97% based on the lower heating value (LHV), which are high values and very close to condensation. Anyway, these values correspond to hot water production at a low temperature (40ºC) and are consistent with the independent simulation of efficiency performed with EES.

The BB modulation has only been studied from 50% to 100% in 5% variation steps, considering the subsequent connection with SE, which will require high temperatures to stay warm and produce electricity.

The following Fig. 7 shows some of the most relevant temperatures of the simulated model (see Fig. 2 for their location), demonstrating a clear trend based on the partial load. For example, the temperature difference $T_{g,1}$ for the gases toward the water jacket varies by about 150°C between the minimum and maximum loads (539–382°C). It is also very interesting to analyse the temperature difference between the gas volume and its metal wall ($T_{s,i}$–$T_{p,i}$), which has 80 l of water in its jacket on the other side. A difference of 400–350°C is maintained for high loads, decreasing to 350–300°C for the lowest loads, given the lower temperatures in the combustion chamber. It can also be seen that the gas decay profile ($T_{h,i}$) inside the jacket is much higher at the beginning than at the end of its path, and the water temperature increase ($T_{w,i}$), in countercurrent and upwards, heats up according to this thermal jump on the flue gas side. Regarding the actual measurements, the temperature probe is located approximately at the height of $T_{g,2}$; the values obtained are very reasonable, from 597°C to 440°C. It must be said that this parameter has much higher safety limits in the commercial BB, but it is not a control parameter since the boiler is mainly controlled by the O_2 measured with a lambda probe.

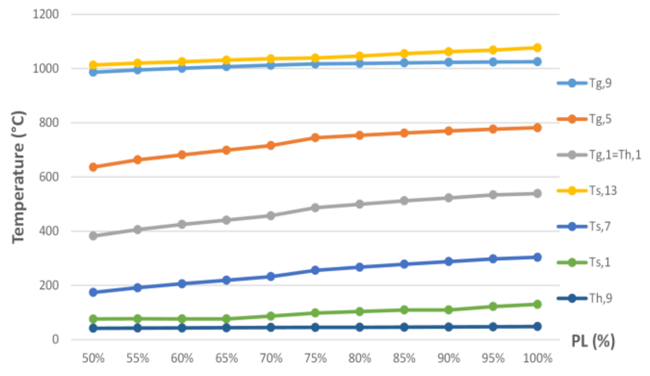

Fig. 7. Temperature profiles of the BB depending on the PL applied.

3.2. Stirling engine

The effects of the boiler performance on SE are significant in that the temperature values obtained for the heater ($T_{s,7}$), depending on the partial load of the BB, proportionally affect both the thermal efficiency and the expected electrical production. In calculating this temperature, there are two fundamental parameters that affect its final value: the proposed emissivity for the heater and the conduction resistance of the SE assembly. In this case, an emissivity value of 0.5 was taken for the SE heater, considering it a polished receiver but exposed to fouling from the combustion of various types of biomass. Regarding the resistance value, a figure of 0.5 K/W has been selected. This implies temperature values in the range of 190–305°C depending on the boiler load, with an electrical production in the range of 200–650 W (see Fig. 8) and increasing electric efficiencies in the order of 8–22% (simple model, see Fig. 9). Those values are comparable for the reduced number of commercial SEs. It is also evident in the previous figures that there is a reduction in production and efficiency loss as a more detailed and realistic thermodynamic model is gradually included. The difference between the isothermal and adiabatic models is that they are not so crucial in estimation of efficiency and produced power, as shown in other studies [5,9,26].

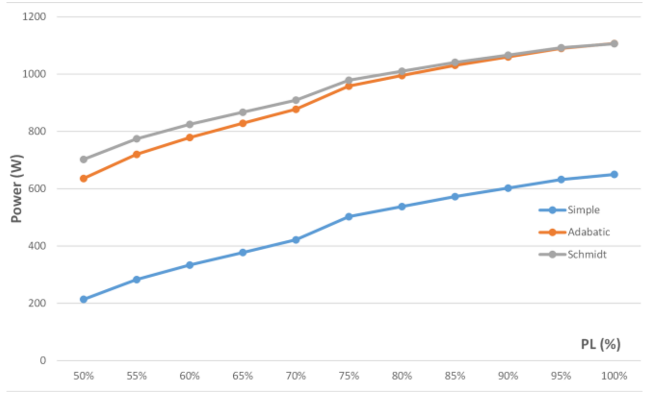

Fig. 8. Projected power generation in SE depending on the applied BB part load and SE model.

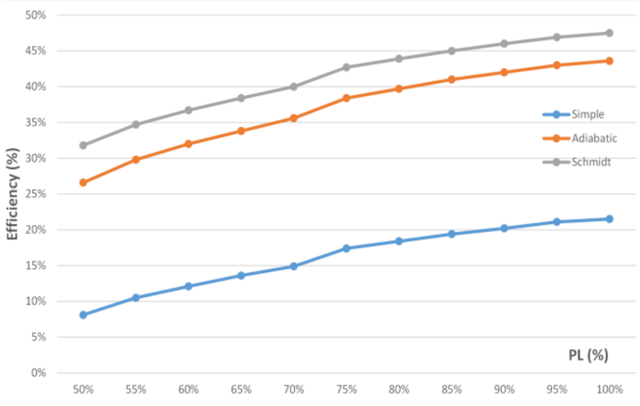

Fig. 9. Electrical efficiency of SE as a function of the BB part load and SE model applied.

The greatest difference is shown in the jump from the adiabatic model to the simple one, where, above all, the impact of the regenerator effectiveness (about 0.6 on average) is much more significant than the power losses associated with the pressure drop of the three SE exchangers (heater, regenerator and cooler). In the same studies, the difference could also be seen.

It is important to note that heat recovery in this BB is different from other systems where the heat recovery unit is located behind the combustion chamber, and this does not favour heat capture by SE, which is the main reason for not reaching the nominal power and find relatively low heater temperatures. On the other hand, in the actual SE installation, the temperature of the cold focus will be limited by the cooling capacity of the system associated with the cooler. In this case, this effect has not been considered, and the cooling temperature taken was 300 K for the model. Although this value is less important than the heater temperature, it must be controlled within reasonable limits to have a good efficiency.

Furthermore, it should be noted that the SE heater design may vary, given the variety of models, and, in particular, the design required for the heater, considering the potential fouling that occurs during biomass combustion, which prevents the installation of fins to increase heat capture.

4. Conclusions

In this article, an integrated model of a biomass boiler is presented, which includes the zonal method for radiative exchange using the WSGG model and energy balances in the meshing performed for the zonal method, as well as a combustion model to estimate gas production, its composition and estimated gas and water outlet temperatures. The calculations were carried out using Excel and, subsequently, three successive EES files. The internal temperature values and the efficiency for a partial load ranging from 50% to 100% were obtained from the model.

The main advantage of this BB model is that it also provides the temperature values available in the area where the heat receiver of SE is expected to be installed. In the successive modelling of this SE in MATLAB, production values of up to 650 W and efficiencies of 22% were obtained in the best cases, assuming an emissivity of 0.5 for the engine receiver. This figure is very similar to the average production offered by a biomass boiler manufacturer that incorporates SE in its upper part.

Regarding the model error analysis, its validation is planned to be carried out shortly using experimental data obtained from the recently completed facility, including the real-time acquisition of specific measurements for both BB and SE. In any case, it will only be possible to validate some values since the real instrumentation only measures values such as $T_{g,2}$, the temperatures of the gas ($T_{h,9}$) and water inlet and outlets ($T_{w,9}$, $T_{w,1}$) in BB, and the temperature of the SE head ($T_{s,7}$) in the SE controller. It should also be made clear that the model is a simplification of the actual installation since SE will have a specific vertical movement and, therefore, the combustion chamber will not be precisely a cylinder, which gives it a particular uncertainty associated with the validation due to these undesirable geometrical effects. Since the BB model is based on a zonal radiation model, it depends on the meshing used to create it. According to Larsen and Howell [31], the maximum error in temperatures or heat fluxes is less than 1.5% for a similar meshing example. In the case of SE, the articles mentioned in section 3.2 have found an error relative to a real SE of around 3-4% in the best cases. With all reservations, the model is expected to yield an error of less than 10% in the experimental measurements taken.

This model is more flexible than the actual installation as it allows for modification of aspects that are not feasible in said installation, and therefore, once validated, can be a way of proposing improvements to the installation because of the results. In any case, it is necessary to comment that the sequential model is very sensitive. Any modification of a substantial parameter in the model requires recalculating all downstream modules from the modified one till its convergence. Nevertheless, certain parameters have already been identified as crucial in these models, such as:

- The emissivities ε of the internal surfaces of the boiler enclosure, especially that of SE and the surface where combustion (flame, $T_{s,13}$) takes place;
- The treatment of the area adjacent to the burner outside the irradiated enclosure. Currently, it has been considered that there is no participatory medium in the radiation between the inner walls of BB ($T_{s,i}$) and the outer walls of the water jacket ($T_{p,i}$);
- The thermal resistance is assumed for the entire SE assembly since, in the energy balance of the combustion chamber, it is a relevant loss that greatly affects the value obtained from $T_{s,7}$ (input of the SE model);
- The excess air in combustion would vary the gas temperature profiles and thus produce less (or more) hot water and electricity from this hybrid system;
- The section considered for the exit of combustion gases in the burner involves the treatment of gaseous convection in the internal boiler enclosure, which is very sensitive to existing passage sections.

The ultimate goal is to produce enough power from this boiler, making it a self-sufficient system in isolated and wooded areas where solar resources are scarce but biomass is abundant. This can be achieved by maintaining the SE head temperature above 350ºC.

Acknowledgements

This publication is part of the R+D+i project ENSURE (TED2021-131397B) funded by MCIN/AEI/10.13039/501100011033/ and European Union NextGenerationEU/PRTR.

References

[1] Schneider, T., Müller, D., & Karl, J. (2020). A review of thermochemical biomass conversion combined with Stirling engines for the small-scale cogeneration of heat and power. *Renewable and Sustainable Energy Reviews*, 134, 110288. doi: 10.1016/j.rser.2020.110288

[2] Zhu, G., Yu, K., Liang, W., Dai, W., & Luo, E. (2021) A review of Stirling-engine-based combined heat and power technology. *Applied Energy,* 294, 116965. doi: 10.1016/j.apenergy.2021.116965

[3] Hachem, H., Gheith, R., Aloui, F., & Nasrallah, S.B. (2018) Technological challenges and optimization efforts of the Stirling machine: A Review. *Energy Conversion and Management,* 171, 1365-1387. doi: 10.1016/j.enconman.2018.06.042

[4] Zare, S., & Tavakolpour, A. (2020) Free piston Stirling engines: A review. *International Journal of Energy Research*, 44, 5039–5070. doi: 10.1002/er.4533

[5] Ahmadi, M.H., Ahmadi, M.A., & Pourfayaza, F. (2017) Thermal models for analysis of performance of Stirling engine: A review. *Renewable and Sustainable Energy Reviews,* 68, 168–184. doi: 10.1016/j.rser.2016.09.033

[6] Jiménez, P., Cardozo, E., Choque, L.A., & Araoz, J.A. (2020) Performance Analysis of a Stirling Engine Hybrid Power System. *Energies,* 13, 980. doi: 10.3390/en13040980

[7] Laazaar, K., & Boutammachte, N. (2020) New approach of decision support method for Stirling engine type choice towards a better exploitation of renewable energies. *Energy Conversion and Management,* 223, 113326. doi: 10.1016/j.enconman.2020.113326

[8] Udeh, G.T., Michailos, S., Ingham, D., Hughes, K.J., Ma, L, & Pourkashanian, M. (2020) A techno-enviro-economic assessment of a biomass fuelled micro-CCHP driven by a hybrid Stirling and ORC engine. *Energy Conversion and Management,* 227, 113601. doi: 10.1016/j.enconman.2020.113601

[9] Auñón, J.A., Pérez, J.M., Martín, M.J., Auñón, F., & Núñez, D. (2023) Development and validation of a software application to analyse thermal and kinematic multimodels of Stirling engines. *Helyon,* 9, 18487. doi: 10.1016/j.heliyon.2023.18487

[10] Jiang, Z., Yu, G., Zhu, S., Dai, W., & Luo, E. (2022) Advances on a free-piston Stirling engine-based micro-combined heat and power system. *Applied Thermal Engineering,* 217, 119187. doi: 10.1016/j.applthermaleng.2022.119187

[11] Kwankaomeng, S., Silpsakoolsook, B., & Savangvong, P. (2014) Investigation on Stability and Performance of a Free-Piston Stirling Engine. *Energy Procedia,* 52, 598–609. doi: 10.1016/j.egypro.2014.07.115

[12] González-Pino, I., Pérez-Iribarren, E., Campos-Celador, A., Terés-Zubiaga, J., & Las-Heras-Casas, J. (2020) Modelling and experimental characterization of a Stirling engine-based domestic micro-CHP device. *Energy Conversion and Management,* 225, 113429. doi: 10.1016/j.enconman.2020.113429

[13] Valenti, G., Campanari, S., Silva, P., Fergnani, N., Ravidà, A., Di Marcoberardino, G., & Macchi, E. (2014) Modeling and testing of a micro-cogeneration Stirling engine under diverse conditions of the working fluid. *Energy Procedia,* 61, 484–487. doi: 10.1016/j.egypro.2014.11.1154

[14] Choque, L.A., & Araoz, A. (2023) A Case Study of the Development Experience of Using a Prototype Stirling Engine in A Novel Bioenergy Driven Co-Generation Plant in Bolivia. *Heat Transfer Engineering,* doi: 10.1080/01457632.2023.2185492

[15] Cardozo, E., Erlich, C., Malmquist, A., Jiménez, & Alejo L. (2014). Integration of a wood pellet burner and a Stirling engine to produce residential heat and power. *Applied Thermal Engineering,* 73, 671–680. doi: 10.1016/j.applthermaleng.2014.08. 024

[16] Damirchi, H., Najafi, G., Alizadehnia, S., Mamat, R., Sidik., N. A.C. Azmi, W.H., & Noor M.M. Micro Combined Heat and Power to provide heat and electrical power using biomass and Gamma-type Stirling engine. *Applied Thermal Engineering*, 103, 1460–1469. doi: 10.1016/j.applthermaleng.2016.04.118

[17] Arashnia, I., Najafi, G., Ghobadian, B., Yusaf, T., Mamat, R., & Kettner, M. (2015) Development of micro-scale biomass-fuelled CHP system using Stirling Engine. *Energy Procedia,* 75, 1108–1113, doi: 10.1016/j.egypro.2015.07.505

[18] Cardozo, E., & Malmquist, A. (2019) Performance comparison between the use of wood and sugarcane bagasse pellets in a Stirling engine micro-CHP system. *Applied Thermal Engineering,* 159, 113945, doi: 10.1016/j.applthermaleng.2019.113945

[19] Araoz, J.A., Cardozo, E., Salomon, M., Alejo, L., &. Fransson, T.H. (2015) Development and validation of a thermodynamic model for the performance analysis of a gamma Stirling engine prototype. *Applied Thermal Engineering,* 83, 16–30. doi: 10.1016/j.applthermaleng.2015.03.006

[20] Esteban, I. (2014) *Análisis y caracterización de la combustión de pélets en una caldera Solarfocus TII30 de llama invertida*. Universidad de Valladolid (in Spanish).

[21] Hottel, H.C., & Sarofim, A.F. (1967) *Radiative Transfer.* McGraw Hill Book Company, New York.

[22] Noble, J.J. (1975) The zone method: Explicit matrix relations for total exchange areas. *Int. J. Heat Mass Transfer,* 18, 261-269.

[23] Hofgren, H., & Sunden, B. (2015) Evaluation of Planck mean coefficients for particle radiative properties in combustion environments. *Heat Mass Transfer,* 51, 507–519. doi: 10.1007/s00231-014-1431-0

[24] Rhine, J.M., & Tucker, R.J. (1991) *Modelling of gas-fired furnaces and boilers and another industrial processes*. British Gas plc.

[25] Walker, G., & Senft, J.R. (1985) *Free Piston Stirling Engines.* (1st ed.). Springer-Verlag.

[26] Urieli, I., & Berchowith, D.M: (1984) *Stirling Cycle Engine Analysis.* Adam Hilger Ltd.

[27] Urieli, I. (2002) *Stirling Cycle Machine Analysis.* https://www.ohio.edu/mechanicalfaculty/urieli/stirling/Index.html [accessed 28 September 2023].

[28] Scarpin, G. (2012) *Modelo Simple de Motores Stirling.* Informe Técnico: DMA-012/12. Instituto Universitario Aeronáutico, Córdoba, Argentina (in Spanish).

[29] Araoz, J.A., Salomon, M., Alejo, L., &. Fransson, T.H. (2014) Non-ideal Stirling engine thermodynamic model suitable for the integration into overall energy systems. *Applied Thermal Engineering,* 73, 205–221. doi: 10.1016/j.applthermaleng.2014.07. 050

[30] CTE UNE124 (2023) Generadores y emisores de calor. Norma Española UNE-EN 303-5:2022+A1. *Heating boilers. Part 5: Heating boilers for solid fuels, manually and automatically stoked, nominal heat output of up to 500 kW. Terminology, requirements, testing, and marking.* Madrid (in Spanish).

[31] Larsen, M.E., & Howell, J.R. (1985) The Exchange Factor Method: An Alternative Basis for Zonal Analysis of Radiation Enclosures. *Journal of Heat Transfer,* 107(4), 936–942. doi: 10.1115/1.3247524

Co-published by
Institute of Fluid-Flow Machinery
Polish Academy of Sciences
Committee on Thermodynamics and Combustion
Polish Academy of Sciences

http://www.imp.gda.pl/archives-of-thermodynamics/

ARCHIVES OF THERMODYNAMICS

Numerical Study on Nozzle Group Atomization Cooling: Effects of Pressure, Tilt Angle and Spacing on Enhanced Heat Transfer

Li Li[a,b,*], Rong Li[a,b], Lei Zhang[a,b]

[a]Hebei Key Laboratory of Man-machine Environmental Thermal Control Technology and Equipment, Xingtai, 054000, China
[b]Hebei Vocational University of Technology and Engineering, Xingtai, 054000, China
*Corresponding author email: lili@xpc.edu.cn

Received: 25.12.2024; revised: 23.04.2025; accepted: 27.05.2025

Abstract

This study investigates the improved heat transfer process of multi-nozzle arrangements through numerical analysis. A discrete phase based numerical model is developed to analyse the secondary atomization and heat transfer characteristics under different conditions. The effects of pressure, spacing and tilt angle of the nozzle group on the atomization cooling performance are evaluated. The results indicate that increasing the pressure can significantly improve the heat transfer capacity. The higher the pressure, the lower the hot wall temperatures and the higher the heat transfer coefficient. The nozzle tilt angle also has a significant impact. The heat transfer performance for a 30° tilt angle is optimal, while for a 15° tilt angle is poor. Increasing the number of nozzles can improve the cooling to a limited extent. In addition, nozzle spacing will affect temperature distribution, thereby achieving optimal cooling at intermediate distances. The results can provide valuable insights for optimizing multi-nozzle configurations of efficient heat transfer in industrial applications.

Keywords: Nozzle atomization; Pressure change; Tilt angle; Nozzle spacing; Heat transfer

Vol. 46(2025), No. 2, 143–152; doi: 10.24425/ather.2025.154913

Cite this manuscript as: Li, L., Li, R., & Zhang, L. (2025). Numerical Study on Nozzle Group Atomization Cooling: Effects of Pressure, Tilt Angle and Spacing on Enhanced Heat Transfer. *Archives of Thermodynamics*, 46(2), 143–152.

1. Introduction

The increasing demand for high-performance cooling solutions in various industrial and technological applications such as power generation, electronics and manufacturing has driven the development and optimization of advanced heat transfer techniques. One of the most promising methods is spray cooling, which involves optimizing the liquid into fine droplets on a hot surface, providing rapid and effective heat dissipation. This technique has achieved significant attention due to its ability for high heat transfer coefficients and low thermal resistance [1–4]. Recent advancements in spray cooling have focused on optimizing various parameters, including droplet size, velocity and distribution, to enhance the overall cooling performance [5–8].

In the context of spray cooling, the configuration of nozzle groups is a critical factor influencing the effectiveness of the process. Pressure, spacing and tilt angle of the nozzles can significantly affect the heat transfer characteristics. For instance, higher pressures typically result in finer droplets and increased momentum, leading to improved heat transfer coefficients [9−11]. The spacing between nozzles is also important, as it affects the uniformity of the spray coverage and the overlap of the atomization cones, which in turn impacts the heat transfer efficiency [12,13]. Furthermore, the tilt angle of nozzles can alter the impingement pattern and the distribution of droplets on the target surface, thereby affecting the heat transfer rate [14]. Understanding these relationships is essential for the design and optimization of efficient spray cooling systems.

Nomenclature

Abbreviations and Acronyms

CHF – critical heat flux
DPM – discrete phase model
PISO – pressure implicit split operator
SMD – Sauter mean diameter
TAB – Taylor analogy breakup

Numerous studies have shown the effects of different nozzle configurations on the heat transfer performance of spray cooling. Durmus et al. [15] examined the heat transfer performance and pressure drop characteristics in concentric heat exchangers of a volute inlet, and analysed the heat transfer efficiency and fluid resistance under different operating conditions. Abbasi and Kim [16] explored the application of nano-fluids in spray cooling, and found that the addition of nanoparticles can significantly enhance the heat transfer coefficient. Combined with a newly designed conical wire blade, Oflaz et al. [17] investigated the thermal properties of SiO_2-water nano-fluid. The study also highlighted the potential of nano-fluids to improve thermal performance. Cheng et al. [18] experimentally and numerically investigated the impact of different nozzle configurations on spray cooling, demonstrating that optimal spacing and inclination angles can improve the cooling efficiency. Wang et al. [19] studied the heat transfer performance of spray cooling under low mass flux conditions and highlighted the importance of droplet size and velocity.

Hou [20] conducted numerical simulations and experimental validations to multi-nozzle spray cooling systems, providing valuable insights into the optimal nozzle arrangements for improved heat transfer. Zhang et al. [12] and Muthukrishnan et al. [21] developed the correlations to predict the critical heat flux (CHF) in spray cooling, which is crucial for the safe and efficient operation of cooling systems. The applications of implementing spray cooling in real-world applications are also concerned. Pautsch and Shedd [8] measured the thickness of liquid film during spray cooling of FC-72, providing data that can be used to optimize the cooling process. Liao et al. [22] developed a comprehensive model to predict the performance of simplex atomizers, which are commonly used in spray cooling systems. Si et al. [23] tested an integrated refrigeration-spray cooling system for high-power solid-state lasers and demonstrated the potential of spray cooling in specialized applications. These studies emphasize the importance of considering theoretical and practical aspects for designing and optimizing spray cooling systems.

Despite the above advancements in spray cooling, a comprehensive understanding of the intricate interactions in different parameters remains to be fully explained. This study aims to develop a gas-liquid two-phase atomization and heat transfer model for a pressure swirl nozzle array, and systematically analyse the influence of nozzle atomization cooling on improved heat transfer performance. This study focuses on different configurations of nozzle groups, simulating atomization and heat transfer processes on heated walls by numerically calculating the droplet ejection at the nozzle outlet and its subsequent trajectory in the computational domain. Based on these simulations, an in-depth examination is conducted considering the effects of pressure, tilt angle and spacing on the atomization characteristics of the nozzle array. These findings can not only provide essential insights for optimizing nozzle atomization cooling parameters, but also provide robust data support for advancing the comprehension of enhanced heat transfer mechanisms. The practical significance lies in its capacity to improve the efficiency and reliability of industrial cooling systems through refining nozzle configurations. This is particularly important in power generation, electronics and manufacturing. Efficient cooling solutions are indispensable in these fields, and can provide scientific foundations and technical guidance.

2. Research method

A numerical model utilizing ANSYS Fluent software based on the discrete phase model (DPM) is developed to investigate the secondary atomization and heat transfer characteristics of multiple nozzles under different operating conditions. The examined parameters include nozzle group pressure, spacing and tilt angle. The DPM model is selected to accurately track individual droplets and predict their interactions with heated surfaces. To ensure the reliability of the model, grid independence is verified. The numerical results are validated with experimental data from previous studies to evaluate the impact of these parameters on atomization cooling performance.

2.1. Verification of grid independence

In this study, pressure swirl nozzles are used for numerical simulation of the atomization characteristics of the nozzle group and for the numerical simulation of cooling. The cooling medium is accelerated by the cyclone sheet, and then enters the central cyclone chamber to form a central air column under centrifugal force. When the cooling medium leaves the nozzle outlet, it is already in the state of liquid film. This is because the surface tension of the liquid film is unstable at this time, and then it decomposes into filamentous liquid or liquid droplets. Due to the fact that the numerical simulation mainly explores the spatial injection of droplets in the nozzle group of the computational domain, as well as the formation of liquid film and the heat transfer on the bottom hot surface, the central region is encrypted and the boundary layer grid is set on the bottom surface when dividing the grid. To further verify the grid independence of this model, the rectangular computational domains with about 50 000, 263 000, 386 000, 483 000 and 781 000 grid cells are used to verify the grid independence, respectively. The DPM condition of the bottom surface is set as escape and the time step is 1×10^{-5} s to run for 2000 steps. The Sauter mean diameter (SMD) of droplets injected by the nozzle is recorded for judgment based on the change in SMD of droplets. The results are shown in Fig. 1.

When the number of grid cells reaches 483 000, SMD of droplets hardly changes with this increase. Therefore, to shorten the calculation time, the calculation model with 483 000 grid cells is adopted to establish the independence of the model grids.

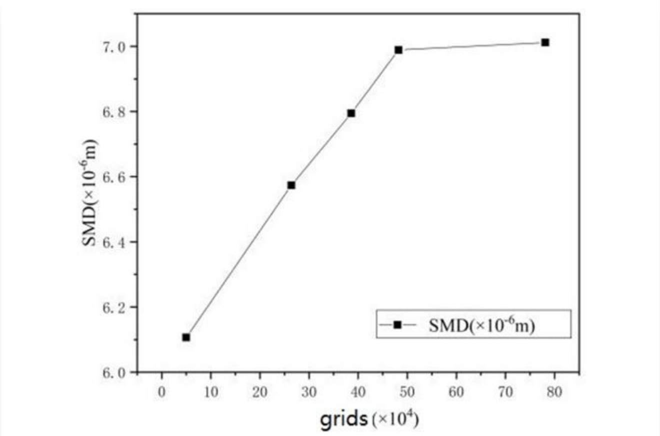

Fig. 1. Mesh independence verification.

2.2. Numerical calculation settings

ANSYS Fluent is used for numerical simulation. The boundary conditions for the continuous phase are established with a pressure inlet, while the flow of the continuous gas phase (air) in the computational domain is induced by liquid droplets ejected from a lateral injection source. The bottom boundary of the computational domain is modelled as an adiabatic wall without slip, maintained at a temperature of 293 K. All other boundaries in the computational domain are designated as pressure outlets. A realizable k–ε turbulence model is adopted. A second-order upwind scheme is used for pressure and momentum calculations via the pressure implicit with splitting of operator (PISO) algorithm.

Under the background of setting discrete phase boundary conditions, a pressure cyclone nozzle is used to precisely define parameters such as the inlet pressure and flow rate. The DPM boundary conditions on the upper surface around the computational domain and at the nozzle location are specified as escape, while those on the bottom surface are configured to trap particles. A random tracking model is used for particle tracking, and a dynamic drag model and a Taylor analogy breakup (TAB) model are used to explain the effect of gravity on droplets.

The inlet temperature of the cooling medium (water) and the ambient temperature are both maintained at 293 K. The material of the bottom heating wall is copper. The thermal wall is configured to be non-slip, with a heat flux set at 100 W/cm². Droplets are tracked as they reach the hot wall surface to form a liquid film. Consequently, the above Eulerian wall film model is activated, and the bottom boundary condition is defined as wall-jet.

2.3. Model reliability verification

To validate the reliability of the heat transfer model for the nozzle group, numerical simulations are conducted using the experimental conditions in Ref. [17]. Figure 7 shows the simulation results of nozzle atomization cooling in a wall temperature range of 40–90℃. As shown in Fig. 2, the discrepancy between the numerical simulations and experimental results remains within 10% in the temperature range of 40–90℃. This deviation may be attributed to the experimental conditions and measurement inaccuracies. The uncertainty related to temperature readings and droplet size distributions can affect the interpretation of results. Although the DPM model is effective for simulating discrete phase flow, its limitations in predicting secondary droplet fragmentation and coalescence under specific conditions should also be considered. Given that the error is in an acceptable range, the used heat transfer model is reliable.

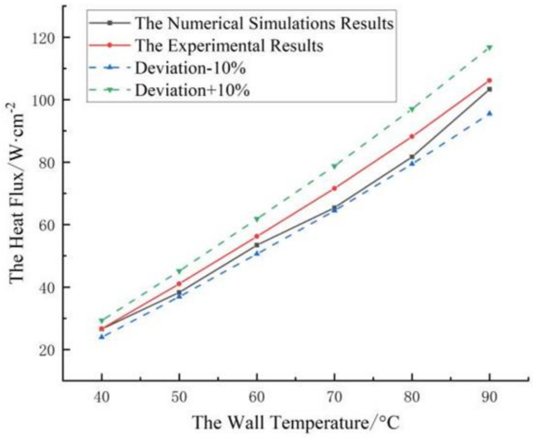

Fig. 2. Comparison between numerical simulations and experimental results of the heat transfer model.

3. Results and discussion

3.1. Effect of different pressures

The heat transfer mechanisms in spray cooling include the direct thermal exchange between the cooling medium and high-velocity liquid droplets impacting on the heating surface via the nozzle, as well as the heat transfer from the liquid film formed by these droplets on the hot surface, the flow of this liquid film over said surface, and its subsequent evaporation. To investigate how pressure influences the heat transfer characteristics of the nozzle array, a constant heat flux of 100 W/cm² is maintained while simulating spray cooling pressures ranging from 1.0 MPa to 2.0 MPa. Figure 3 shows the changes in bottom surface temperature under different pressure conditions.

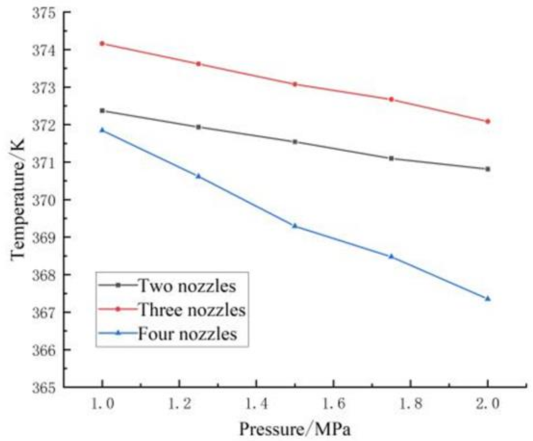

Fig. 3. Temperature curves under different pressure conditions.

The data indicate that the two, three and four nozzles have similar trends. Specifically, as pressure increases, there is a corresponding decrease in average hot wall temperature. This phenomenon can be attributed to the increased atomization effect caused by the increase in pressure, which increases the energy of droplet fragmentation, reduces droplet size, accelerates droplet velocity, and thus enhances their heat transfer ability.

Figures 4, 5 and 6 show the temperature distribution on the bottom surface of the two, three and four nozzles under different pressure conditions. As nozzle pressure increases from 1.0 MPa to 2.0 MPa, the strong impact region and the blue low-temperature zone within the atomization cone both transition from a discontinuous state to a completely continuous state. At the same time, the area occupied by red high-temperature regions associated with weak impacts within the atomization cone gradually decreases. It is worth noting that an extension of this red high-temperature region occurs near the atomization cone. However, it decreases along with the temperature. This phenomenon, which can be attributed to an increase in droplet velocity, will increase the pressure, resulting in a decrease in average droplet diameter while promoting a more uniform distribution of droplets. Therefore, the heat transfer capabilities in the impact areas of the atomizing cone can be enhanced, and the thermal effects related to liquid film flow outside this region can be improved.

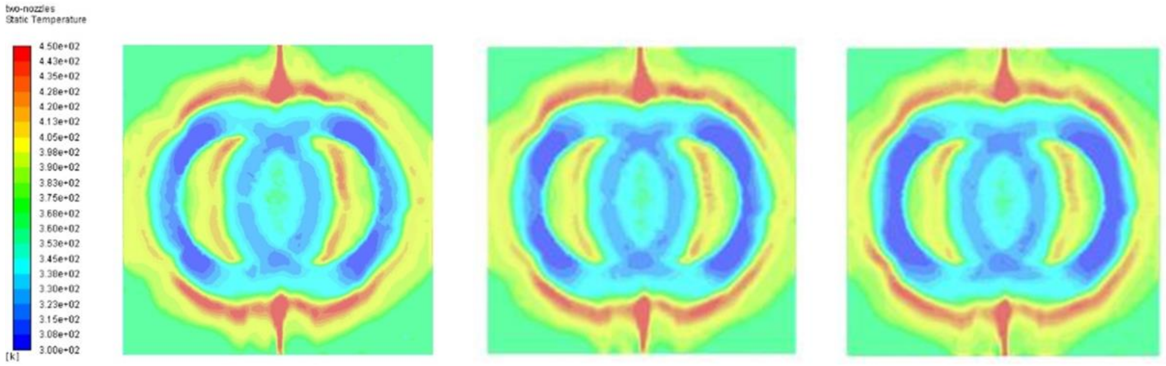

(a) 1.0 MPa (b) 1.5 MPa (c) 2.0 MPa

Fig. 4. Temperature distribution on the bottom surface of two nozzles under different pressures.

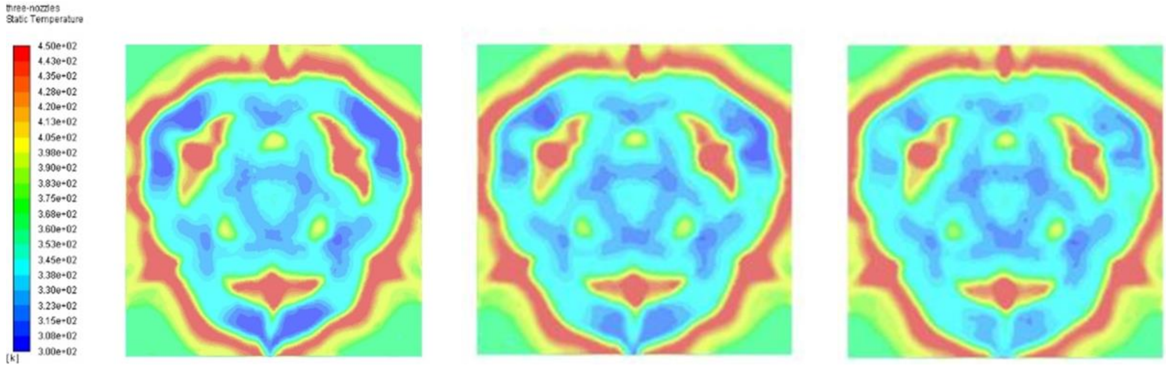

(a) 1.0 MPa (b) 1.5 MPa (c) 2.0 MPa

Fig. 5. Temperature distribution on the bottom surface of three nozzles under different pressures.

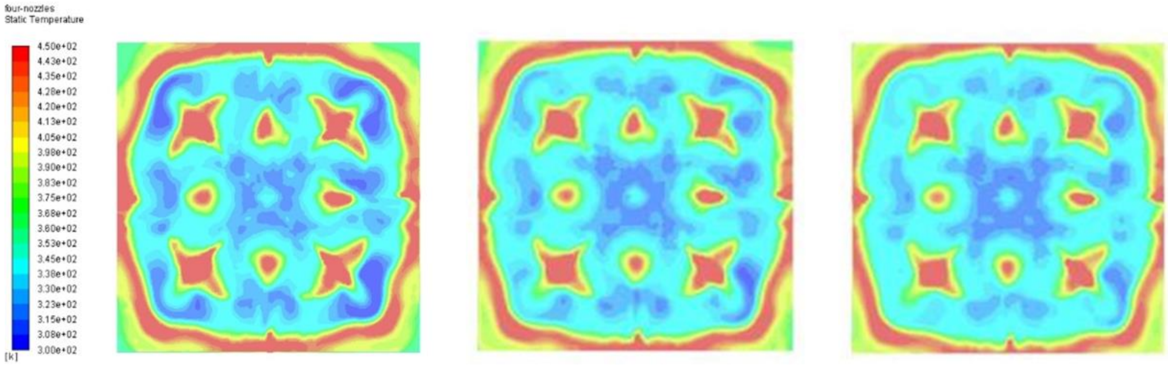

(a) 1.0 MPa (b) 1.5 MPa (c) 2.0 MPa

Fig. 6. Temperature distribution on the bottom surface of four nozzles under different pressures.

Under consistent pressure conditions, an increase in the number of nozzles leads to a gradual expansion of the coverage area of the atomization cone. The blue low-temperature region in the atomization cone extends outward, while the interference zone becomes more dispersed. However, the central blue low-temperature area has a significant increase. The number of red high-temperature regions with weak impact inside the atomization cone increases, showing a clear regularity. On the contrary, the area and temperature of the extrapyramidal region will decrease. This phenomenon can be attributed to the increase in the number of nozzles, which leads to an increase in the atomization region and an expanded interference zone between nozzles, thereby improving the heat transfer area and efficiency.

Figure 7 shows the variation in the hot wall heat transfer coefficient for the two, three and four nozzles under different pressures. The data indicates that as the pressure increases, the heat transfer coefficient of the hot wall also increases. Notably, the range of variation in this coefficient is most significant for four nozzles and least pronounced for two nozzles. The heat transfer coefficients in all three nozzle configurations exceed 15 000 W/(m^2·K). This suggests that increasing the number of nozzles can significantly enhance the heat transfer of the atomizing cooling system on the bottom surface of the nozzle group.

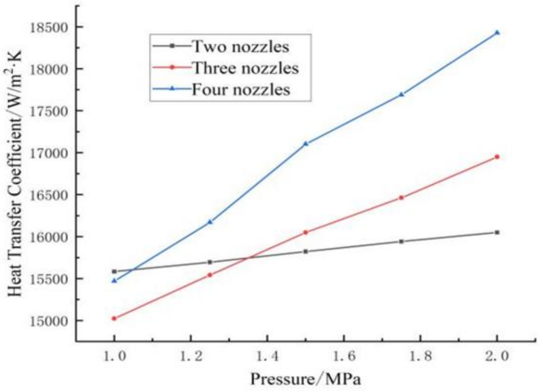

Fig. 7. Heat coefficient curves under different pressure inlet conditions.

According to Figs. 3 through 7, as shown in Table 1 below, the parameters of different nozzle groups change under different pressures: as the pressure increases, the average droplet velocity increases; the bottom surface average temperature decreases, and the bottom heat transfer coefficient increases.

Table 1. Parameters of the nozzle group under different pressures.

Number of nozzles	P, MPa	Average bottom surface temperature, K	Average liquid film temperature, K	Heat transfer coefficient, W/(m²·K)
Two	1.0	372.37	308.19	15582.54
	1.5	371.54	308.33	15821.40
	2.0	370.81	308.50	16049.54
Three	1.0	374.16	307.59	15023.26
	1.5	373.07	310.76	16048.27
	2.0	372.08	313.08	16949.58
Four	1.0	371.84	307.20	15469.86
	1.5	369.29	310.81	17101.45
	2.0	367.35	313.08	18426.51

This indicates that increasing pressure can improve the atomization effect of the nozzle group and its heat transfer capability, which is crucial for designing efficient multi-nozzle array cooling systems.

3.2. Effect of different tilt angles

Figure 8 shows the trend of the average bottom surface temperature of the two, three and four nozzles at different tilt angles. The findings indicate that as the nozzle tilt angle increases, the bottom temperature first increases and then decreases. Notably, the two and three nozzles exhibit a similar trend, reaching a comparable minimum temperature at 30°. The four nozzles display a more pronounced variation in temperature and achieve a similar temperature at both 0° and 30°.

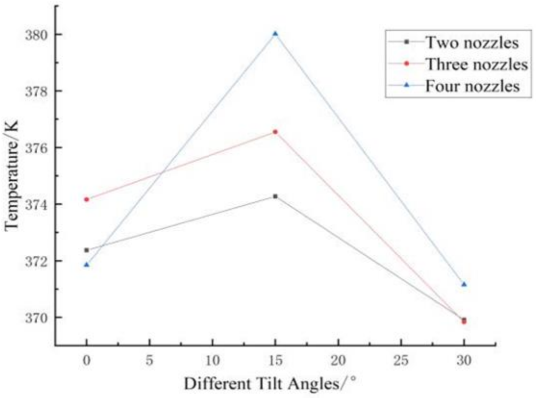

Fig. 8. Temperature curves at different tilt angles.

Based on the temperature distribution of the hot wall in Figs. 9, 10, and 11, it is observed that the coverage area of the atomization cone changes as the tilt angle increases. The temperature in the strong impact region of the cone increases, while the weak impact region first decreases and then increases, followed by the decreased temperature. On the contrary, the interference area expands with the decreased temperature. The outer region of the cone experiences atomization without significant changes in temperature. This phenomenon can be attributed to an even distribution of bottom surface temperatures at a nozzle tilt angle of 0°. The droplets are densely concentrated in the strong impact and interference areas with low temperatures. As the tilt angle escalates to 15°, an overlap occurs between the weak impact and interference regions, leading to a decline in temperature. However, droplet kinetic energy decreases due to nozzle interference from different directions, resulting in elevated temperatures within the strong impact zone. At a tilt angle of 30°, the kinetic energy of the droplets passing through the interference areas further decays, causing the droplets near the nozzle to almost vertically strike against the bottom surface. The interaction between these factors leads to an increase in the temperature distribution of the bottom surface within the interference regions. In the strong impact regions, the temperature outside these regions decreases.

Figure 12 shows the variation of the average heat transfer coefficient of the bottom surface at different tilt angles. The data indicates that as the tilt angle increases, the average heat transfer coefficient for the two and four nozzles first decreases and then increases. For the three nozzles, it first increases slightly and then increases significantly. Compared with the two and four nozzles, the difference in behaviour of the three nozzles can be attributed to the changes in the spray coverage area. Specifically, as the tilt angle increases, this area first decreases before expanding again. However, due to their asymmetric arrangement, the three nozzles have an impact on coverage distribution and liquid film uniformity. When the inclination angle of all three nozzles reaches 15°, the interaction between these factors increases slightly in the heat transfer coefficient of the bottom surface.

The increase of the tilt angle can improve the heat transfer ability of the nozzle group. Optimizing the nozzle tilt angle (especially at 30°) can achieve a more uniform temperature distribution and significantly improve heat transfer efficiency. Table 2 shows the variations of nozzle group parameters under different tilt angles.

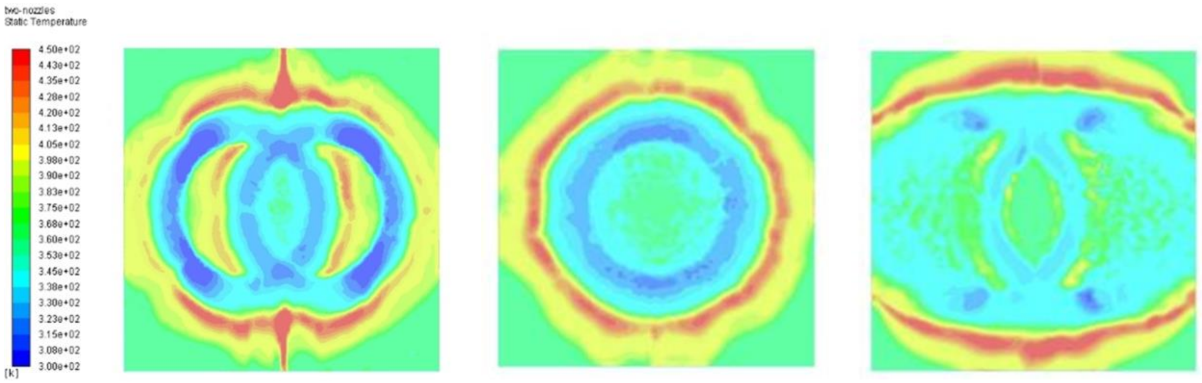

(a) 0° (b) 15° (c) 30°

Fig. 9. Temperature distribution on the bottom surface of two nozzles at different tilt angles.

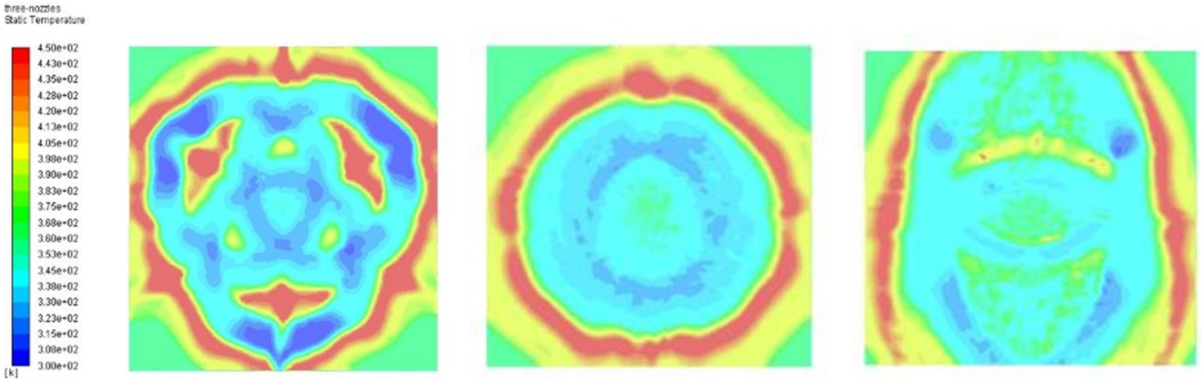

(a) 0° (b) 15° (c) 30°

Fig. 10. Temperature distribution on the bottom surface of three nozzles at different tilt angles.

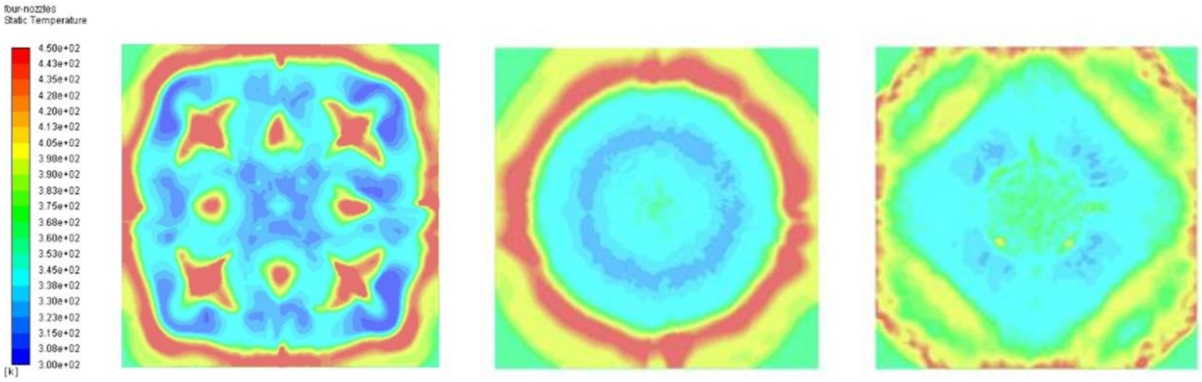

(a) 0° (b) 15° (c) 30°

Fig. 11. Temperature distribution on the bottom surface of four nozzles at different tilt angles.

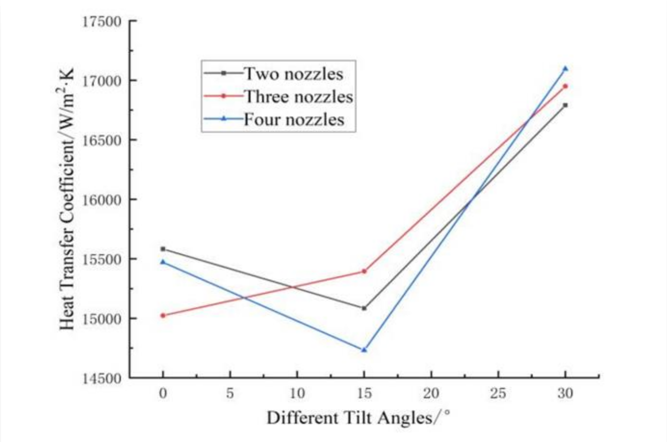

Fig. 12. Heat transfer coefficient curves at different tilt angles.

Table 2. Parameters of the nozzle group at different tilt angles.

Number of nozzles	Tilt angles, °	Average bottom surface temperature, K	Average liquid film temperature, K	Heat transfer coefficient, W/(m²·K)
Two	0	372.37	308.19	15582.54
	15	374.27	307.97	15084.03
	30	369.91	310.36	16790.07
Three	0	374.16	307.59	15023.26
	15	376.54	311.58	15393.46
	30	369.83	310.83	16948.77
Four	0	371.84	307.20	15469.86
	15	380.01	312.12	14731.37
	30	371.15	312.65	17095.22

3.3. Effect of nozzle group spacing

Figure 13 shows the variation of the average temperature on the bottom surfaces of the two, three and four nozzles with different nozzle group spacing. As the nozzle group spacing increases, the temperature of the three and four nozzles first increases and then decreases, while that of the two nozzles always shows a downward trend. This phenomenon can be attributed to significant interference effects between the three and four nozzles at a spacing of 2 mm. When this distance increases to 4 mm, although the coverage area of the spray is expanded, the interference effect will be weakened. Consequently, the average temperature on the bottom surface is observed to increase.

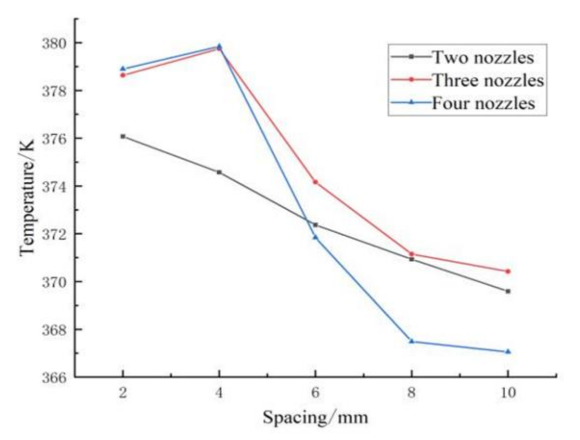

Fig. 13. Temperature curves at different nozzle distance.

Figures 14, 15, and 16 show the average temperature distribution on the bottom surface of configurations with two, three and four nozzles at different nozzle group spacing. At a nozzle spacing of 2 mm, there will be obvious interference between nozzles, resulting in overlapping of spray coverage areas and lower temperatures in the droplet impact zones. As the spacing between nozzles increases by 6 mm, this interference decreases. Consequently, the spray coverage area expands outward, causing a decreased temperature in the regions of strong impact while the temperature in the weak impact regions increases. In addition, the high-temperature region outside the atomization cone transitions from a continuous to discontinuous pattern. When the nozzle group spacing increases to 10 mm, the spray coverage area continuously expands, while the interference region decreases. The overall temperature is also decreasing. Specifically, the temperature in the weak hitting area of the atomization cone decreases, while that in strong hitting areas increases. High-temperature regions outside the atomization cone are concentrated at the upper and lower ends of this area, resulting in a more uniform temperature distribution.

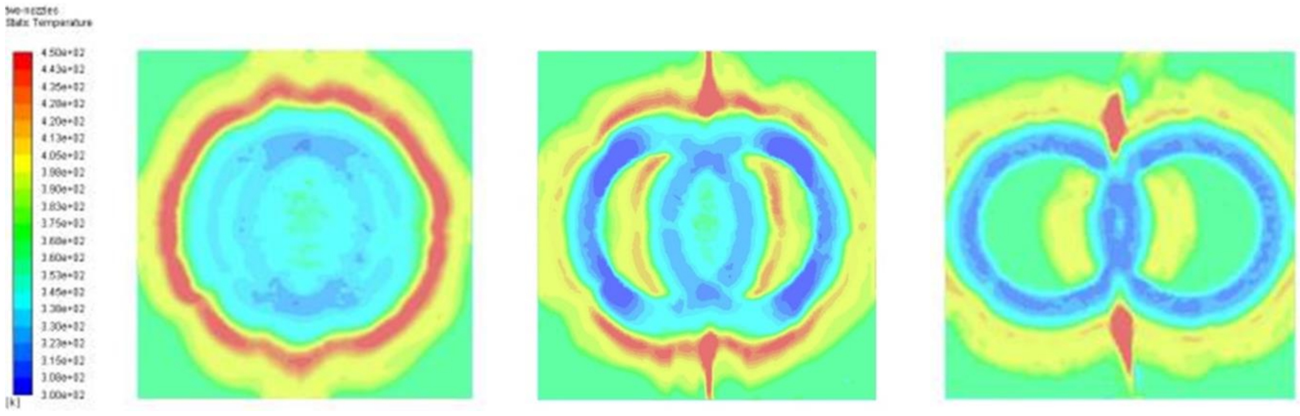

(a) 2 mm (b) 6 mm (c) 10 mm

Fig. 14. Temperature distribution on the bottom surface of two nozzles at different spacing.

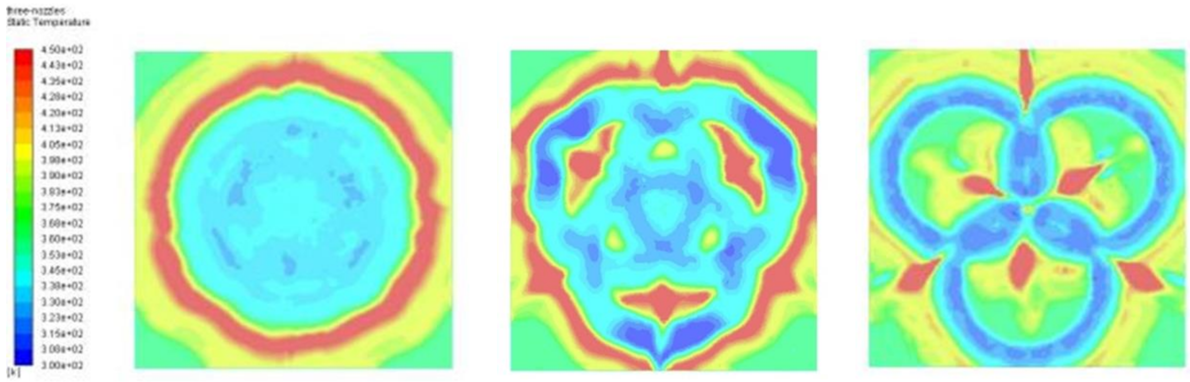

(a) 2 mm (b) 6 mm (c) 10 mm

Fig. 15. Temperature distribution on the bottom surface of three nozzles at different spacing.

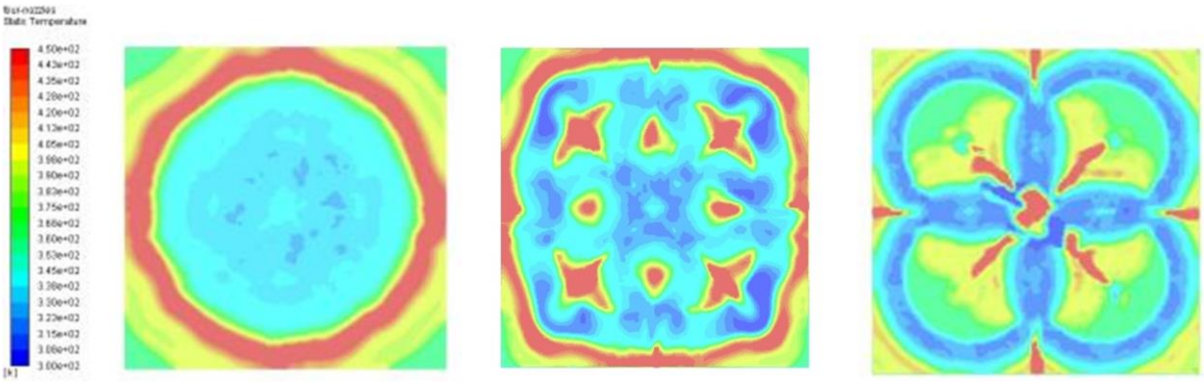

(a) 2 mm (b) 6 mm (c) 10 mm

Fig. 16. Temperature distribution on the bottom surface of four nozzles at different spacing.

As shown in Fig. 17, for two nozzles, the heat transfer coefficient of the bottom surface increases with the nozzle group spacing. In contrast, for three and four nozzles, a decrease is observed at a spacing of 6 mm, followed by a significant increase as the spacing continues to expand. This phenomenon can be attributed to the reduction of interference between nozzles when the spacing reaches 6 mm, which results in a dispersion of the droplet impact area.

However, it is worth noting that although the spray impact area does not fully cover the thermal wall and some liquid film overflows from its boundary, effective heat transfer would still occur at this stage. The temperature on the bottom surface decreases, and the average heat transfer coefficient also decreases. It is worth noting that during the temperature atomization cooling processes, the heat transfer coefficient of the bottom surface exceeds 14 750 W/(m^2·K).

Increasing the nozzle spacing within a specified range can significantly enhance the atomization cooling effect through improving droplet coverage and reducing interference zones, thereby enhancing heat transfer area and efficiency. Table 3 shows the variations of nozzle array parameters at different nozzle spacing.

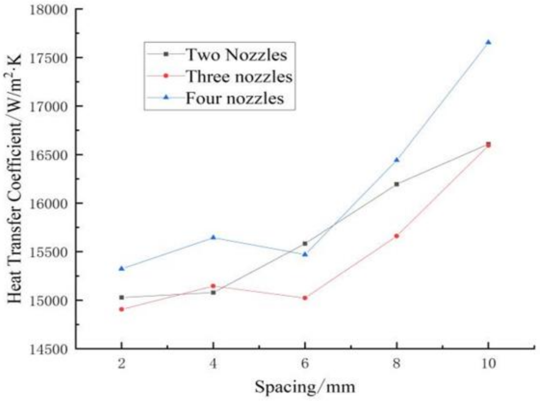

Fig. 17. Heat coefficient curves at different nozzle spacing.

Table 3. Parameters of the nozzle group at different nozzle spacing.

Number of nozzles	Spacing, mm	Average bottom surface temperature, K	Average liquid film temperature, K	Heat transfer coefficient, W/(m^2·K)
Two	2	376.07	309.53	15027.56
	6	372.37	308.19	15582.54
	10	369.59	309.38	16608.27
Three	2	378.63	311.54	14904,62
	6	374.16	307.59	15023.26
	10	370.42	310.15	16593.26
Four	2	378.90	313.63	15322.48
	6	371.84	307.20	15469.86
	10	367.05	310.40	17653.33

This study demonstrates that nozzle pressure, tilt angle and spacing have a significant impact on atomization cooling efficiency. External factors such as ambient temperature and fluid properties should not be ignored. Changes in ambient temperature can affect the evaporation rates of droplets and alter heat transfer efficiency. Moreover, the viscosity and density of different liquids will directly affect droplet size and velocity distribution, which in turn impacts cooling performance. In practical applications, these parameters should be adjusted according to specific operating conditions to optimize the cooling efficiency. Future research should further investigate the influence of these variables to improve the universality and practicality of the model.

4. Conclusions

This study analyses the effects of different pressures, tilt angles and spacing on the bottom temperature, liquid film temperature, liquid film thickness and heat transfer coefficient of the thermal wall of the nozzle array after atomization and cooling. The findings are drawn as follows:

(1) The increase in pressure can significantly improve the heat transfer capacity of the nozzle group. As the pressure increases, the thickness of the liquid film in the high-impact region of the atomization cone decreases. This leads to an increase in liquid film temperature, a reduction in bottom surface temperature, and an increase in heat transfer coefficient.

(2) The tilt angle of the nozzle significantly influences the heat transfer characteristics of the nozzle group. When the tilt angle reaches 30°, the average temperature of the bottom surface decreases, enabling the optimal heat transfer performance of the nozzle group. Under this configuration, a peak average heat transfer coefficient is observed. In addition, the bottom temperature distribution has good uniformity, and the liquid film is elliptical and can effectively reduce the retention areas. Conversely, at a tilt angle of 15°, the heat transfer efficiency of the nozzle group significantly decreases. Although the average temperature within the weak impact area of the atomization cone decreases, this will lead to an increase in the average temperature of the bottom surface and poor atomization cooling effects.

(3) The increase in nozzle spacing can increase the spray coverage area and improve the uniformity of temperature distribution in the nozzle array. When the distance between nozzles is set to 10mm within the range of 2 mm to 10 mm, the heat transfer performance is optimal. However, for the arrays with a limited number of nozzles, increasing the spacing may reduce the interaction between nozzles, which may lead to a decrease in overall heat transfer efficiency.

(4) Increasing the number of nozzles can improve the cooling efficiency of the nozzle array in a certain range. However, this enhancement is limited. In practical applications, economic factors such as costs related to nozzle manufacturing should be taken into account.

The relative impact on the heat transfer efficiency of the nozzle group ranks as: pressure > tilt angle > spacing > number of nozzles. When the nozzle group pressure is 2.0 MPa, the tilt angle is 30°, the nozzle spacing is 10 mm and the number of nozzles is 4, the heat transfer performance of the nozzle group is optimal. The numerical model has provided significant insights for optimizing atomization cooling parameters, and future work should combine experiments to validate these findings. An experimental study conducted under controlled conditions similar to those modelled in this study is crucial for verifying the accuracy and applicability of our results. This experimental validation may involve testing various nozzle configurations, pressures, tilt angles and spacing in real-world environments to ensure the robustness and reliability of our proposed guidelines.

Acknowledgements

This study was supported by the Applied Innovation Project of Hebei Vocational University of Technology and Engineering (No. 202307).

References

[1] Khandekar, S., Jaiswal, A.K., & Sahu, G. (2022). Spray cooling: From droplet dynamics to system level perspectives. *Advances in Heat Transfer*, 54, 135–177. doi: 10.1016/bs.aiht.2022.07.002

[2] Li, W., Zheng, Y., Shao, H., Wang, X., Chen, X., & Gao, Y. (2024). Experimental and Numerical Simulation Studies on the Atomization Characteristics of the Internal Mixing Nozzle and Its Field Application. *Mining, Metallurgy & Exploration*, 41(2), 1099–1120. doi: 10.1007/s42461-024-00955-x

[3] Mertens, R.G., Chow, L., Sundaram, K.B., Cregger, R.B., Rini, D.P., Turek, L., & Saarloos, B.A. (2007). Spray cooling of IGBT devices. *Journal of Electronic Packaging*, 129(3), 316–323. doi: 10.1115/1.2753937ss

[4] Zhang, H., Li, Y., Mao, Y., Tian, S., Liu, Y., & Yang, L. (2015). Optimization Design of a Novel Closed-Loop Spray Cooling System. *2015 IEEE International Conference on Advanced Intelligent Mechatronics*, Busan, Korea (South), IEEE, 324–329. doi: 10.1109/AIM.2015.7222552

[5] Pang, L.P., Luo, K., Guo, Q., Li, S.X., & Yang, C. (2017). Numerical study of high-overload effect on liquid film of spray cooling. *Applied Thermal Engineering*, 127, 1015–1024. doi: 10.1016/j.applthermaleng.2017.07.209

[6] Zheng, D., & Wang, M. (2022). Measurement of spray droplet velocity and size distribution by a tapered optical fiber probe. *2022 IEEE International Instrumentation and Measurement Technology Conference*, Ottawa, ON, Canada, IEEE, 1–6. doi: 10.1109/I2MTC48687.2022.9806586

[7] Majhool, A.A.A.K., & Jasim, N.M. (2020). Prediction of the Initial Drop Size and Velocity Distribution in the Cold Cryogenic Spray. *International Journal of Heat and Technology*, 38(3), 629–640. doi: 10.18280/ijht.380307

[8] Pautsch, A.G., & Shedd, T.A. (2006). Adiabatic and Diabatic Measurements of the Liquid Film Thickness During Spray Cooling with FC-72. *International Journal of Heat and Mass Transfer*, 49(15–16), 2610–2618. doi: 10.1016/j.ijheatmasstransfer.2006.01.024

[9] Selvam, R.P., Hamilton, M., & Silk, E.A. (2007). Spray cooling modeling: liquid film thickness effect on heat transfer. *AIP Conference Proceedings*, 880(1), 110–117. doi: 10.1063/1.2437447

[10] Liu, L., Wang, X., Ge, M., & Zhao, Y. (2021). Experimental study on heat transfer and power consumption of low-pressure

spray cooling. *Applied Thermal Engineering*, 184, 116253. doi: 10.1016/j.applthermaleng.2020.116253

[11] Li, J.X., Li, Y.Z., Li, E.H., & Li, T. (2020). Numerical Investigation on the Thermodynamic Characteristics of a Liquid Film upon Spray Cooling Using an Air-Blast Atomization Nozzle. *Entropy*, 22(3), 308. doi: 10.3390/e22030308

[12] Zhang, Z., Hu, D., Li, Q., Liu, C., & Zhou, F. (2021). Visualization study on atomization characteristics and heat transfer performance of R1336mzz flash spray cooling. *Science China Technological Sciences*, 64(10), 2099–2109. doi: 10.1007/ s11431-021-1853-4

[13] Hsieh, S.S., & Tsai, H.H. (2006). Thermal and flow measurements of continuous cryogenic spray cooling. *Archives of Dermatological Research*, 298(2), 82–95. doi: 10.1007/ s00403-006-0663-3

[14] Sapit, A., Razali, M.A., Mohammed, A.N., Manshoor, B., Khalid, A., Salleh, H., & Hushim, M.F. (2019). Study on Mist Nozzle Spray Characteristics for Cooling Application. *International Journal of Integrated Engineering*, 11(3), 299–303. doi: 10.30880/ijie.2019.11.03.033

[15] Durmuş, A., Durmuş, A., & Esen, M. (2002). Investigation of heat transfer and pressure drop in a concentric heat exchanger with snail entrance. *Applied Thermal Engineering*, 22(3), 321–332. doi: 10.1016/S1359-4311(01)00078-3

[16] Abbasi, B., & Kim, J. (2011). Development of a General Dynamic Pressure Based Single-Phase Spray Cooling Heat Transfer Correlation. *ASME Journal of Heat and Mass Transfer*, 133(5), 052201. doi: 10.1115/1.4002779

[17] Oflaz, F., Keklikcioglu, O., & Ozceyhan, V. (2022). Investigating thermal performance of combined use of SiO_2-water nanofluid and newly designed conical wire inserts. *Case Studies in Thermal Engineering*, 38, 102378. doi: 10.1016/j.csite.2022.102378

[18] Cheng, W.L., Liu, Q.N., Zhao, R., & Fan, H.L. (2010). Experimental Investigation of Parameters Effect on Heat Transfer of Spray Cooling. *Heat and Mass Transfer*, 46(8–9), 911–921. doi: 10.1007/s00231-010-0631-5

[19] Wang, Y., Liu, M., & Liu, D. (2017). Theoretical and Experimental Investigation of Heat Transfer Performance of Spray Cooling Under Low Mass Flux. *Journal of Engineering Thermophysics*, 31(6), 1027–1030. doi: 10.1007/s11630-017-1015-4

[20] Hou, Y. (2019). The Experimental Study and Numerical Simulation of Multi-Nozzle Spray Cooling. *Journal of Engineering Thermophysics*, 40(4), 678–683. doi: 10.1007/s11630-019-1127-7

[21] Muthukrishnan, S., Tan, X., & Srinivasan, V. (2023). High-efficiency spray cooling of rough surfaces with gas-assist atomization. *Applied Thermal Engineering*, 221, 119764. doi: 10.1016/ j.applthermaleng.2022.119764

[22] Liao, Y., Sakman, A.T., Jeng, S.M., Jog, M.A., & Benjamin, M.A. (1999). A Comprehensive Model to Predict Simplex Atomizer Performance. *Journal of Engineering for Gas Turbines and Power*, 121(2), 285–294. doi: 10.1115/1.2817119

[23] Si, C., Shao, S., & Tian, C. (2018). Experimental Study on Integrated Refrigeration-Spray Cooling System for High-Power Solid-State Laser. *Chinese Journal of Lasers*, 38(1), 44–48. doi: 10.3788/CJL20113801.0102008

Co-published by
Institute of Fluid-Flow Machinery
Polish Academy of Sciences
Committee on Thermodynamics and Combustion
Polish Academy of Sciences

http://www.imp.gda.pl/archives-of-thermodynamics/

ARCHIVES OF THERMODYNAMICS

Linear method for the determination of Newton's heat transfer coefficient in the gap under conditions of limited convection

Ewa Pelińska-Olko*, Emilija Zagórska

Department of Thermodynamics and Renewable Energy Sources, Faculty of Mechanical and Power Engineering,
Wroclaw University of Science and Technology, Wybrzeże Stanisława Wyspiańskiego 27, 50-370 Wrocław, Poland
*Corresponding author email: Ewa.Olko@pwr.edu.pl

Received: 21.02.2025; revised: 16.05.2025; accepted: 27.05.2025

Abstract

This study investigates heat transfer under conditions of limited (undeveloped) convection within a narrow 5 cm gap between a centrally positioned heater and the inner walls of a closed chamber. A simplified approach − the linear method − is proposed for estimating Newton's heat transfer coefficient, assuming a weak linear dependence on temperature. Experimental data and known convection models were used to verify the method. The convective component obtained using the linear method was compared to experimental values and theoretical bounds, showing that the linear method slightly overestimates but remains within a valid range. Artificial neural networks supported the estimation of steady-state temperatures and voltages. This work is a continuation of earlier research and confirms the practical value of the linear method in constrained thermal environments. Further development of the experimental rig is planned to expand the study.

Keywords: Limited convection; Gap; Artificial neural network; Newton heat transfer coefficient

Vol. 46(2025), No. 2, 153–165; doi: 10.24425/ather.2025.154914

Cite this manuscript as: Pelińska-Olko, E., & Zagórska, E. (2025). Linear method for the determination of Newton's heat transfer coefficient in the gap under conditions of limited convection. *Archives of Thermodynamics*, 46(2), 153−165.

1. Introduction

Convection refers to the macroscopic movement of fluid molecules—liquids and gases—with specific velocity profiles [1]. It is classified as either natural, driven solely by gravitational forces, or forced, involving additional external forces [2]. The phenomenon arises from the imbalance between buoyancy forces, resulting from temperature-dependent density variations, and viscous forces [3]. Instabilities in the fluid lead to the formation of convective cells, first described by Bénard (see Aubin [3]). Rayleigh-Bénard convection occurs when the lower fluid layers are hotter than the upper ones. Such structures, resembling biological cells, are observed in Newtonian and non-Newtonian fluids, in homogeneous liquids and in nanoparticle suspensions [4]. Nanoparticles added to the base fluid may be metallic, such as Al_2O_3 or Cu [5], or non-metallic, such as SiO_2 [6].

Convection processes occur at both large scales, such as in stellar interiors [7], and in small-scale systems with complex geometries. Applications include nuclear reactor design and electronics cooling systems [8]. Experimental methods, such as the Schlieren technique, which is an optical method, allow for imaging the flow of liquids with different densities [9].

The presence of obstacles can influence the convective flow, modifying the structure of the thermal boundary layer and affecting heat transfer rates above or below a horizontally placed plate [10]. In particular, obstacles below a horizontally placed plate can lead to laminarization and thickening of the boundary

Nomenclature

A – area of surface, m^2
B, C, D, E – constants
Gr – Grashof number
h – Newton's coefficient, $W/(m^2\,K)$
m – number of neurons
Nu – Nusselt number
P – power, W
Pr – Prandtl number
$\dot{Q}$ – heat flux, W
R – electrical resistance, Ω
R^2 – coefficient of determination
$r_{y_{ei}y_i}$ – Pearson's coefficient
T – temperature, K
t – time, s
U – voltage, V

Greek symbols

δ – thickness of a gap, m
ε – relative emissivity coefficient
ε_z – correction factor
λ – thermal conductivity, $W/(m\,K)$
σ – Stefan-Boltzmann constant, $W/(m^2\,K^4)$

Subscripts and Superscripts

b – solid body
f – fluid
ch – chamber
k – convection part
h – heater
r – radiation part
S – using Solver function
tgc – theoretical gap model
toc – theoretical open model

Abbreviations and Acronyms

ANN – artificial neural networks
GNU R – interpreted language
GPL – general public license
HL – hidden layer
IN – input layer
ML – linear method
OUT – output layer
SEM – electromotive force
RMSE – root mean square error
TB – training base

layer, decreasing the heat transfer coefficient [11]. The concept of the thermal boundary layer was introduced by Prandtl and remains essential for understanding convection phenomena. The Prandtl number (Pr) expresses the ratio of momentum diffusivity to thermal diffusivity, with heat conduction dominating within the thermal boundary layer [12].

Scaling effects of convective cells, involving their expansion or contraction with volume changes, significantly impact thermal resistance in engineering structures. Key factors include gap dimensions, wall displacement and temperature differences, which collectively influence convective patterns [13]. Convection in rotating [14] and stationary [15] partitions has been studied experimentally, with results generalized for practical applications [16]. These findings are especially important for industrial systems and modern construction technologies [17].

Given the widespread occurrence and technological significance of natural convection, continued research in this area remains fully justified. Moreover, the development of methods for analysing thermal phenomena on a small scale − particularly in closed or semi-closed spaces − has increased the need for a deeper understanding of heat transport mechanisms in narrow gaps. This is driven by technological demands, as many modern applications tend toward component miniaturization, such as in microelectronics, materials engineering, and the design of advanced passive cooling systems. In such confined geometries, classical convection models often prove insufficient. This further reinforces the relevance and justification of the research topic undertaken in this study.

In the present study, the term 'convection' refers specifically to natural convection in Newtonian fluids, where viscosity depends only on temperature. This work builds upon previous studies involving the experimental determination of the emissivity of black paint to assess the radiative component of the convection coefficient in this study (h_r) [18], as well as the use of artificial neural networks (ANN) for predicting steady-state temperature distributions within the analysed range of heater power [19].

2. Theory

The basic equation describing the phenomenon of heat transfer between a fluid and a solid body is the energy balance equation for a system with a "lumped capacitance model". This model is used under the assumption that the whole body has a uniform temperature, which changes only in time – and not in space (no temperature gradients in the body). In its general form, this equation represents the change in enthalpy of the body, which affects the change in temperature and enthalpy of the body fluid environment, which can be written in the form of Newton's classical equation. After taking into account the radiation from the body to other material bodies, the energy balance has the form known from the literature Eq. (1) [2]:

$$\begin{cases} mc_p\,\dfrac{d\theta}{dt} = hA_h\left(T_h - T_f\right) \\ hA_h\left(T_h - T_f\right) = h_kA_h\left(T_h - T_f\right) + \varepsilon\sigma A_h\left({T_h}^4 - {T_{ch}}^4\right), \end{cases} \tag{1}$$

where: $mc_p \cdot d\theta/dt$ is the enthalpy change of the considered body with mass m and specific heat c_p, and the change in temperature over time measured in its centre $d\theta/dt$; h is the convection coefficient, A_h and T_h are the surface area of the solid body and its surface temperature, respectively; T_{ch} is the average surface temperature of other solid bodies in the environment at temperature T_f, ε – relative radiation coefficient characteristic, for a given material, $\sigma = 5.67 \cdot 10^{-8}\ W/(m^2\,K^4)$ – Stefan-Boltzmann constant.

The upper row of Eq. (1) represents convective heat transfer directly to the surroundings of the body, such as the surrounding air. The symbol h denotes the convection coefficient under these conditions. The lower row presents a heat balance that includes radiative heat transfer to other material bodies located at a considerable distance. Heat, treated as an extensive quantity, is expressed as the sum of the 'pure' convective heat flux, incorporating the convective component of Newton’s coefficient, and the radiative heat flux directed toward distant material objects.

After introducing the assumption that, for good thermal conductors, the internal temperature of the body (θ) is equal to the surface temperature (T_h), Eq. (1) becomes nonlinear due to the presence of the temperature term raised to the fourth power. To linearize it, certain simplifications are applied: the ambient temperature and the temperature of the surrounding bodies are assumed to be similar ($T_h \approx T_f$). Under this condition, the radiation term can be expressed in the form of a convection-like equation, as shown in Eq. (2):

$$\varepsilon\sigma A_h\left(T_h{}^4 - T_{ch}{}^4\right) = h_r A_h\left(T_h - T_f\right), \tag{2}$$

or, after its prior linearization around, e.g., a certain average temperature $T_{av} = (T_h + T_f)/2$, where h_r is described by Eq. (3), [20]:

$$h_r \approx 4\varepsilon\sigma T_{av}{}^3. \tag{3}$$

As its result, the temperature term raised to the fourth power in Eq. (1) disappears. On the other hand, Newton’s coefficient is expressed as the sum of the purely convective component h_k and the radiative component h_r.

Under steady-state conditions, the term involving enthalpy can be calculated as the heat generated by the heat-generating element, as in the case described in the work:

$$mc_p\frac{d\theta}{dt} = UI, \tag{4}$$

where: U, I are the voltage and current intensity, respectively, at the power input of the heat-generating element at a steady state.

In the rest of the article, the term h_k is used to emphasize the purely convective character of Newton’s coefficient.

In the literature, two main models are known that calculate h_k in two extreme cases. The first concerns the situation when a solid body is surrounded by a medium and is in an open, unbounded space. In the second case, the medium is located in a gap between walls at a short distance from each other [21]. The first model describes phenomena in a typical open system. In the second case, the studied space is limited to a narrow, small gap, which may be located in another enclosed space [22]. As reported by the authors [23], both open and closed systems differ not only in their ability to interact with the environment, but also in the type and intensity of thermal phenomena occurring, which is reflected in the values of the coefficients in the equations describing these phenomena. The first model, mentioned earlier, describes the criterion for determining the value of h_k in unbounded space, under free convection conditions as in Eq. (5):

$$\mathrm{Nu} = \mathrm{B}\,(\mathrm{Gr}\cdot\mathrm{Pr})^{\mathrm{C}}, \tag{5}$$

where: Nu, Gr, Pr are the numbers of Nusselt, Grashof and Prandtl, respectively, and B, C are constant coefficients, the values of which are shown in Table 1 [22].

Table 1. B and C constants of the Eq. (5).

B	C	Gr·Pr
1	0	$\mathrm{Gr}\cdot\mathrm{Pr} < 10^{-3}$
1.18	0.13	$10^{-3} < \mathrm{Gr}\cdot\mathrm{Pr} < 500$
0.54	0.25	$500 < \mathrm{Gr}\cdot\mathrm{Pr} < 2\cdot10^{7}$
0.13	0.333	$2\cdot10^{7} < \mathrm{Gr}\cdot\mathrm{Pr} < 10^{13}$

In the case of the gap, rising convection currents from the warmer wall cannot develop freely and come into direct contact with descending currents from the cooler wall. As a result, fluid circulation is not fully developed. The way of heat flow is treated here as heat conduction between walls. The thermal conductivity coefficient, called equivalent λ_z is modified by applying a certain correction resulting from incomplete convection ε_k:

$$\lambda_z = \varepsilon_k\,\lambda, \tag{6}$$

where λ_z is the equivalent heat transfer coefficient, ε_k is the convection coefficient for this case, λ is the heat conduction coefficient for the fluid, for the arithmetic mean of the walls temperatures.

The correction ε_k is calculated from an experimental formula that relates the numbers Gr and Pr as in Eq. (7):

$$\varepsilon_k = \mathrm{D}\cdot(\mathrm{Gr}\cdot\mathrm{Pr})^{\mathrm{E}}, \tag{7}$$

where D and E are constants as in Table 2 [21].

Finally h_k is expressed by the formula:

$$h_k = \frac{\lambda_z}{\delta}, \tag{8}$$

where δ is the thickness of a gap.

Table 2. D and E constants of Eq. (7).

D	E	Gr·Pr
1	0	$\mathrm{Gr}\cdot\mathrm{Pr} < 10^{-3}$
0.105	0.3	$10^{3} < \mathrm{Gr}\cdot\mathrm{Pr} < 10^{6}$
0.4	0.2	$10^{6} < \mathrm{Gr}\cdot\mathrm{Pr} < 2\cdot10^{10}$

These two models for the two extreme cases of convection are described in detail. The authors expected that convection in the gap created between the heater (1) and the inner surface of the chamber (2) on the test rig sketched in Figs. 1 and 2 would not fully develop, and therefore the values of the convection coefficient h_k should be between those calculated in the literature models and the actual values obtained directly from the experiment. The topic was also very interesting due to the so-called scaling of convection cells, described in the introduction. It is not possible to clearly determine whether and how scaling may have occurred; however, the h_k values obtained using the ML model, being closer to reality, should allow for the rejection of some values derived from selected literature models.

3. The test rig

Figure 1 shows the sketch of the rig, along with its basic components.

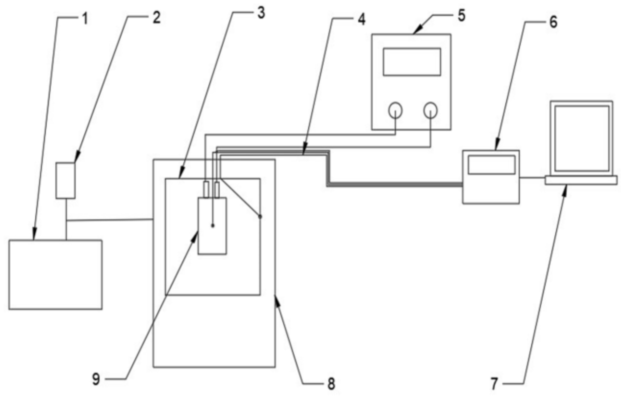

Fig. 1. The sketch of the rig: 1 − vacuum pump, 2 − digital vacuum gauge, 3 − chamber, 4 − thermocouple, 5 − DC power supply, 6 − Keithley multimeter, 7 − computer, 8 − desiccator, 9 – heater.

The experiments took place under dynamic vacuum at a pressure of about 300 Pa (2500 microns Hg). A cubic aluminium chamber along with a rectangular heater at its geometric centre, was placed in a desiccator that was connected to a vacuum pump. The chamber had an inner side that was 14 cm long. The heater had dimensions of 3 cm × 3 cm × 4 cm. The average resistance of the heater at 20ºC was 9,6677621 Ω and the resistance of the cables connecting the heater at this temperature was 0,037 Ω.

Data from the rig were collected using the Keithley multimeter (hereafter referred to as the meter), which provided relatively accurate readings of the output signals in the form of resistance or voltage.

Figure 2 shows an axonometric mapping of the interior of the chamber, including the heater with external surface area A_h and temperature T_h (1), inner surface of the chamber with area A_{ch} and temperature T_{ch} (2). The gap, which is mentioned in the work topic, is created between the heater (1) and the inner surface of the chamber (2). In the gap, there is a fluid with temperature T_f. The black dots (3) mark the location of the thermocouples. Chamber (2) in Fig. 2 corresponds to position 3 in Fig. 1, which is located in the desiccator (8) in Fig. 1.

Thermocouples 1 and 3 are located at the intersection of the diagonals of the respective walls of the heater. Thermocouples 2 are located about 5 mm horizontally and 10 mm vertically from the edge of the heater wall. Thermocouples 4 and 5 located on the chamber wall are parallel to thermocouples 1 and 2. Thermocouple 6 is placed loosely in the space between the heater and the chamber wall and measures the temperature of the air in the chamber.

The temperature of the free ends of the K-type thermocouples was measured using a PT1000 sensor [24,25]. This was a class A sensor, so its tolerance is ± 0.15ºC for the temperature range tested [26]. As for the thermocouples themselves [27], their tolerance in the range of tested temperatures was due to their initial calibration against each other. In addition, they were verified against PT100 [28]. They were assumed to have an accuracy of 0.2 K [29].

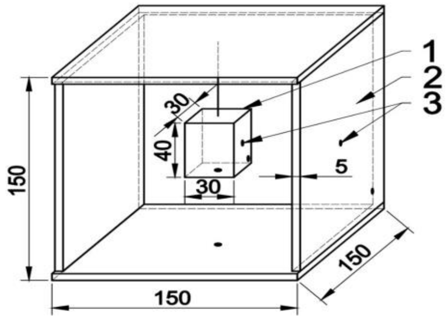

Fig. 2. Axonometric mapping of the interior of the chamber (2) including the heater (1) and temperature measurement locations (3). The gap is created between the heater (1) and the inner surface of the chamber (2) [18].

All temperature sensors were calibrated before the actual measurements.

The complete measurement cycle included reaching steady-state conditions at selected measurement points, including the stage after air evacuation, for a given heater power level. The test measurement time ranged between approximately 3−6 hours depending on the measurement series. However, this study focused exclusively on the phenomena occurring up to the activation of the vacuum pump, i.e. on phenomena involving only convection.

The quadratic approximation of the K-type thermocouple characteristic [30], in the form of Eq. (9), was used to convert the voltage signal in mV from the meter to degrees Celsius.

$$T = -0.1412 \cdot SEM^{2} + 24.9231 \cdot SEM + 0.1462, \tag{9}$$

where: T is the temperature value expressed in ºC, SEM is the electromotive force value measured on the thermocouple in mV.

The detailed design of the experimental setup, along with more extensive descriptions, is presented in previously published works [18] and [19]. Each of these studies addresses distinct physical phenomena and targets different research objectives. Paper [18] focuses on the determination of the relative emissivity coefficient of black paint, essential for further analyses, under dynamic vacuum conditions at a pressure of 300 Pa. For the purposes of the present investigation, a value of 0.97 ± 0.03 for this coefficient (h_r) was adopted. Paper [19] discusses the use of an artificial neural network (ANN) to predict transient temperature responses and to assess the accuracy of steady-state (far-future) temperature distributions obtained during the heating process of a black-paint-coated heater, under power ranges corresponding to those employed in the current experiments. In contrast, the present study is devoted to the analysis of heat transfer in a gap under conditions of undeveloped convection.

3.1. The test results

As a result of temperature measurement at selected points of the test rig, a number of temperature characteristics changing over time were obtained. An example plot of SEM in mV versus time is shown on Fig. 3.

Figure 3 consists of two parts. The first part, lasting up to approximately 4000 seconds (up to point P), presents the temperature evolution under convection conditions within the gap formed between the surfaces of the heater and the chamber, at all monitored points. The second part, after point P, shows the temperature changes under near-vacuum conditions, after the air has been evacuated, where heat transfer occurs via electromagnetic radiation. At this stage, the Newton coefficient decreases by the purely convective component, which impedes heat transfer in the region. The minimum amount of data for the so-called ANN Training Base (TB) is determined by the tangent method and is indicative – it contains data up to point A. The actual length of TB is longer and contains data up to point P.

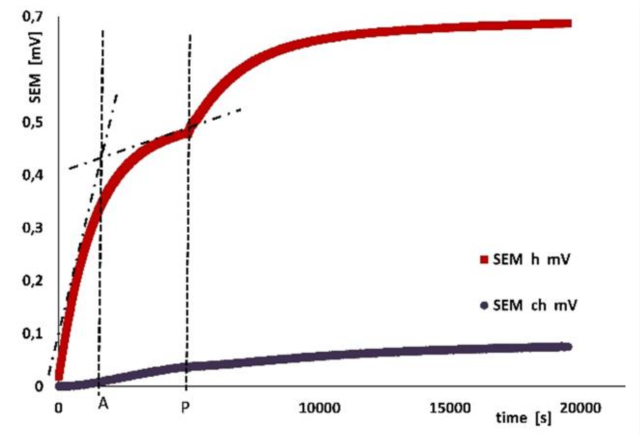

Fig. 3. Evolution of temperature over time as measured by thermocouples in mV on the heater – SEM h mV (top line), and on the inner surface of the chamber – SEM ch mV (bottom line). Point A on the OX-axis determines the minimum amount of training data for ANN returning the temperature value in steady states, point P – the actual amount of data constituting two so-called Training Bases.

3.2. Application of Artificial Neural Networks for the determination of selected steady-state temperature values

Figure 3 refers to the temperature evolution during the entire measurement cycle, as mentioned. The part that is the subject of this work covers the time from the beginning of the cycle to point P, where the vacuum pump was activated. The data up to the mentioned point P form TB for ANN, which included between 3.8 and 4.5 thousand data points recorded by the meter approximately every 3−6 seconds for all experiments. During the studies [19], it was determined that ANN was able to reproduce the curve $T = f(t)$ and predict the steady-state value of this function with relatively good accuracy, notably faster, approximately up to point A, determined for example using the tangent method (as shown in the figure). In this case, TB was significantly larger, which provides greater confidence that the values predicted by ANN relate to the sought steady-state temperature.

Figure 4 shows only the experimental data up to point P, which constitute TB. The temperature graphs are very predictable, with no distortions, so the chosen ANN may have had a very simple architecture.

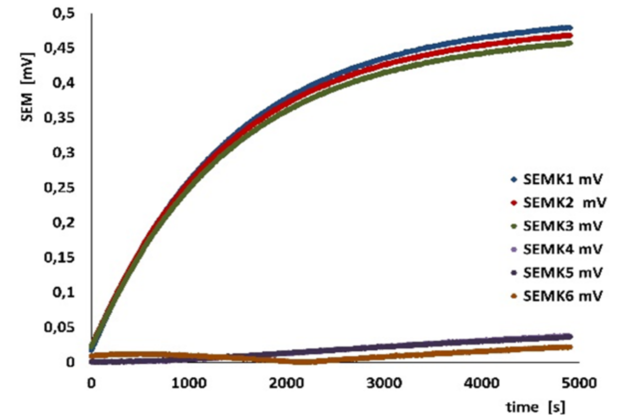

Fig. 4. Example training dataset for ANN. The data set at each monitored measurement point (1, 2, 3, 4, 5, 6) was free from significant noise and unexpected signal distortions, making a simple ANN architecture sufficient for effective learning, without the need for more advanced solutions such as Wavelet Neural Networks (WNN) or similar methods.

In this case, ANN was used to determine the steady-state temperature values [30], which − compared to the latest available experimental data at point P − differ by no more than 0.5–0.8 K across all convection-related experiments. The ANN used in this study [31] had a simple architecture: one neuron in the input layer (IN), several or a dozen neurons in the hidden layer (HL), and one neuron in the output layer (OUT). In general, the hidden layer may contain *m* neurons, and their number is typically selected by trial and error [32]. The network employed the backpropagation error algorithm [33]. Its principle is based on detecting an error, defined as the difference between the output signal from a given layer and the reference signal from the training sequence. This error is then corrected by adjusting the so-called weights, which are back propagated to all neurons providing input to the neuron where the error was detected.

A proprietary program based on the *nnet* package, integrated with the R programming language, was used in the study. The GNU R language belongs to the group of interpreted languages, and its source code is distributed under the GNU-GPL license [34]. This code is compatible with Excel spreadsheets.

Using ANN, the steady-state values of temperature expressed in mV (SEM) and the voltage at the terminals of the heat-generating element were ultimately determined. As demonstrated in [19], for simple functions − such as the temperature rise function during heating − using an ANN with a simple (IN-HL-OUT) structure allows for rapid prediction of the steady-state value with an accuracy of up to 0.03 K. The number of neurons (m) in the hidden layer should be at least $m = 6$ [33]. The length of the constructed TB is crucial for the learning process of the network and its sensitivity to disturbances in input data, which results from the nature of the backpropagation algorithm [35].

It is assumed that the steady state of the temperatures on the heater and the inner surface of the chamber is the state in which the temperature change rate at the designated points is less than 0.03 K/h. The number of neurons in the hidden layer was selected by trial and error, using statistical criteria.

3.2.1. Statistical functions for evaluating ANN data

One of the statistical techniques is regression analysis, which allows for determining the relationships between variables. In this case, the variables are the values returned by ANN for a specific subset of data, compared with their corresponding experimental data values. Pearson's coefficient is a tool that allows for the evaluation of whether there is a strong correlation between these quantities or not. A high correlation, i.e. a coefficient value close to 1, indicates that ANN accurately represents the real values. A low correlation, such as a value close to zero, suggests a poor fit of the model to the data. For this reason, Pearson's coefficient ($r_{y_{ei}y_i}$) in Eq. (10) and the commonly used root mean square error (RMSE) in Eq. (11) [36] were used to optimize the number of neurons in the hidden layer (HL)

$$r_{y_{ei}y_i} = \frac{\sum_{i=1}^{n}(y_{ei}-\overline{y_e})(y_i-\bar{y})}{\sqrt{\sum_{i=1}^{n}(y_{ei}-\overline{y_e})^2}\sqrt{\sum_{i=1}^{n}(y_i-\bar{y})^2}}, \tag{10}$$

$$RMSE(m) = \sqrt{\frac{\sum_{i=1}^{n}(y_{ei}-y_i)^2}{n}}, \tag{11}$$

where: y_{ei} – consecutive data from the experiment at the measurement point recorded in the i-th cell of the sheet, y_i is the corresponding value returned by ANN, $\overline{y_e}$ is the arithmetic mean value of experimental data, $\bar{y}$ is the arithmetic mean value of the results returned by ANN, n – the number of measurement data, m – the number of neurons.

As mentioned before, the selection of the best number of neurons was determined by the minimum value of RMSE and $r_{y_{ei}y_i}$ close to one. Tables 3 and 4 show an example comparison of the results obtained using ANN depending on the results of the selected functions.

Table 3. Example of optimization of the number of neurons *m* in HL based on the criteria of regression analysis for heater surface temperature.

m	$r_{y_{ei}y_i}$	RMSE	$T_{h\mathrm{ANN}}$, ^{0}C
25	0.9999977	0.000345	38.37
28	0.9999977	0.000349	38.06
30	0.9999978	0.000343	38,02

Table 4. Example of optimization of the number of neurons *m* in HL based on the criteria of regression analysis for inner chamber surface temperature.

m	$r_{y_{ei}y_i}$	RMSE	$T_{ch\mathrm{ANN}}$, ^{0}C
25	0.9378	0.00231	21.42
28	0.9986	0.00033	21.54
30	0.8287	0.00450	21.22

The columns devoted to the heater and the inner surface of the chamber contain, from the top, the number of neurons *m* in HL, RMSE and Pearson's coefficient values. In the last column, there is the temperature on a given surface in the far future, in steady states calculated by ANN with the mentioned number of neurons *m* in HL: $T_{h\mathrm{ANN}}$ on the heater and $T_{ch\mathrm{ANN}}$ on the inner surface of the chamber.

The best criterion fits were obtained for the heater: $m = 28$ and 30, and for the inner surface of the chamber: $m = 28$ and 25.

For ANN, the type of physical parameter whose value is to be determined is not important; only the quantity and quality of the data on which the network is trained matter. Figure 5 shows an example of graphs of temperature evolution in the form of the experimental dependence of SEM in mV on time and the response of ANN as it reaches its steady state, for the heater and for the inner surface of the chamber.

ANN was appropriately optimized by selecting the number of neurons *m*. Here, the selected number of neurons in the hidden layer (HL) was $m = 28$ (heater) and $m = 25$ (chamber). The thicker line represents the experimental data that constitute the training databases (TBs) for ANN, up to point P (Fig. 3).

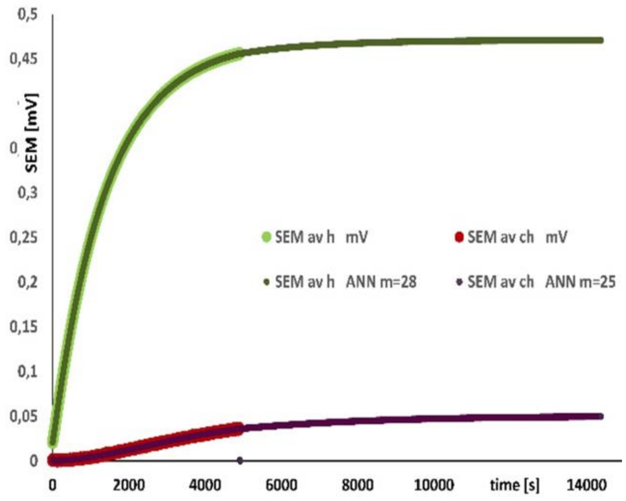

Fig. 5. Responses of ANN with an optimized number of neurons *m*, showing the evolution of temperature to its steady state value: for a higher heater temperature and a lower temperature on the inner surface of the chamber (thin lines in both mentioned cases). Training bases for ANN are indicated by bold lines.

As for the accuracy of the obtained RMSE and Pearson's coefficient values, they are shown with a large decimal expansion in Tables 3 and 4. The goal was to determine as accurately as possible which number of neurons in the hidden layer is most optimal.

Similarly, ANN was also used to determine the steady-state voltage at the heater terminals. Experimental data (thicker line) and ANN responses for $m = 28$ in HL are shown in Fig. 6. Compared to the latest available experimental data at point P, the values differ by no more than 6 mV across all convection-related experiments.

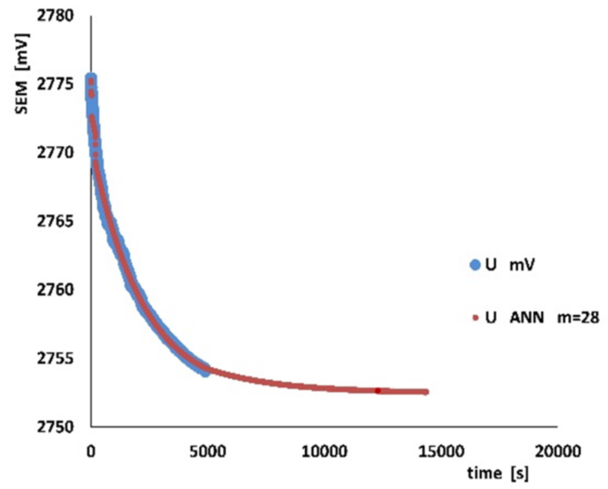

Fig. 6. Responses of ANN with an optimized number of neurons *m* determining the voltage on the heater in the steady state. Training bases for ANN are indicated by bold lines.

The computational power in further calculations was determined based on the steady-state voltage value returned by ANN and the average value of the heater resistance as in the formula in Eq. (12):

$$P = U^2/R, \tag{12}$$

where: P – the power of the heater, U – the value of the steady-state voltage returned by the ANN, R – the average resistance of the heater over the considered temperature range.

The heat flux dissipated by the heater has been reduced by the losses at the test rig as in Eq. (13):

$$\dot{Q} = P - \dot{Q}_\lambda - \dot{Q}_v, \tag{13}$$

where: $\dot{Q}$ is the heat flux dissipated by the heater in the chamber, $\dot{Q}_\lambda$ – heat flux losses conducted through the thermocouple wires connecting the heater to the meter, $\dot{Q}_v$ – enthalpy flux losses.

Thermal losses denoted as $\dot{Q}_\lambda$ are associated with the temperature gradient along the thermocouple wires and compensating leads, as well as with convection around the chamber in the desiccator environment $\dot{Q}_v$. These losses resulted from the routing of the measurement wires − from the test chamber, through the desiccator, and further to the measuring device located outside the desiccator.

In the experiment, six type K thermocouples were used, each with a diameter of 0.15 mm and a length of 1.2 m. The thermal conductivity coefficient was assumed to be λ = 20 W/(m K). Three of the thermocouples were used to measure temperatures of up to approximately 100°C, while the remaining three operated in the range of up to 30°C. Due to the unavailability of dedicated compensating cables (e.g. of type KX), 1.5 m long extensions were made using copper wires (λ = 400 W/(m K)) of the same diameter (0.15 mm), routed outside the desiccator. The temperature drop along the section outside the desiccator was estimated to be up to 10°C.

For twelve copper conductors (accounting for two leads per thermocouple), the estimated total thermal losses amounted to approximately $\dot{Q}_\lambda$ = 0.105 mW. In comparison, the heat power dissipated by the heater, calculated using Eq. (12), was approximately 5 W. For similar temperature conditions on the heater, chamber and outside the desiccator, the value determined using the method of total differential was characterized by an uncertainty of approximately 1.5 mW.

Therefore, it was concluded that the thermal losses $\dot{Q}_\lambda$ were negligible in this case.

Similarly, the temperature of the outer surface of the desiccator was comparable to the ambient temperature.

For this reason, both loss values: $\dot{Q}_\lambda$ and $\dot{Q}_v$ were neglected, and this way: $\dot{Q} = P$.

Nevertheless, considering future research and the potential need for higher measurement precision, these regions were identified as possible sources of uncertainty worth addressing in subsequent analyses.

Table 5 summarizes the steady-state temperatures returned by ANN with respect to the heat flux dissipated by the heater ($\dot{Q} = P$).

Table 5. Steady-state temperatures on the heater and on the inside surface of the chamber returned by ANN.

$\dot{Q}$, W	T_{hANN}, °C	ΔT_{hANN}, K/h	T_{chANN}, °C	ΔT_{chANN}, K/h	T_o °C
0.218	25.72	0.012	22.34	0.029	21.84
0.769	29.09	0.002	18.64	0.011	17.25
1.340	38.02	0.006	21.54	0.028	19.82
1.374	35.68	0.028	19.07	0.003	16.88
2.096	45.63	0.001	20.7	0.031	17.11
5.113	74.06	0.005	26.17	0.030	19.36

From left: $\dot{Q}$ – dissipated heat flux, T_{hANN} – steady-state heater temperature returned by ANN and $\Delta T_{hANN} = f(\tau)$ being the rate of its increase over time τ, T_{chANN} – steady-state chamber surface temperature returned by ANN and $\Delta T_{chANN} = f(\tau)$ being the rate of its increase over time, T_o – ambient temperature.

4. Linear method for determining the Newton’s coefficient

The linear method (ML) for determining Newton’s coefficient proposed in this work assumes its linear change with temperature, according to Eq. (14)

$$h_S = h_0 + \beta T, \tag{14}$$

where: h_S is the so-called “total” Newton’s coefficient, containing both radiative and convective parts, determined by the ML method using the Solver function, h_0, β are constant, T is the temperature at the given location.

The only inconvenience in ML is the need to solve a system of several equations, where some solutions can only be approximate. For this purpose, the Solver function available in the Excel spreadsheet was used.

Solver is included by default in every office suite. It is integrated with Excel, which means that no external programs or coding are required. It works like a mini-math engine. Solver uses numerical methods such as Simplex LP, GRG Nonlinear, or Evolutionary Solver. It handles nonlinear problems, constraints, and integers well. It helps solve various computational problems where no simple formula exists. It works by iteratively finding the best result for a selected cell, manipulating others until it meets the conditions.

Solver was used here to optimize the thermodynamics and heat transfer problem [37]. As shown in [38], the optimized Excel can successfully support optimization analyses of a similar type as in the article, but also in other areas of thermal technology, including recuperators.

The unknowns here are the temperatures prevailing in the space between the heater and the inner surface of the chamber T_{S1}, T_{S2}, and the constants h_0, β, which can be found from the system of equations with a unique solution:

$$\begin{cases} \dot{Q}_1 = A_h(h_0 + \beta T_{h1})(T_{h1} - T_{S1}) \\ \dot{Q}_1 = A_{ch}(h_0 + \beta T_{ch1})(T_{ch1} - T_{S1}) \\ \dot{Q}_2 = A_h(h_0 + \beta T_{h2})(T_{h2} - T_{S2}) \\ \dot{Q}_2 = A_{ch}(h_0 + \beta T_{ch2})(T_{ch2} - T_{S2}) \end{cases}, \tag{15}$$

where: $\dot{Q}_1$, $\dot{Q}_2$ are heat flux dissipation by the heater in the 1st or 2nd measurement, A_h and A_{ch} are the heater surface and the internal surface of the chamber, respectively, h_0 and β are constants from Eq. (14). T_{h1}, T_{h2} and T_{ch1}, T_{ch2} are experimental temperatures of the heater and the inner surface of the chamber in the 1st or 2nd measurement. T_{S1}, T_{S2} are the temperatures in the gap between the heater and the chamber returned by Solver, the average of which corresponds to the temperature of the heater surroundings.

To solve the system of Eq. (15), data from the two closest series of measurements with similar temperatures resulting from similar experimental powers were selected. The total surface areas for the heater and chamber are: A_h = 0.008996 m^2 and A_{ch} = 0.11745 m^2 [18]. The objective function used in Solver is the sum of squares, the unknowns being T_{S1}, T_{S2}, h_0, β. It is assumed that the value of β should be positive, but not zero, while h_0 can be zero. In this way, Newton's coefficient always increases with increasing power. Finally, from each case of power, two values of Newton's coefficient were calculated for the layer near the heater h_{hs} and for the layer near the inner surface of the chamber h_{chs}. The total value of coefficient h_s is the arithmetic average for a given series of measurements and the temperature in the gap T_S calculated by Solver is the arithmetic average of T_{S1}, T_{S2}. The results are shown in Table 6.

Table 6. Newton's heat transfer coefficient and gap temperature values calculated using the Solver function in ML.

$\dot{Q}$, W	T_s, °C	h_{hs}, W/(m²K)	h_{chs}, W/(m²K)	h_s, W/(m²K)
0.218	22.24	7.46	7.45	7.45
0.769	17.2	8.16	7.99	8.08
1.340	20.69	9.47	8.97	9.22
1.374	18.22	10.02	9.48	9.75
2.096	19.85	11.72	11.30	11.51
5.113	25.33	12.83	12.82	12.82

4.1. Comparison of experimental results for different theoretical models

Based on the known relative emissivity of the black paint ε, the radiative component of the heat transfer coefficient h_r was calculated using Eq. (2).

Subsequently, the total heat transfer coefficient h was determined from experimental data using Eq. (1). By subtracting the radiative component h_r, from the total value of h, the convective part of the Newton heat transfer coefficient h_{ke} was directly determined from the experiment.

Using Eq. (5), the convective part of Newton's coefficient calculated in the open model h_{ktoc} was calculated.

The gap thickness is assumed to be the distance between the heater surface and the inner surface of the chamber, which is 5.5 cm. Using Eqs. (6)−(8), the convective part of Newton's coefficient in the gap model h_{ktgc} was calculated.

On the other hand, the convective part of Newton's coefficient h_{kS} in the proposed ML method was calculated according to Eq. (15), as the difference between the Newton's coefficient determined using the Solver function in Eq. (14) h_S and the radiative component h_r (Eq. (2))

$$h_{kS} = h_S - h_r, \tag{16}$$

where: h_{kS} and h_S are the convective part of Newton's coefficient and its total value in ML, respectively.

Table 7 presents the values of the convective parts of Newton's coefficient for selected theoretical models and compares them with the values obtained in ML and the experimental values, accurate to the second decimal place. From left: convective part of Newton's coefficient obtained experimentally h_{ke}, convective part of Newton's coefficient obtained in ML h_{kS}, convective part of Newton's coefficient calculated in the gap model h_{ktgc}, convective part of Newton's coefficient calculated in the open model h_{ktoc}.

Table 7. Comparison of the convective parts of Newton's coefficient under limited convection conditions from the experiment with its values from different models.

$\dot{Q}$, W	h_{ke}, W/(m²K)	h_{kS}, W/(m²K)	h_{ktgc}, W/(m²K)	h_{ktoc}, W/(m²K)
0.218	1.33	1.75	1.33	4.34
0.769	1.78	2.39	1.85	5.77
1.340	2.72	3.32	2.11	6.41
1.374	2.99	3.71	2.12	6.42
2.096	3.58	5.26	2.37	7.05
5.113	4.28	5.46	2.81	8.14

In Fig. 7, it can be seen that the values of the convective part of Newton's coefficient obtained experimentally h_{ke} and calculated from ML h_{kS} lie between their counterparts from the open and gap model.

Figure 7 illustrates that the analysed relationship is generally satisfied, with the exception of the first and second positions from the origin of the coordinate system, which correspond to the lowest tested power levels: 0.218 W and 0.769 W. In these specific cases, the experimental values of the Newton heat transfer coefficient (h_{ke}) closely match those obtained using the gap model (h_{ktgc}) whereas the values predicted by ML are consistently higher than the actual measured values.

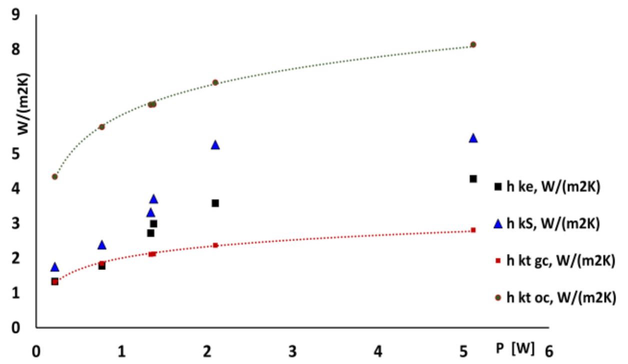

Fig. 7. Validation of the ML model based on comparison of the convective part of Newton’s coefficient h_{ke} as a function of (here) heater power P. Experimental data are compared with values obtained from the ML model (h_{kS}), the gap model (h_{ktgc}), and the open model (h_{ktoc}). Slightly higher ML predictions confirm the presence of convection suppression in the gap.

For all other cases − particularly those involving higher power levels − a clear convergence is observed between the experimental data and the values predicted by the ML model. Notably, the ML-based estimations tend to approach the arithmetic mean of the results derived from the two classical models commonly cited in the literature.

In general, slightly higher ML predictions confirm the presence of convection suppression in the gap.

Nevertheless, the ML approach appears to offer a relatively simple yet more accurate means of estimating the Newton heat transfer coefficient across the tested power range of the heater.

5. Overview of materials, methods and measurement uncertainties

In terms of the applied methods, the study was divided into an experimental part and a computational part, utilizing numerical software, including an ANN and the Solver module. The work is a continuation of previous research concerning the determination of the relative emissivity coefficient of black paint. The value of this coefficient is one of the key parameters used to determine the convection coefficient in the gap.

The research method described and applied in “Emissivity measurement of black paint using the calorimetric method” [18] was the calorimetric method, which requires maintaining the system, both internally and externally, in stable conditions for a relatively long period to obtain appropriate parameters in steady-state conditions, i.e. states in the distant future. Such procedures are generally time-consuming and expensive, which is a drawback of this method. On the other hand, all values of material constants are typically determined under steady-state conditions due to their stability and the precisely defined physical conditions under which they are determined. Papers [18] and [19] describe and illustrate in detail the construction of the experimental setup. Figure 2 of this paper presents an axonometric mapping of the chamber’s interior, including the heater’s location and temperature measurement points, taken directly from [18], along with the main dimensions of the chamber placed in the desiccator (8), in accordance with the sketch of the test rig (Fig. 1).

Since the time required to reach a steady state in convection conditions should be significantly shorter due to the faster stabilization of temperature, and one research cycle included both the temperature evolution at selected locations under convection conditions and in a vacuum (after air evacuation from the chamber), there was uncertainty whether the system actually reached the required steady state in its first stage, i.e. under convection conditions, necessary for determining steady-state convection coefficients. The criterion for achieving a steady state was a temperature change of less than 0.03 K per hour.

To verify whether the experimentally measured temperatures at selected points corresponded to their steady-state values, an ANN was used. The network architecture included: 1 neuron in the input layer, m neurons in the hidden layer (selected by trial and error), and 1 neuron in the output layer, as described in “Numerical prediction of steady-state temperature based on transient measurements” [19]. Due to its simplicity, this architecture is commonly used to predict values in the so-called distant future (steady states).

Here, two data analysis methods were used: ANN and the least squares approximation method, to predict steady-state temperature values based on short-term measurements. It was found that in the case of heater heating functions in the chamber, ANN was able to predict steady-state temperature values after only about one-third of the experiment time required by the classical calorimetric method. Thus, the use of ANN effectively reduced the duration of the experiments.

The ANN program was written in R, version 3.4.2 (X86 = 64-in 64-mgw32/x64), using the nnet library, which contains the Fit Neural Network module. Due to ANN’s compatibility with Excel, the Solver module was also used to solve systems of equations with four unknowns, characterized by its ease of use and wide availability.

The values of the Newton coefficient h_{kS} calculated in ML were then compared with values obtained using two literature models mentioned in this work and derived from experiment h_{ke}. These models describe: natural convection in an open system, allowing full development of convection in an unbounded space, and in a gap-type system, suppressing its mechanisms.

The value of the relative emissivity coefficient of black paint, along with the error of the method, is presented in [18]. The obtained values ranged from 0.958 ±0.07 to 1.049 ±0.102. Assuming that the relative emissivity coefficient should not exceed 1, values greater than 1 were excluded from further calculations. The overestimation of the coefficient resulted from the very low power of the heater, which led to relatively large measurement errors. The average value of the coefficient, after rejecting the overestimated values, was 0.97 ±0.03, and this value was used for further calculations. Determining its value was a necessary step in calculating the radiative part of h_r (Eq. (2)).

The length of the elements needed to determine surface areas was measured using a precise micrometer, with a reading error of 0.01 mm and a systematic error of 0.001 mm. A measurement error of ±0.000011 m was adopted. The ambient temperature was measured using a PT100 sensor, with an accuracy of ±0.2 K.

Type A thermocouples, calibrated against each other and verified against the PT100 sensor, also had an accuracy of ±0.2 K.

Voltage was measured using a Keithley Model 2000 multimeter, capable of measuring DC voltage up to 100 mV, AC voltage up to 10 V, and resistance up to 100 Ω. In the range of up to 100 mV, the basic accuracy was 0.0035% + 0.0002, which did not significantly affect thermocouple temperature measurements, as the additional error in the 0–100°C range was below 15.3 mK (0.015 K).

The heater supply voltage, required for calculating the design power, was measured with an accuracy of ±1 mV (0.001 V).

The resistance of the heater at ambient temperature was measured up to 100 Ω and was 9.667621 Ω. After accounting for the resistance of the measurement leads, the total resistance was 9.70472 ±0.00084 Ω. The heat stream from Eq. (12) was calculated with an uncertainty of about 1 mW.

For illustrative purposes, additionally, the heater power was also estimated based on power supply readings, with an accuracy of 0.1 W.

The absolute uncertainty in determining h_r using the total differential method (based on Eq. (2)) consists of the corresponding partial uncertainties associated with the respective differentials, as shown below:

$$\begin{cases} \frac{\partial h_r}{\partial T_h} = \frac{\varepsilon\sigma(4{T_h}^3)}{T_h - T_f} - \frac{\varepsilon\sigma({T_h}^4 - {T_{ch}}^4)}{(T_h - T_f)^2} \\ \frac{\partial h_r}{\partial T_{ch}} = -\frac{\varepsilon\sigma(4{T_{ch}}^3)}{T_h - T_f} \\ \frac{\partial h_r}{\partial T_f} = -\frac{\varepsilon\sigma({T_h}^4 - {T_{ch}}^4)}{(T_h - T_f)^2} \end{cases}. \tag{17}$$

Since all temperatures were measured with an accuracy of ±0.2 K, and after calculating and summing all partial uncertainties, the total uncertainty of the determined h_r within the examined range is approximately 0.3 W/(m²·K) on average.

Similarly, the partial derivatives for calculating the uncertainty h are calculated based on a modified Eq. (1), due to the steady state on the heater, Eq. (18):

$$\begin{cases} \frac{\partial h}{\partial \mathrm{P}} = \frac{1}{A_h(T_h - T_f)} \\ \frac{\partial \mathrm{h}}{\partial A_h} = -\frac{P}{{A_h}^2(T_h - T_f)} \\ \frac{\partial h}{\partial T_h} = \frac{P}{A_h(T_h - T_f)^2} \\ \frac{\partial h}{\partial T_f} = -\frac{P}{A_h(T_h - T_f)^2} \end{cases}, \tag{18}$$

The average uncertainty of h in the examined range is approximately 0.2 W/(m²·K), with the highest value about 0.4 W/(m²·K) occurring at the lowest heat flux dissipated by the heater. The average uncertainty of the difference $h - h_r$, treated as the square root of the sum of squares of the individual components, is 0.36 W/(m²·K).

In the context of using ANN and Solver, the classical understanding of measurement accuracy − referring to instrument limitations, tolerances or random conditions − becomes less relevant. Instead, the concept of prediction accuracy or numerical solution accuracy becomes crucial. In the case of ANN, the model quality was assessed using the root mean square error (RMSE) and the Pearson correlation coefficient, whose values are presented in Tables 2 and 3. For Solver, it was expected that the final result would fall between values determined according to the models describing natural convection in an open system and in a gap system.

6. Reconstructing the rig with a view to further research

In this article, the simple formula of ML in the form of Eq. (14) is analysed for the "total" Newton coefficient.

Now a formula is proposed as in Eq. (19) for its convective part only (h_k):

$$h_k = h_0 + \beta T, \tag{19}$$

Research should be continued in two directions:

1. Analysis of the damping effect of the gap geometry (i.e. reduction of its thickness and/or height),
2. Investigation of the influence of temperature difference on convection enhancement.

In reality, both mechanisms interact and partially cancel each other, so the experimental rig should be reconstructed to quantitatively and qualitatively determine their interplay.

6.1. Idealized model "Nusselt sphere"

In the first conceptual approach, it is proposed to use the idea of the "Nusselt sphere," where the gap of thickness L is formed between two concentric spheres with radii, respectively: R_h − radius of the heater (inner sphere), with external surface area $A_h = 4\pi R_h^2$, R_{ch} − radius of the chamber (outer sphere), with internal surface area $A_{ch} = 4\pi R_{ch}^2$:

$$R_{ch} - R_h = L. \tag{20}$$

Temperature sensors are installed: in the heater ($T_h = T_h(R_h)$ − heater surface temperature), in the surrounding air (with T_o), on the chamber wall ($T_{ch} = T_{ch}(R_{ch})$).

6.1.1. Heat conduction in the heater

The Poisson equation with a uniform volumetric heat source in a steady state can be written as:

$$\frac{1}{r^2}\frac{d}{dr}\left(r^2 \lambda_g \frac{dT_h}{dr}\right) + q_v = 0 \ , \ r \in [0, R_h], \tag{21}$$

where: $q_v = \dot{Q}/(4/3 \cdot \pi R_h^3)$ is the volumetric heat generation rate (so-called "internal heat sources").

Boundary conditions**:**

- at the heater centre (symmetry):

$$\left.\frac{dT_h}{dr}\right|_{r=o} = 0, \tag{22}$$

- at the heater surface:

$$-\lambda_g \frac{dT_h}{dr}\bigg|_{r=R_h} = \alpha(T_h - T_o) + \varepsilon\sigma\left({T_h}^4 - {T_o}^4\right). \qquad (23)$$

6.1.2. Heat balance in the gap

The heat flux dissipated by the heater leaving it (Eq. (13)) passes through the air in the gap and reaches the chamber wall:

$$\dot{Q} = A_h h_{kh}(T_h - T_o) + A_h\varepsilon\sigma\left({T_h}^4 - {T_o}^4\right) = A_{ch}h_{kch}(T_o - T_{ch}), \qquad (24)$$

where: h_{kh} – convective heat transfer coefficient at the heater surface, h_{kch} – convective heat transfer coefficient at the chamber surface.

6.1.3. Extended formula for h_k

To account for both the position and temperature dependence, it is proposed:

$$h_k(r,T) = h_0 + \gamma\frac{r}{L} + \beta T(r)\,,\ r \in [R_h, R_{ch}]. \qquad (25)$$

The corresponding steady-state energy balance for $r \in [R_h, R_{ch}]$ can be written as:

$$\dot{Q} - A_h\varepsilon\sigma\left({T_h}^4 - {T_{ch}}^4\right) = \left(h_0 + \gamma\frac{r}{L} + \beta T(r)\right)\times A_h(T_h - T_o). \qquad (26)$$

Measurements at $r = R_h$, $r = L/2$, $r = R_{ch}$ allow the determination of h_0, γ, β.

If technical challenges arise, a simplified model can be adopted by omitting the position-dependent term:

$$h_k(r) = h_0 + \beta T(r), \qquad r \in [R_h, R_{ch}]. \qquad (27)$$

This linear model underlies ML described in the article.

6.1.4. Modified ANN on the reconstructed rig

In the future, the use of more advanced artificial neural networks (ANN) will be advisable. Valuable insights in this area are provided in articles [39–41]. In [39] two methods for modelling the ground-coupled heat pump system (GCHP) were compared: artificial neural networks (ANN) and adaptive neuro-fuzzy inference systems (ANFIS). The article used the coefficient of determination (R^2) to assess the model fit. This coefficient is calculated using the formula:

$$R^2 = 1 - \frac{\sum_{i=1}^{n}(y_{ei} - \overline{y_e})}{\sum_{i=1}^{n}(y_{ei} - y_i)}\,, \qquad (28)$$

where: y_{ei} – consecutive data from the experiment at the measurement point recorded in the i-th cell of the sheet, y_i is the corresponding value returned by the ANN, $\overline{y_e}$ is the arithmetic mean value of experimental data, n – the number of measurement data.

Equation (28) is used to evaluate how well the model explains the variability of the observed data, with a focus on the quality of fit. Due to its simple structure and ease of application to specific cases, it may serve as an additional statistical criterion in future analyses.

It is also advisable to facilitate the ANN learning process. For example: similar to [40], to appropriately process the input data based on the weights assigned to them – both manually and using statistical functions such as RMSE (root mean square error) or R^2. This approach supports the ANN learning process, improving prediction accuracy by eliminating noise and random disturbances from measurement devices during the data pre-processing stage.

In the case of highly sensitive measurement equipment, it may be observed that during variations in the size of the gap, the temperature − which influences the function $h_k(r)$ − evolves in an unexpected manner. It is therefore essential to determine whether such fluctuations are due to measurement noise or constitute a significant aspect of the underlying physical phenomenon occurring within the gap.

Wavelet functions, as discussed in [41], may prove particularly useful in such analyses. In the referenced study, the authors compare traditional artificial neural networks (ANNs) with wavelet neural networks (WNNs) for modelling a solar air heater system.

In WNNs, wavelet basis functions − such as those derived from mother wavelets like Haar or Symlets − are employed in the hidden layers instead of conventional activation functions such as tanh or sigmoid.

Networks trained in this manner exhibit high flexibility when analysing nonlinear and non-stationary signals. Wavelet transformations decompose a signal across multiple scales (frequencies) and locations (time), allowing the network to capture both fine-grained features and potential disturbances originating from the measurement apparatus.

6.1.5. Influence of atmospheric composition

An additional advantage of the improved rig is the possibility of testing various gas mixtures in the gap, as the desiccator, which is an element of the setup, allows for testing different gases, effectively separating the atmosphere in the gap from the external environment. It is possible to study, for example, nanofluids, mixtures of air with water vapour, and air with CO_2. Considering radiation and absorption by gases is essential:

- monoatomic and diatomic gases (except CO and HCl) are nearly transparent to thermal radiation,
- triatomic gases (CO_2, H_2O) significantly absorb and emit in specific frequency bands.

For example:

- at approximately −50°C, both water vapour (H_2O) and carbon dioxide (CO_2) absorb heat,
- around 0°C, CO_2 becomes inactive, while H_2O strongly absorbs heat with the wavelength near $\lambda \approx 6$ µm,
- at 25°C, H_2O dominates in radiation and absorption,
- at 100°C, water vapour still intensively absorbs heat, while CO_2 remains nearly inactive.

Studying the influence of these effects on the heat balance in the gap and on the coefficients $h_k(r)$, $h_{kh} = h_k(R_h)$, $h_{kch} = h_k(R_{ch})$ (e.g. by comparison with pure nitrogen) seems to be a valuable direction for future research, especially in times when there is so much talk about the topic of the so-called "climate warming".

7. Conclusions

This study presents a simplified ML method for determining the Newton coefficient under conditions of limited (undeveloped) convection in a gap, within the heater power range of approximately 0.2 W to 5 W. A weak linear dependence of the Newton coefficient on temperature was assumed.

To verify the value of the Newton coefficient obtained using ML, the first stage involved experimental determination of its convective component h_{ke} and experimental radiative component h_r. The convective part calculated by ML h_{kS} was obtained by subtracting the radiative component h_r from the "total" Newton coefficient determined using the Solver program h_S, and was subsequently compared with the convective part measured experimentally h_{ke}. The radiative component was determined based on previous experimental studies, taking into account measurements of the relative emissivity of the black paint covering the heater and the internal surfaces of the chamber.

It was demonstrated that the experimental values of the convective part of the Newton coefficient fall between the values obtained from the gap model h_{ktgc} (lower bound Fig. 7) and those calculated using ML. Moreover, both the experimental and ML-derived values fall between the results obtained from literature based models (gap model h_{ktgc} and open model gap model h_{ktoc} – lower and upper bounds at Fig. 7, respectively). And the values obtained using ML slightly exceed those real ones, derived from the experiment.

- It was thus shown that convection in the gap of the test rig is suppressed due to geometric constraints, meaning the convective flow could not fully develop.
- This validates the ML-based approach.
- ML seems to be a very simple method for estimating the convective heat transfer coefficient in a gap under limited convection conditions.

Artificial Neural Networks (ANN) were employed in this study to determine selected steady-state parameters, namely, the temperature and the voltage at the heater terminals. The number of neurons m in the hidden layer (HL) was selected using a trial-and-error method, optimizing RMSE and Pearson's correlation coefficient as objective functions. Additionally, a separate optimization problem was solved to find the solution to a system of four equations using the Solver program used in ML.

In light of the obtained results, a reconstruction of the test rig is planned to enable further investigation of convection phenomena in the gap and to validate ML methods over a broader range of measurement conditions.

References

[1] McAdams, W.H. (1954). *Heat Transmission*. McGraw-Hill Book Company.

[2] Lienhard IV, J.H., & Lienhard V, J.H. (2019). *Heat Transfer Textbook*. Phlogiston Press Cambridge.

[3] Aubin, D. (2008). The memory of life itself: Bénard's cells and the cinematography of self-organization. *Studies in History and Philosophy of Science, Part A*, 39(3), 359−369. doi: 10.1016/j.shpsa.2008.06.007

[4] Aliouane, I., Kaid, N., Ameur, H., & Laidoud, H. (2021). Investigation of the flow and thermal fields in square enclosures: Rayleigh-Bénard's instabilities of nanofluids. *Thermal Science and Engineering*, 25. doi: 10.1016/j.tsep.2021.100959

[5] Mathews, J., & Hymavathi, T. (2024). Unsteady magnetohydrodynamic free convection and heat transfer flow of Al2O3–Cu/water nanofluid over a non-linear stretching sheet in a porous medium. *Archives of Thermodynamics*, 45(1), 165–173. doi: 10.24425/ather.2024.150449

[6] Mathews, J., & Hymavathi, T.(2024). Unsteady flow of silica nanofluid over a stretching cylinder with effects of different shapes of nanoparticles and Joule heating. *Archives of Thermodynamics*, 45(3), 115–126.445. doi: 10.24425/ather.2024.151222

[7] Houdek, G., & Dupret, M.A.(2015) Interaction Between Convection and Pulsati. *Living Reviews in Solar Physics*, 12(8), doi: 10.1007/lrsp-2015-8, 10.48550/arXiv.1601.03913

[8] Husain, S., Adil, M., Arqam, M., & Shabani, B. (2021). A review on the thermal performance of natural convection in vertical annulus and its applications. *Renewable and Sustainable Energy Reviews*, 150, doi: 10.1016/j.rser.2021.111463

[9] Misale, M., Fossa, M., & Tanda, G.(2014). Investigation of free convection in a vertical water channel. *Experimental Thermal and Fluid Science*, 59, 252−257. doi: 10.1016/j.expthermflusci.2014.01.022

[10] Pretot, S., Zeghmati, B., & Palec Le, G. (2000), Theoretical and experimental study of natural convection on a horizontal plate. Applied Thermal Engineering, 20(10), 873−891. doi. 10.1016/S1359-4311(99)00067-8

[11] Radziemska, E., & Lewandowski, W.M, (2001). Heat transfer by natural convection from an isothermal downward-facing round plate in unlimited space, Applied Energy, 68(4), 347−366. doi: 10.1016/S0306-2619(00)00061-1

[12] Rohsenow, W.M., & Hartnett, J.P. (1998). *Handbook of heat transfer*. The McGraw-Hill Companies.

[13] Ghoben, Z.K., & Hussein, A.K. (2002). Natural Convection Inside a 3D Regular Shape Enclosures - A Brief Review. *International Journal of Heat and Technology*, 40(1), 32−246. doi: 10.18280/ijht.400128

[14] Chithrakumar, V., Venugopal, G., & Rajkumar, M. (2019). Convection in vertical annular gap formed by stationary heated inner cylinder and rotating unheated outer cylinder. *Heat and Mass Transfer*, 55, 2873–2888. doi: 10.1007/s00231-019-02614-0

[15] Petrichenko, M., & Petrochenko, M. (2022). Hydraulics of natural convection flows in building walling with air gap. *Magazine of Civil Engineering*, 26, 63−69. doi: 10.5862/MCE.26.8

[16] Said, S.A.M, & Krane, R.J. (1990). An analytical and experimental investigation of Natural Convection Heat Transfer in vertical channels with single obstruction. *International Journal of Heat Mass Transfer*, 33, 1121−1134. doi: 10.1016/0017-9310(90)90245-P

[17] De Giorgi, L., Bertola, V., & Cafaro, E.(2011). Thermal convection in double glazed windows with structured gap. *Energy and Buildings*, 43(8), 2034-2038. doi:10.1016/j.enbuild.2011.03.043

[18] Pelińska-Olko, E. (2023). Emissivity measurement of black paint using the calorimetric method. *Archives of Thermodynamics*, 44(3). doi:10.1007/s10765-011-1010-2

[19] Lewkowicz, M., & Pelińska-Olko, E. (2018). Numerical prediction of steady state temperature based on transient measurements. *MATEC Web of Conferences*, 240(05024). doi: 10.1051/matecconf/201824005024

[20] Hobler, T. (1971). *Heat movement and exchangers*. WNT Warszawa (in Polish).

[21] Pudlik, W. (2012). *Heat exchange and exchangers.* Wydawnictwo Politechniki Gdańskiej (in Polish).

[22] Kostowski, E. (2003). *Collective work*. Wydawnictwo Politechniki Śląskiej (in Polish).

[23] Mikielewicz, J., & Mikielewicz, D. (2024). Influence of thermodynamics on the development of technology and science. *Archives of Thermodynamics*, 45(2), 51–61. doi: 10.24425/ather.2024.150851

[24] Batagelj, V., & Bojkovski, R.J. (2011). Calibration by comparison of platinum resistance thermometers using slow resistance bridges. *Journal of Thermophysics*, 32, 1409−1417. doi: 10.1007/s10765-011-1010-2

[25] Wędrychowicz, W. (2015). *Temperature measurement with metal and semiconductor resistance thermocouples*. Wydawnictwo Politechniki Wrocławskiej (in Polich).

[26] Lundström, H., & Mattsson, M. (2020). Radiation influence on indoor air temperature sensors: Experimental evaluation of measurement errors and improvement methods. *Experimental Thermal and Fluid Science*, 115. doi: 10.1016/j.expthermflusci.2020.110082

[27] Wędrychowicz, W. (2017). *Temperature measurement with thermocouples.* Wydawnictwo Politechniki Wrocławskiej (in Polish).

[28] Liu, H.T., Shao, D., & Li, B.Q. (2012). Theory Analysis of Thermocouple Temperature Measurement. *Applied Mechanics and Materials*, 239−240, 749−753. doi: 10.4028/www.scentific.nett/AMM.239-240.749

[29] Liu, B., Huang, Q.H., & Wang, P.Y. (2020). Influence of sur rounding gas temperature on thermocouple measurement. *Case Studies in Thermal Engineering*, 19. doi: 10.1016/j.csite.2020.100627

[30] Czujniki termoelektryczne. Katalog-Edycja 2023. Termoaparatura, Wrocław (in Polish). https://termoaparatura.com.pl/media/wysiwyg/docs/type-k-table-pl.pdf [accessed 22 Feb. 2025].

[31] Tadeusiewicz, R., & Szaleniec, M. (2015). *Neural Network Lexicon*. Wydawnictwo Fundacji „Projekt Nauka" (in Polish).

[32] Cantú-Paz, E. (2003). Pruning neural networks with distribution estimation algorithms. *Genetic and Evolutionary Computation Conference* (GECCO, LNCS, 2723, 790–800), 12−16 Jul., Chicago, IL, USA. doi: 10.1007/3-540-45105-6_93

[33] Pavlidis, N.G., Tasoulis, O.K., Plagianakos, V.P., Nikiforidis, G., & Vrahatis, M.N. (2005). Spiking Neural Network training Using Evolutionary Algorithms. In: *Proceedings. 2005 IEEE International Joint Conference on Neural Networks*, vol. 4, 2190–2194. doi: 10.1109/IJCNN.2005.1556240

[34] Ripley, B., &. Venables, W. (2022). Package 'nnet'. https://cran.r-project.org/web/packages/nnet/nnet.pdf [accessed 22 Feb. 2025].

[35] Rigler, A.K., Irvine, J.M., *&* Vogl, T.P. (1991). Rescaling of variables in back propagation learning. *Neural Networks*, 4, 225−229. doi: 10.1016/0893-6080(91)90006-Q

[36] StatSoft Electronic Statistics Textbook (1984−2024). https://www.statsoft.pl/textbook [accessed 22 Feb. 2025].

[37] Stachurski, A. (1999). *Optimization Basics.* Oficyna Wydawnicza Politechniki Warszawskiej (in Polish).

[38] El-Awad, M.M., & Al-Saidi, M.S. (2022). Excel as an educational platform for design analyses of fluid-thermal systems. *World Journal of Engineering and Technology*, 10(20), 434−443. doi: 10.4236/wjet.2022.102025

[39] Esen, H., Inalli, M., Sengur, A., & Esen, M. (2008). Artificial Neural Networks and adaptive neuro-fuzzy assessments for ground-coupled heat pump system, *Energy and Buildings*, doi: 10.1016/j.enbuild.2007.10.002

[40] Esen, H., Inalli, M., Sengur, A., & Esen, M (2008). Forecasting of a ground-coupled heat pump performance using neural networks with statistical data weighting pre-processing, International Journal of Thermal Sciences, 47(4), 431−441. doi: 10.1016/j.ijthermalsci.2007.03.004

[41] Esen, H., Ozgen, F., Esen, M., & Sengur, A. (2009). Artificial neural network and wavelet neural network approaches for modelling of a solar air heater. *Expert Systems with Applications*, 36(8), 11240−11248. doi: 10.1016/j.eswa.2009.02.073

Co-published by
Institute of Fluid-Flow Machinery
Polish Academy of Sciences
Committee on Thermodynamics and Combustion
Polish Academy of Sciences

http://www.imp.gda.pl/archives-of-thermodynamics/

ARCHIVES OF THERMODYNAMICS

A Fast Fourier Transform Solution for 1D Unsteady Heat Transfer Model Bounded by Varying Temperature

Dan Wu[a], Yao Wang[b], Yuezan Tao[c*], Xian Li[c], Honglei Ren[c], Qiang Yang[d]

[a]School of Urban Construction and Transportation, Hefei University, Hefei, 230601 China
[b]School of Environment and Energy Engineering, Anhui Jianzhu University, Hefei 230601, China
[c]School of Civil and Hydraulic Engineering, Hefei University of Technology, Hefei, 230009 China
[d]Northwest Engineering Corporation Limited, Xi'an 710065, China
*Corresponding author email: taocs163@126.com

Received: 13.12.2024; revised: 21.02.2025; accepted: 03.03.2025

Abstract

Using the Fourier transform to solve a one-dimensional heat conduction model with temperature *f*(*t*) as the boundary requires complex integral transformation operations. According to the property of the Fourier transform, *f*(*t*) is regarded as a symbol in the process operation, and the universal theory resolution of such a problem is established without directly solving the *f*(*t*) transformation. *f*(*t*) is then substituted into the theoretical solution to obtain the solution of the actual model. Using the theoretical solution, the solutions of 3 types of common functions are given. Combined with the characteristics of the model, precautions during the solving process are proposed. The example application demonstrates the establishment and application process of inversing model parameters based on the inflection point of temperature variation over time.

Keywords: Thermal conduction; Fourier transform; Theoretical solution; Common functions; Inflection point

Vol. 46(2025), No. 2, 167–172; doi: 10.24425/ather.2025.154915

Cite this manuscript as: Wu, D., Wang, Y., Tao, Y., Li, X., Ren, H., & Yang, O. (2025). A Fast Fourier Transform Solution for 1D Unsteady Heat Transfer Model Bounded by Varying Temperature. *Archives of Thermodynamics*, 46(2), 167–172.

1. Introduction

One-dimensional (1D) heat conduction model bounded by varying temperature is a classic problem [1,2]. In this problem, the edge temperature *f*(*t*) is set as $\varDelta T_0$ (that is the instantaneous increase of boundary temperature $\varDelta T_0$ remains unchanged) [3,4]. This model can be directly solved by the Laplace and Fourier transform [5,6].

Numerical algorithms are more and more widely used in solving heat conduction models in complex calculation regions [7–12], boundary conditions [13–15] and source/sink terms [14–16]. Although the analytical solution of the model is strictly limited [17,18] and difficult to solve [19,20], the solution is an important theorem to discuss the mathematical laws of the model [18–20]. The analytical solution of the model corresponding to various conditions such as heat transfer in porous media [21–23] and pollutant transport [24–26] has always been difficult, and a hot spot in related fields. The Fourier transform and other integral transformation methods are basic tools for finding the solution [21–29]. For the solution of a 1D heat conduction model, a complex integral transformation operation is required to solve the problem with different *f*(*t*) [5,6]. To avoid the above complex integral transformation and solve the unsteady model of unconfined groundwater near a canal, Wu et al. [30] proposed to make full use of the nature of Fourier transformation and a fast Fourier transformation solution method when *f*(*t*) is not in transformation. Wei et al. [31] studied a 1D thermal conduction problem with *f*(*t*) being $e^{-\lambda t.}$ using fast solving methods.

Fast solution is a theoretical solution applicable to such problems based on the Fourier transform convolution theorem. Then,

Nomenclature

a – thermal diffusivity, m^2/s
erfc(u) – the complementary error function
f – boundary temperature, °C
F – Fourier transform operator
F^{-1} – inverse Fourier transform operator
$\bar{u}$ – image function for Fourier transform
s – Fourier operator
t – time, d
T – temperature of calculation point, °C
T_0 – boundary temperature, °C
x – distance of the calculation point from the boundary, m

Greek symbols

$\delta(t-t_{i-1})$ – Heaviside function
Δ – instantaneous change
λ – boundary temperature variation rate, °C/d
φ – temperature variation rate of the calculation point, °C/h
ω – the conversion factor

Subscripts and Superscripts

a – air
g – inflection-point
n – time step number
t – time

Abbreviations and Acronyms

1D – one-dimensional
$*$ – convolution operator

$f(t)$ is substituted into the theoretical solution to obtain an example solution. This solving process can eliminate complex integral transformation, making it fast and convenient.

The establishment process of the fast Fourier transform method is systematically presented. The solutions of 3 type functions are given using the fast solution method, and the precautions during the process are discussed. Based on the example applications, a method is established and applied for calculating the parameters using the inflection point in the temperature variation process.

2. Basic model

The 1D thermal conduction model is shown in Figs. 1 and 2, assuming:

(1) There is a heat source $f(t)$ with the temperature changing over time at the edge (x = 0) of a homogeneous sheet with an infinite length;
(2) The temperature at x is $T(x, t)$, and $T(x, 0) = 0$;
(3) The surface of the thin plate has no thermal exchange outside, and the edge thermal source forms 1D heat conduction.

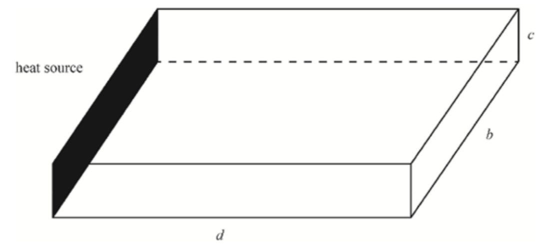

Fig. 1. Experimental materials.

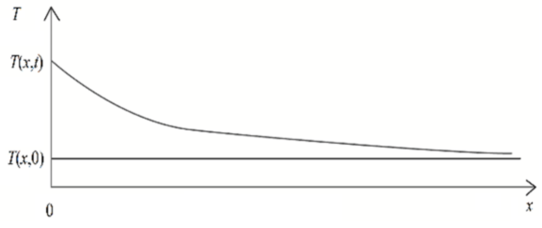

Fig. 2. Temperature change in the x direction.

The problem mentioned can be considered as the model (I):

$$
\text{(I)}\begin{cases}
\dfrac{\partial T}{\partial t} = a\dfrac{\partial^2 T}{\partial x^2} \quad (0 < x < +\infty, t > 0), & \text{(10} \\
T(x,t)|_{t=0} = 0 \quad (x > 0), & (2) \\
T(x,t)|_{x=0} = f(t) \quad (t \geq 0), & (3)
\end{cases}
$$

where a [m^2/s] is the thermal diffusivity.

3. Theoretical solution

Let $u(x, t) = T(x, t) - T(x, 0)$, (I) be rewritten as the model (II):

$$
\text{(II)}\begin{cases}
\dfrac{\partial u}{\partial t} = a\dfrac{\partial^2 u}{\partial x^2} \quad (0 < x < +\infty, t > 0, & (4) \\
T(x,t)|_{t=0} = 0 \quad (x > 0), & (5) \\
u(x,t)|x = 0 = f(t) \quad (t \geq 0), & (6)
\end{cases}
$$

Fourier transform about x is found for the model (II). In the model, x is a variable of (0, +∞) using a Fourier sine transform. From the Fourier laws, it can be obtained as follows:

$$F[u(x,t)] = \int_0^\infty u(x,t) \sin \omega x dx = \bar{u}(\omega,t), \tag{7}$$

$$F\left\{\frac{\partial[u(x,t)]}{\partial t}\right\} = \frac{d[\bar{u}(\omega,t)]}{dt}, \tag{8}$$

$$F\left\{\frac{\partial^2[u(x,t)]}{\partial x^2}\right\} = \int_0^\infty \frac{\partial^2[\bar{u}(\omega,t)]}{\partial x^2} \sin \omega x dx =$$

$$= \omega u|_{x=0} - \omega^2 \bar{u}(\omega,t), \tag{9}$$

$$F[u(x,t)|_{x=0}] = \omega f(t), \tag{10}$$

where $\bar{u}$ is the function after the Fourier transformation of x; ω is the conversion factor; F is the Fourier conversion, and F^{-1} is the Fourier inverse conversion.

From Eqs. (4), (8) and (9), we can obtain:

$$\frac{d[\bar{u}(\omega,t)]}{dt} = a[\omega u(x,t)|_{x=0} - \omega^2 \bar{u}(\omega,t)]. \tag{11}$$

The basic solution is derived from Eq. (11) and the boundary condition Eq. (10) is introduced as follows:

$$\bar{u}(\omega,t) = exp(-\omega a t) \int_0^t [\omega a f(\tau) \, exp(-\omega^2 a \tau)] d\tau. \tag{12}$$

The inverse Fourier transform of Eq. (12) is obtained as follows:

$$u(\omega,t)=F^{-1}[\bar{u}(\omega,t)]=\frac{2}{\pi}\int_0^\infty\left\{\exp(-\omega^2at)\int_0^t[a\omega f(\tau)\exp(-\omega^2a\tau)]d\tau\right\}sin\,\omega\,xd\omega=$$
$$=\frac{2a}{\pi}\int_0^t f(\tau)\left[\int_0^\infty \omega\,exp[-\omega^2a(t-\tau)]\,sin\,\omega\,xd\omega\right]d\tau=$$
$$=\frac{2a}{\pi}\int_0^t\frac{f(\tau)}{2a(t-\tau)}\{-\exp[-\omega^2a(t-\tau)]|_0^\infty+\int_0^\infty\exp[-\omega^2a(t-\tau)]x\,cos\,\omega\,xd\omega\}d\tau=$$
$$=\frac{x}{\pi}\int_0^t\frac{f(\tau)}{t-\tau}\left\{\int_0^\infty exp[-\omega^2a(t-\tau)]\,cos\,\omega\,xd\omega\right\}d\tau. \tag{13}$$

According to the characteristic function of the Fourier transform:

$$\int_0^\infty\exp(ax)\,cos\,\omega\,xdx=\frac{\sqrt{\pi}}{2\sqrt{a}}\exp(-\omega^2/4a). \tag{14}$$

From Eqs. (13) and (14), we have:

$$u(\omega,t)=\frac{x}{2\sqrt{\pi a}}\int_0^t\frac{f(\tau)}{(t-\tau)^{3/2}}\exp[-x^2/4a(t-\tau)]d\tau. \tag{15}$$

Eq. (15) is the solution of the 1D model under *f*(*t*). From Eq. (15), based on the convolution theorem, we have:

$$u(x,t)=\frac{x}{2\sqrt{\pi a}}\int_0^t\frac{f(\tau)}{(t-\tau)^{3/2}}exp[-x^2/4a(t-\tau)]\,d\tau=$$
$$=f(t)*\frac{x}{2\sqrt{\pi at}}exp(-x^2/4at)= \tag{16}$$
$$=f(t)*\frac{d}{dt}\left[\frac{2}{\sqrt{\pi}}\int_{\frac{x}{2\sqrt{at}}}^\infty exp(-\tau^2)d\tau\right]=f(t)*\frac{d}{dt}\left[\text{erfc}\left(\frac{x}{2\sqrt{at}}\right)\right],$$

where * is the convolution operator and erfc(*x*) is a complementary error function.

According to the differential property of convolution, it is obtained that:

$$f(t)*\frac{d}{dt}\left[\text{erfc}\left(\frac{x}{2\sqrt{at}}\right)\right]+\text{erfc}\left(\frac{x}{2\sqrt{at}}\right)\Big|_{t=0}f(t)=$$
$$=\text{erfc}\left(\frac{x}{2\sqrt{at}}\right)*\frac{d[f(t)]}{dt}+f(t)|_{t=0}\text{erfc}\left(\frac{x}{2\sqrt{at}}\right). \tag{17}$$

From the relationship between Eq. (16) and Eq. (17), $\text{erfc}(\frac{x}{2\sqrt{at}})\Big|_{t=0}=0$, and $u(x,t)=T(x,t)-T(x,0)$. According to Eq. (17), it is obtained that:

$$T(x,t)=f(t)|_{t=0}\text{erfc}\left(\frac{x}{2\sqrt{at}}\right)+\int_0^t\left[\frac{d[f(t)]}{dt}\text{erfc}\left(\frac{x}{2\sqrt{a\tau}}\right)\right]d\tau. \tag{18}$$

Equation (18) is the solution of the model obtained without finding its Fourier transform image function of *f*(*t*). It is true for all boundary functions *f*(*t*) constituting the Dirichlet condition, that is Eq. (18) is the theoretical resolution of this problem. The application of Fourier and Laplace transform properties will facilitate the solution of the problem [17]. When *f*(*t*) of the practical problem is determined, a solution can be obtained by submitting *f*(*t*) into Eq. (18).

4. Solution for a common boundary function

Providing functional expressions applicable to actual boundaries is the foundation of mathematical models [32]. For the convenience of application, based on the theoretical solution, the solution is given when *f*(*t*) is a constant function, polynomial function and basic elementary common function.

4.1. Constant function

Function $f(t)=\Delta T_0$, where ΔT_0 is a constant. It is the boundary condition of the classical 1D model, that is when $t\to 0^+$, the boundary temperature will remain constant after an instantaneous change of T_0.

Substituting $f(0)=\Delta T_0$ into Eq. (18), due to $d[f(t)]/dt=d[\Delta T_0]/dt=0$, we have:

$$T(x,t)=\Delta T_0\text{erfc}\left(\frac{x}{2\sqrt{at}}\right). \tag{19}$$

4.2. Multi-order function

In practical work, since the observation of the time-varying process *f*(*t*) of the target variable is discrete, piecewise functions are usually used to represent *f*(*t*) based on discrete measurement data. Among them, step functions and linear interpolation functions are commonly used forms in engineering technology.

1) Step function

For the boundary temperature $f(t_i,t_{i+1})$ between $t_\text{i}-t_{\text{i}+1}$ ($I\geq 2$), when using the average temperature in the period $(f_\text{i}+f_{\text{i}+1})/2$ or the increment of $f_{i+1}-f_\text{i}$, we have:-

$$f(t)=\Delta T_0+\textstyle\sum_{i=2}^n(f_i-f_{i-1})\delta(t-t_{i-1}),$$
$$(t>t_{i-1},i\in N^*), \tag{20}$$

when $t<t_{i\text{-}1}$, $\delta(t-t_{i\text{-}1})=0$ and when $t\geq t_{i\text{-}1}$, $\delta(t-t_{i\text{-}1})=1$.

Substituting Eq. (20) into Eq. (18), $\delta(t-t_{i\text{-}1})$ functionality and $f(0)=\Delta T_0$ are noted as follows:

$$T(x,t)=\Delta T_0\text{erfc}\left(\frac{x}{2\sqrt{at}}\right)+$$
$$+\textstyle\sum_{i=2}^n(f_i-f_{i-1})\int_0^t\text{erfc}\left[\frac{x}{2\sqrt{a(\tau-t_{i-1})}}\right]d\tau. \tag{21}$$

Note: ΔT_0 means that variation occurs at $t\to 0^+$ and maintains for a long period of time. The time that remains unchanged is t_1-t_0, and $i=2-n$.

2) Lagrange linear interpolation function

When the variables have certain changes in each test period t_i-t_{i+1}, linear interpolation methods could be used for *f*(*t*), representing as follows:

$$f(t)=\Delta T_0+\textstyle\sum_{i=2}^n(f_i-f_{i-1})\frac{t-t_{i-1}}{t_i-t_{i-1}}\delta\,(t-t_{i-1}). \tag{22}$$

Substituting Eq. (22) into Eq. (18), we obtain:

$$T(x,t)=\Delta T_0\text{erfc}\left(\frac{x}{2\sqrt{at}}\right)+\textstyle\sum_{i=2}^n\frac{f_i-f_{i-1}}{t_i-t_{i-1}}\int_{t_{i-1}}^t\text{erfc}\left(\frac{x}{2\sqrt{a\tau}}\right)d\tau. \tag{23}$$

Based on the definition of ΔT_0, when establishing the *f*(*t*) piecewise function, attention should be paid to the expression methods of each time interval.

4.3. Basic elementary function

1) Exponential decay function.

When $f(t) = \Delta T_0 \exp(-\lambda t)$（$\lambda > 0$), substituting it into Eq. (18), we obtain the following formula:

$$T(x,t) = \Delta T_0 \text{erfc}\left(\frac{x}{2\sqrt{at}}\right) + \\ -\lambda \Delta T_0 \int_0^t \exp(-\lambda\tau)\,\text{erfc}\left[\frac{x}{2\sqrt{a(t-\tau)}}\right] d\tau. \qquad (24)$$

2) Logarithmic function.

When $f(t) = \Delta T_0 log_a(t)$, substituting it into Eq. (18), it can be obtained that:

$$T(x,t) = \Delta T_0 \text{erfc}\left(\frac{x}{2\sqrt{at}}\right) + \frac{1}{ln\,a}\int_0^t \frac{1}{\tau}\,\text{erfc}\left[\frac{x}{2\sqrt{a(t-\tau)}}\right] d\tau. \quad (25)$$

3) Trigonometric function.

Taking $f(t) = \Delta T_0\cos(t)$ for example, substituting it into Eq. (18), it can be obtained that:

$$T(x,t) = \Delta T_0 \text{erfc}\left(\frac{x}{2\sqrt{at}}\right) - \Delta T_0 \int_0^t sin(\tau)\,\text{erfc}\left[\frac{x}{2\sqrt{a(t-\tau)}}\right] d\tau. \qquad (26)$$

After the edge condition is determined, $f(t)$ is substituted into the equation, and the analytical solution of the model can be obtained more conveniently and quickly. The solutions of 3 function types are obtained, which are convenient for practical reference and application. When $f(t)$ is determined, the above solution may be further expanded by using the step-by-step integration. Numerical algorithms for analytical solutions can also be established based on [31], providing convenience for frequent applications.

5. Application of solution

One of the important purposes of researching problem-solving solutions is to establish inversion model parameters based on the analytical solution of the model and the observed data of the target variable changing over time [33–37]. Based on the solution of Eq. (21), when $i = 2$, the curve is shown in Fig. 3.

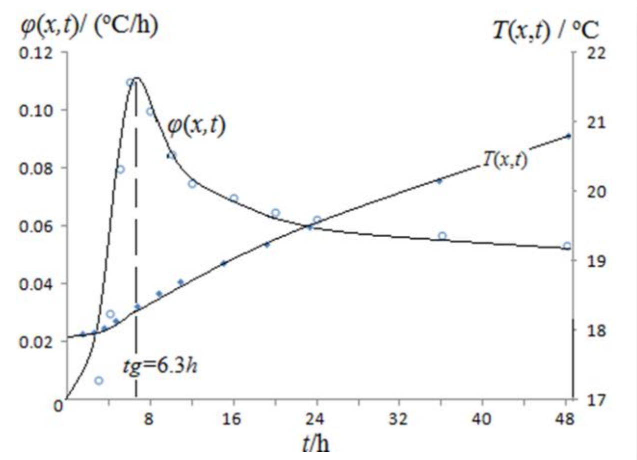

Fig. 3. Temperature variation rate at x = 0.5 m.

5.1. Calculation of model parameters

The partial derivative of T in Eq. (21) is calculated, $\varphi(x, t) = \partial T(x, t)/\partial t$, $\varphi(x, t)$ is the temperature variation rate at point x, then:

$$\phi(x,t) = \Delta T_0 \frac{2^{-3/2}}{2\sqrt{\pi a}} exp\left(\frac{x^2}{4at}\right) + \sum_{i=2}^{n} \frac{f_i - f_{i-1}}{t_i - t_{i-1}}\,\text{erfc}\left[\frac{x}{2\sqrt{a(t-t_{i-1})}}\right]. \qquad (27)$$

As $n = 2$, Eq. (27) can be rewritten as follows:

$$\phi(x,t) = \Delta T_0 \frac{t^{-3/2}}{2\sqrt{\pi a}} exp\left(\frac{x^2}{4at}\right) + \lambda\,\text{erfc}\left(\frac{x}{2\sqrt{at}}\right), \qquad (28)$$

where $\lambda = (f_2 - f_1)/(t_2 - t_1)$ expresses the slope change of the boundary temperature in the period of $t_1 - t_2$.

For Eq. (28), the partial derivative about t is found as follows:

$$\frac{\partial\phi(x,t)}{\partial t} = \frac{1}{2\sqrt{\pi a t^5}} \exp\left(-\frac{x^2}{4at}\right)\left[\Delta T_0\left(-\frac{3}{2} + \frac{x^2}{4at}\right) + \lambda t\right]. \quad (29)$$

At the inflection point of the curve in Fig. 3, $\partial\varphi(x,t)/\partial t = 0$, $t = t_g$. Two roots can be obtained from Eq. (29), where the mathematically and physically reasonable roots are expressed as follows:

$$\frac{\partial\phi(x,t)}{\partial t} = \frac{1}{2\sqrt{\pi a t^5}} exp\left(-\frac{x^2}{4at}\right)\left[\Delta T_0\left(-\frac{3}{2} + \frac{x^2}{4at}\right) + \lambda t\right]. \quad (30)$$

According to Eq. (28), the model parameter a can be obtained (at time t_g, ΔT_0, λ, x are known) as follows:

$$a = \frac{x^2}{2t_g(3 - 2\lambda t_g)/\Delta T_0}. \qquad (31)$$

It should be noted that due to the differences in model boundary conditions [30,31,38] and source/sink term [14], the calculation formula for the parameter a at the inflection point method is also different.

5.2. Case study

A sample of silty mudstone obtained from the ground-source heat pump drilling site in Anhui Province with dimensions of d = 3.0 m, b = 1.5 m, and c = 0.3 m was used (refer to Fig. 1). A steel pipe with an outer diameter of 0.15 m was pre-installed at one end of this sample. In addition, a detailed insulation treatment was carried out on the surrounding environment as well as at the top and bottom surfaces of the steel pipes and concrete specimens. According to the standard protocol outlined in "Determination of Steady-State Thermal Resistance and Related Properties of Thermal Insulation Materials – Guarded Hot Plate Method (GB10294)", the specimen has undergone a guarded heat treatment procedure. The "steady-state method" is used to ensure a controlled and consistent thermal environment throughout the testing phase. A temperature measuring optical fibre was installed at 0.2 m from the steel pipe in the sample for continuous testing.

In a 2-day test, the initial temperature was $T(x, 0)$ = 18.06°C. At the beginning, 36°C water was imported into the boundary slot, and then $T(x, t)$ was reduced slowly. At the end of the test, the boundary temperature was 35.5℃. So, $\Delta T_0 = 17.94$℃, and $\lambda = -0.25$℃/d.

The temperature measurements taken at 0.5 m from the heating device are shown in Table 1 (during the first two hours of the experiment, the temperature response was insensitive).

To ascertain the inflection point, the interpolation technique based on the recorded temperatures is used to calculate the temperature change rate $\varphi(x, t)$. To improve the calculation accuracy, it is recommended to increase the data density near the inflection point.

It can be seen from Fig. 3 that $\varphi(x, t) - t$, $t_g = 6.3$ h. According to Eq. (31), $a = 1.85 \times 10^{-6}$ m^2/s.

During the experiment, using forward or backward interpolation to calculate the temperature change rate $\varphi(x, t)$ will have a certain impact on determining the inflection point time. However, this impact can be effectively minimized by applying multiple encryption methods.

Table 1. Temperature at a distance of $x = 0.50$ m.

t* / *h	**2**	**3**	**4**	**5**	**7**	**9**	**11**	**15**	**18**	**24**	**36**	**48**
***T*(*x*,*t*), °C**	17.86	17.87	17.93	18.04	18.25	18.43	18.6	18.78	19.14	19.39	20.07	20.71
***φ*(*x*,*t*), °C/h**	0.006	0.009	0.059	0.109	0.104	0.089	0.084	0.069	0.064	0.062	0.056	0.052

6. Conclusions

Based on the research of the one-dimensional heat conduction model with variable temperature constraints, the following conclusions are drawn in establishing the fast Fourier transform method:

1) For the variable temperature boundary $f(t)$, a theoretical resolution of such models has been established using the differential properties of Fourier's law and the convolution theorem.
2) Based on theoretical solutions, there is an urgent need for practical models to avoid the tedious and complex Fourier transform.
3) There was an inflection point in the temperature over time, which can be used to invert the model parameter a.
4) Calculating the temperature change rate $\varphi(x,t)$ based on actual measured temperatures, using forward or backward interpolation can cause a degree of interference to the experimental results. To mitigate this effect, it is recommended to increase the frequency of data recording near the inflection point when determining the time of occurrence based on recorded data.

It should be noted that in the solving process, when the operator $f(t)$ is used for the Fourier transform, $f(t)$ should meet the specification of Fourier conversion [39], that is $f(t)$ should satisfy the Dirichlet condition: $f(t)$ is a succession function or has only a finite number of first-order discontinuities and only a finite number of extreme points.

The one-dimensional heat conduction model uses a fast Fourier transform solution that leverages the properties of the Fourier transform. This method simplifies the solution process by excluding boundary conditions from the complex transformation procedures. Using dynamic temperature monitoring data from the temperature field, the method can calculate the thermophysical properties of the experimental material [40] (i.e. thermal diffusivity or thermal conductivity coefficient of the model). This calculation represents a significant objective in studying such problems. In addition, this method has a significant reference for models controlled by the heat conduction equation, including groundwater flow models and pollutant diffusion models [40–44].

Acknowledgements

The research work was funded by the National Natural Science Foundation of China (42107082), the Natural Science Research Foundation of Anhui Universities (CN) (2024AH051537).

References

[1] Tao, W.Q. (2019). *Heat Transfer Theory* (5th ed.). Higher Education Press, Beijing, China, 75–77.

[2] Fourier, J., & Gui, Z.L. (2008). *The Analytic Theory of Heat*. Peking University Press, Beijing, China, 89–95.

[3] Gu, C.H., Li, D.Q., & Chen, S.X. (2012). *Mathematical Physical Equation* (3rd ed.). Higher Education Press, Beijing, China, 148–150.

[4] Ozisik, M.N. (1989). *Boundary value problems of heat conduction*. Dover Publications, New York, America, 37–42.

[5] Jiang, Y.S., Xu, Y.Q., & Wang, X.M. (2014). *Equations of mathematical physics*. Tsinghua University Press, Beijing, China, 76–79.

[6] Su, B.P., & Chen, D.L. (2018). *Complex Variables and Integral Transformation*. High Education Press, Beijing, China, 103–106.

[7] Li, Y.T., Xu, H.J., Gong, L., & Zhang, K.F. (2014). Numerical study of fluid flow and heat transfer characteristics in metal-foam filled microchannel heat sink. *Applied Mathematics and Mechanics*, 35(3), 287–294.

[8] Zhou, F.L., Yuan, X.H., YU, J.H., Qin, Y., & Pan, X.Y. (2022). Transient heat conduction analysis of heat dissipation structure based on time domain boundary element method. *Journal of Hunan University of Technology*, 36(3), 22–28.

[9] Ou, G.B., & Fei, J.S. (1991). Boundary element method for solving transient heat conduction. *Nuclear Power Engineering*, (4), 76–80, 96.

[10] Abouelregal, A.E. (2016). Fractional heat conduction equation for an infinitely generalized, thermoelastic, long solid cylinder. *International Journal for Computational Methods in Engineering Science and Mechanics*, 17(5–6), 374–381. doi: 10.1080/15502287.2012.698700

[11] Povstenko, Y., & Klekot, J. (2019). Time-fractional heat conduction in two joint half-planes. *Symmetry*, 11(6), 800. doi: 10.3390/sym11060800

[12] Zhang, X.Y., & Li, X.F. (2017). Transient thermal stress intensity factors for a circumferential crack in a hollow cylinder based on generalized fractional heat conduction. *International Journal of*

Thermal Sciences, 121, 336–347. doi: 10.1016/j.ijthermalsci.2017.07.015

[13] Povstenko, Y., & Klekot, J. (2018). Fractional heat conduction with heat absorption in a sphere under Dirichlet boundary condition. *Computational and Applied Mathematics*, 37, 4475–4483. doi: 10.1007/s40314-018-0585-7

[14] Zhou, H.L., Yan, J., Yu, B., & Chen, H.L. (2018). Identification of thermal diffusion coefficients for transient heat conduction problems with heat sources. *Applied Mathematics and Mechanics*, 39(2), 160–169. doi: 10.21656/1000-0887.380199

[15] Povstenko, Y. (2016). Time-fractional heat conduction in a half-line domain due to boundary value of temperature varying harmonically in time. *Mathematical Problems in Engineering*, 2016(1), 8605056. doi: 10.1155/2016/8605056

[16] Fabre, A., & Hristov, J. (2017). On the integral-balance approach to the transient heat conduction with linearly temperature-dependent thermal diffusivity. *Heat and Mass Transfer*, 53, 177–204. doi: 10.1007/s00231-016-1806-5

[17] Dai, Y., & Xiao, B. (2019). Application of Fourier integral and Fourier transform in heat conduction equation. *Journal of Xinjiang Normal University (Natural Sciences Edition)*, 38(2), 5–15. doi: 10.14100/j.cnki.1008-9659.2019.02.002

[18] Liu, H., Mao, Q.X., An, E.K., & Mei, H.S. (2002). Contacting Heat Conduction between Two Bars with Different Temperatures. *Journal of Tongji University (Natural Science)*, 30(6), 686-689.

[19] Xiong, H., & Yang, G. (2014). Dynamics of a complex-valued heat equation. *Applied Mathematics and Mechanics*, 35(9), 1055–1062.

[20] Tang, S.H., Luo, Y.S., & Peng, X.H. (2013). Analytical solutions of temperature field in the concrete slab on fire. *Chinese Journal of Applied Mechanics*, 30(4), 544–549, 646–647.

[21] Lu, Y.H., & Duan, G.L. (2018). Analytic solution of velocity and temperature distribution about plate channel filled with and without a porous medium. *Journal of Engineering Thermophysics*, 39(3), 633–639.

[22] Wang, K.Y., Wang, D.Z., & Li, P.C. (2015). Two decoupling methods for the heat transfer model of a plate channel filled with a porous medium. *Applied Mathematics and Mechanics*, 36(5), 494–504 (in Chinese).

[23] Xi, S.L., Shi, G., & Wei, Z.H. (2023). Heat Transfer Model of a Single U-tube Energy Pile With Variable Heat Flow Considering Heat Exchange Between Circulating Water and Energy Pile. *Journal of Engineering Thermophysics*, 44(6), 1709–1719.

[24] Jiang, W.H., Li, J.S., Huang, X., & Cheng, X. (2023). Analytical model for one-dimensional transient transport of organic contaminants in composite liner considering thermal diffusion. *China Civil Engineering Journal*, 56(9), 146–157, 188. doi: 10.15951/j.tmgcxb.21121205

[25] Zhang, W.J., Zhao, P., & Jia, W.Q. (2015). Boundary conditions of one-dimensional convection-diffusion column tests and unified analytical solution. *Rock and Soil Mechanics*, 36(10), 2759–2764. doi: 10.16285/j.rsm.2015.10.003

[26] Chen, Y.M., Xie, H.J., Ke, H., & Tang, X.W. (2006). Analytical solution of one-dimensional diffusion of volatile organic compounds through composite liners. *Chinese Journal of Geotechnical Engineering*, 28(9), 1076-1080.

[27] Xu, H.Y., Wang, X.P., & Qi, H.T. (2017). Fractional dual-phase-lag heat conduction model for laser pulse heating. *29th Chinese Control and Decision Conference*, 28–30 May, Chongqing, China. *IEEE*, 7833–7837. doi: 10.1109/CCDC.2017. 7978615

[28] Fu, J.W., Hu, K.Q., & Qian, L.F. (2020). Non-Fourier Heat Conduction of a Functionally Graded Cylinder Containing a Cylindrical Crack. *Advances in Mathematical Physics*, 2020(1), 8121295. doi: 10.1155/2020/8121295

[29] Zhang, L.J., & Shan, X.C. (2016). Semi-analytic solution of the non-Fourier thermal propagation on the surface of material irradiated by laser beam. *Journal of Hebei University (Natural Science Edition)*, 36(5), 449–454. doi: 10.3969/j.issn.1000-1565.2016.05.001

[30] Wu, D., Tao, Y.Z., & Lin, F. (2018). Application of unsteady phreatic flow model and its solution under the boundary control of complicated function. *Journal of Hydraulic Engineering*, 49(6), 725–731. doi: 10.13243/j.cnki.slxb.20171014

[31] Wei, T., Tao, Y.Z., Ren, H.L., & Wu, D. (2022). The solution to one-dimensional heat conduction problem bounded by the exponential decay condition and its application. *Chinese Journal of Applied Mechanics*, 39(6), 1135–1139, 1202.

[32] Li, B., & Liu, L.H. (2008). An algorithm for geometry boundary identification of heat conduction problem based on boundary element discretization. *Proceeding of the Chinese Society of Electrical Engineering*, 28(20), 38–43.

[33] Zhang, J.P. (1994). Principles and methods of expressing segmented functions as a single equation using unit step functions. *Journal of Lanzhou Petrochemical University of Vocational Technology*, (1), 24–26 (in Chinese).

[34] Jiang, Z.Y. (1995). Discussion on the properties of δ function. *Journal of Shaoyang College*, 8(3), 203–206.

[35] Chen, H.L., & Liu, Z.L. (2021). Solving the inverse heat conduction problem based on data driven model. *Chinese Journal of Computational Mechanics*, 38(3), 272–279. doi: 10.7511/jslx20210115004

[36] Yang, J., Xu, R., Huang, Q., Shao, Q., Huang, W., & Hu, H. (2020). Date-driven computational mechanics: a review. *Chinese Journal of Solid Mechanics*, 41(1), 1–14. doi: 10.19636/j.cnki.cjsm42-1250/o3.2020.001

[37] Xue, Q.T., & Wei, W. (2010). Parameters identification of nonlinear inverse heat conduction problem. *Engineering Mechanics*, 27(8), 5–9.

[38] de Andrade, G.S., Nascimento, E.J., & de Lemos, M.J. (2024). Finite integral transform with homogenized boundary conditions solution of transient heat conduction applied to thermal plug and abandonment of oil wells. *Geoenergy Science and Engineering*, 233, 212530. doi: 10.1016/j.geoen.2023.212530

[39] Teng, Y.M. (2015). Some problems in integral transform. *College Mathematics*, 31(1), 105–109.

[40] de Andrade, G.S., Nascimento, E.J., & de Lemos, M.J. (2024). Finite integral transform solution of unsteady heat conduction applied to thermal plug and abandonment of oil wells. *Applied Thermal Engineering*, 236(Part B), 121576. doi: 10.1016/j.applthermaleng.2023.121576

[41] Feng, D., Zhao, Z., Li, P., Li, Y., Zha, J., Hu, J., & Feng, Y. (2024). Multifunctional performance of carbon nanotubes in thermal energy storage materials. *Materials Today*, 75, 285–308. doi: 10.1016/j.mattod.2024.04.005

[42] Ouyang, D., Qin, C., Qin, X., Qing, L., & Yu, T. (2024). Thermal response of DNAN based explosives considering thermodynamic coupling: Under different charge quantity and diameter changes. *Case Studies in Thermal Engineering*, 58, 104290. doi: 10.1016/j.csite.2024.104290

[43] Alves, E.B., da Veiga, A.P., Fancello, E.A., & Barbosa Jr, J.R. (2024). A coupled model of wellbore-formation thermal phenomena and salt creep in offshore wells. *Geoenergy Science and Engineering*, 233, 212548. doi: 10.1016/j.geoen.2023.212548

[44] Tripathi, B.M., & Shukla, S.K. (2024). A comprehensive review of the thermal performance in energy efficient building envelope incorporated with phase change materials. *Journal of Energy Storage*, 79, 110128. doi: 10.1016/j.est.2023.110128

Co-published by
Institute of Fluid-Flow Machinery
Polish Academy of Sciences
Committee on Thermodynamics and Combustion
Polish Academy of Sciences

http://www.imp.gda.pl/archives-of-thermodynamics/

ARCHIVES OF THERMODYNAMICS

The impact of the behaviour of individual users in single-family households on the values of internal heat gains in a building

Alicja Wiącek[a*], Sebastian Werle[b], Mariusz Ruszel[c]

[a]Ignacy Łukasiewicz Doctoral School of Rzeszów University of Technology, Powstańców Warszawy 12, Rzeszów, 35-959, Poland
[b]Silesian University of Technology, Akademicka 2A, Gliwice, 44-100, Poland
[c]Rzeszow University of Technology, Powstańców Warszawy 12, Rzeszów, 35-959, Poland
*Corresponding author email: alicja.kardysz07@gmail.com

Received: 07.08.2024; revised: 04.01.2025; accepted: 03.03.2025

Abstract

The aim of this study is to analyse the presence and activity of users in individual households by means of quantitative and qualitative research – questionnaires and interviews. The users' behaviour has a significant impact on the thermal-flow processes taking place in the building, so their verification, ultimately, makes it possible to reduce the difference between the calculated and actual energy consumption of the building. The literature review revealed a lack of updated building occupancy schedules, which changed significantly after the COVID-19 pandemic. Based on the data collected, 6 household occupancy profiles were proposed, which, when combined, form a model describing behaviours (occupancy profile, profile of electrical appliances, lighting, natural ventilation, heating installations and supporting appliances). The model took into account the effect of internal heat gains on the energy balance of the building, including the working system – home office mode. The collected data was fed into a reference building model and an hourly dynamic simulation was carried out using commercial DesignBuilder software. Using outdoor climate parameters for selected cities, the reference building's annual heat demand was demonstrated and an assessment of the building's indoor microclimate was provided. The multi-criteria empirical approach resulting in a set of revised data can be generalised and adapted to a larger group of actors, a selected area and a building.

Keywords: Human behaviour; Schedules; Heat-flow processes; Heat demand

Vol. 46(2025), No. 2, 173–183; doi: 10.24425/ather.2025.154916

Cite this manuscript as: Wiącek, A., Werle, S., & Ruszel, M. (2025). The impact of the behaviour of individual users in single-family households on the values of internal heat gains in a building. *Archives of Thermodynamics*, 46(2), 173–183.

1. Introduction

The construction sector is widely recognised as one of the most energy-intensive [1]. In 2020, electricity and heat consumption in the residential sector in the European Union (EU) was 714 TWh, which amounts to 1.6 MWh (1595 kWh) per capita. The correct application of methodologies for determining the energy performance of buildings influences the accuracy of the scale of the problem and the improvement in their energy efficiency [2]. Static methods are subject to a large calculation error, and the use of dynamic methods, which give more accurate results, requires the introduction of a large number of parameters in complex calculation procedures [3]. Modelling these parameters is very labour-intensive, so many researchers use simplified static methods and, in the case of dynamic methods, parameter values derived from outdated literature data. The rapid development of technology has

Nomenclature

d – permissible error, %
m – fraction size
n – population size
$\mathbf{n}$ – sample size
u_α – value resulting from the adopted confidence level, %

Abbreviations and Acronyms

ASHRAE – American Society of Heating, Refrigerating and Air-Conditioning Engineers
Cfb – C = warm temperate, f = fully humid, b = warm summer
Dfb – D = continental, f = fully humid, b = warm summer
Dfc – D = continental, f = fully humid, c = cool summer
DHW – domestic hot water
DOE – Department of Energy
EPW – energy plus weather
ET – E = polar, T = tundra
EU – European Union
HDD – heating degree day
HDI – human development index
HVAC – heating, ventilation, air conditioning
IEA – International Energy Agency
MOTIE – Ministry of Trade, Industry and Energy
NOAA – National Oceanic and Atmospheric Administration
TMY – typical meteorological year

resulted in human dependence on appliances, which is why electricity consumption has increased very strongly in recent decades [4]. Consequently, the consideration of internal heat gains has become an important element in determining the thermal load of residential buildings.

Many researchers stress the importance of using the most realistic model of occupant presence and activity to perform dynamic energy analyses of buildings [5]. Despite this, authors still typically adopt the ASHRAE 90.1 standard in their energy analyses [6]. Lee et al. [7] conducted an analysis of the effect of internal heat gain levels on the determination of building envelope insulation standards for a large-scale office building. Although the analysis carried out was very detailed, the modelling of internal heat gains was based on standards and literature data: Department of Energy (DOE), American Society of Heating, Refrigerating and Air-Conditioning Engineers (ASHRAE), Ministry of Trade, Industry and Energy (MOTIE). Literature data on European electrical and hot water load profiles by the International Energy Agency (IEA) [8] were also used by Ampatzi and Knight [9]. In their work, the authors included patterns of daily electricity consumption to model internal heat gains, which have important implications for the performance design of solar thermal systems in multifamily buildings. Ferdyn-Grygierek et al. [10] included values of internal heat gains in their validation studies of daily heat demand, where for a school building, the values were adopted according to ASHRAE recommendations [11], and for a multi-family building, random tests were performed. On the basis of the results from random tests, the authors assumed constant heat gains, which is a major simplification with a high risk of calculation error with regard to performing dynamic simulations [11]. The results of the analysis of the influence of static and dynamic internal heat gains on heat demand by Elsland et al. [12] show that the static values used in the study are underestimated. In comparison with the existing knowledge, Firląg et al. [13] also showed that the standard values of internal heat gains differ from the actual measured values.

Furthermore, the literature shows that internal heat gains have mostly been modelled for office buildings [14]. Liang et al. [15] conducted a prediction of internal heat gains in an office building using artificial intelligence methods. The analysis was performed for an office building in China. The use of artificial intelligence methods is very time-consuming, and often, engineers do not have the expertise to perform internal heat gain prediction by such means. The use of fuzzy logic methods appears to be a faster and simpler solution for this type of modelling. Samaan et al. [16] built time schedules of internal heat gains using DesignBuilder software, but only for rooms located in the Mansoura University building. The authors focused their attention on the effect of heat gains from population and daylight on the cooling load of the rooms, abandoning any attempt to predict the heat demand due to the location of the building. As a result, it can be assumed that the analysis makes a significant contribution to the area of knowledge studied, but only for buildings located in tropical climates.

Detailed modelling of internal heat gains in relation to single-family and multi-family buildings has been conducted by several authors. Few analyses have referred to modelling the behavioural variables of individual occupants and their impact on the level of energy demand in single-family passive buildings [17]. Given that passive buildings currently do not account for a large share of the total number of households, the model is only applicable to a very narrow group of consumers. Such studies should be carried out for existing buildings that need to be thermally upgraded. Elsland et al. [12] performed an internal heat gain model for single-family and multi-family buildings at different age groups. The base year was 2008 and an electricity consumption projection scenario was considered until 2050. The scenario took an upward trend in electricity consumption into account, especially with regard to the increasing number of mobile devices. The authors subjected a very large survey sample (27 EU countries) to the study, thus giving indicative results. In this article, the patterns of daily electricity consumption were determined on the basis of the quantitative research carried out – questionnaires that were targeted at a smaller group of people. The individual approach allowed internal heat gains to be modelled with greater accuracy. In addition, the dynamic increase in electricity consumption caused, among other things, by the change to a home office system that occurred during the COVID-19 pandemic, and its continuation and trend towards persistence, indicates an update of the existing scenarios. The literature review showed a lack of such analysis in the last decade. Therefore, one of the key objectives of this study was to present an empirical approach identifying patterns of hourly electricity consumption in single-family buildings and modelling internal heat gains from these.

The analysis was performed in four stages:

1) Identify the area, subject and object of research;
2) Carry out a survey consisting of an on-site visit to a residential building and quantitative and qualitative research to collect datasets;
3) Performing modelling based on the empirical survey data obtained;
4) Carrying out dynamic simulations.

The approach presented here aims to build a theoretical database for engineers and researchers in an effort to improve their work. The modelling of behaviours and their variables makes it possible to accurately determine the heat demand of a building and thus to accurately size heating, ventilation and air-conditioning (HVAC) systems. Efficient operation of HVAC systems contributes to lowering the overall energy demand and thus to maintaining environmental sustainability. As a result, the approach presented aims to improve energy efficiency in residential buildings.

2. Method of solving the research problem

With the aim of building an authentic and contemporary model describing the behaviour of individual users in single-family households and determining its impact on the values of internal heat gains and thus on the heat balance of the building, the research was carried out using descriptive-analytical and simulation methods.

2.1. Descriptive-analytical method

The research was conducted in Norway in 2023. The validity of the choice is emphasised by the HDI (human development index) indicators, according to which Norway is the most developed country in the world after Switzerland [18]. The high standard of living of the population is ensured by the effective operation of state instruments for raw material policy. The revenue generated from oil and gas exports allows, among other things, the formation of a welfare state with the main focus on levelling income inequality in the country. The high national income per capita is synonymous with the desire to improve the quality of everyday life through, among other things, the purchase of high-end household appliances. This translates into the result of average electricity consumption in the residential sector, which fell by 18.5% between 2005 and 2020 [19]. However, the potential to reduce total energy consumption in the residential sector is even higher. Thus, the government's efforts are directed towards introducing financial support mechanisms for retrofitting older buildings and the scientific community’s efforts to identify the scale and scope of the problem and to search for the best building and architectural solutions to support the government’s efforts, which are already seen worldwide as a pioneering energy policy that is a model for many economies around the world.

With this in mind, selected Norwegian cities were taken as the study area in this paper, the subject was single-family households and the subject was Norwegian society. The exact study area was delineated according to the Köppen-Geiger climate classification [20] and the ANSI/ASHRAE 90.1 and 90.2 [21,22] classification system. An analysis of the literature and statistical data together with their interpretation was used to determine the research subject. However, the minimum size of the research subject (research sample) was determined using the following formula [23]:

$$\mathbf{n} = \frac{u_\alpha^2 \frac{m}{n}\left(1-\frac{m}{n}\right)}{d^2}, \qquad (1)$$

where **n** is the sample size, u_α is the value resulting from the adopted confidence level, m/n is the estimated proportion in the population (m − fraction size, n − population size) and d is the permissible error.

The confidence level was assumed to be 99% as the survey is targeted at a specific audience. The size of the fraction was assumed to be 50%, assuming that half the respondents may be users of single-family dwellings and half are not. The size of the survey population was calculated using statistics from Statistics Norway 2021. A margin of error of 5% was assumed for the survey sample selection [23].

In the next stage of the research, the data sets necessary to carry out energy simulations and thus determine the scale of the problem – the amount of energy demand in the selected households – were collected. The geometric and technical data sets of the building were constructed using the results from the site visit. On the other hand, the dataset describing the uses of the building was created using the results of quantitative (questionnaires made using Google Forms) and qualitative (interviews) research. Based on the collected dataset from the empirical research, a reference single-family residential building was modelled and a model was created to describe the behavioural patterns of the building’s occupants. Modelling was carried out in the commercial simulation software DesignBuilder [24]. Simulations of the dynamic distribution of internal heat gain values were performed using hourly weather data. A set of 8760 data records containing meteorological parameters, being a typical meteorological year (TMY), was downloaded from the international EnergyPlus database [25]. The EnergyPlus Weather (EPW) files in the repository were developed based on the methodology in ISO 15927-4:2005 [26] and weather data provided by the NOAA (National Oceanic and Atmospheric Administration).

3. Course of research

The course of the research consisted of identifying the research area, subject, and object. The research area was defined based on the Köppen-Geiger climate classification. Four main climate zones were distinguished, considering the significant impact of varying solar radiation gains and modeled internal lighting (dependent on daily solar insolation) on the amount of internal heat gains in buildings. Next, the subject of the research was defined, focusing on single-family residential buildings, which are characterized by the highest electricity consumption within the residential sector. In the final stage, the research sample (research object) was selected for survey distribution in order to develop a model describing the users' behavioral patterns.

3.1. Research area

Four major cities in Norway, located in four different climate zones – Bergen, Oslo, Tromsø and Vardø – were selected for the study. The weather conditions in these cities according to the Köppen-Geiger classification [20] were defined as oceanic climate (Cfb), continental, warm, humid climate (Dfb), subarctic climate (Dfc) and tundra climate (ET), respectively. The affiliation of these cities to climate zones according to the division by ASHRAE [27] is shown in Table 1.

Table 1. Division of Norwegian climate zones according to ASHRAE [27].

City	Climate zone	Description	Criteria
Bergen	5A	cool - moist	$3000 < HDD^{*}_{18°C} \leq 4000$
Oslo	6A	cool - moist	$4000 < HDD_{18°C} \leq 5000$
Tromsø	7	very cold	$5000 < HDD_{18°C} \leq 7000$
Vardø	8	subarctic	$HDD_{18°C} > 7000$

*HDD – heating degree day.

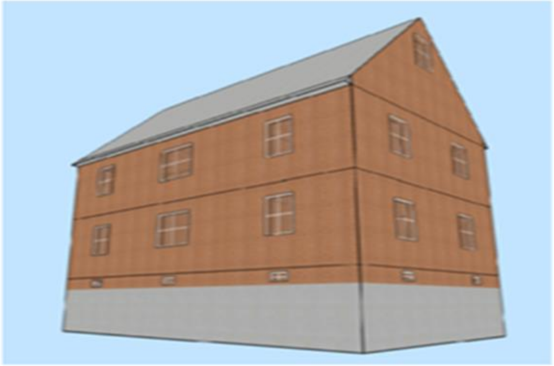

Fig. 1. The building under consideration. This model was created with DesignBuilder software.

Fig. 2. Layout of zones on the first floor. This model was created with DesignBuilder software.

3.2. Subject of the study

On the basis of the literature data, the residential buildings with the highest energy consumption were singled out. These are single-family households built before 1960 [28]. Their share of the total set of single-family households located in Norway is 30%, which means that this group has a significant impact on sectoral energy consumption and the level of emissions from energy consumption [29]. A detailed summary of the results from the analysis of statistical data on the number of single-family households built before 1960, relative to 2021, in the identified study area is presented in Table 2.

In order to collect geometrical and technical data, an on-site visit was made to a reference building, built before 1960, with a typical Norwegian timber-frame construction. The total volume of the building is 279 m^2, of which only 91 m^2 is the usable area of the heated part of the building. The basement level is unused, only one room is developed – the boiler room, where the electric hot water heater is located. The second storey is an enclosed, unheated area that serves as a utility room. The third storey is a usable, heated area which includes a kitchen, bathroom, hallway, living room and two bedrooms. The third storey is connected to the attic. The attic is occasionally used and heat is provided by convection. The measures for separating the unheated zone (basement, ground floor) and the heated zone (1st floor) aim to reduce the heat demand. A model of the building is shown in Fig. 1 and Table 3 summarises the parameters of the zones located on the first floor, which constitute the heated floor area (Fig. 2).

Table 2. Study subject selection - analysis of the number of single-family dwellings by year and locality [29].

Area	Number of single-family houses built before 1960	Number of single-family houses built between 1960 and 2021
Norway	380 819	1 284 892
Oslo	9407	27 210
Bergen	11647	36 008
Tromsø	2254	15 605
Vardø	365	787

Table 3. Area of usable space.

Zone	Purpose	Area of the room (m^2)
Corrido	Corridor	19.1
Bathroom	Bathroom	3.1
Kitchen	Kitchen	12.5
Living room	Living room with dining area	24.8
Bedroom 1	Parents' bedroom	13.2
Bedroom 2	Children's bedroom	18.3
Total usable area	Usable, heated	91.0

Table 4. Building envelope data. Infiltration is 10 air changes per hour at a pressure difference of 50 Pa.

Partition type	Building material	Unit (W/m²K)
External wall	exterior wood cladding (spruce) unventilated air void tar paper (windproofing) timber frame construction (trusses) interior wood cladding (spruce)	1.45
Inner wall	wood cladding (spruce) wooden construction unventilated air void wood cladding (spruce)	2.17
Exterior doors	wooden double doors	4.92
Floor on the ground	compacted threshing floor	3.13
Foundation wall (basement)	clinker brick plaster	3.57
Exterior windows	single pane	5.00
Lower internal ceiling	wooden ceiling joists unventilated air void wooden planks joists clay floorboards (spruce)	1.53
Internal upper floor	wooden ceiling joists unventilated air void wooden planks joists clay floorboards (spruce)	2.14
Roof	slate tar paper unventilated air void timber frame construction interior wood cladding (spruce)	2.83

A technical and structural inventory of the residential building under study was carried out in order to determine the measurement of all structural elements that are a source of heat loss and gain (Table 4). On the other hand, the heat transfer coefficients for windows and doors were adopted on the basis of data and information from the European building classification database TABULA – EPISCOPE [28].

In addition, on the basis of a site visit and an interview with the users of a reference residential building, the following relationships were introduced into the model:

1) The building is supplied with electricity from a single-phase low-voltage network − 230V IT system;
2) The primary source of heat is 5 electric radiators, supporting an air conditioner with heating function and a wood-burning fireplace; in the bathroom the source of heat is electric underfloor heating made of heating cables;
3) A water heater located in the basement (unheated zone) is used to cover the domestic hot water (DHW) demand, so the total heat transfer coefficient between hot water and air was assumed to be 2.6 W/K;
4) The building has natural displacement ventilation (duct in the chimney), exhaust grilles in the bathroom and a 120 m/h exhaust package in the kitchen. Local fresh air supply is provided by window leaks.

Quantitative research – questionnaires – and qualitative research – interviews – were carried out to build a model describing the behaviour of users located in the reference building, the subject of this study. The size of the research sample was calculated according to Eq. (1). Current statistics from Statistics Norway [30] were used in the calculations. Based on these data, it was assumed that there are two adults per household. Also, taking into account data on the number of buildings built before 1960 in Oslo, Bergen, Tromsø and Vardø (Table 2), the population size was calculated to be 47 346 people. A margin of error of 5% was assumed for the survey sample selection. An anonymous survey was conducted among 654 people, using Google Forms. The questions on the form were structured to build a model describing behaviour consisting of six areas based on their answers:

1) usage profile that affects human heat gain,
2) usage profile that affects heat gain from lighting,
3) usage profile that affects heat gains from electrical appliances,
4) usage profile that has the effect of reducing electricity and heat demand as a result of lowering the setpoint temperature,
5) usage profile that affects the ventilation of the premises,
6) usage profile that affects the heat gain from burning wood in a fireplace.

4. Results

4.1. Results of the descriptive-analytical study

On the basis of a preliminary analysis of the results from the environmental survey, a study group was identified, with the subjects being traditional Norwegian families with a size of 2+2. In turn, assumptions were made about the timing of daily activities, based on the findings, which are necessary for modelling the usage profiles.

4.1.1. Usage profile 1

Assumptions:

1) From Monday to Friday, both adults work. One works remotely (at home) from 8.00−16.00, while the other works at the company's premises (away from home) from 8.00−18.00;
2) From Monday to Friday, three people are in the kitchen from 7.00−8.00;
3) From Monday to Friday, two children are in school from 8.00−16.00;
4) Monday to Friday, after school and work, from 16.00−18.00, one adult and two children stay in the kitchen;
5) Every weekday from 18.00 to midnight, two adults stay in the lounge;
6) Every weekday from 18.00 to 8.00, two children are in bedroom 2;
7) Every weekday from 0.00 to 8.00, two adults stay in bedroom 1;

Table 5. Usage profiles for calculating human heat gains.

Usage profiles (human heat gains)					
Hours of use		Zone	Value		Purpose
Monday to Friday	Saturday and Sunday		Monday to Friday	Saturday and Sunday	
8 h (8.00–16.00)	10 h (8.00–18.00)	Lounge	0.25	1.0	Inactive rest
1 h (7.00–8.00) 2 h (16.00–18.00)	0	Kitchen	0.75	0.0	Active relaxation
6 h (18.00–24.00)	6 h (18.00–24.00)	Lounge	0.50	0.5	Inactive rest
7 h (24.00–7.00)	7 h (24.00–7.00)	Bedroom 1	0.50	0.5	Sleeping
9 h (18.00–7.00)	9 h (18.00–7.00)	Bedroom 2	0.50	0.5	Sleeping

8) On Saturday and Sunday, the whole family is in the lounge from 8.00–18.00;
9) On Saturday and Sunday, the kitchen is not in use.

Based on the assumptions quoted, a usage profile schedule was constructed and tabulated (Table 5).

4.1.2. Usage profile 2

In order to build a second occupancy profile that influences the heat gain from lighting in each of the zones analysed, time slots were defined in the separate cities in which people are simultaneously present and using lighting that imitates daylight. A schedule (Table 6) was constructed based on the hours of occupancy in each room (Table 5) and based on an analysis of hourly reports showing typical weather conditions for Oslo, Bergen, Tromsø and Vardø. This analysis made it possible to extract the dependent variables – the hours of sunrise and sunset and the number of hours of sunshine – which, in combination with the occupancy schedule, determine the duration of lighting use during the day.

The modelled profile was also supplemented with information resulting from the quantitative survey, participatory observation and the technical and structural inventory. Based on the collected research material, assumptions were made, stating that:

1) More than half of the respondents surveyed are away from work and school during their free period (lasting at least 3 days);
2) 70% of these people declared that the period falls during the Easter holidays, during the May holidays enacted as public holidays and during the summer holidays. According to respondents, the most common month for summer holidays is July, with the holiday itself lasting 3 weeks. In order to input this data into the simulation software, these periods were assumed to fall on the following dates:
    - 14.04 − 18.04,
    - 03.06 − 06.06,
    - 04.07 − 24.07;
3) The majority of the Norwegian population has lights on in the corridor 24 hours a day, as a result of the habits they have retained;
4) The density of lighting power installed in each room is:
    - in the living room: 1.00 W/m^2,
    - in the corridor: 0.27 W/m^2,
    - in the kitchen: 0.63 W/m^2,
    - in bedroom 2: 0.28 W/m^2,
    - in bedroom 1: due to the usage profile, the lighting density is 0,
    - in the bathroom: the density of the luminous flux falling on the surface is negligible and has therefore not been taken into account.

4.1.3. Usage profile 3

The third use profile refers to the schedule of hours of use of electrical appliances (Table 7). The operation of these units results in heat exchange through the movement of gas streams (convection) creating heat gains, which are important in the energy balance of a building. By implementing the first schedule, which describes the occupancy profiles at specific time intervals in specific rooms (Table 5), it can be concluded that:

1) Throughout the living room, individual users use electrical appliances;
2) Between 7.00 and 8.00, individual users use a kettle and microwave;
3) During the two-hour period (16.00−18.00), the family uses the induction hob and oven in the kitchen. During this time, individual users programme the automatic switching on of the washing machine, dryer and dishwasher during the night time interval (0.00−3.00), due to the financial savings resulting from the lower price of electricity in the night zone;
4) The washing machine and dryer are located in the hallway. The washing machine operates from 0.00−01.00, while the dryer operates from 1.00−3.00;
5) The family does not use electrical appliances in the bedrooms and bathroom.

4.1.4. Usage profile 4

Based on the quantitative study carried out – a questionnaire, addressed to a selected sample of the Norwegian population, living in single-family households built before 1960, it can be concluded that the respondents surveyed are highly consumer-conscious people. Almost 70% of the respondents answered that, during a prolonged absence, the set temperature, which is 20°C, is lowered to 16°C, in each room. A prolonged absence was defined as the absence of all occupants of a household during the Easter holidays, the May break and the holiday season. Based on these assumptions and the geometry of the building, the occupancy profile presented in Table 8 was constructed.

Table 6. Usage profiles for calculating heat gains from lighting.

Usage profiles (heat gains from lighting)					
Hours of use Monday to Sunday*					
Month	**City**				**Zone**
	Oslo	Bergen	Tromsø	Vardø	
January	10 h (8.00–9.00 & 15.00–24.00)	10 h (8.00–9.00 & 15.00–24.00)	16 h (8.00–24.00)	16 h (8.00–24.00)	Lounge
	3 h (7.00–8.00 & 16.00–18.00)	3 h (7.00–8.00 & 16.00–18.00)	3 h (7.00–8.00 & 16.00–18.00)	3 h (7.00–8.00 & 16.00–18.00)	Kitchen
	2 h (18.00–20.00)	2 h (18.00–20.00)	2 h (18.00–20.00)	2 h (18.00–20.00)	Bedroom 2
	24h	24h	24h	24h	Corridor
February	8 h (16.00–24.00)	9 h (8.00–9.00 & 16.00–24.00)	11 h (8.00–9.00 & 14.00–24.00)	12 h (8.00–9.00 & 13.00–24.00)	Lounge
	3 h (7.00–8.00 & 16.00–18.00)	3 h (7.00–8.00 & 16.00–18.00)	3 h (7.00–8.00 & 16.00–18.00)	3 h (7.00–8.00 & 16.00–18.00)	Kitchen
	2 h (18.00–20.00)	2 h (18.00–20.00)	2 h (18.00–20.00)	2 h (18.00–20.00)	Bedroom 2
	24 h	24 h	24 h	24 h	Corridor
March	7 h (17.00–24.00)	6 h (18.00–24.00)	8 h (16.00–24.00)	9h (15.00–24.00)	Lounge
	1 h (17.00–18.00)	0 h	2 h (16.00–18.00)	2 h (16.00–18.00)	Kitchen
	2 h (18.00–20.00)	2 h (18.00–20.00)	2 h (18.00–20.00)	2 h (18.00–20.00)	Bedroom 2
	24h	24 h	24 h	24 h	Corridor
April	4 h (20.00–24.00)	4 h (20.00–24.00)	5 h (19.00–24.00)	5 h (19.00–24.00)	Lounge
	0 h	0 h	0 h	0 h	Kitchen
	0 h	0 h	1 h (19.00–20.00)	1h (19.00–20.00)	Bedroom 2
	24 h	24h	24 h	24 h	Corridor
May	3 h (21.00–24.00)	3 h (21.00–24.00)	2 h (22.00–24.00)	3 h (21.00–24.00)	Lounge
	0 h	0 h	0 h	0 h	Kitchen
	0 h	0 h	0 h	0 h	Bedroom 2
	24 h	24 h	24 h	24 h	Corridor
June	2 h (22.00–24.00)	2 h (22.00–24.00)	0 h	0 h	Lounge
	0 h	0 h	0 h	0 h	Kitchen
	0 h	0 h	0 h	0 h	Bedroom 2
	24 h	24 h	24 h	24 h	Corridor
July	2 h (22.00–24.00)	1 h (23.00–24.00)	0 h	0 h	Lounge
	0 h	0 h	0 h	0 h	Kitchen
	0 h	0 h	0 h	0 h	Bedroom 2
	24 h	24 h	24 h	24 h	Corridor
August	3 h (21.00–24.00)	2 h (22.00–24.00)	1 h (23.00–24.00)	2 h (22.00–24.00)	Lounge
	0 h	0 h	0 h	0 h	Kitchen
	0 h	0 h	0 h	0 h	Bedroom 2
	24 h	24 h	24 h	24 h	Corridor
September	4 h (20.00–24.00)	4 h (20.00–24.00)	4 h (20.00–24.00)	5 h (19.00–24.00)	Lounge
	0 h	0 h	0 h	0 h	Kitchen
	0 h	0 h	0 h	1 h (19.00–20.00)	Bedroom 2
	24 h	24 h	24 h	24 h	Corridor
October	6 h (18.00–24.00)	5 h (19.00–24.00)	6 h (18.00–24.00)	7 h (17.00–24.00)	Lounge
	0 h	1 h (7.00–8.00)	0 h	1 h (17.00–18.00)	Kitchen
	2 h (18.00–20.00)	1 h (19.00–20.00)	2 h (18.00–20.00)	2 h (18.00–20.00)	Bedroom 2
	24 h	24 h	24 h	24 h	Corridor
November	8 h (16.00–24.00)	8 h (16.00–24.00)	10 h (14.00–24.00)	11 h (13.00–24.00)	Lounge
	2 h (16.00–18.00)	3 h (7.00–8.00 & 16.00–18.00)	3 h (7.00–8.00 & 16.00–18.00)	3 h (7.00–8.00 & 16.00–18.00)	Kitchen
	2 h (18.00–20.00)	2 h (18.00–20.00)	2 h (18.00–20.00)	2 h (18.00–20.00)	Bedroom 2
	24 h	24 h	24 h	24 h	Corridor
December	9 h (8.00–9.00 & 15.00–24.00)	10 h (8.00–9.00 & 15.00–24.00)	16 h (8.00–24.00)	16 h (8.00–24.00)	Lounge
	3 h (7.00–8.00 & 16.00–18.00)	3 h (7.00–8.00 & 16.00–18.00)	3 h (7.00–8.00 & 16.00–18.00)	3 h (7.00–8.00 & 16.00–18.00)	Kitchen
	2 h (18.00–20.00)	2 h (18.00–20.00)	2 h (18.00–20.00)	2 h (18.00–20.00)	Bedroom 2
	24 h	24 h	24 h	24 h	Corridor

*On Saturday and Sunday, the number of hours the kitchen is lit is 0 h.

*In the periods: 14.04–18.04 (Easter holidays), 3.06–06.06 (Pentecost), 4.07–24.07 (holiday period) the residential building is unoccupied, heat gains are 0 h.

Table 7. Usage profiles for calculating heat gains from electrical appliances.

Usage profiles (heat gains from electrical appliances)					
Hours of use		**Zone**	**Electrical equipment**	**Total power of appliances in the room (W)***	
Monday to Friday	**Saturday and Sunday**			**Monday to Friday**	**Saturday and Sunday**
8 h (8.00–16.00) 6 h (18.00–24.00)	10 h (8.00–18.00) 6 h (18.00–24.00)	Lounge	Laptop TV	315	315
3 h (7.00–8.00 & 16.00–17.00)	0	Kitchen	Kitchen appliances	3800	100**
3 h (24.00–01.00 & 01.00–03.00)	0	Corridor	Washer and dryer	1500	100**

*   Power of equipment is based on specifications provided by the manufacturer.

** Assuming that only the fridge works for 24 hours on Saturday and Sunday.

Table 8. Usage profile, which influences the reduction in electricity and heat demand as a result of lowering the set-point temperature.

Room	Setpoint temperature (°C)	Set-back temperature (°C)
Lounge	20	16
Kitchen	20	16
Bathroom	24	16
Corridor	20	16
Bedroom 1,2	20	16

4.1.5. Usage profile 5

The interdependence of the presented schedules and the assumptions derived from them also has a significant impact on the effectiveness of the natural ventilation. For the purpose of the simulation, it was assumed that the presence of any of the individual users in the building is equivalent to the operation of the natural air exchange system. A study involving participant observation showed that, when present, the individual users ventilate the building by opening the windows, provided that the outside air temperature is not below 10°C. Based on Table 5, it can be concluded that at least one individual user is in the household 24 hours a day, except during holidays and vacation periods.

4.1.6. Usage profile 6

The technical and structural inventory carried out showed that an additional supporting heat source is the fireplace. Due to its sporadic operation depending directly on usage, a schedule of operation for this heat source was developed at the input stage. A review of weather data from meteorological files (Oslo, Bergen, Tromsø, Vardø) showed that the winter period runs from 1 October to 30 April. According to a schedule defining the hourly range of individual users in the room, and according to the conclusions presented from the participatory observation, assumptions were extracted regarding the fireplace use profile. According to this, the fireplace is used for two hours from 18.00−20.00 in the living room, by two people, during the winter period.

As assumed by the manufacturer, the nominal power of the fireplace used by individual domestic users is 6000 W. Based on the assumptions outlined above, it can be inferred that this fireplace is operating at around 50%, thus showing that the final power is 3000 W. To simplify the model, the chimney loss was assumed to be approximately 30%, meaning that the usable power is 2100 W. According to the calculation methodology for combustion heat gains contained in DesignBuilder, in which the radiant factor is 0.3 W, it can be tentatively concluded that the radiant power that influences the level of warm comfort and the heating of the walls, located in the vicinity of the fireplace, is 630 W. From this assumption, on the other hand, it follows that the convective power that heats the air is 1470 W.

4.2. Results of the hourly building energy simulation study

All the data and assumptions collected through the empirical studies carried out were entered into DesignBuilder and energy simulations were then carried out on the reference building. The results are shown in Tables 9−12.

Table 9. Annual contribution of gains and losses to the annual heat balance – Oslo.

Profit and loss statement – reference building in Oslo			
Heat gains	**Value (kWh)**	**Heat losses**	**Value (kWh)**
from lighting	102.7	through transparent partitions	–6 202.8
from electrical appliances	4 511.6	through the building envelope	–15 975.7
from people	1 778.3	through the ceiling	–12 974.8
from solar radiation	4 823.1	through the floor	–1 462.6
		ventilation	–2 215.2
		infiltration	–5 161.0
Total profits	11 215.7	**Total profits**	–43 992.1

Table 10. Annual contribution of gains and losses to the annual heat balance – Bergen.

Profit and loss statement – reference building in Bergen			
Heat gains	**Value (kWh)**	**Heat losses**	**Value (kWh)**
from lighting	102.7	through transparent partitions	–5 688.4
from electrical appliances	4 511.6	through the building envelope	–16 517.8
from people	1 783.6	through the ceiling	–12 249.7
from solar radiation	3 389.0	through the floor	–1 307.4
		ventilation	–945.4
		infiltration	–4 735.1
Total profits	9 786.9	**Total profits**	–41 443.8

Table 11. Annual contribution of gains and losses to the annual heat balance − Tromsø.

Profit and loss statement – reference building in Tromsø			
Heat gains	**Value (kWh)**	**Heat losses**	**Value (kWh)**
from lighting	102.7	through transparent partitions	–8 383.1
from electrical appliances	4 511.6	through the building envelope	–24 131.6
from people	1 786.7	through the ceiling	–16 531.1
from solar radiation	3 565.3	through the floor	–1 568.7
		ventilation	–293.5
		infiltration	–5 949.9
Total profits	9 966.3	**Total profits**	–56 857.9

Table 12. Annual contribution of gains and losses to the annual heat balance − Vardø.

Profit and loss statement – reference building in Vardø			
Heat gains	**Value (kWh)**	**Heat losses**	**Value (kWh)**
from lighting	102.7	through transparent partitions	–8 157.8
from electrical appliances	4 511.6	through the building envelope	–24 638.3
from people	1 778.3	through the ceiling	–16 603.0
from solar radiation	3 269.7	through the floor	–1 528.2
		ventilation	–175.5
		infiltration	–6 164.3
Total profits	9 672.0	**Total profits**	–57 267.1

Numerical simulations of heat-flow processes have shown that the energy demand of the reference building in Vardø is the highest at 46 937 kWh (including the heat from burning wood in the fireplace -657.4 kWh). This compares with 32 119 kWh in Oslo, 30 999 kWh in Bergen and 46 234 kWh in Tromsø.

The calculations carried out with an hourly calculation step for the whole year (8 760 hours) also made it possible to determine the technical condition of the residential building under study and to assess the microclimate inside. The simulations carried out showed that there was an air exchange problem in the reference building as a result of the impaired operation of the natural ventilation system responsible for removing excess heat from the building and supplying fresh air to the interior. As a result, there was a loss of thermal comfort for the individual occupants and a decrease in indoor air quality.

5. Conclusions and discussion

The data collected from the empirical research conducted made it possible to build a model to describe the behaviour of individual users, thus reducing the discrepancy between actual and assumed premises. Undoubtedly, the accurately developed model has contributed to results with less calculation error across the entire energy balance. On the basis of the calculations carried out, it has been shown that the percentage of heat gain from people, lighting, appliances and solar radiation in the energy balance, respectively, is for Oslo 20%, Bergen 35%, with reference to Tromsø 32%, while taking into account the climatic conditions in Vardø, the percentage is 22%. Such a high share of heat gain equates to the need for accurate modelling of behaviour. Thus, simplified monthly calculation methods, often used to determine energy characteristics for single-family households, which take into account implicit internal heat gain parameters should not be implemented. As the literature review in the introduction showed, this problem is already known, but researchers are still working to solve it. The model presented in this paper describing the behaviours that influences the level and distribution of heat gains in the energy balance is undoubtedly one solution. It seems that the biggest problem lies with national regulations, which, despite many recommendations, allow the use of monthly methods to calculate annual energy demand. On the other hand, if changes are made to the need for the hourly method, there is a high risk of job losses for those currently performing energy performance based on basic knowledge and simplified calculation methods.

In highly developed countries such as Norway, people's awareness is at a very high level, so that even though national regulations allow a simplified, monthly method for determining annual energy demand to be used, only software based on the hourly method is used in practice. Therefore, the question arises of whether one solution to the research problem of determining the influence of behaviour on the value of internal heat gains in a building is to raise public awareness of the use of the calculation method.

Furthermore, it should be noted that the use of time-varying internal heat gains that affect the dynamics of the heat flow through the building allows the precise determination of the heating power of the equipment, the selection of which, in actual use, determines its final efficiency and energy performance. Thus, the introduction of accurate data also makes it possible to verify the problems occurring in the heat flow performance of buildings, and thus provides the opportunity to build an appropriately adapted retrofit scenario and avoid a number of mistakes in the future. Although internal heat gains have a significant impact on the selection of heating power of devices, uncertainty in their determination is still caused by future climate changes. The size of the heat demand is largely determined by the parameters of the external climate. Taking into account the lifespan of buildings, the authors also recommend taking into account climate analyses in the selection of heating systems.

References

[1] Deka, P., & Szlęk, A. (2022). Thermal energy storage in buildings: Opportunities and challenges. *Archives of Thermodynamics*, 43(4), 21−61. doi:10.24425/ather.20220144405

[2] Kreider, J.F., & Haberl, J.S. (1994). Predicting hourly building energy use: The great energy predictor shootout – Overview and discussion of results. *ASHRAE Transactions*, 100(2), 1104−1118.

[3] Ziębik, A., & Stanek, W. (2020). Energy efficiency – selected thermo-ecological problems. *Archives of Thermodynamics*, 41(2) 277−279. doi: 10.24425/ather.2020.133633

[4] Mikielewicz, J., & Mikielewicz, D. (2024). Influence of thermodynamics on the development of technology and science. *Archives of Thermodynamics*, 45(2) 51−61. doi: 10.24425/ather.2024.150851

[5] Karlsson, F., Rohdin, P., & Persson, M.-L. (2007). Measured and predicted energy demand of a low energy building: important aspects when using Building Energy Simulation. *Building Services Engineering Research and Technology*, 28, 223−235. doi: 10.1177/0143624407077393

[6] Destro, N., Benato, A., Stoppato, A., & Mirandola, A. (2016). Components design and daily operation optimization of a hybrid system with energy storages. *Energy*, 117(2), 569−577. doi: 10.1016/j.energy.2016.05.097

[7] Lee, J., Kim, J., Song, D., & Jang, Ch. (2017). Impact of external insulation and internal thermal density upon energy consumption of buildings in a temperate climate with four distinct seasons. *Renewable and Sustainable Energy Reviews*, 75, 1081−1088. doi: 10.1016/j.rser.2016.11.087

[8] Knight, I., Kreutzer, N, Manning, M., Swinton, M., & Ribberink, H. (2007). *European and Canadian non-HVAC electric and DHW load profiles for use in simulating the performance of residential cogeneration systems* [A report of Subtask A of FC+COGEN-SIM: The simulation of building-integrated fuel cell and other cogeneration systems: Annex 42 of the International Energy Agency, Energy Conservation in Buildings and Community Systems Programme]. IEA.

[9] Ampatzi, E., & Knight, I. (2012). Modelling the effect of realistic domestic energy demand profiles and internal gains on the predicted performance of solar thermal systems. *Energy and Buildings*, 55, 285−298. doi: 10.1016/j.enbuild.2012.08.031

[10] Ferdyn-Grygierek, J., Bartosz, D., Specjal, A., & Grygierek, K. (2018). Analysis of accuracy determination of the seasonal heat demand in buildings based on short measurement periods. *Energies*, 11(10), 2734. doi: 10.3390/en11102734

[11] American Society of Heating, Refrigerating and Air-Conditioning Engineers (1997). *ASHRAE Handbook Fundamentals* (SI edition).

[12] Elsland, R., Peksen, I., & Wietschel, M. (2014). Are internal heat gains underestimated in thermal performance evaluation of buildings? *Energy Procedia*, 62, 32−41. doi: 10.1016/j.egypro.2014.12.364

[13] Firląg, S., & Zawada, B. (2013). Impacts of airflows, internal heat and moisture gains on accuracy of modeling energy consumption and indoor parameters in passive building. *Energy and Buildings*, 64, 372−383. doi: 10.1016/j.enbuild.2013.04.024

[14] Saelens, D., Parys, W., & Baetensa, R. (2011). Energy and comfort performance of thermally activated building systems including occupant behavior. *Building and Environment*, 46(4), 835−848. doi: 10.1016/j.buildenv.2010.10.012

[15] Liang, R., Ding, W., Zandi, Y., Rahimi, A., Pourkhorshidi, S., & Khadimallah, M.A. (2022). Buildings internal heat gains prediction using artificial intelligence methods. *Energy and Buildings*, 258, 111794. doi: 10.1016/j.enbuild.2021.111794

[16] Samaan, M.M., Farag, O., & Khalil, M. (2018). Using simulation tools for optimizing cooling loads and daylighting levels in Egyptian campus buildings. *HBRC Journal*, 14(1), 79−92. doi: 10.1016/j.hbrcj.2016.01.001

[17] Blight, T.S., & Coley, D.A. (2013). Sensitivity analysis of the effect of occupant behaviour on the energy consumption of passive house dwellings. *Energy and Buildings*, 66, 183−192. doi: 10.1016/j.enbuild.2013.06.030

[18] UNDP (2024). *Human Development Report 2023/2024. Breaking the gridlock: Reimagining cooperation in a polarized world*. United Nations Development Programme.

[19] Statistisk sentralbyrå - SSB. (2021). *Production and consumption of energy, energy balance and energy account*. Statistics Norway (in Norwegian).

[20] Köppen, W., & Geiger, R. (1936). *The Geographical System of Climate.* In *Handbook of Climatology*. Verlag Gebrüder Borntraeger (in German).

[21] ANSI/ASHRAE/IESNA (2016). *ANSI/ASHRAE/IESNA Standard 90.1-2016. Energy standard for buildings except low-rise residential buildings*. American Society of Heating, Refrigerating and Air-Conditioning Engineers, Inc.

[22] ANSI/ASHRAE (2007). ANSI/ASHRAE *Standard 90.2-2007. Energy-efficient design of low-rise residential buildings*. American Society of Heating, Refrigerating and Air-Conditioning Engineers, Inc.

[23] Matuszak, A., & Matuszak, Z. (2011). Definition of the sample and its size in pedagogical research. *General and Professional Education*, 2, 33–39 (in Polish).

[24] DesignBuilder software. https://designbuilder.co.uk/

[25] *Repository of Building Simulation Climate Data*. Climate.OneBuilding.Org. https://climate.onebuilding.org/ [accessed 10 June 2024].

[26] ISO (2005). *ISO 15927-4:2005*. *Hygrothermal performance of buildings – calculation and presentation of climatic data*. *Part 4: data for assessing the annual energy for heating and cooling*. International Organization for Standardization.

[27] ANSI/ASHRAE (2013). *ANSI/ASHRAE Addendum a to ANSI/ASHRAE Standard 169-2013. Climatic data for building design standards*. American Society of Heating, Refrigerating and Air-Conditioning Engineers, Inc.

[28] Brattebø, H., O'Born, R., Sartori, I., Klinski, M., & Nørstebø, B. (2016). *Typologies for Norwegian residential buildings − Examples of measures for energy efficiency*. TABULA – EPISCOPE - prosjektet (in Norwegian).

[29] Statistisk sentralbyrå - SSB. (2021). *Housing by building type and year of construct*ion. Statistics Norway (in Norwegian).

[30] Statistisk sentralbyrå - SSB. (2021). *Population in Norway*. Statistics Norway (in Norwegian).

Co-published by
Institute of Fluid-Flow Machinery
Polish Academy of Sciences
Committee on Thermodynamics and Combustion
Polish Academy of Sciences

http://www.imp.gda.pl/archives-of-thermodynamics/

ARCHIVES OF THERMODYNAMICS

Simplified dynamic heat exchanger models for heat recovery steam generators

Nabil Youssef[a,b*], Assaad Zoughaib[a], Valentin Drouet[b]

[a]Mines Paris – PSL, 60 Boulevard Saint Michel, 75006 Paris, France
[b]Metroscope, 63 Boulevard Haussmann, 75008 Pairs, France
*Corresponding author email: nabil.youssef@metroscope.tech

Received: 30.12.2024; revised: 05.02.2025; accepted: 09.02.2025

Abstract

Monitoring power plants necessitates sophisticated methods and reliable dynamic models, especially with the increasing flexibility demand. The primary challenge of this work is to develop a modelling strategy for heat recovery steam generators (HRSG) that enables simple yet accurate simulation of their dynamic behaviour, accounting for the delayed response of their heat exchangers to load variations caused by high thermal inertia. The proposed modelling methodology aims to build models suitable for monitoring power plants based on a set of sensor measurements, which can realistically be found in a power plant. This approach eliminates the need for extensive system design information, which may not always be accessible to the modeller. First, fully detailed, pseudo three dimensional Modelica model of the monophasic heat exchangers is developed. The model is then simplified progressively while the impact on accuracy is assessed. A more simplified model is later developed by assuming a lumped global heat transfer coefficient and a mass. The simplified model provides promising results, demonstrating a good compromise between simple calibration process and accuracy. A model of the evaporator is also presented and validated based on literature. Finally, a qualitative analysis of the full HRSG model is conducted. The dynamic behaviour as well as the time constants of the heat exchangers are analysed. The results demonstrate a good agreement with the expected physical behaviour.

Keywords: Dynamic modelling; Steam generation; Heat exchanger; Model calibration; Model reduction

Vol. 46(2025), No. 2, 185–197; doi: 10.24425/ather.2025.154197

Cite this manuscript as: Youssef, N., Zoughaib, A., & Drouet, V. (2025). Simplified dynamic heat exchanger models for heat recovery steam generators. *Archives of Thermodynamics*, 46(2), 185–197.

1. Introduction

Power generation is simultaneously the largest carbon dioxide emitter and a key driver in the transition to zero emissions. This is insured by a rapid expansion of renewable energy sources, which are expected to overtake coal as the largest source in 2025 [1]. The net additions to renewable energy capacity are dominated by wind and solar, which are inherently variable, contributing to a fluctuating feed-in power to the grid. This poses a challenge to grid operators in maintaining the load and supply balance [2].

Several solutions, such as energy storage and operational flexibility, are being deployed. Existing conventional power plants, like combined cycle gas turbines (CCGTs), will operate alongside renewable energies to ensure flexibility from the supply side in the short to medium term.

CCGT power plants offer a combination of advantages compared to other types of power plants, such as high efficiency, including during part load operations, fast start-up and good operational flexibility [3]. However, the dynamic flexibility of CCGT is restricted by its heat recovery steam generator (HRSG) because of its thick-walled components, requiring more transi-

Nomenclature

A – heat exchange area, m^2
C_p – specific heat capacity at constant pressure, J/(kg K)
D – diameter, m
e – thickness, m
g – gravitational acceleration, m/s^2
H – height, m
h – specific enthalpy, J/(kg K)
k – heat transfer coefficient, W/(m^2 K)
l – water level, m
L – length, m
$\dot{m}$ – mass flow rate, kg/s
m – mass, kg
n – number of discretization elements
N_r – number of rows
Nu – Nusselt number
P – pressure, Pa
Pr – Prandtl number
$\dot{q}$ – heat flow, W
r – radius, m
r_{UA} – ratio
Re – Reynolds number
S – pitch, m
t – time, s
T – temperature, K
$\bar{T}$ – average temperature, K
u – specific internal energy, J/(kg K)
v – flow speed, m/s
U – overall heat transfer coefficient, W/(m^2 K)
V – volume, m^3
x_r – steam quality at the riser outlet
$\overline{x_v}$ – average volume fraction in the riser

Greek letters

α – thermal diffusivity, m^2/s
β – constant parameters in drum equations
ζ – friction coefficient
η – efficiency
λ – thermal conductivity, W/(m K)
μ – dynamic viscosity, kg/(m s)
ρ – density, kg/m^3
τ – time constant, s

Subscripts and Superscripts

a – air
c – condensation
conv– convection
d – drum
e – along tube thickness
f – fins
fg – flue gas
fw – feedwater
i – inner side of the tube
in – inlet
l – longitudinal
o – outer side of the tube
out – outlet
n – time step number
r – riser
s – steam
t – transversal
tot – total
w – water
wall– tubes wall
z – along tube length

Abbreviations and Acronyms

HRSG – heat recovery steam generator
CCGT – combined cycle gas turbine
HP – high pressure
IP – intermediate pressure
LP – low pressure
Eco – economizer

tion time.

The increasing frequency of flexible operation modes in power generation assets promotes the use of digital solutions to help maintain safety, availability, and efficiency. In [4,5], dynamic models are developed to improve the start-up time of a CCGT while assessing the state of stressed components to maintain safe operation. In [6], two models are compared to estimate the reduction of the residual life of a CCGT power plant due to its flexible operation. It states that load cycling triggers damage, failures, and frequent unplanned maintenance work. In [7], dynamic simulations are carried out to highlight the advantages of a new hybrid once-through and natural circulation HRSG over conventional natural circulation ones. Moreover, model-based and model-free fault detection and diagnosis techniques are applied to prevent power generation losses and extended downtimes, such as in [8,9]. Models presented in the literature often rely heavily on detailed design information. While this dependence can improve their accuracy, it also introduces challenges such as increased calibration complexity and slower simulation times. These factors can limit their scalability and applicability in scenarios where comprehensive design data is not available or where computational efficiency is critical.

In this study, a modelling methodology of the HRSG is presented. Figure 1 shows a diagram of a simplified CCGT. The HRSG is placed at the gas turbine's exhaust to recover the remaining energy contained in the hot flue gases. It is composed of a series of heat exchangers. Water flows inside the tubes while the hot flue gas flows from the outside. Three main types of heat exchangers are used:

- Economizer: liquid water is heated to a point near saturation;
- Evaporator: liquid water is evaporated in once-through or drum-type evaporators [10];
- Superheaters: steam is superheated before it is sent to steam turbines to maximize efficiency while respecting the mechanical limits of the blades.

In economizers and superheaters, water flows as a single-phase fluid, liquid, or steam, while in evaporators, phase change occurs. Single-phase heat exchangers dominate the space of the

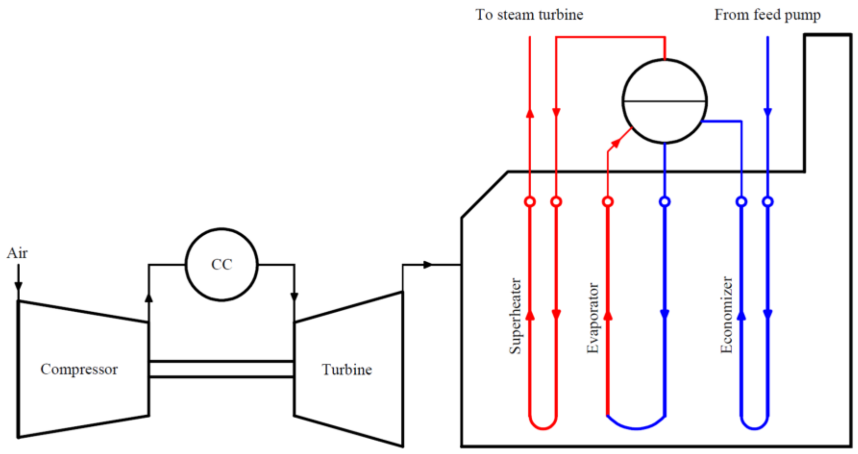

Fig. 1. Simplified diagram of a combined cycle gas turbine: CC – combustion chamber.

HRSG, and temperature gradients happen in both fluids across the tubes. Depending on the phase of the water and the exchange surface, the global heat transfer coefficient can be limited from the flue gas or the liquid water sides. However, in two-phase heat exchangers, the heat transfer coefficient on the water side is much higher than that of the flue gas, making the latter the limiting side. The temperature of the mixture is constant during the phase change, so the temperature gradient is present only on the flue gas side. Nevertheless, hydrodynamics plays a critical and complex role in evaporators, particularly in natural circulation evaporators, and this aspect will be discussed in detail later in the paper.

In HRSG, each heat exchanger is composed of a number of rows (N_r) of finned tubes to enhance heat exchange: Headers at both ends of the tubes bundle are used to distribute the water/steam or mix it, as shown in Fig. 2. In one-pass heat exchangers, water flows in the same direction in each row of tubes as seen in Fig. 3a. However, in multiple pass heat exchangers, water changes its direction throughout the row, by separators placed in the upper and lower headers, as in Fig. 3b.

While the HRSG is globally a counter-flow system, each individual tube row functions as a crossflow heat exchanger. Modelling the dynamic response of heat exchangers in the HRSG, especially when the gas turbine load varies, requires detailed information about their design and properties.

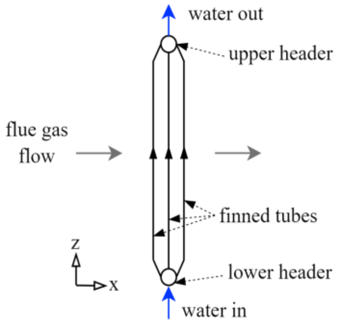

Fig. 2. Heat exchanger with 3 rows in the *x-z* plane.

The objective of this work is to develop a simplified model of the HRSG, balancing the complexity and accuracy. The methodology and results are divided into three sections. In the first one, starting from a fully detailed, pseudo three-dimensional model, a simplified monophasic heat exchanger model is developed. The simplification steps and their impact on the accuracy of the model, both on steady-state, and dynamic responses are analyzed. In the second section, a model of a natural recirculation evaporator-drum system is presented in detail. It is based on a well-known publication in literature. Validation was performed through comparison with results reported in the literature. Finally, in the third section, a full model of an industrial

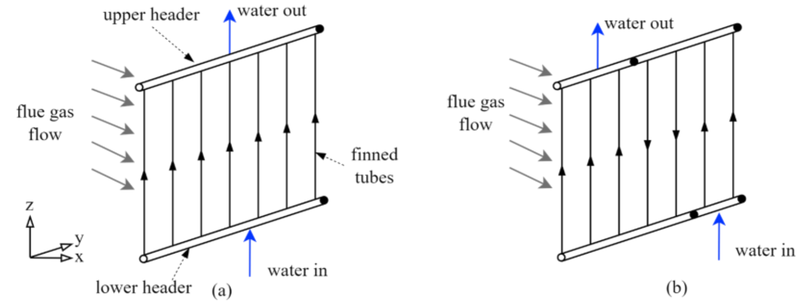

Fig. 3. View of one row of tubes in (a) 1-pass, and (b) 3-pass heat exchangers.

HRSG is developed. The dynamic response is studied by introducing perturbation to the boundary conditions. The time constants of different heat exchangers are outlined.

2. Monophasic heat exchanger modelling

In this section, a mathematical model of a single-phase dynamic heat exchanger is presented with the possible discretization strategies and main assumptions. Then, a sensitivity analysis is conducted on various discretization parameters, as well as an assessment of simplification assumptions impact on the model's precision on both the steady-state and dynamic behaviours. Finally, a simplified model based on an overall heat transfer coefficient and a lumped mass is developed. This model necessitates the specification of a predefined ratio of heat transfer coefficients that can be estimated without precise knowledge of the design of the heat exchangers. The impact of this ratio on the model's outputs is studied to define the validity range. The main mathematical equations, modelling assumptions, and empirical correlations employed in the model are outlined. Finally, the discretization strategy of the heat exchanger model across different directions is described.

2.1. Heat exchange model

In this section, the main mathematical equations used to describe the monophasic heat exchange are listed. One tube element is considered with average properties on the flue gas and the water side, as shown in Fig. 4.

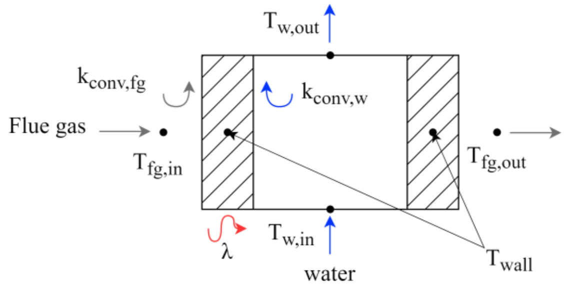

Fig. 4. Heat exchanger with 3 rows in the *x-z* plane.

First, dynamic mass balance is applied on water and flue gas, respectively:

$$V_w \frac{d\rho_w}{dt} = \dot{m}_{w,in} - \dot{m}_{w,out}, \tag{1}$$

$$V_{fg} \frac{d\rho_{fg}}{dt} = \dot{m}_{fg,in} - \dot{m}_{fg,out}, \tag{2}$$

where *V* represents the constant volume of the tubes and channels, $\dot{m}$ − the mass flow rate, ρ − the density, and *t* − the time. Subscripts *w* and *fg* denote water and flue gas, respectively, while the subscripts *in* and *out* indicate inflow and outflow. The time variation of density can be neglected due to its minimal impact on the mass flow rate. Therefore, in Eqs. (1) and (2), terms $\frac{d\rho_w}{dt}$ and $\frac{d\rho_{fg}}{dt}$ can be neglected.

The energy balances on both sides are given by

$$V_w \frac{d(\rho_w u_w)}{dt} = \dot{m}_{w,in} h_{w,in} - \dot{m}_{w,out} h_{w,out} + \dot{q}_w, \tag{3}$$

$$V_{fg} \frac{d(\rho_{fg} u_{fg})}{dt} = \dot{m}_{fg,in} h_{fg,in} - \dot{m}_{fg,out} h_{fg,out} + \dot{q}_{fg}, \tag{4}$$

where *u* represents the specific internal energy, *h* − the specific enthalpy, and $\dot{q}$ − the heat flow.

The energy balance on the tube's wall is given by

$$\dot{q}_w + \dot{q}_{fg} + m_{wall} C_{p,wall} \frac{dT_{wall}}{dt} = 0, \tag{5}$$

where *m* represents the mass, C_p − the specific heat, and *T* − the temperature. Subscript *wall* denotes the tubes wall.

The heat capacities of water and flue gas are negligible in comparison to the capacity of the metal. Consequently, the terms $\frac{d(\rho_w u_w)}{dt}$ and $\frac{d(\rho_{fg} u_{fg})}{dt}$ in Eq. (3) and (4) can be neglected. Given that the pressure drop in a monophasic flow exerts a minor influence on the heat transfer, this phenomenon will be ignored in this model.

Convection heat transfer equations are applied on water and flue gas sides. The heat flow of water $\dot{q}_w$ and flue gas sides $\dot{q}_{fg}$ are computed by

$$\dot{q}_w = k_{conv,w} A_i (T_{wall} - \bar{T}_w), \tag{6}$$

$$\dot{q}_{fg} = k_{conv,fg} (T_{wall} - \bar{T}_{fg})(A_o + \eta_f A_f). \tag{7}$$

In these equations, k_{conv} represents the convection heat transfer coefficient, *A* the surface and η the efficiency. Subscripts *i* and *o* refer to the inner and outer smooth sides of the tube, respectively, while *f* denotes fins. Since heat is transferred from flue gas to water, it is expected that $\dot{q}_w > 0$ and $\dot{q}_{fg} < 0$. The mean temperatures $\bar{T}_w$ and $\bar{T}_{fg}$ are computed by

$$\bar{T}_w = \frac{T_{w,in} + T_{w,out}}{2}, \tag{8}$$

$$\bar{T}_{fg} = \frac{T_{fg,in} + T_{fg,out}}{2}. \tag{9}$$

The convection heat transfer coefficients are computed according to empirical correlations. First, the Reynolds (Re) and Prandtl (Pr) numbers are calculated for both water and flue gas sides as

$$\mathrm{Re} = \frac{\rho v D}{\mu}, \tag{10}$$

$$\mathrm{Pr} = \frac{C_p \mu}{\lambda}, \tag{11}$$

where *v* represents the velocity, *D* − the diameter, μ − the dynamic viscosity and λ − the thermal conductivity.

For water, the Dittus-Boelter [11] correlation is applied as

$$\mathrm{Nu}_w = 0.023 \mathrm{Re}_w^{0.8} \mathrm{Pr}_w^{0.4}, \tag{12}$$

where Nu is the Nusselt number.

For the flue gas side, the Escoa (Extended Surface Corporation of America) correlation [12] is used to calculate the external convection heat transfer coefficient for segmented finned-tubes at staggered arrangement:

$$\mathrm{Nu}_{fg} = C_1 C_3 C_5 \mathrm{Re}_{fg} \mathrm{Pr}_{fg}^{0.33} \left(\frac{T_{fg}}{T_f}\right)^{0.25} \left(\frac{D_f}{D_o}\right)^{0.5}, \tag{13}$$

where $C_1 = 0.25\mathrm{Re}^{-0.35}$, $C_3 = 0.55 + 0.45\exp\left(\frac{0.35H_f}{S_f - e_f}\right)$ and $C_5 = 0.7 + [0.7 - 0.8\exp(-0.15N_r^2)]\exp\left(-\frac{S_l}{S_t}\right)$, H is the height, S – the pitch, e – the thickness, N_r – the number of rows. Subscripts l and t denote longitudinal and transverse, respectively.

Knowing the Nusselt number for each fluid, the convection heat transfer coefficients can finally be calculated by

$$k_{conv} = \mathrm{Nu}\frac{\lambda}{D}. \tag{14}$$

Heat is transferred from the flue gas to the water through the tube's wall by conduction. Assuming that heat transfer is only in one direction, the following can be applied:

$$\frac{1}{\alpha}\frac{\partial T}{\partial t} = \frac{1}{r}\frac{\partial}{\partial r}\left(r\frac{\partial T}{\partial r}\right), \tag{15}$$

where α is the thermal diffusivity and r is the radius.

The time constant τ is an important parameter to characterize a transient phenomenon. It represents the time a system takes to achieve approximately two-thirds of its final equilibrium value in response to a perturbation of an input [13]. This parameter will be used to evaluate the dynamic response of the models later in the paper.

2.2. Discretization

The wall is discretized into n_e elements to capture the temperature distribution along the tubes' thickness as seen in Fig. 5. In Eqs. (6) and (7), T_{wall} is substituted with that of the corresponding node temperature on the side of the fluid. For instance, in Eq. (6), heat is exchanged through the inner surface of the tube, so $T_{wall,1}$ is used. $T_{wall,ne}$ is used in Eq. (7). Equation (15) is then solved for the tube nodes.

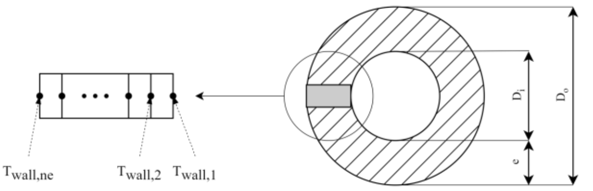

Fig. 5. Tube wall radial temperature distribution.

The fluid properties in the heat exchanger vary in a non-linear way. Therefore, it is necessary to discretize it in small control volumes to ensure high accuracy [14]. In this case, several tube elements are assembled. Figure 6 shows the 2D discretization of a section of a heat exchanger. Flue gas flows across the tube bundle from left to right, while water flows upwards inside the tubes. Tubes are divided into n_z elements along the tube length. Two main assumptions are considered: (1) the flue gas does not mix between the different elements in the tube length direction, (2) all tubes, in parallel, in the same row (y-direction in Fig. 3) with the same water flow direction have identical temperature evolution along the tube length.

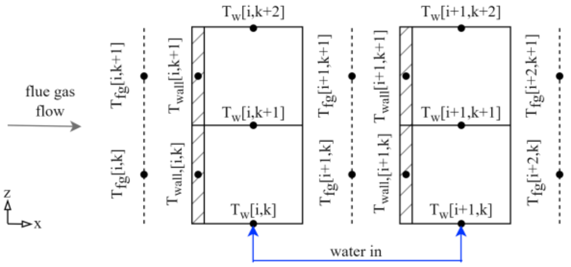

Fig. 6. 2D discretization strategy of a heat exchanger.

The dynamic heat exchanger model is developed using Modelica [15], an object-oriented, equation-based language, powerful to model complex systems containing multi-physics components with a causal connection between them. Dymola [16], a multi-engineering modelling and simulation software based on Modelica, is used to build and simulate this model. This model is developed within Metroscope Modeling Library (MML) [17], which contains the necessary components for the thermodynamic modelling of CCGTs and the secondary cycles of nuclear power plants.

2.3. Sensitivity analysis on discretization strategy and simplification assumptions

The impact of varying the discretization parameters of the heat exchanger is detailed. Moreover, some simplification assumptions are investigated to ensure that the model keeps an acceptable precision. Both the steady state and dynamic responses are investigated on one heat exchanger, then on two consecutive heat exchangers. The models are initialized under steady state conditions. At $t = 100$ s, a sudden decrease of 20°C in the flue gas temperature is applied to trigger a dynamic response, mimicking a load decrease of the turbine. Then, a sensitivity analysis is performed for each assumption. Validation is performed on the outlet water temperature of the exchanger, as it is typically the only measured property on an industrial HRSG: the convergence value is used to validate the steady-state response, and the time constant is used to validate the dynamic response.

2.3.1. Impact on one heat exchanger

A typical high pressure superheater is considered with the following boundary conditions at its inlet: flue gas side $T = 630$°C, $P = 1$ bar, $\dot{m} = 660$ kg/s and on the water side $T = 250$°C, $P = 120$ bar and $\dot{m} = 84$ kg/s. The main design specifications of this superheater are: tubes length $L = 22$ m, tubes outer diameter $D_o = 40$ mm, tubes wall thickness $e = 3$ mm, heat exchanger mass $m = 38\ 200$ kg, number of rows $N_r = 2$, number of tubes per row of 180, transversal pitch of 75 mm, longitudinal pitch of 95 mm, fins efficiency of 0.8 and fins pitch of 9.5 mm.

Tube wall temperature distribution. As discussed in Section 2.2, the wall is discretized into several elements. The reference model for this sensitivity analysis has 5 temperature nodes.

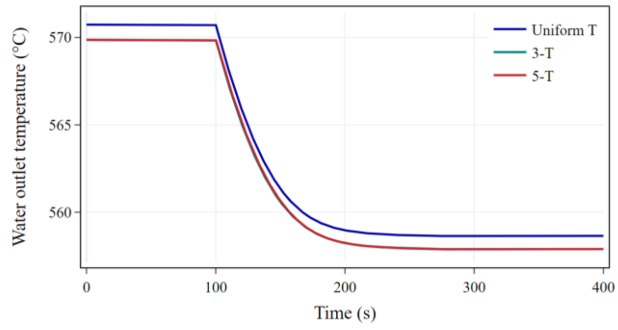

Fig. 7. Evolution of water outlet temperature for the 3 cases of tube wall temperature distribution.

Two other cases are investigated: one with a uniform temperature and the other with 3 temperature nodes. Figure 7 shows the simulation results of the 3 cases. The uniform temperature model presents a steady state error of 0.87°C compared to the 5 nodes model. However, the 3 nodes model shows no error in the steady state response compared to the 5 nodes model, as their curves overlap. This low error was expected due to the thin tube walls and the low Biot number.

The reference model of 5 nodes has a time constant of 36.7 s, while the models with uniform temperature and 3 nodes have 35.9 s and 36.0 s, respectively. Therefore, 0.8 s and 0.7 s errors are induced by each of the two models. According to the data acquisition frequency (typically 1 s), these errors can be considered insignificant. This dynamic error is due to the variations in the repartition of the energy stored in the wall. Thus, a model with 3 nodes appears to be enough to provide accurate steady state and dynamic responses.

Discretization along the tube length. A sensitivity analysis is performed on the number of elements n_z used to discretize the tubes. Figure 8 shows the steady-state and the dynamic impacts of varying n_z from 1 to 15 on the model's outputs. Considering the case with $n_z = 15$ as a reference, the outlet temperature error decreases rapidly from 3.61°C to 0.19°C as the number of elements increases from $n_z = 1$ to $n_z = 4$, before stabilizing close to zero. Similarly, the time constant error follows the same trend, decreasing from 7.62 s at $n_z = 1$ to 0.4 s at $n_z = 4$. This error is induced by the non-linear evolution of the steam's temperature throughout the finned tube. Therefore, for this heat exchanger, a model with $n_z = 4$ is considered satisfactory compared to the sensors measurements uncertainties.

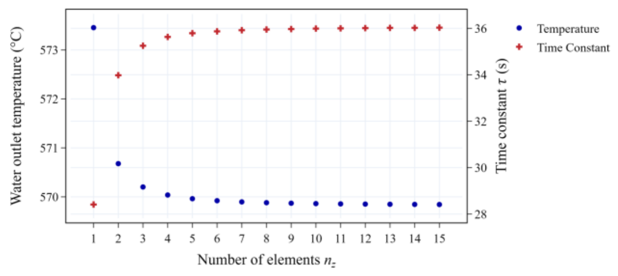

Fig. 8. Sensitivity analysis of element count n_z on steady-state and dynamic responses.

2.3.2. Impact on two consecutive exchangers

In HRSG, the flue gas flows through multiple heat exchangers. Therefore, it is also essential to study the dynamic response of a series of exchangers. For this purpose, a reheater is connected to the outlet of the high pressure (HP) superheater, as shown in Fig. 9. This time, the water outlet temperature, and the time constant of the reheater are used as quantities of interest to assess the model's precision under various assumptions.

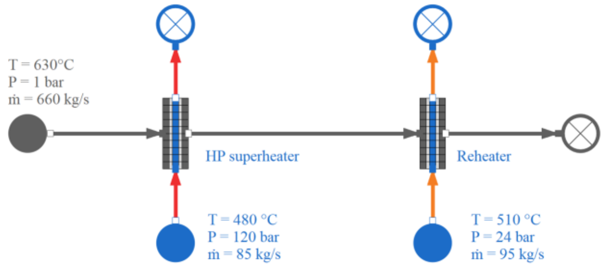

Fig. 9. Model diagram of HP superheater and reheater in the HRSG.

Fuel gas temperature distribution. When the heat exchanger is discretized along the tube length, the flue gas temperature distribution between both heat exchangers can be computed. In this section, the impact of mixing the flue gas flow before entering the second heat exchanger is assessed. Three different cases are compared, all having an element count along the tube length $n_z = 4$, as suggested in the previous section:

- Case 1: no flue gas mixing and water flows in the same direction in both heat exchangers (as seen in Fig. Fig. 9);
- Case 2: no flue gas mixing and water in the reheater flows in the opposite direction compared to the superheater (downwards);
- Case 3: flue gas is mixed between the heat exchangers, thus the water flow direction is irrelevant.

Table 1 displays the simulation results of the reheater for the 3 cases. Analysing the water outlet temperature of the reheater, case 3 presents 1.40 and 1.43°C gaps compared to cases 1 and 2, respectively. On the dynamic level, 0.33 and 0.24 s time constant errors are calculated compared to cases 1 and 2, respectively. This section shows that averaging the flue gas temperature between heat exchangers, while maintaining an appropriate elements count, can give interesting precision levels, regardless of the water flow direction. The acceptability of this precision depends on the uncertainty of the available measurements, as well

Table 1. Reheater simulation results of the 3 cases.

	$T_{w,out}$ (°C)	τ (s)
Case 1	580.36	38.86
Case 2	577.53	38.29
Case 3	578.96	38.53

as the application requirements. Moreover, in a real exchanger, depending on the turbulence of the flue gas, which is enhanced by the fins and the tubes spacings, some mixing occurs.

Single pass assumption. As shown in Fig. 3, water can undergo a single or multiple passes through the heat exchanger. Considering the number of passes complicates the model and requires accurate design information of the heat exchanger. In this section, the impact of assuming a multiple-pass heat exchanger as a single pass one on two consecutive heat exchangers is evaluated. Two 4-pass HP economizers in series are considered, as seen in Fig. 10.

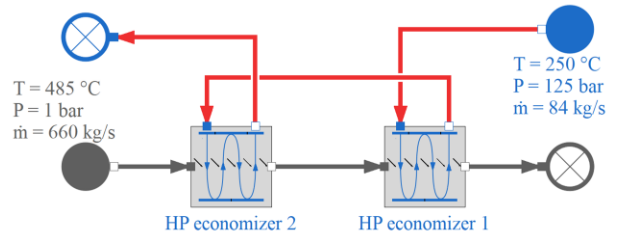

Fig. 10. Model diagram of two 4-pass HP economizers in series.

The reference case has $n_z = 10$ and a 2D flue gas temperature distribution between the heat exchangers. Two simplification cases are studied:

- Case 1: $n_z = 10$, 4-pass heat exchanger models, and an averaged flue gas temperature between both economizers;
- Case 2: $n_z = 10$, equivalent single pass heat exchanger models, and an averaged flue gas temperature between both economizers.

Table 2 presents the results for the reference model, as well as the two cases. The errors in the water outlet temperatures for both cases are significantly less than 0.1°C. Similarly, only case 2 presents a time constant error of 0.1 s. This section suggests that simplifying multi-pass heat exchangers into single-pass ones is a plausible assumption.

We conclude from the previous study that the discretization along the tube length is necessary in modelling dynamic heat exchangers. Averaging flue gas temperature between heat exchangers in series is an acceptable assumption. Moreover, a three nodes discretization of the tube wall is enough to capture the temperature distribution in the wall and its impact of the time constant. Finally, multi-pass heat exchangers can also be replaced by equivalent single-pass ones with negligible impact on the model's output accuracy. In the next section, the impact of further simplifications is assessed to facilitate easier calibration.

Table 2. Simulation results of the 3 models of 2 multi-pass economizers in series.

Model	**Eco1** $T_{w,out}$ (°C)	**Eco2** $T_{w,out}$ (°C)	**Eco1** τ (s)	**Eco2** τ (s)
Ref.	289.6	321.1	55.4	73.0
Case 1	289.6	321.1	55.4	73.0
Case 2	289.6	321.1	55.3	73.0

2.4. Simplified model

As previously stated, the detailed model requires design information that might not always be available to the modeller. Models of existing power plants require calibration based on site data. However, calibration of such models is also complex due to the considerable number of parameters that need to be adjusted for each heat exchanger. In addition, the simulation of complex models with fine discretization requires high computational resources. Therefore, a simplified model of a single monophasic heat exchanger is introduced based on the results of Section 2.3 to overcome these limitations. It is built to be easily calibrated, with a focus on the precision measurable quantities in actual HRSG.

2.4.1. Heat exchange model

Instead of computing the convection and conduction heat transfer coefficients, an overall heat transfer coefficient (U) is used. If the design information is available, it can be computed by

$$\frac{1}{UA} = \frac{1}{(UA)_w} + \frac{1}{(UA)_{fg}}, \tag{16}$$

where A is the heat exchange surface.

The ratio (r_{UA}) between the overall heat transfer coefficients of the water and flue gas sides is introduced. It is calculated as

$$r_{UA} = \frac{(UA)_w}{(UA)_{fg}}. \tag{17}$$

The heat flows for the water and flue gas sides are calculated by, respectively:

$$\dot{q}_w = (UA)_w(T_{wall} - \bar{T}_w), \tag{18}$$

$$\dot{q}_{fg} = (UA)_{fg}\left(T_{wall} - \bar{T}_{fg}\right). \tag{19}$$

The tube wall temperature is considered uniform along the tube's thickness. The energy balance on the tube's wall is the same as in Eq. (5).

2.4.2. Calibration and discretization

The steady-state calibration of the simplified model consists of imposing $T_{w,out}$ and r_{UA} calculated by a reference model (superheater model with $n_z = 10$) and getting the UA as an output. The simplified model is discretized along tube length, therefore, for each element count n_z, a separate calibration simulation is conducted. At the end of the calibration process, the simplified models with different n_z values, give all the same steady-state response as the reference model since they were calibrated with the same $T_{w,out}$. However, the dynamic response represented by the time constant τ depends on n_z, as seen in Fig. 11. The reference τ is equal to 36.46 s, consequently, the error is reduced to less than 0.5 s when n_z is equal or greater than 4.

2.4.3. Sensitivity analysis on r_{UA}

Without the detailed design information of the heat exchanger, ratio r_{UA} cannot be determined. For this purpose, this section conducts a sensitivity analysis on the ratio r_{UA} to assess the im-

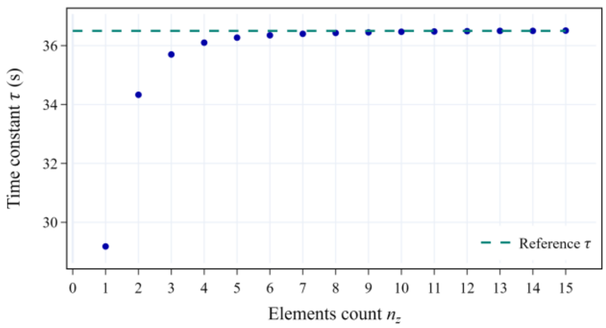

Fig. 11. Simplified model – time constant dependency on element count n_z.

pact of an error in a guessed value on the outputs of the model. A model with $n_z = 4$ is considered. The ratio r_{UA} is varied between 1 and 30. The reference model computes a ratio $r_{UA} = 7.54$ for the HP superheater. Figure 12 shows that the time constant depends on r_{UA}. However, compared to the reference τ, choosing a ratio r_{UA} higher than 4 keeps the time constant error less than 1 s. Therefore, an approximation of the ratio r_{UA} for each type of heat exchanger can give a satisfactory dynamic response simulation. Ideally, this ratio could be computed using a detailed heat exchanger model, such as the one presented in Section 2. If the available information is insufficient for this calculation, estimations based on similar heat exchanger models can be used without significantly compromising accuracy, as demonstrated in this section. Besides the temperature and mass flow rate measurements, this simplified model only requires the metal mass of the heat exchanger. If not available, calibration on a dynamic scenario is required. This is not covered in this study.

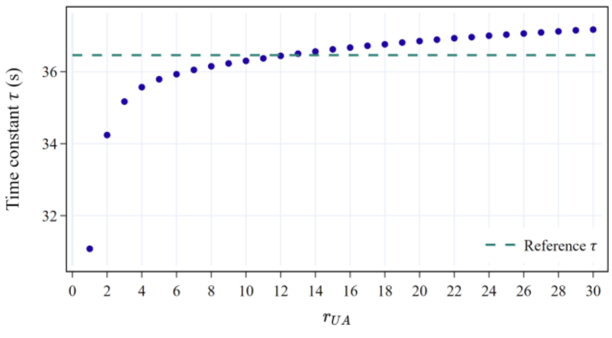

Fig. 12. Simplified model – time constant in function of r_{UA} for $n_z = 4$.

3. Evaporator

This section details the model of a natural circulation evaporator-drum based on the work presented in [18]. First, a general description of the system is shown. Then, the main equations that describe the behaviour of the system are listed. Finally, a Modelica model is validated by comparing its results with those presented in the literature using the same parameters.

3.1. General description

Figure 13 shows a diagram of the evaporator-drum system and its working principle. Pre-heated feedwater from the economizers enters the drum and mixes with the saturated liquid. The downcomers are vertical tubes connecting the drum to the risers and allowing the recirculation. They are placed outside the HRSG casing, allowing heat transfer to be neglected in this part of the system. The risers consist of finned tubes through which the two-phase water flows and exchange heat with flue gas. In other words, the risers section is the heat exchanger of the system. The drum is the core component. It consists of a thick walled, horizontal, cylindrical tank, in which steam is separated from the mixture by force of density difference between the vapour and liquid phases.

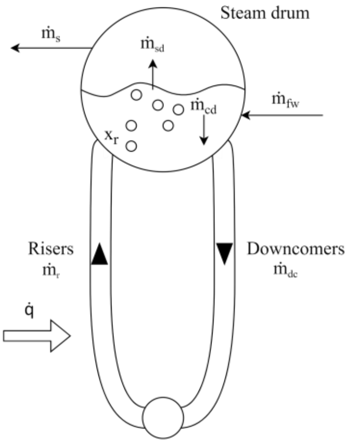

Fig. 13. Evaporator diagram.

The level of water in the drum is critical for the power plant operation. It is mainly controlled by adjusting the mass flow rate of the feedwater $\dot{m}_{fw}$. Steam bubbles are present below the liquid level of the drum, causing a shrink-and-swell phenomenon when the heat flow varies, which makes the water level control difficult. Modelling this level is therefore mandatory to accurately simulate the behaviour of the system.

Saturated steam flows through the liquid surface in the drum before being extracted and sent to the superheaters. In some cases, saturated steam is sent directly to the steam turbine without superheating. Steam dryers might be implemented to avoid droplets carrying on to the blades.

3.2. Evaporator-drum model

Water and steam occupy the whole volume of the system; therefore, the total volume V_{tot} of the evaporator-drum can be calculated as

$$V_{tot} = V_{stot} + V_{wtot}, \tag{20}$$

where V_{stot} and V_{wtot} represent the total volumes of steam and water, respectively.

Considering the entire system, the global mass and energy balances are given by the following equations:

$$\frac{d}{dt}(\rho_s V_{stot} + \rho_w V_{wtot}) = \dot{m}_{fw} - \dot{m}_s, \tag{21}$$

$$\frac{d}{dt}(\rho_s u_s V_{stot} + \rho_w u_w V_{wtot} + m_{wall} C_{p,wall} T_{wall}) =$$

$$= \dot{q} + \dot{m}_{fw} h_{fw} - \dot{m}_s h_s, \tag{22}$$

where $\dot{q}$ represents the heat flow rate to the risers. Subscripts *s*, *w*, and *fw* denote saturated steam, saturated liquid water and feedwater, respectively. The mass flow rates going in and out of the system are the feedwater $\dot{m}_{fw}$ and the steam $\dot{m}_s$, respectively.

As mentioned earlier, the heat exchange with the flue gas occurs in the risers, which are finned tubes, like the economizers and superheaters. The steam quality increases from the bottom of the risers to their connection with the drum. In [18], a linear mass fraction of steam along the risers is assumed. This assumption fits well with the experimental data, and significantly simplifies the risers' modelling. The average volume fraction can therefore be computed by

$$\overline{x_v} = \frac{\rho_w}{\rho_w - \rho_s}\left[1 - \frac{\rho_s}{(\rho_w - \rho_s) x_r} \ln\left(1 + \frac{\rho_w - \rho_s}{\rho_s} x_r\right)\right]. \tag{23}$$

In this equation, $\overline{x_v}$ is the average volume fraction of steam in the riser, and x_r is the steam quality at the riser outlet.

With $\overline{x_v}$ known, the mass and energy balances on the riser section can be calculated by the following equations:

$$\frac{d}{dt}[\rho_s \overline{x_v} V_r + \rho_w (1 - \overline{x_v}) V_r] = \dot{m}_{dc} - \dot{m}_r, \tag{24}$$

$$\frac{d}{dt}\left[\rho_s h_s \overline{x_v} V_r + \rho_w h_w (1 - \overline{x_v}) V_r - P V_r + m_r C_{p,wall} T_{wall}\right] =$$

$$= \dot{q} + \dot{m}_{dc} h_w - (x_r h_c + h_w) \dot{m}_r, \tag{25}$$

$$h_c = h_s - h_w, \tag{26}$$

where h_c is the condensation specific enthalpy, $\dot{m}_{dc}$ is the downcomer's mass flow rate, V_r is the riser tube internal volume and P is the drum pressure.

Recall that downcomers are placed outside the HRSG casing, so the heat transfer in this section can be neglected. However, the dimensions of the downcomers have a major influence on the natural recirculation loop. The flow is driven by the density difference between steam and liquid water in the risers and downcomers. The time constant of the recirculation flow is low, therefore, a steady state relation is used as

$$\frac{1}{2} \zeta \dot{m}_{dc}^2 = \rho_w A_{dc} (\rho_w - \rho_s) g \overline{x_v} V_r, \tag{27}$$

where ζ is a dimensionless friction coefficient, A_{dc} – the downcomers cross-section area, and g – the standard gravitational acceleration.

Considering only the steam under the water level, the mass balance is given by

$$\frac{d}{dt}(\rho_s V_{sd}) = x_r \dot{m}_r - \dot{m}_{sd} - \dot{m}_{cd}, \tag{28}$$

where $\dot{m}_{sd}$ and $\dot{m}_{cd}$ represent the steam mass flow rate through the liquid surface and the condensation mass flow rate in the drum, respectively.

The condensation mass flow rate is computed by

$$\dot{m}_{cd} = \frac{h_w - h_{fw}}{h_c} \dot{m}_{fw} + \frac{1}{h_c}\left[\rho_s V_{sd} \frac{dh_s}{dt} + \rho_w V_{wd} \frac{dh_w}{dt} - \right.$$

$$\left. (V_{sd} + V_{wd}) \frac{dp}{dt} + m_d C_{p,wall} \frac{dT_{wall}}{dt}\right]. \tag{29}$$

An empirical model that fits well with the experimental data is used to compute the steam flow through the water surface:

$$\dot{m}_{sd} = \frac{\rho_s}{t_d}(V_{sd} - V_{sd}^0) + x_r \dot{m}_{dc} + x_r \beta (\dot{m}_{dc} - \dot{m}_r) \tag{30}$$

with V_{sd}^0 – the volume of steam in the drum when no condensation is occurring, t_d – the residence time of the steam in the drum and β a constant parameter.

The liquid water in the drum is calculated by

$$V_{wd} = V_{wtot} - V_{dc} - (1 - \overline{x_r}) V_r. \tag{31}$$

The drum is considered a horizontal cylinder. The volume of water and steam under the drum level can be calculated as a function of the level:

$$V_{wd} + V_{sd} = \left[\pi {r_d}^2 - \cos^{-1}\left(\frac{r_d - l}{r_d}\right) {r_d}^2 - \right.$$

$$\left. (r_d - l)\sqrt{(2 r_d l - l^2)}\right] L_d, \tag{32}$$

where r_d is the drum radius, l is the water level in the drum, and L_d is the drum length.

The heat exchange model in the risers is based on the simplified approach presented in Section 2.4. As mentioned earlier, the heat transfer coefficient of the water side is much higher than that of the flue gas side. Therefore, this coefficient is correlated to the flue gas mass flow rate.

3.3. Model validation

The model of the evaporator-drum presented earlier is implemented in Modelica. It was validated by comparing the simulated response of the system to the results presented in [18]. Step changes of the inputs were applied to the model, and the evolution of the outputs was observed. The simulation starts from steady state and at t = 50 s a step change is applied to a single input.

It was necessary to have the same parameters as in [18]. Some of them were explicitly given and used. The remaining parameters and inputs, all of which are listed in Table 3, were calculated based on the steady-state period. For the sake of validation, the following relation is applied:

$$l = \frac{V_{wd} + V_{sd}}{A_d} \tag{33}$$

to link the level to the volume in function of the drum area A_d at nominal operating level, as in [18]. For real applications, Eq. (32) is used.

A 10 MW step increase to the heat flow to the risers is applied. All other inputs ($\dot{m}_{fw}$, $\dot{m}_s$ and T_{fw}) are kept constant. The step increase of the heat flow, as well the responses of other variables are shown in Fig. 14. Since the steam and the feedwater flows are constant inputs, and the steam generation accelerates with the increased heat flow, the drum pressure builds up linearly. The steam quality at the risers outlet initially increases rapi-

Table 3. Evaporator-drum parameters for validation.

Parameter	Symbol	Value	Unit
Drum volume	V_d	40	m³
Risers volume	V_r	37	m³
Downcomer volume	V_{dc}	11	m³
Drum area	A_d	20	m²
Total mass	m_t	300 000	Kg
Risers mass	m_r	160 000	kg
Friction coefficient	ζ	25	
Constant parameter	β	0.3	
Residence time	t_d	12	s
Heat flow	$\dot{q}$	85.2	MW
Feedwater flow	$\dot{m}_{fw}$	50.5	kg/s
Steam flow	$\dot{m}_s$	50.5	kg/s
Feedwater temperature	T_{fw}	242	°C
Theoretical volume of steam	V_{sd}^0	7.6	m³

dly before slowing down with the adaptation of the recirculation flow. The step increase in the heat flow disturbs the balance of the mass flow rates in the risers and downcomers due to the sudden change in density. After about 25 s, the balance is restored. Both mass flow rates decrease linearly with increasing pressure, due to the linear decrease in density difference between saturated liquid and vapour. The drum level undergoes an initial rapid increase, which corresponds to the 'swell' phenomenon. It is caused by accelerated steam generation, which shortly increases the volume of steam under the water surface. The increasing pressure slows down the level increase by reducing the volume of steam and increasing the condensation flow.

These results are consistent with the conclusions of [18]. It should be noted that in this reference, the model was validated on real data from a power plant. The main challenge of this model is to have a good estimation of the residence time t_d and the constant parameter β. Their calibration is not covered by this study.

4. Full heat recovery steam generator model

In this section, a full dynamic model of an industrial heat recovery steam generator (HRSG) is developed and simulated. Its diagram is shown in Fig. 15. The monophasic heat exchangers and the drum-evaporator models are based on the methodologies presented earlier. First, a description of the power plant is given. The model is then developed. Finally, the dynamic response is assessed by applying a step increase in the flue gas mass flow rate. The control system is not included in this model, thereby limiting the scope of the analysis to the free response.

4.1. Power plant description

In the context of this study, a collaboration with a CCGT power plant has been established to validate the proposed methodology. It has a 1–1–1 (one gas turbine, one HRSG and one steam turbine line), multi-shaft (two generators: one for the gas turbine and one for the steam turbine) configuration. Due to the significantly fast response of the gas turbine compared to the steam cycle, it has been excluded from the scope of this study. Therefore, the exhaust temperature and mass flow rate will be used as boundary conditions at the inlet of the HRSG, with the exhaust flow rate serving as an indicator of the power plant's load. The HRSG has three natural-circulation evaporator-drum systems, at different pressure levels to maximize heat recovery: high pressure (HP), intermediate pressure (IP) and low pressure (LP).

The extraction pump supplies liquid water from the condenser to the HRSG. Water is first preheated in a series of 7 economizers before entering the LP steam drum. In addition to saturated steam generation, the LP drum serves as a feedwater tank for the IP and HP circuits. Therefore, a feedwater pump with two pressure levels outlets is supplied directly from the LP drum. This configuration complicates the drum levels control due to its strong interdependencies. The LP steam flows in a superheater before being sent to the LP turbine. The IP line consists of 3 economizers, 1 evaporator-drum, 1 superheater, and 3 reheaters. The HP line consists of 8 economizers, 1 evaporator-drum,

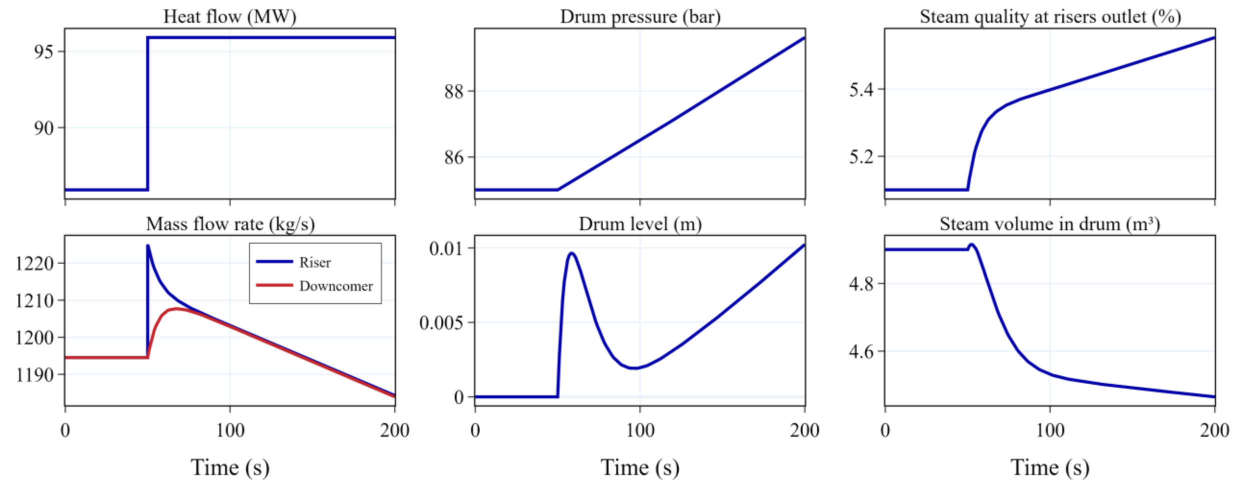

Fig. 14. Evaporator-drum dynamic response.

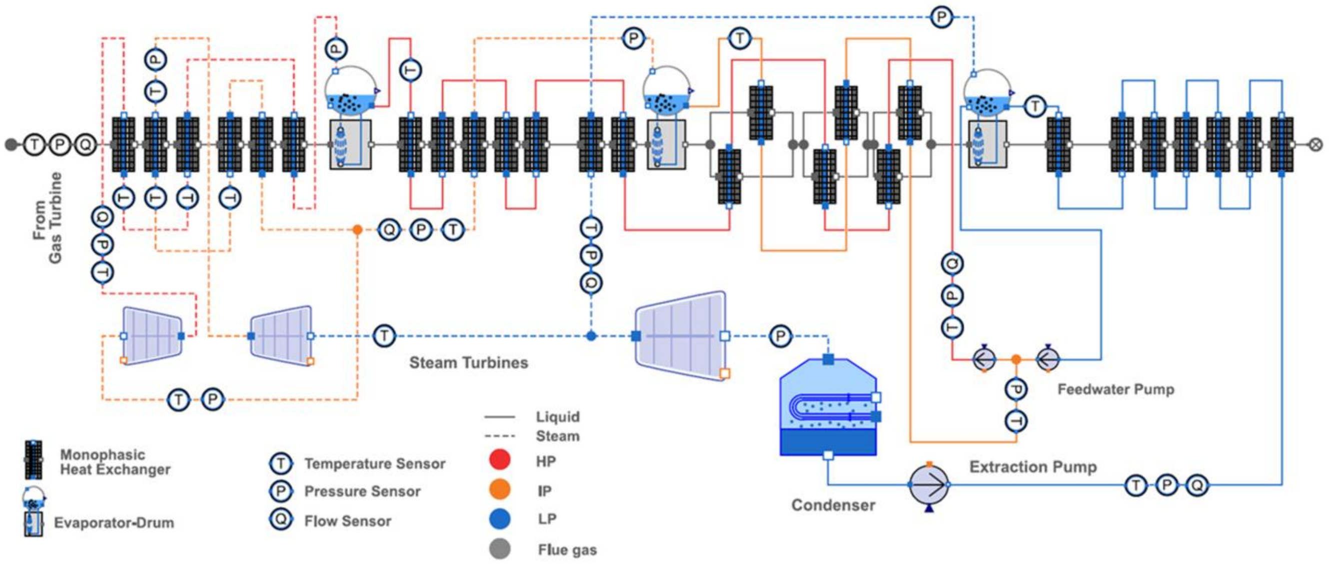

Fig. 15. Full steam cycle model diagram.

and 3 superheaters. The outlet of the HP turbine mixes with the flow from the IP superheater before being heated in the reheaters. The IP turbine discharges directly to the LP turbine. The condenser finally ensures the condensation of the liquid-vapour mixture at the LP turbine outlet. Several control systems, like flue gas condensation, drum levels and steam de-superheating nozzles, are implemented to ensure safe operation. Since the control system is not covered, these systems are excluded.

4.2. Model

The HRSG consists of 26 monophasic heat exchangers and 3 drum-evaporators. The monophasic heat exchangers are modelled based on the simplified approach presented in section 2.4. Therefore, an average flue gas temperature is applied between heat exchangers, which are considered single-pass ones. The tubes are discretized into 6 elements. A global heat transfer coefficient UA, as well as a ratio between the water and flue gas coefficients r_{UA} is applied for each heat exchanger. Using the sensor measurements, the UA can be determined. However, some heat exchangers are not fully instrumented; therefore, assumptions must be made, such as assigning equal coefficients or using other estimates based on the available design information. The mass of each heat exchanger is obtained from design data, as its calibration falls outside the scope of this study.

Reminding the simplification process of monophasic heat exchanger, the 5th HP economizer is given as an example. It has a 3-row, 4-pass configuration. First, the temperature of the wall is considered uniform. Instead of the 4-pass configuration, a single-pass assumption is adopted, implying that temperatures remain uniform across the width of the heat exchanger. Finally, the heat exchanger is modelled as a discretized tube, with a global heat transfer coefficient UA and a ratio r_{UA}. Using the outlet water temperature as an input, the overall heat transfer coefficient can be calculated. Its mass is applied from the manufacturer data.

Evaporator-drum systems are modelled based on Section 3. The risers heat exchange module is also based on a simplified approach, as presented in section 2.4. The dimensions and masses for the components are obtained from design datasheets. Since the level is an important parameter of the power plant operation, its modelling is crucial for an accurate representation. Therefore, further simplifications are not possible.

The condenser is also built as a simplified model. The turbine and pumps have low inertia compared to the heat exchangers, therefore their inertia is neglected. Their parameters are calibrated based on operational data.

In terms of causality, the model uses the gas turbine exhaust mass flow rate and temperature, the condenser cooling loop inlet temperature, and the atmospheric pressure as input boundary conditions. Since the control system is not included, the feedwater mass flow rates of the different pressure levels are also imposed as inputs. The model is able to predict all the states of the cycle, including the key measured variables, such as temperatures, pressures, and water levels in the HRSG, as seen in Fig. 15.

4.3. Response to step increase in power

The free response of the steam cycle, without including the control system is analysed. A step increase in the mass flow rate of the flue gas from the gas turbine exhaust is applied at $t = 50$ s, representing a gas turbine load increase. The feedwater mass flow rates are maintained constant, allowing the level to fluctuate freely.

Figure 16 shows the evolution of different variables in function of time. The three drum pressures increase gradually due to the increase in steam generation in the risers section. In the three drums, the swell phenomenon initially appears due to the fast increase of steam volume under the water. The condensation in the drum also increases with increasing pressure, contributing to the water volume in the drums. However, the increasing pressure shrinks the steam volume. The steam mass flow rate in-

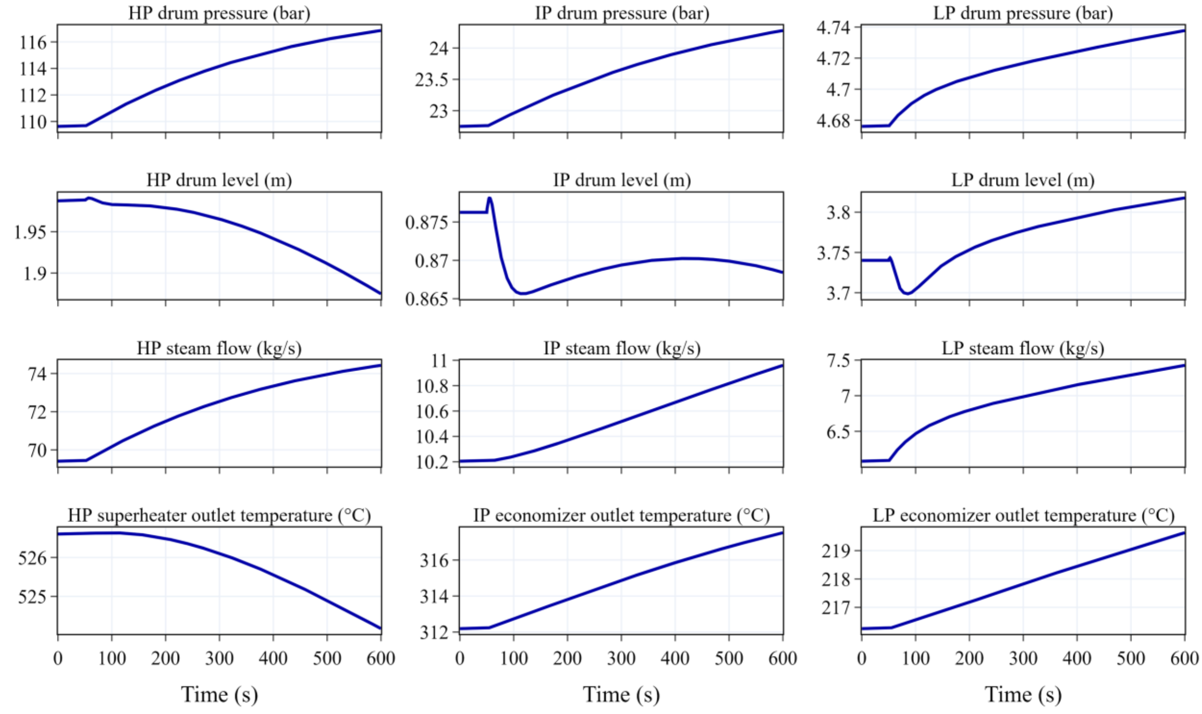

Fig. 16. HRSG model response to load change.

creases due to the increase in the pressure difference between the drums and the condenser. If run for a longer time with a constant feedwater flow, all three drum levels will fall to zero. Figure 16 also shows the evolution of three temperatures. The HP superheater outlet temperature slowly decreases with time, due to the increase in the HP steam flow. The HP and IP economizers outlet temperature gradually increase due to increased flue gas mass flow rate and constant feedwater mass flow rates.

The simulation time is extended till the system reaches a new steady state. It should be noted that the drums levels keep decreasing due to the difference between the steam and feedwater flows. The water temperature sensors at the outlet of the heat exchangers and the drum pressure sensors were used to compute the time constants of the heat exchangers. The results are shown in Table 4. The time constants vary between 6 and 73.5 min, which is a much higher order of magnitude compared to the individual heat transfer time constants calculated in the first section. This shows that the delay is propagated in the HRSG, with strong interdependencies between different heat exchangers. When comparing heat exchangers of the same type across different pressure levels, the HP exchangers show the lowest time constants, followed by the IP exchangers, with the LP exchangers having the highest. Although the thickness of the tube walls increases with pressure, the HP components are closer to the source of the perturbation. While the mass of individual components can significantly influence their response, in interconnected systems, the distance from the perturbation source plays a more critical role in determining the time constant.

The results of this section demonstrate the applicability of the modelling methodology to a real industrial HRSG. The model can predict the complex dynamics of the steam drums, especially its level variations. It can provide predictions of sensors during dynamic operation. Coupled with the steam turbines and the condenser, the steam mass flow rate's dependency on evaporator pressure is also simulated. The delay in reaching a new steady state is well represented with the propagation of time constants throughout the HRSG.

Table 4. Time constants of different components.

Component	τ (min)
HP superheaters	20
HP evaporator	6
HP economizers	16
Reheaters	34.5
IP superheater	10
IP evaporator	9
IP economizers	17.5
LP superheater	73.5
LP evaporator	10
Preheaters	28

5. Conclusions

This paper proposed a dynamic model of a heat recovery steam generator in the context of reducing the dependency on design information and simulation time. The model balances the numerical simplification and accuracy to capture the main dynamic response indicators after a calibration based on measures. First, a mathematical model of monophasic heat exchanger of HRSG has been presented. The discretization methodology and assumptions are investigated to assess their impact on the model's steady-state and dynamic responses. For instance, a 3-nodes discretization of the tube wall thickness is sufficient to drastically reduce both the steady-state and dynamic errors. The discretization along the tube length is critical to improve the model's precision. Depending on the required precision, the flue gas temperature between heat exchangers can be averaged with minimal impact on errors. Similarly, multi-pass heat exchangers models can be replaced by equivalent one-pass models with negligible impact on the results. Moreover, a simplified model based on the overall heat transfer coefficient has been developed that requires minimal design information. This model can be easily calibrated using the typical instrumentation on the HRSG, however, a preset value for the ratio of the heat transfer coefficients times the area (UA) of water and flue gas sides should be established. The sensitivity analysis on this ratio shows that when the heat exchanger is discretized, the model achieves good precision across a wide range of guessed values. In the second section, a simple model of an evaporator-drum system based on the literature is presented. The model is then validated by comparison of the simulation results with the literature. Finally, a full model of the steam cycle is developed. The heat exchangers in the HRSG were modelled based on the simplified method presented in the first section. The evaporator-drum systems are based on the model from the second section. The free dynamic response, without any control system influence, is analysed by applying a step increase in the flue gas mass flow rate. The behaviour of the main measurable quantities was studied, as well as the time constants of different components. The results demonstrate that this simplified approach effectively simulates the system's dynamic response while maintaining physical accuracy. The time constants of components show that the distance from the perturbation source has a considerable influence on delay to reach a new steady state. Therefore, HP components have lower time constants, followed by IP and then LP components. To go further in this analysis, a calibration based on real measures should be performed. The control system should be implemented, allowing the model to follow the operation of the HRSG in real time, therefore improving its accuracy for different purposes. After that, data validation can be performed. The reliance on real data measurements for calibrating the parameter UA limits the applicability of this modelling methodology to existing systems equipped with sufficient instrumentation. Consequently, it cannot be employed during the design phase of heat exchangers. Although this approach provides a simplified modelling approach with minimal reliance on design data and enables faster simulations, it should be coupled by a calibration strategy to account for parameter variations under different boundary conditions. This is achieved by the conventional heat exchanger modelling methodologies through empirical correlations that relate the heat transfer coefficient to various operating conditions, such as changes of mass flow rates.

References

[1] IEA (2024). *Electricity 2024*. https://www.iea.org/reports/electricity-2024 [accessed 30 Nov. 2024].

[2] Holttinen, H. (2012). Wind integration: experience, issues, and challenges. *WIREs Energy and Environment*, 1(3), 243–255. doi: 10.1002/wene.18

[3] IRENA (2019). *Innovation landscape brief: Flexibility in conventional power plants*. International Renewable Energy Agency, Abu Dhabi. https://www.irena.org/-/media/Files/IRENA/Agency/Publication/2019/Sep/IRENA_Flexibility_in_CPPs_2019.pdf?la=en&hash=AF60106EA083E492638D8FA9ADF7FD099259F5A1 [accessed 25 Oct. 2024].

[4] Casella, F., & Pretolani, F. (2006). Fast start-up of a combined-cycle power plant: A simulation study with Modelica. *5th International Modelica Conference*, Sep. 6-8, Vienna, Austria. https://modelica.org/events/modelica2006/Proceedings/sessions/Session1a1.pdf [accessed 15 Sept. 2024].

[5] Alobaid, F., Postler, R., Ströhle, J., Epple, B., & Kim. H.-G. Modeling and investigation start-up procedures of a combined cycle power plant. *Applied Energy*, 85(12), 1173–1189. doi: 10.1016/j.apenergy.2008.03.003

[6] Benato, A., Stoppato, A., & Bracco, S. (2014). Combined cycle power plants: A comparison between two different dynamic models to evaluate transient behaviour and residual life. *Energy Conversion and Management*, 87, 1269–1280. doi: /10.1016/j.enconman.2014.06.017

[7] Farahani, Y., Jafarian, A., & Mahdavi Keshavar, O. (2022). Dynamic simulation of a hybrid once-through and natural circulation heat recovery steam generator (HRSG). *Energy*, 242, 122996. doi: 10.1016/j.energy.2021.122996

[8] Jain, P., Poon, J., Singh, J.P., Spanos, C., Sanders, S.R., & Panda, S.K. (2020). A digital twin approach for fault diagnosis in distributed photovoltaic systems. *IEEE Transactions on Power Electronics*, 35(1), 940–956. doi: 10.1109/TPEL.2019.2911594

[9] Allard De Grandmaison, I., Muszynski, L., & Schwartz, A. (2019). AI diagnosis for maintenance teams: building of a digital twin. *VGB PowerTech*, 99(8), 67–72.

[10] Mertens, N., Alobaid, F., Starkloff, R., Epple, B., & Kim, H.-G. (2015). Comparative investigation of drum-type and once-through heat recovery steam generator during start-up. *Applied Energy*, 144, 250–260. doi: 10.1016/j.apenergy.2015.01.065

[11] Dittus, F.W., Boelter, L.M.K. (1985). Heat transfer in automobile radiators of the tubular type. *International Communications in Heat and Mass Transfer*, 12(1), 3–22. doi: 10.1016/0735-1933(85)90003-X

[12] Walter, H., & Hofmann, R. (2011). How can the heat transfer correlations for finned-tubes influence the numerical simulation of the dynamic behavior of a heat recovery steam generator? *Applied Thermal Engineering*, 31(4), 405–417. doi: 10.1016/j.applthermaleng.2010.08.015

[13] Can Gülen, S., & Kim, K. (2014). Gas turbine combined cycle dynamic simulation: A physics based simple approach. *Journal of Engineering for Gas Turbines and Power*, 136(1), 011601. doi: 10.1115/1.4025318

[14] Dechamps, P.J. (1995). Modelling the transient behaviour of heat recovery steam generators. *Proceedings of the Institution of Mechanical Engineers, Part A: Journal of Power and Energy*, 209(4), 265–273. doi: 10.1243/PIME_PROC_1995_209_005_01

[15] Modelica Association (2000). *ModelicaTM – A Unified Object-Oriented Language for Physical Systems Modeling Version 1.4 – Tutorial*. https://modelica.org/documents/ModelicaTutorial14.pdf [accessed 11 Aug. 2023].

[16] *Dymola — Dassault Systèmes*. https://www.3ds.com/products-services/catia/products/dymola/ [accessed 18 July 2023].

[17] Metroscope (2023). *Metroscope Modeling Library*. https://github.com/Metroscope-dev/metroscope-modeling-library [accessed 18 July 2023].

[18] Åström, K.J., & Bell, R.D. (2000). Drum-boiler dynamics. *Automatica*, 36(3), 363–378. doi: 10.1016/S0005-1098(99)00171-5

Co-published by
Institute of Fluid-Flow Machinery
Polish Academy of Sciences
Committee on Thermodynamics and Combustion
Polish Academy of Sciences

http://www.imp.gda.pl/archives-of-thermodynamics/

ARCHIVES OF THERMODYNAMICS

Numerical study of radiating Casson fluid past a permeable stretching sheet in a Darcy-Forchheimer porous medium

Shish Ram Dhwal[a*], Rajendra Singh Yadav[a], Oluwole Daniel Makinde[b]

[a]Department of Mathematics, University of Rajasthan, Rajasthan, Jaipur 302004, India
[b]Faculty of Military Science Stellenbosch University, Stellenbosch, Western Cape, South Africa
*Corresponding author email: shishramdhwal75@gmail.com

Received: 21.11.2024; revised: 16.02.2025; accepted: 20.03.2025

Abstract

This research investigates the mixed convection of an incompressible, non-Newtonian radiating Casson fluid in a Darcy-Forchheimer porous medium over a slippery, permeable, stretching surface. The study further examines the influences of thermal buoyancy and viscous dissipation. Through appropriate similarity transformations, the governing nonlinear partial differential equations are transformed into nonlinear ordinary differential equations. These nonlinear ordinary differential equations are solved using MATLAB with the fourth-order Runge-Kutta method combined with the shooting technique. This work aims to assess the influence of Casson parameter, porosity parameter, radiation parameter, suction parameter, Eckert number, mixed convection parameter, local inertia coefficient, Prandtl number and slip parameter on the velocity and temperature. The findings show that increasing Casson parameter results in decreased velocity and temperature, while an increase in the radiation parameter leads to a rise in temperature. Velocity decreases with an increase in slip parameter for velocity, but as the similarity variable exceeds 2.4, it experiences a slight increase due to the stretching effect of the sheet. Conversely, temperature is directly proportional to slip parameter for velocity.

Keywords: Darcy-Forchheimer porous medium; Permeable stretching sheet; Radiating Casson fluid; Thermal buoyancy; Viscous dissipation

Vol. 46(2025), No. 2, 199–208; doi: 10.24425/ather.2025.154918

Cite this manuscript as: Dhwal, S.R., Yadav, R.S., & Makinde, O.D. (2025). Numerical study of radiating Casson fluid past a permeable stretching sheet in a Darcy-Forchheimer porous medium. *Archives of Thermodynamics*, 46(2), 199–208.

1. Introduction

The exponential stretching surface in boundary layer flow has significant applications in manufacturing engineering, such as the production of copper wires and determining the quality of various industrial products. A substantial portion of contemporary research focuses on the study of boundary layer flow over stretching sheets. For instance, Gupta and Gupta [1] analysed the transfer of momentum, mass, and heat within the boundary region of a stretching sheet. Magyari and Keller [2], along with Elbashbeshy [3], investigated heat transfer over an exponentially stretched sheet, considering the effects of suction and blowing. Pramanik [4] examined heat transfer in the boundary layer of an exponentially stretching surface. Jain et al. [5] studied boundary layer flow over a suction surface with slip and mixed convection conditions. Similarly, researchers like Partha et al. [6], Khan [7], and Sajid and Hayat [8] explored exponentially stretching sheets under various fluid dynamics scenarios.

Nomenclature

C_p – specific heat coefficient, J/(kg K)
C_f – skin friction coefficient
e_{ij} – (ij)th component of the deformation rate
Ec – Eckert number
f – dimensionless stream function
F – drag coefficient
Fr – local inertia coefficient
g – gravitational acceleration, m/s^2
Gr – Grashof number
h – heat transfer coefficient, W/ (m^2 K)
K – porous medium permeability, m^2
K_1 – porosity parameter
k^* – mean absorption coefficient, 1/m
L – characteristic length, m
N – radiation parameter
Nu – Nusselt number
Pr – Prandtl number
q – heat flux, W/m^2
R – slip length coefficient, m
Re – Reynolds number
S – suction/blowing parameter
T – temperature, K
u, v – velocity in x- and y-direction, m/s
U – stretching velocity, m/s
V – velocity over the sheet, m/s

Greek symbols

β – Casson parameter
β^* – thermal expansion coefficient, 1/K
θ – dimensionless temperature
ϑ – kinematic viscosity, m^2/s
κ – thermal conductivity, W/(m K)
λ – mixed convection parameter
λ_u – slip parameter for velocity
λ_t – slip parameter for temperature
μ – viscosity of fluid, Pa·s
η – similarity variable
ρ – density, kg/m^3
σ – Stefan-Boltzmann coefficient, 5.67×10^{-8} W/(m^2 K^4)

Subscripts and Superscripts

r – radiation,
t – temperature
u – velocity
W – sheet surface
0 – initial
∞ – fluid surface
$(\cdot)'$ – differentiation with respect to η

Abbreviations and Acronyms

PDE – partial differential equation
ODE – ordinary differential equation

The study of radiating Casson fluid flow holds diverse engineering and industrial applications, particularly in fluid dynamics and complex fluid behaviours. It is relevant in processes such as polymer processing, food manufacturing, paint production, and oil drilling. Additionally, the non-Newtonian behaviour of blood can be described using the Casson fluid model, which is critical for designing medical devices like artificial heart valves and understanding blood circulation mechanics. Radiating Casson fluid also plays a role in studying blood flow under different physiological conditions. For example, during cardiac surgeries, external heating or cooling is used to regulate blood flow and prevent complications. Bejawada et al. [9] investigated the effects of radiating Casson fluid flow in a porous medium with an inclined non-linear sheet, while Rassol et al. [10] explored Casson nanofluid flow in a porous medium over a non-linear stretching sheet. Bilal et al. [11] provided an analytical study on Casson fluid flow over an isothermal sloping Riga sheet with thermal radiation. Other notable works include Raju et al. [12], who analysed heat and mass transfer characteristics of Casson fluid on a rotating wedge under thermal radiation, and Mehmood et al. [13], who studied the behaviour of non-aligned Casson fluid on a stretching surface in the presence of radiation. Research by Sinha et al. [14] focused on mixed convection in fluid flow with dissipation and radiation effects, while Loganathan and Deepa [15] examined electromagnetic and radiative Casson fluid flow near a permeable vertical plate. Additional studies by Kumar and Sugunamma [16] and Samrat et al. [17] investigated magnetohydrodynamic (MHD) radiative Casson fluid over various geometries.

Viscous dissipation, an essential concept in fluid mechanics, refers to the conversion of mechanical energy into thermal energy due to internal friction within a fluid. This phenomenon is influenced by fluid viscosity and shear forces and plays a vital role in applications like heat exchangers, cooling systems, and electronics cooling. Gebhart [18] was the first to discuss the viscous dissipation term in natural convection, while Hadhrami et al. [19] studied its effects on porous media and permeable surfaces. Hayat et al. [20] explored the impact of viscous dissipation in Casson fluid flow combined with nanofluid and thermal conductivity. Praveen et al. [21] examined Joule heating and heat generation effects on a permeable stretching cylinder. Researchers such as Koo and Kleinstreuer [22] and Winter [23] have also investigated the role of viscous dissipation in energy equations.

The Darcy-Forchheimer porous medium is used to model fluid flow in filtration processes, water treatment systems, and oil and gas filtration. It is also applied in geotechnical engineering to estimate groundwater flow rates and pressure distributions and has biomedical applications in tissue engineering, drug delivery, and blood flow through tissues. For example, Khan [24] analysed velocity slip, viscous dissipation, heat sources/sinks, and Ohmic heating in a Darcy-Forchheimer porous medium. Mukhopadhyay et al. [25] studied boundary layer convective flow over a porous plate in such a medium. Ganesh et al. [26] investigated heat transfer in non-Newtonian Reiner-Philippoff fluid flow within a Darcy-Forchheimer medium, while Prasad [27] examined thermal diffusion in MHD mixed convection over an accelerating vertically wavy plate in a porous medium. Shoaib et al. [28] analysed the effects of a Forchheimer porous medium on Casson fluid over a non-linear surface, and Bansal and Yadav [29] explored slip velocity effects in Newtonian fluid flow over a stretching surface with a porous medium.

This research expands on the work of Pramanik [4] by incorporating the effects of slippery, permeable Darcy-Forchheimer porous medium and mixed convection. The effects of slip conditions, viscous dissipation, and thermal buoyancy are also investigated. The governing nonlinear partial differential equations are transformed into nonlinear ordinary differential equations using similarity transformations. These equations are solved numerically using the fourth-order Runge-Kutta method.

2. Mathematical model

This study focuses on the incompressible, non-Newtonian radiative Casson fluid over a slippery, permeable, stretching flat surface. The flow occurs within a Darcy-Forchheimer porous medium, with the flat plate aligned parallel to the *x*-axis (Fig. 1). Fluid stream is restricted to $y > 0$. Further assumptions include that two identical but adverse stresses are used along with the flow direction to stretch the sheet while maintaining the origin static. The phenomena impacting the fluid flow include radiative heat transfer, drag effects, buoyancy forces, and viscous dissipation.

The following equation is the rheological expression for an incompressible, isotropic, and viscous Casson fluid:

$$\tau_{ij}=\begin{cases}2\left(\mu_B+\frac{p_y}{\sqrt{2\pi}}\right)e_{ij,} & \pi>\pi_c\\ 2\left(\mu_B+\frac{p_y}{\sqrt{2\pi_\epsilon}}\right)e_{ij,} & \pi<\pi_c\end{cases},$$

where $\pi = e_{ij}e_{ij}$ is the product of the component of deformation rate, e_{ij} is the (*ij*)th component of the deformation rate, μ_B is the plastic dynamic viscosity of a non-Newtonian fluid, p_y is the yield stress of the fluid, and π_c is the critical value of the product.

The governing continuity equation, derived from the principle of mass conservation for an incompressible fluid in two dimensions, is expressed as

$$\frac{\partial u}{\partial x}+\frac{\partial v}{\partial y}=0, \tag{1}$$

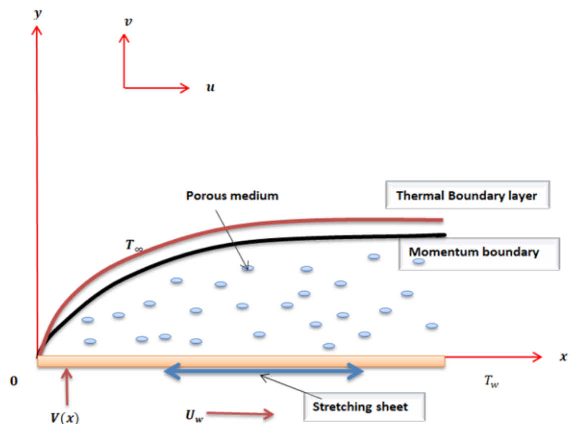

Fig. 1. Diagram of the flow case under consideration.

where u is the velocity in the *x*-direction, and v is the velocity in the *y*-direction.

The momentum equation, also called the Navier-Stokes equation, is derived from Newton's second law of motion for an incompressible non-Newtonian fluid, incorporating additional effects such as permeability, buoyancy and a stretching sheet, and is expressed as

$$u\frac{\partial u}{\partial x}+v\frac{\partial u}{\partial y}=\vartheta\left(1+\frac{1}{\beta}\right)\frac{\partial^2 u}{\partial y^2}-\vartheta\left(1+\frac{1}{\beta}\right)\frac{u}{K}+$$
$$-\frac{Fu^2}{\rho\sqrt{K}}+g\beta^*(T-T_\infty), \tag{2}$$

where ρ is the density, β^* is the thermal expansion, ϑ is the kinematic viscosity, F is the drag coefficient, g is the gravitational acceleration, K is the permeability of the porous medium, T is the temperature, and $\beta=\mu_B\frac{\sqrt{2\pi_c}}{p_y}$ is the Casson parameter.

The energy equation, derived from the first law of thermodynamics (the conservation of energy), for an incompressible non-Newtonian fluid with effects, such as porous medium, viscous dissipation, Forchheimer drag, and radiative heat transfer, is expressed as

$$u\frac{\partial T}{\partial x}+v\frac{\partial T}{\partial y}=\frac{\kappa}{\rho C_p}\frac{\partial^2 T}{\partial y^2}+\frac{\mu}{\rho C_p}\left(1+\frac{1}{\beta}\right)\left(\frac{\partial u}{\partial y}\right)^2+$$
$$+\left(1+\frac{1}{\beta}\right)\frac{\mu u^2}{K\rho C_p}+\frac{Fu^3}{\rho C_p\sqrt{K}}-\frac{1}{\rho C_p}\frac{\partial q_r}{\partial y}. \tag{3}$$

where C_p is the specific heat, q_r is the radiative heat flux, κ is the thermal conductivity, and μ is the viscosity. We are able to write an expression of the Rosseland estimation as

$$q_r=-\frac{4\sigma}{3k^*}\frac{\partial T^4}{\partial y}, \tag{4}$$

where σ is the Stefan-Boltzmann constant and k^* is the mean absorption coefficient. Then, expanding T^4 along with T_∞ with the help of Taylor series, taking zero of higher-order terms in fluid flow yields:

$$T^4\equiv 4T_\infty^3T-3T_\infty^4. \tag{5}$$

Using Eqs. (4) and (5), Eq. (3) is converted into

$$u\frac{\partial T}{\partial x}+v\frac{\partial T}{\partial y}=\left(\frac{\kappa}{\rho C_p}+\frac{16\sigma T_\infty^3}{3\rho C_p k^*}\right)\frac{\partial^2 T}{\partial y^2}+\frac{\mu}{\rho C_p}\left(1+\frac{1}{\beta}\right)\left(\frac{\partial u}{\partial y}\right)^2+$$
$$+\left(1+\frac{1}{\beta}\right)\frac{\mu u^2}{K\rho C_p}+\frac{Fu^3}{\rho C_p\sqrt{K}}. \tag{6}$$

The boundary conditions adopted in this study are:

$$\left.\begin{aligned}u&=U_w+\frac{\mu}{R}\left(1+\frac{1}{\beta}\right)\frac{\partial u}{\partial y},\\ v&=-V(x),\\ -\kappa\frac{\partial T}{\partial y}&=h(T_w-T),\end{aligned}\right\}\quad \text{at } y=0, \tag{7}$$

$$u\to 0,\quad T\to T_\infty\quad \text{as } y\to\infty \tag{8}$$

Here, $U_w=U_0e^{\frac{x}{L}}$ is the stretch velocity, where L is the is the characteristic length and U_0 is the reference velocity, R is the slip length coefficient, $T_w = T_0 e^{\frac{x}{2L}}$ is the temperature over the surface, T_0 is the reference temperature, $V(x) = V_0 e^{\frac{x}{2L}}$ is a velocity over the sheet, where V_0 is considered as constant, while $V(x) > 0$ is the velocity for suction and $V(x) < 0$ is the velocity for blowing.

3. Numerical solution

Dimensionless variables are defined as:

$$\eta = \sqrt{\frac{U_0}{2\vartheta L}}\, e^{\frac{x}{2L}} y, \quad v = -\sqrt{\frac{\vartheta U_0}{2L}} e^{\frac{x}{2L}} [f(\eta) + \eta f'^{(\eta)}],$$

$$u = U_0 e^{\frac{x}{L}} f'(\eta), \quad T = T_\infty + T_0 e^{\frac{x}{2L}} \theta(\eta), \tag{9}$$

where f is the dimensionless stream function and θ is the dimensionless temperature, and the prime mark denotes differentiation with respect to η.

Using Eqs. (9), Eqs. (2) and (6) transform to dimensionless forms, respectively:

$$\left(1+\frac{1}{\beta}\right) f''' + f f'' - \left(1+\frac{1}{\beta}\right) K_1 f' - (\mathrm{Fr}+2) f'^2 + 2\lambda\theta = 0, \tag{10}$$

$$\left(1+\frac{4}{3}N\right)\theta'' - \mathrm{Pr}(\theta f' - f\theta') +$$

$$+\left(1+\frac{1}{\beta}\right)\mathrm{EcPr}\left(f''^2 + K_1 f'^2\right) + \mathrm{FrEcPr} f'^3 = 0, \tag{11}$$

where higher order derivatives with respect to η are represented by adding more primes (the second and third derivatives).

Applying similarity transformation from Eq. (9), Eqs. (7) and (8) can be converted as follows:

$$\begin{cases} f'(0) = 1 + \left(1+\frac{1}{\beta}\right)\lambda_u + f'', \\ f'(0) = S, \\ \theta(0) = 1 + \lambda_t \theta'(0), \end{cases} \quad \text{at } \eta = 0, \tag{12}$$

$$f'(\infty) \to 0, \quad \theta(\infty) \to 0, \qquad \text{as } \eta \to \infty. \tag{13}$$

Here, $S = \frac{V_0}{\sqrt{\frac{\vartheta U_0}{2L}}} > 0$ is the suction or $S < 0$ is the blowing parameter, $\lambda_u = \frac{\mu}{R}\sqrt{\frac{U_0}{2\vartheta L}} e^{\frac{x}{2L}}$ is the velocity slip parameter, $\lambda_t = \frac{\kappa}{h}\sqrt{\frac{U_0}{2\vartheta L}} e^{\frac{x}{2L}}$ is the slip parameter of temperature distribution, $\mathrm{Gr} = \frac{g\beta^*(T_w - T_\infty)L^3}{\vartheta^2}$ is the Grashof number, $\mathrm{Pr} = \frac{\mu C_p}{\kappa}$ is the Prandtl number, $\mathrm{Ec} = \frac{{U_w}^2}{C_p(T_w - T_\infty)}$ is the Eckert number, $\mathrm{Fr} = \frac{2FL}{\rho\sqrt{\kappa}}$ is the local inertia coefficient, $\lambda = \frac{\mathrm{Gr}}{\mathrm{Re}^2}$ is the mixed convection parameter, $\mathrm{Re}^2 = \frac{{U_w}^2 L^2}{\vartheta}$ is the local Reynolds number, $K_1 = \frac{2\vartheta L}{U_w K}$ – the porosity parameter, $N = \frac{4\sigma T_\infty^3}{\kappa k^*}$ – the radiation parameter.

The skin friction coefficient C_f and Nusselt number Nu, which are the factors of physical interest, are calculated as

$$C_f = \frac{\tau_w}{\frac{1}{2}\rho U_w^2}, \quad \mathrm{Nu} = \frac{L q_w}{\kappa(T_w - T_\infty)},$$

where τ_w is the shear stress at the surface and q_w is the heat flux at the surface:

$$\tau_w = \mu\left(\frac{\partial u}{\partial y}\right)_{y=0}, \quad q_w = -\kappa\left(\frac{\partial T}{\partial y}\right)_{y=0}.$$

By using Eq. (8), the above are converted as follows:

$$C_f \frac{\sqrt{\mathrm{Re}}}{\sqrt{2}} = f''(0), \quad \mathrm{Nu}\frac{\sqrt{2}}{\sqrt{\mathrm{Re}}} = -\theta'(0).$$

3.1. Numerical methodology

Using Eqs. (12) and (13), the solution of governing Eqs. (10) and (11) has been computed numerically by means of the fourth-order Runge-Kutta (RK4) method. The momentum and energy equations are converted from higher order to first order differential equations using the following substitution:

$$f = f_1,$$

$$f' = f_2,$$

$$f'' = f_3,$$

$$f'_3 = \frac{1}{\left(1+\frac{1}{\beta}\right)}\left[\left(1+\frac{1}{\beta}\right) K_1 f_2 + (2+\mathrm{Fr}) f_2^2 - f_1 f_3 - 2\lambda f_4\right], \tag{14}$$

$$\theta = f_4,$$

$$\theta' = f_5,$$

$$f'_5 = \frac{1}{1+\frac{4}{3}N}\left[\mathrm{Pr}(f_4 f_2 - f_1 f_5) - \left(1+\frac{1}{\beta}\right)\mathrm{EcPr}(f_3^2 + K_1 f_2^2) + \right.$$

$$\left. - \mathrm{FrEcPr} f_2^3\right] \tag{15}$$

with the boundary conditions:

$$\begin{cases} f_1(0) = S, \\ f_2(0) = 1 + \left(1+\frac{1}{\beta}\right)\lambda_u f_3(0), \\ f_2(0) = 1 + \left(1+\frac{1}{\beta}\right)\lambda_u f_3(0), \\ f_4(0) = 1 + \lambda_t f_5(0), \\ f_2(\infty) \to 0, \\ f_4(\infty) \to 0. \end{cases} \tag{16}$$

The values of $f_3(0)$ and $f_5(0)$ are required to integrate the initial value problems in Eqs. (14) and (15) with the boundary conditions given by Eqs. (16), but these values are not provided. It is crucial to set a finite value for η_∞ when using the shooting technique. We begin with random initial estimate values to obtain $f_3(0)$ and $f_5(0)$ for a finite value of η_∞. Repeating this process for the significant value of η_∞, a finite value of $\eta_\infty = 10$ for all physical parameters is used to integrate the boundary value problem with a difference of 0.01, applying the RK4 method. We set the better approximation of $f_3(0)$ and $f_5(0)$ for the given boundary conditions of $f_2(10) = 10$ and $f_4(10) = 0$ until the output reaches the required decimals of accuracy 10^{-5}.

3.2. Validation of the code

To verify the present code, the guessed value of $f_3(0)$ for ($\beta = \infty$) is similar to the result provided by Sahoo and Poncet [30],

Table 1. Comparison of $-\theta'(0)$ against Prandtl number for K_1 = S = Fr = Ec = λ = λ_u = λ_t = 0, β = ∞.

	Bidin &Nazar [31]		Pramanik [4]		Present study	
N Pr	**0.5**	**1**	**0.5**	**1**	**0.5**	**1**
1	0.6765	0.5315	0.6765	0.5315	0.6775	0.5353
2	1.0735	0.8627	1.0734	0.8626	1.1074	0.8628
3	1.3807	1.1214	1.3807	1.1213	1.3807	1.1214

Keller and Magyari [2], and Pramanik [4] in their seminal works. The value $f_3(0) = -1.281816$ is correct up to 10^{-6}, which is a sufficient accuracy compared with $f_3(0) = -1.281811$, $f_3(0) = -1.28180$, and $f_3(0) = -1.28182$. Table 1 validates the program's coding by comparing the current outcome with the results reported by Pramanik [4] and Bidin [31].

4. Results and discussion

The combined effects of various parameters on velocity and temperature are analysed for the Casson parameter, porosity parameter, radiation parameter, suction parameter, Eckert number, mixed convection parameter, local inertia coefficient, Prandtl number, and slip parameter, while keeping the fixed values $\beta = 0.5$, $K_1 = 0.1$, $\mathrm{Pr} = 0.7$, $N = 1$, $\mathrm{Fr} = 1$, $\mathrm{Ec} = 0.2$, $\lambda = 0.5$, $\lambda_u = 0.1$, and $\lambda_t = 0.1$. Figures 2 and 3 illustrate the influence of the Casson parameter (β) on the velocity and temperature profiles. For velocity, an increase in β enhances the flow in the region approximately between $0 \le \eta \le 0.62$ $(S = 0.5)$ and $0 \le \eta \le 0.86$ $(S = -0.5)$. Beyond these points, an opposite trend is observed. Initially, the velocity increases due to the effect of the slippery surface. However, as β continues to rise, the fluid's yield stress increases, resulting in higher resistance forces, which ultimately reduce the fluid velocity. In terms of temperature, an increase in β leads to a reduction in the temperature profile. This behaviour is attributed to the same resistance effect caused by the increased yield stress. Additionally, when comparing the effects of blowing and suction, it is evident that suction significantly reduces both the fluid velocity and temperature.

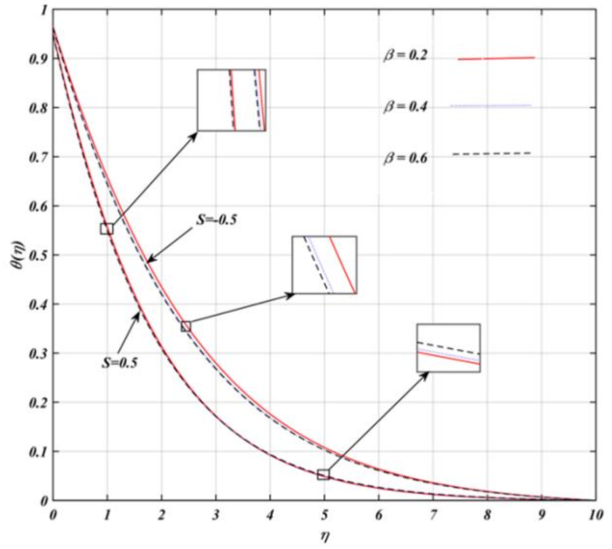

Fig. 3. Change in temperature profiles with β in the existence of S.

Figures 4 and 5 depict the effect of the suction parameter (S) on the velocity and temperature profiles. When $S > 0$ (suction), the velocity profile significantly decreases. The case $S = 0$ represents a non-permeable stretching sheet. Conversely, for $S < 0$ (blowing), the velocity exhibits an increasing trend. The temperature profile also decreases with an increase in $S > 0$, whereas it rises when $S < 0$. This behaviour can be attributed to the fact that blowing increases pressure, allowing the warmed fluid to move farther from the surface, accelerating both velocity and temperature. In contrast, suction exerts an opposite influence by

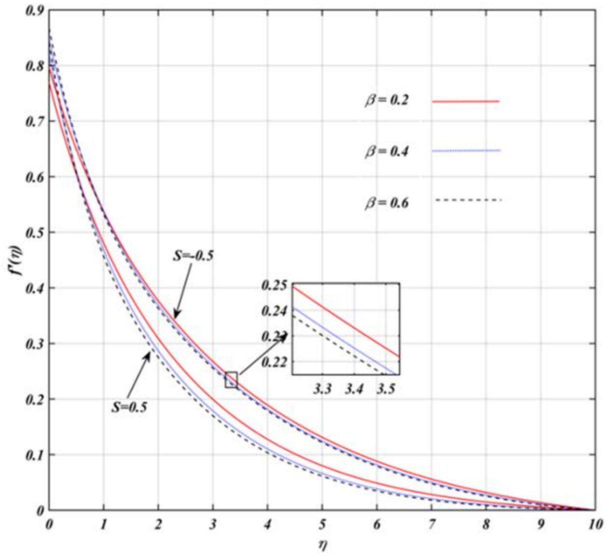

Fig. 2. Change in velocity profiles with β in the existence of S.

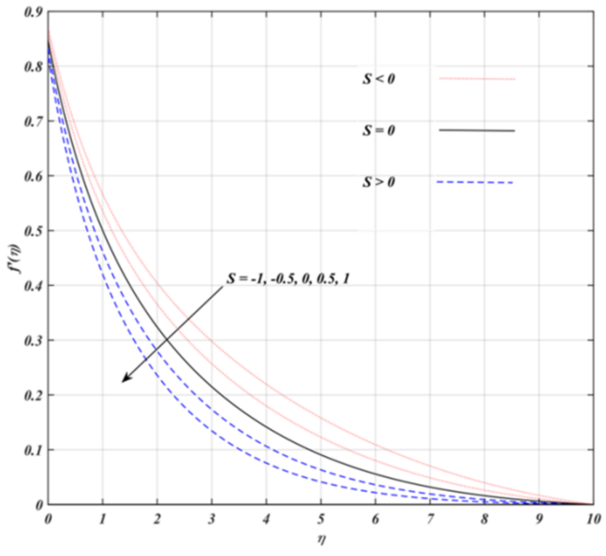

Fig. 4. Velocity profiles for varying S.

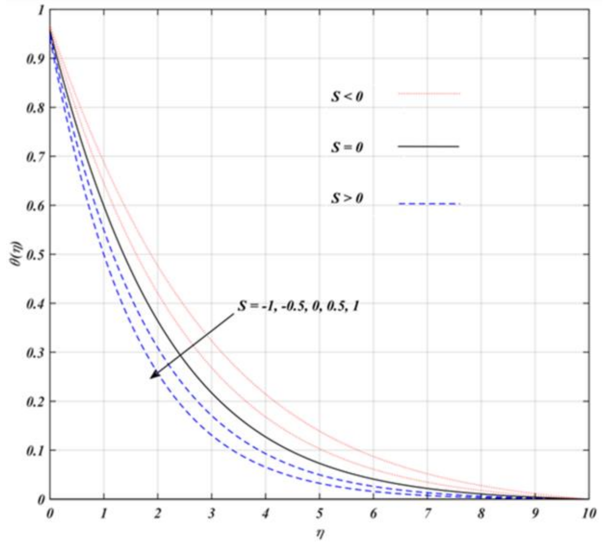

Fig.5. Temperature profiles for varying S.

pulling the fluid closer to the surface, reducing both velocity and temperature.

Figures 6 and 7 present the effect of the porosity parameter (K_1) on the temperature and velocity profiles. As K_1 increases, permeability of the porous medium decreases. This reduced permeability leads to stronger resistance and, consequently, lower fluid velocity. The Forchheimer effect also contributes to increased resistance, further decreasing the velocity. This reduction in permeability and the presence of the Forchheimer effect cause an increase in resistance, which in turn leads to a higher temperature profile as K_1 increases.

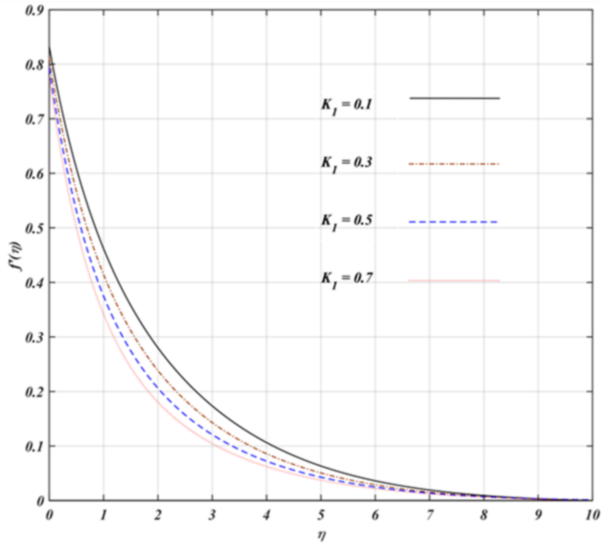

Fig.6. Change in velocity profiles with $\boldsymbol{K_1}$.

Figures 8 and 9 show the influence of the local inertia coefficient (Fr) on velocity and temperature. Here, the Forchheimer drag in porous medium increases internal resistance; higher Fr increases flow resistance, reducing fluid velocity in the porous medium. Forchheimer inertial drag generates heat, so a higher

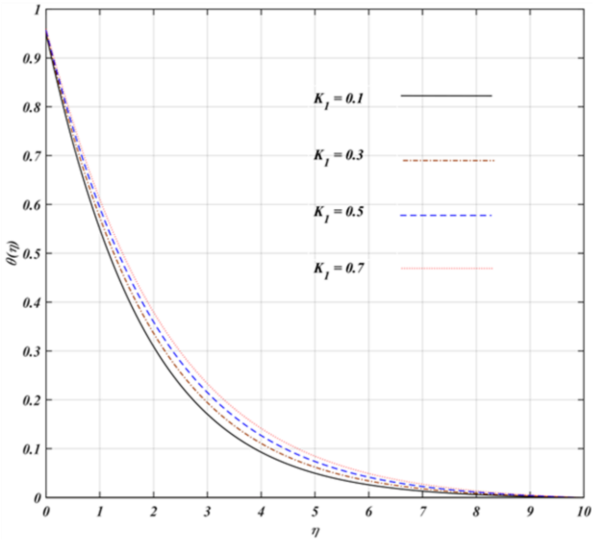

Fig. 7. Change in temperature profiles with K_1.

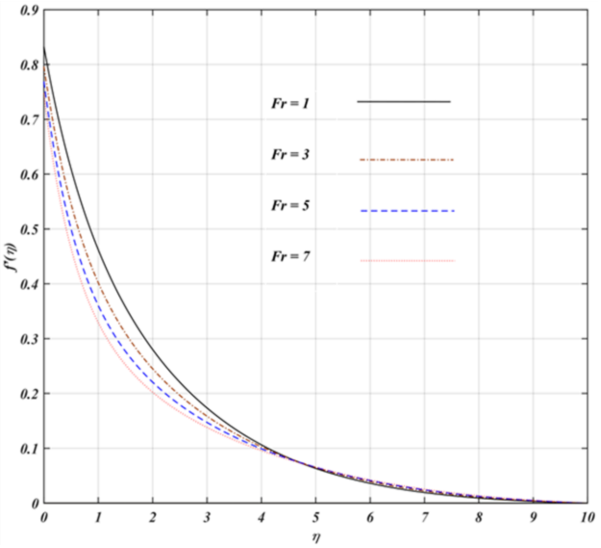

Fig. 8. Change in velocity profiles with Fr.

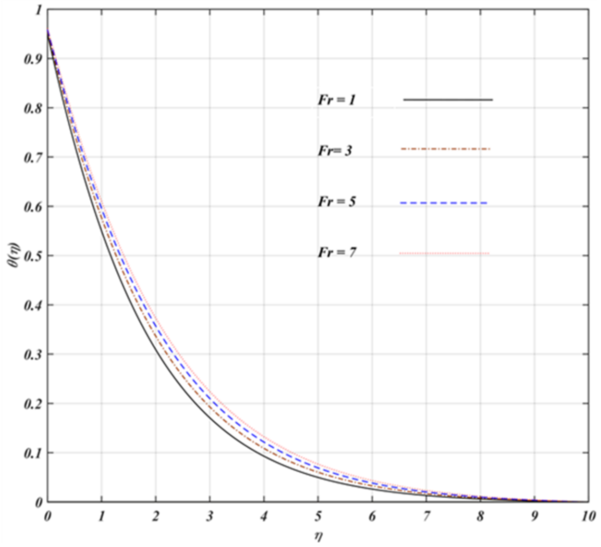

Fig. 9. Change in temperature profiles with Fr.

Fr increases heat generation, leading to a rise in fluid temperature.

Figures 10 and 11 explore the effect of the mixed convection parameter (λ) on the velocity and temperature. The results indicate that temperature decreases and velocity increases with rising λ. This occurs because the temperature difference is directly proportional to λ; the temperature gradient at the wall increases, leading to a higher Nusselt number (more efficient heat dissipation). The thermal boundary layer thickness decreases as more heat is convected away. In the velocity case, the buoyancy force acts in the direction of the flow, which leads to an increase in velocity with an increase in λ.

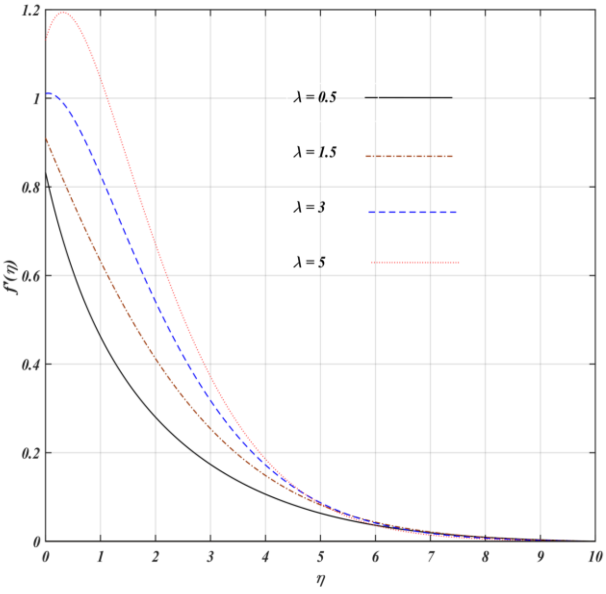

Fig. 10. Velocity profile change with λ.

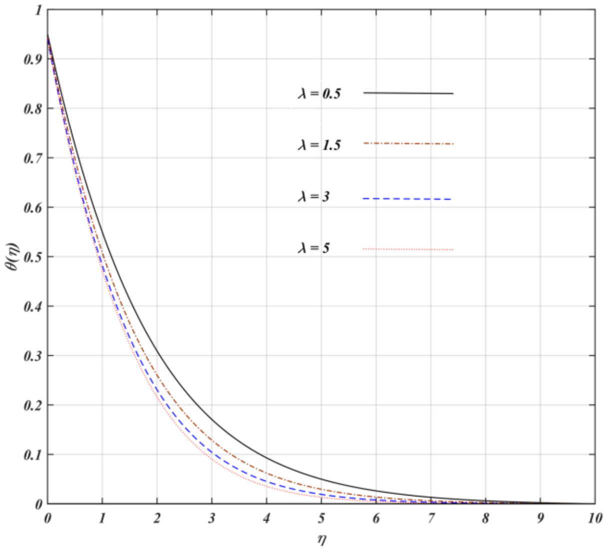

Fig. 11. Temperature profile change with λ.

Figure 12 shows the effect of the radiation parameter (N) on the temperature profile. An increase in N results in a continuous rise in temperature, because higher N enhances radiative heat transfer, increasing energy transport in the fluid. This leads to a higher temperature throughout the boundary layer. Figure 13 illustrates the effect of the Prandtl number (Pr) on temperature, showing a decrease in temperature as Pr increases. A higher Pr signifies greater thermal conductivity (κ), which lowers the fluid temperature.

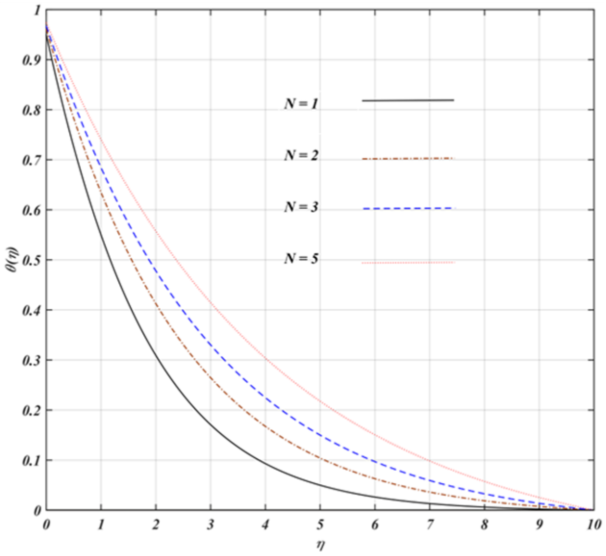

Fig. 12. Temperature profile change with N.

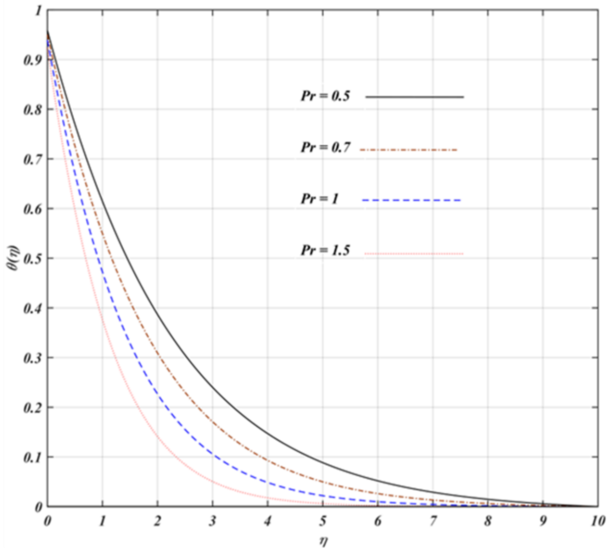

Fig. 13. Temperature profile change with Pr.

Figure 14 demonstrates that the temperature profile expands with an increase in the Eckert number (Ec). This is because Ec reflects the conversion of mechanical energy into thermal energy. When Ec is high, more mechanical energy is converted into heat, leading to a rise in the fluid temperature. Figure 15 examines the impact of the slip parameter for the temperature (λ_t), showing that temperature decreases with higher λ_t as less heat is transferred from the sheet to the fluid. The thermal boundary layer becomes thinner as less heat is conducted to the fluid. Figures 16 and 17 depict the influence of the velocity slip

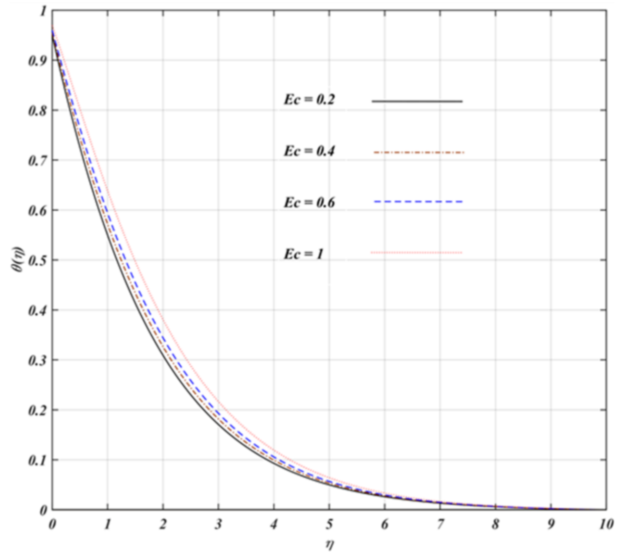

Fig. 14. Temperature profile change with Ec.

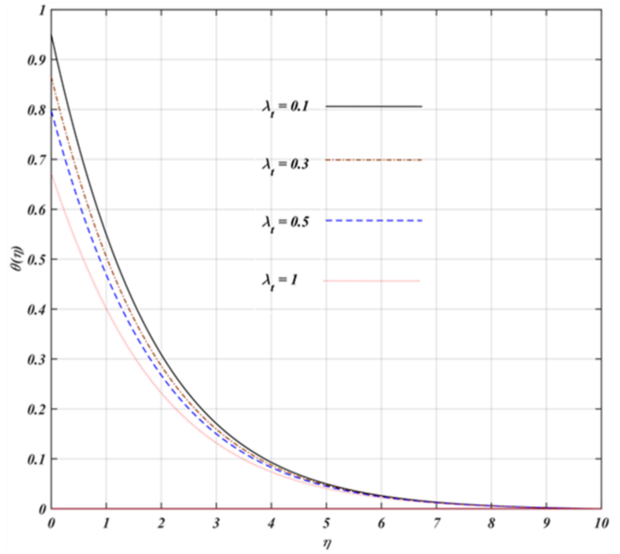

Fig. 15. Temperature profile change with λ_t.

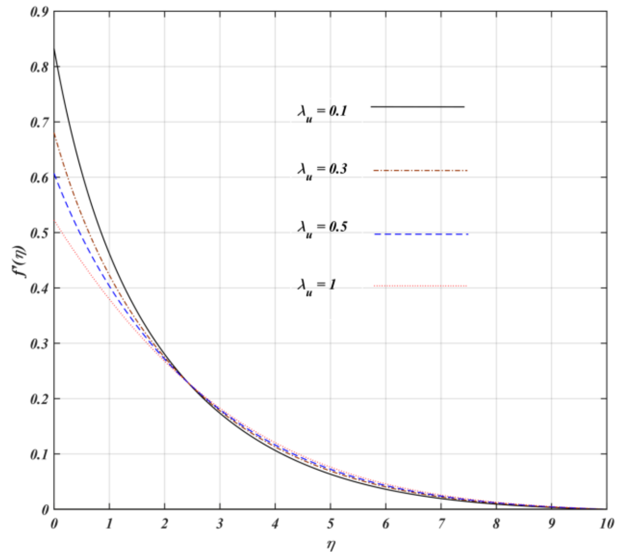

Fig. 16. Velocity profile change with λ_u.

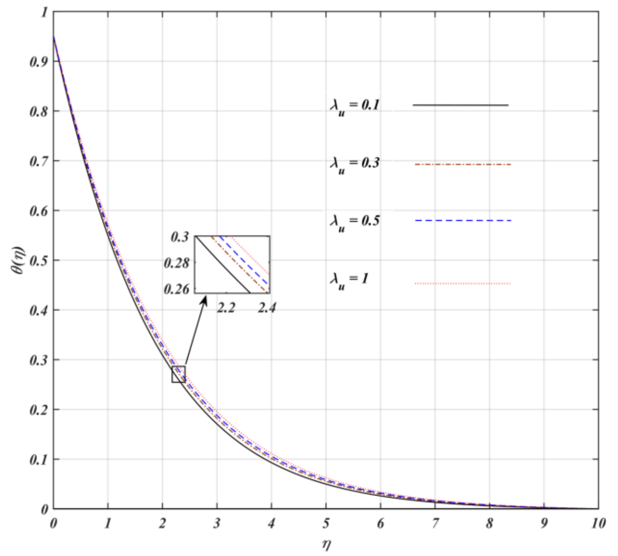

Fig. 17. Temperature profile change with λ_u.

parameter (λ_u) on the velocity and temperature. Velocity decreases with an increase in λ_u, because of a reduction in wall shear stress, but as η exceeds 2.4, it slightly increases due to the stretching effect of the sheet. Conversely, temperature is directly proportional to λ_u, increasing with λ_u. This results in an increase in thermal boundary layer thickness because of weaker momentum transfer.

The skin friction coefficient (C_f) and Nusselt (Nu) number play crucial roles in analysing the effects of shear stress and heat transfer at the surface of the stretching sheet. Table 2 summarizes the effect of various parameters on C_f and Nu for a fixed Reynolds number, Re = 1. The Nusselt number increases with S, Pr, β, and λ, but decreases with K_1, Fr, N, Ec, λ_u and λ_t. Meanwhile, the skin friction coefficient C_f increases with N, Ec, λ and λ_u, while it decreases with K_1, β, S, Fr, Pr and λ_t. A higher skin friction coefficient means increased drag force on the stretching sheet due to resistance from fluid motion. A higher Nusselt number implies more efficient heat transfer, which is crucial in applications like cooling processes and thermal management in industrial systems.

5. Practical significance and usefulness

The findings of this study offer valuable insights into the behaviour of Casson non-Newtonian fluid flow and heat transfer over a stretching sheet, considering various physical effects, such as porous media, thermal radiation, mixed convection, velocity slip and suction/blowing. These results have significant applications across multiple industrial and engineering fields, particularly in areas where non-Newtonian fluids and porous media play a crucial role.

The study demonstrates that parameters, such as the Prandtl number, suction parameter, Casson parameter and mixed convection parameter, notably enhance the Nusselt number, thereby improving heat dissipation. This is particularly important for cooling electronic devices, thermal coating processes and poly-

Table 2. $f''(0)$ and $-\theta'(0)$ for physical parameters β, λ, N, Pr, S, K_1, Fr, Ec, λ_u and λ_t.

K_1	β	S	Fr	N	Pr	Ec	λ	λ_u	λ_t	$f''(0)$	$-\theta'(0)$
0.1	0.5	0.5	1	1	0.7	0.2	0.5	0.1	0.1	-0.558356	0.499664
0.3	0.5	0.5	1	1	0.7	0.2	0.5	0.1	0.1	-0.626966	0.464039
0.5	0.5	0.5	1	1	0.7	0.2	0.5	0.1	0.1	-0.687742	0.433837
0.1	0.2	0.5	1	1	0.7	0.2	0.5	0.1	0.1	-0.383669	0.485282
0.1	0.4	0.5	1	1	0.7	0.2	0.5	0.1	0.1	-0.513380	0.497690
0.1	0.6	0.5	1	1	0.7	0.2	0.5	0.1	0.1	-0.595488	0.500780
0.1	0.5	0.0	1	1	0.7	0.2	0.5	0.1	0.1	-0.511995	0.430546
0.1	0.5	0.5	1	1	0.7	0.2	0.5	0.1	0.1	-0.558356	0.499664
0.1	0.5	1.0	1	1	0.7	0.2	0.5	0.1	0.1	-0.610393	0.499664
0.1	0.5	0.5	1	1	0.7	0.2	0.5	0.1	0.1	-0.558356	0.499664
0.1	0.5	0.5	3	1	0.7	0.2	0.5	0.1	0.1	-0.679037	0.451246
0.1	0.5	0.5	5	1	0.7	0.2	0.5	0.1	0.1	-0.769847	0.416987
0.1	0.5	0.5	1	1	0.7	0.2	0.5	0.1	0.1	-0.558356	0.499664
0.1	0.5	0.5	1	2	0.7	0.2	0.5	0.1	0.1	-0.538443	0.388077
0.1	0.5	0.5	1	3	0.7	0.2	0.5	0.1	0.1	-0.526579	0.327710
0.1	0.5	0.5	1	1	0.5	0.2	0.5	0.1	0.1	-0.543258	0.413735
0.1	0.5	0.5	1	1	0.7	0.2	0.5	0.1	0.1	-0.558356	0.499664
0.1	0.5	0.5	1	1	1.0	0.2	0.5	0.1	0.1	-0.575659	0.611694
0.1	0.5	0.5	1	1	0.7	0.2	0.5	0.1	0.1	-0.558356	0.499664
0.1	0.5	0.5	1	1	0.7	0.4	0.5	0.1	0.1	-0.554952	0.451332
0.1	0.5	0.5	1	1	0.7	0.6	0.5	0.1	0.1	-0.549534	0.403111
0.1	0.5	0.5	1	1	0.7	0.2	0.5	0.1	0.1	-0.558356	0.499664
0.1	0.5	0.5	1	1	0.7	0.2	1.5	0.1	0.1	-0.299004	0.556375
0.1	0.5	0.5	1	1	0.7	0.2	3.0	0.1	0.1	-0.034755	0.592747
0.1	0.5	0.5	1	1	0.7	0.2	0.5	0.1	0.1	-0.558356	0.499664
0.1	0.5	0.5	1	1	0.7	0.2	0.5	0.3	0.1	-0.355079	0.488848
0.1	0.5	0.5	1	1	0.7	0.2	0.5	0.5	0.1	-0.262017	0.480791
0.1	0.5	0.5	1	1	0.7	0.2	0.5	0.1	0.1	-0.558356	0.499664
0.1	0.5	0.5	1	1	0.7	0.2	0.5	0.1	0.3	-0.570966	0.447053
0.1	0.5	0.5	1	1	0.7	0.2	0.5	0.1	0.5	-0.581328	0.404767

extrusion, where efficient heat removal is essential to prevent overheating.

Additionally, the study examines the influence of the porosity parameter and local inertia coefficient on the velocity and temperature. This knowledge is beneficial in oil extraction, geothermal energy systems, and chemical filtration, where understanding fluid flow resistance through porous media is essential for optimizing performance.

The Casson fluid models are widely used to describe blood flow in arteries. The effects of suction and porosity on the velocity and temperature can provide insights into blood perfusion in biological tissues and aid in the design of porous medical implants for improved heat dissipation.

Furthermore, stretching sheet problems are common in polymer manufacturing, fibre spinning, and metal extrusion. The influence of mixed convection and porous media effects is also crucial in applications, such as solar energy collection, geothermal heat exchangers, and thermal energy storage systems.

6. Conclusions

The mathematical approaches of steady boundary layer flow for a radiating Casson fluid on a permeable stretching sheet under the existence of both velocity and temperature slip conditions with a Darcy-Forchheimer porous medium and viscous dissipation were analysed. The findings of the current investigation are briefly summarised below.

1) The velocity increases with increasing Ec and λ, but falls with increasing K_1, $S > 0$, β and Fr;
2) The temperature increases with an increase of K_1, Fr, N and λ_u, but declines with increasing λ, β, Pr, $S > 0$ and λ_t;
3) Fr first decreases the velocity, then as $\eta > 4.75$ (approximately) increases it due to the mixed convection effect. Boundary layer thickness increases with increasing local inertia coefficient;
4) The velocity profile enhances with increased β before $\eta = 0.62$ for $S = 0.5$ ($\eta = 0.86$ for $S = -0.5$), but after that, it decreases because of the slip velocity effect;
5) The velocity profile increases when λ increases, but the temperature decreases;
6) The skin friction coefficient C_f enhances with increasing values of N, Ec, λ and λ_u, while it reduces with a rise in values of K_1, β, S, Fr, Pr and λ_t;
7) Nu enhances with increasing values of S, Pr, β and λ, but decreases with rising values of K_1, Fr, N, Ec, λ_u and λ_t.

While the current study provides significant insights, several aspects require further exploration, such as three-dimensional flow effects, unsteady flow conditions, and nanofluid and hybrid nanofluid flow, chemical reaction and magnetic field effects.

References

[1] Gupta, P., & Gupta, P. (1977). Heat and mass transfer on a stretching sheet with suction or blowing. *Journal of Chemical Engineering*, 55(6), 744–746. doi: 10.1002/cjce.5450550619

[2] Magyari, E., & Keller, B. (1999) Heat and mass transfer in the boundary layers on an exponentially stretching continuous sur-

face. *Journal of Physics D: Applied Physics*, 32(5), 577–585. doi: 10.1088/0022-3727/32/5/012

[3] Elbashbeshy, E. (2001). Heat transfer over an exponentially stretching continuous surface with suction. *Archives of Mechanics*, 53(6), 643–651.

[4] Pramanik, S. (2014). Casson fluid flow and heat transfer past an exponentially porous stretching surface in presence of thermal radiation. *Ain Shams Engineering Journal*, 5(1), 205–212. doi: 10.1016/j.asej.2013.05.003

[5] Jain, R., Mehta, R., Mehta, T. & Yadav, R.S. (2020). Numerical study of chemically reactive MHD hydrodynamic boundary layer fluid flow over an absorptive surface in the presence of slip and mixed convection. *Advances in Mathematics: Scientific Journal*, 9(9), 7057–7064. doi: 10.37418/amsj.9.9.55

[6] Partha, M.K, Murthy, P.V., & Rajasekhar, G.P. (2005). Effect of viscous dissipation on the mixed convection heat transfer from an exponentially stretching surface. *Heat and Mass Transfer*, 41, 360–366. doi: 10.1007/s00231-004-0552-2

[7] Khan, S.K. (2006). Boundary layer viscoelastic fluid flow over an exponentially stretching sheet. *International Journal of Applied Mechanics and Engineering*, 11(2), 321–335.

[8] Sajid, M., & Hayat, T. (2008). Influence of thermal radiation on the boundary layer flow due to an exponentially stretching sheet. *International Communications in Heat and Mass Transfer*, 35(3), 347–356. doi: 10.1016/j.icheatmasstransfer.2007.08.006

[9] Bejawada, S.G., Reddy, Y.D., Jamshed, W., Nisar, K.S., Alharbi, A.N., & Chouikh, R. (2022). Radiation effect on MHD Casson fluid flow over an inclined non-linear surface with chemical reaction in a Forchheimer porous medium. *Alexandria Engineering Journal*, 61(10), 8207–8220. doi: 10.1016/j.aej.2022.01.043

[10] Rasool, G., Chamkha, A.J., Muhammad, T., Shafiq, A., & Khan, I. (2020). Darcy-Forchheimer relation in Casson type MHD nanofluid flow over non-linear stretching surface. *Propulsion and Power Research*, 9(2), 159–168. doi: 10.1016/j.jppr.2020.04.003

[11] Bilal Ashraf, M., Hayat, T. & Alsaedi, A. (2017). Mixed convection flow of Casson fluid over a stretching sheet with convective boundary conditions and Hall effect. *Boundary Value Problems*, 137. doi: 10.1186/s13661-017-0869-7

[12] Raju, C.S., Hoque, M.M., & Sivasankar, T. (2017). Radiative flow of Casson fluid over a moving wedge filled with gyrostatic microorganisms. *Advanced Powder Technology*, 28(2), 575–583. doi: 10.1016/j.apt.2016.10.026

[13] Mehmood, R., Rana, S., Akbar, N.S., & Nadeem, S. (2018). Non-aligned stagnation point flow of radiating Casson fluid over a stretching surface. *Alexandria Engineering Journal*, 57(2), 939–946. doi: 10.1016/j.aej.2017.01.010

[14] Sinha, S., & Yadav, R.S. (2022). MHD mixed convective slip flow along an inclined porous plate in presence of viscous dissipation and thermal radiation. *Trends in Sciences*, 19(4), 2685. doi: 10.48048/tis.2022.2685

[15] Loganathan, P., & Deepa, K. (2019). Electromagnetic and radiative Casson fluid flow over a permeable vertical Riga-plate. *Journal of Theoretical and Applied Mechanics*, 57(4), 987– 998. doi: 10.15632/jtam-pl/112421

[16] Kumar, K.A., Sugunamma, V., & Sandeep, N. (2020). Effect of thermal radiation on MHD Casson fluid flow over an exponentially stretching curved sheet. *Journal of Thermal Analysis and Calorimetry*, 140, 2377–2385. doi: 10.1007/s10973-019-08977-0

[17] Samrat, S.P., Reddy, M.G., & Sandeep, N. (2021). Buoyancy effect on magnetohydrodynamic radiative flow of Casson fluid with Brownian moment and thermophoresis. *The European Physical Journal Special Topics*, 230, 1273–1281. doi: 10.1140/epjs/s11734-021-00043-x

[18] Gebhart, B. (1962). Effects of viscous dissipation in natural convection. *Journal of fluid Mechanics*, 14(2), 225–232. doi: 10.1017/S0022112062001196

[19] Al-Hadhrami, A., Elliott, L. & Ingham, D. (2003). A new model for viscous dissipation in porous media across a range of permeability values. *Transport in Porous Media*, 53, 117–122. doi: 10.1023/A:1023557332542

[20] Hayat, T., Khan, M.I., Waqas, M., Yasmeen, T., & Alsaedi, A. (2016). Viscous dissipation effect in flow of magnetonanofluid with variable properties. *Journal of Molecular Liquids*, 222, 47–54. doi: 10.1016/j.molliq.2016.06.096

[21] Kumar, P., Yadav, R.S, & Makinde, O.D. (2023). Numerical study of Williamson fluid flow and heat transfer over a permeable stretching cylinder with the effects of joule heating and heat generation/absorption. *Heat Transfer*, 52(4), 3372–3388. doi: 10.1002/htj.22832

[22] Koo, J., & Kleinstreuer, C. (2004). Viscous dissipation effects in microtubes and microchannels. *International Journal of Heat and Mass Transfer*, 47(14-16), 3159–3169. doi: 10.1016/j.ijheatmasstransfer.2004.02.017

[23] Winter, H.H. (1987). Viscous dissipation term in energy equations. American Institute of Chemical Engineers, *Modular Instruction, Series C: Transport, Vol. 7. Calculation and Measurement Techniques for Momentum, Energy and Mass Transfer*, 27–34.

[24] Khan, M.I., Alzahrani, F., & Hobiny, A. (2020). Simulation and modeling of second order velocity slip flow of micropolar ferrofluid with Darcy-Forchheimer porous medium. *Journal of Materials Research and Technology*, 9(4), 7335–7340. doi: 10.1016/j.jmrt.2020.04.079

[25] Mukhopadhyay, S., De, P.R., Bhattacharyya, K & Layek, G.C. (2012). Forced convective flow and heat transfer over a porous plate in a Darcy-Forchheimer porous medium in presence of radiation. *Meccanica*, 47, 153–161. doi: 10.1007/s11012-011-9423-3

[26] Kumar, K.G., Reddy, M.G., Khan, M.I., Alzahrani, F., Khan, M.I., & El-Zahar, E.R. (2021). Heat transfer and melting flow of a Reiner-Philippoff fluid over a surface with Darcy-Forchheimer medium. *Case Studies in Thermal Engineering*, 28, 101649. doi: 10.1016/j.csite.2021.101649

[27] Prasad, D.K., Chaitanya, G.K., & Raju, R.S. (2019). Double diffusive effects on mixed convection Casson fluid flow past a wavy inclined plate in presence of Darcian porous medium. *Results in Engineering*, 3, 100019. doi: 10.1016/j.rineng.2019.100019

[28] Shoaib, M., Kausar, M., Nisar, K.S., Raja, M.A.Z., & Morsy, A. (2022). Impact of thermal energy on MHD Casson fluid through a Forchheimer porous medium with inclined non-linear surface: A soft computing approach. *Alexandria Engineering Journal*, 61(12), 12211–12228, doi: 10.1016/j.aej.2022.06.014

[29] Bansal, S., & Yadav, R.S. (2024). Effect of slip velocity on Newtonian fluid flow induced by a stretching surface within a porous medium. *Journal of Engineering and Applied Science*, 71, 153. doi: 10.1186/s44147-024-00481-z

[30] Sahoo. B., & Poncet, S. (2011). Flow and heat transfer of a third grade fluid past an exponentially stretching sheet with partial slip boundary condition. *International Journal of Heat and Mass Transfer*, 54(23-24), 5010–5019. doi: 10.1016/j.ijheatmasstransfer.2011.07.015

[31] Bidin, B., & Nazar, R. (2009). Numerical solution of the boundary layer flow over an exponentially stretching sheet with thermal radiation. *European Journal of Scientific Research*, 33(4), 710–717.

Co-published by
Institute of Fluid-Flow Machinery
Polish Academy of Sciences
Committee on Thermodynamics and Combustion
Polish Academy of Sciences

http://www.imp.gda.pl/archives-of-thermodynamics/

ARCHIVES
OF THERMODYNAMICS

Gibbs-Duhem equation used to describe uncompensated and apparent heat transfer applied to spray cooling

Stephanie Lacour[a*], Michel Feidt[b]

[a]Université Paris-Saclay, INRAE - Unite de recherche FRISE, Pierre-Gilles de Gennes 1, CS 10030, Antony 92761, Cedex, France
[b]University of Lorraine, Laboratory LEMTA, 2 Av. de la Forêt de Haye, 54500 Vandœuvre-lès-Nancy, France
*Corresponding author email: stephanie.lacour@inrae.fr

Received: 06.12.2024; revised: 25.03.2025; accepted: 06.04.2025

Abstract

Entropic analysis makes it possible to determine the equilibrium of a system with its environment, but heat exchange at boundaries is a difficulty in this exercise. In this article, we establish the energy balance of a water liquid and air mixture: the Gibbs-Duhem equation is used to describe the balance. Diffusion terms are expressed while accounting for volume changes and their entropic contributions, leading to an expression for fugacity. After mixing, the mixture spontaneously evolves combining mechanical, chemical and thermal changes towards equilibrium. This latest is solved assuming either an isenthalpic or isentropic transformation in the balance, to highlight the energy exchange between the system and its environment. Some irreversibilities are included in transformations and primarily affect the chemical path. The comparison reveals heat transfer terms corresponding to uncompensated heat. This analysis illustrates the concept of uncompensated heat and introduces its complement, the apparent heat, which corresponds to enthalpy. The models explain the limiting phenomena involved in spray cooling, whose efficiency varies depending on whether the process follows an adiabatic or an isenthalpic path. The isenthalpic model was applied to literature data to estimate experimental cooling efficiencies over a wide range of operating conditions. However, further modelling work is needed to express the scaling factor for fugacity as a function of the droplet size distribution. The mechanical pathway also requires more attention and dedicated measurements are needed to include pressure drops in the analysis.

Keywords: Gibbs-Duhem equilibrium; Uncompensated heat transfer; Irreversibility analysis; Misting process; Evaporating cooling

Vol. 46(2025), No. 2, 209–219; doi: 10.24425/ather.2025.154919

Cite this manuscript as: Lacour, S., & Feidt, M. (2025). Gibbs-Duhem equation used to describe uncompensated and apparent heat transfer applied to spray cooling. *Archives of Thermodynamics*, 46(2), 209–219.

1. Introduction

Spray cooling of air, heat exchangers or electronic devices allows adapting heat-releasing systems to our actual atmosphere, overheated by climate change. Many studies were carried on to describe the spray cooling efficiencies and their related operating parameters in various evaporative applications: for a direct use outdoors [1], in direct heating, ventilation, and air conditioning (HVAC) systems [2−7], in indirect or M-cycle air coolers [8−11], for heat releases in chillers [12−15] or cooling towers [16−21], or electronic applications [22,23]. Most of the time, results are given according to a simplified thermal analysis: efficiency is found by comparing results to the guess state, which is the saturated state of air. Because of the spontaneous and uncontrolled nature of evaporation, attention is not paid to the physical processes that alleviate efficiency. The complete evaporation of a spray is rarely observed in experimental studies reported in the literature [1,3,6]. Actual development in spray cooling techniques relies on intermittent injection, in order to save water and

Nomenclature

C_p – molar heat capacity, J mol^{-1} K^{-1}
d – droplet diameter, m
H – enthalpy, J
HR – relative humidity, %
H_{vap}– enthalpy for water phase change, J mol^{-1}
k – scaling factor
M – mass of compound, kg
$\widehat{M}$ – molar mass, kg/mol
n – mole of compound, mol
N – number of droplets, m^{-3}
P – pressure, Pa
R – ideal gas constant, J mol^{-1} K^{-1}
S – entropy, J K^{-1}
S_d – entropy for partial pressure change, J K^{-1}
S_v – entropy for volume change, J K^{-1}
S_{vap}– entropy for water phase change, J mol^{-1} K^{-1}
T – temperature, K
V – volume, m^3
x – evaporated mole of water, mol

Greek symbols

α – exponent in the scaling factor
β_i – coefficient in the evaporation temperature relation
γ – adiabatic index
ρ – phase density, kg m^{-3}
μ_i – chemical potential of water in phase i, J mol^{-1}
δQ – heat exchange, J
δW – work exchange, J

Subscripts and Superscripts

d – droplet
eq – equilibrium
f – final state
g – gas
i – initial state
l – liquid
v – water vapour
vap – vaporisation
m – initial mix (liquid+gas)
t – total of compounds
x – related to vapour at the early stage of evaporation
0 – standard state

let the system dry out regularly [24]. Nevertheless, spray cooling techniques would surely be improved if more care was paid to the exceeding liquid water, remaining as a result of non-ideal, not the so-called adiabatic, cooling. Hence, irreversibilities have to be studied, which can be done using entropy analysis.

Entropic analysis in classical thermodynamics allows the study of the irreversibilities of a system that undergoes transformations. Advances in thermodynamics of finite physical dimensions integrate these irreversibilities into methods of optimizing energy systems [24]. Entropy is often used for spray in order to predict the size of spray droplets using the maximum entropy formalism [26]. Le Moyne et al. in [27] explored the concept of scale entropy, shifting from the self-similarity theory to the so-called ‘close-to-fractal’ evolution to describe spray atomization. Such mechanistic approaches are less suited when dealing with evaporative cooling because the focus is mainly on the thermal change, not addressed in mechanics. Combined heat and mass transfer phenomena are also usual problems handled with thermodynamics. Water in moist air is one of the well-documented ones [25,28]. The entropy of moist air was studied in atmospheric problems. Dynamic and thermal pathways were examined to assess the entropy production in the Earth's atmosphere and study the piston effect of convection with moist air [29]. The chemical pathway is added to describe convective motion in cloud formation [30]. In the latest, local entropy deficits explain convective air entrainment and cloud size evolution. Piston effect in spray and moist air was even exploited for an evaporative engine in [31]. For an evaporative cooler, the entropy analysis is a basis for exergy assessments [28,32,33]. Most of the key psychrometrics processes used in HVACR (heating, ventilating, air conditioning and refrigeration) were studied by Ratlamwala and Dincer [33], using various definitions for energy and exergy efficiencies. For an evaporative cooler, they considered a complete evaporation of the liquid water in the process. Energy efficiencies were, however, highly different according to the benefits brought by such an ideal process and its related efficiency definition. In the work of Santos and Barros [34], the second law gives an interesting insight for assessing the exergy efficiency of air washers. In the same way, entropy analysis was successfully used by Wang et al. [35] for the optimization of a M-cycle cooler. Smekar et al. in [16] also used the entropy approach to link local temperature fluctuations and their related entropy to the efficiency of a cooling tower. Majunath et al. [36] used the second law of thermodynamics in a heat exchanger to reduce irreversibilities with an optimal design. Like in [34] or [35], the entropy generation is used for quantifying irreversibilities. However, in an adiabatic cooling method, such as spray cooling, both entropy generation and entropy transfer are critical factors that influence cooling efficiency. The transformation during spray cooling involves multiple pathways related to chemical, thermal and mechanical changes. Therefore, it is essential to integrate these pathways into a comprehensive energy analysis of the system.

Defining a system consists of delimiting a portion of the Universe, whose behaviour is described in detail and which is opposed to the rest, that is, “its environment”. The existence of the system is thus based on the notion of the geometric dimensions assigned to the system by defining it. The transfer of mass and energy at the boundary is generally described, but that of entropy at the boundary is rarely addressed. Bejan [28] evokes the difficulty associated with accounting for these transfers in his work. He underlines the problem of boundaries of isolated systems, which are often subjected to temperature gradients.

The isolated system is a limit case, with no transfer of mass or energy to the environment. The absence of transfer simplifies the description of system transformations, making it ideal. The actual state observed generally differs from the ideal state: this is then attributed either to imperfections in the insulation of the system (transfers), or to irreversibilities (internal productions) which prevent a return to the initial state. The distinction between irreversibility and transfer is delicate: the two terms, generally second-order, are often confused. In open systems, energy transfer at the boundaries occurs, internal irreversibilities are present and are easily confused with the irreversibilities of transfers. Exchange at the boundaries also includes the transfer of matter, but the latter does not better explain the distinction between entropic and thermal transfer at the boundaries. The purpose of this paper is to highlight the distinction between transfer terms and internal irreversibilities in spray cooling. Therefore, we study the spontaneous evolution of a mixture of air and liquid water in free conditions. Mixing generates an imbalance, which causes the two phases to evolve towards a state of equilibrium. In the Lagrangian approach, the mixture evolves spatially in a tunnel at the entrance of which we carry out the mixing, and at the exit of which we recover a mixture assumed to be in equilibrium: we describe an open system in a permanent steady state. In the Eulerian approach, the description involves the temporal evolution of the mixture in a spatially limited closed space, which exchanges energy at its boundaries. A succession of transformations details the chemical, thermal and mechanical processes at work in the evolution of the mixture. The Gibbs-Duhem equation, extended to this non-isolated system, brings together these three types of thermal, mechanical and chemical processes in a global equation of evolution. The equilibrium is expressed with an assumption regarding chemical equilibrium and two alternatives for the thermal equilibrium. The internal irreversibilities for this system control the position of the chemical equilibrium, while the heat transfer terms are of small amplitudes. Entropic transfers systematically differ from thermal transfers and analytically explain the notion of uncompensated heat.

2. Materials and methods

2.1. Mixing moist air with liquid water

Mixing operation induces a temporary non-equilibrium state in the system's components, enabling the extraction of a useful effect such as cooling during the relaxation back to equilibrium. Mixing is often used to quicker obtain an equilibrium state, adding convection transport to diffusion processes. Optimization serves to minimize the cost of creating an imbalance state, while maximizing the service provided. This approach is not the subject of our description and we are not interested here in the energy cost of unbalancing. On the other hand, we use entropic analysis to identify the parameters that impose the final position of the equilibrium. Indeed, these parameters describe the accessible final state. We use a method based on the control volume approach [37] to describe the evolution of the energy terms corresponding to the movement towards equilibrium of our mixture.

Entropy analysis allows identify the intrinsic physical limitations of our mixture. Just as Chambadal and Curzon-Alborn [38] demonstrated that Carnot's efficiency was inaccessible due to the need to have a temperature gradient to carry out heat transfer, we seek here to express the effective cooling obtained from the mixture of air and water. Entropy analysis is one way to achieve this. We apply it here to operating mixing conditions, given a quantity of humid air at a known temperature and humidity (T, M_g, HR) and a quantity of liquid water (M_l, T_w = T). In a stationary or permanent dynamic regime, (M_g) and (M_l) will be quantities per unit of time, while they will be the extensive quantities in the Eulerian approach. Such a mixture of humid air and water is a classic thermodynamic system. Many authors have shown that the evolution of these mixtures involves a path of transformations, which combines thermal, mechanical and chemical modifications [32,39]. Most of the time, particularly in exergy approaches [36], the final state is assumed to correspond to the adiabatic saturation state of the air. Adiabatic saturation is related to the reference state, assuming infinite air volumes. In a finite volume, the final equilibrium state differs from adiabatic saturation. To describe the effective cooling, a succession of transformations makes it possible to express the mechanical, thermal and chemical contributions. These are detailed in the following paragraph. Physical processes are broken down to simply express transformation terms.

2.2. Path of transformations

2.2.1. Evaporation stage

A quantity of water (x) is transformed into vapour and this physicochemical transformation modifies enthalpy, entropy and chemical potential by modification of the reference values. For enthalpy, the reference values are preferred to its definition with internal and PV energies (where PV energy arises from the pressure (P) and volume (V) of fluid): enthalpy is more likely used in this form in evaporative cooling. Thus, we have:

$$dH = (H_g^0 - H_l^0)dx = H_{vap}dx, \tag{1}$$

$$dS = (S_g^0 - S_l^0)dx = S_{vap}dx, \tag{2}$$

$$d\mu = (H_{vap} - TS_{vap})dx. \tag{3}$$

2.2.2. Vapour diffusion stage

Water in the vapour state occupies a volume V_x greater than the volume occupied in the liquid state. This volume of gas diffuses into the total volume of air V_g and generates entropy. This contribution is obtained by writing the variation in volume entropy, between the initial state V_i and the final volume V_f, for each component j of the gas mixture containing n_g moles of air, and by deriving with respect to the evaporated quantity dx:

$$S_v = R\sum_j n_j \ln\frac{V_{jf}}{V_{ji}} = R\left(n_g \ln\frac{V_{gf}}{V_{gi}} + x\ln\frac{V_{xf}}{V_{xi}} + n_l \ln\frac{V_{lf}}{V_{li}}\right).$$

Neglecting the volume variation for the liquid content and assuming that water evaporates at a constant atmospheric pressure, one obtains

$$S_v = R\left(n_g \ln\frac{n_g + x}{n_g} + x\ln\frac{n_g + x}{x}\right) \Rightarrow dS_v = -R\ln\frac{x}{n_g + x}dx. \tag{4}$$

This term corresponds to the diffusion of vapour in the gas volume. At constant pressure and temperature, it represents the non-ideality resulting from the gas volume and molar increase associated with the phase change. Due to its form, this term is assumed to balance the fugacity required for a non-ideal reaction. The homogenization of the partial pressures of water vapour and liquid water is also accounted for by expressing the diffusion entropy according to the mixing law, known as Amagat's diffusion. The Amagat's diffusion is also balanced with partial pressure terms in the chemical potential.

2.2.3. Compression stage

Our diffusion model does not keep the volume. Hence, a compression step is added to keep an isochoric evolution. The gas volume (V_g + V_x) is compressed to retrieve the initial volume V_g through an isentropic compression following:

$$PV^{\gamma} = \text{const.} \tag{5}$$

Temperature, pressure and volume are modified and affect all three paths. Although the mix composition does not vary during this step, all changes are related to the evaporated quantity, which determines the initial volume of this step. For an ideal gas, we get

$$PdV = -\gamma RT_m \left(\frac{n_g+x}{n_g}\right)^{\gamma} dx, \tag{6}$$

from which the pressure drop and thermal changes are established, where T_m is the initial mixing temperature, used here to alleviate notations.

2.2.4. Cooling stage

The energy required to convert *dx* moles of water from liquid to vapour produces a significant decrease in thermal energy, which results in a decrease in the temperature of a mixture and a pressure drop. The pressure change modifies the chemical potential:

$$dH = n_t C_{p,m} dT, \tag{7}$$

$$VdP = n_g R dT, \tag{8}$$

$$(\mu_g - \mu_l)dx = RT \ln \frac{P_f}{P_i} dx. \tag{9}$$

2.3. Gibbs-Duhem equation

The Gibbs-Duhem equation brings together the different contributions of the thermal (*dH*), mechanical (*VdP*) and chemical ((μ_g - μ_l)*dx*) pathways, revolving around the evolution of entropy, written in the form

$$dH = VdP + \left(\mu_g - \mu_l\right)dx + TdS. \tag{10}$$

This equation makes it possible to track the energy redistributions, which take place as the transformations progress. The order of the transformations does not matter. All the terms detailed before are reported in Table 1 and brought together in Eq. (10) by equating all terms of the first column to all those of the second, third and fourth columns.

Any modification of the thermal state (*dH*) has repercussions on the entropy. Similarly, the chemical and mechanical states also contribute to the entropy term *TdS*. In all the transformations, the Gibbs-Duhem energy terms are balanced. The exhaustive writing of the terms makes it possible to analyse the energy redistributions from one path to another, as shown in Fig. 1.

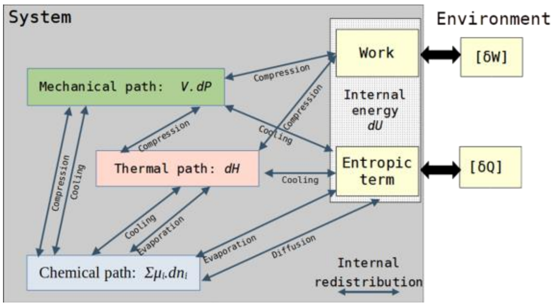

Fig. 1. Energy variation of control volume in its evolution towards a state of equilibrium: storage in internal energy, energy redistributions and exchange with the environment.

Table 1. Decomposition of energy terms in Gibbs-Duhem equation corresponding to *dx* moles of liquid water, which evaporates at a constant volume (see text for the stage description).

	Thermal path	Mechanical path	Chemical path	δQ	−δW
Operation	$dH =$	$VdP +$	$(\mu_g - \mu_l)dx$	$+ TdS$	
Evaporation	$H_{vap}dx$		$(H_{vap} - TS_{vap})dx$	$TS_{vap}dx$	
Mixing **S_v**	0	0	$RT \ln\left(\frac{x}{n_g + x}\right)dx$	$-RT \ln\left(\frac{x}{n_g + x}\right)dx$	$RT_m dx$
S_d			$RT \ln\left(\frac{n_v + x}{n_l - x}\right)dx$	$-RT \ln\left(\frac{n_v + x}{n_l - x}\right)dx$	
Compression	$\gamma RT_m \left(\frac{x}{n_g + x}\right)^{\gamma} dx$	$\gamma RT_m \left(\frac{x}{n_g + x}\right)^{\gamma} dx$	$RT \ln\left(\frac{n_g + x}{n_g}\right)^{\gamma} dx$	$-RT \ln\left(\frac{n_g + x}{n_g}\right)^{\gamma} dx$	$-RT_m \left(\frac{x}{n_g + x}\right)^{\gamma} dx$
Cooling	$n_t C_{p,m} dT$	$n_g R dT$	$RT \ln\left[\frac{T}{T_m}\left(\frac{n_g + x}{n_g}\right)^{1-\gamma}\right]dx$	$(n_t C_{p,m} - n_g \mathrm{R})dT$ $-RT \ln\left[\frac{T}{T_m}\left(\frac{n_g + x}{n_g}\right)^{1-\gamma}\right]dx$	

Likewise, the term TdS_d corresponds to the balancing of partial pressures. It was identified by Amagat as a diffusion entropy, which reflects the irreversibility of mixing. In our proposal, we brought out dS_v, the variation in entropy associated with the change in volume: this term balances with the fugacity in the chemical potential. The pressure drop recovers mechanical dissipation, marking the irreversibility of cooling. The whole entropic term TdS therefore contains dissipations, related to diffusion and mechanical degradations. It is not in exact correspondence with the thermal term dH, in the sense of [35]: the first describes the thermal energy transfer with the environment, while the second characterizes conversion processes that modify the thermal state of the system.

The entropic term governs heat exchange with the environment. In this, it is difficult to assess the reversible or irreversible nature of the subterms. Many terms are associated with the reduction of chemical potential and pressure. Others correspond to the thermal change in enthalpy and the change in the entropy of formation.

3. Results and discussion

3.1. Chemical potential of moist air with liquid water

Evaporation is driven by the chemical potential. The chemical potential, in exergy approaches concerning moist air, is expressed with the change of state term ($H_{vap} - TS_{vap}$) and the partial pressure equilibrium (S_d). For pure water, the potential is positive at ambient temperature and becomes negative at 100°C. Spontaneous evaporation is not possible. Mixed with ambient air, the chemical potential is set to zero at adiabatic saturation conditions for the air; it is the reference state − or dead − state used in exergy approaches [28]. In the present work, the entropy of volume change was used to express the fugacity without using a reference state.

Thus, the chemical potential is completely defined and evolves during evaporation: very negative at start, it increases with the quantity of water evaporated, as can be observed in Fig. 2. The spontaneous evaporation ends when the chemical potential becomes positive. At zero, an equilibrium is found and the evaporation is stopped. This occurs before saturation, because the contribution of fugacity (S_v) is larger than the constant related to saturation conditions.

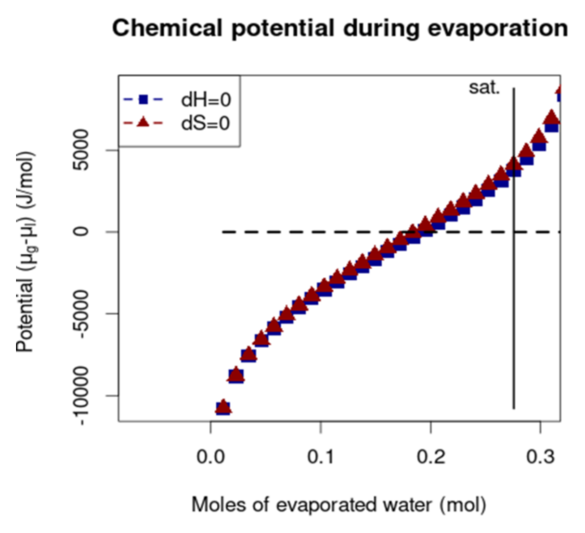

Fig. 2. Evolution during evaporation of the chemical potential, for an isenthalpic or isentropic transformation.

The vapour diffusion term (S_v, entropy of volume change, in red in Fig. 3) compensates for the positive terms. It is enough for a water molecule to break away from the liquid phase and pass into the much larger volume of gas; the number of possible positions (probable state) of this molecule is very large. This is the meaning of the entropy of volume change in a probabilistic approach (statistical mechanics). This entropy, very important at the start of the reaction, reduces as the number of vapour molecules increases. Hence, the diffusion of vapour initiates and controls the evaporation. As the liquid was neglected, this model applies only to a disperse spray mixture but gives, at $\Delta\mu = 0$, an estimate for the cooling efficiency of a mixture for the given operating conditions inside a finite volume.

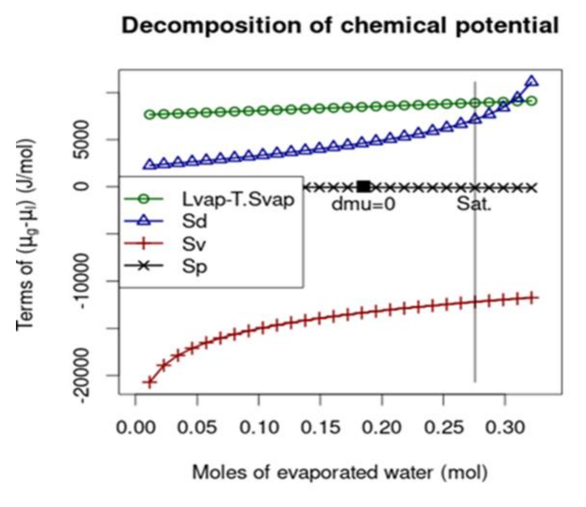

Fig. 3. Process contributions to the chemical potential.

3.2. Towards the equilibrium state

The evaporation of liquid water in air is a spontaneous reaction requiring a negative chemical potential. Also, setting the chemical potential to zero (the third column of Table 1 equals zero) is the condition for ending spontaneous evaporation and defining the chemical equilibrium. The cancellation of the chemical potential does not involve dx, nor dT, and is written as

$$0 = H_{vap} - TS_{vap} + RT\ln\left(\frac{n_v+x}{n_l-x}\frac{x}{n_g}\frac{T}{T_m}\right). \qquad (11)$$

Furthermore, cooling by evaporation of water in air is generally called adiabatic, which provides a second boundary condition. Classically, the overall process is assumed to be isenthalpic with $dH = 0$. The temperature gradient is then written as a function of the quantity of water evaporated, by making a series expansion of the exponent term (γ), which gives for the isenthalpic case:

$$dT = -dx\left(\frac{H_{vap}+\gamma RT_m}{n_t C_{p,m}} + x\,\frac{\gamma^2 RT_m}{n_g n_t C_{p,m}}\right). \tag{12}$$

Integrating gives:

$$T = T_m - \beta_1 x - \beta_2 \frac{x^2}{2} \tag{13}$$

with $\beta_1 = \frac{H_{vap}+\gamma RT_m}{n_t C_{p,m}}$ and $\beta_2 = \frac{\gamma^2 RT_m}{n_g n_t C_{p,m}}$.

The adiabatic system is without heat exchange with the outside, meaning that the entropic term is cancelled, $TdS = 0$. There, entropy reaches an extremum. As the production of entropy in the system can only be positive or zero, the isentropic equilibrium position corresponds to a minimum of entropy. By making the chemical equilibrium match with the minimum entropy, Eq. (11) is introduced into the entropic term to express the temperature gradient as a function of the quantity of evaporated water:

$$dT = -dx\left(\frac{H_{vap}}{n_t C_{p,m} - Rn_g}\right). \tag{14}$$

After integration, it yields:

$$T = T_m - \beta_1 x \quad \text{with} \quad \beta_1 = \frac{H_{vap}}{n_t C_{p,m} - Rn_g}. \tag{15}$$

Introducing this latest expression of $T(x)$ into the isentropic equation $dS = 0$ gives the expression for the chemical equilibrium at the minimum entropy:

$$\begin{aligned} 0 = H_{vap} - \ (T_m - \beta_1 x)S_{vap} + \\ + R\,(T_m - \beta_1 x)\ln\left(\frac{n_v+x}{n_l-x}\,\frac{x}{n_g}\,\frac{T_m-\beta_1 x}{T_m}\right). \end{aligned} \tag{16}$$

3.3. Comparing isenthalpic and isentropic solutions

The root of Eq. (16), namely, the isentropic solution, is assessed using an equation solver between 0 and n_l, the molar quantity of injected liquid water. The same procedure is applied to the isenthalpic case, combining Eqs. (11) and (13) (results are written later, in Eq. (18)).

Differences between the isenthalpic and isentropic approaches are illustrated for the following given operating conditions:

$M_g = 1145$ g, $T_g = T_l = 33$°C, $M_l = 6$ g, HR = 40%.

Solutions are given in Table 2 for both cases. Chemical equilibrium is reached before evaporating all the injected liquid water in both cases.

Table 2. Temperature and evaporated liquid mass at chemical equilibrium of mixture for two cases.

Case	Equilibrium temperature (°C)	Evaporated mass (g)
Isenthalpic	25.3	3.5
Isentropic	23.6	3.3

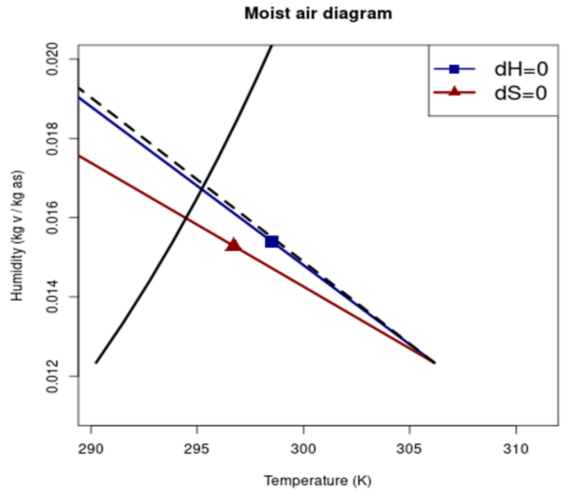

Fig. 4. Temperatures and quantities of liquid evaporated at equilibrium, assuming isenthalpic or isentropic transformation. Marks represent the equilibrium positions, the black curve is the saturation curve and the dotted black one is the air isenthalp curve.

The isentropic line, corresponding to Eq. (14), is represented in red in Fig. 4 and the blue line corresponds to the isenthalpic– Eq. (12). These curves represent the isentropic and isenthalpic evolution of temperatures with the evaporation. The equilibrium points are represented with the marks. In both cases, the final equilibrium state has a temperature above and a humidity below the adiabatic saturation point. Isentropic cooling, i.e. without heat exchange with the environment, provides access to a lower equilibrium temperature and ensures better cooling by evaporating less water. In the isenthalpic case, the surrounding environment transfers heat to the mixture: equilibrium temperatures are higher and water consumption is slightly higher than in the isentropic case. To increase cooling, the quantity of liquid water injected can be increased, as shown in [40].

3.4. Exchange with the environment

In the isentropic case, there is no heat exchange with the surrounding environment. It is the ideal case, where cooling is maximum. The real case, closer to the isenthalpic model, is not adiabatic, because $dS_{eq} > 0$ ($dS_{eq} = 32$ J/K, in the previous conditions). Heat ($\delta Q = TdS$) is transferred from the hot surrounding environment to the cooled system: the entropy of the system increases despite the drop in temperature. Inserting the isentropic equation (Eq. (14)) into the TdS term gives the following equation, where redistributions are identified:

$$\delta Q = TdS = dx \begin{bmatrix} (T_m - \beta_1 x)S_{vap} \\ + R(T_m - \beta_1 x)\ln\left(\frac{T_m-\beta_1 x}{T_m}\,\frac{x}{n_g}\,\frac{n_v+x}{n_l-x}\right) \\ + Rn_g\beta_1 \\ - n_t C_{p,m}\beta_1 \end{bmatrix} \quad \left| \begin{array}{c} TdS\ [\text{formation}] \\ TdS[\mu] \\ TdS\ [P] \\ TdS\ [H] \end{array} \right. \tag{17}$$

Entropic terms resulting from energy redistributions, via chemical, mechanical and thermal pathways, are identified according to the following methods: the thermal path is balanced with terms in the first column, the mechanical path with terms in the second column and the chemical path with terms in the third column. This latest includes only the diffusion process and the phase change was separated. Entropic contributions are quantified at equilibrium for the previous test conditions and compared for the isentropic and isenthalpic cases in Table 3.

Table 3. Heat exchange *TdS* according to chemical, thermal and mechanical paths (Eq. (17)).

***TdS* at equilibrium**	**Isenthalpic**	**Isentropic**
Formation: *TS_{vap}*	35160	34940
Chemical: *TdS* [μ]	8510	8710
Mechanical: *TdS* [*dP*]	13230	16940
Thermal: *TdS* [*dH*] = apparent heat	–47260	–60550
Total transfer	9646	~ 0

As δQ and dS have the same sign, the entropy production pathways are identified. Thus, the phase change corresponds to a net creation of entropy (*TdS* [formation]). The reduction of the chemical potential by diffusion corresponds to an increase in the entropy of the system (*TdS* [μ]). The loss of pressure is also a source of increase in entropy (*TdS* [*dP*]). Thermal cooling decreases the total entropy. Cooling is the only operation that absorbs entropy (*TdS* [*dH*]), while changing state is the operation that produces the most (see Fig. 5).

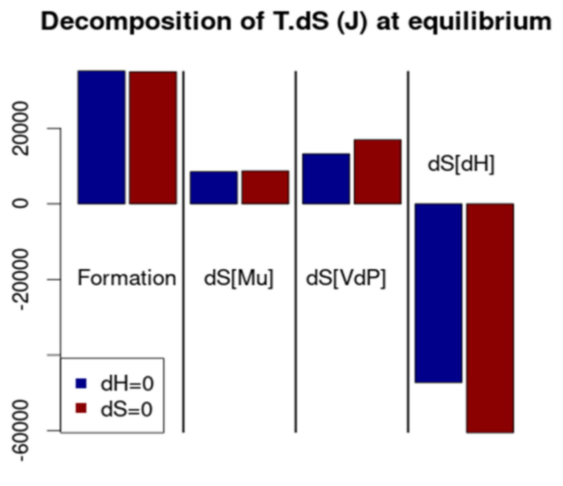

Fig. 5. Heat exchange with the environment for the isenthalpic and isentropic cases.

Apparent heat corresponds to the transfer of latent energy into sensible energy (*TdS* [*dH*]). The term ‘apparent heat’ is the usual term, although it is here a question of cooling. This energy transfer is internal to the system, but perceptible by measuring its temperature. In the isenthalpic case, this term is more or less equal to the latent energy transfer, i.e. the energy required for modifying the enthalpy of formation due to phase change.

In the isentropic case, there is no exchange with the environment. The case is however irreversible, because irreversible diffusion processes are taken into account in the Gibbs-Duhem equation. This case is truly adiabatic (without any exchange with the environment), even if irreversible. Compared to the isenthalpic case, the energy dissipated in the pressure loss and diffusion is increased. So, the irreversibilities rise in the isentropic case. But the apparent heat increases more, as shown in Fig. 5: at equilibrium, the system is colder because the latent energy transfer is increased. This internal transfer is sufficient to compensate for the energy dissipation. The absence of heat input from the outside prevents any heating of the system.

In the isenthalpic case, heat from the outside (remaining term: 9646 J) corresponds to uncompensated heat; it is not linked to the system temperature and represents 20% of the apparent heat. It is not perceptible by a temperature measurement, but contributes to the reactive blocking. It includes some *PV* energy changes related to pressure drop by cooling and irreversible diffusion as well.

Irreversibilities and cold production both increase in the isentropic case compared to the isenthalpic case. Comparisons to measurements show that real cases are close to the isenthalpic and are not truly adiabatic.

3.5. Efficiency of spray cooling

The isenthalpic equilibrium, described by Eq. (11) with the temperature coming from the isenthalpic Eq. (13), is given by

$$0 = H_{vap} - \left(T_m - \beta_1 x - \beta_2 \frac{x^2}{2}\right) S_{vap} + \\ + R\left(T_m - \beta_1 x - \beta_2 \frac{x^2}{2}\right) \ln\left(\frac{n_v + x}{n_l - x} \frac{kx}{n_g} \frac{T_m - \beta_1 x - \beta_2 \frac{x^2}{2}}{T_m}\right). \quad (18)$$

It is solved for various operating conditions using real data for cooling air with a spray. Measurements were obtained by Surheshkumar et al. [4] for the first series, and by Tissot et al. [5] for the second series. In both papers, operating conditions (T_l, T_g, M_l, M_g, RH) at the wind tunnel inlet are fully given (or retrieved from air volume rate and wet bulb temperature). The atmospheric pressure was not given and we take the standard value in calculations (101 325 Pa).

The standard spray cooling efficiency is given by the ratio between the air temperature decrease between the inlet and the outlet, versus the maximal decrease, given by the difference between wet and dry bulb temperature:

$$\eta = \frac{T_{real} - T_{g,inlet}}{T_{wb,g,inlet} - T_{g,inlet}}. \quad (19)$$

An average temperature at the outlet was computed from operational conditions and Eq. (18). Modelled temperatures are compared with measurements made at the wind tunnel exit in Fig. 6 for the first series and in Fig. 7 for the second one. A perfect efficiency would have been achieved if blue temperatures were aligned with the red ones. In all these experiments, saturation was not reached.

A good agreement was found between the real efficiency of spray and the temperature derived from modelling chemical and thermal equilibrium (Figs. 6 and 7). The evaporation rate is also

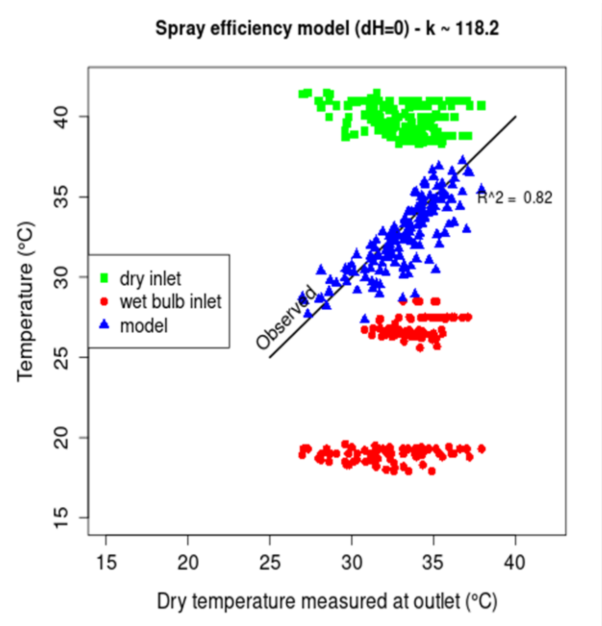

Fig. 6. Temperatures measured by Sureshkumar et al. [4]: dry bulb (green) and wet bulb (red) at the wind tunnel inlet, modelled (blue) and observed (black line) at the wind tunnel outlet. The green-red interval corresponds to the ideal cooling.

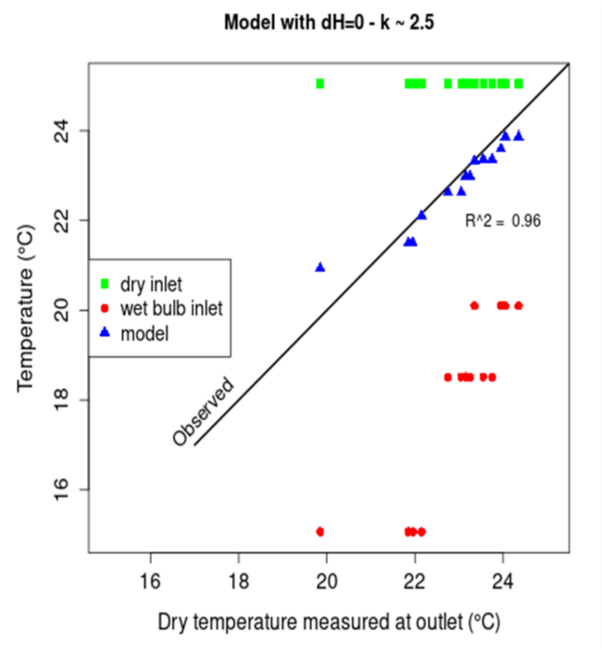

Fig. 7. Temperatures measured by Tissot et al. [5]: dry bulb (green) and wet bulb (red) at the wind tunnel inlet, modelled (blue) and observed (black line) at the wind tunnel outlet.

close to measurements and the temperatures at the outlet were close to an equilibrium. However, the isenthalpic model needs scaling for obtaining such results; the fugacity term was scaled with a scaling factor *k*.

$$dS_v = -RT \ln \frac{kx}{n_g + x}. \tag{20}$$

The scaling was needed because the liquid content was neglected in writing the entropy of volume change. The volume of vapour starts from small volumes around droplets and should therefore depend on the droplet concentrations. This is the meaning of the scaling factor, which is related to the volume concentration of droplets:

$$k = \frac{n_g + x}{n_t}\left(\frac{n_l - x}{n_l}\frac{\rho_l}{\rho_g}\right)^{\alpha}. \tag{21}$$

Differences between the experiments depend precisely on the droplet concentrations and sizes. The reported sizes are about 10−30 µm in Tissot et al. [5] and bigger in Sureshkumar et al. [4], of about 100 µm to 300 µm. The surface of the liquid was, however, equivalent in the experiment, because Sureshkumar et al. compensated for the small specific surface of droplets by injecting more water. Evaporation of large droplets is more likely related to a droplet size reduction. Due to the high capillary pressure inside the liquid, evaporation reduces droplet numbers rather than the diameters for small droplets [41]. The volume of liquid is expressed by

$$V_l = \frac{(n_l - x)\,\widehat{M_l}}{\rho_l} = \frac{N_d \pi d_d^3}{6}. \tag{22}$$

Reducing the size of droplets (d_d) does not have the same effect on the volume concentration as reducing the number of droplets (N_d). The volumetric concentration depends on whether N_d or d_d varies with x, according to Eq. (22). This changes the exponent α in the scaling factor (Eq. (21)), which is 6/8 for the evolution of d_d [4] and 1/8 for the evolution of N_d [5]. The average value for k (all data of each series) is given in the figures' titles and is related to the hypothesis made on how the volume fraction of droplets decreases with evaporation.

As shown in Fig. 8, heat exchange at the boundaries accounts for more than 20% of the cooling power in the study of Tissot et al. [5], and for approximately 10% in the case of Sureskumar et al. [4]. The relationship between boundary heat and the system follows a linear trend with the temperature gradient for Tissot's measurements, but more discrepancies are observed in Sureskumar's measurements. This can be attributed to the higher water content; the temperature gradients are scattered by the water temperature during mixing. The liquid content also influences the calorific capacities of mixtures. The heat exchange corresponds to the uncompensated heat involved in irreversible processes, such as water vapour diffusion or pressure drop. The more evaporation and efficient cooling, the greater the irreversibility of the processes. Even when cooling is balanced by water evaporation, other energy redistributions are involved in evaporative cooling. These energies prevent the system from reaching the saturated state and govern the effective cooling efficiency.

The model accounts for some of the observed phenomena reported by the authors. The measurements made by Tissot et al. were made at 5 cm and 20 cm downwards the injection point. Measurements were very close in both sections for most of the cases. As the chemical equilibrium was reached, the maximum permissible cooling was achieved under the operational conditions. Hence, the chemical potential explains why evaporation was rather null between sections. Results also indicate that the

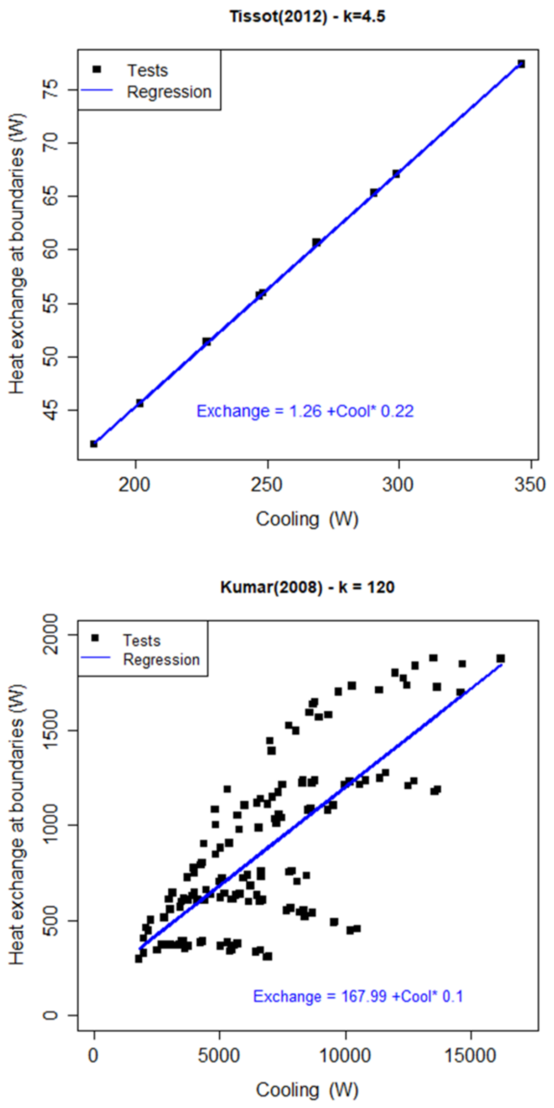

Fig. 8. Heat exchange at the boundaries according to the cooling power related to equilibrium in Tissot et al. [5] experiments (top) and in Sureshkumar et al. [4] experiments (bottom).

equilibrium is rapidly achieved. In half of the data of [4], the injection of water was in the counter-current direction of the air flow. Such an orientation fails to improve cooling efficiency notably, which is mainly limited by the chemical blockage. It may help, however, to get more homogeneous temperatures at the outlet, but was not seen as an explanation factor for improving our estimate.

4. Conclusions and perspectives

By using the Gibbs-Duhem equation to describe the evaporation of liquid water in air, it is possible to study the irreversible processes in the evolution of such a mixture. Four stages are used to distinguish processes and quantify the governing energy pathways of the system, involving mechanical, chemical and thermal energy changes. The Gibbs-Duhem equation allows to study energy redistributions and identify the limiting phenomena when multiple pathways are involved.

With spray cooling, the physicochemical evaporation reaction governs the evolution of the mixture and rules the cooling efficiency. The chemical potential is depleted before the air reaches the adiabatic saturation, due to irreversibilities associated with the diffusion of water vapour in gas: the variation of the volume entropy allows expressing a chemical fugacity and thereby sizes the ending state of the mixture. The chemical potential limits the quantity of spontaneously evaporable water, although vapour diffusion is a process that requires little energy. Other entropic contributions, such as the change of state of water molecules or loss of pressure through cooling, are more important sources of entropy production. Apparent heat (here, apparent cooling) absorbs this production.

In an isentropic transformation, the cooling is maximum and fully compensates for the entropic production, half of which is linked to irreversibilities in the chemical (diffusion, formation) and mechanical (pressure drop) pathways. The transformation takes place without any heat exchange with the outside. In an isenthalpic transformation, the quantity of water evaporated is quite similar, but the cooling is less. Heat is received from the hot surrounding environment and provides an increase of entropy of this system. For such a transformation, the chemical potential also limits the cooling, but the heat received from the environment reduces it. The isenthalpic transformation is not adiabatic, due to the need for this uncompensated heat, which is necessary for the system evolution. An isentropic cooling is more efficient than the isenthalpic cooling and it corresponds to a minimum of entropy. However, entropy production is higher for the isentropic cooling and is compensated by a higher destruction. Both cases do not reach the adiabatic saturation when considering a finite volume.

The isenthalpic equilibrium was applied to real measurements. A scaling was made to account for the volume concentration of droplets in the fugacity model. When scaled, results were found in good agreement with the literature data regarding the spray cooling efficiency. The equilibrium equation gives estimates of efficiencies over a wide range of operating conditions and could help in improving management of spray cooling. The entropic analysis also provides insights about some reported observations and gives an estimate of heat transferred from the surrounding into the system. Surface tension phenomena have to be further described to provide more details about the scaling factor used to correct fugacity. Further experiments, including pressure measurements, are required to assess the ability of the approach to handle with combined pathways, to assess the mechanical energy depletion in such systems.

References

[1] Meng, X., Meng, L., Gao, Y., & Li, H. (2022). A comprehensive review on the spray cooling system employed to improve the summer thermal environment: Application efficiency, impact factors, and performance improvement. *Building and Environment*, 217, 109065. doi: 10.1016/j.buildenv.2022.109065

[2] Kachhwaha, S.S., Dhar, P.L., & Kale, S.R. (1998). Experimental studies and numerical simulation of evaporative cooling of air with a water spray — I. Horizontal parallel flow. *International Journal of Heat and Mass Transfer*, 41(2), 447–464. doi: 10.1016/S0017-9310(97)00133-6

[3] Hamlin, S., Hunt, R., & Tassou, S.A. (1998). Enhancing the performance of evaporative spray cooling in air cycle refrigeration and air conditioning technology. *Applied Thermal Engineering*, 18(11), 1139–1148. doi: 10.1016/S1359-4311(98)00028-3

[4] Sureshkumar, R., Kale, S.R., & Dhar, P.L. (2008). Heat and mass transfer processes between a water spray and ambient air – I. Experimental data. *Applied Thermal Engineering*, 28(5-6), 349–360, doi: 10.1016/j.applthermaleng.2007.09.010

[5] Tissot, J., Boulet, P., Labergue, A., Castanet, G., Trinquet, F., & Fournaison, L. (2012). Experimental study on air cooling by spray in the upstream flow of a heat exchanger. *International Journal of Thermal Sciences*, 60, 23–21, doi: 10.1016/j.ijthermalsci.2012. 06.005

[6] Zheng, K., Ichinose, M., & Wong, N.H. (2018). Parametric study on the cooling effects from dry mists in a controlled environment. *Building and Environment*, 141, 61–70. doi: 10.1016/j.buildenv. 2018.05.053

[7] Sun, Y., Alkhedhair, A.M., Guan, Z., & Hooman, K. (2018). Numerical and experimental study on the spray characteristics of full-cone pressure swirl atomizers. *Energy*, 160, 678-692. doi: 10.1016/ j.energy.2018.07.060

[8] Caliskan, H., Hepbasli, A., Dincer, I., & Maisotsenko, V. (2011). Thermodynamic performance assessment of a novel air cooling cycle: Maisotsenko cycle. *International Journal of Refrigeration*, 34(4), 980−990. doi: 10.1016/j.ijrefrig.2011.02.001

[9] Zhan, C., Duan, Z., Zhao, X., Smith, S., Jin, H., & Riffat, S. (2011). Comparative study of the performance of the M-cycle counter-flow and cross-flow heat exchangers for indirect evaporative cooling – Paving the path toward sustainable cooling of buildings. *Energy*, 36(12), 6790−6805. doi: 10.1016/j.energy. 2011.10.019

[10] Jia, C., Sun, D., Hu, X., & Jing, C. (2023). Optimization of the performance of M-Cycle indirect evaporative cooling via thermodynamic approach. *Journal of Asian Architecture and Building Engineering*, 22(6), 3612−3626. doi: 10.1080/13467581.2023. 2183774

[11] Yang, H., Shi, W., Chen, Y., & Min, Y. (2021). Research development of indirect evaporative cooling technology: An updated review. *Renewable and Sustainable Energy Reviews*, 145, 111082. doi: 10.1016/j.rser.2021.111082

[12] Wang, T., Sheng, C., & Agwu Nnanna, A.G. (2014). Experimental investigation of air conditioning system using evaporative cooling condenser. *Energy and Buildings*, 81, 435−443. doi: 10.1016/ j.enbuild.2014.06.047

[13] Wen, M.-Y., Ho, C.-Y., Jang, K.-J., & Yeh, C.-H. (2014). Experimental study on the evaporative cooling of an air-cooled condenser with humidifying air. *Heat and Mass Transfer*, 50, 225–233. doi: 10.1007/s00231-013-1243-7

[14] Heidarinejad, G. As'adi Moghaddam, M.R., & Pasdarshahri, H. (2019). Enhancing COP of an air-cooled chiller with integrating a water mist system to its condenser: Investigating the effect of spray nozzle orientation. *International Journal of Thermal Sciences*, 137, 508−525. doi: 10.1016/j.ijthermalsci.2018.12.013

[15] Yang, H., Rong, L., Liu, X., Liu, L., Fan, M., & Pei, N. (2020). Experimental research on spray evaporative cooling system applied to air-cooled chiller condenser. *Energy Reports*, 6, 906−913. doi: 10.1016/j.egyr.2020.04.001

[16] Smrekar, J., Oman, J., & Širok, B. (2006). Improving the efficiency of natural draft cooling towers. *Energy Conversion and Management*, 47(9-10), 1086−1100. doi: 10.1016/j.enconman. 2005.07.012

[17] Muangnoi, T., Asvapoositkul, W., & Wongwises, S. (2008). Effects of inlet relative humidity and inlet temperature on the performance of counterflow wet cooling tower based on exergy analysis. *Energy Conversion and Management*, 49(10), 2795− 2800. doi: 10.1016/ j.enconman.2008.03.019

[18] Alkhedhair, A., Guan, Z., Jahn, I., Gurgenci, H., & He, S. (2015). Water spray for pre-cooling of inlet air for Natural Draft Dry Cooling Towers – Experimental study. *International Journal of Thermal Sciences*, 90, 70−78. doi: 10.1016/j.ijthermalsci. 2014. 11.029

[19] Kim, M.-H., & Jeong, J.-W. (2013). Cooling performance of a 100% outdoor air system integrated with indirect and direct evaporative coolers. *Energy*, 245−257. doi: 10.1016/j.energy. 2013.02.008

[20] Zunaid, M., Murtaza, Q., & Gautam, S. (2017). Energy and performance analysis of multi droplets shower cooling tower at different inlet water temperature for air cooling application. *Applied Thermal Engineering*, 121, 1070−1079. doi: 10.1016/j.applthermaleng.2017.04.157

[21] Tejero-González, A., & Franco-Salas, A. (2021). Optimal operation of evaporative cooling pads: A review. *Renewable and Sustainable Energy Reviews*, 151. 111632. doi: 10.1016/j.rser.2021. 111632

[22] Lee, Y.-C., Chen, K.-Y., Yan, W.-M., Shih,Y.-C., & Chao, C.-Y. (2023). Evaporative cooling method to improve energy management of overhead downward flow-type data center. *Case Studies in Thermal Engineering*, 45, 102998. doi: 10.1016/j.csite.2023. 102998

[23] Mi, R., Bai, X., Xu, X., & Ren, F. (2023). Energy performance evaluation in a data center with water-side free cooling. *Energy and Buildings*, 295, 113278. doi:10.1016/j.enbuild.2023.113278

[24] Elahi, S.H., & Farhani, S.D. (2021). Increasing evaporative cooler efficiency by controlling water pump run and off times. *International Communications in Heat and Mass Transfer*, 127, 05525. doi: 10.1016/j.icheatmasstransfer.2021.105525

[25] Feidt, M. (2013). *Thermodynamique optimale en dimensions physiques finies*. In Collection Thermique, par Denis Lavoisier. Lavoisier − Hermes Science Publications.

[26] Dumouchel, C. (2009). The Maximum Entropy Formalism and the Prediction of Liquid Spray Drop-Size Distribution. *Entropy*, 11(4), 713−747. doi: 10.3390/e11040713

[27] Le Moyne, L., Freire, V. & Queiros Conde, D. (2008). Fractal dimension and scale entropy applications in a spray. *Chaos, Solitons & Fractals*, 38(3), 696−704, doi: 10.1016/j.chaos.2007. 01.004

[28] Bejan, A. (2016). *Advanced Engineering Thermodynamics.* John Wiley & Sons, Inc.

[29] Pauluis, O. M. (2004). Chapter 7: Water vapor and entropy production in the earth's atmosphere. In , *Non-equilibrium thermodynamics and the production of entropy: Life, Earth and Beyond* (A. Kelidon, R. D. Lorenz, Eds.). Springer-Verlag.

[30] Duane, G.S. & Curry, J.A. (1997). Entropy of a convecting water-air system and the interpretation of cloud morphogenesis. *Quarterly Journal of the Royal Meteorological Society*, 123 (539), 605−629. doi: 10.1002/qj.49712353905

[31] Barton, N.G. (2008). An evaporation heat engine and condensation heat pump. *Anziam Journal*, 49(4), 503−524. doi: 10.1017/ S1446181108000035

[32] Chengqin, R., Nianping, L. & Guangfa, T. (2002). Principles of exergy analysis in HVAC and evaluation of evaporative cooling schemes. *Building and Environment*, 37(11), 1045−1055. doi: 10.1016/S0360-1323(01)00104-4

[33] Ratlamwala, T.A.H. & Dincer, I. (2013). Efficiency assessment of key psychometric processes. *International Journal of Refrigeration*, 36(3), 1142−1153, doi: 10.1016/j.ijrefrig.2012.10.038

[34] Santos, J.C., Barros, G.D.T., Gurgel, J.M. & Marcondes, F. (2013). Energy and exergy analysis applied to the evaporative cooling process in air washers. *International Journal of Refrigeration*, 36(3), 1154−1161. doi: 10.1016/j.ijrefrig.2012.12.012

[35] Wang, L., Zhan, L.C., Zhang, J. & Zhao, X. (2019). Optimization of the counter-flow heat and mass exchanger for M-cycle indirect evaporative cooling assisted with entropy analysis. *Energy*, 171, 1205−1216. doi:10.1016/j.energy.2019.01.099.

[36] Manjunath, K. & Kaushik, S.C. (2014). Second law thermodynamic study of heat exchangers: A review. *Renewable and Sustainable Energy Reviews*, 40, 348−375. doi: 10.1016/j.rser.2014.07.186

[37] Niven, R.K. & Noack, B.R. (2013). Control volume analysis, entropy balance and the entropy production in flow systems. In *Beyond the Second Law: Entropy Production and Non-Equilibrium Systems* (R.C. Dewar, C. Lineweaver, R.K. Niven., K. Regenauer-Lieb, Eds.) (pp. 129−162). Springer-Verlag.

[38] Feidt, M. (2016). *Thermodynamique et optimisation énergétique des systèmes et procédés*. Hors collection, Lavoisier.

[39] Farmahini-Farahani, M., Delfani, S. & Esmaeelian, J. (2012). Exergy analysis of evaporative cooling to select the optimum system in diverse climates. *Energy*, 40(1), 250−257, doi: 10.1016/j.energy.2012.01.075

[40] Lacour, S.O.L., Diango, K.A. & Feidt, M. (2022). Entropy analysis in spray cooling for dosing water injection. *Entropie: thermodynamique – énergie – environnement – économie*, 3(1) (in French). doi: 10.21494/ISTE.OP.2022.0829

[41] Lefebvre, A. (1988). *Atomization and Sprays* (1st ed.). CRC Press. doi: 10.1201/9781482227857